AERODYNAMIC AND ELECTROMECHANICAL DESIGN, MODELING AND IMPLEMENTATION OF PIEZOCOMPOSITE AIRFOILS

by

Onur Bilgen

Dissertation submitted to the faculty of the Virginia Polytechnic Institute and State University in partial fulfillment of the requirements for the degree of

Doctor of Philosophy
in
Mechanical Engineering

Daniel J. Inman, Chair
Kevin B. Kochersberger, Co-Chair
Nakhiah C. Goulbourne
Michael W. Hyer
Donald J. Leo

August 02, 2010
Blacksburg, Virginia, USA

Key Words: Variable-Camber Airfoil, Piezoceramic, Macro-Fiber Composite, Unimorph, Bimorph

AERODYNAMIC AND ELECTROMECHANICAL DESIGN, MODELING AND IMPLEMENTATION OF PIEZOCOMPOSITE AIRFOILS

Onur Bilgen

ABSTRACT

Piezoelectrics offer high actuation authority and sensing over a wide range of frequencies. A Macro-Fiber Composite is a type of piezoelectric device that offers structural flexibility and high actuation authority. A challenge with piezoelectric actuators is that they require high voltage input; however the low power consumption allows for relatively lightweight electronic components. Another challenge, for piezoelectric actuated aerodynamic surfaces, is found in operating a relatively compliant, thin structure (desirable for piezoceramic actuators) in situations where there are relatively high external (aerodynamic) forces. Establishing an aeroelastic configuration that is stiff enough to prevent flutter and divergence, but compliant enough to allow the range of available motion is the central challenge in developing a piezocomposite airfoil. The research proposed here is to analyze and implement novel electronic circuits and structural concepts that address these two challenges.

Here, a detailed theoretical and experimental analysis of the aerodynamic and electromechanical systems that are necessary for a practical implementation of a piezocomposite airfoil is presented. First, the electromechanical response of Macro-Fiber Composite based unimorph and bimorph structures is analyzed. A distributed parameter electromechanical model is presented for interdigitated piezocomposite unimorph actuators. Necessary structural features that result in large electrically induced deformations are identified theoretically and verified

experimentally. A novel, lightweight electrical circuitry is proposed and implemented to enable the peak-to-peak actuation of Macro-Fiber Composite bimorph devices with asymmetric voltage range.

Next, two novel concepts of supporting the piezoelectric material are proposed to form two types of variable-camber aerodynamic surfaces. The first concept, a simply-supported thin bimorph airfoil, can take advantage of aerodynamic loads to reduce control input moments and increase control effectiveness. The structural boundary conditions of the design are optimized by solving a coupled fluid-structure interaction problem by using a structural finite element method and a panel method based on the potential flow theory for fluids. The second concept is a variable-camber thick airfoil with two cascading bimorphs and a compliant box mechanism. Using the structural and aerodynamic theoretical analysis, both variable-camber airfoil concepts are fabricated and successfully implemented on an experimental ducted-fan vehicle. A custom, fully automated low-speed wind tunnel and a load balance is designed and fabricated for experimental validation. The airfoils are evaluated in the wind tunnel for their two-dimensional lift and drag coefficients at low Reynolds number flow. The effects of piezoelectric hysteresis are identified.

In addition to the shape control application, low Reynolds number flow control is examined using the cascading bimorph variable-camber airfoil. Unimorph type actuators are proposed for flow control in two unique concepts. Several electromechanical excitation modes are identified that result in the delay of laminar separation bubble and improvement of lift. Periodic excitation to the flow near the leading edge of the airfoil is used as the flow control method. The effects of amplitude, frequency and spanwise distribution of excitation are determined experimentally using the wind tunnel setup.

Finally, the effects of piezoelectric hysteresis nonlinearity are identified for Macro-Fiber Composite bimorphs. The hysteresis is modeled for open-loop response using a phenomenological classical Preisach model. The classical Preisach model is capable of predicting the hysteresis observed in 1) two cantilevered bimorph beams, 2) the simply-supported thin airfoil, and 3) the cascading bimorph thick airfoil.

DEDICATION

to my grandfather,
Kadri Bilgen

and to my parents,
Deniz and Ahmet Saim Bilgen

ACKNOWLEDGEMENTS

First, I would like to thank Dr. Daniel J. Inman and Dr. Kevin B. Kochersberger for their support and for the direction that they provided. Without their leadership and expertise in their fields, none of this work would have been possible. They have treated me with sincerity and respect, which built the foundation of my academic character. Also thanks to Dr. Mary E. Kasarda and Dr. Andrew J. Kurdila for serving as my previous advisors, as they contributed to the foundation of my research abilities. Dr. Nakhiah C. Goulbourne, Dr. Michael W. Hyer and Dr. Donald J. Leo are also acknowledged for serving in my committee. Also, sincere thanks to Ms. Margaret E. Howell (Beth) for her support to me over the last three years.

Sincere thanks to Mr. Osgar J. Ohanian (John) for his patience, calm personality and his research advice as these were fundamental in developing the concepts presented in Chapters 4, 5 and 6. I would like to acknowledge Dr. Carlos De Marqui, Jr. for his sincere personality, friendship and the academic collaboration. The research presented in Chapter 7 is possible with his expertise and help. Thanks to Mr. Muhammad A. Karami (Amin) for his sincere friendship and character as well as his collaboration in the subjects presented in Section 2.3 and Section 3.3. I would also like to thank Ms. Ya Wang for her collaboration on the experiments presented in Section 2.2.2. Thanks to Mr. Nicholas J. Konchuba for his help with the preliminary wind tunnel experiments. I also would like to acknowledge the help of Mr. Nikolai Vozza for his help with the design and fabrication of the variable-camber airfoil demonstrator and the converging nozzle inlet of the wind tunnel. Thanks to Mr. Daniel J. Inman II, and Ms. Emily Armentrout for their help with the fabrication of the first iteration of the flow straightener for the wind tunnel used in this dissertation. Fabrication of approximately 9000 pieces of three inch long drinking straws would be unbearable without their youth and energy.

I would like to acknowledge my colleagues at the Center for Intelligent Material Systems and Structures (CIMSS) for their friendship and for sharing their ideas and expertise in theoretical, computational, and experimental subjects. The complete list of people to thank are too numerous due to the number of subjects that were studied over the last three years. The following acknowledgement is only a sincere attempt. First and foremost, thanks to Dr. Pablo A.

Tarazaga for teaching me vibrations and his influence in making me part of CIMSS. His expertise in vibration helped build my foundation in theoretical and experimental subjects. Thanks for everything Pablo! Dr. Stephen A. Sarles (Andy) helped me with (literally) everything in the lab and in the office from the beginning to the end of my Ph.D. study. Mr. Steven R. Anton (Steve) helped me with developing numerous experimental codes, and he has been a helpful lab co-manager. Thanks to Mr. Jacob D. Davidson for his sincere character and help in theoretical and experimental questions. Furthermore, Dr. Vishnu Baba Sundaresan, Dr. Barbar Akle, Mr. David A. Neal, Mr. M. Austin Creasy, Dr. Jamil M. Renno and Mr. Jason W. Fox have been great colleagues and they have been very helpful in several theoretical and experimental topics. Also thanks to Mr. Justin R. Farmer for his kind assistance in the lab.

The preliminary wind tunnel tests (although not presented in this dissertation) were possible with the help of Dr. Srinath Ekkad. I would like to thank Dr. Demetri P. Telionis at the Engineering Science and Mechanics Department for his kind assistance with equipment for wind tunnel experimentation. Thanks to Dr. Christopher B. Williams for his kind assistance with the rapid prototyping technique. Also thanks to Mr. Christopher Mesrobian for his help with experimentation. I would like to acknowledge Mr. Danny Reed, Mr. David R. Simmons and Mr. Darrell L. Link at the Engineering Science and Mechanics Department for their kind assistance with experimentation and prototype fabrication. Thanks to Mr. Derwin E. Stafford at the Mechanical Engineering Department for his kind assistance with fabrication.

Thank you to my parents, Dr. Deniz Bilgen and Dr. Ahmet Saim Bilgen, for making this all possible 27 some years ago. They have laid the foundation of my personal and academic character. Thanks to my extended family for being as close as my parents. Finally, I would like to extend a sincere thanks to the Bousquet family for supporting me in many ways.

Finally, I would like to acknowledge friends who have indirectly helped me with this dissertation. Mr. Umut Onat, who I've known since second year of middle school in Ted Ankara Koleji in Ankara, Turkey, has always been there to talk to me. Mr. Danoosh Kapadia is also another friend and a great personality whose expertise helped me in numerous times. Ms. Evrim Dalkiran has been a great friend and continues to support me as this dissertation is being written. Mr. Mustafa Ali Arat and Mrs. Seda Arat are the two most sincere people that I've known in Blacksburg, and their friendship is invaluable. Also thanks to Ms. Mana Afshari and Mr. Moataz B. M. A. S. Khalifa for being good friends.

This work is partially supported by the G. R. Goodson Professorship endowment. The research presented in Chapters 2, 4, 5 and 6 are partially funded by the U.S. Air Force Research Laboratory (AFRL) through a Phase II Small Business Innovation Research (SBIR) contract with AVID LLC. The author is grateful for the support of Air Force Office of Scientific Research (AFOSR) Grant Number FA9550-09-1-0625 "Simultaneous Vibration Suppression and Energy Harvesting" under the direction of "Les" Lee for the research presented in Chapters 3, 4, 7 and 8. Additional financial support (for these chapters) is provided by the Office of Naval Research (ONR) through Multidisciplinary University Research Initiative (MURI) grant # N00014-08-1-0654. Furthermore, I would like to thank the CIMSS for additional funding contributions to this research.

TABLE OF CONTENTS

LIST OF FIGURES

LIST OF TABLES

CHAPTER 1

INTRODUCTION AND LITERATURE REVIEW

The past few decades have seen the development and integration of active materials into a variety of host structures as a superior means of measuring and controlling their behavior. Piezoelectrics remain the most widely used "smart" or active material because they offer actuation and sensing over a wide range of frequencies. Specifically, piezoelectrics have been employed in aerospace structures by performing shape and flow control. A Macro-Fiber Composite (MFC) is a type of piezoelectric device that offers structural flexibility and high actuation authority (up to 0.2% in-plane strain). A challenge with piezoelectric actuators is that they require high voltage input. In contrast, the current drain is extremely low which creates small power consumption and requires relatively lightweight electronic components. Active materials became feasible in small platforms such as unmanned air vehicles (UAVs) or micro air vehicles (MAVs) with the continuing developments in the electronic systems.

From a research and commercial standpoint, development of smaller and lighter aircraft has driven a need to investigate the use of smart materials for flight and flow control. These small unmanned aircraft are pushing the limits and driving the designs to include smart materials and systems. For example, field-deployable aircraft have flexible wings that can be folded during transportation, and they can be unfolded for operation. These compliant wings can be realized with the integration of smart materials. For smart material actuated devices, another challenge is found in operating a relatively compliant, thin structure (desirable for piezoelectric actuators) in situations where there are relatively high external forces. *Establishing a wing configuration that is stiff enough to prevent flutter and divergence, but compliant enough to allow the range of available motion is the central challenge in developing a piezocomposite airfoil.* Novel methods of supporting the actuator can take advantage of aerodynamic loads to reduce control input moments and increase control effectiveness.

There are several benefits of employing continuous shape (or more specifically camber) control via active materials over the discrete trailing edge control using conventional control

surfaces in small air-vehicles. In aerodynamics, camber represents the effective curvature (or shape) of an airfoil. The term camber control simply refers to the change of the curvature of the airfoil by means of actuators. First, the low Reynolds number flow regime can result in flow separation that reduces the effectiveness of a trailing edge control surface. Second, small UAVs and MAVs cannot afford to lose energy through control surface drag because of their severe power limitations. Finally, the opportunity for flow control is inherent in the active material due to its direct effect on circulation and its high operating bandwidth. In addition to replacing conventional control surfaces for camber control, these actuators can be effective in dynamic laminar separation bubble (LSB) control (also referred to as flow control). The bandwidth advantage of a conformal actuator also opens the possibility for dynamic actuation that may have significant advantages. This dissertation addresses aerodynamic and electromechanical challenges that arise with the incorporation of piezocomposite materials into aerodynamic control surfaces.

1.1. Background and Literature Review

The following sections present the relevant background information on the research conducted in this dissertation. First, morphing applications for aircraft are described, and recent morphing wing applications are presented. Next, research background in small unmanned aircraft is presented. Piezoelectric materials are introduced and the Macro-Fiber Composite is described with attention to recent research. Next, the electromechanical modes of smart material devices are demonstrated. Finally, applications of smart materials in aerodynamics are reviewed.

1.1.1. Morphing Wing Aircraft

A morphing aircraft changes its configuration to maximize its performance in significantly different flight environments. Wing morphing has been of interest to researchers because wings directly affect flight performance. The Wright Brothers' first controlled, powered, heavier-than-air flight in 1903 was primarily a success due to the application of the morphing concept. The Wright's were convinced that control of the flying machine was the key challenge. They decided that a "good" way for flying was to "bank" or "lean" into the turn just like a bird, and just like a person riding a bicycle. They puzzled over how to achieve this effect with man-

made wings and eventually discovered wing-warping when Wilbur twisted a long inner tube box at their bicycle shop [Wright].

The early mechanical method of morphing led to the current search for a morphing technique with maximum efficiency. Morphing is necessary for several reasons. A long-endurance aircraft can loiter over a target for an extended time because it utilizes a high aspect ratio, unswept wing. However, this choice of planform is in direct conflict with the design of a high speed aircraft requiring a low aspect ratio, swept wing design. Jha and Kudva [2004] studied how increasing or decreasing a wing parameter affects the performance of an aircraft, demonstrating that an optimal design requires large geometric changes to satisfy a multi-role mission. Table 1.1 shows the effect of change in geometric properties to the aircraft performance.

Table 1.1: Effects of increase / decrease of geometric wing parameters on aircraft performance. [Jha and Kudva, 2004] [Used under the fair use guidelines.]

Parameter	Effects of variation with all other parameters constant
Wing Plan Area	↑ Increase lift, load factor capability ↓ Decreased parasitic drag
Wing Aspect Ratio	↑ Increased L/D, loiter time, distance, turn rates; Decreased engine requirements ↓ Increased maximum speed; Decreased parasitic drag
Wing Dihedral	↑ Increased rolling moment capability, lateral stability ↓ Increased maximum speed
Wing Sweep	↑ Increased critical Mach number, dihedral effect; Decreased high-speed drag ↓ Increased CL max
Wing Taper Ratio	Wing efficiency (Spanwise lift distribution; Induced drag)
Wing Twist Distribution	Prevents tip stall behavior; Spanwise lift distribution
Airfoil Camber	Zero-lift angle of attack, airfoil efficiency, separation behavior
Airfoil Thickness / Chord Ratio	↑ Improved low-speed airfoil performance ↓ Improved high-speed airfoil performance
Leading Edge Radius	↑ Improved low-speed airfoil performance ↓ Improved high-speed airfoil performance
Airfoil Thickness Distribution	Airfoil characteristics, laminar/turbulent transition

While efficient low-speed flight requires a high aspect ratio and low sweep angle, high-speed flight requires exactly the opposite. In order to have the same aircraft fly diversified missions, it should be capable of making large geometric changes in an efficient manner. Jha and Kudva [2004] reviewed several morphing wing concepts that have been utilized. Examples will be briefly discussed below.

Camber control of wings using control surfaces has been extensively utilized in the industry as a morphing concept. Most of these designs use discrete and rotating leading and trailing edge controls. Trailing edge control is the more popular of the two. The F-16 Fighting Falcon uses leading edge flaps to change the camber of the wings. In 2002, the Active Aeroelastic Wing program of NASA demonstrated twisting of wings for primarily roll control at transonic and supersonic speeds for an F/A-18 Hornet. Twist was achieved by creating aerodynamic moments on the wings by leading edge flap and aileron deflection.

The NASA-Ames Mission Adaptive Wing Research program focused on producing smooth camber change by using a flexible internal mechanism to flex the outer skin. Drag was reduced by around 7 percent at the wing design cruise point, and by 20 percent at an off-design condition.

Smooth cambering was applied in a Northrop Grumman Unmanned Combat Air Vehicle (UCAV) test model. The unmanned aircraft demonstrated high actuation rate (80deg/s), large deflection (20°), hinge-less, smoothly contoured control surfaces with chord-wise and span-wise shape variability. Piezoelectric motors were used as actuators [Bartley-Cho et al., 2002].

Along with the developments listed above, inflatable wings were mostly developed within the last few decades. Aspects of inflatable technologies and a review of inflatable wing and related technologies are included in Cadogan et al. [2003, 2004]. More recent interest in inflatable wings was demonstrated through the development of an inflatable wing UAV for NRL by Vertigo, Inc. Flight tests of deployment and low-altitude flight of the design were conducted in 2001 by researchers at NASA Dryden [2005]. The skeleton of the wing was made of inflatable tubes, surrounded with crushable foam to provide the airfoil cross-section. Simpson and Jacob [2005] presented research on developing UAVs using inflatable wings with wing warping for roll control. The inflatable wings are constructed with internal bladders and flexible external restraints and inflatable wing stiffness varies with internal pressure. A small-scale UAV with inflatable wings using wing warping roll control is demonstrated.

1.1.2. Small Unmanned Aircraft

Micro air vehicles represent a new challenge for aerodynamics, propulsion and control design. Typical MAV missions are projected to be flown either by inexperienced operators or via autonomous control. This requires robust flying characteristics. It is well known that during flight in the Reynolds number range between 10,000 and 100,000, flow separation around an airfoil can lead to sudden increases in drag and loss of efficiency. The effects of flow separation can be seen in nature where large species soar for extended periods of time while small birds have to flap vigorously to remain airborne. The Reynolds numbers of the larger species are well above 100,000 whereas hummingbirds fly at below 10,000 if they attempt to soar [Ifju et al., 2001].

The researchers at the University of Florida have developed a series of MAVs that incorporate a unique, thin, reflexed, flexible wing design [Waszak et al., 2001, Ifju et al., 2002]. The wings are constructed of a carbon fiber skeleton and a thin flexible latex membrane. There is some evidence that the flexible wing design reduces the adverse effects of gusty wind conditions and unsteady aerodynamics, exhibits desirable flight stability, and enhances structural durability.

There have been numerous experimental and analytical studies on flexible wing MAVs. Albertani et al. [2004] investigated the effects of a propeller on the aerodynamic characteristics of MAVs and the coupling with the wing flexibility in steady conditions. The MAV was placed in a wind tunnel and subjected to different flow conditions and different motor speeds. Data were gathered through a sting balance and two cameras for stereovision and image correlation. The test data provided a detailed account of aerodynamics as they relate to the propeller effects and to the structural deformations, namely the wing flexibility.

Garcia et al. [2003] investigated the use of a morphing method to provide control authority. A torque tube actuated by servos twisted or curled the flexible wing. Flight tests show that wing twisting or curling was a good strategy to command roll maneuvers. The vehicles were easy to fly and were suitable for autopilot control.

The aerodynamic characteristics of isolated MAV wings and complete aircraft are considered a good base examination for general aerodynamic considerations and a necessary step for a sound MAV wing design [Torres, 2002]. Prandtl [1921] and Hoerner [1975] and many others studied the general aerodynamic effects of propellers on the wing and the aircraft. Barlow et al. [1999] established standard wind tunnel testing techniques.

1.1.3. Piezoelectric Materials

The field of smart materials has advanced rapidly in the last 15 years due to an increasing awareness of material capabilities, the development of new materials and transducer designs, and increasingly stringent design and control specifications in aerospace, aeronautic, industrial, automotive, biomedical, and nano-systems [Smith, 2005]. A piezoelectric material is a type of smart material. The history of piezoelectricity dates to 1880 when Pierre and Jacques Curie discovered the effect in several substances such as the quartz crystal (which is a naturally occurring piezoelectric material). The term piezoelectricity is used for certain materials and substances that generate charge (or voltage) when pressure is applied to them [Inman and Cudney, 2000]. These materials are also capable of changing their shape when they are exposed to an electric field. The direct effect is the charge generated due to pressure. The converse effect is the mechanical response of the material to the electrical field.

Applications of piezoelectric materials are very broad. Although the electrically induced strains are relatively small (around 0.1%), the force outputs can be relatively large, resulting in high energy density. Response times are also very short which allows for high frequency applications. Piezoelectric materials exhibit high-sensitivity to mechanical deformation which allows them to be used as sensors [Lloyd, 2004].

A common synthetic piezoelectric material composition is Lead-Ziconate-Titanate, PZT for short. Selected electrical and mechanical properties of common piezoelectrics can be seen in Table 1.2. Uses for PZT-5A include accelerometers, hydrophones, low power structural control, and stable sensors. PZT-5H is used in areas requiring sensitive receivers, fine motion control, and low power structural control. The single crystal piezoelectric, PMN-PT, is best suited to low induced-stress, high strain, and deflection applications [Wilkie, 2006].

Table 1.2: Selected properties for common piezoelectric materials. The boundary condition superscripts are: T = constant stress; E = constant field. [Wilkie, 2006] [Used under the fair use guidelines.]

Bulk Properties	PZT-5A	PZT-5H	PMN-PT
Density, ρ (g/cm^3)	7.8	7.8	8.05
Relative Dielectric Constant, K_3^T {1kHz}	1900	3800	7151
Electromechanical Coupling, k_{33}	0.72	0.75	0.91
Strain / applied field, d_{33} (pm/V)	390	650	2285
Strain / applied field, d_{31} (pm/V)	-190	-320	-1063
Compliance, s_{11}^E (10^{-12} m^2/N)	16.4	16.5	59.7
Compliance, s_{13}^E (10^{-12} m^2/N)	-7.22	-9.21	-45.3
Compliance, s_{33}^E (10^{-12} m^2/N)	18.8	20.7	86.5
Compliance, s_{44}^E (10^{-12} m^2/N)	47.5	43.5	14.4

Two types of piezoelectric devices are monolithic piezoelectric wafers and piezoelectric fiber composites. For structural actuation and sensing, piezoelectric materials are usually implemented in the form of monolithic wafers. The term monolithic refers to a single, contiguous piece of piezoelectric material, free from added materials or augmenting structural components [Lloyd, 2004]. Structural control, sensing and vibration suppression applications typically rely on in-plane actuation and sensing. In most cases piezoelectric wafers are subjected to out-of-plane electric field. As a result of in-plane sensing/actuation and out-of-plane electric field, piezoelectric wafers commonly operate in what is referred to as the *31* mode. This technique fails to exploit the full electro-mechanical coupling of piezoelectrics (note the relatively larger d_{33} coefficients in Table 1.2). Limiting energy density and strain output, the *31* is a much weaker phenomenon than the *33* mode, where the applied or sensed electric field is in the same direction of the strain. A piezoceramic is a type of piezoelectric material and it used commonly used in many applications; however the inherent brittle nature of piezoelectric ceramics (or piezoceramics) and primary mode of operation limit applications employing monolithic wafers. These types of piezoceramics are difficult to instrument on non-flat surfaces due to their stiff mechanical properties, thereby making them impractical for control of membranes, irregularly shaped surfaces or for large deflections required in shape changing materials.

The second type of a piezoelectric device is known as piezoelectric fiber composites or piezocomposites for short. Piezocomposites generally consist of unidirectional PZT fibers embedded in a polymer matrix. Typically, crystalline materials have much higher strengths in

fibrous form, where the decreased volume fraction of flaws leads to an increase specific strength. Since they will be encased in a polymer and laminated with other flexible layers, the fibers can be thinner, thus less stiff in bending than a monolithic layer. A major limitation in the use of piezoceramics is their rigid and brittle nature making them questionable for applying in-plane or out-of-plane deformation. However fibrous piezoceramics offer flexibility but at the expense of reduced effective area.

A fundamental problem that has been overlooked in designing piezoelectric (and more specifically piezoceramic) actuators for structural integration is to align the electric field with the direction of strain. Applying electric fields in the out-of-plane direction and actuating in the in-plane direction is easier to employ, however is far less effective than aligning the electric field and actuation direction because of the smaller coupling coefficient. Many combinations of electroding methods and piezoelectric materials have been designed and fabricated. More recent benefits of piezoelectric composites include the ability to use larger *33* electromechanical coupling, more robustness, increased flexibility, and the ability to tailor the direction of actuation strains and sensing capability. The current state of the art for piezoelectric fiber composite actuators with interdigitated electrodes has been arrived at by several smaller steps which advanced and combined pre-existing technologies. The following sections outline the development of such devices through a chronological discussion of the cornerstone publications.

Hagood and Bent [1993], and Hagood et al. [1993] attempted to improve planar actuation by using interdigitated electrodes (IDEs) to apply in-plane fields to monolithic piezoceramic wafers. This technique succeeded in applying such an electric field, which was used to pole and then actuate that material through the stronger *33* piezoelectric effect. However, high electric field gradients near the edges of the electrodes caused stresses large enough to crack the brittle ceramic. Nevertheless, the electric field between the electrodes was shown to be relatively uniform and in the desired planar direction. Thus, the idea of interdigitated electrodes was a significant contribution and the critical component of today's high strain actuators.

Around this same time, piezoceramic fiber composites (PFCs) with uniform electrodes were developed in an effort to achieve in-plane orthotropic actuation. This concept utilized round, extruded piezoceramic fibers embedded in an epoxy matrix. Electric fields were applied to the device through uniform electrode layers on the top and bottom of a single orthotropic layer of fibers. Of course, this type of electroding poles the actuator through its thickness; therefore

planar actuation was achieved through the weaker *31* piezoelectric effect. Nevertheless, the device showed much larger deflections parallel to the fibers than in the transverse direction. This directional actuation offered a designer the ability to excite only specific deformation modes of a host structure. However, the large dielectric mismatch between the piezoceramic and epoxy greatly reduced the electric field available to the fibers. The result was a device with actuation capability comparable to the relatively weak piezo-polymer material, PVDF.

Soon after, the piezoceramic fiber composite and interdigitated electrode technologies were combined to form Interdigitated Electrode Piezoelectric Fiber Composites (IDEPFCs). This union exploited the directional actuation, increased flexibility, and improved durability of the PFC, along with the increased strain output obtained by using IDEs in lieu of uniform electrodes [Bent and Hagood, 1997]. As expected, the values of the free-strain constants were five times higher than PFCs with uniform electrodes, indicating much improved actuation performance. Also, the maximum free-strain output in the fiber direction was approximately three times greater than in the transverse direction, under comparable fields of ±6.6 kV/m.

In his doctoral dissertation, Bent [1997] coined the term "Active Fiber Composite (AFC)," to take the place of IDEPFC, and presented a detailed design analysis, including constituent material characterization and selection. Additionally, a thorough derivation of the linear uniform fields and finite element models was presented, and the results were used to examine design tradeoffs between various fiber and matrix combinations. Manufacturing of several selected AFC designs and the experimental measurement of their relevant electromechanical properties was discussed. It was shown that the behavior of the AFC was well described by the linear uniform fields model, however, actuation under high fields led to more complex nonlinear material behavior.

A great deal of information was learned about interdigitated electrodes and piezoceramic fiber composites through the development of the AFC. However, its performance was ultimately limited by design and manufacturing issues. Most importantly, the round cross-section fibers tended to have minimal contact area with the copper electrodes. This limitation, combined with the epoxy beneath the electrodes but adjacent to the contact region, made for an inefficient transfer of the electric field into the PZT fibers. Additionally, the PZT fibers used in the AFC are obtained individually from an extrusion process, which required the thin, brittle fibers to be aligned by hand. This procedure oftentimes resulted in broken, poorly aligned fibers.

Furthermore, the vacuum infiltration process that was used to apply the epoxy to the fibers can leave air bubbles (voids) and particulate inclusions, both of which greatly increased the chance of electrical failure.

1.1.4. Macro-Fiber Composites

The Macro-Fiber Composite (MFC) was developed at NASA Langley Research Center [Wilkie et al., 2000]. The MFC is a layered, planar actuation device that employs rectangular cross-section, unidirectional piezoceramic fibers (PZT-5A) embedded in a thermosetting polymer matrix. This active, fiber reinforced layer is then sandwiched between copper-clad Kapton film layers that have an interdigitated electrode pattern. The MFC device is shown in Figure 1.1.

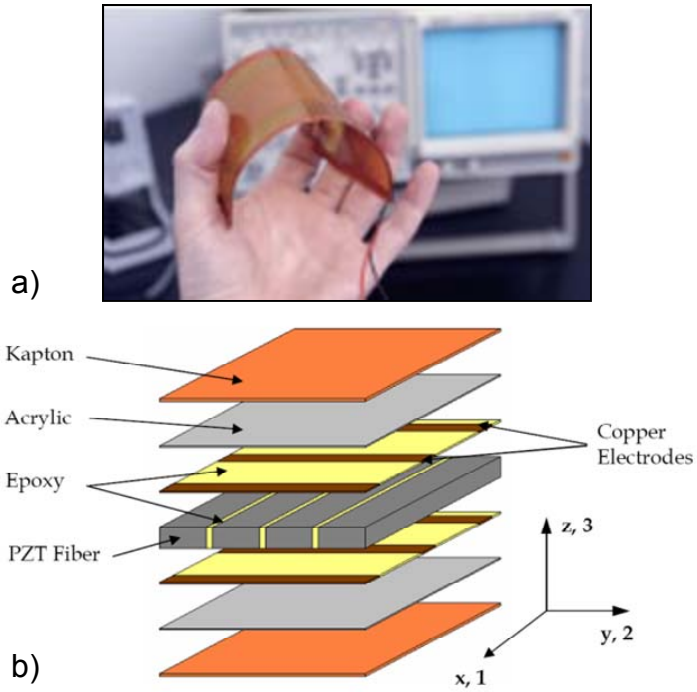

Figure 1.1: a) A demonstration of the flexibility of the Macro-Fiber Composite. [www.smart-material.com] b) Layers of the MFC. [Williams, 2004] [Used under the fair use guidelines.]

The in plane poling and subsequent voltage actuation allows the MFC to utilize the *33* piezoelectric effect, which is much stronger than the *31* effect used by traditional PZT actuators with through-the-thickness poling [Hagood et al., 1993]. MFC has a uniform geometry, including PZT fiber and electrode spacing and continuity, as well as the absence of air voids or particulate

inclusions. The use of rectangular fibers also promotes improved contact between the piezoceramic and the adjacent electrode finger, thus ensuring more efficient transfer of electric field into the fibers.

There has been extensive analytical and experimental research focused on utilizing MFC as an actuator (or sensor) for structural control. Williams [2004] provides a detailed nonlinear characterization of the mechanical and piezoelectric behavior of the MFC actuator. A classical lamination model was developed to predict MFC's short circuit linear-elastic properties. Piezoelectric characterization is achieved using a nonlinear actuation model whose parameters are experimentally determined. Common linear piezoelectric strain coefficients are presented as a function of electric field and applied stress.

Moses et al. [2001] used both Active Fiber Composite (AFC, an earlier version of MFC) and MFC to actively reduce vibration levels in the tail fins of a wind tunnel model of a fighter jet subjected to buffet loads. The model was tested at a Mach number of 0.105 and a 25 degree angle of attack. One fin had five MFCs, while the other had five AFCs. Using a maximum closed-loop control signal input of 1 kV to the actuators, the fin-tip peak acceleration was reduced by about 70% with the MFCs and about 85% with the AFCs at frequencies near the first bending resonance frequency. Torsional peak vibration levels were reduced 30% and 40% by delivering a closed-loop control signal to the MFCs and AFCs respectively.

Ruggiero et al. [2002] used several MFCs as both actuators and sensors to measure the dynamic behavior of the same inflated Kapton torus and to control its vibration. The flexibility of MFC made attachment convenient to the curved surface. The MFC was found to outperform other actuators and to have sensitivity comparable to other monolithic piezoelectric sensors.

Sodano et al. [2003] experimentally investigated the suitability of using the MFC for structural vibration applications. Ground testing and active vibration control of an inflated Kapton torus was performed using an MFC. By measuring changes in impedance, the MFC was able to accurately detect damage in a lap joint whose bolt preload was reduced, and in a cantilevered beam whose clamped end was loosened. In addition, self-sensing technology was used with the MFC to reduce the vibration levels of a cantilevered aluminum beam.

Park and Kim [2005] presented an analytical development of single crystal MFC actuators for active twist rotor blades. Wilkie et al. [2006] presented a research on incorporating single crystal piezoelectrics in to piezocomposite actuators (such as the MFC actuator). The three

types of MFC actuators are fabricated and tested with PMN-PT single crystals and PZT-5A and PZT-5H type polycrystalline piezoceramics.

1.1.5. Electromechanical Transduction Modes

This section describes the basic electro-mechanical relationship between strain and electric field. Piezoelectrics are employed in two common forms, unimorph and bimorph configuration. Figure 1.2 shows the clamped free unimorph and bimorph actuators [Inman and Cudney, 2000].

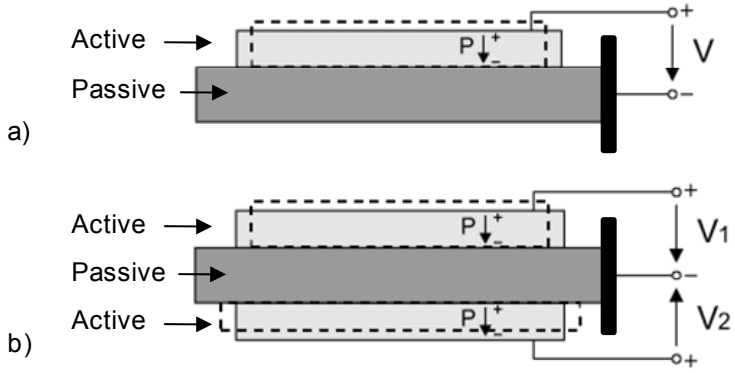

Figure 1.2: Clamped-free actuator configurations. a) Unimorph and b) bimorph. In both cases, the active material is bonded to an elastic and conductive passive substrate material. [Used under the fair use guidelines.]

In unimorph configuration, the active piezoelectric material is bonded to a passive material so that the net effect is bending. In the bimorph configuration, where both sides of the substrate are active, the bending is achieved by asymmetric actuation of the active materials. The piezoelectric constitutive relation is given by:

$$S_{ij} = s^{E}_{ijkl} T_{kl} + d_{kij} E_k \quad i,j,k,l = 1,2,3 \tag{1.1}$$

where S is the mechanical strain, T is the mechanical stress, E is the applied electric field, s^E is the mechanical compliance tensor at constant electric field, and d is the piezoelectric constant. Applied electric field is defined as:

$$E_k = \frac{\Delta V_k}{\Delta e_k} \tag{1.2}$$

where ΔV is the voltage applied to the piezoelectric material, and Δe is the electrode spacing assuming that an isotropic piezoelectric material is sandwiched between two uniform electrodes. To increase the strain induced due to electrical field, one can increase the electro-mechanical coupling coefficient (d) by using newer single crystal piezoelectrics, PMN-PTs or PMN-PZTs. Another improvement can be obtained with the choice of poling direction, where the in plane poling and subsequent voltage actuation utilizes the d_{33} piezoelectric constant, which is higher than the d_{31} piezoelectric constant (see Table 1.2). Figure 1.3 demonstrates the most common electrode arrangement of a piezoelectric wafer actuator (A monolithic PZT layer is placed between two electrodes).

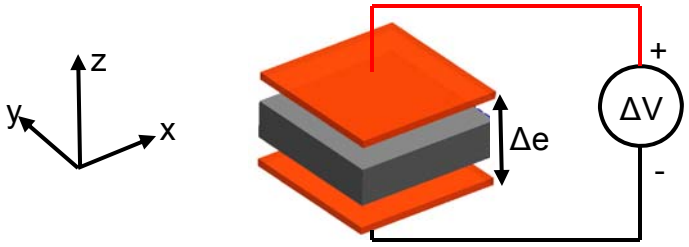

Figure 1.3: Commonly used electrode arrangement for piezoelectric wafers.

This type of configuration is generally used to induce bending on the substrates that they are bonded to. Highest deformation is obtained in the in-plane direction (*x-y plane*) which induces shear forces on the host material that they are bonded to.

Another configuration, known as the stack actuator, uses the out-of-plane displacement of the piezoelectric material shown in Figure 1.4, which employs *33* coupling. Since the out-of-plane length of the PZT is small, the displacement generated is also small; however the force output is very large due to large planform of the PZT layer. The total displacement could be increased by stacking several piezoelectric-electrode layers.

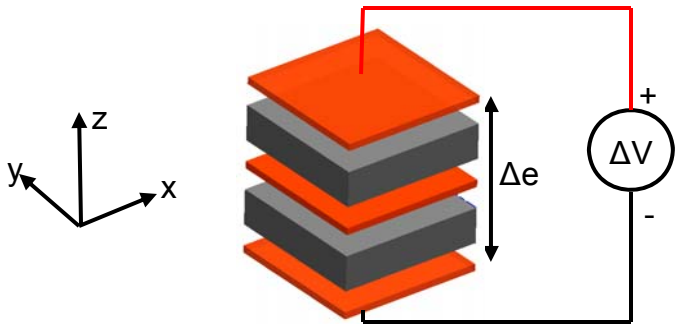

Figure 1.4: Stack actuator that employs multiple piezoelectric elements and electrodes.

In order to use the *33* coupling mode for an actuator that induces shear forces on a substrate, the interdigitated electrode concept is introduced. The electrodes could be placed on one or both sides of the piezoelectric material. The electric field is aligned with x-axis which the direction of maximum induced strain allowing *33* coupling as shown in Figure 1.5.

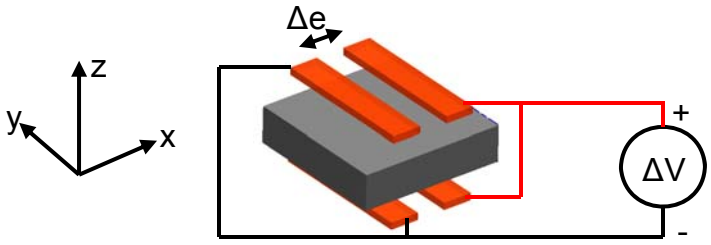

Figure 1.5: Application of interdigitated electrodes on a monolithic piezoelectric material.

In this configuration, a nonuniform electric field is applied to the piezoelectric material due to the surface bonded interdigitated electrodes. There are electric field concentrations on the edge of the electrode closest to the nearby, oppositely-poled electrode. Although the higher *33* coupling is employed, the piezoelectric material is not placed in a uniform electric field; therefore the *33* coupling is not efficiently used. One can argue that not all of the piezoelectric material is employing the *33* coupling because electric field is not parallel with the in-plane direction everywhere in the actuator. Figure 1.6, adopted from Williams [2004], demonstrates the electric field distribution for a piezoelectric material with interdigitated electrodes.

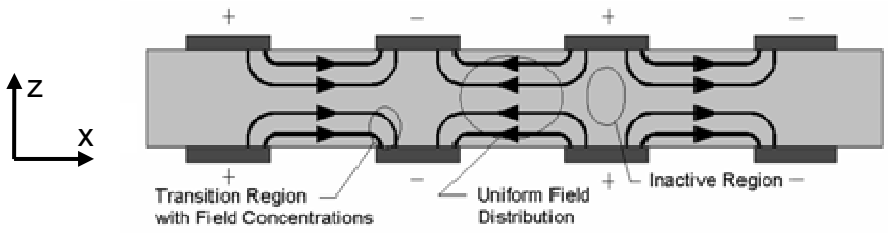

Figure 1.6: Electric field distribution for interdigitated electrodes. [Williams, 2004] [Used under the fair use guidelines.]

The area under each electrode is inactive because theoretically there is zero electric field. There are several improvements that can be employed to reduce the penalty of IDEs placed off-plane with respect to the PZT fibers. The number of inactive areas could be reduced by decreasing the number of electrodes per unit length. This will increase the distance between each oppositely poled electrode (Δe). To keep the same electric field (E), the voltage (ΔV) must be increased. As the electrode space is increased, the effective field through the piezoelectric material becomes uniform.

Both, the single layer actuator with regular or interdigitated electrodes and the stack actuator are typically made from brittle, monolithic piezoceramic wafers. The brittle nature of these configurations makes them a poor choice for curved surfaces. An alternative is to employ piezoceramic fibers or sliced monolithic wafers. Figure 1.7 demonstrates the rectangular piezoceramic fibers with regular electrodes on the top and bottom surfaces.

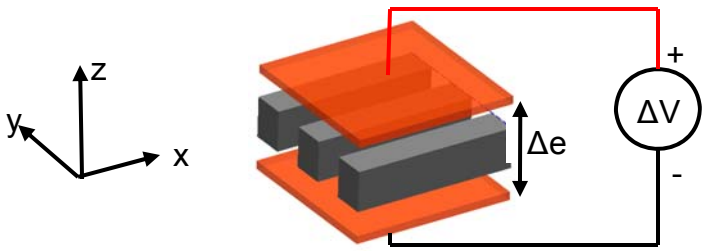

Figure 1.7: Piezoceramic fiber composite actuator with flat electrodes.

This configuration operates in the *31* mode where the electric field is aligned in the out-of-plane direction (*z-axis*). A disadvantage is that the electrodes restrict the strain output, which may be a significant performance reduction.

Recently, the interdigitated electrode pattern and the fibrous piezoceramic concepts have been combined to create a flexible actuator that can induce high shear forces and high strains.

The *33* coupling is employed in such actuators. The fibers could be round (as in the AFC) or rectangular (as in MFC). Figure 1.8 demonstrates piezo-fiber-composite actuators with interdigitated electrodes.

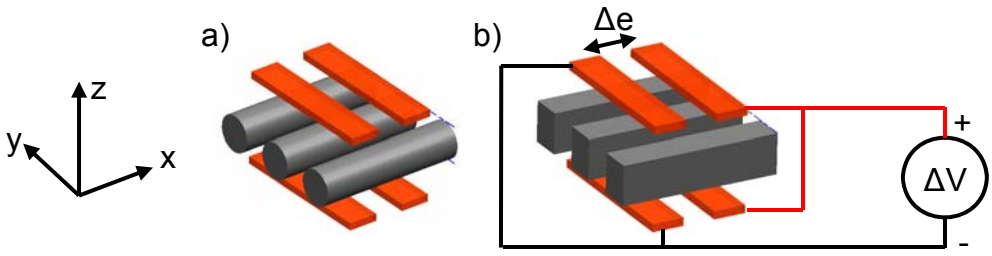

Figure 1.8: a) AFC actuator with round fibers. b) MFC actuators with rectangular fibers.

The actuator with round fibers is known to have less electromechanical coupling because the electrode contact is minimum when compared to the actuator with rectangular fibers. Rectangular fibers allow maximum contact with the electrode and they are cheaper to fabricate because the fibers can be cut from larger monolithic wafers. Figure 1.9 demonstrates the contact issues between the round piezoceramic fibers and the electrodes.

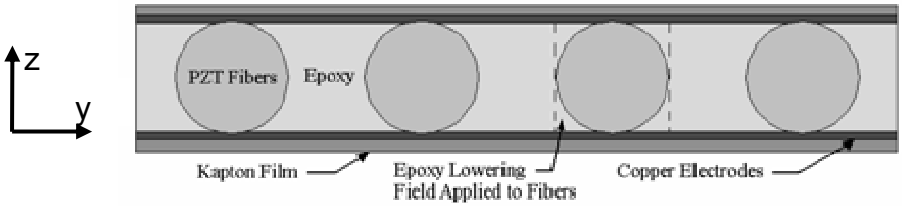

Figure 1.9: Cross-section of AFC actuator. Electrodes are perpendicular to the round piezoceramic fibers. [Williams, 2004] [Used under the fair use guidelines.]

Both the AFC and MFC actuators operate in the more effective *33* mode, however they suffer nonuniform electric field distribution and inactive piezoceramic material.

Other designs based on rectangular fibers and interdigitated electrodes are possible with the development of fabrication techniques. The interdigitated electrodes allow the use of better electro-mechanical coupling mode. A concept piezocomposite device uses the IDEs in the same plane as the fibers, still perpendicular to the piezoceramic fibers. This configuration allows uniform field distribution along the cross-section of the fiber. Figure 1.10 demonstrates the device before and after the application of the electrodes.

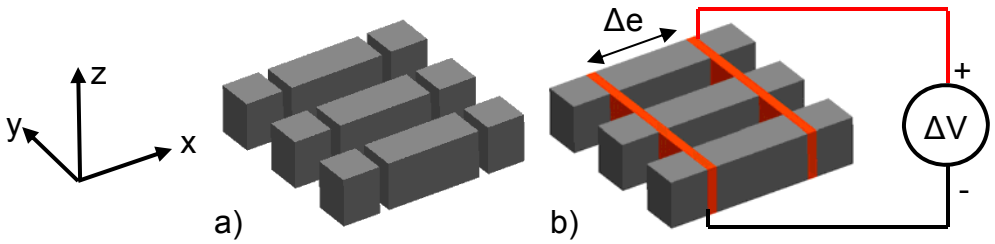

Figure 1.10: a) PZT fibers after dicing in the lateral direction. b) IDEs applied between the fibers.

The fabrication of the concept includes a repeated step in the fabrication process for an MFC type actuator. The MFC is fabricated by a well established fabrication process, described in High and Wilkie [2003]: 1) Slicing (dicing) a monolithic wafer into thin fibers. 2) The gaps between the fibers are filled with epoxy by covering the complete surface with filling material. The excess filling material is removed with mechanical polishing techniques. 3) The IDEs are applied on a separate film to the top and bottom surfaces of the orthotropic fiber-epoxy layer. Up to step 3, the fabrication of the MFC actuator is followed. The proposed concept could be achieved by slicing the orthotropic fiber-epoxy layer in perpendicular direction to the PZT fibers. The IDEs are applied in the new "channels" by using electronic circuit printing techniques, or metal deposition via chemical vapor or physical vapor deposition methods.

Figure 1.11 demonstrates two geometric alternatives to the new piezoceramic actuator concept. First, monolithic piezoceramic wafers sliced only along the lateral direction (*y-axis*), and electroded along the *y-axis*. This design will create an actuator flexible along the *x-axis* and stiff along the *y-axis*. If flexibility along both in-plane directions is required, the wafers can be cut along the *x*-axis leaving a rectangular piezoceramic planform. The in-plane electrodes can be applied along the *y-axis*.

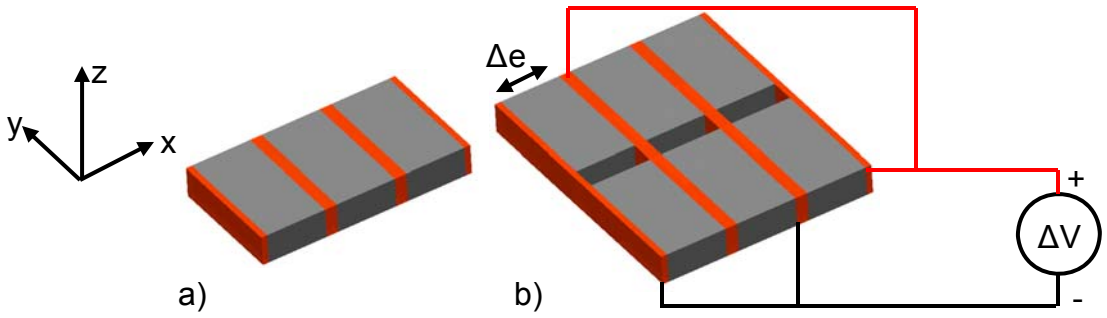

Figure 1.11: Two design considerations that induce uniform electric field to the PZT.

This concept could be viewed as a very thin stack actuator on its side, generating shear force on the substrate instead of normal force. The geometric property that allows this concept to work is the fact that the out-of-plane length (thickness) of the PZT "micro-wafer" is smaller compared to the in-plane dimensions (length and width). This geometric feature allows the overall actuator to be compliant to large deformations. Single crystal piezoelectrics could be a candidate material for this concept. High electro-mechanical coupling coefficient from the single crystal wafer combined with the uniform field *33* mode is a key improvement to current concepts in the market. According to Table 1.2, this actuator concept theoretically results in *three times* the coupling coefficient of currently designed piezocomposites.

1.1.6. Smart Materials in Aerodynamic Applications

Smooth control surface designs have been a research interest since the beginning of the modern aviation, the first controlled, powered and heavier-than-air flight by Wright Brothers in 1903. During the past few decades, smart materials have been implemented to control the shape of continuous aerodynamic surfaces. Smart materials have also been used in flow control by adding energy to the flow by means of synthetic jets. Therefore, the following sections will list the developments in the past few decades in aerodynamic applications via smart material systems.

Rotorcraft Applications: Lazarus et al. [1991] examined the feasibility of using representative box wing adaptive structures for static aeroelastic control. It was found that greater control authority along with a lower weight penalty is achievable using adaptive aeroelastic structures for a variety of wing designs. Roglin et al. [1994] presented an adaptive airfoil that uses a shape memory alloy (SMA) actuator mechanism to actively change the camber of an airfoil for a remotely piloted helicopter. Steadman et al. [1994] showed an application of a

piezoceramic actuator for camber control in helicopter blades. Structure-control interaction was employed to develop an adaptive airfoil that can be used in the cyclic and vibration control of the helicopter. Giurgiutiu et al. [1994] has researched improvement on rotor blades using several smart material based technologies. A comprehensive review paper was published in 2000. In this paper, Giurgiutiu [2000] reviewed achievements in the application of smart-materials actuation to counteract aeroelastic and vibration effects in helicopters and fixed wing aircraft. Experiments of active flutter control, buffet suppression, gust load alleviation, and sonic fatigue reduction are discussed.

Fixed-Wing Platforms: Conventional or smart material actuated continuous control surface designs have also been employed in fixed-wing aircraft. In recent years, several important advances have been centered on squeezing more performance out of existing adaptive materials and enhancing the performance of materials yet to come. Post-Buckled-Precompression (PBP) concept, in its earliest incarnation was primarily intended to increase the coupling coefficient exhibited by piezoelectric transducer elements [Lesieutre and Davis, 1997]. Experiments showed that apparent coupling coefficients approaching one could be achieved by axially loading bending elements with forces that approached the buckling load of the beam. Vos et al. [2007] conducted research to improve the PBP concept for aerodynamic applications. In this work, the design, modeling, and testing of a morphing wing for flight control of an UAV is presented. Axial precompression was generated in the piezoelectric elements by an elastic skin which covered the outside of the wing and served as the aerodynamic surface. It was shown that static trailing edge deflections of ±3.1° could be attained statically and dynamically through 34 Hz. The PBP concept was employed in a ducted-fan aircraft [Barrett et al., 2005].

Seigler et al. [2007] focused on modeling and flight control of large-scale planform altering flight vehicles. The equations of atmospheric flight are derived in a general form, methods of integrating the aerodynamic forces are examined, and various approaches and methods of flight control are distinguished.

Flow Control with Smart Material Actuators: The use of conformal, zero mass flux actuators in aerodynamic flow control has been presented recently as a novel means of controlling laminar separation bubble (LSB) on small aircraft subjected to low Reynolds number flows. Passive separation control methods, such as trip wires, are known to be ineffective at low Reynolds number flow [Gad-el-Hak, 1990, Joslin, 1998]. Conformal zero mass flux actuators

include synthetic jets [Glezer et al., 2005], plasma actuators [Pern et al. 2006] and piezo-ceramic actuators that move in the out-of-plane direction [Ramakumar and Jacob, 2005]. The motivation for designing such an actuator is to increase the bandwidth of actuation, where the ability to delay or re-attach the LSB is dependent on the excitation frequency and amplitude. Mechanical actuators are limited in frequency due to mass loading effects while the MEMS actuators can operate at orders of magnitude higher frequency. The opportunity for flow control is inherent in the smart material device due to its direct effect on circulation and its high operating bandwidth.

There are also non-zero mass flux trailing edge blowing (TEB) for circulation control, demonstrated in applications from helicopters [Rogers et al., 1985] to turbine blades. The complexity and weight of TEB actuators make them a poor choice for small aircraft applications where size, weight and power are primary concerns. Acharya et al. [2004] presented the application of flow control technology to the compressor of a gas-turbine engine designed for a UCAV. Pulsed blowing was employed in suction surface of stator vanes to delay or eliminate flow separation in the vane passage, thereby enabling higher vane loadings. Trailing-edge-blowing was used in the inlet guide vanes (IGVs) to vector the flow leaving the vane row to desired flow angles.

Santhanakrishnan et al. [2005] discussed several technologies for use on low speed UAVs. This includes adaptive wing technology that controls separation via active changes in the camber, use of large scale surface roughness to control separation, plasma actuators to control stall and enhance lift, and inflatable wings that can be tailored using wing warping. In the research, the THUNDER piezoelectric actuators are employed in a cavity on the wing where the actuator oscillation changes the profile of the suction surface.

Gomes et al. [2006] investigated on the effect of geometry and actuation variables on peak jet velocity of a piezoelectric diaphragm synthetic jet actuator. Patel et al. [2007] presented the use of dielectric barrier discharge plasma actuators for hingeless flow control over a 47-degree 1303 UCAV wing. When compared with the conventional trailing edge devices, the plasma actuators demonstrated a significant improvement in the control authority in the 15 to 35 degree angle of attack range.

Greenblatt and Wygnanski [2000] presented a review of control of flow separation from solid surfaces by periodic excitation. The paper pays attention to the separation control on airfoils by considering controlling parameters such as optimum reduced frequencies and

excitation levels, performance enhancement efficiency, reduction of post-stall unsteadiness, compressibility and other important features. Seifert et al. [2000] demonstrated several experimental flow control studies on a NACA 0015 airfoil at various Reynolds numbers. It was shown that two dimensional periodic excitation is effective in delaying the boundary layer separation, reattaching flows and stabilizing unsteady wakes at chord Reynolds numbers ranging from $O(10^4)$ to $O(10^7)$.

1.1.7. Macro-Fiber Composites in Small Unmanned Aircraft

Kim and Han [2006, 2008, 2009] designed and fabricated a smart flapping wing by using a graphite/epoxy composite material and an MFC actuator. This research was aimed to mimic the flapping motion of birds. The wind tunnel tests were performed to measure the aerodynamic characteristic and performance of the surface actuators. A test stand was also designed to measure the lift and thrust generated by the flapping device. The tests were done on the Cybrid-P2 commercial ornithopter with and without the MFC actuator. A twenty percent increase in lift was achieved by changing the camber of the wing at different stages of flapping motion.

Wickramasinghe et al. [2009] recently presented the design and verification of a smart wing for an MAV. The proposed smart wing structure consists of a composite spar and ailerons that have bimorph active ribs consisting of MFC actuators with interdigitated electrodes. Actuation is enhanced by preloading the piezoceramic fiber actuators with a compressive axial load. The preload is exerted on the actuators through a passive latex or electro active polymer skin that wraps around the airfoil.

Recently, Bilgen, et al. [2007a, 2007b, 2009] presented a new application for piezo-composite actuators on a 0.76 meter wingspan morphing wing air vehicle with approximately 0.815 kg total weight. In this application, two MFC patches are bonded to the wings of a small demonstration vehicle, and the camber of the wing is changed with actuator voltage. This morphing control directly affects the circulation by changing the wing's camber, and adequate roll control authority is demonstrated in the wind tunnel as well as in flight. The aircraft demonstrates that lightweight, conformal actuators can be used as primary control surfaces on an aircraft. All electronics, including MFC power electronics (103 grams), are powered by an 11.1 V Lithium-Polymer battery (106 grams), a common choice for remotely controlled aircraft. The

aircraft uses a 150 W brushless motor for thrust; in contrast the MFC power electronics consume only 3.0 Watts during peak actuation.

1.2. Objectives

The goal of this research is to exploit the electromechanical properties of Macro-Fiber Composites to perform shape and flow control of an airfoil on small platforms and to determine the feasibility and advantages of smooth control surface deformations.

The first objective is to quantify the electromechanical capabilities and limitations of a piezoceramic based structure and determine the feasibility of a variable-camber airfoil that is actuated with MFCs. Since the MFC device can also sense and harvest mechanical strains, the energy harvesting characteristics are also desired along with actuation characteristics. The goal is to determine the extent of the usage of the MFC actuator when coupled with a structure for open-loop control and energy harvesting. Nonlinear effects (if any) need to be identified for development of a linear response (for flight control purposes). In order to develop an overall efficient system (for power and weight), lightweight driving circuitry designs are also desired.

The second objective is to employ active material actuation and structural boundary conditions to perform structural shape control and aerodynamic flow control of airfoils. The advantages of smooth control surface deformations can be evaluated by developing a variable-camber airfoil employing piezoceramics. The effectiveness of different flow control techniques induced by piezoelectric materials is also desired.

1.3. Outline of the Dissertation

Chapter 2 discusses the modeling and experimentation conducted to understand and compare the behavior of several piezoelectric actuated unimorph structures. The mathematical modeling of MFC actuated unimorph beams is conducted using a distributed parameter Euler-Bernoulli beam theory. Predictions of the tip displacement are validated against experimental measurements with several beam-like specimens. The MFC unimorphs are compared to other piezoelectric devices.

Chapter 3 presents the experimental analysis of energy harvesting capabilities of several unimorph beam-like specimens. The power outputs of base excited clamped-free beams are

determined using a resistive shunt circuit. Constitutive nonlinear effects (that arise from piezoceramic hysteresis) are identified.

Chapter 4 introduces a novel, solid-state electrical voltage divider circuit. The circuit allows a single bipolar amplifier to control a bimorph composed of two MFC actuators. First, the challenges and conventional solutions to high voltage actuation are presented. Next, the novel circuit design is presented. The input-output characteristics of the circuit are evaluated experimentally. Several bimorphs employing MFC actuators are excited with the circuit to prove the effectiveness of the design. The electromechanical response of the bimorphs is experimentally characterized.

Chapter 5 presents the design and analysis of a thin, variable-camber bimorph airfoil that is actuated by MFCs. The coupled static fluid-structure interaction problem is solved by a structural finite element method and panel method employing a potential flow theory. Two prototypes are fabricated and compared to conventional NACA airfoils through wind tunnel experimentation. The lift and drag forces generated by the airfoils are measured using a mechanical beam balance in a two-dimensional (2D) wind tunnel test section. The 2D lift and drag coefficient of the airfoils are compared to results from the literature. Aerodynamic and structural nonlinear effects are identified.

Chapter 6 presents a novel, high load output, bi-directional variable-camber airfoil employing MFC bimorphs. The chapter focuses on actuation modeling and response characterization under aerodynamic loads. A parametric examination of the aerodynamic response is employed to optimize kinematic parameters of the airfoil. Two prototypes of the concept is fabricated and tested in an experimental ducted-fan vehicle. Additional 2D wind tunnel experiments are conducted to quantify the aerodynamic and structural performance results. Nonlinear effects due to aerodynamic and piezoceramic hysteresis are identified and discussed. Results are compared to conventional, symmetric NACA and other airfoils.

Chapter 7 presents the development and implementation of a variable-camber airfoil with a flow control feature. First, using the electromechanical model of a unimorph (presented in Chapter 2), a parametric examination is conducted to identify an actuator to output high deformations at the desired frequency for lift improvement at post-stall angles. The optimum frequency and amplitude for increasing lift coefficient are identified experimentally. Along with aerodynamic force and structural displacement measurements, helium bubble flow visualization

is used to verify existing separated flow, and the attached flow induced by flow control. The lift coefficient enhancement induced by several flow control techniques are compared.

Chapter 8 presents the modeling of piezoceramic hysteresis nonlinearity observed in MFC bimorphs. The hysteresis is modeled for open-loop response using a phenomenological classical Preisach model. Open-loop response is predicted and the model results are compared to experimental results for several bimorph specimens.

Chapter 9 provides a summary of the results from the research. The publications stemming from the research are listed. A discussion of conclusions, recommendations and future work is also presented.

In addition to the chapters outlined above, the dissertation includes a set of appendices that present additional information related to the chapters. Appendix A presents additional unimorph actuation experimental results to the experiments introduced in Chapter 2. Appendix B presents additional energy harvesting results related to Chapter 3. Appendix C presents the experimental stress-strain measurements on several composite materials. The test data presented in this appendix are used to aid the analysis presented in Chapters 4 through Chapter 8. Appendix D presents physical parameters and additional experimental data of the bimorph devices that are presented in Chapter 4. Appendix E presents the low-speed, open circuit wind tunnel that is used for 2D aerodynamic characterization presented in Chapters 5, 6 and 7. The iterations of the wind tunnel and the corresponding calibration data are shown. Appendix F presents additional information for the airfoils presented in Chapters 5, 6 and 7. Finally, Appendix G presents additional hysteresis experiment results from Chapter 8.

CHAPTER 2

ACTUATION CHARACTERIZATION OF UNIMORPH STRUCTURES

This chapter presents experimental and theoretical characterization of beam-like unimorph structures. The goal of the chapter is to understand the actuation capabilities of several active material configurations so that optimal material choices can be employed in lightweight, low power aircraft applications. In order to conduct the analysis, unimorph cantilevered beams are investigated (due to their structural simplicity). The results from this chapter are then used to aid the design of two piezocomposite variable-camber airfoil concepts (presented in Chapter 5 and Chapter 6), and cantilevered beam flow control actuators (presented in Chapter 7).

First, in Section 2.1, a thin, uniform cross-section MFC actuated unimorph is evaluated through analytical modeling and experimental measurements. A distributed parameter analytical model of an MFC actuated thin clamped-free beam is presented. The model prediction of the tip velocity frequency response function is compared to the experimental results. Next, in Section 2.2, the actuation comparison of four nonuniform cross-section unimorph beams with thick substrates is presented. Each beam employs a different kind of piezoelectric material; hence the comparison is aimed to determine the actuator with highest control authority. Finally, in Section 2.3, uniform cross-section beams with single crystal piezoelectrics are experimentally compared to other conventional piezoceramics. As with the previous two sections, the goal is to determine the advantages and disadvantages of different piezoelectrics so that a practical piezocomposite airfoil can be realized. The chapter ends with the summary of conclusions from each section.

2.1. Unimorph Beams with Thin Substrates

In order to predict the transverse vibration response of a cantilevered MFC unimorph due to a dynamic voltage excitation, a distributed parameter formulation is employed here. A similar

distributed parameter model, applied to monolithic piezoceramic cantilevered beam energy harvesters, is presented by Erturk and Inman [2008]. The unimorph cantilever is modeled as a uniform Euler-Bernoulli beam because the interdigitated electrodes have negligible thickness and the beam cross section is small with respect to the bending wavelength at the highest frequency of interest. The unimorph is illustrated in Figure 2.1.

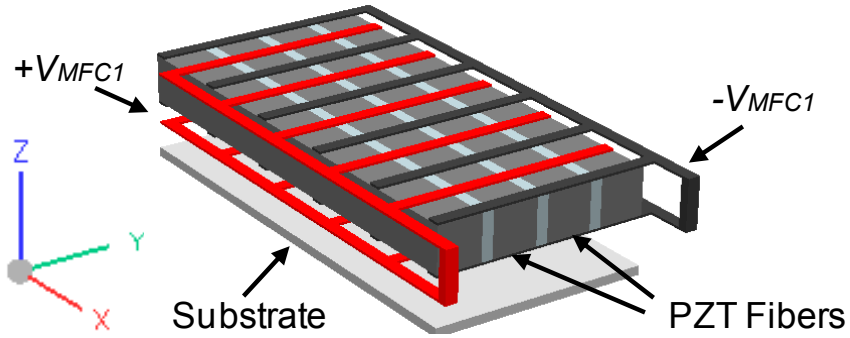

Figure 2.1: A unimorph with piezocomposite fibers and interdigitated electrodes. PZT fibers are scaled up (in relationship to the substrate) to aid the illustration.

The MFCs studied here operate in the *33* mode of piezoelectricity and the respective (well-known) constitutive relation is:

$$T_3 = c_{33}^E S_3 - e_{33} E_3 \tag{2.1}$$

where T_3 is the stress component, S_3 is the strain component, E_3 is the electric field component, e_{33} is the piezoelectric constant and c_{33}^E is elastic stiffness component at constant electric field (reduced for the thin beam theory).

Undamped free vibrations of the beam are governed by:

$$\frac{\partial^2 M(x,t)}{\delta x^2} + c_s I \frac{\partial^5 w(x,t)}{\delta x^4 \delta t} + c_a \frac{\delta w(x,t)}{\delta t} + m \frac{\partial^2 w(x,t)}{\delta t^2} = 0 \tag{2.2}$$

where $M(x,t)$ is the internal bending moment (excluding the strain rate effect), $w(x,t)$ is the transverse deflection, I is the cross-section area moment of inertia, $c_s I$ is the Kelvin-Voigt damping term, c_a is the viscous damping coefficient and m is the mass per unit length of the beam. After expressing the strain component in terms of the curvature and the electric field in terms of the voltage ($E_3(t) = -v(t)/\Delta_{el}$ where $v(t)$ is the voltage across the interdigitated

electrodes and Δ_{el} is the effective electrode spacing) one can integrate the moment of Eq. (2.1) and substitute in Eq. (2.2) to obtain the coupled equation for the forced vibrations of the beam:

$$YI\frac{\partial^4 w(x,t)}{\delta x^4} + c_s I\frac{\partial^5 w(x,t)}{\delta x^4 \delta t} + c_a\frac{\delta w(x,t)}{\delta t} + m\frac{\partial^2 w(x,t)}{\delta t^2} = -v(t)\frac{\partial^2 \Gamma(x)}{\delta x^2} \qquad (2.3)$$

where Y is the elastic modulus and therefore YI is the bending stiffness obtained from the transformed cross-section. $\Gamma(x)$ accounts for the spatial distribution of the electric potential [Erturk et al., 2008] and is defined by:

$$\Gamma(x) = \vartheta\sum_{i=1}^{N_e}\left\{\left(1+\frac{x-x_{i0}}{x_{i0}-x_{i1}}\right)[H(x-x_{i0})-H(x-x_{i1})] + \left(\frac{x-x_{i2}}{x_{i3}-x_{i2}}\right)[H(x-x_{i2})-H(x-x_{i3})]\right\} \qquad (2.4)$$

where N_e is the number of electrode pairs over the beam length ($N_e \cong L_{act}/2(u_e+u_0)$ where L_{act} is the active beam length, u_e is the width of each electrode in the direction of beam axis, u_0 is the width of each non-electroded region in the direction of beam axis), H is the Heaviside function and ϑ is a coupling constant which will be discussed later. At an arbitrary instant of the motion, the electric potential is assumed to be linearly decreasing from $v(t)$ to 0 in $x_{i0} \le x \le x_{i1}$ whereas it is assumed to be linearly increasing from 0 to $v(t)$ in $x_{i2} \le x \le x_{i3}$. The coupling treatment given by Eq. (2.4) is a summation of N_e terms due to the piezoelectric coupling on small fiber elements under the electric field applied. Therefore, the positions x_{i0}, x_{i1}, x_{i2} and x_{i3} change with the index i. As one moves from the clamped end to the free end, the index number increases. For instance, starting from the clamped end, (i.e., for $i = 1$):

$$x_{10} = \frac{u_e}{4}, x_{11} = x_{10} + u_0 + \frac{u_e}{2}, x_{12} = x_{11} + \frac{u_e}{2}, x_{13} = x_{12} + u_0 + \frac{u_e}{2} \qquad (2.5)$$

and so on for $i = 1 \ldots N_e$ with the increasing index number until the end of the active length. Figure 2.2 shows the index scheme for electrodes.

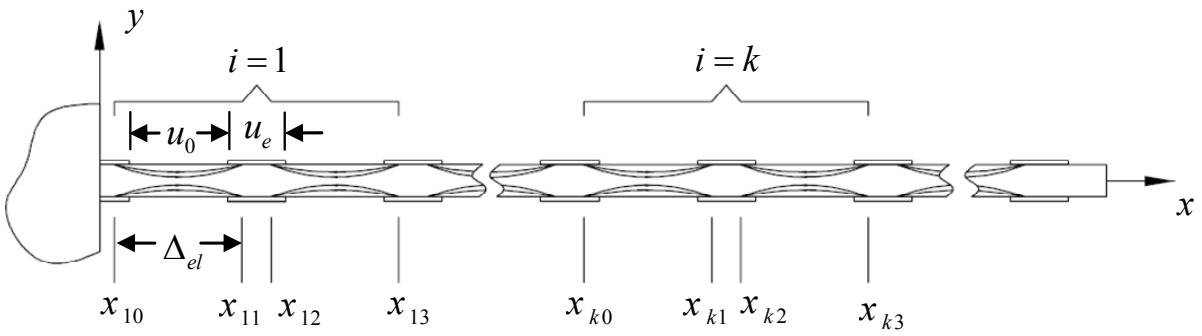

Figure 2.2: Geometric parameters of the interdigitated electrodes used in the coupling term (substrate is excluded). The electrodes are normal to the page.

The effective electrode spacing is calculated by $\Delta_{el} = u_0 + u_e/2$. In Eq. (2.4), the coupling constant is given by:

$$\vartheta = -\frac{e_{33} b_{pt} \left[\left(h_d - \alpha h_p \right)^2 - \left(h_c + \alpha h_p \right)^2 \right]}{2\Delta_{el}} \tag{2.6}$$

where e_{33} is the piezoelectric constant (reduced for the thin beam theory), b_{pt} is the total width of the piezoceramic fibers, h_p is the thickness of the piezoceramic fibers, h_c is the position of the bottom of the piezoceramic layer from the neutral axis and h_d is the position of the top of the piezoceramic layer from the neutral axis. Note that, the electric field is assumed to be uniform over the effective electrode spacing Δ_{el}. The form of the coupling constant given by Eq. (2.6) is similar to the coupling constant given for a unimorph cantilever with a monolithic ceramic where the electric field is uniform and the *31* mode is used instead of the *33* mode with nonuniform electric field in reality. In Eq. (2.6), α is an empirical constant that reduces the thickness of the piezoceramic to an effective value due to nonuniform electric field.

The solution of Eq. (2.3) can be expressed as:

$$w(x,t) = \sum_{r=1}^{\infty} \phi_r(x) \eta_r(t) \tag{2.7}$$

where $\phi_r(x)$ and $\eta_r(t)$ are the mass normalized eigenfunction and the modal response of the clamped-free beam for the *r*-th mode, respectively. For a proportionally damped system, the mass normalized eigenfunctions denoted by $\phi_r(x)$ are given by:

$$\phi_r(x) = \sqrt{\frac{1}{mL}} \left[cosh\frac{\lambda_r}{L}x - cos\frac{\lambda_r}{L}x - \sigma_r \left(sinh\frac{\lambda_r}{L}x - sin\frac{\lambda_r}{L}x \right) \right] \tag{2.8}$$

where the dimensionless frequency numbers (λ_r) are obtained from

$$1 + cos\,\lambda_r\, cosh\,\lambda_r = 0 \tag{2.9}$$

and σ_r is expressed as

$$\sigma_r = \frac{sinh\lambda_r - sin\lambda_r}{cosh\lambda_r + cos\lambda_r}. \tag{2.10}$$

Moreover, ω_r is the undamped natural frequency of the *r*-th mode:

$$\omega_r = \lambda_r^2 \sqrt{\frac{YI}{mL^4}} \tag{2.11}$$

which is approximately the resonance frequency (for light mechanical damping) of the unimorph when the electrodes are shorted. The eigenfunctions satisfy the following orthogonality conditions:

$$\int_{x=0}^{L} m\phi_s(x)\phi_r(x)dx = \delta_{rs}, \int_{x=0}^{L} YI\phi_s(x)\frac{d^4\phi_r(x)}{dx^4}dx = \omega_r^2\delta_{rs}. \tag{2.12}$$

Using Eq. (2.7) in Eq. (2.3) and applying the orthogonality conditions of the eigenfunctions gives the electromechanically coupled ordinary differential equation for the modal response of the beam as:

$$\frac{d^2\eta_r(t)}{dt^2} + 2\zeta_r\omega_r\frac{d\eta_r(t)}{dt} + \omega_r^2\eta_r(t) = -\chi_r v(t) \tag{2.13}$$

where

$$\chi_r = \vartheta\sum_{i=1}^{N_e}\left(\frac{\phi_r(x_{i0}) - \phi_r(x_{i1})}{x_{i0} - x_{i1}} + \frac{\phi_r(x_{i2}) - \phi_r(x_{i3})}{x_{i3} - x_{i2}} + \frac{d\phi_r(x)}{dx}\Big|_{x_{i0}}^{x_{i3}}\right) \tag{2.14}$$

and based on the proportional damping assumption, ζ_r is the modal mechanical damping ratio and it is related to the physical damping parameter through:

$$\zeta_r = \frac{c_s I\omega_r}{2YI} + \frac{c_a}{2m\omega_r}. \tag{2.15}$$

For harmonic excitation of the bimorph (i.e., $v(t) = V_0 e^{j\omega t}$ where ω is the driving frequency and j is the unit imaginary number), the steady state response of Eq. (2.13) becomes:

$$\eta_r(t) = \frac{-\chi_r V_0 e^{j\omega t}}{\omega_r^2 - \omega^2 + 2j\zeta_r\omega_r\omega}. \tag{2.16}$$

Physical steady state response of the beam is then obtained by substituting Eq. (2.16) into Eq. (2.7):

$$w(x,t) = \sum_{r=1}^{\infty} \frac{-\chi_r \phi_r(x)}{\omega_r^2 - \omega^2 + 2j\zeta_r\omega_r\omega} V_0 e^{j\omega t}. \tag{2.17}$$

Hence the steady state response of the beam at its free end is:

$$w(L,t) = \sum_{r=1}^{\infty} \frac{-\chi_r \phi_r(L)}{\omega_r^2 - \omega^2 + 2j\zeta_r\omega_r\omega} V_0 e^{j\omega t}. \tag{2.18}$$

2.1.1. Parametric Evaluation of Unimorph Actuators

The theoretical actuation response of the MFC actuated unimorph is presented here. Before the development of the theoretical model, 12 unimorphs specimens are fabricated (presented in the next section,) and their electromechanical properties are measured to determine the parameters of the model. The unimorph considered here employs a single M8507-P1 type MFC manufactured by Smart Material Inc., Germany [MFC M8507-P1] which use the *33* mode of piezoelectricity. In-order to accurately model the PZT fibers and the interdigitated electrodes, a sample of (non-bonded) MFC M8507-P1 type actuator, shown in Figure 2.3, is examined under a microscope.

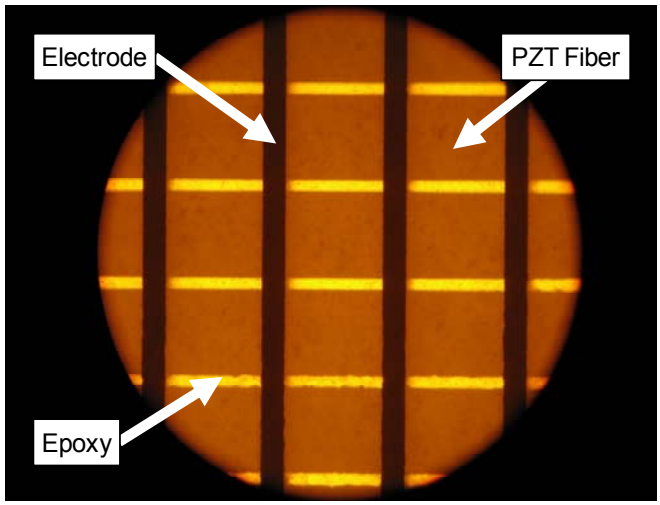

Figure 2.3: Digital photograph of the planar view of a MFC M8507-P1 actuator under a microscope.

The measured values are cross-checked with the ones provided by the manufacturer and the following values are used: Thickness and width of each piezoceramic fiber are approximately 180 μm and 355 μm respectively, and each epoxy layer between the fibers has a width of 51.25 μm. The total thickness of the active region is *MFC th* = 305 μm and therefore each of the top and bottom Kapton layers in the active region is 60 μm thick. Since the total active width is approximately 7.3 mm, each sample has approximately 18 piezoceramic fibers, yielding a total piezoceramic width of $b_{pt} = 6.4$ mm. The width of each electrode in the direction of beam length is $u_e = 97$ μm and the spacing between the electrodes is $u_0 = 410$ μm. Therefore, the number of electrode pairs over the beam length is $N_e \cong 72$ (~144 electrode fingers) and the effective electrode spacing is about $\Delta_{el} = 458.5$ μm. The M8507-P1 uses Navy II piezoceramics, for which the effective value of the piezoelectric constant is approximately $e_{33} = 19.1$ C/m^2. Additional images and data of the MFC M8507-P1 type device can be seen in Appendix A.2.

Three different substrate materials (with a range of thicknesses) are examined. Total overhang length of the unimorphs are approximately 80 mm and the overhang length of the active area is set to be $L_{act} \cong 73$ mm during clamping. The total width of each unimorph is 16.28 mm (which is also the original width of the MFC M8507-P1 type actuator). The substrate materials investigated are aluminum (Al), brass (Br) and stainless-steel (Ss) available from McMaster-Carr, Aurora, OH, USA. The Young's moduli for these substrate materials are taken as 70 GPa, 105 GPa and 200 GPa respectively. The Young's modulus of the Kapton is 3.0 GPa. The Young's modulus of the piezoceramic fibers (alone) is taken as 64 GPa. The epoxy type used for bonding the substrate and MFC layers is 3M DP460 and its shear strength is approximately 31 MPa. The substrate thicknesses and the average thicknesses of the epoxy layers between the substrate and the MFC layers are presented in the next section. Mass-per-length of the MFC and the epoxy layers is estimated experimentally as 0.0123 kg/m. Total mass-per-length of each sample is estimated by adding this value to the mass per length of each substrate. Here, the mass densities of the aluminum, brass and stainless-steel substrates are taken as 2700 kg/m^3, 9000 kg/m^3 and 7800 kg/m^3 respectively.

A parametric examination is conducted using the solution given in Eq. (2.18) and the parameters given above. A damping ratio of 0.005 is assumed for all modes. It is important to note that the effect of damping ratio is dominant in the absolute values of the model prediction;

therefore the predictions below can have small absolute value differences from the actual response. The purpose of this section is to understand the relative response due to the effects of thickness ratio and substrate modulus. The solution is obtained for different Young's modulus and thickness ratio of substrate with respect to the constant MFC thickness of 0.305 mm. The effect of the empirical correction factor is also demonstrated. An average value of α=0.20 is identified by matching the model predictions for a set of experiments (discussed later) using M8507-P1 type MFC with different substrates. The maximum tip-velocity-per-excitation-voltage (at the corresponding resonance frequency) is presented in Figure 2.4.

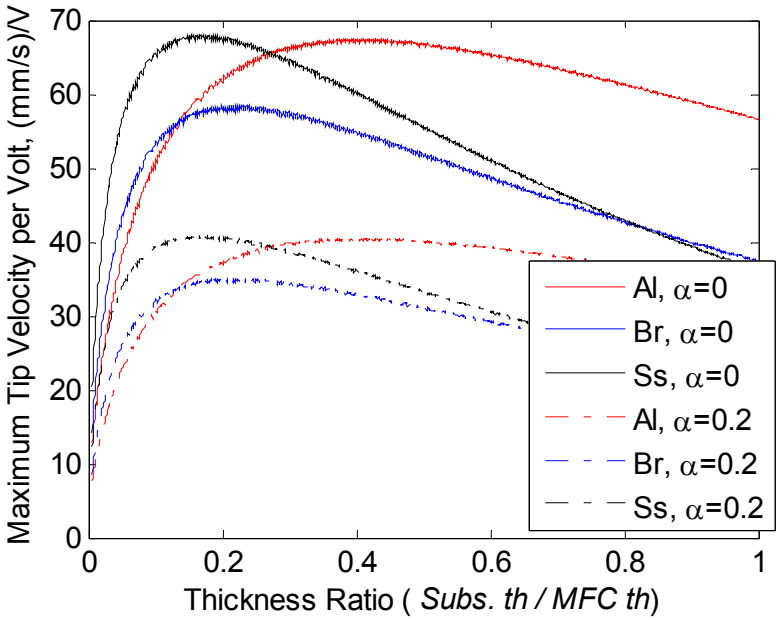

Figure 2.4: Theoretical maximum tip velocity response to harmonic excitation for a range of thickness ratios. Response corresponds to the 1st bending resonance of a cantilevered beam.

It is important to note that the empirical correction factor (α) does not change the "optimum" thickness ratio, and that it is only an amplitude-wise effect. The tip velocity shown is the maximum velocity achieved by the unimorph free end at its first bending resonance frequency. The effect of empirical electric field correction factor (α) can also be seen. Note that the frequency of maximum velocity (the first resonance frequency) changes from sample to sample because the moment of inertia and the mass per length are different between each sample.

The specific trend observed in Figure 2.4 is also specific to the mass density of aluminum, brass and stainless-steel. The trend would be different (for a set of hypothetical) substrates if their density is constant; however the axial stiffness (E_1) is varied. Such case is illustrated (qualitatively) with a three dimensional plot in Figure 2.5, where the substrate Young's modulus is varied between 0.01 GPa through 2000 GPa, representing materials from rubbers to carbon nanotubes. The two dimensional version of the figures in this section (for selected Young's moduli) are presented in Appendix A.3 for better quantitative representation. Note that the material density is assumed constant at 2700 kg/m^3 for the three dimensional plots presented next. In addition, the large bending strains and stresses are assumed to be acceptable by the substrate material and the MFC actuator.

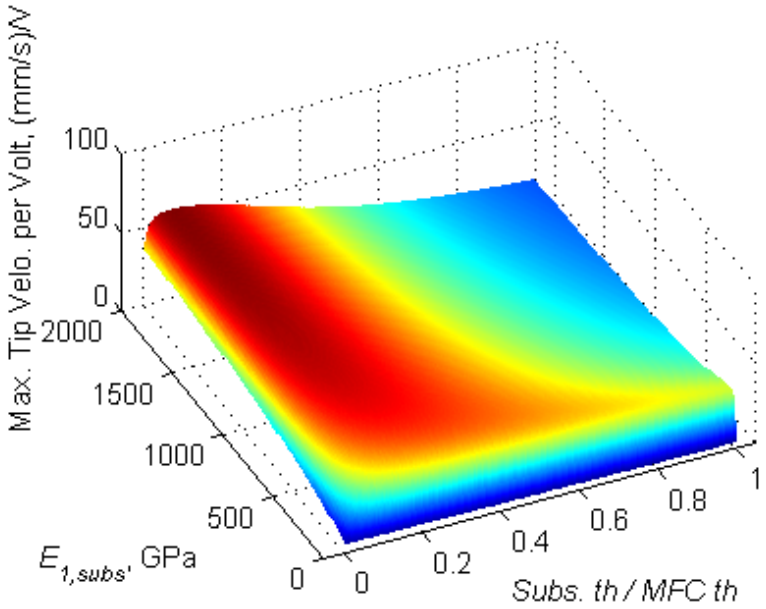

Figure 2.5: Theoretical maximum tip velocity response to harmonic excitation for a range of substrate Young's moduli and thickness ratios. (α = 0.2, ρ_{subs} = 2700 kg/m^3)

The variation of the first natural frequency of MFC unimorphs with aluminum, brass and steel substrates is given in Figure 2.6. Note that the empirical correction factor does not have any effect on the resonance frequency variation.

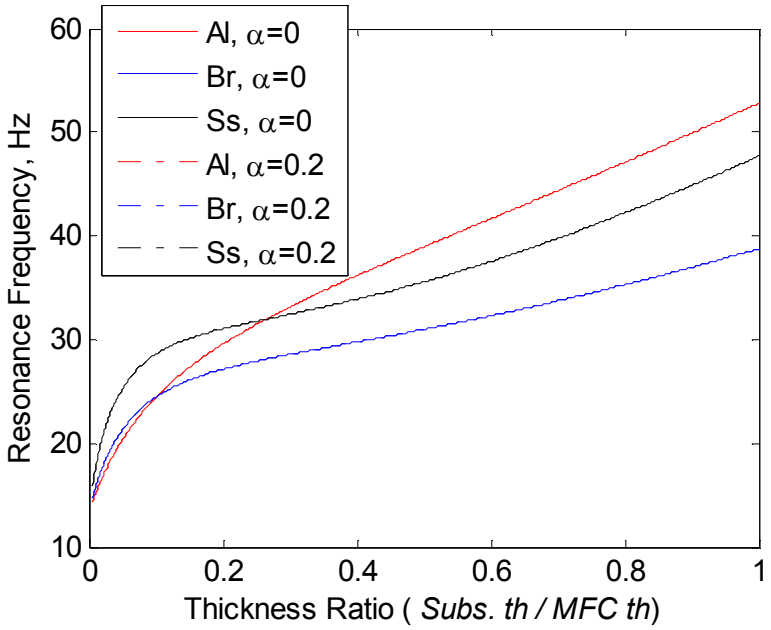

Figure 2.6: Theoretical variation of 1st bending resonance frequency (in response to harmonic excitation) with substrate thickness and material.

Similar to maximum tip velocity (presented in Figure 2.4), the resonance frequency is also dependent on the substrate density; therefore the trends presented in Figure 2.6 will be different if other materials are used. Figure 2.7 presents the resonance frequency response for a fixed density (2700 kg/m^3) and variable Young's moduli substrate material. As expected, the resonance frequency is monotonically increasing with substrate stiffness when the substrate density is kept constant.

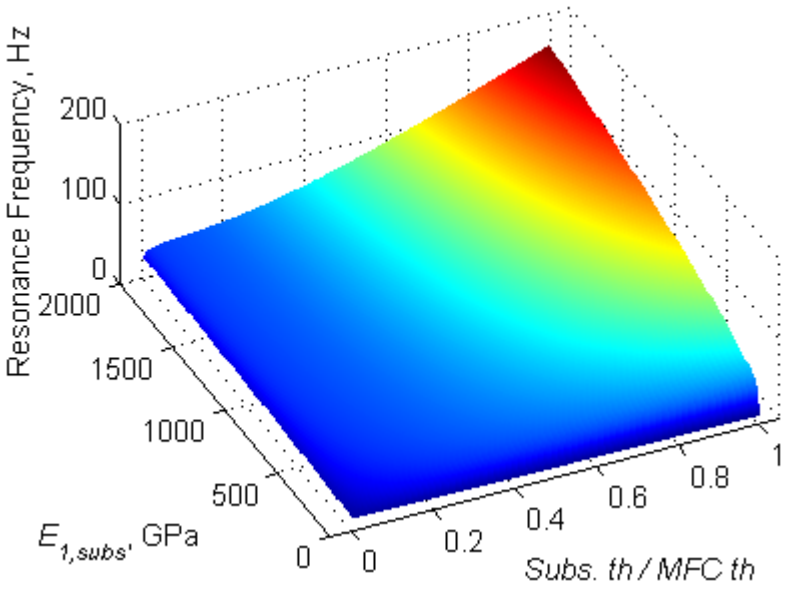

Figure 2.7: Theoretical variation of 1st bending resonance frequency for a range of substrate Young's moduli and thickness ratios. (α = 0.2, ρ_{subs} = 2700 kg/m^3)

Note that the substrate density (and mass-per-length of the unimorph) effects only 1) velocity output (shown in Figure 2.4 and Figure 2.5) and 2) resonance frequency (shown in Figure 2.6 and Figure 2.7).

The tip-velocity-per-excitation-voltage FRF is integrated in the frequency domain (assuming zero for the constant of integration) to get the maximum tip displacement, again at the corresponding 1st bending resonance frequency. Figure 2.8 shows the displacements for aluminum, brass and stainless-steel substrate materials and thickness ratios.

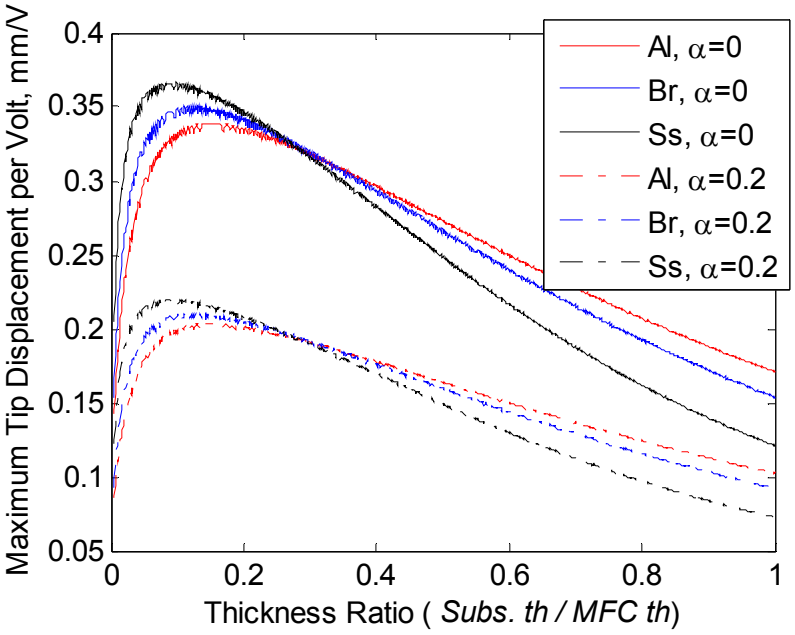

Figure 2.8: Theoretical maximum tip displacement response to harmonic excitation for a range of thickness ratios. Response corresponds to the 1st bending resonance of a cantilevered beam.

The effect of the substrate material Young's modulus shows as a change in the maximum displacement (and the corresponding optimum thickness ratio). The stainless-steel substrate shows the highest displacement, however the thickness ratio is less when compared to aluminum substrate. Figure 2.9 presents the maximum tip displacement per excitation voltage for a range of thickness ratios and substrate Young's moduli. It is observed that larger deformations can be achieved for substrate materials that have very high Young's modulus (or high axial stiffness) and very low thicknesses (resulting in low bending stiffness).

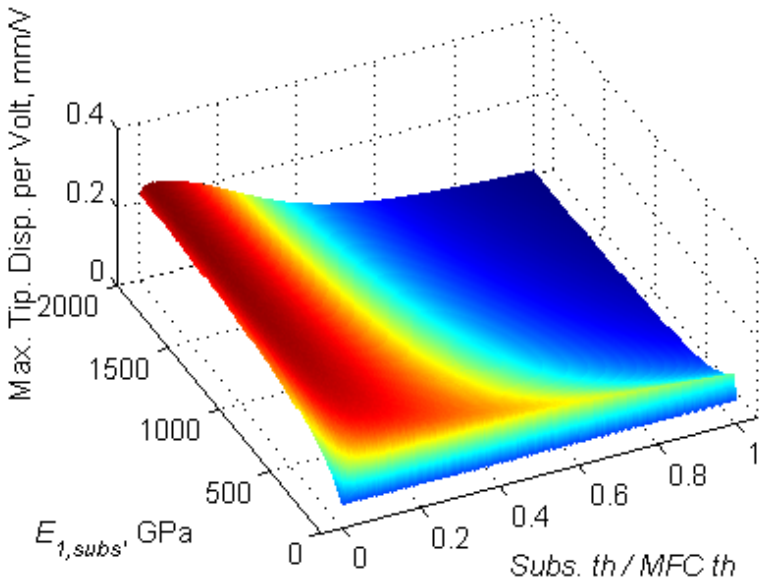

Figure 2.9: Theoretical maximum tip displacement response to harmonic excitation for a range of substrate Young's moduli and thickness ratios. (α = 0.2)

For the displacement output predictions, the effect of substrate material density is diminished; therefore Figure 2.9 actually applies to any material density. Finally, the analysis is presented for static actuation (sufficiently below the first natural frequency) where the inertial effects simply vanish. The peak tip displacement for static actuation of unimorph actuators are presented in Figure 2.10.

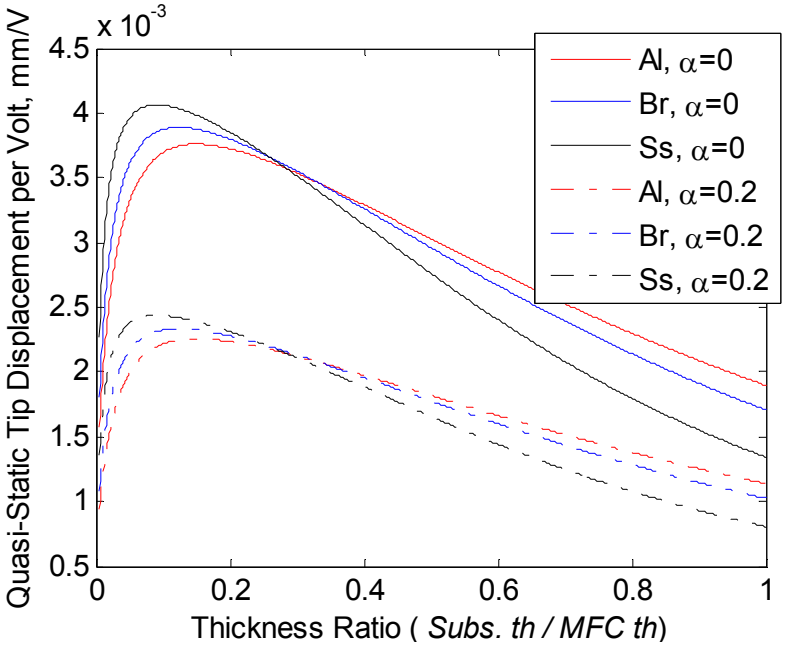

Figure 2.10: Theoretical static tip displacement per volt for a range of thickness ratios.

The results given in Figure 2.10 for a unimorph actuator are modeled and experimentally verified in the literature [Inman and Cudney, 2000]. As mentioned earlier, the value of the empirical correction factor (α) shifts the amplitude of displacement, but not the optimum thickness ratio. The model presented here considers the linear and low amplitude actuation, so a geometrically nonlinear and highly hysteretic high amplitude actuation may not be predicted well. The static tip displacement analysis is extended to range of Young's moduli and thickness ratios.

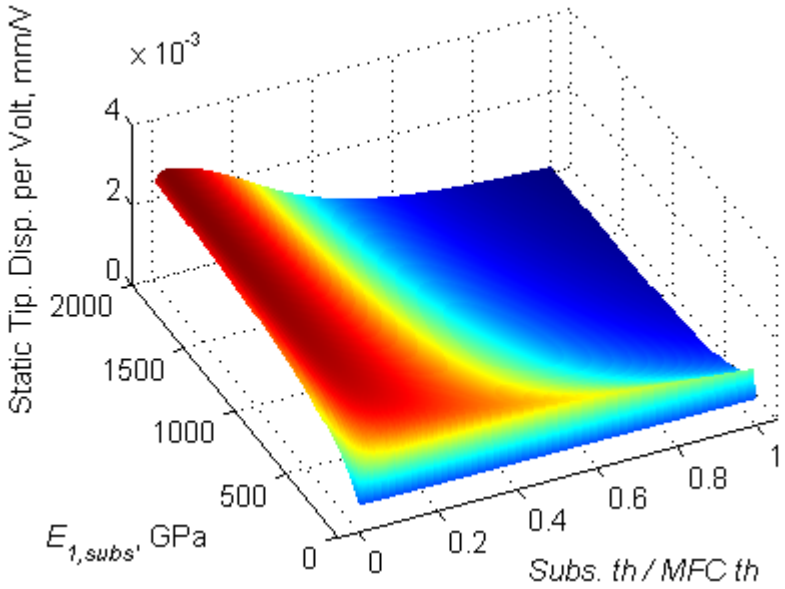

Figure 2.11: Theoretical static tip displacement per volt for a range of substrate Young's moduli and thickness ratios. (α = 0.2)

Looking at the effect of substrate properties presented in this section, clearly a thin and axially stiff substrate material is the best choice for and MFC actuated unimorphs. The increase in displacement-output-per-excitation-voltage is significant for soft materials; however beyond a certain Young's moduli, the response does not change. For an MFC actuated unimorph, substrate modulus of 1000 GPa (carbon nanotube) achieves 98% and 200 GPa (stainless-steel) achieves 91% of the maximum bending displacement.

2.1.2. Experimental Validation

Twelve unimorphs are fabricated by bonding an MFC actuator to commercial sheet metal substrates with epoxy to validate the analytical model. Samples are bonded in vacuum bag to minimize variation in epoxy thickness, and air gaps. Each sample employs a single M8507-P1

type MFC manufactured by Smart Material Inc [MFC M8507-P1] which use the *33* mode of piezoelectricity. The details of the MFC actuator are presented in the previous section. Substrate thicknesses and the average thicknesses of the epoxy layers between the substrate and the MFC layers are shown in Table 2.1. Note that the epoxy thickness has a relatively large variation of ±0.02 mm which is an important source of uncertainty. The epoxy thicknesses listed in the table are fine tuned for the model predictions by comparing the analytical first natural frequency and the experimental natural frequency when the system is close to short circuit condition. It is observed that the amplifier(s) used in this section (and other chapters dealing with actuation) have 1) negligible electrical dynamics and 2) have very low output impedance, therefore the short circuit assumption is valid.

Table 2.1: Thickness properties of each unimorph and its epoxy layer. MFC has an active area thickness of 0.305 mm.

Sample	Substrate	*Subs. th* (mm)	*Subs. th / MFC th*	*Epoxy th* (mm)
Al 2	Aluminum	0.0547	0.18	0.0187
Al 3	Aluminum	0.0776	0.25	0.0152
Al 4	Aluminum	0.1071	0.35	0.0474
Al 5	Aluminum	0.1218	0.40	0.0376
Br 1	Brass	0.0300	0.10	0.0077
Br 2	Brass	0.0551	0.18	0.0189
Br 3	Brass	0.0772	0.25	0.0133
Br 4	Brass	0.0975	0.32	0.0359
Ss 1	Stainless-Steel	0.0274	0.09	0.0100
Ss 2	Stainless-Steel	0.0537	0.18	0.0165
Ss 3	Stainless-Steel	0.0776	0.25	0.0050
Ss 4	Stainless-Steel	0.1007	0.33	0.0454

The frequency response prediction of the model is compared to the experimental measurements of the 12 MFC unimorphs. Figure 2.12 presents the tested unimorph actuators and the clamp used for testing. The design of the clamp and the details of the boundary conditions are discussed in Appendix A.1. A Polytec PDV-100 laser vibrometer is used to measure the tip velocity of the cantilevers, 79 mm from the clamped end. The actuators are excited with a 2.5 Vpeak pure sine tone generated by the data acquisition system. The excitation signal is buffered

by an HP 6826A bipolar amplifier with unity gain. A Siglab 20-42 frequency analyzer system is used for data processing.

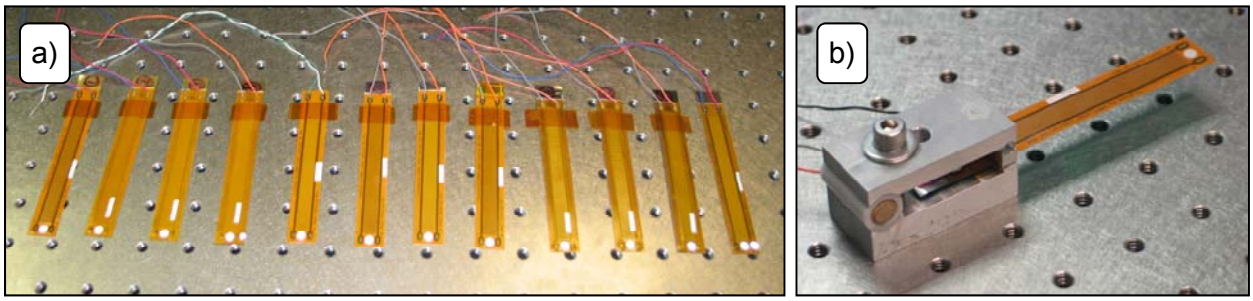

Figure 2.12: a) Twelve unimorphs. b) One of the unimorphs clamped for testing.

A virtual sine sweep is used for the frequency response function (FRF) measurements, where the excitation is a pure sine tone at constant frequency. The frequency is incremented only when transients are decayed from the previous frequency. This method is utilized to avoid transients caused by more common (and faster) techniques, such as a chirp excitation. The FRF is measured for tip-velocity-to-harmonic-voltage-excitation. Comparison of the model predictions and the experimental measurements are presented in Figure 2.13 through Figure 2.15. Note that only two thicknesses for each material are shown for plot clarity.

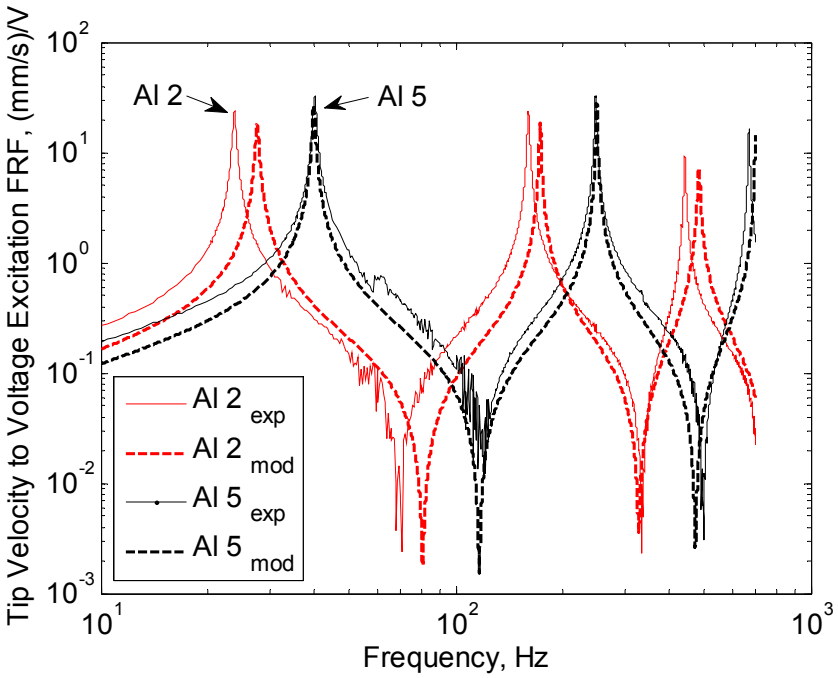

Figure 2.13: Tip-velocity-to-actuation FRF comparison of experiments to model for unimorph samples Al 2 and Al 5.

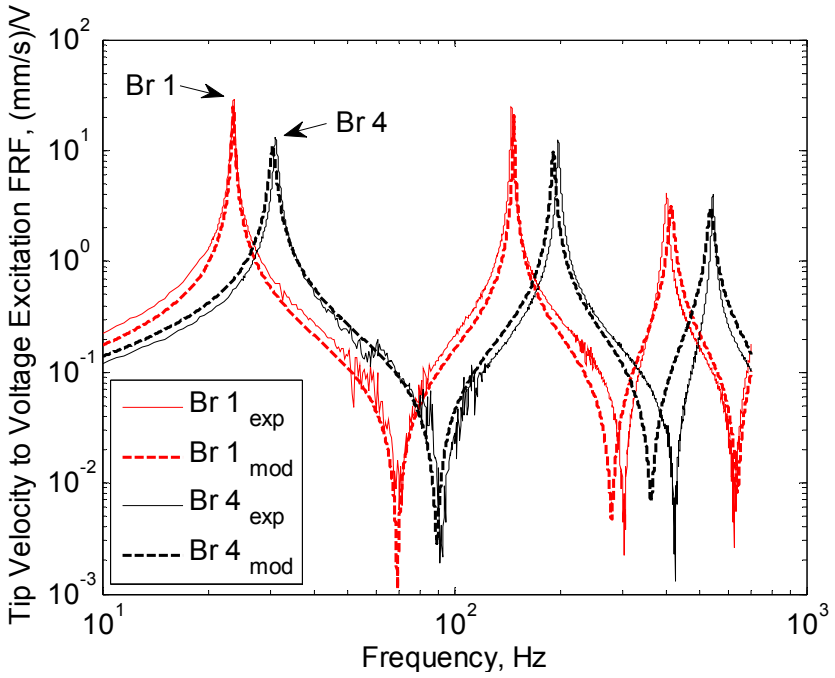

Figure 2.14: Tip-velocity-to-actuation FRF comparison of experiments to model for unimorph samples Br 1 and Br 4.

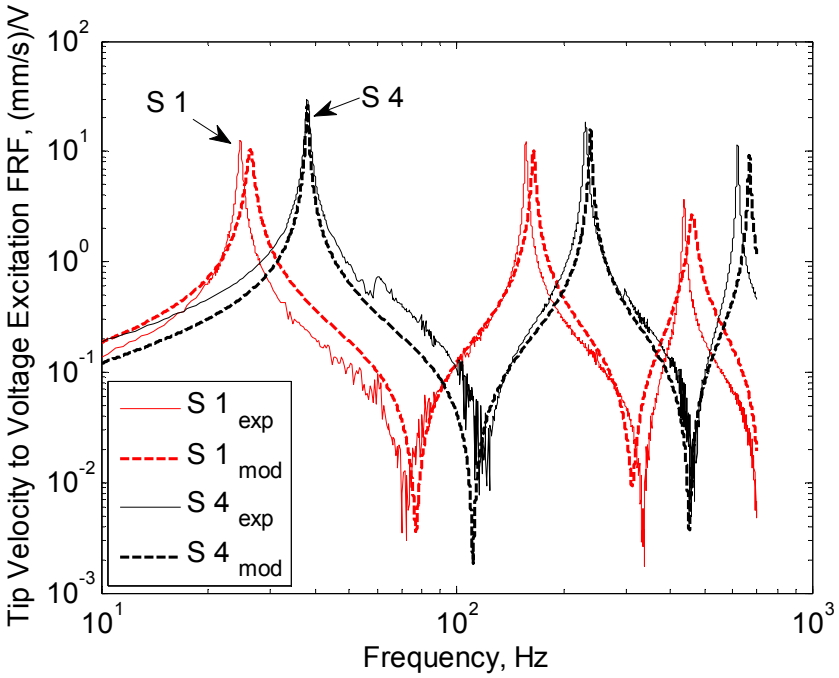

Figure 2.15: Tip-velocity-to-actuation FRF comparison of experiments to model for unimorph samples Ss 1 and Ss 4.

Additional results are presented in Appendix A.4. The FRFs presented above shows the unimorphs with aluminum, brass and steel substrates with two different thicknesses. The model predictions and the experimental results correlate very well. It must be noted that bending stiffness used for the model is purely theoretical so there is a small mismatch between the experimental and the model prediction for the first natural frequency. One can "calibrate" the bending stiffness to match the prediction to the experimental values; however such a method is not utilized here. Table 2.2 shows a comparison of first three natural frequency predictions to the experimental values for all 12 unimorphs.

Table 2.2: Comparison of experimental and predicted natural frequencies in Hz.

	ω_1 exp	ω_1 mod	ω_1 %error	ω_2 exp	ω_2 mod	ω_2 %error	ω_3 exp	ω_3 mod	ω_3 %error
Al 2	23.8	27.6	16.0	160.0	172.9	8.1	441.9	484.0	9.5
Al 3	31.5	32.9	4.4	194.9	206.2	5.8	530.2	577.2	8.9
Al 4	34.3	34.2	-0.4	227.3	214.3	-5.7	612.8	600.1	-2.1
Al 5	40.1	39.8	-0.6	247.4	249.6	0.9	669.3	698.7	4.4
Br 1	23.7	23.6	-0.4	145.5	147.7	1.5	401.5	413.7	3.0
Br 2	25.5	25.4	-0.6	165.2	158.9	-3.8	454.4	445.0	-2.1
Br 3	29.1	28.9	-0.7	178.6	181.2	1.4	486.4	507.3	4.3
Br 4	31.1	30.6	-1.8	197.5	191.3	-3.1	543.2	535.8	-1.4
Ss 1	24.7	26.3	6.5	156.6	164.7	5.1	436.9	461.2	5.6
Ss 2	30.7	30.5	-0.5	192.2	191.1	-0.6	521.0	535.1	2.7
Ss 3	32.0	31.6	-1.3	200.6	197.7	-1.4	550.4	553.7	0.6
Ss 4	38.1	38.1	0.0	230.5	238.4	3.4	617.9	667.4	8.0

The prediction of the model for higher modes is simply a shift in the same direction relative to the shift observed in the first frequency. Considering the Euler-Bernoulli assumptions, this consistent shift is expected since it over-predicts the natural frequencies (due to effectively stiffer assumptions of material behavior). The nonuniform shear layer (at the epoxy interface) is also neglected here (due to low excitation voltages) which is another source of variance of the structure from the model assumptions.

2.2. Unimorph Beams with Thick Substrates

This section presents an electromechanical comparison of the actuation capabilities of a clamped-free Macro-Fiber Composite (MFC) actuated unimorph to other unimorphs employing monolithic piezoceramic wafers. Four unimorphs are fabricated by bonding different commercially available piezoceramic devices to four identical clamped-free aluminum beams. The unimorphs are evaluated for their actuation performance via displacement induced with voltage excitation.

Four identical clamped free aluminum beams are used as substrate for the piezoceramic devices. Unimorph devices are fabricated by bonding the piezoceramic to the beam close to the base of the beams with 3M DP460 epoxy. Samples are bonded in vacuum bag to minimize variation in epoxy thickness, and air gaps, hence achieving a minimum variation in dynamic response. The following four piezoceramic devices are used: 1) PSI PZT-5A4E [PSI PZT-5A4E], 2) PSI PZT-5H4E [PSI PZT-5H4E], 3) MIDE QP10N [MIDE QP10N] and 4) MFC M8528-P1 [MFC M8528-P1], which will be referred to as Beam 1 through 4 respectively. In this section, the *31* mode devices are monolithic piezoceramic wafers and the *33* mode device is a piezoelectric fiber composite. Monolithic piezoceramics considered are models PZT-5A4E and PZT-5H4E (labeled PZT-5A and PZT-5H respectively) from Piezo Systems, Inc., Woburn, MA, USA and model QP10N device from MIDE Technologies, Medford, MA, USA. Uses for industry-type 5A include accelerometers, hydrophones, low power structural control, and stable sensors. The industry-type 5H piezoceramic is used in areas requiring sensitive receivers, fine motion control, and low power structural control. The *33* type device, MFC M8528-P1 is manufactured by Smart Material Corp, Germany, which uses industry-type 5A ceramic.

The sizes of these piezoceramic devices are chosen so that the ceramic thickness and total ceramic mass are relatively close one another. In this research, transduction effectiveness is evaluated both by maximum values achieved (such as displacement, power output, control authority, etc.,) and also by those values normalized by the total ceramic mass. The substrate material is chosen as an aluminum beam with 3.05 mm thickness, 28 mm width, 450 mm length. The beams weigh 140 grams each. The dimensions are chosen so that the transverse displacement of the system can be represented by Euler-Bernoulli beam theory with uniform cross-section; hence the effort is concentrated on the piezoceramic device comparison and not the beam dynamics. Here, it is assumed (and later verified in Section 3.2 and Section B.2) that

the addition of the active material has 1) a small effect on the mass-per-length and the stiffness of the beam and 2) a negligible effect on the mode shapes due to the large substrate-to-actuator mass and thickness ratios. Since the mode shapes are not changed by the addition of the piezoceramic, the unimorph is assumed to have a uniform cross-section (through its length). Figure 2.16 shows the four beams and the experimental setup used for actuation and control experiments.

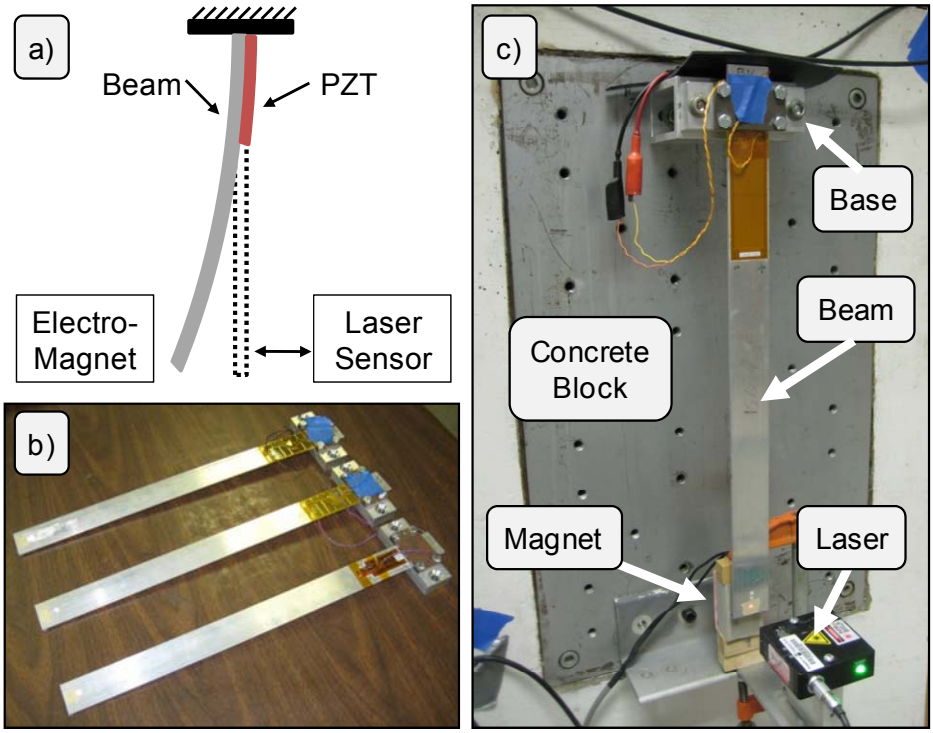

Figure 2.16: a) Illustration of the cantilevered unimorph. b) Beam 1-3 with monolithic ceramics. c) Experimental setup for actuation and control experiments with Beam 4 installed. The Polytec vibrometer is not shown.

Figure 2.16a illustrates the cantilevered unimorph beam setup with the laser (displacement and velocity) sensor and the electro-magnet for release in feedback control experiments. Note that the electro-magnet is used only during the control experiments to achieve a repeatable release of the beam from a non-zero displacement and zero velocity initial condition. Figure 2.16b shows the three beams with the monolithic ceramics (Beams 1-3). In Figure 2.16c, the beam with MFC M8528-P1, mounted vertically on an inertial mass (concrete block) is shown. The properties of the piezoceramic devices on the beams are given in Table 2.3.

Table 2.3: Piezoceramic properties of four test specimens.

Piezoelectric Properties	PSI PZT-5A	PSI PZT-5H	MIDE QP10N	MFC M8528-P1
Beam Designation	1	2	3	4
Electromechanical Mode	*31*	*31*	*31*	*33*
Navy / Industry Type	II / 5A	VI / 5H	II / 5A	II / 5A
Length, l_{pzt} (mm)	72.4	72.4	46	85
Width, w_{pzt} (mm)	34.7	34.7	20.6	28
Thickness, *PZT th* (mm)	0.267	0.267	0.254	0.180
Thickness Ratio, *Subs. th / PZT th*	11.4	11.4	12.0	16.9
Mass, *m* (gr)	5.23	5.23	1.88	2.92
Density, ρ (gr/cm^3)	7.8	7.8	7.8	7.8
Mechanical Quality, Q_M	80	32	80	80
Relative Dielectric Constant, K_3^T {1kHz}	1900	3800	1900	1900
Electromechanical Coupling, k_{33}	0.72	0.75	0.72	0.72
Electromechanical Coupling, k_{31}	0.35	0.44	0.35	0.35
Strain / applied field, d_{33} (pm/V)	390	650	390	460
Strain / applied field, d_{31} (pm/V)	-190	-320	-190	-210
Electrode Spacing (mm)	0.267	0.267	0.254	0.5
Initial Depolarizing Field, *Ec* (10^5 V/m)	5	3	5	30
Coercive Field, *Ec* (10^5 V/m)	12	8	12	12
Maximum Voltage (V)	±134	±80	±200	+1500 (-500)
Curie Temperature, T_C (°C)	350	230	350	350
Compliance, s_{11}^E (10^{-12} m^2/N)	16.4	16.5	16.4	16.4
Compliance, s_{13}^E (10^{-12} m^2/N)	-7.22	-9.21	-7.22	-7.22
Compliance, s_{33}^E (10^{-12} m^2/N)	18.8	20.7	18.8	18.8
Compliance, s_{44}^E (10^{-12} m^2/N)	47.5	43.5	47.5	47.5

2.2.1. Electrical Impedance Characteristics

Electrical impedance spectroscopy is performed using an Autolab PGSTAT12 (Eco Chemie) Potentiostat/Galvanostat with a FRA2 module controlled by FRA and GPES software. Electrical impedance measurements of the beams are obtained using a 250 mV_{RMS} sinusoidal potential swept from 10 kHz to 10 mHz. For these measurements, a 120 kOhm resistive load is connected parallel with the piezoceramic. The measurement system applies a controlled

sinusoidal signal to the system, and current is measured. The experimental impedance magnitude and phase and the parallel resistor-capacitor (RC) circuit fit is shown in Figure 2.17.

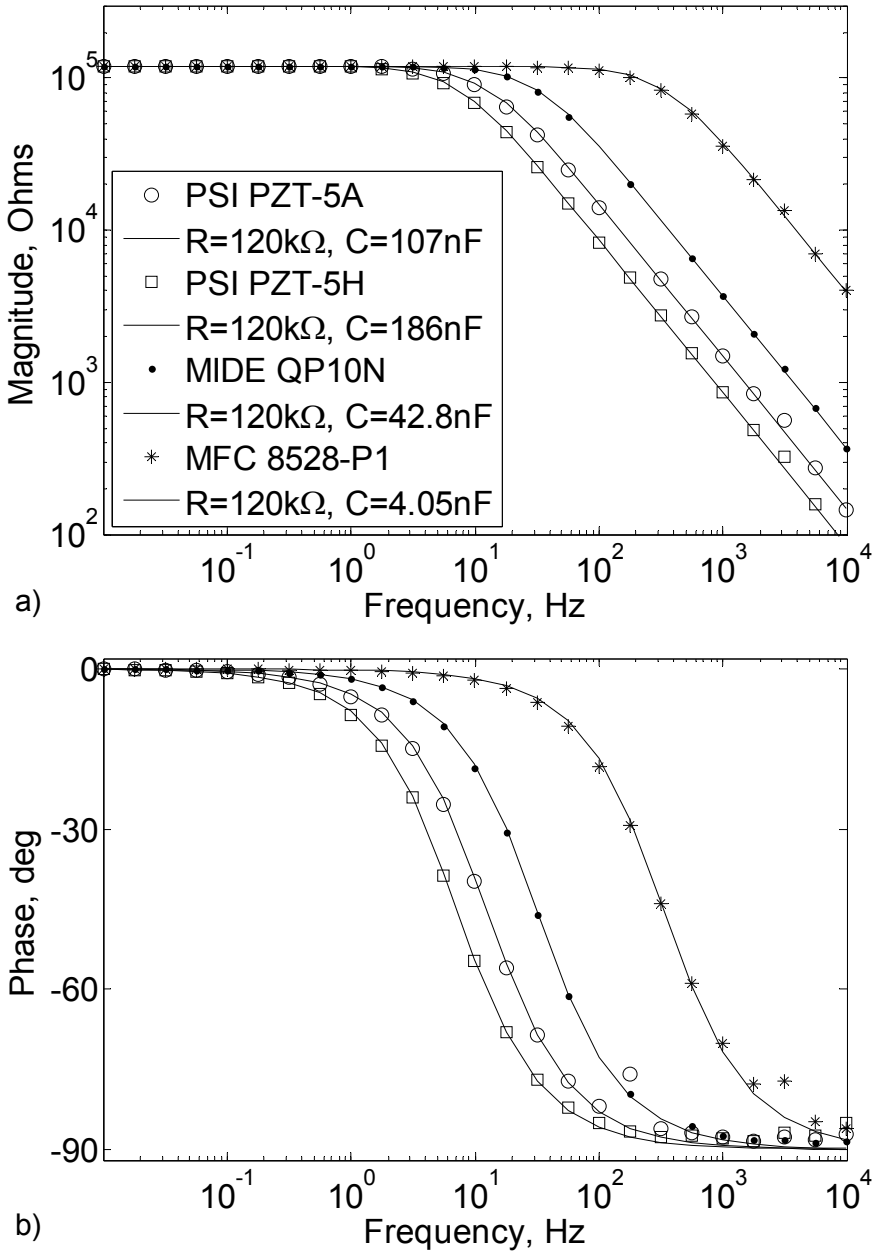

Figure 2.17: Electrical impedance a) magnitude and b) phase of four clamped-free unimorph beams with 120k Ohm resistive shunt.

The results are deduced from the complex impedance measurement of the system. The resistor of 120 kOhm is estimated with high accuracy. As expected, the MFC has very low

capacitance (due to its interdigitated electrodes in the fiber direction) when compared to the other monolithic ceramics with through-the-thickness electrode configuration.

2.2.2. Actuation Characteristics

The devices studied here are clamped-free benders that are composed of an active material bonded on a metal substrate. The linear electromechanical actuation modeling of the MFC unimorph (which is the more complex of the four beams) is briefly described in this section, and in more detail in Section 2.1.

A parametric examination is conducted (not shown here) using the solution given in Eq. (2.18) to understand the effect of the small ceramic thickness variation between the four beams. A damping ratio of 0.005 is assumed for all modes. The solution is found for a thickness ratio of an aluminum substrate with respect to the constant total MFC thickness of 0.305 mm (with 0.180 mm ceramic thickness). The Young's modulus and mass density for aluminum is taken as 70 GPa and 2700 kg/m^3 respectively. The Young's modulus of the piezoceramic fibers (alone) is taken as 64 GPa. The epoxy type used for bonding the substrate and MFC device is 3M DP460 and its shear strength is approximately 31 MPa. Note that the epoxy thickness has a negligible variation between each sample due to the thickness ratio considered in this research. Beam 4 employs an M8528-P1 type MFC actuator, which uses the *33* mode of piezoelectricity.

It is well known that the resonance frequency of the unimorph actuator is affected by its moment of inertia and the mass per length. Therefore, the maximum tip displacement of the unimorph free-end occurs at different frequencies for different substrate thicknesses. An optimum thickness ratio of substrate-to-ceramic (*Subs. th / PZT th*) exists which achieves the highest displacement-per-excitation-voltage. For the current beam dimensions, the thickness ratios considered are significantly higher than this optimum thickness ratio. As the thickness ratio is increased, the strain transfer to and from the active material is monotonically decreasing for the thickness ratio range of interest of 11.4 to 16.9.

The frequency response prediction of the model is compared to the experimental case for the MFC unimorph beam. A Polytec OFV-303 laser vibrometer and a Siglab 20-42 frequency analyzer is used to measure the tip velocity of the cantilevers. A virtual sine sweep is used for the frequency response function (FRF) measurements, where the excitation is a pure sine tone at constant frequency. The frequency is incremented only when transients are decayed from the

previous frequency excitation. This method is utilized to avoid windowing and transients caused by more common (and faster) techniques, such as a chirp excitation. The reference signal (from the Siglab Analyzer) is amplified with a TREK 2220 high voltage amplifier with a gain of 200. The amplifier has a current monitor that allows the measurement of actual current flow during the acquisition.

Figure 2.18 presents tip-velocity-per-excitation-voltage FRF (near the 1st bending resonance frequency) of the MFC actuated unimorph beam in response to harmonic excitation. The linear model prediction (for low excitation values) is represented by a dashed line. All other (solid) lines show the experimental measurements.

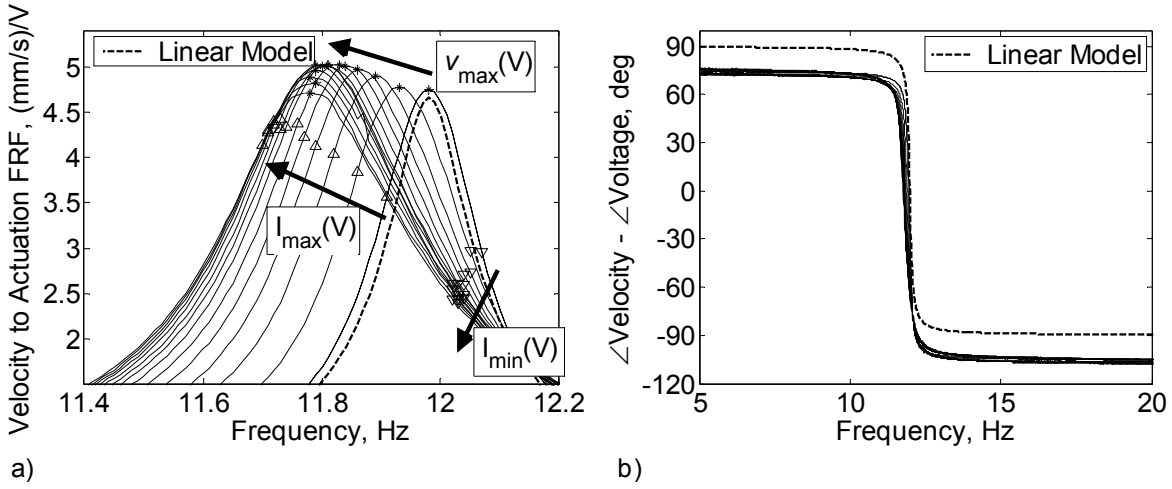

Figure 2.18: Tip-velocity-to-actuation FRF a) magnitude and b) phase comparison of experiments (solid lines) to model (dashed line). Clamped free aluminum beam with MFC M8528-P1 actuator with no tip-mass.

Three "paths" of excitation are marked in Figure 2.18. The first one is the set of operational points where maximum mechanical output (displacement, velocity, etc.). are achieved which is considered as the "mechanical resonance". This path is labeled as $v_{max}\ (V)$. The second operational path, electrical resonance labeled as $I_{max}\ (V)$, is where the highest level of current (and power) is drawn by the actuator, however mechanical output is lower than the mechanical resonance path. The third path is the electrical anti-resonance path labeled as $I_{min}\ (V)$, where low mechanical output is achieved by the lowest level of power consumption.

The linear model (which is developed for low excitation amplitudes) is in good agreement (for magnitude) with the experiments for the first three operational modes in the 0-

500 Hz acquisition bandwidth. The second and third bending operational modes are not shown. The beam has its 1st bending resonance frequency around 11.95 Hz. Two important differences should be noted. First, the experimental velocity phase (with respect to the input voltage) has a constant offset throughout the spectrum of analysis. For a linear Euler-Bernoulli beam (as assumed here) the pre-resonance displacement phase is expected to be zero degrees, and velocity phase to be 90 degrees (leading the voltage). The phase offset observed in the experiment is due to the piezocomposite and hysteretic nature of the actuator. Second, as the excitation level is increased, the actual response deviates from the linear model prediction. If this constitutive nonlinearity is ignored, the small shift in resonance frequency can result in large amplitude prediction errors due to the low damping of the system. In the current research, the excitation level dependence of the unimorph beam is due to several reasons. These reasons are briefly discussed here; however the influence of each nonlinearity is beyond the scope of this dissertation: 1) As the excitation levels are increased, the aluminum beam reaches very high strain levels; therefore a linear stress-strain relationship is not accurate. 2) Note that the MFC actuated unimorph is a slender body however it includes nonlinearities due to MFCs composite nature (including piezoceramic hysteresis). 3) The nonuniform shear layer (at the epoxy interface) is neglected here. Figure 2.19 shows the electrical power input to Beam 4 with the MFC M8528-P1 actuator. The figure represents the response for different levels of peak harmonic excitation voltage (V).

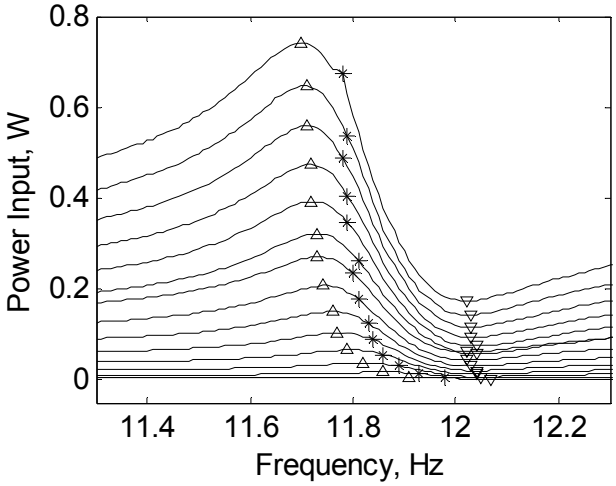

Figure 2.19: Peak power consumption of Beam 4 at different peak excitation levels. Response to harmonic voltage excitation.

The comparison of the actuation response of the four beams is given in Figure 2.20. The results represent the maximum mechanical response; hence the frequency is not constant as shown in Figure 2.18a. The displacement output, normalized by total ceramic mass, is presented Figure 2.20.

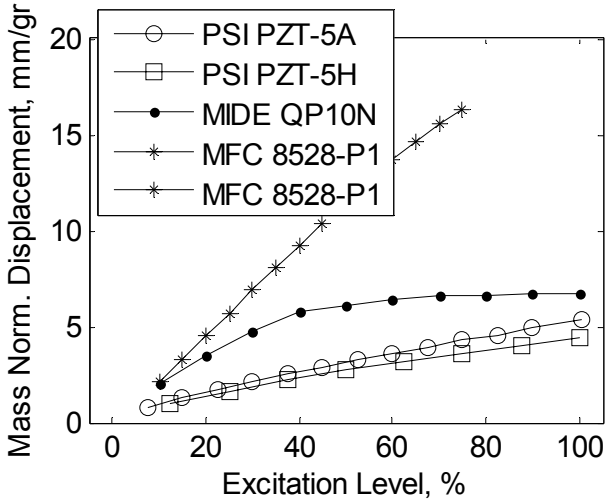

Figure 2.20: Mass normalized peak tip displacement comparison of four clamped-free unimorphs in response to harmonic voltage excitation.

Note that two separate set of points are presented for the beam with the MFC actuator. The curve for low excitation level has zero DC voltage offset; therefore the maximum excitation

amplitude is 500 Vpeak. In the second set of points, a DC voltage offset of 500 V is applied so that the complete excitation range (1000 Vpeak) can be utilized. The power consumption of the actuators (also mass normalized) is presented in Figure 2.21.

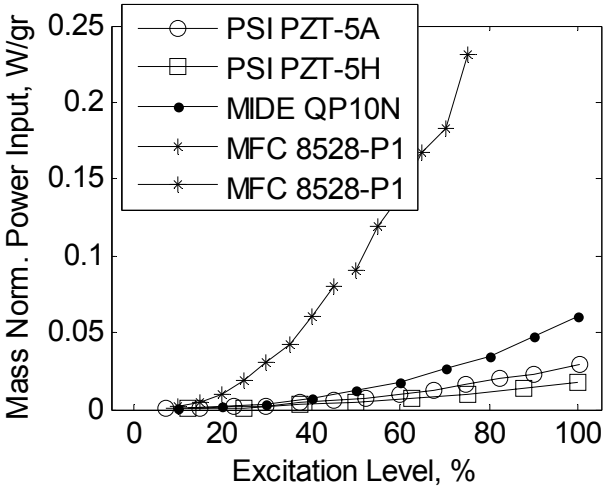

Figure 2.21: Mass normalized peak power input comparison of four clamped-free unimorphs in response to harmonic voltage excitation.

As noted earlier, due to the dimensions of the piezoceramic material in relationship to the beam dimensions, the length scales have a linear effect on the actual strain output, therefore the mass normalization results in a fair comparison of the four actuators with variation in area and ceramic thickness. The independent variable is the percent excitation level, which is the actuation voltage normalized by the maximum voltage allowed for the device. These maximum voltages can be found in Table 2.3. As expected, the MFC actuated beam shows the largest actuator authority due to its large *33* electromechanical configuration. The normalization mass used here is only for the ceramic; hence it does not include actuator specific electrode or packaging mass. The total ceramic mass is previously presented in Table 2.3. Also note that the beam with the MFC is only actuated up to 75% because the deformations obtained were too large for the laser sensor to detect.

2.2.3. Response to Positive Position Feedback Control

The actuation characteristics of the four beams (presented in Section 2.2.2) are further evaluated by the use of a simple linear feedback control law. The Positive Position Feedback (PPF) controller is originally proposed and developed by Goh [1983], and Goh and Caughey

[1985]. The controller is developed as an alternative to collocated direct velocity feedback and it has the following advantages: 1) the stability condition is non-dynamic; 2) it is not sensitive to spillover for low modal density; 3) it is not destabilized by finite actuator dynamics; 4) it is amenable to a strain-based sensing approach, which are experimentally validated in Fanson and Caughey [1990]. In addition, it offers quick damping for a particular mode if the modal characteristics are well known. PPF controllers have been extensively used in flexible structure vibration control applications, such as in a programming structure by Dosch et al. [1993], a thermally induced vibration by Friswell et al. [1997], a slewing flexible frame by Leo and Inman [1994], and a thin film rigidizable inflatable boom by Tarazaga et al. [2007]. As illustrated in Figure 2.22, the PPF control algorithm introduces a second-order filter (G1) to the system (H), which is fed by the sensed position signal. The position response of the filter is then fed back to give the force input to the structure.

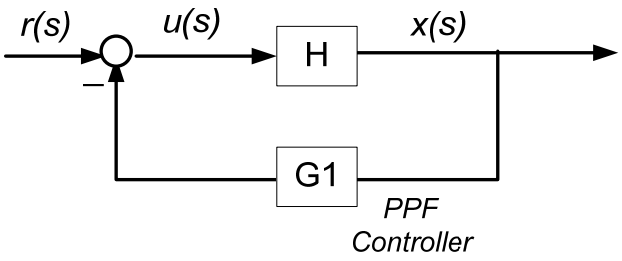

Figure 2.22: Block diagram of PPF controller.

where r is the reference signal, u corresponds to the voltage output to the piezoceramic and the x is the tip displacement of the beam in meters. The structure and the PPF controller equations for the scalar case is:

$$\ddot{x} + 2\zeta\omega_n \dot{x} + {\omega_n}^2 x = b\, u\,, \tag{2.19}$$

$$\ddot{u} + 2\zeta_f\omega_f \dot{u} + {\omega_f}^2 u = g_f\, {\omega_f}^2\, x \tag{2.20}$$

where, $\zeta\ and\ \omega_n$ indicate the first mode damping ratio and natural frequency and b is the input gain. The actual value of input gain b is not constant as the voltage/strain level changes, which is confirmed in Section 2.2.2 earlier and also discussed in Crawley and Anderson [1990]. In this section, an average b value is found experimentally. The controller parameters $\zeta_f\ and\ \omega_f$

correspond to damping ratio and natural frequency respectively. The control gain is g_f. The transfer functions of the structure and controller in Laplace form are given by:

$$H(s) = \frac{b}{s^2 + 2\xi\omega_n\, s + {\omega_n}^2}, \tag{2.21}$$

$$G1(s) = \frac{g_f\, {\omega_f}^2}{s^2 + 2\xi_f\omega_f\, s + {\omega_f}^2}. \tag{2.22}$$

Table 2.4 presents the parameters of the beam and the PPF controller. From Eq. (2.22) and Table 2.4 we can see that the PPF controller has the same form as the Eq. (2.21), but with much higher damping ratio.

Table 2.4: Parameters for the flexible beam and PPF controller.

	Operating Frequency	Damping Ratio	Gain
Beam	$\omega_n = 75.5\, rad/s$	$\zeta = 0.0032$	$b = 0.005$
PPF Controller	$\omega_f = 80\, rad/s$	$\zeta_f = 0.15$	$g_f = 10 - 500$

The PPF controller is implemented using Simulink, a toolbox in MATLAB software. The system layout is presented in Figure 2.23. The tip displacement of the beam is measured with an MTI Instruments LTC-50-20 type laser displacement sensor. The output of the controller is fed back to the MFC actuator using a TREK 2220 high voltage amplifier. As shown in Figure 2.23, both the dSPACE output to the TREK amplifier and the displacement laser output (measured with dSPACE) are low-pass filtered at 1k Hz cut-off frequency using a DC-coupled ITHACO 6032 24dB/Octave analog filter.

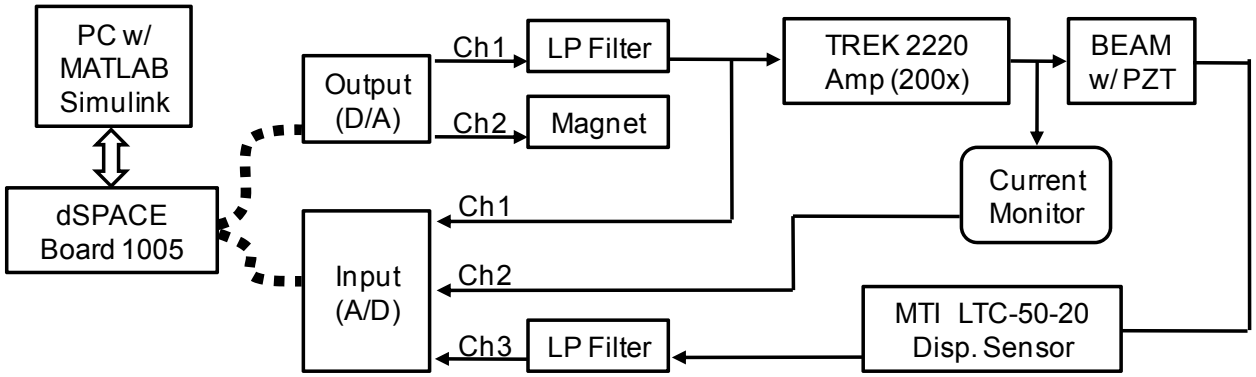

Figure 2.23: Illustration of PPF control experiment.

The beam is initially displaced at a fixed distance and held in place with an electronically controlled electromagnet. The initial conditions are set at a constant displacement of about 5.0 mm and a zero velocity. A simple code written in Control Desk software is used to implement the controller on a dSPACE 1005 real time control board. Figure 2.24 shows (an example case of) the tip displacement as a function of time for the open and closed-loop cases for Beam 4 with MFC M8528-P1 type piezoceramic. The controller gain, g_f, is 300 for this example. For this beam, the maximum control output voltage is limited to approximately ±500 V.

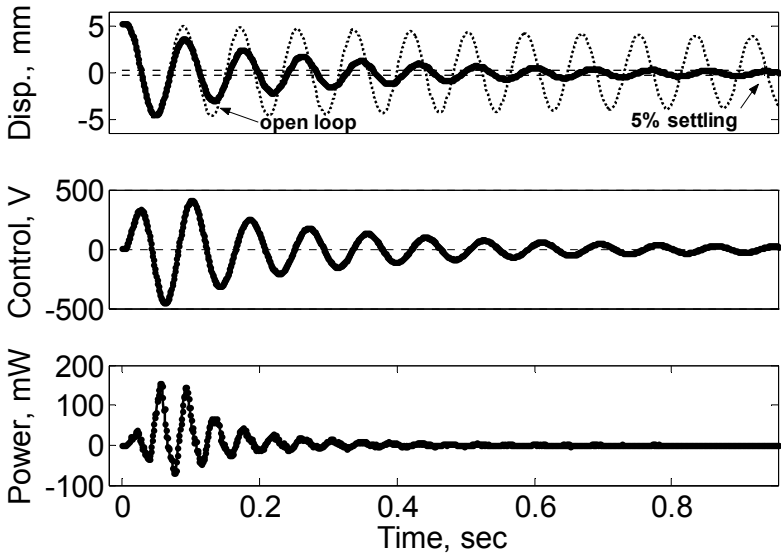

Figure 2.24: Experimental time history of open-loop-open-circuit response and closed-loop response with PPF controller. The response starts from an initial tip displacement and zero velocity.

The instantaneous power presented (in Figure 2.24) is calculated by multiplying the measured control voltage and the measured current output at each time step of the acquisition (at 1k Hz sampling rate). The current is measured by the current monitor function that is available on the amplifier. Due to 1) the capacitive nature of the piezoceramic and 2) the effectively short circuit condition of the output of the TREK 2220 amplifier, there is a significant amount of "reactive" power returned to the amplifier and this power is dissipated through the output impedance of the amplifier. The net electrical energy, which is the summation of electrical energy that is applied and returned, is defined as:

$$E_{NET} = \int_0^{T_s} V(t) * I(t)\, dt. \tag{2.23}$$

The electrical energy consumption (from the release of the beam to the 5% settling time) is presented in Figure 2.25.

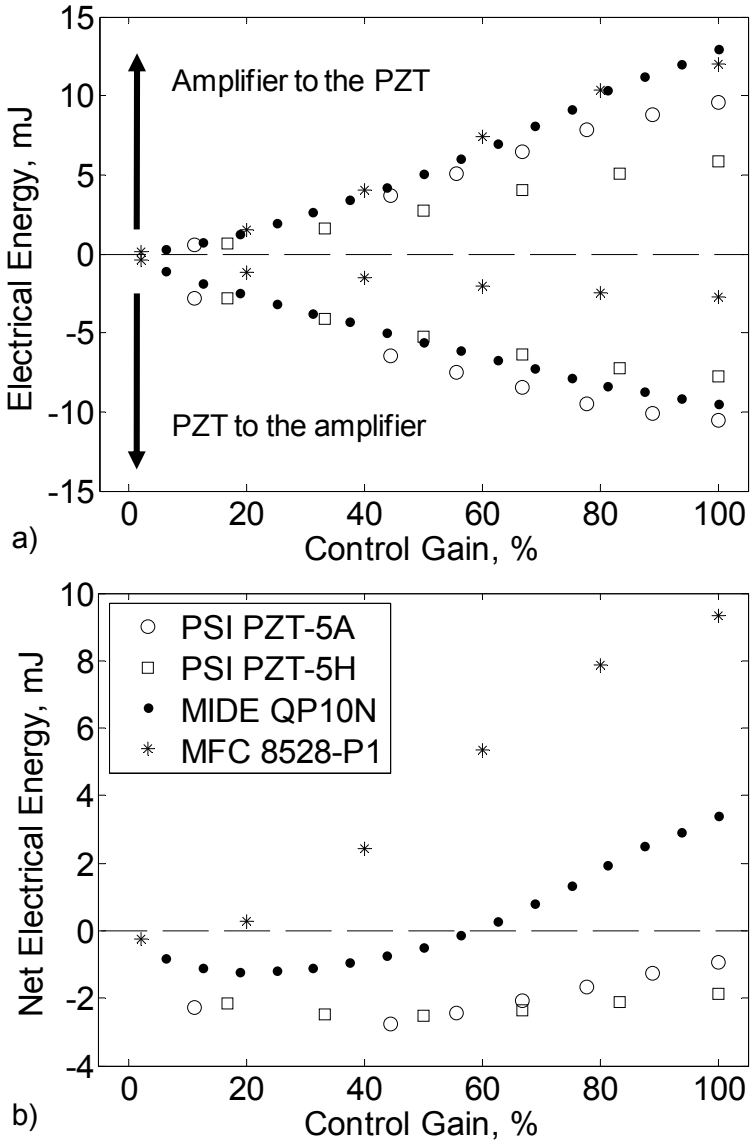

Figure 2.25: a) Electrical energy flux and b) net electrical energy consumption of four beams during the control experiments.

Figure 2.25a shows the electrical energy that is transferred into the piezoceramic (positive area of the integral) as well as the energy returned from the piezoceramic (negative area of the integral) as a function of the percent control gain. The percent control gain is calculated by normalizing the peak control voltage by the maximum allowed voltage to the piezoceramic. Figure 2.25b shows the net energy flux (defined earlier).

It is important to note that a very small portion of the returned electrical energy is due to the "harvesting" of the elastically stored potentially energy (induced by the initial tip displacement). First, there is a significant amount of reactive power returned from the (capacitive) piezoceramic material. The beams 1 and 2 with PSI PZT-5H and -5A type ceramics have the high capacitance (as shown earlier); hence the reactive power is large. Second, as demonstrated in the "Actuation Characteristics" section, the mechanical and electrical variables have a hysteresis induced phase offset of about -20 degrees. Due to this constant phase offset, some of the control effort actually promotes the vibration in the system and some of this additional vibration is captured (by direct electromechanical coupling) and dissipated through the output impedance of the amplifier. For the Beams 1-3 (with monolithic ceramics) the electromechanical coupling is larger; therefore a significant amount of energy can still be recovered during the "inefficient" control effort. For Beam 4 (with the MFC device) the returned energy is low; however due to its large control authority, the control effectiveness is the highest. Figure 2.25b shows that, up to a certain control gain, the net sum of electrical energy flux is negative, indicating that some of the elastically stored potential energy is returned. The potential energy stored in the beams for an initial tip displacement (δ_{tip}) can be approximated by:

$$U = \frac{3{\delta_{tip}}^2 EI}{2L^3} \tag{2.24}$$

where EI is the bending stiffness and L is the length of the beam. For the initial displacement of δ_{tip}=5.38 mm, the stored energy is U = 3.0 mJ. For example, in the case of a shunt circuit, only a very small portion of this energy is expected to be harvested. In addition to the PPF controller and the amplifier used here, further effort is required to 1) reduce the reactive power dissipation through the output impedance of the amplifier by storing it to a capacitor, 2) reduce the undesired control effort by compensating the phase lag in the piezoceramic and 3) to harvest the elastically stored energy simultaneously. These efforts are beyond the scope of this section.

The effect of control effort in the 5% settling time is presented in Figure 2.26. The settling time with zero control gain simply represents the open-loop-open-circuit settling time.

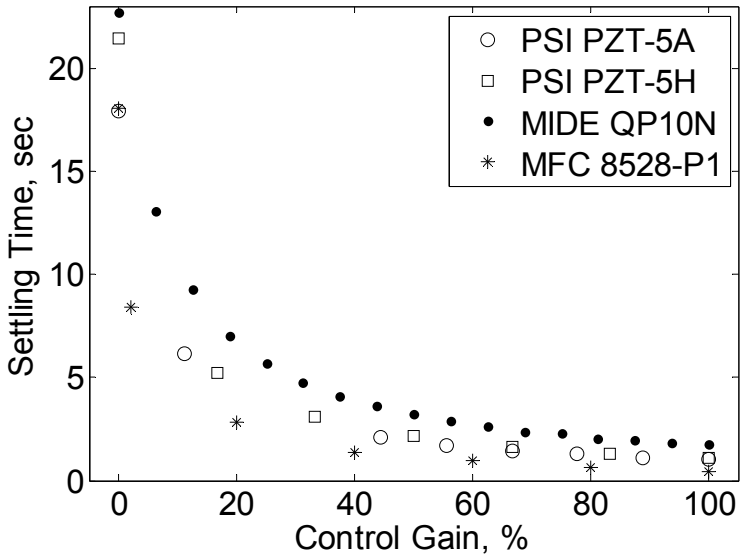

Figure 2.26: Five percent settling time of four beams as a function of control gain.

Each beam has a slightly different open-loop settling time because each beam does not have the same "absolute" equilibrium position with respect to the position of the electromagnet, hence resulting in a different initial displacement. Regardless of the open-loop response, the MFC M8528-P1 actuated Beam 4 shows the best control effectiveness, which is consistent with the actuation characterization.

2.3. Unimorph Beams with Single Crystal Piezoelectrics

This section presents an electromechanical comparison of the actuation capabilities of several clamped-free single crystal actuated unimorphs to other unimorphs employing conventional polycrystalline monolithic piezoceramics. The unimorphs are evaluated for their actuation performance via measuring the tip velocity output induced with voltage excitation. A total of 24 unimorphs are fabricated by bonding Ceracomp PMN-PZT [Ceracomp PMN-PZT], PSI PZT-5A4E [PSI PZT-5A4E], PSI PZT-5H4E [PSI PZT-5H4E] type monolithic ceramics to aluminum and stainless-steel substrates. The substrates are CNC machined to the exact size of the piezoelectric devices and bonded with Tower Hobbies Build-it Thin CA (commonly known as super glue). Samples are bonded by applying pressure by hand; hence there could be a

relatively high variation in glue thickness. The electrode surface of the piezoelectrics (that is bonded to the substrate) is accessed by a small hole through the clamped end of the substrate. A small wire is bonded to the "interior" electrode with a two-part silver epoxy (AI Technology Prime-Solder EG8050) with 0.40 mOhm-cm electrical resistivity.

The substrate materials are metal beams with four different thicknesses and they all have 5.0 mm width, 30 mm total length. The overhang lengths of the cantilever are set to be 22.5 mm. Figure 2.27 shows the experimental setup used for actuation experiments.

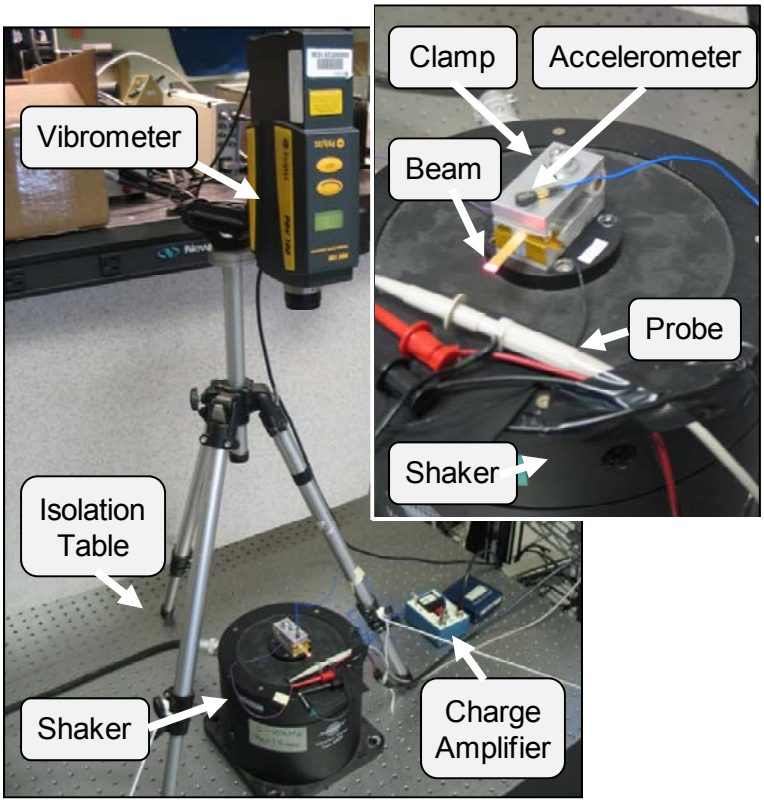

Figure 2.27: The cantilevered unimorph actuation (and energy harvesting) test setup with a single crystal unimorph installed on the clamp.

The design of the clamp can be seen in Appendix A.1. Figure 2.27 illustrates general cantilevered unimorph beam setup with the laser velocity sensor and the electromagnetic shaker. Note that the shaker is used only during the energy harvesting experiments which will be presented in Chapter 3. The assumed properties of the piezoelectric devices on the beams are given in Table 2.5. All of the piezoelectric materials used in this section operate in the *31* mode and they are monolithic devices. The single crystal piezoelectrics are manufactured by Ceracomp

Co., Ltd., Chungcheongnam-do, South Korea. These crystals are fabricated by the cost-effective solid-state crystal growth (SSCG) method. The specific model used is CPSC 160-95 type 31 mode PMN-PZT single crystal. These types of single crystals are reported to have 1) high piezoelectric coupling constants (d_{33} and d_{31}), 2) high relative permittivity (K_3^T), 3) low mechanical quality factor (Q_M), 4) low Rhombohedral-to-Tetragonal transition temperature (T_{RT}) and 5) no internal bias. The other two (polycrystalline) monolithic piezoceramics used are models PZT-5A4E and PZT-5H4E from Piezo Systems, Inc., Woburn, MA, USA. All three piezoelectric devices are poled in the through-the-thickness direction.

Table 2.5: Typical properties of the tested piezoelectric materials.

Piezoelectric Properties	Ceracomp PMN-PZT	PSI PZT-5A	PSI PZT-5H
Model	CPSC 160-95	PZT-5A4E	PZT-5H4E
Electromechanical Mode	*31*	*31*	*31*
Type	PMN-PZT	II / 5A	VI / 5H
Length, l_{pzt} (mm)	30.0	30.0	30.0
Width, w_{pzt} (mm)	5.00	5.00	5.00
Thickness, *PZT th* (mm)	0.2800	0.2670	0.2670
Density, ρ (gr/cm^3)	8.0	7.8	7.8
Mechanical Quality, Q_M	41*	80	32
Relative Dielectric Constant, K_3^T {1kHz}	4663*	1900	3800
Electromechanical Coupling, k_{33}	0.93	0.72	0.75
Electromechanical Coupling, k_{31}	0.88*	0.35	0.44
Strain / applied field, d_{33} (pm/V)	2000	390	650
Strain / applied field, d_{31} (pm/V)	-1582*	-190	-320
Electrode Spacing (mm)	0.280	0.267	0.267
Initial Depolarizing Field, *Ec* (10^5 V/m)	n/a	5	3
Coercive Field, *Ec* (10^5 V/m)	4	12	8
Maximum Voltage (V)	n/a	±134	±80
Curie Temperature, T_C (°C)	160	350	230
Compliance, s_{11}^E (10^{-12} m^2/N)	77.7*	16.4	16.5

The manufacturer, Ceracomp Co. Ltd. provided the typical and the measured properties of the CPSC 160-95 type PMN-PZT type single crystals. In Table 2.5, the values presented with "*" are average values calculated from the values specific to the piezoelectrics used in this

research. Both the typical and the measured properties of the CPSC 160-95 (reported by the manufacturer) are presented in Appendix A.5. The length, width dimensions are measured with a digital caliper (with 0.0005" resolution). The thicknesses of the piezoelectrics are measured with a digital micrometer (with 0.00001" resolution). Table 2.6 presents the complete list of the 24 specimens tested and their respective thickness properties.

Table 2.6: Thickness properties of unimorph cantilevers with PZT-5A, PZT-5H and PMN-PZT type polycrystalline and single crystal piezoelectrics.

Sample	Code	Type	*PZT th* (mm)	Subs.	*Subs. th* (mm)	*Tot. th* (mm)	*Glue th* (mm)
1	5H01	PZT-5H	0.2667	Al	0.38608	0.68148	0.0287
2	5H02	PZT-5H	0.2667	Ss	0.38608	0.70866	0.0559
5	SC05	PMN-PZT	0.2800	Ss	0.10947	0.40919	0.0197
6	SC06	PMN-PZT	0.2800	Ss	0.25806	0.55626	0.0182
7	SC07	PMN-PZT	0.2800	Ss	0.38583	0.67335	0.0075
8	SC08	PMN-PZT	0.2800	Ss	0.51079	0.79807	0.0073
9	SC09	PMN-PZT	0.2800	Ss	0.62992	0.92608	0.0162
10	SC10	PMN-PZT	0.2800	Al	0.13995	0.49581	0.0759
11	SC11	PMN-PZT	0.2800	Al	0.25400	0.59766	0.0637
12	SC12	PMN-PZT	0.2800	Al	0.38659	0.79248	0.1259
13	SC13	PMN-PZT	0.2800	Al	0.50597	0.85192	0.0659
14	SC14	PMN-PZT	0.2800	Al	0.81890	1.15722	0.0583
16	SC16	PMN-PZT	0.2800	Al	0.13284	0.49987	0.0870
17	SC17	PMN-PZT	0.2800	Ss	0.38684	0.66954	0.0027
20	5H20	PZT-5H	0.2667	Ss	0.10922	0.39903	0.0231
21	5H21	PZT-5H	0.2667	Ss	0.25730	0.54559	0.0216
22	5H22	PZT-5H	0.2667	Ss	0.38608	0.68961	0.0368
23	5H23	PZT-5H	0.2667	Ss	0.50876	0.80772	0.0323
24	5H24	PZT-5H	0.2667	Ss	0.62662	0.91415	0.0208
25	5A25	PZT-5A	0.2667	Ss	0.10693	0.39345	0.0198
26	5A26	PZT-5A	0.2667	Ss	0.25984	0.55499	0.0284
27	5A27	PZT-5A	0.2667	Ss	0.38049	0.68326	0.0361
28	5A28	PZT-5A	0.2667	Ss	0.50673	0.79807	0.0246
29	5A29	PZT-5A	0.2667	Ss	0.62154	0.91161	0.0234

Note that the glue thickness has an average measured value of 0.0375 mm and a large standard deviation of 0.0293 mm. The piezoelectric, substrate and total weight measurements are presented in Appendix A.5.

2.3.1. Electrical Impedance Characteristics

Electrical impedance spectroscopy is performed using an Autolab PGSTAT12 (Eco Chemie) Potentiostat/Galvanostat with a FRA2 module controlled by FRA and GPES software. Electrical impedance measurements of the beams are obtained using a 100 mV_{RMS} sinusoidal potential swept from 100 kHz to 1.00 Hz. The measurement system applies a controlled sinusoidal signal to the system, and current is measured. The test setup is presented in Figure 2.28.

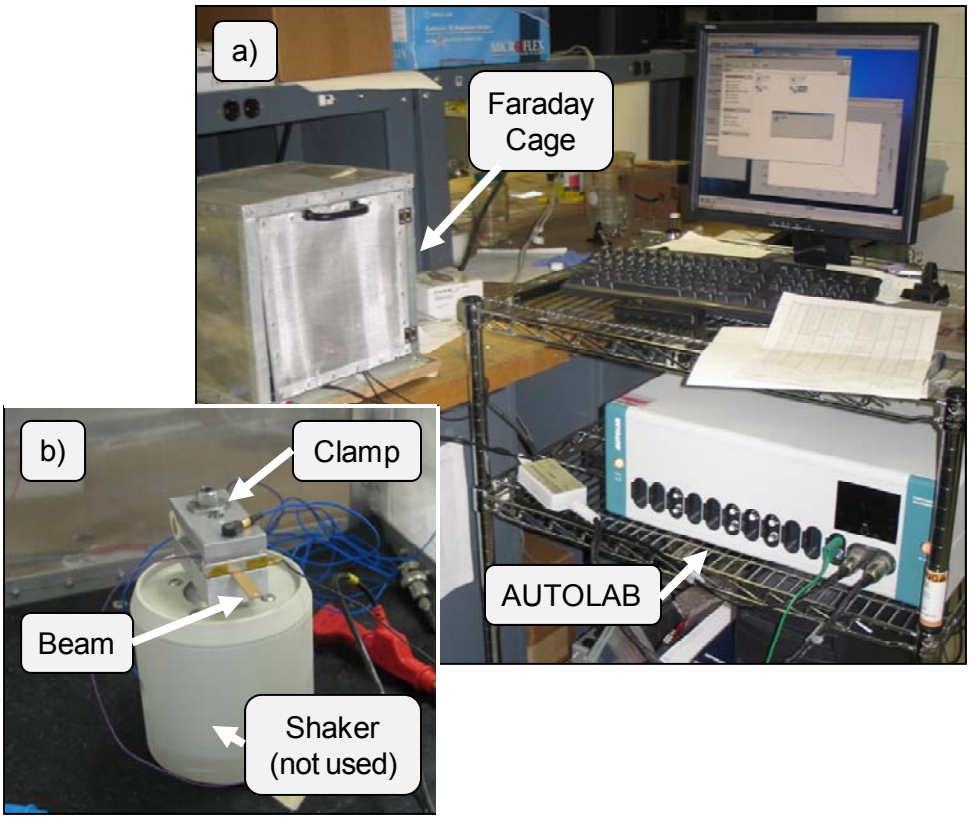

Figure 2.28: a) The impedance measurement test setup. b) Clamped-free unimorph beam inside the Faraday cage.

The samples are clamped-free (as shown in Figure 2.27 and Figure 2.28). The clamp and the specimen (mounted on a small shaker) are placed in a Faraday cage during the measurements to reduce the electrical noise in current measurements. The overhang length is set to be approximately 22.5 mm. The experimental impedance magnitude and phase and the capacitor (*C*) circuit fit is shown in Figure 2.29. The capacitor model fit is applied to frequencies well below the first resonance frequency.

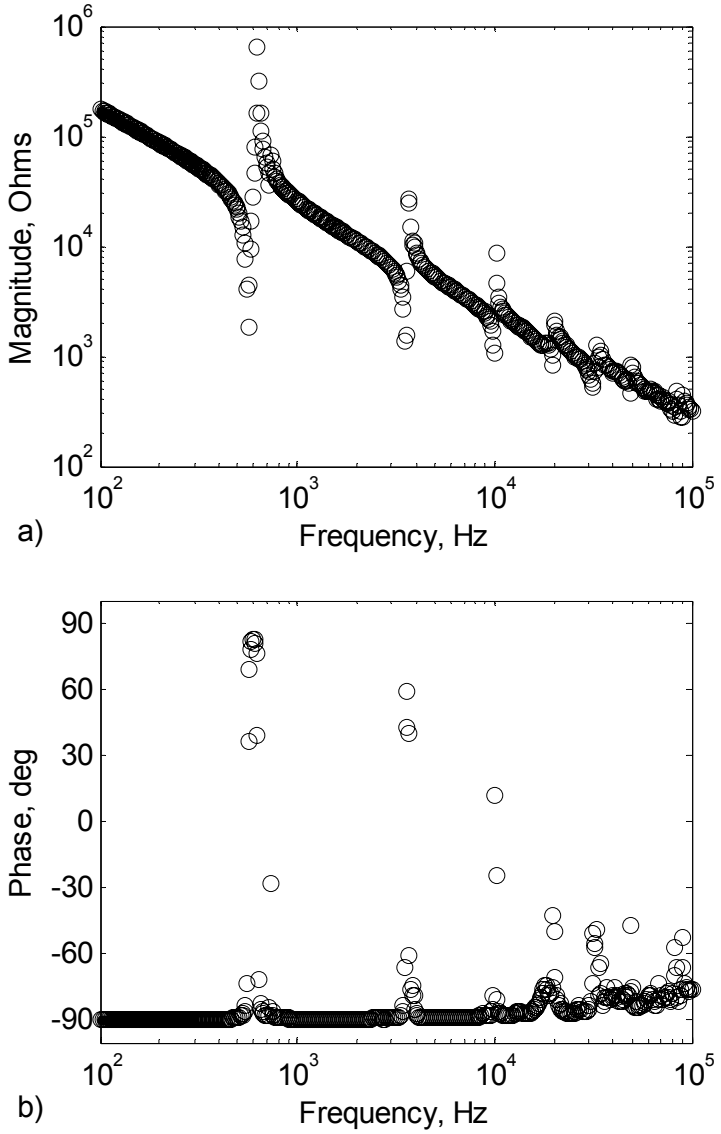

Figure 2.29: Electrical impedance a) magnitude and b) phase of unimorph Sample 17 with PMN-PZT single crystal and stainless-steel substrate. a) Magnitude and b) phase.

The results are deduced from the complex impedance measurement of the system. The mechanical effects are clearly visible from the electrical impedance measurements. Effective capacitance values are deduced from the pre-resonance spectrum. These values are presented in Table 2.7.

Table 2.7: Effective capacitance (*C*) measurements of 24 unimorph specimens.

Sample	Code	*C* (nF)	Sample	Code	*C* (nF)
1	5H01	16.88	16	SC16	19.00
2	5H02	14.88	17	SC17	9.14
5	SC05	15.31	20	5H20	15.53
6	SC06	11.66	21	5H21	15.31
7	SC07	n/a	22	5H22	15.56
8	SC08	8.17	23	5H23	14.34
9	SC09	7.55	24	5H24	13.50
10	SC10	15.25	25	5A25	9.19
11	SC11	13.97	26	5A26	9.27
12	SC12	11.44	27	5A27	8.50
13	SC13	10.50	28	5A28	8.42
14	SC14	8.66	29	5A29	8.13

2.3.2. Actuation Characteristics

The tip-velocity-to-voltage-excitation frequency response function is measured through experimentation for all 24 unimorph beams. A Polytec PDV-100 laser vibrometer and a Siglab 20-42 frequency analyzer is used to measure the tip velocity of the cantilevers. A virtual sine sweep is used for the frequency response function (FRF) measurements, where the excitation is a pure sine tone at constant frequency. The frequency is incremented only when transients are decayed from the previous frequency. This method is utilized to avoid windowing and transients caused by more common (and faster) techniques, such as a chirp excitation. The 500 mVpeak pure sine tone excitation signal (from the Siglab Analyzer) is buffered through an HP 6826A bipolar amplifier with a fixed unity gain. The acquisition is conducted in the 5 Hz to 10 kHz bandwidth, with 1 Hz resolution. Three samples are taken at each frequency and averaged. The laser measurement is taken at 21.4 mm from the base of the clamped-free beams. As noted earlier, the overhang lengths of the beams are 22.5 mm. Figure 2.30 presents tip-velocity-per-excitation-voltage FRF of the four unimorph beams with approximately 0.25 mm thick

substrates. Sample 6, 21 and 26 (labeled SC06, 5H21 and 5A26) have stainless-steel substrates, and Sample 11 (labeled SC11) has an aluminum substrate. The first three bending resonances can be seen for the two single crystal specimens.

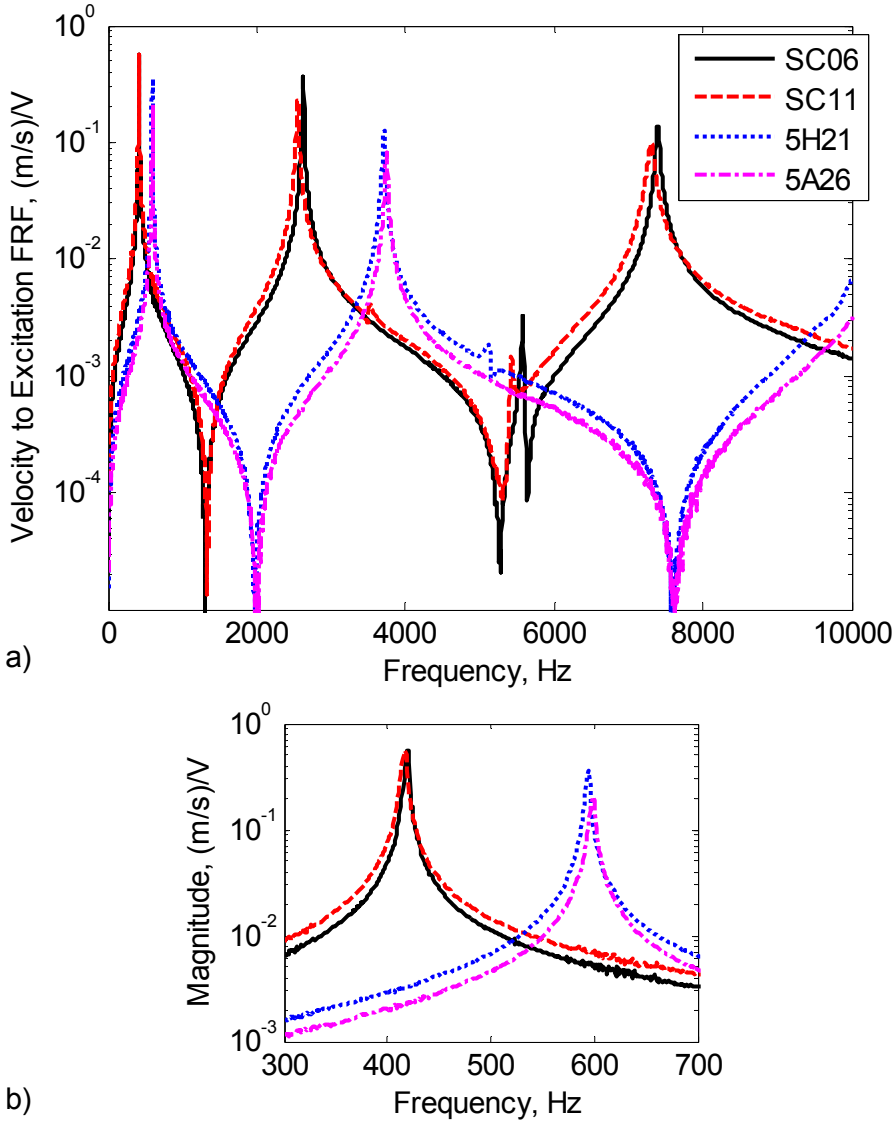

Figure 2.30: Tip-velocity-to-excitation FRF a) complete measurement spectrum and b) spectrum around 1st bending frequency. Four FRF examples of clamped-free unimorphs.

Additional actuation response characterization plots are presented in Section A.5. The interesting results from these FRF measurements are the frequency and amplitude of displacement response at the 1st operational bending frequency. Figure 2.31 presents the resonance response of the all specimens to harmonic excitation.

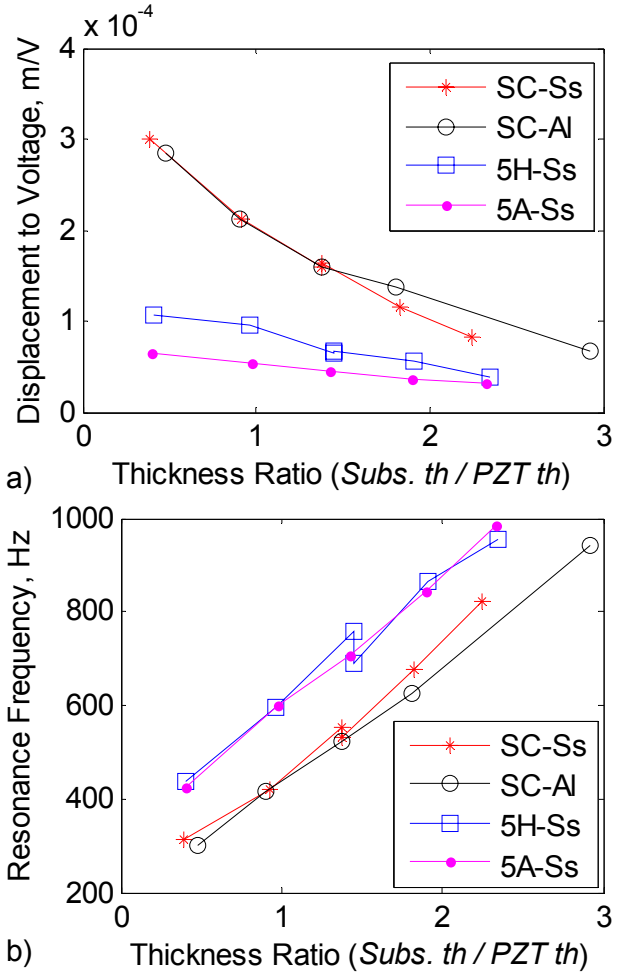

Figure 2.31: Response of all 24 specimens at their 1st bending resonance frequency to harmonic voltage excitation. a) Peak tip displacement per voltage and b) resonance frequency (at the peak displacement operation point).

In Figure 2.31a, the peak tip displacement per excitation voltage is presented against the substrate-to-piezoelectric thickness ratio. The peak tip displacement is deduced from the tip-velocity-to-excitation-voltage FRF measurements at the resonance frequency. The thicknesses of substrates and the piezoelectrics are presented in Table 2.6. Finally, the displacement response at the quasi-static range (or static displacement) derived from low frequency velocity FRFs is presented in Figure 2.32.

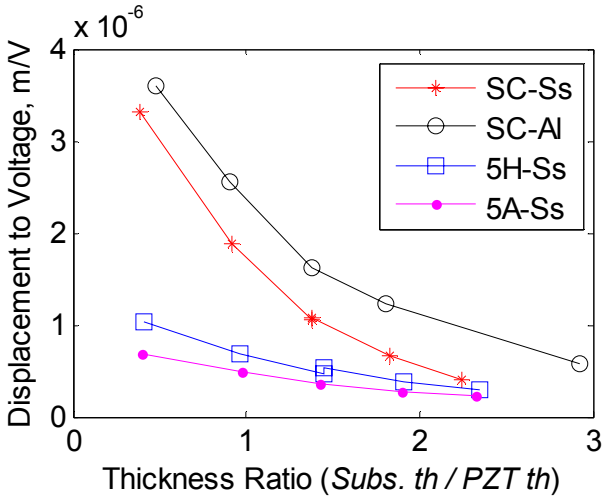

Figure 2.32: Quasi-static displacement-to-voltage response for all 24 specimens.

Both for dynamic and quasi-static response, the single crystal PMN-PZT type unimorphs show superior actuation response when compared to polycrystalline PZT-5A and PZT-5H type ceramics. It is also noted that the thickness ratios of the tested specimens are larger than the optimum thickness ratio (that results in highest mechanical output). The overall displacement-output-to-thickness-ratio trend described in Section 2.1 also applies here. Also note that the active material stiffness with respect to the substrate stiffness plays an important role in addition to the substrate-to-active-material thickness ratio. Single crystal piezoelectrics are significantly softer when compared to polycrystalline ceramics as presented in Table 2.5.

2.4. Conclusions

Overall, the MFC actuator demonstrated the highest actuation capability due to 1) their use of the *33* mode (due to interdigitated electrodes), 2) their flexibility (due to fibrous ceramics). From a practical perspective, the MFC actuators are far superior to other evaluated in this section due to its flexibility and ease of application. As presented by Park and Kim [2005] and Wilkie et al. [2006] and demonstrated here by experiments, the single crystal piezoelectrics can improve the actuation performance when compared to polycrystalline ceramics; however only under certain electromechanical conditions.

The following sections present a brief summary of the conclusions. First, the conclusions from the analytical and experimental results on MFC actuated unimorph structures with thin substrates are presented. Next, conclusions on actuation characterization of MFC actuated

unimorphs with thick substrates are given. Finally, the practical limitations of single crystal piezoelectrics are discussed.

2.4.1. Thin Unimorphs

A distributed parameter model is proposed for the MFC actuated unimorphs with interdigitated electrodes and *33* electromechanical mode. The model is validated against experimental measurements by using 12 unimorph samples with a wide range of structural properties. Considering that the predicted values are without any bending stiffness corrections, the model is capable of capturing the dynamics for a wide range of physical cases.

The MFC actuated thin unimorph is a slender body however it includes nonlinearities due to MFCs composite nature (including piezoceramic hysteresis). The effect of hysteresis is frequency and amplitude dependent, and is not observed during the low-amplitude and high frequency experiments conducted in Section 2.1. Due to nature of piezoceramics, and important nonlinearity, material hysteresis, arises for high-voltage actuation. Further experimental investigation needs to be conducted in order to determine the development of the hysteresis, and the find the limits of the linear model. Section 2.2 addresses this issue.

2.4.2. Thick Unimorphs

In Section 2.2, the electromechanical comparison of the transduction capabilities of four clamped-free unimorphs employing piezoceramics in two different types of applications: open-loop control and closed-loop control. The unimorph with the MIDE QP10N device (with industry-type 5A ceramic) shows the largest mass-normalized-power-output which is identified during the resistive-shunt and feedback control experiments. For all four piezoceramic devices, it is discovered that some energy can be harvested during the feedback control effort. Although not addressed here, intelligent design of electronics and nonlinear control laws can take advantage of the existing energy in the environment and use it to aid the control effort for vibration suppression. Due to its large *33* coupling, the MFC M8528-P1 type device shows the largest actuation output and control authority. Significant nonlinearities are identified (in the constitutive relationships, but not in the governing equations) during the actuation experiments, where development of large strains in the aluminum beams caused an material softening effect, and the natural frequency is slightly reduced and the displacement amplitudes and the power consumption is no longer linear. The piezoceramic hysteresis induces a constant phase shift

between the mechanical and electrical variables, such as displacement (or velocity) with respect to the input voltage.

2.4.3. Single Crystal Unimorphs

A total of 24 small unimorph specimens with PMN-PZT, PZT-5H and PZT-5A type piezoelectrics are experimentally evaluated for their tip velocity and displacement output to voltage excitation. Single crystal type unimorphs demonstrated superior actuation response when compared to unimorphs with polycrystalline ceramics. As noted earlier, the PMN-PZT type single crystals used here are reported to have 1) high piezoelectric coupling constant (d_{33} and d_{31}), 2) high relative permittivity (K_3^T), 3) low mechanical quality factor (Q_M), 4) low Rhombohedral-to-Tetragonal transition temperature (T_{RT}) and 5) no internal bias. The single crystals are known to be "soft" piezoelectrics which is a major practical issue. During the fabrication and testing of the single crystal based unimorphs, several specimens were broken with very small forces applied. The lack of grain boundaries (as in the polycrystalline material) makes the single crystals to be very "brittle" and susceptible to stress concentrations. Another important limitation is the low transition temperature. The electrodes can't be soldered using regular solder materials and temperatures, therefore relatively expensive and slow methods (such as two part conductive epoxies) have to be used for wiring.

CHAPTER 3

ENERGY HARVESTING CHARACTERIZATION OF UNIMORPH STRUCTURES

Recently, there is a significant effort for utilizing smart materials for energy harvesting applications in aircraft. As noted in the "Objectives" section, smart material devices can sense and harvest mechanical stimuli, therefore the energy harvesting characteristics are also desired along with actuation characteristics (studied in Chapter 2). The aim here is to determine the capabilities of Macro-Fiber Composites coupled to a structure as a multifunctional transducer. The motivation for a multifunctional MFC based aerodynamic structure that can actuate and harvest (or sense) mechanical energy is due to the following reasons: 1) The MFCs are already proposed as an actuator for the aerodynamic application (i.e. variable-camber piezocomposite airfoil) and 2) the necessary electronics that allow actuation and energy harvesting (or sensing) simultaneously would not be a burden on the total weight of the complete system and most importantly 3) the harvested energy can be used for additional tasks such as vibration suppression that allows the aeroelastic conditions to be more favorable. This chapter complements Chapter 2 and it deals with energy harvesting from base excited unimorph clamped-free beams.

Cantilever type energy harvesting devices use a substrate to support a piezoelectric transduction element. The maximum power output of such a device occurs when the fundamental frequency is near the dominant frequency of ambient vibration insuring a resonance response maximizing the strain into piezoelectric material. The topic of energy harvesting has been of great interest in the recent literature as well as in applications for wireless sensing. The ambient energy from solar loads, wind loads, thermal gradients or mechanical vibration can be harvested and used at various sensor nodes to provide the energy needed for necessary tasks. Sodano et al. [2004, 2006] investigated the transduction performance of several monolithic and piezocomposite devices. Electromechanical models and experimental validation are presented in

Erturk and Inman [2008, 2009]. The results shown in Erturk et al. [2009] illustrate that the power output is not just a function of coupling but also a function of piezoelectric material stiffness and material damping. Recent reviews of the literature on energy harvesting are given in Anton and Sodano [2007], Cook-Chennault et al. [2008] and Priya and Inman [2008].

The chapter is organized identical to Chapter 2. First, in Section 3.1, the same MFC actuated thin unimorphs (evaluated for actuation in Section 2.1) are evaluated for power output capability over a resistive shunt by experimental measurements. Next, in Section 3.2, the energy harvesting comparison of four nonuniform cross-section unimorph beams with thick substrates is presented. The actuation characterization for these beams is presented in Section 2.2. Finally, in Section 3.3, the energy harvesting characterization is conducted on the 24 specimens of uniform cross-section beams with single crystal and polycrystalline piezoelectrics. The chapter ends with the summary of conclusions from each section.

3.1. Unimorphs with Thin Substrates

The energy harvesting characterization of the MFC actuated unimorph thin beams (presented in Section 2.1) are conducted by measuring the voltage output of the piezoceramic across a variable resistive load; typically know as a resistive shunt. The properties of the specimens are presented in Section 2.1.1, Section 2.1.2 and in Appendix A.2. The mechanical input (base excitation) is obtained by an LDS electromagnetic shaker driven by an HP 6826A bipolar amplifier with unity gain. The acceleration input to the systems is measured with a PCB Piezotronics Model U352C67 shear accelerometer with 115 mV/g sensitivity and 0.5 Hz to 10 kHz frequency bandwidth. The signal from the accelerometer is amplified with a PCB model 482A16 type charge amplifier with 10x gain. The experimental setup is shown in Figure 3.1. A Polytec PDV-100 laser vibrometer (with 125 mm/s/V sensitivity) is used to measure the tip velocity of the beams.

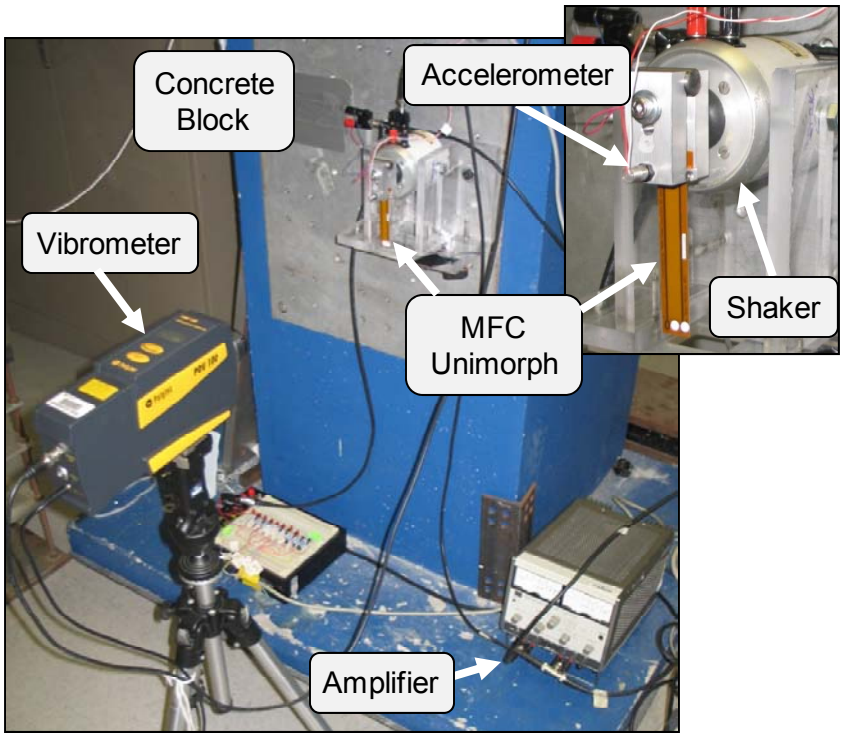

Figure 3.1: Energy harvesting experimental setup for MFC unimorphs.

The resistive loads used are 4.61k, 14.6k, 21.3k, 52.3k, 89.6k, 179k, 320k, 662k and 996k Ohms. A Siglab 20-42 frequency analyzer is used to measure the tip-velocity-to-base-acceleration and voltage-output-to-base-acceleration FRFs of the cantilevers. A virtual sine sweep is used for the FRF measurements, where the excitation is a pure sine tone at constant frequency. The experiments are conducted in the 5 - 700 Hz bandwidth with three averages at each frequency increment. The frequency increment is set to 1/20 Hz around the resonance frequencies. Figure 3.2 shows the tip-velocity-to-base-acceleration FRFs that are measured for specimen Al2 with MFC M8507-P1 type actuator and 0.0547 mm thick aluminum substrate. The frequency response to nine resistive loads are shown.

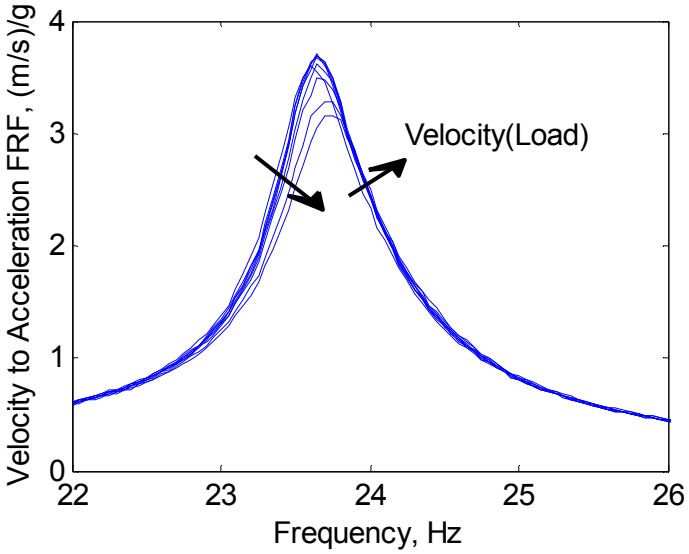

Figure 3.2: The measured tip-velocity-to-base-acceleration FRFs for harmonically base-excited clamped-free sample Al2.

Figure 3.2 is a good illustration of the effect of the electrical load to the mechanical response. For devices with low (direct) electromechanical coupling (such as the unimorphs tested here with the MFC M8507-P1 type device) this shift in resonance frequency is very small, and ignored for most practical applications. Figure 3.3 presents the voltage-output-to-base-acceleration FRF of sample Al2. The frequency response to nine resistive loads is shown.

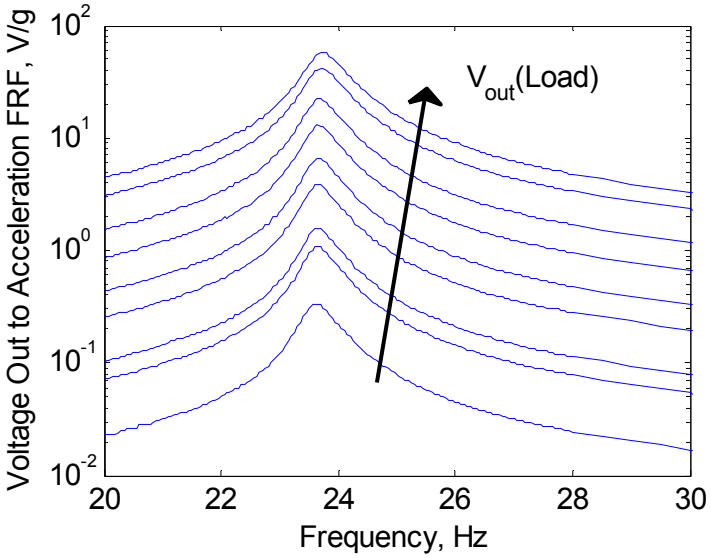

Figure 3.3: The measured voltage-output-to-base-acceleration FRFs for harmonically base-excited clamped-free sample Al2.

Similar to the mechanical response, the voltage output shows very little shift in resonance frequency, indication that the MFC M8507-P1 type device does not have good direct electromechanical coupling. Note that the open circuit response is not achieved with the range of resistors used here. The Siglab 20-42 frequency analyzer has an input impedance of 0.994 MOhm which is the largest load resistance that can be applied to the piezoceramic (without the use of a voltage divider probe). Due to the unavailability of a 10 MOhm voltage probe (at the time of the experiments,) the maximum effective resistance resulted to be 0.996 MOhm. Note that all of the results presented next (current and power output) are deduced from these two measured FRFs.

Figure 3.4 shows the voltage-per-acceleration and current-per-acceleration as a function of load resistance for four unimorph beams with aluminum substrates. Substrate information is presented in Table 2.1. All of the presented curves represent the response at the short circuit natural frequency. The response at open circuit natural frequency or the maximum response were not attained due to the maximum resistance restriction of the signal analyzer. Since the electromechanical coupling is the low in MFC M8507-P1 type devices, the shift in natural frequency (due to electrical loading) is negligible; therefore only the short circuit resonance values are close to those curves for open circuit and the maximum (variable frequency) response.

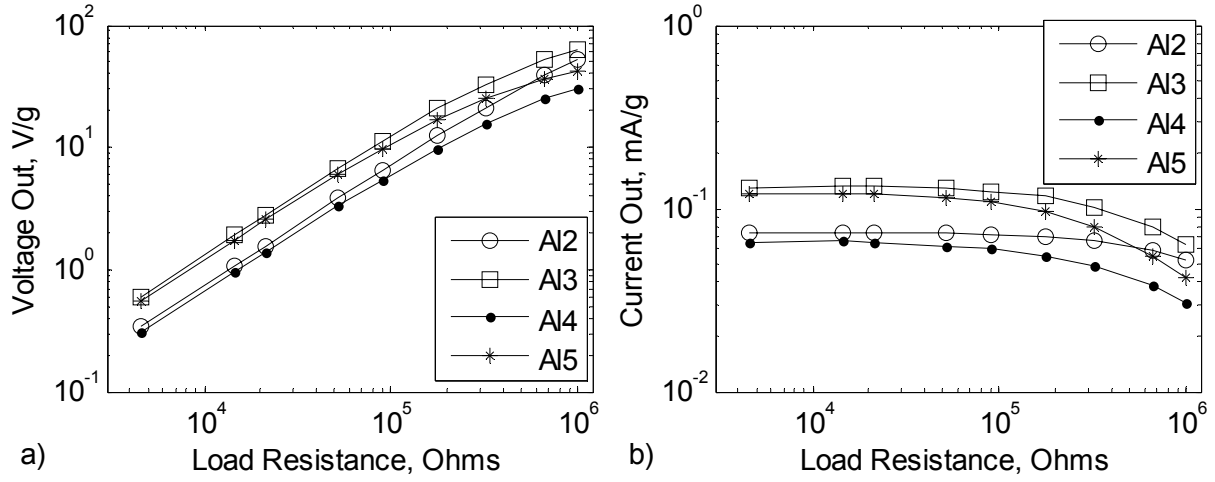

Figure 3.4: a) Voltage-output and b) current-output -to-base-acceleration of four unimorphs with aluminum substrates as a function of load resistance. Response is at the short circuit natural frequency (ω_{sc}).

Figure 3.5 presents the power output of for unimorphs with aluminum substrates. The optimum load resistance (for maximum available power output) is realized for three of the four samples with aluminum substrates. The sample Al3 demonstrates the highest short circuit power output.

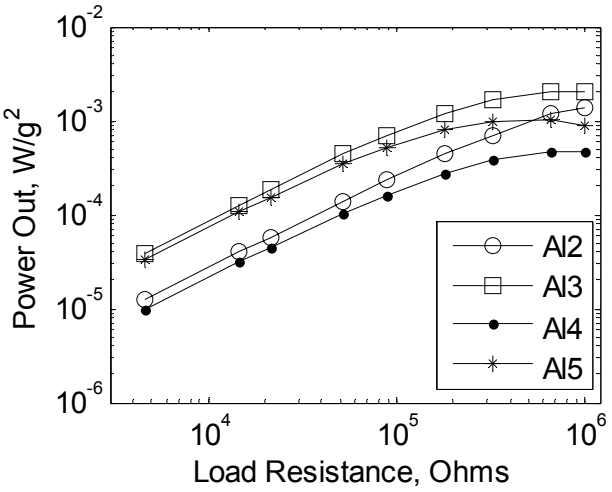

Figure 3.5: Power-output-per-harmonic-base-acceleration comparison as a function of load resistance. Response is at short circuit natural frequency (ω_{sc}).

The mechanical and electrical response of unimorphs with brass (samples Br1 – Br4) and stainless-steel (samples Ss1 – Ss4) substrates are presented in Appendix B.1. The electrical responses of all 12 MFC unimorphs are summarized by plotting the values of interest against the substrate-to-MFC-actuator thickness ratio. Figure 3.6 presents the maximum power output measured for each sample and the respective frequency (which is in-between the open circuit resonance and short circuit resonance).

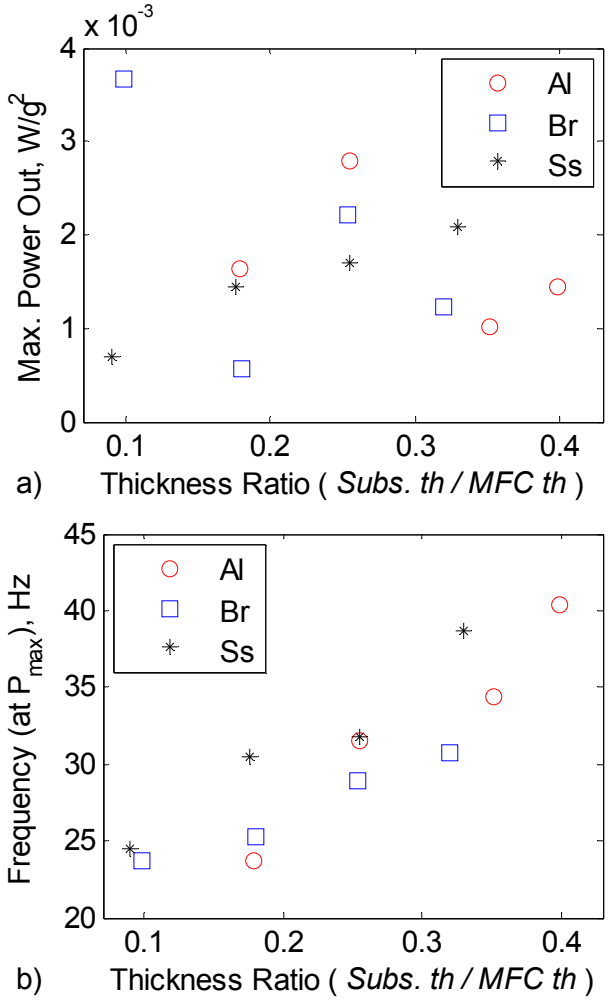

Figure 3.6: a) Maximum power output per harmonic base excitation. b) Frequency of base acceleration that results in maximum power.

It is observed that the thickness ratio does not have a conclusive effect on maximum power output for MFC unimorphs with aluminum and brass substrate materials. For the axially stiff (compared to the active material) stainless-steel material, the power output monotonically increases as the thickness ratio is increased. Figure 3.7 presents the electrical response at short circuit natural frequency.

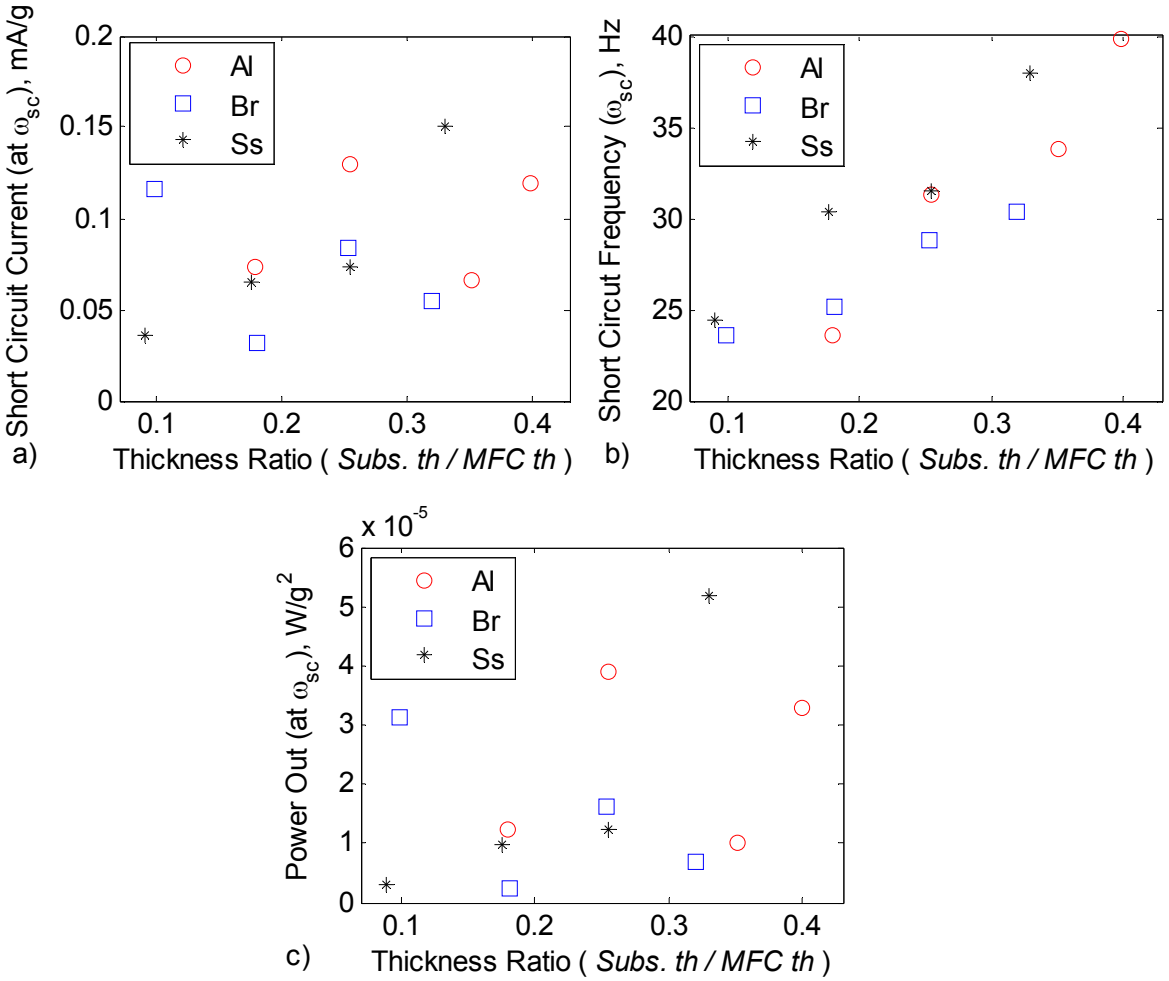

Figure 3.7: Response at short circuit natural frequency (ω_{sc}). a) Current-output-per-harmonic-base-acceleration, b) frequency of base acceleration and c) power-output.

Figure 3.7a presents the current output at short circuit condition and at ω_{sc}. Figure 3.7b presents the short circuit natural frequency which is close to the values presented in Figure 3.6b. Finally, power-output-per-base acceleration is presented in Figure 3.7c for the short circuit condition and also at ω_{sc}. The electrical output at the short circuit condition appears to have non-conclusive electrical output dependence on thickness-ratio for the aluminum and brass substrates. The electrical output results are summarized in Table 3.1 for all 12 MFC unimorph specimens.

Table 3.1: Energy harvesting response of MFC unimorphs to harmonic base acceleration.

Sample	*Subs. th / MFC th*	V_{max} (ω_{oc}) (V/g)	I_{max} (ω_{sc}) (μA/g)	P_{max} (mW/g^2)	$\omega(P_{max})$ (Hz)
Al 2	0.18	57.1	73	1.64	23.8
Al 3	0.25	74.5	130	2.79	31.6
Al 4	0.35	44.8	66	1.01	34.4
Al 5	0.40	53.6	120	1.44	40.4
Br 1	0.10	85.4	117	3.66	23.7
Br 2	0.18	33.9	32	0.58	25.3
Br 3	0.25	66.3	83	2.21	28.9
Br 4	0.32	49.6	54	1.24	30.7
Ss 1	0.09	37.1	36	0.69	24.6
Ss 2	0.18	53.8	65	1.45	30.5
Ss 3	0.25	58.2	73	1.70	31.8
Ss 4	0.33	64.3	150	2.08	38.7

As noted earlier, the thickness ratio does not appear to have a conclusive effect on maximum power output of the specific MFC unimorphs used here with aluminum and brass substrate materials. For the stainless-steel material however, the power output monotonically increases as the thickness ratio is increased. This effect (observed in the Ss 1-4 samples) is expected due to the following reasons: 1) The stainless-steel substrate stiffness (in the unimorph axial direction) is significantly larger than the MFC stiffness. 2) As the thickness ratio is increased, the effective neutral axis of the unimorph approaches the (original) neutral axis of the substrate material. On the other hand, the active material is moving away from the neutral axis; therefore it is subjected to larger strains causing larger voltage outputs. 3) The change in thickness ratio applied in the experiments is through the increase of the thickness of the substrate while the MFC device and its thickness are kept constant. Remember that all 12 unimorphs have the MFC M8507-P1 type piezocomposite device; therefore the change in thickness ratio does not change the capacitance of the active material. The net result of these three conditions is a monotonic increase of power as the substrate thickness is increased (while the active material choice is kept same). Note that the conclusions presented above apply to a certain range of thickness ratios and an optimum thickness ratio is expected in a wider thickness ratio range. Additional discussion is presented in Section 3.4.1.

3.2. Unimorphs with Thick Substrates

The energy harvesting characterization of the thick unimorph beams (evaluated for actuation in Section 2.2) are conducted by measuring the voltage output of the piezoceramic across a variable resistive load. The properties of the beams are presented in Section 2.2. The mechanical input (base excitation) is obtained by an APS Electro Seis Model 113 seismic shaker with linear bearings. The acceleration input to the systems is measured with a PCB Model U352C67 shear accelerometer. The experimental setup is shown in Figure 3.8. A Polytec PDV-100 laser vibrometer is used to measure the tip velocity of the beams.

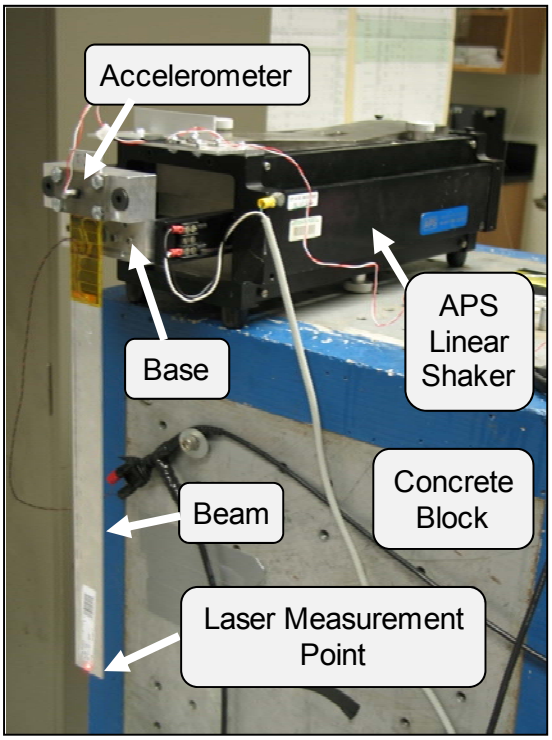

Figure 3.8: Energy harvesting experimental setup. The Polytec PDV-100 laser vibrometer is not shown.

The resistive loads used are 99.0, 4.61k, 9.77k, 21.3k, 52.6k, 89.8k, 179k, 495k and 996k Ohms. A Siglab 20-42 frequency analyzer is used to acquire the tip-velocity and voltage-output FRFs of the cantilevers with respect to the input base acceleration. A virtual sine sweep is used for the FRF measurements, where the excitation is a pure sine tone at constant frequency. The experiments are conducted in the 5 - 500 Hz bandwidth with three averages at each frequency increment. Figure 3.9 shows the two frequency response functions that are measured for Beam 2

with PSI PZT-5H ceramic. All other calculations (current and power output) are deduced from these two measured FRFs. The FRFs for other beams are presented in Appendix B.2.

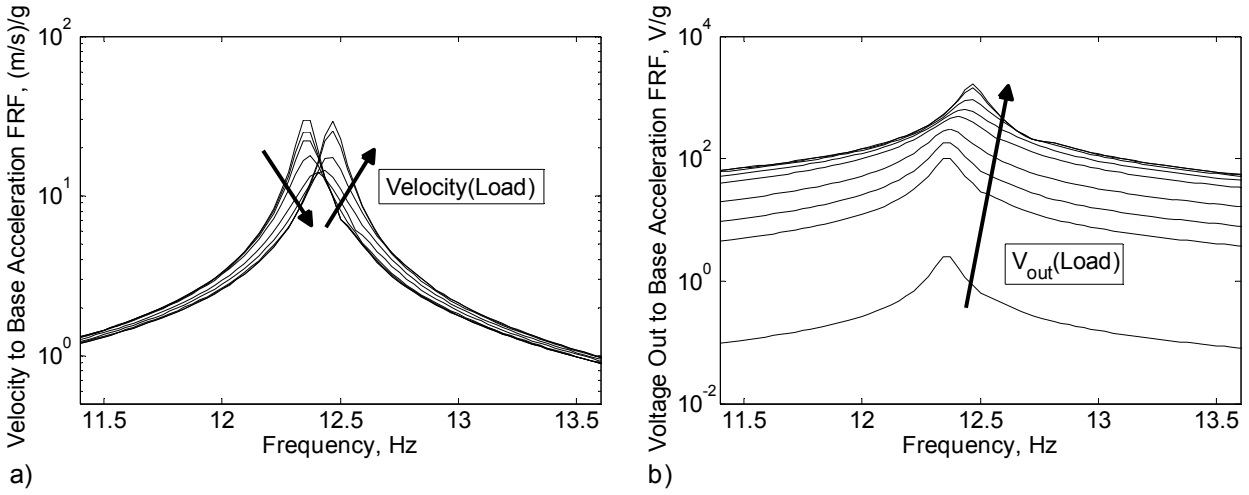

Figure 3.9: The measured a) tip-velocity and b) voltage-output to base acceleration FRFs for harmonically base-excited clamped-free Beam 2. Response is shown for a range of loads between the open-circuit and short circuit conditions.

Figure 3.9a shows that the electromechanical coupling is (relatively) strong in Beam 2 with the PZT-5H piezoceramic and the electrical load induces a significant change to the mechanical response. In Figure 3.9a and Figure 3.9b, the arrows indicate the increasing electrical load; therefore indicating the mechanical response going from the short-circuit condition to the open-circuit condition. For devices with low (direct) electromechanical coupling (such as Beam 4 with the MFC device) this shift in resonance frequency is very small. Figure 3.10 shows the voltage-per-acceleration and current-per-acceleration as a function of load resistance for two beams: 1) Beam 2 with PSI PZT-5H and 2) Beam 4 with MFC M8528-P1. Beam 2 has the largest power output; hence the highest electromechanical coupling. For the Beam 2, three curves are shown. The first curve (shown in the legend of Figure 3.10) is the maximum voltage and current output which occurs at a load dependent frequency. The second power curve shows the power variation at a fixed frequency, the short circuit natural frequency of 12.3 Hz for Beam 2. The third power curve is at the open-circuit natural frequency of 12.5 Hz. Since the electromechanical coupling is the lowest in Beam 4 (with the MFC), the shift in natural frequency is negligible; therefore only the maximum power vs. load curve is shown.

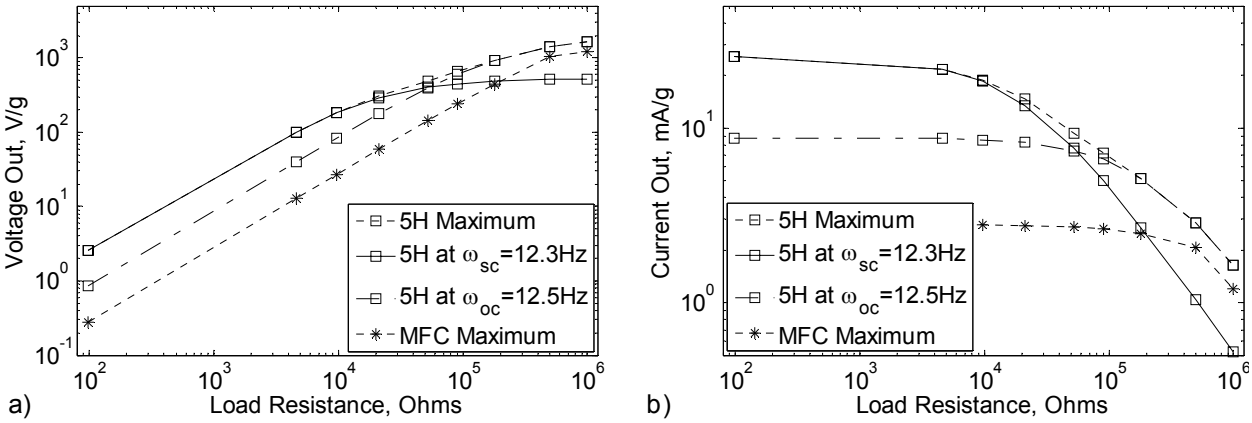

Figure 3.10: a) Voltage-output-per-input-acceleration and b) current-output-per-input-acceleration of two beams as a function of load resistance.

Figure 3.11a presents the power output of Beam 2 and Beam 4. Figure 3.11b shows the maximum power output (at variable frequency) normalized by the ceramic mass for all four beams. Beam 2 (with PSI PZT-5H ceramic) has the highest power output which is consistent to its size and the electromechanical coupling coefficient. The optimum load resistance (for maximum available power output) is measured as 89.8k Ohms producing 2.35 W/g^2. Beam 4 has the lowest power output of 1.07 W/g^2 at the measured optimum load resistance of 495k Ohms.

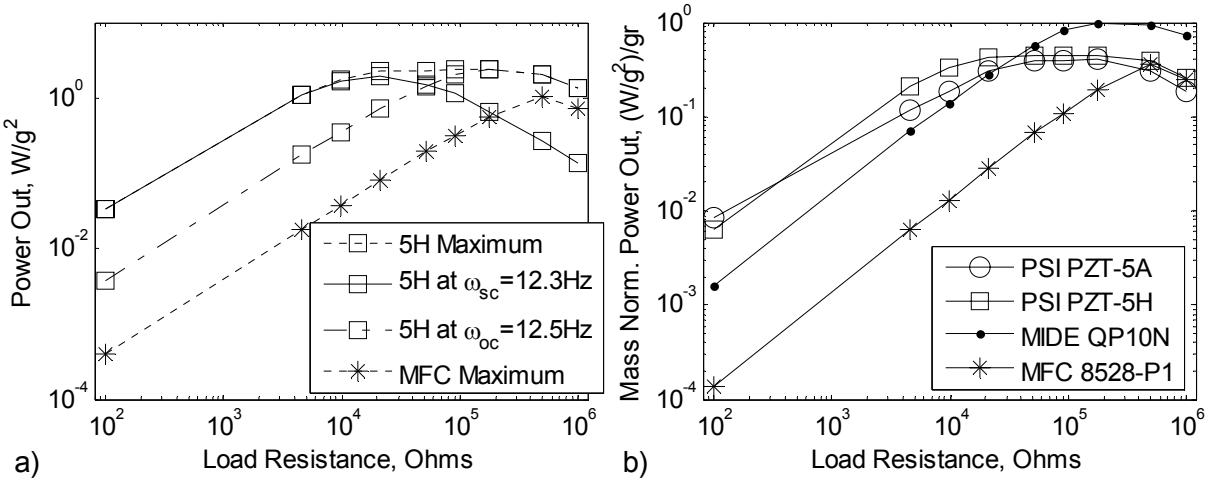

Figure 3.11: a) Power-per-acceleration and b) mass normalized power-per-acceleration comparison as a function of load resistance.

Additional results as a function of load resistance are presented in Appendix B.2. Similar to the actuation characterization, the mass normalization of the power output results in a fair comparison of the four devices with variation in area and ceramic thickness. In Figure 3.11b, the MIDE QP10N shows the highest power output density. The MIDE patch is a commercially sealed and packaged device with electrodes distributed over the ceramic. Although the ceramic used in the MIDE patch is type 5A, similar to Beam 2, the commercial application of the electrodes shows significant benefit over the in-house application of the electrodes on the ceramic (for Beams 1 and 2). Additional discussion is presented in 3.4.2.

3.3. Unimorphs with Single Crystal Piezoelectrics

This section presents the energy harvesting comparison of the single crystal monolithic piezoelectrics to polycrystalline monolithic ceramics. The actuation characterizations of these unimorph thin beams are presented in Section 2.3. The energy harvesting performance is evaluated by measuring the voltage output of the piezoelectric across a variable resistive load. The properties of the specimens are presented in Section 2.3.1, Section 2.3.2 and in Appendix A.5. The mechanical input (base excitation) is obtained by an Bruel & Kjaer 4808 electromagnetic shaker (with 5 Hz to 10 kHz bandwidth) driven by an HP 6826A bipolar amplifier with unity gain. The acceleration input to the systems is measured with a PCB Piezotronics Model U352C22 shear accelerometer with 9.88 mV/g sensitivity and 0.5 Hz to 10 kHz frequency bandwidth. The signal from the accelerometer is amplified with a PCB Piezotronics model 480E09 type charge amplifier with 100X gain. The voltage output of the piezoelectrics is measured through a 10:1 probe with 10 MOhm total resistance. The experimental setup is (previously) presented in Figure 2.27. A Polytec PDV-100 laser vibrometer (with 25 mm/s/V sensitivity) is used to measure the tip velocity of the beams. The overhang lengths of the unimorphs are set to be 22.5 mm. The laser measurement point is 21.4 mm from the base of the beam. A total of 18 resistive loads used ranging from 15 Ohm to 10 MOhm. A Siglab 20-42 frequency analyzer is used to measure the tip-velocity-to-base-acceleration and voltage-output-to-base-acceleration FRFs of the cantilevers. A virtual sine sweep is used for the FRF measurements, where the excitation is a pure sine tone at constant frequency. The experiments are conducted in the 5 Hz to 10 kHz bandwidth with three averages at each frequency increment of 1 Hz. Figure 3.12 shows the tip-velocity-to-base-acceleration FRFs that

are measured for the specimen SC17 with PMN-PZT single crystal actuator and 0.387 mm thick stainless-steel substrate. The frequency responses to a range of resistive loads (varying from short circuit to open circuit) are shown. Note that the phase is wrapped between ±180 degrees.

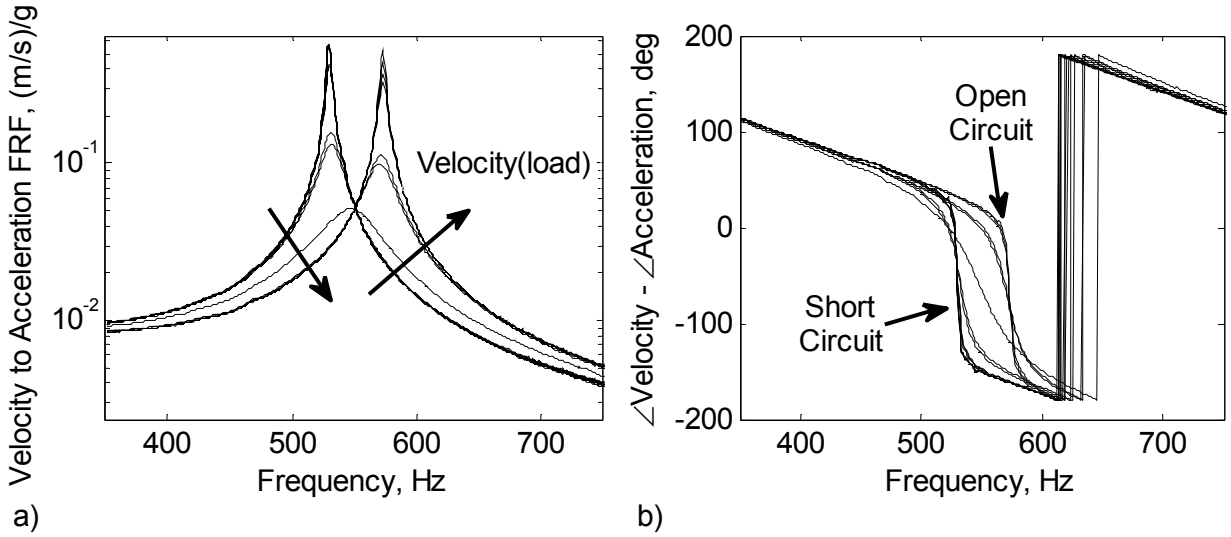

Figure 3.12: The measured tip-velocity-to-base-acceleration FRF a) magnitude and b) phase for harmonically base-excited clamped-free sample SC17.

For the single crystal and polycrystalline monolithic unimorph devices tested here, the direct electromechanical coupling is relatively high therefore the shift in resonance frequency is significant. Figure 3.13 presents the voltage-output-to-base-acceleration FRF of sample SC17.

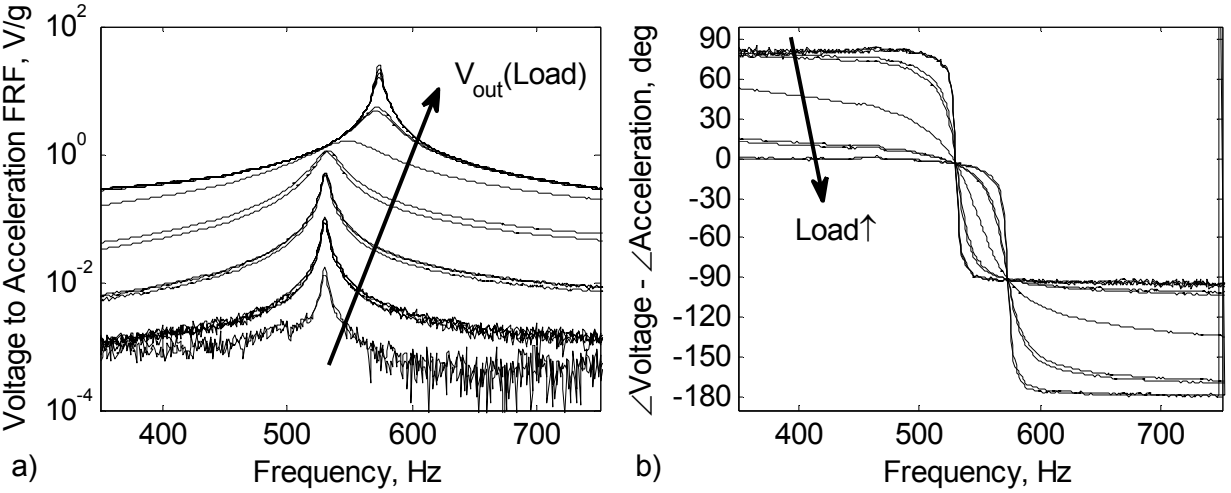

Figure 3.13: The measured voltage-output-to-base-acceleration FRF a) magnitude and b) phase for harmonically base-excited clamped-free sample SC17.

Similar to the mechanical response, a large shift in resonance frequency indicates the high direct electromechanical coupling. Note that all of the results presented next (current and power output) are deduced from these two measured FRFs for each unimorph sample.

Figure 3.14 presents the electrical response by the voltage-output-per-base-acceleration and current-output-per-base-acceleration as a function of load resistance for two unimorph beams with stainless-steel substrates. The first unimorph is the sample SC17 with PMN-PZT type single crystal piezoelectric and a 0.387 mm thick stainless-steel substrate. The second unimorph is the sample 5H22 with PZT-5H type polycrystalline ceramic and 0.386 mm stainless-steel substrate. The plots present 1) the response at short circuit natural frequency (ω_{sc}) and 2) the response at open circuit natural frequency (ω_{oc}). The "identical" PMN-PZT type piezoelectrics (used in the SCxx samples) have constant thickness of 0.2800 mm. Both the PZT-5H and the PZT-5A materials have a constant thickness of 0.2667 mm. The difference in the piezoelectric material thicknesses is negligible; therefore the comparison of the piezoelectric material properties (presented in this section) is reasonable.

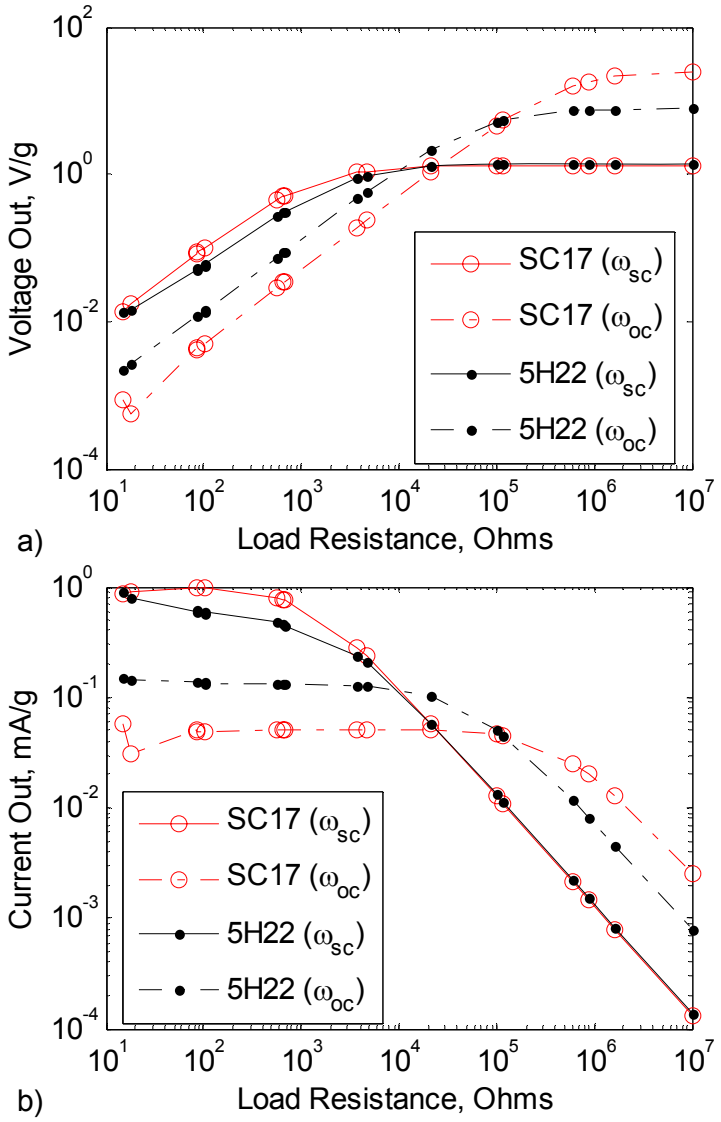

Figure 3.14: a) Voltage-output-per-harmonic-base-acceleration and b) current-output-per-base-acceleration of samples SC17 and 5H22 as a function of load resistance.

The mechanical response is represented in Figure 3.15a by the variation of resonance frequency due to electrical load and in Figure 3.15b by the variation in tip-velocity-to-base-acceleration also as a function of load resistance.

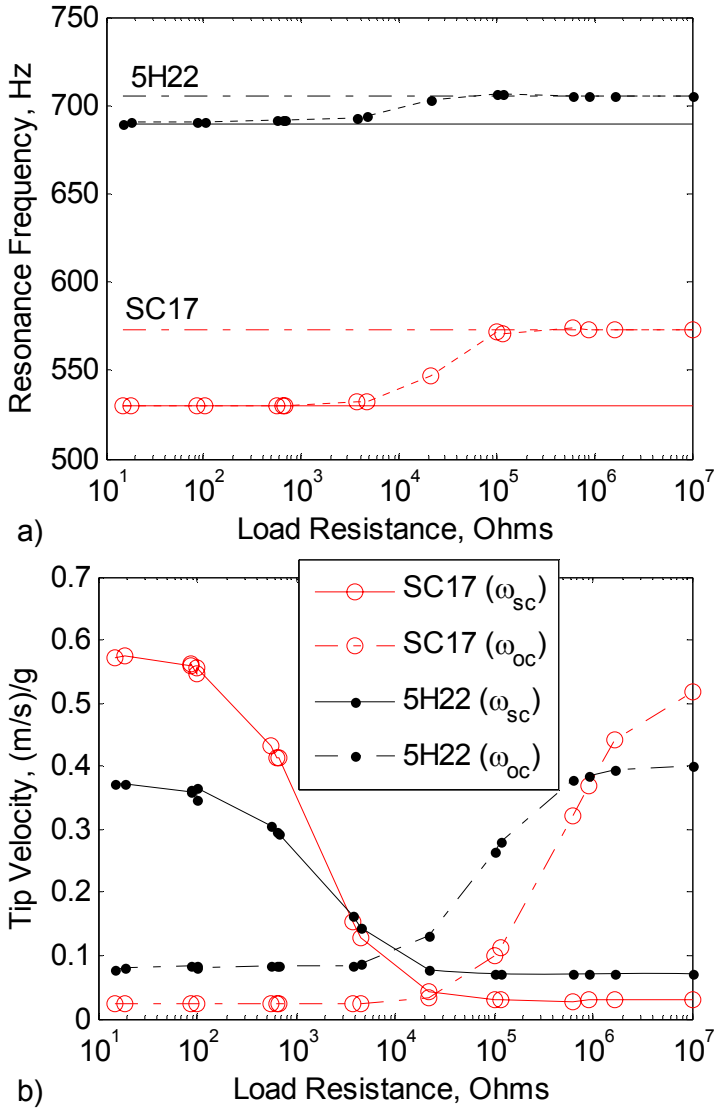

Figure 3.15: a) Resonance frequency variation and b) tip-velocity-per-base-acceleration response of samples SC17 and 5H22 as a function of load resistance.

Finally, Figure 3.16 presents the power output of the two unimorphs. The optimum load resistance (for maximum available power output) is realized for both the open circuit natural frequency and the short circuit natural frequency.

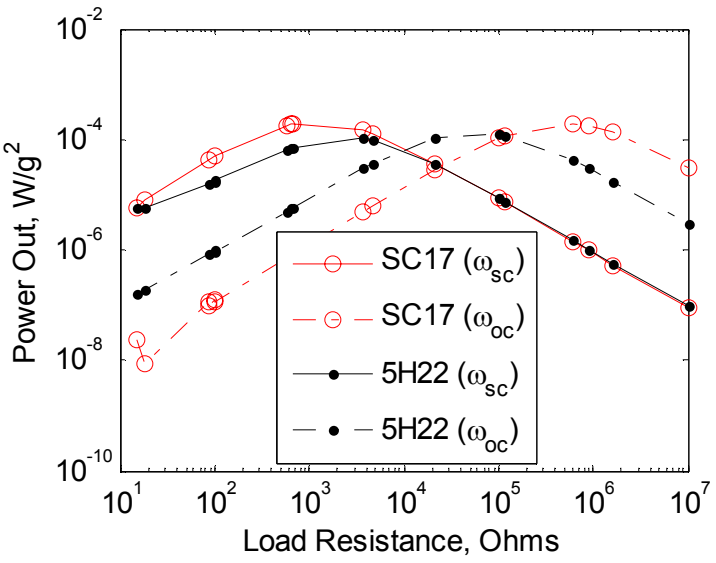

Figure 3.16: Power-output-per-harmonic-base-acceleration comparison as a function of load resistance for samples SC17 and 5H22.

As expected, the sample SC17 with the single crystal piezoelectric demonstrates high power output when compared to the PZT-5H material. Note that both samples use the same substrate material and thickness. It should be also noted that the thickness ratio is 1.38 for the SC17 and 1.45 for the PZT-5H. Such high thickness ratio coupled with the stiff substrate material (in comparison to the piezoelectric) guarantees that the comparison made here is fair because the mechanical strains induced on the PMN-PZT and the PZT-5H material are very close (if not same).

The mechanical and electrical responses of the other 22 samples are presented in Appendix B.3. In this section, the energy harvesting capabilities of all unimorphs (listed in Table 2.6) are summarized by plotting the values of interest against the substrate-to-piezoelectric thickness ratio and total unimorph mass. Figure 3.17 presents the maximum-power-output-per-base-acceleration measured for each unimorph. The maximum power output can occur at variable input frequency.

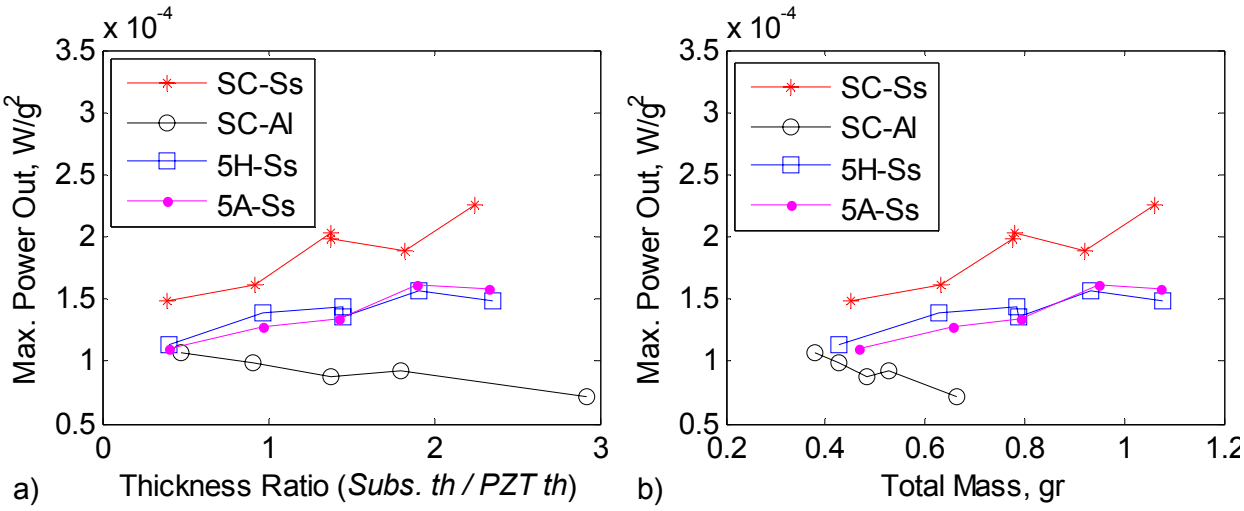

Figure 3.17: Maximum power output per harmonic base excitation as a function of a) thickness ratio and b) total unimorph mass.

It is observed that the thickness ratio (hence the total mass) has the expected effects on maximum power output for the piezoelectric and the substrates considered in this section. For the axially stiff (compared to the active material) stainless-steel material, the power output monotonically increases as the thickness ratio is increased. This effect confirms that the piezoelectric is moving away from the effective neutral-axis; therefore the strains induced (on the piezoelectric material) are getting larger. In contrast, the unimorphs with "softer" aluminum substrates show a decreasing power output as the thickness ratio is increased. The reason will be discussed shortly. Note that samples SC07 and SC17 both have the same piezoelectric and the substrate material and thickness. This also applies to samples 5H02 and 5H22. Due to the fabrication limitations, these two pairs of "identical" specimens have slightly different electrical and mechanical response. The differences are more apparent in the mechanical response presented next.

Figure 3.18 presents the mechanical response that corresponds to the maximum power operating point (P_{max}). Figure 3.18a presents the frequency at P_{max} which is in-between the open circuit resonance and short circuit resonance frequencies. Similarly, Figure 3.18b shows the tip-displacement-per-base-acceleration at the Pmax operating point.

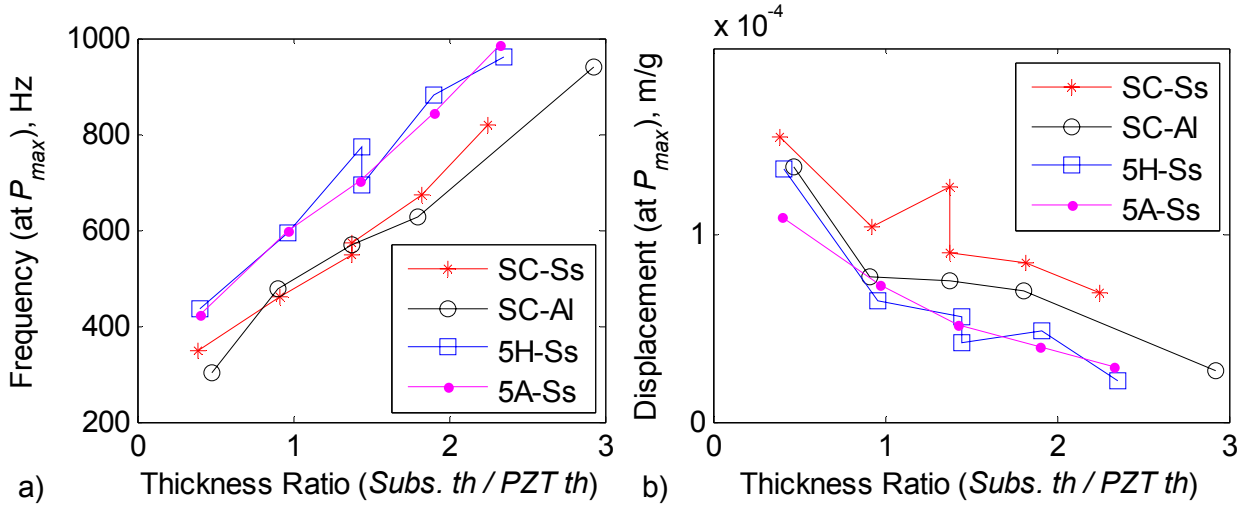

Figure 3.18: a) Frequency and b) displacement-per-base-acceleration at the maximum power operating condition as a function of thickness ratio.

As the substrate material is getting thicker, the unimorph is getting stiffer and heavier, and the net effect is an overall increase in natural frequencies and increase in bending stiffness. The electrical and mechanical response presented in Figure 3.17 and Figure 3.18 can also be presented for the short circuit natural frequency (ω_{sc}) and the open circuit natural frequency (ω_{oc}). These analyses result in similar trends that are observed in the variable frequency P_{max} operating condition; therefore the data is presented in Appendix B.3. The electrical output results are summarized in Table 3.2 for all 24 unimorph specimens with PMN-PZT, PZT-5H and PZT-5A piezoelectrics with aluminum and stainless-steel substrates.

Table 3.2: Energy harvesting response of unimorphs with PMN-PZT, PZT-5H and PZT-5A type monolithic piezoelectrics.

Sample	PZT Type	Subs.	*Subs. th / PZT th*	V_{max} (ω_{oc}) (V/g)	I_{max} (ω_{sc}) (mA/g)	P_{max} (μW/g^2)	$\omega(P_{max})$ (Hz)
1	PZT-5H	Al	1.45	7.12	0.54	100	747
2	PZT-5H	Ss	1.45	8.66	0.68	144	773
5	PMN-PZT	Ss	0.39	25.13	1.16	148	348
6	PMN-PZT	Ss	0.92	24.75	1.29	162	462
7	PMN-PZT	Ss	1.38	24.18	0.86	202	550
8	PMN-PZT	Ss	1.82	20.46	0.79	189	671
9	PMN-PZT	Ss	2.25	19.35	1.37	226	819
10	PMN-PZT	Al	0.50	14.05	0.91	86	346
11	PMN-PZT	Al	0.91	21.87	0.93	99	477
12	PMN-PZT	Al	1.38	15.59	0.66	88	569
13	PMN-PZT	Al	1.81	14.98	0.53	92	626
14	PMN-PZT	Al	2.92	15.42	0.94	72	939
16	PMN-PZT	Al	0.47	17.45	0.97	107	303
17	PMN-PZT	Ss	1.38	25.05	0.88	199	574
20	PZT-5H	Ss	0.41	7.35	0.60	114	436
21	PZT-5H	Ss	0.96	8.68	0.90	139	592
22	PZT-5H	Ss	1.45	7.72	0.88	135	693
23	PZT-5H	Ss	1.91	8.66	0.94	156	881
24	PZT-5H	Ss	2.35	8.20	0.59	149	960
25	PZT-5A	Ss	0.40	6.66	0.27	110	422
26	PZT-5A	Ss	0.97	8.25	0.64	127	600
27	PZT-5A	Ss	1.43	8.00	0.67	135	704
28	PZT-5A	Ss	1.90	9.83	0.55	162	843
29	PZT-5A	Ss	2.33	8.72	0.79	159	984

As noted earlier, the thickness ratio has a significant effect on maximum power output of the specific unimorphs used here with aluminum and stainless-steel substrate materials. For the stainless-steel material, the power output monotonically increases as the thickness ratio is increased. This effect (which is also discussed in Section 3.1) is expected due to the following reasons: 1) The stainless-steel substrate stiffness (in the unimorph axial direction) is significantly larger than both of the polycrystalline and single crystal piezoelectric stiffness. 2) As the thickness ratio is increased, the effective neutral axis of the unimorph approaches the (original) neutral axis of the substrate material. On the other hand, the active material is moving away from the neutral axis; therefore it is subjected to larger strains causing larger voltage outputs. 3) The

change in thickness ratio applied in the experiments is through the increase of the thickness of the substrate while the piezoelectric material thickness is kept constant. Remember that change in thickness ratio does not change the capacitance of the active material (for the samples considered in this section). The net result of these three conditions is a monotonic increase of power as the substrate thickness is increased (while active material choice is kept same).

In contrast to the stiff stainless-steel material, the "softer" aluminum shows a different power vs. thickness ratio relationship. The maximum power output (shown in Figure 3.17, Figure B.12 and Figure B.13) decreases as the thickness ratio is increased. This effect indicates that the effective unimorph neutral axis is not far enough from the neutral axis of the piezoelectric material. In the case where the substrate and piezoelectric material Young's moduli are close, the effect of thickness ratio becomes similar to the displacement-to-input-voltage response presented in Section 2.1 (for actuation characterization of MFC unimorphs) and in 2.3 (for actuation characterization of single crystal unimorphs). Additional discussion is presented in Section 3.4.3.

3.4. Conclusions

In conclusion, the unimorph energy harvester with MFCs demonstrated the lowest harvesting capability (per piezoelectric material mass) due to its low capacitance. In general, the MFC actuator is far superior in aerodynamic applications when compared to other piezoelectric materials evaluated in this section due to its flexibility and ease of application. Monolithic polycrystalline and single crystal piezoelectrics do offer better harvesting capabilities when compared to fibrous, interdigitated polycrystalline piezoceramics (such as MFCs); however the application of monolithic piezoelectric materials are not practical for large strain aerodynamic applications.

The following sections present a brief summary of the conclusions. First, the conclusions from the energy harvesting results of the thin unimorphs with MFCs are presented. Next, conclusions on harvesting characterization of unimorphs with thick substrates are given. Finally, the results are discussed for single crystal piezoelectrics in relationship to the polycrystalline materials. The effect of substrate-to-piezoelectric thickness ratio on the power output is summarized.

3.4.1. Thin Unimorphs

The thickness ratio does not appear to have a conclusive effect on maximum power output of the specific MFC unimorphs used here with aluminum and brass substrate materials. For the stainless-steel material, the power output monotonically increases as the thickness ratio is increased. This effect is due to the following reasons: 1) The stainless-steel substrate stiffness (in the unimorph axial direction) is significantly larger than the MFC stiffness. 2) As the thickness ratio is increased, the effective neutral axis of the unimorph approaches the (original) neutral axis of the substrate material. On the other hand, the active material is moving away from the neutral axis; therefore it is subjected to larger strains causing larger voltage outputs. 3) The change in thickness ratio applied in the experiments is through the increase of the thickness of the substrate while the MFC device and its thickness are kept constant. An optimum thickness ratio is expected in a wider thickness ratio range.

3.4.2. Thick Unimorphs

The experimental analysis of four clamped-free thick unimorphs employing polycrystalline piezoceramics showed that the interdigitated MFC type piezocomposites are not as effective in energy harvesting performance as its monolithic counterpart. The unimorph with the MIDE QP10N device (with industry-type 5A ceramic) shows the largest mass-normalized-power-output which is identified during the resistive-shunt experiments. For all four piezoceramic devices, it is discovered that some energy can be harvested during the feedback control effort (see Section 2.2.3). Although not addressed here, intelligent design of electronics and nonlinear control laws can take advantage of the existing energy in the environment and reduce the power consumption of the control effort.

3.4.3. Single Crystal Unimorphs

The expected effect of thickness ratio on maximum power output is realized with unimorphs with monolithic piezoceramics. For the stiff substrate materials (in comparison to the piezoceramic), the power output monotonically increases as the thickness ratio is increased. In contrast to the stiff stainless-steel material, the “softer” aluminum shows a different power vs. thickness ratio relationship. The maximum power output decreases as the thickness ratio is increased. This effect indicates that the effective unimorph neutral axis is not far enough from the neutral axis of the piezoceramic. In the case where the substrate and piezoceramic Young’s

moduli are close, the effect of thickness ratio becomes analogous to the displacement-to-input-voltage response presented in Section 2.1 (for actuation characterization of MFC unimorphs) and in 2.3 (for actuation characterization of single crystal unimorphs). One can expect an "optimum" substrate-to-piezoelectric thickness ratio for comparable values of Young's moduli (of substrate and piezoelectric material). For pre-optimum thickness ratios, the power output (due to bending) goes to zero as the axial strain in the piezoelectric material is diminished. In the post-optimum thickness ratios, the power output is expected to drop.

CHAPTER 4

LIGHTWEIGHT CIRCUITS FOR PIEZOELECTRIC BIMORPH ACTUATORS

There are two main drawbacks in implementing open-loop shape control with Macro-Fiber Composites: 1) Its high voltage input requirement (1500 V) and 2) its asymmetry in the positive and negative applied voltage directions. The Macro-Fiber Composite actuators are demonstrated to be excellent in inducing high strains to the substrate materials that they are bonded on (see Section 2.1 and Section 2.2). On the other hand, the MFC actuator has an asymmetric actuation voltage range of -500 V to 1500 V. Another challenge is added if an MFC bimorph is employed (instead of an MFC unimorph) to achieve larger strain outputs. A bimorph device with MFC actuators and with a conventional serial or parallel electrical connection (using a single bipolar amplifier) limits the actuation to the -500 V to 500 V range in order not to exceed the -500 V limit on both of MFCs. To remedy this situation, a solid-state electrical circuit employing diodes and resistors is proposed and tested in this section. The circuit allows a single bipolar amplifier to actuate a bimorph composed of two MFC actuators to its peak-to-peak input voltage range.

The circuit proposed in this section allows the division of the input voltage so that: 1) The MFC that is in extension receives 1500 V (which is the maximum positive voltage), and 2) The MFC that is in compression receives -500 V (which is the maximum negative voltage). The circuit also allows the actuation in the opposite direction without any physical changes (i.e. not using any electromechanical switches). The input-output relationship of the circuit is characterized experimentally.

The section is organized as follows. First, the electrical requirements for a bimorph are presented. Next, conventional methods of high voltage actuation are presented. Next, the novel circuit design is presented. The input-output characteristics of the circuit are evaluated

experimentally. Finally, several MFC bimorphs are driven with the circuit to prove the effectiveness of the design. The chapter concludes with the summary of results.

4.1. Requirements for MFC Actuated Bimorphs

The bimorph actuated via MFC actuators require several electronic components for achieving maximum actuation range. In contrast to the traditional bimorph (with *31* mode monolithic piezoceramic), the *33* mode interdigitated MFC has an asymmetric (-500 V to +1500 V) actuation range. For a monolithic ceramic based bimorph, a serial (or parallel depending on the polarization direction) electrical connection provides equal voltage drop across both ceramics, hence there is no risk of de-polarization. If an MFC is connected in serial, the negative limit of -500 V can be exceeded (with the application of 1500 V to the opposite layer) and the piezoceramic will be de-polarized.

For a bimorph employing monolithic ceramics (shown in Figure 1.2), the voltages *V1* and *V2* can be tied together (and supplied from the same source). Therefore, a single bipolar power source is sufficient for peak-to-peak actuation. If an MFC is connected in the same fashion, the actuation range will be limited to -500 V to +500 V. In most applications and specifically the aerodynamic applications considered in this dissertation, it is critical that the peak-to-peak range is employed. Figure 4.1 illustrates the functional components of the bimorph employing two *33* mode interdigitated MFC actuators.

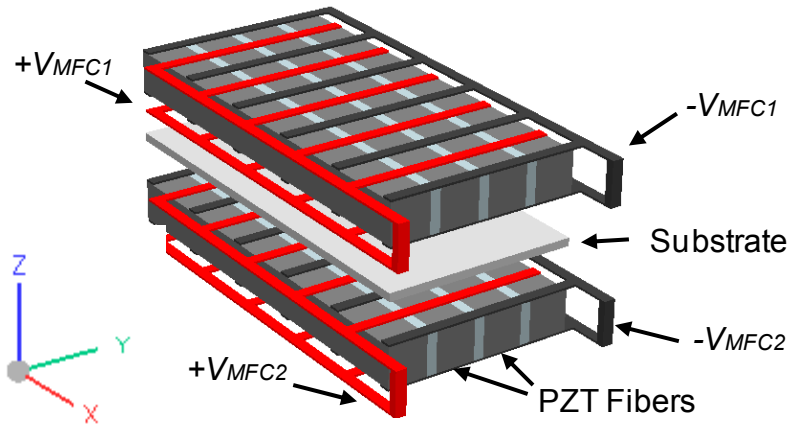

Figure 4.1: Illustration of the MFC bimorph.

In a bimorph device, a thin substrate is typically sandwiched between two active materials (or MFCs). In Figure 4.1, the interdigitated electrodes and PZT fibers are scaled up to aid illustration.

4.2. High Voltage Circuit Configurations

The effective application of the electromechanical actuators requires attention to the electronics as well as the structure. The highest deformation (per active material mass density) by a piezoceramic based actuator can be achieved by a bipolar bimorph configuration [Inman and Cudney, 2000]. In the bimorph configuration, the electronics can supply currents in both directions, and the actuator has two MFCs that can to be actuated in opposite polarity (and the voltage regulated depending on that polarity).

For a lightweight implementation of a piezoceramic actuator (i.e. in an aerospace application), there are several approaches with incremental increases in complexity and performance. First, a single unipolar direct-current-to-direct-current (DC-DC) converter allows the conversion of low voltage (typically 3 V – 24 V) high current (0.1 A – 1 A) source to a high voltage (0 – 10 kV) and low current output. Although the name suggests DC to DC conversion, these converters are typically capable of dynamic output up to the high frequency limit of 10 to 20 Hz. Using a single DC-DC converter focuses on actuation in one direction (since the converter is unipolar) and leverage approximately 75% of the MFC input voltage range. To attain an actuation range of 100%, a unipolar voltage signal to the MFC can be switched depending on the desired actuation direction. An electromechanical relay or multiple bipolar converters can be used; however it is known that relays do not provide fast switching and cause electrical discontinuities. On the other hand, using multiple (dedicated) converters to achieve bipolar actuation of the MFC can increases the weight and power consumption by two (or four for some cases). The configuration that allows the maximum actuation range can also introduce the penalties of increased weight and complexity, and a reduction of overall efficiency and energy density. The following sections will describe (in order of complexity) the individual components and typical configurations.

4.2.1. DC-DC Converters

A DC-DC converter is a relatively simple device that amplifies a DC signal depending on a desired voltage and power output. The DC-DC converters that must be used for this application tend to be specific to piezoceramics (as well as lasers) because of the (relatively) low power consumption of these systems. A low voltage power source can be converted using a DC-DC converter with approximately 45% electrical efficiency at a bandwidth of 0 - 10 Hz. These converters typically receive 0.7 to 24 V input and can output up to 10 kV proportional to the input range. Maximum power output is typically 1 - 10 Watts. A buffer amplifier is typically used to drive the DC-DC converter, where current can be drawn from a power source (i.e. battery) and the voltage output is controlled by a reference voltage (i.e., from a data acquisition system). Figure 4.2 shows model AM1505 DC-DC converter from AM Power Systems, NV, USA [AM1505].

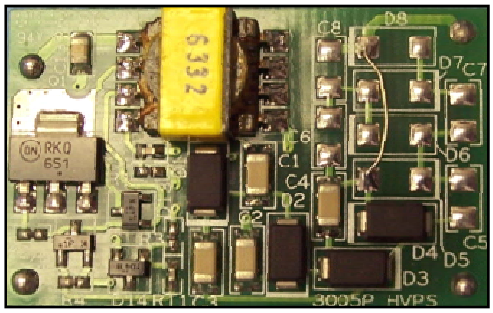

Figure 4.2: The AM Power Systems standard PCB mount unipolar DC-DC converter. The board is 23 mm tall and 36 mm wide, and has a mass of 4.60 grams.

Several DC-DC converters are experimentally analyzed to understand their electrical properties. Figure 4.3 shows the electrical response of an AM2505 type converter (with 0.7 – 5 V input and 0 – 2500 V output) from AM Power Systems. The voltage input-output relationship is given for static voltage inputs.

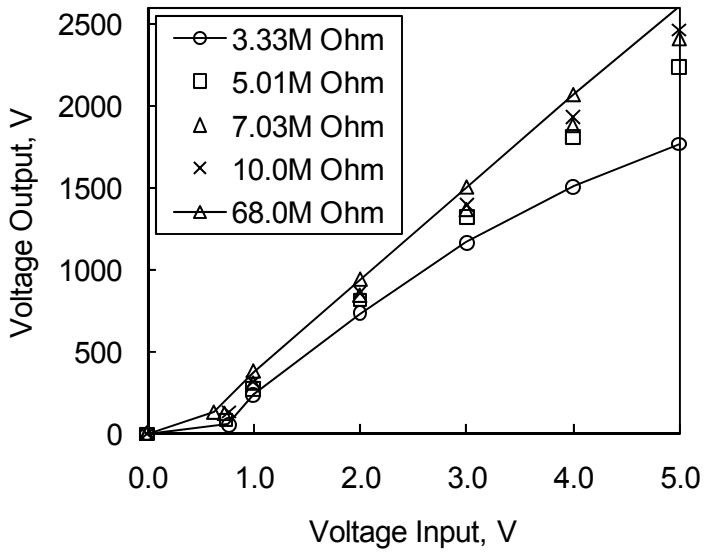

Figure 4.3: Voltage input-output characteristics of the AM2505 DC-DC converter.

The output of the converter is measured by a Fluke 80K-15 probe (with 1 GOhm resistance and 1000:1 ratio) and a Fluke 87III multimeter. The input is provided by an Agilent digital DC power supply. The power supply provides readout of the current output; hence the power calculations presented next represent the actual power consumption. Figure 4.4a presents the power consumption for several resistive loads. Figure 4.4b shows the electrical conversion efficiency (which is the ratio of the experimentally measured output power to input power).

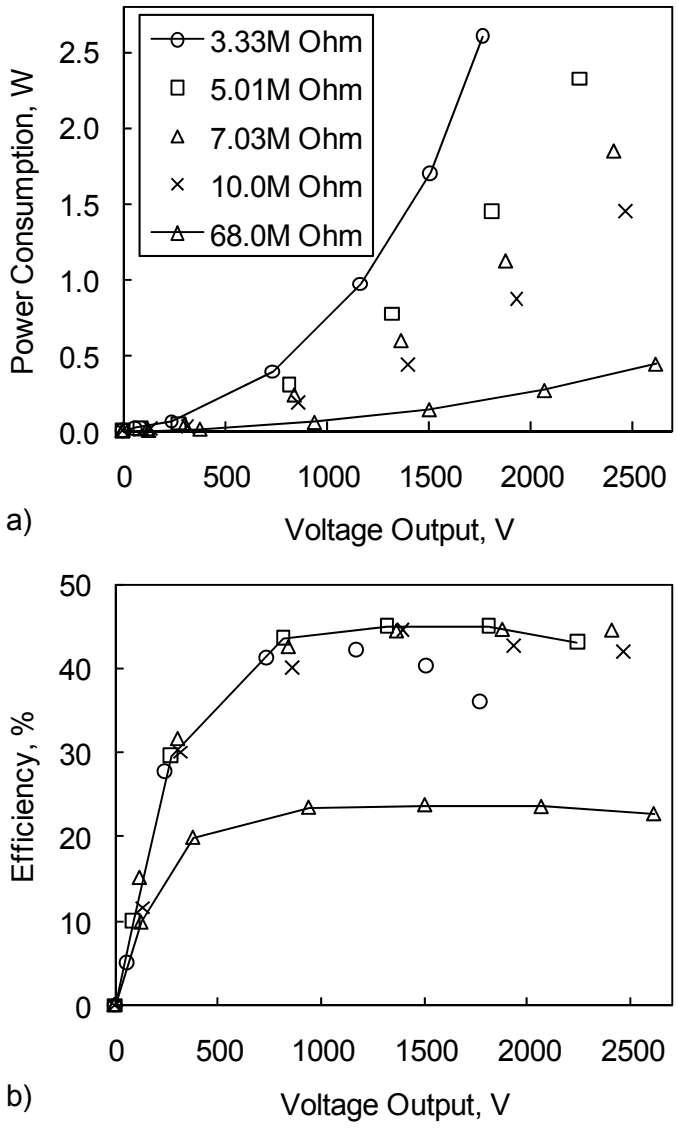

Figure 4.4: Electrical characteristics of the AM2505 DC-DC converter. a) Total power consumption and b) electrical efficiency. Legends are the same for both plots.

The DC-DC converter with 5.01 MOhm load shows a relatively high efficiency and it is capable of reaching 2 kV output (which will be necessary for the designs illustrated next). Performance characteristics of other relevant DC-DC converters are presented in Appendix D.1.

4.2.2. Unipolar Unimorph Configuration

The simplest electrical configuration is the unipolar unimorph device. A single unipolar DC-DC converter is used to power the single MFC on the unimorph actuator. Figure 4.5 shows a typical electrical circuit for this configuration.

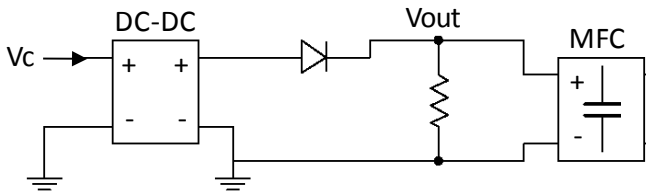

Figure 4.5: Unipolar unimorph configuration.

where *Vc* represents the control input, *Vout* is the output voltage (proportional to *Vc*). The MFC can be represented as a capacitor for the purposes of the discussion in this chapter. In contrast to conventional electrical amplifiers, DC-DC converters have very high output impedance and they can't sink currents returned from the load. Therefore, a diode is placed on the output to limit currents into the converter. If the output potential falls below the potential stored in the MFC, the current is "bled" through the resistor in parallel. In the discharging phase, the MFCs response becomes first-order, where the discharge rate can be increased (hence the response made faster) by reducing the resistance. In this configuration, the bleed resistor constantly consumes power which creates a trade-off between response time and power consumption. A single MFC can be actuated from 0 to 1500 V with this configuration.

4.2.3. Bipolar Unimorph Configuration

A single DC-DC converter does not allow a bipolar (both negative and positive) output, thus it does not allow the MFC to reach the peak-to-peak actuation range. Bipolar converters are available, however due to their complex electrical architecture they are heavier and more expensive. To achieve a bipolar signal (without a bipolar amplified), a simple configuration can be utilized which uses two unipolar DC-DC converters and diodes. A diagram of the bipolar unimorph design can be seen in Figure 4.6.

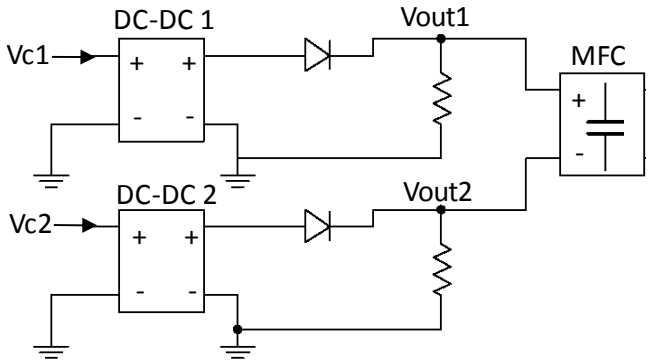

Figure 4.6: Bipolar unimorph configuration.

Depending on the voltage difference between the two "opposing" DC-DC converters, the current is able to flow in either direction across the load (or the MFC). The voltage across the MFC is simply the difference of the two outputs (*Vout1*-*Vout2*) which is proportional to the difference of the control voltages (*Vc1*-*Vc2*). An external signal controller (i.e. microcontroller or a data acquisition system) can be used to determine the control voltages sent to each converter; hence achieving a certain potential difference. The amplitude of the converters will affect which way the current flows through the MFC patches, thus which way the patch will morph (and whether the MFC is in tension or compression).

4.2.4. Bipolar Bimorph Configuration

The bipolar unimorph configuration limits the actuation because the morphing structure can be deflected using a single MFC. A more complicated electrical solid-state (meaning that an electromechanical switch is not used) configuration can be implemented by using three unipolar DC-DC converters. This configuration allows for one patch to be fully actuated (+1500 V in extension) while the other is actuated to its full capability in the other direction (-500 V in compression). The configuration is demonstrated in Figure 4.7.

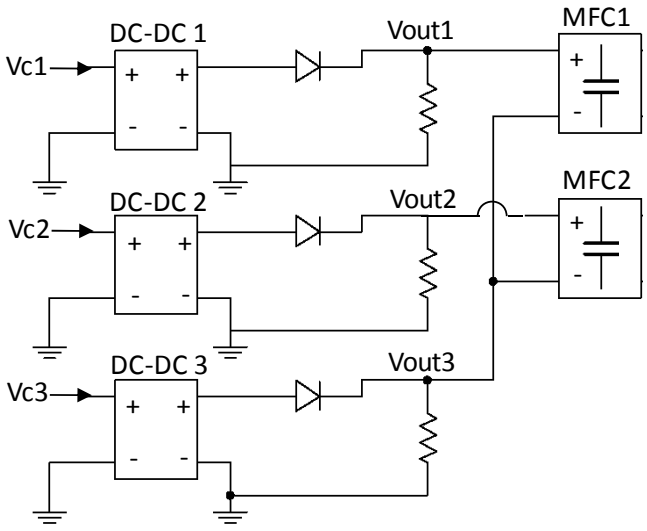

Figure 4.7: Bipolar bimorph configuration employing three unipolar DC-DC converters. In this configuration, the DC-DC converters can be replaced with two bipolar amplifiers.

In this configuration, the DC-DC 3 output (*Vout3*) can be kept at a constant voltage 500 V. As an example, if a maximum positive deformation is desired, the input control (*Vc1*) can be

controlled so that voltage across MFC1 (*Vout1-Vout3*) is 1500 V. Similarly, *Vc2* can be set to zero so that MFC2 voltage (*Vout2-Vout3*) is equal to -500 V. This configuration is the heaviest solution with significant part count, but enables full actuation of an MFC bimorph. Two bipolar amplifiers may be preferred instead of three unipolar amplifiers.

4.3. Novel Solid-State Switching Voltage Divider

As stated earlier, a bimorph actuator can be used to achieve a higher deformation (than unimorphs) employing two piezo-composite actuators operating in *33* mode (MFCs in our case) instead of two monolithic piezoceramics which operate in *31* mode. The current issue is that the maximum driving voltage range is "asymmetric". The proposed novel passive solid-state electrical circuit design allows division of voltage depending on the direction of current. This switching is required for a bimorph in two possible electrical configurations with 1) two unipolar or 2) a single bipolar DC-DC converter. The proposed design consists of solid-state passive electrical components (resistors and diodes). The circuit allows serial actuation of smart-material transducers with asymmetric actuation range. The circuit is presented in Figure 4.8 (highlighted in the large dashed box).

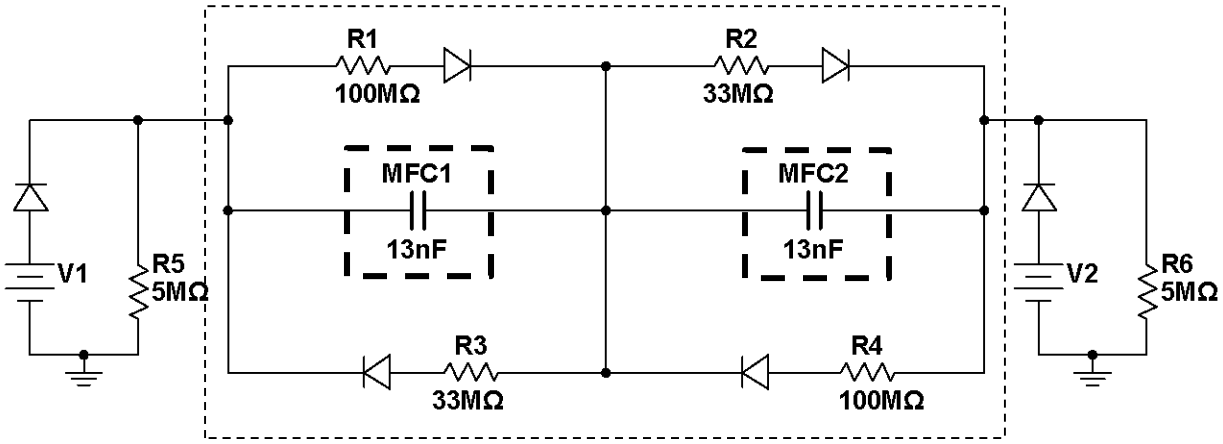

Figure 4.8: Current direction selective voltage divider circuit.

In the figure, the input voltages are represented by sources *V1* and *V2* (which are both grounded with bleed resistors. Note that the MFCs are represented by capacitors with 13 nF value in the circuit diagrams. These capacitors for "representative" purposes and they 1) do not represent the actual (high order) dynamic response of the MFC bimorph and 2) are not a part of

the proposed circuit. In order to analyze the circuit, let's assume two identical MFC actuators (MFC1 and MFC2) with -500 V to +1500 V actuation range that are bonded in a bimorph configuration. In order to continuously drive these two actuators (to their peak-to-peak range) with opposite polarity, two separate driving circuits are required. The proposed circuitry allows a single driving circuit to drive two actuators in opposite fields, and with a ratio depending on the input polarity. The operating scenario follows:

Scenario A: The simplified electrical diagram (for scenario A) is presented in Figure 4.9. Assume that the input driving potential is acting in one direction, where *V1>V2*. In this case, the circuit can apply +1500 V to the MFC1 and -500 V to the MFC2.

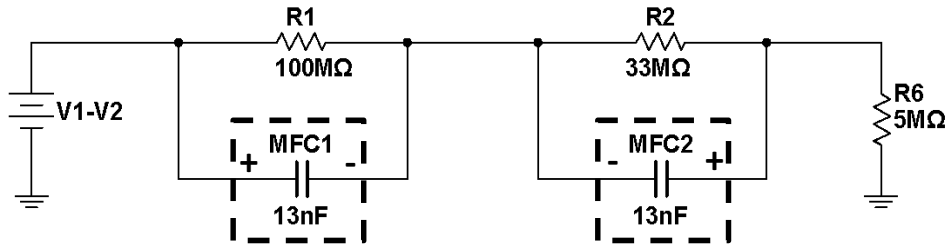

Figure 4.9: Representative circuit for *V1>V2* operating condition.

The division of the input voltage (*Vin = V1 - V2* from the source) is determined by the simple voltage divider rule imposed by the resistances *R1* and *R2* and the bleed resistor *R6*, where

$$V_{MFC1} = (V1 - V2) * \frac{R1}{R1 + R2 + R6} \tag{4.1}$$

and

$$V_{MFC2} = -(V1 - V2) * \frac{R2}{R1 + R2 + R6}. \tag{4.2}$$

It is desired that the bleed resistor is small (relative to the divider resistors) so that most of the voltage drop occurs across the MFCs. On the other hand, the bleed resistor has to be kept high so that power source (i.e. DC-DC converter) is not loaded beyond its limits. The bleed resistor choice of 5 MOhm (shown in Figure 4.8) is due to the converter characterization presented in Figure 4.3.

Scenario B: The simplified electrical diagram (for scenario B) is presented in Figure 4.10. Assume that the input driving potential is acting in the opposite direction (to the given direction in scenario A). In this case, the circuit can apply -500 V to MFC1 and +1500 V to the MFC2.

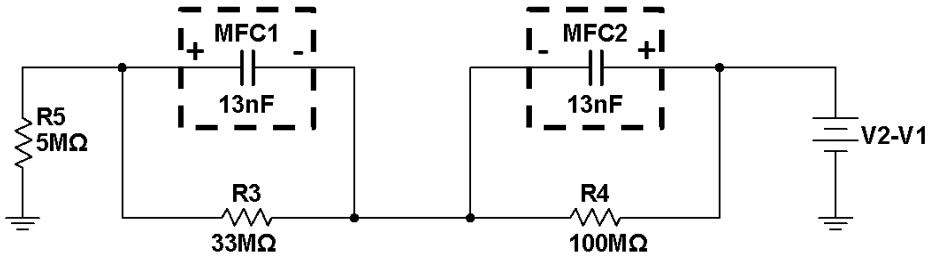

Figure 4.10: Representative circuit for current *V2>V1* operating condition.

Similar to scenario A, the division of the input voltage (*Vin = V2 - V1* from the source) is determined by the simple voltage divider rule imposed by the resistances *R3* and *R4* and the bleed resistor *R5*, where

$$V_{MFC1} = -(V2 - V1) * \frac{R3}{R3 + R4 + R5} \tag{4.3}$$

and

$$V_{MFC2} = (V2 - V1) * \frac{R4}{R3 + R4 + R5}. \tag{4.4}$$

The circuit can switch and operate in both cases (without any physical changes) by employing a total of four diodes. The circuit chooses the specific "voltage divider" resistances depending on the input potential polarity (hence the direction of the current).

The proposed circuit (shown in Figure 4.8) is prototyped on a breadboard and experimentally evaluated. First, the input-output relationship is characterized. The operational prototype will be presented in the next section. Four diodes (model SP5L [SP5L] from HV Component Associates, NJ, USA with 5 kV reverse breakdown voltage) are used along with two 33 MOhm and two 100 MOhm resistors (purchased from DigiKey Corp). The bipolar high voltage potential is generated by a TREK 623B high voltage amplifier. The amplifier is capable of ±2 kV output, and it allows the monitoring of output current and voltage. The voltage output

is connected directly across the circuit. The output of the circuit is measured by a Fluke 80K-15 probe (with 1 GOhm resistance and 1000:1 ratio) and a Fluke 87III multimeter. Figure 4.11a shows the input-output response of the circuit. The input voltage represents the output of the TREK amplifier, and the voltage output corresponds to the two outputs of the circuit (which are connected MFC1 and MFC2 and measured with the Fluke probe). Figure 4.11b shows the voltage loss across the circuit. The voltage loss is calculated by:

$$V_{loss} = V_{input} - (V_{MFC1} + V_{MFC2}). \tag{4.5}$$

This voltage loss is mostly due to the small voltage drops across the diodes. Note that static input voltages are used for this characterization.

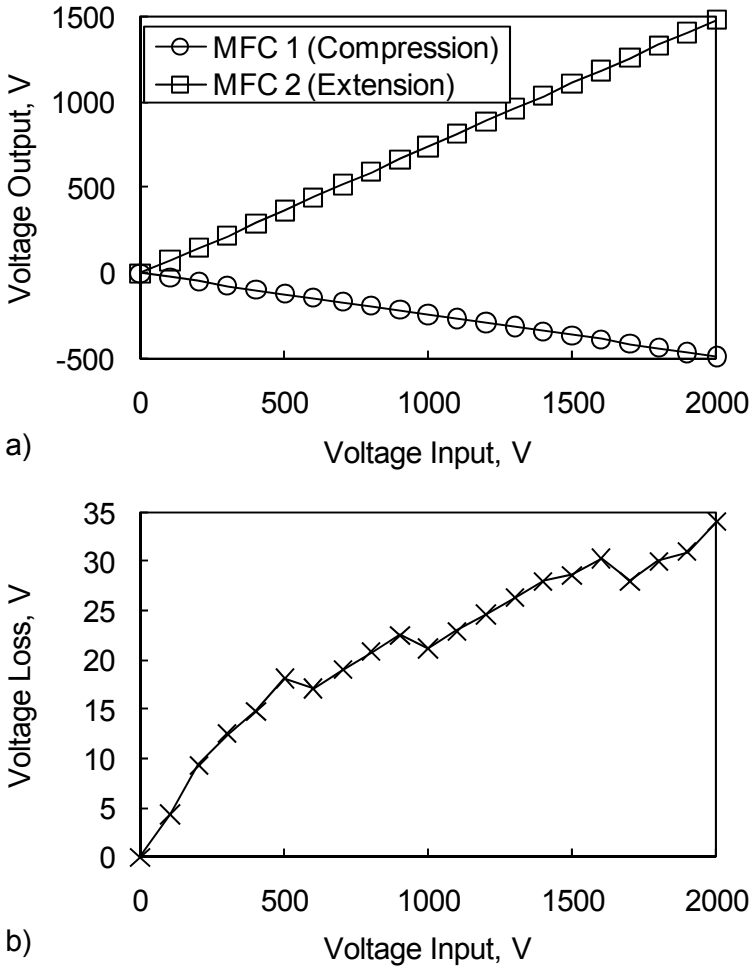

Figure 4.11: Electrical response of the prototype to static voltages. a) Voltage input-output, b) voltage loss across the circuit.

Figure 4.11 shows an excellent linear input output relationship for both outputs. The MFC1 (which is assumed to be in compression) receives up to -500 V. Simultaneously, the MFC2 (which is in extension) is actuated with a +1500 V potential. Only the positive part of the actuation range is shown in the figure for clarity. The total voltage drop across the circuit is low; hence the power loss due to resistive heating is small.

The circuit concept allows a bimorph (with two MFC devices) to be actuated to its full input range using a single bi-polar power source. The circuit can also be connected to two unipolar DC-DC converters as illustrated in Figure 4.8. The circuit is composed of resistors and diodes; therefore the useful bandwidth of the circuit is limited by three factors: 1) frequency limit of the piezoceramic (10 kHz for the MFC actuator), 2) the power input limitation of the piezoceramic (which is a function of both amplitude and frequency) and 3) the frequency and power limitation of the diode (due to the small junction capacitance and heat dissipation limitations). These restrictions are specific to the components used in the system; therefore the reader is referred to the product specifications listed by the manufacturer of the MFC actuator (Smart-Material Inc). and the high voltage diode (HV Component Associates).

The electrical components (four diodes and four resistors) used for the prototype has a total mass of 1.20 grams. The components can easily be assembled on a single layer printed circuit board (PCB) with 10 mm x 20 mm dimensions. A typical single layer PCB with this area has a mass of 0.38 grams. An upper bound of 1.58 grams is estimated for the design implemented on a PCB in a lab environment. The commercial fabrication techniques can easily bring the size and weight down, and implement the design on a single chip.

4.4. Actuation Characteristics of MFC Bimorphs

In order to evaluate the actual dynamic operational performance of the circuit (with a bimorph), a separate experiment is conducted. Several bimorph actuators are used in the tests with each bimorph having two MFC M8507-P1 type actuators. Table 4.1 presents the properties of the bimorphs with different substrates. In addition to conventional metal substrates, fiber-epoxy composites are also considered. Note that the MFC actuator has a thickness of 0.305 mm at its active region.

Table 4.1: Substrate properties of bimorphs with MFC M8507-P1 type actuators.

Sample	Substrate	*Subs. th*, mm
B1	Carbon Veil / Epoxy	0.114
B2	Stainless-Steel	0.027
B3	None	0.000
B4	Aluminum	0.055
B5	Glass Fabric / Epoxy	0.140
B6	None	0.000
B7	Glass Fabric / Epoxy	0.305

The experimental results presented in this section are from the Sample B2 with 0.027 mm thick stainless-steel substrate. Experimental measurements of elastic moduli of the composite substrates are presented in Appendix C. The experimental results from other bimorphs (listed in Table 4.1) are presented in Appendix D.2. A 3M DP460 two part epoxy is used for bonding the MFC patches to the metal substrates (samples B2 and B4) and to themselves (samples B3 and B6). The composite substrates (samples B1, B5 and B7) are bonded to the MFCs during cure process with West System 205 + 105 epoxy-resin system. All bimorphs are cured under 0.8 Atm vacuum for approximately 24 hours.

Figure 4.12 shows the important components of the experimental setup. An MTI Instruments LTC-200-100-SA laser displacement sensor is employed to measure the displacement of the bimorph. The free length of the bimorph is 89 mm and the laser measurement location is 85 mm from the clamped base.

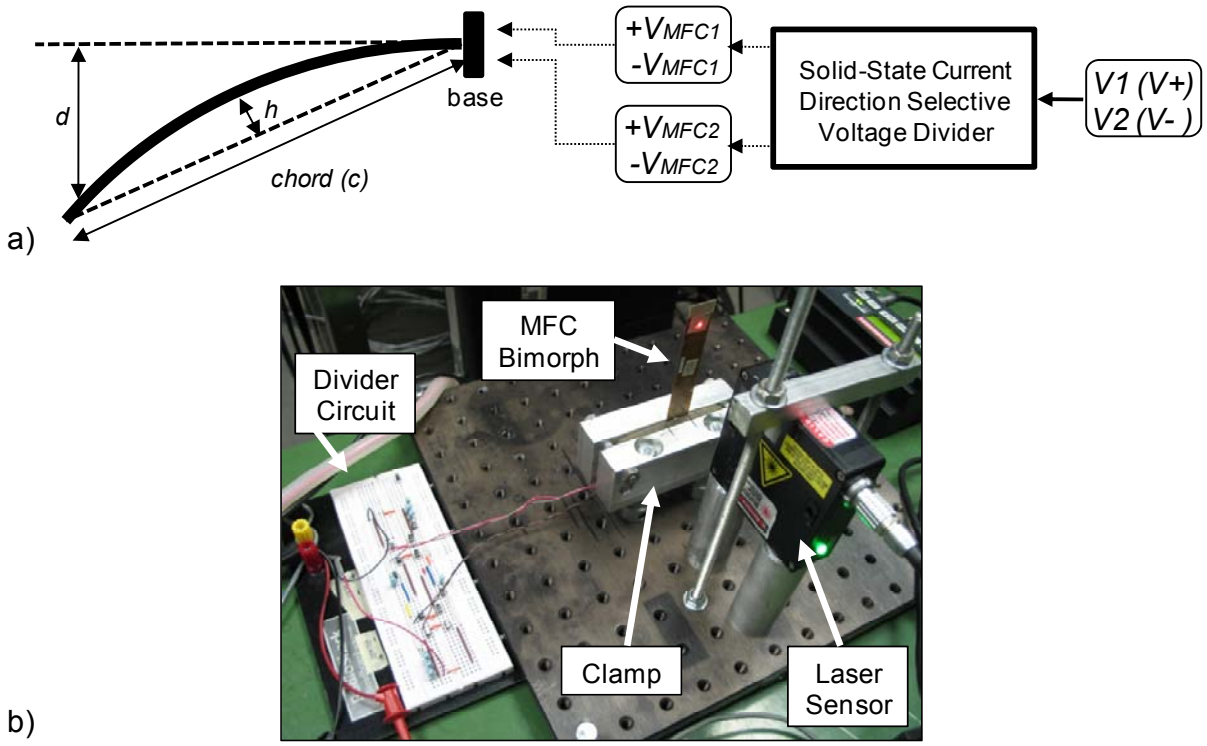

Figure 4.12: Experimental setup for testing the prototype circuit and the MFC bimorphs. a) Diagram of test and description of parameters, b) Picture of the test setup.

In Figure 4.12a, the deformation of the clamped-free MFC bimorph is approximated by a circular arc with constant curvature. This is a good assumption for the range of frequencies that are well below the 1st natural frequency because the active material covers the full length of the substrate. The parameter d is the measured peak displacement, and h is the height of the arc from its chord line with length c. A common measure of deformation in an aerodynamic application, camber, is calculated by $Camber = h/c$. Another measure of the deformation is the curvature, and it is simply $\kappa = 1/r$ where r is the radius of the circular arc. A TREK 623B high voltage amplifier is used to supply the input voltage. A National Instruments (NI) cDAQ data acquisition system with an NI 9215 input module (with isolated 4 channels, 16 bit conversion) and an NI 9263 output module (with 16 bit conversion) is used to control the multi-parameter experiment. A pure sine tone with constant amplitude and frequency is used to actuate the bimorphs. The deformation is recorded for 5 complete cycles and these cycles are averaged. The peak-to-peak displacement of the bimorph is extracted from the nonlinear hysteresis loop. Two types of tests are conducted: 1) Low frequency high amplitude and 2) high frequency and low amplitude. The low frequency tests are conducted between 0.02 – 10 Hz bandwidth with 100 – 2000 V peak

actuation amplitude. The high frequency tests are conducted in the 1 – 500 Hz bandwidth with 100 – 500 V peak actuation amplitude. The high frequency high amplitude tests are not possible simply due to the power input limitations of the MFC M8507-P1 type actuator.

4.4.1. Low Frequency High Amplitude Tests

Figure 4.13 shows an example of the hysteresis loops (for displacement, current input and power consumption vs. voltage) that are measured during the 2 kVpeak (4 kVpp) sine tone actuation at 10 Hz for sample B2. The instantaneous current and power consumption of the bimorph and the circuit are measured with the current monitor on the TREK 623B amplifier.

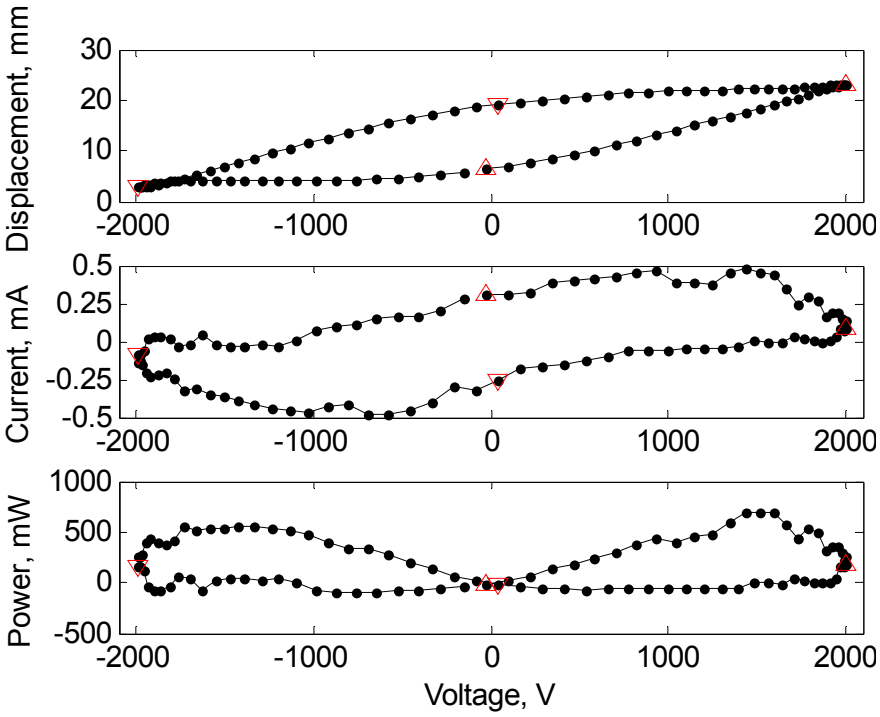

Figure 4.13: Example low frequency hysteresis response of the MFC M8507-P1 bimorph (sample B2) for 2 kVpeak sine tone actuation at 10 Hz.

The tests presented in this section are conducted sufficiently below the first natural frequency, so the dynamic effects are negligible and the results are considered to be in the quasi-static range. The frequency sweep is conducted in the 0.02 Hz to 10 Hz range with 0.02 Hz steps. The peak AC input voltage (or Vpp/2) is swept from 100 V to 2000 V in 100 V steps. Both frequency and amplitude are swept up and down to check for time dependency or other nonlinear effects (such as fatigue and temperature variations in the laboratory). Since negligible difference

is observed between the sweep up and sweep down test, only sweep up results are presented. Figure 4.14a shows the peak displacement output of the free-end of the bimorph actuator that corresponds to a sine tone actuation with constant amplitude and frequency. Figure 4.14b shows the average power consumption of the bimorph and the circuit (measured with the current monitor on the TREK 623B amplifier). The reported average power is calculated by:

$$P_{Average} = \frac{1}{T_s}\int_0^{T_s} V(t) * I(t)\, dt \qquad (4.6)$$

where T_s is the total sampling time for five cycles. Note that average power presents only the actual consumed power; hence the reactive power is not included in the average power values.

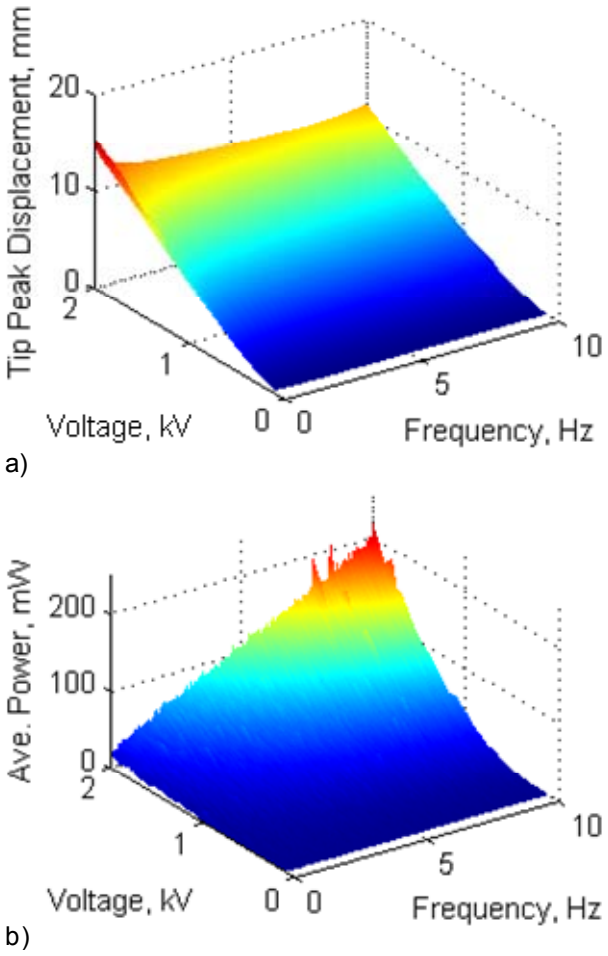

Figure 4.14: Response of the MFC M8507-P1 bimorph (sample B2) driven with the divider circuit. a) Free end peak displacement, b) average power in response to harmonic input.

Figure 4.14 shows the low frequency effectiveness of the circuit. The displacement given in the figure is for the peak level (or peak-to-peak / 2). The same data can be plotted against different set of input parameters. Figure 4.15 shows the deformation characteristics with the inputs being total power input and frequency of excitation.

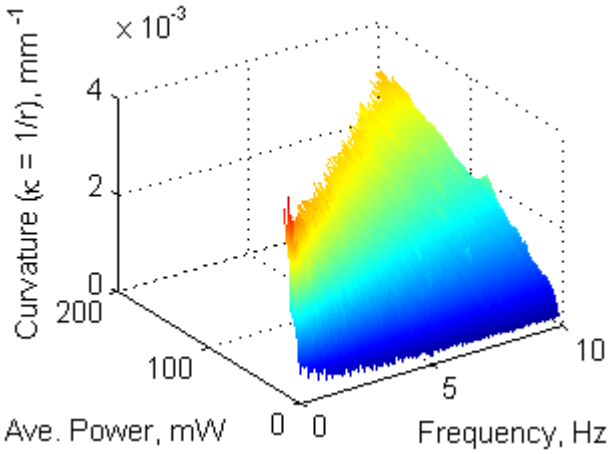

Figure 4.15: Curvature (at peak displacement) of the MFC M8507-P1 bimorph (sample B2) actuated through the voltage divider circuit.

Note that the curvature calculation assumes that the operating deflection shape of the bimorph is a circular arc; therefore this calculation applies only to low frequency (quasi-static) range.

4.4.2. High Frequency Low Amplitude Tests

Figure 4.16 shows an example of the hysteresis loops (for displacement, current input and power consumption vs. voltage) that are measured during the 500 Vpeak (1 kVpp) sine tone actuation at 243 Hz for sample B2. The frequency corresponds to the 2nd bending resonance of the bimorph beam. The tests are conducted in the same way as the low frequency tests.

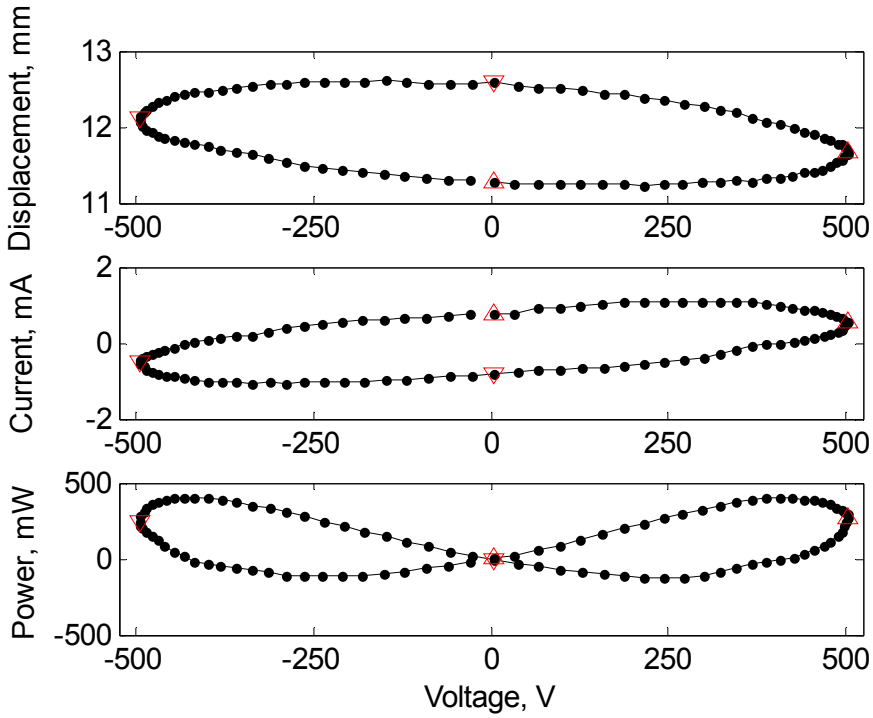

Figure 4.16: Example high frequency hysteresis response of the MFC M8507-P1 bimorph (Sample B2) for 500 Vpeak sine tone actuation at 243 Hz.

For the high frequency tests, the sweep is conducted in the 1 to 500 Hz range with 1 Hz steps. The peak AC input voltage (or Vpp/2) is swept from 100 V to 500 V in 100 V steps. Both frequency and amplitude are swept up and down to check for time dependency or other nonlinear effects (such as fatigue and temperature variations in the laboratory). Since negligible difference is observed between the sweep up and sweep down test, only sweep up results are presented.

Figure 4.17a,b shows the peak displacement output of the free-end of the bimorph actuator that corresponds to a sine tone actuation with constant peak amplitude and frequency. Note that the reported frequency range is 0 – 100 Hz (instead of the full 0 – 500 Hz acquisition bandwidth). In this section, the attention is directed to the 1st bending resonance of the clamped-free bimorphs. Figure 4.17c,d shows the phase angle difference between the displacement output and voltage input.

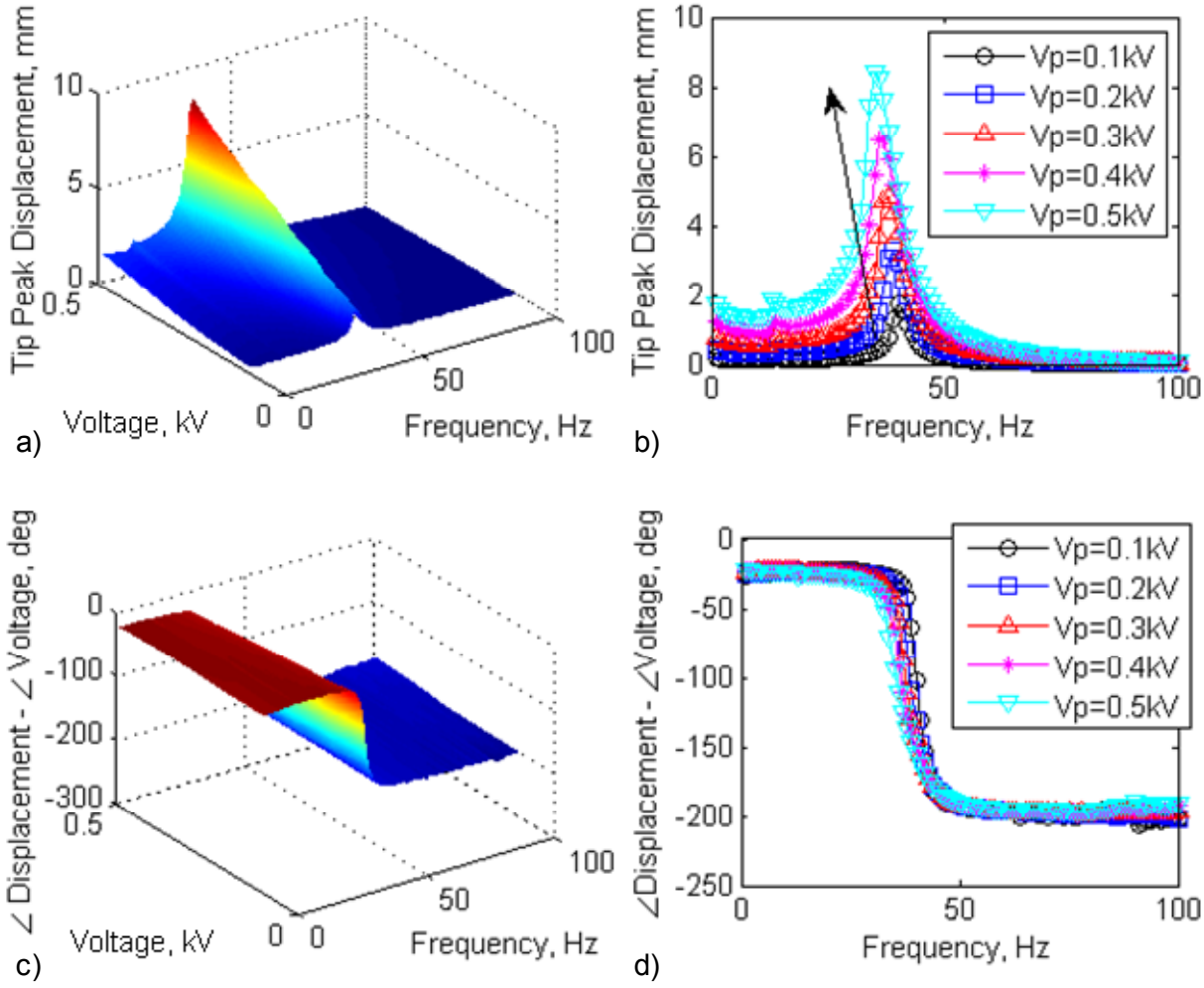

Figure 4.17: Free end peak displacement of the MFC M8507-P1 bimorph (sample B2) driven with the circuit. a,b) Magnitude (3D and 2D) and c,d) phase response (3D and 2D) to harmonic voltage input.

Figure 4.17 shows the high frequency effectiveness of the circuit. The displacement given in the figure is for the peak level. Note that the resonance frequency is dependent on the amplitude of excitation which is due to the constitutive nonlinearity of the bimorphs device. The displacement-to-voltage phase shows a constant offset also due to the same constitutive nonlinearity. Same phenomena are also noted in unimorph devices in Section 2.2.2.

Figure 4.18 presents the average power consumption of the bimorph and the circuit (measured with the current monitor on the TREK 623B amplifier). The reported average power is calculated by Eq. (4.6).

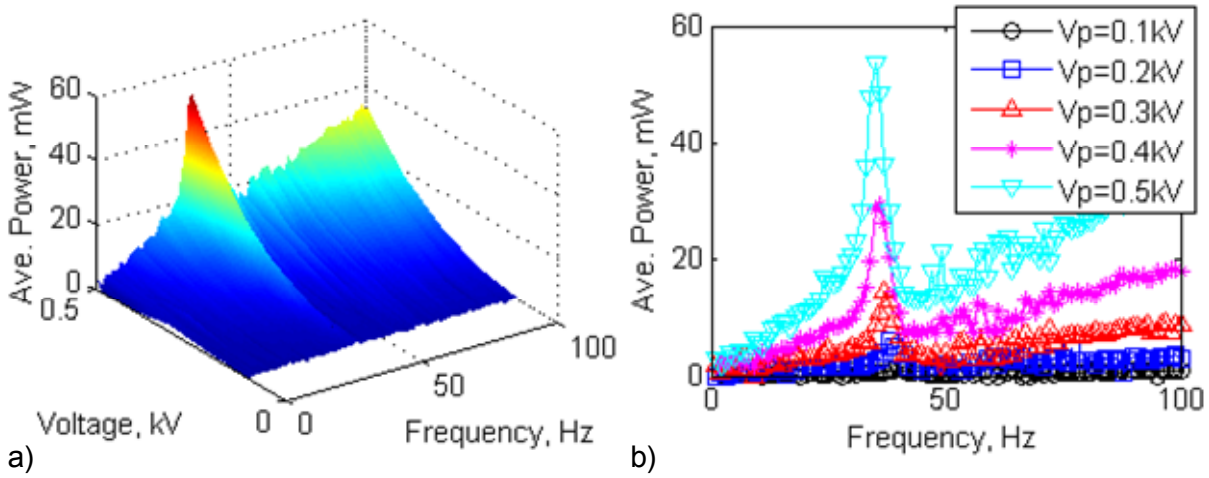

Figure 4.18: Power consumption (3D and 2D) of the MFC M8507-P1 bimorph (sample B2) actuated through the voltage divider circuit.

As noted earlier, the average power presents only the actual consumed power; hence the reactive power is not included in the average power values.

4.5. Conclusions

This chapter presented a novel, solid-state electrical circuit employing passive electrical components such as diodes and resistors. The circuit allows a single bipolar amplifier (or two unipolar amplifiers) to control a bimorph fabricated by two Macro-Fiber Composite actuators. The experimental results show that the proposed circuit allows the division of the input voltage so that: 1) The MFC that is in extension receives 1500 V (which is the maximum positive voltage), and 2) The MFC that is in compression receives -500 V (which is the maximum negative voltage). The circuit also allows the actuation in the opposite direction without any physical changes (i.e. not using any electromechanical switches). The experimentally determined input-output relationship shows an excellent linear trend. An MFC bimorph is used to further demonstrate the wide bandwidth operational capability of the circuit.

CHAPTER 5

MACRO-FIBER COMPOSITE ACTUATED SIMPLY-SUPPORTED THIN AIRFOIL

One of the main goals of this research is to exploit active material actuation and structural boundary conditions to perform structural open-loop shape control of an airfoil for small unmanned aircraft applications. In this chapter, a variable-camber airfoil concept employing piezoceramics is proposed to take advantage of smooth control surface deformations. In particular, the concept is evaluated in a vertical take-off and landing (VTOL) ducted-fan aircraft through experiment. A bimorph configuration is used to create the airfoil surface because 1) it can induce large out-of-plane deformations (see Section 4.4) in comparison to a unimorph (see Section 2.1) and 2) it can be actuated with lightweight electronics (see Section 4.2 and Section 4.3).

This chapter focuses on response characterization under aerodynamic loads for circular-arc bimorph airfoils with variable pinned boundary conditions. A parametric examination of the fluid-structure interaction is employed to find pin locations along the chordwise direction that result in high lift generation. Wind tunnel experiments are conducted on a 1.0% thick, 127 mm chord MFC actuated bimorph airfoil that is simply-supported at 5% and 50% chord. The aerodynamic and structural performance results are presented for a flow rate of 15 m/s and Reynolds number of 127,000. Nonlinear effects due to aerodynamic and piezoceramic hysteresis are identified and discussed.

The chapter is organized as follows. The concept of a two-dimensional (2D) thin airfoil with pinned boundary conditions is first introduced and then evaluated theoretically for lift and drag performance for different flow velocities. The effects of variation in boundary conditions are also studied. Next, qualitative results are presented from wind tunnel tests of the ducted-fan vehicle. Finally, a prototype airfoil is presented and 2D wind tunnel test results are discussed for a flow speed of 15 m/s. The chapter concludes with a brief discussion of the results.

5.1. Thin Bimorph Variable-Camber Airfoil Concepts

A thin bimorph airfoil (with reasonable stiffness and deformation output) is possible with an MFC actuator given that the boundary conditions are favorable. Therefore, the support system for a variable-camber device intended for circulation control is proposed in Figure 5.1. The airfoil surface gains some camber due to the pressure loading between the supports and has a slight loss of camber on the aft end, also due to the pressure loading. The net result is a change in circulation depending on the boundary conditions (hence the structural response). A variable-camber bimorph airfoil is proposed here with total thickness of 1.0% of its chord to simplify fabrication and implementation.

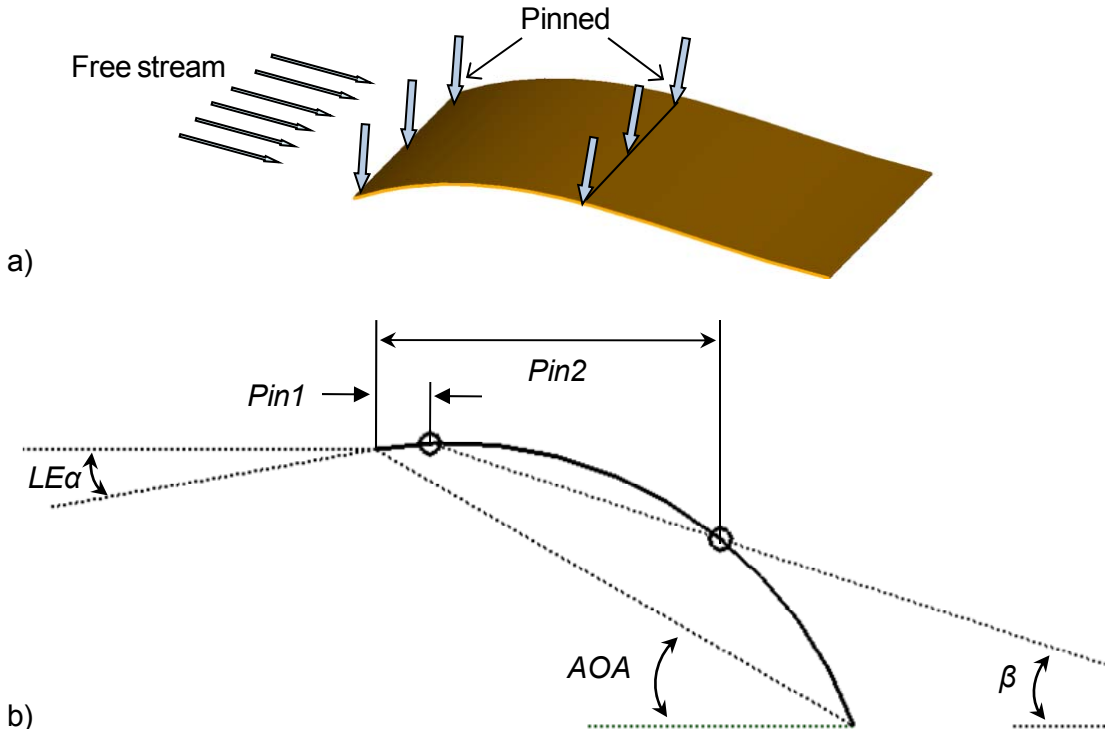

Figure 5.1: a) Variable-camber airfoil concept actuated shape. b) Illustration of the possible chordwise locations of two "pins" and other conventional parameters.

In Figure 5.1b, the label "*AOA*" represents the actual angle of attack, "*β*" represents angle of the support condition, and "*LEα*" represents the leading edge incidence angle with the free-stream velocity. The boundary conditions in the design are pinned-pinned (similar to a simply-supported beam) for ease of implementation; however one can choose the second boundary condition (*Pin2*) as a slider (allowing motion in the chordwise axis and restricting motion in the

lift axis). The pinned-pinned boundary condition theoretically creates an "artificial" nonlinear stiffness but this stiffness is not dominant in an actual implementation of the proposed airfoil geometry and the pin locations (which is presented in Figure 5.7 later). Starting with the base design (given in Figure 5.1a), multiple configurations can be generated (shown in Figure 5.2) by changing the location of the pins.

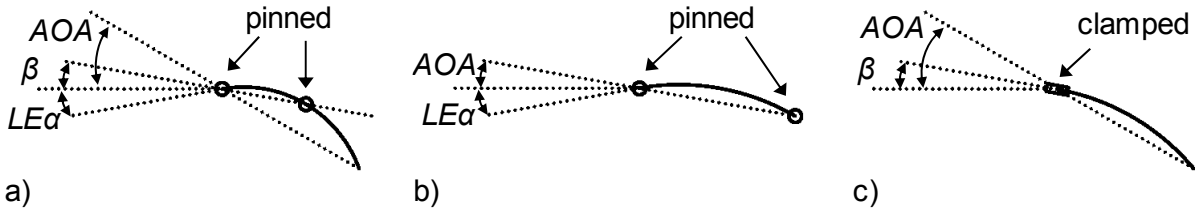

Figure 5.2: a) General configuration, b) simply-supported beam and c) cantilevered beam.

The two extreme configurations are: 1) The middle support is moved to the trailing edge which is similar to a sail or a simply-supported beam; 2) The middle support is moved to the leading edge, hence the airfoil becomes a cantilevered beam.

5.2. Static Aeroelastic Analysis

A theoretical analysis is conducted to determine the effect of pin locations on the 2D aerodynamic response. A MATLAB [MATLAB] based program is developed to solve the static fluid-structure interaction (FSI) problem by iterating between a panel method software XFOIL [XFOIL, Drela, 1989], and a finite element code ANSYS [ANSYS]. Before the iteration starts, the non-aero-loaded airfoil shape is analyzed in XFOIL to initialize the FSI. XFOIL calculates lift and drag coefficients and the pressure distribution and the program enters the iteration loop. First, the pressure distribution is applied to the airfoil geometry in ANSYS which calculates the aero-loaded (deformed) airfoil shape. Second, the deformed airfoil shape is analyzed in XFOIL to calculate change in the lift and drag due to the change in pressure induced deformation. These two steps are continued until no change is observed in the parameters of interest (i.e. deformation and aerodynamic coefficients). Due to the static nature of the problem, the solution converges with a few iterations. Note that the dynamic effects are known to be negligible (and ignored in the analysis) because of previous experimental observations. The model considers only

chordwise distribution of aerodynamic loads and structural deformations (because of the structural and aerodynamic boundary conditions and experimental observations).

The airfoil is assumed to be a thin circular-arc with 1.00% thickness, round leading edge (LE) and tapered trailing edge (TE) with a finite TE thickness of 0.05% chord. A constant curvature is assumed due to the high chordwise coverage of the active material. The nonlinear voltage-camber relationship is experimentally quantified with laser displacement measurements. The curvature and the camber are calculated using geometric properties of the circular-arc. The maximum camber achieved by the airfoil is then used in the theoretical evaluation. The camber vs. voltage curve (with piezoceramic hysteresis) is nonlinear; therefore camber is used as an analysis parameter instead of voltage. For the particular airfoil presented in this chapter, approximately 4.00% camber is achieved at 1400 V actuation. The detailed description of the shape and the actual nonlinear behavior of the airfoil will be discussed in the following sections.

For XFOIL simulations, a 0.85% (of the mean velocity) turbulence level is assumed, which consistent with the measured turbulence level in the wind tunnel. It must be noted that XFOIL predictions for AOA above maximum lift angle are not accurate [Drela, 1989]. Due to the limitation of the deflection of the piezo-composite bimorph, XFOIL analysis presented here never passes beyond this AOA limit. Approximately 800 panels are used in XFOIL to achieve numerical convergence for the thin airfoils considered in this section. As reported in literature [XFOIL, Drela, 1989], XFOIL predicts slightly higher lift coefficients and lower drag coefficients when compared to experimental results; therefore the predictions must be viewed as an upper boundary to actual lift output.

The structure of the bimorph airfoil is modeled as a homogeneous 2D area mesh using PLANE82 high-order quadrilateral (Q8) type element in ANSYS. The plane element type is chosen (instead of the beam element type) because of the dense distributed loading at the leading edge with significant components in the in-plane direction as well as the out-of-plane direction. Figure 5.3 shows the finite element model of the 4.00% cambered airfoil LE. There is a high concentration of aerodynamic loading (shown with arrows normal to the surface) at the leading edge.

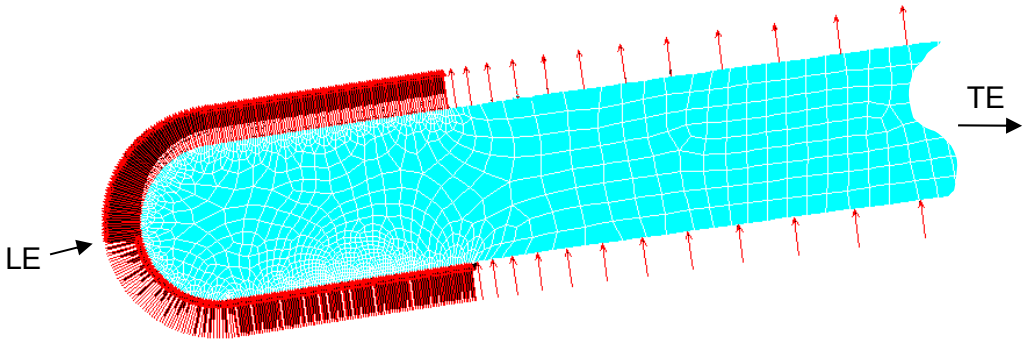

Figure 5.3: 2D mesh and loading of the 4.00% cambered 1.00% thick airfoil. The LE area is shown with high concentration of pressure distribution and elements.

The material properties of the finite element model are experimentally determined and checked by the following method. First, the deformation of the composite airfoil (active/passive/active layered bimorph) is experimentally measured by applying a distributed load along the free-end of a representative bimorph sample in clamped-free configuration. The displacement pattern showed uniform characteristics; hence an effective isotropic material property is assumed for the whole structure. Next, a 16.5 GPa Young's modulus is derived from the experimentally computed bending stiffness and a 0.267 Poisson's ratio is assumed. Finally, this modulus is used in the ANSYS model (with the same loading in the experiment), and a calibrated theoretical response is achieved. Approximately 1900 elements are used to ensure convergence of the finite element model for all airfoil models. The number of elements is chosen relatively high only to accommodate the highly nonuniform pressure distribution data from XFOIL.

The analysis scheme presented above is applied to a parametric examination. The two pin locations are used as independent variables to find the pin location that results in high lift output when the free-stream flow is parallel with the pins (β =0). Pin 1 (*P1*) is varied from 5% chord to 30% chord downstream of the LE. Pin 2 (*P2*) is varied starting from 5% chord downstream of Pin 1 location to the TE in 5% chord increments. With these discrete scenarios, the complete feasible pin locations are considered for the range of interest. For the structural finite element model, Pin 1 is constrained in both x and y directions, however Pin 2 is only constrained in the y direction. This is done to restrict an artificial stiffness caused by the chordwise contraction of the bending airfoil.

Figure 5.4 shows the theoretical change in lift coefficient and AOA for a 1.00% thick circular-arc airfoil with 127 mm chord. The airfoil is actuated to an initial camber (C) of 2.00%, 4.00% and 4.86% (of chord) and subjected to 15 m/s freestream velocity. The plots present both the aero-loaded (solid lines) and non-aero-loaded (dotted lines labeled as "No Load") airfoils. Considering the (experimentally measured) stiffness of the bimorph, the flow induced deformation is negligible at 15 m/s. All results presented in this section are for a constant β angle of zero degrees.

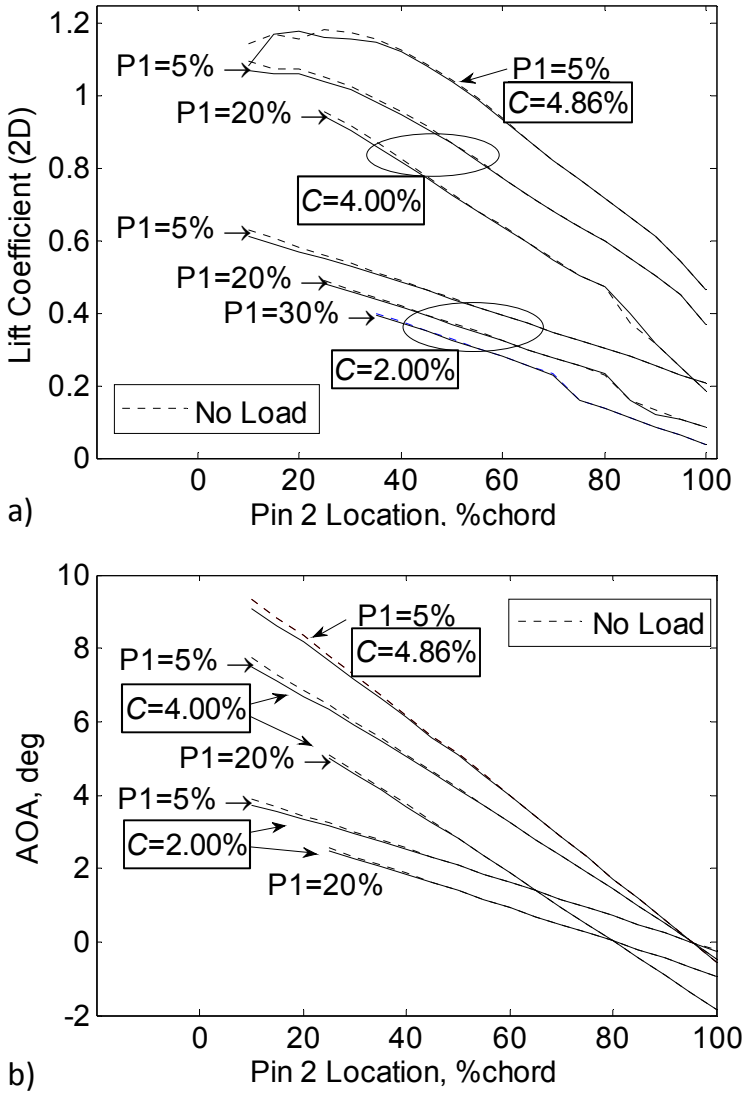

Figure 5.4: Theoretical (2D) a) lift coefficient and b) angle of attack response for a 1.00% thick airfoil at 15 m/s flow. Initial camber is labeled as "*C*". Re_{chord} = 1.27x10^5.

The analysis shows that placing Pin 1 at or close to the leading edge results in the highest lift output. At 5.00% camber, the lift response is close to the theoretical CL_{max}. The accuracy of the numerical analysis starts to degrade beyond this point. We also note that a smooth surface is assumed for the analysis which will cause a deviation of lift curve from actual performance around CL_{max}. The remainder of this section considers the cases with Pin 1 located at 5% chord. The evaluation is extended to higher freestream velocities (observed in the ducted-fan) of 30 and 60 m/s. Figure 5.5 presents the effective camber and the AOA. Both aerodynamically loaded and non-loaded cases are presented.

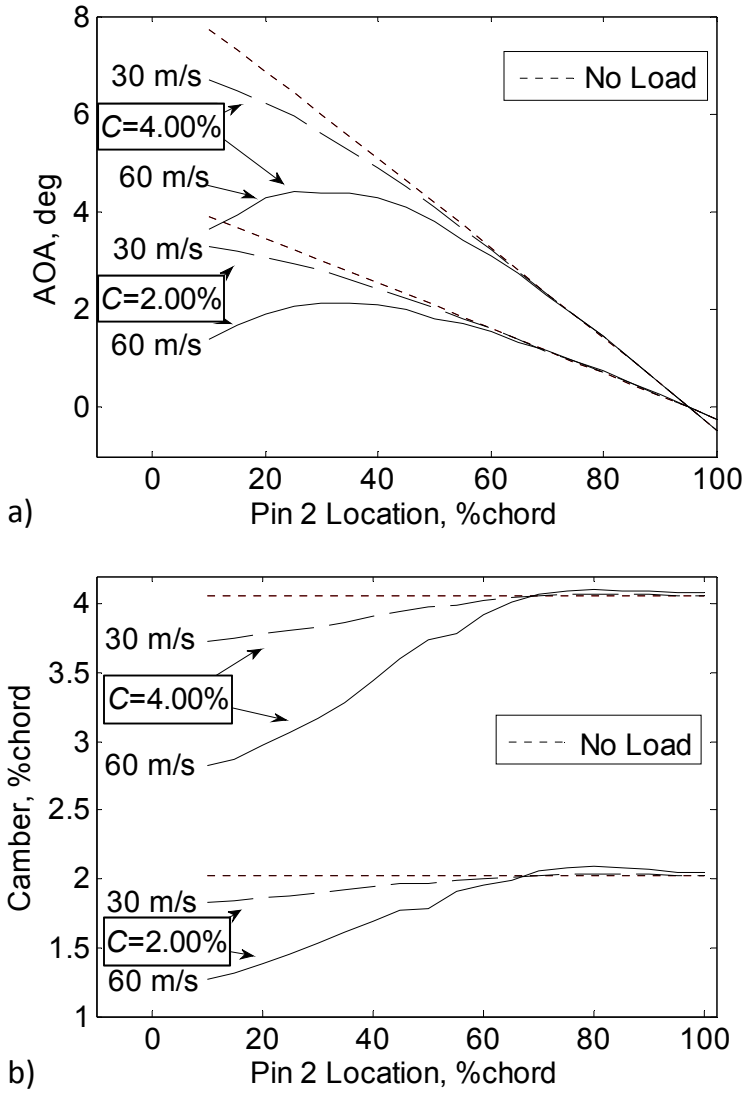

Figure 5.5: Theoretical (2D) a) AOA and b) effective camber response for a 1.00% thick airfoil with Pin1 at 5% chord and variable Pin2 location, subjected to 30 and 60m/s.

In Figure 5.5, the initial camber (with no aerodynamic loading) is labeled as "*C*". As the velocity is increased, a large reduction in camber and AOA is observed for Pin 2 locations up to 60% chord. Pin 2 locations beyond this point results in a small (favorable) increase in camber and AOA. Figure 5.6 presents the variation of lift coefficient and lift-over-drag (*L/D*) ratio due to change in Pin 2 location.

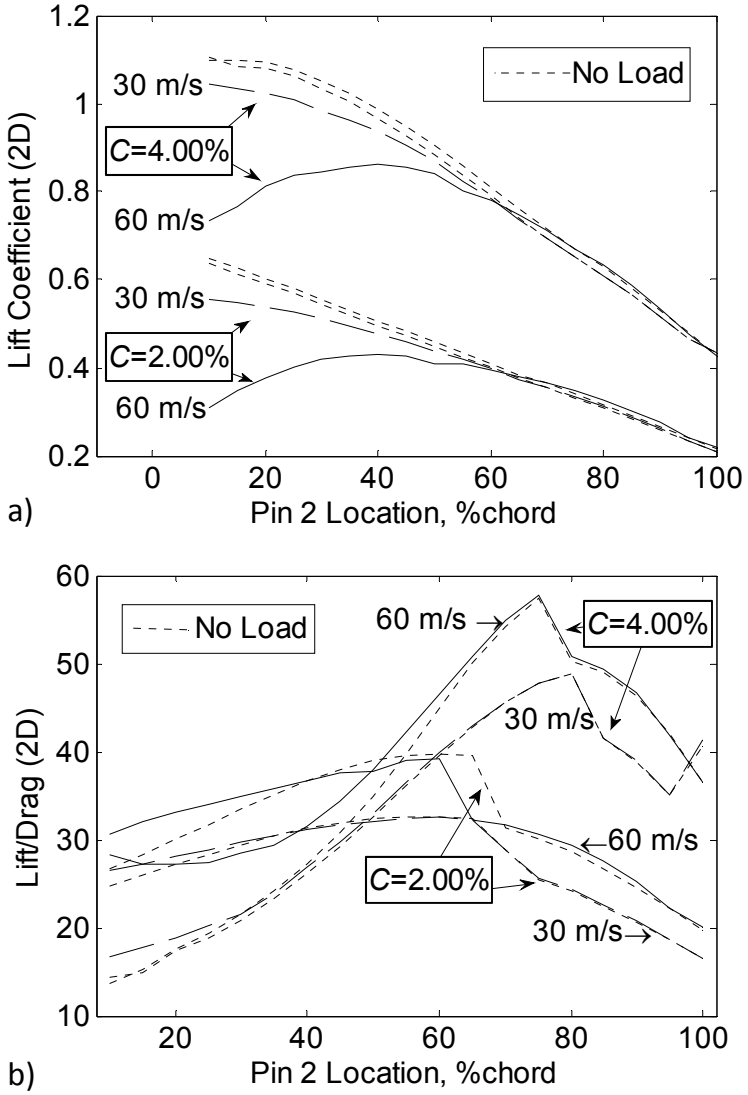

Figure 5.6: Theoretical (2D) a) lift coefficient and b) lift-over-drag response for a 1.00% thick airfoil with Pin1 at 5% chord subjected to freestream velocity of 30 and 60 m/s.

The effect of higher dynamic pressures becomes clearly visible at 60 m/s between the loaded and non-loaded airfoils. In the ducted-fan aircraft wind tunnel tests (presented in the next

section), the airfoil with pinned-pinned boundary condition showed no aerodynamic instability or failure at speeds exceeding 45m/s. In summary, the theoretical analysis shows that a 1.00% thick airfoil presents adequate stiffness at 15 m/s for all support conditions analyzed. At higher dynamic pressures, adverse deformations (that can reduce circulation) can be avoided by more "conservative" pin locations at the expense of reduced aerodynamic output. The configuration with P1 at 5% chord and P2 at 40% chord results in the highest possible lift output for the upper boundary of aerodynamic loading (60 m/s).

5.3. Structural and Aerodynamic Experiments

This section presents the structural and aerodynamic experiments conducted on a bimorph, variable-camber airfoil prototype. First, the fabricated airfoil is introduced. The preliminary evaluation of the airfoil in a VTOL application is presented next. The 2D wind tunnel experimental setup is introduced. Finally, the experimental measurement of the structural and aerodynamic response is presented.

5.3.1. Variable-Camber Airfoil Specifications

Using the conclusions derived from the analysis presented in Section 5.2 and the geometric constraints of the VTOL aircraft (presented next), two MFC actuated thin bimorph airfoils are fabricated. Four total stainless-steel pins (two on each end) are bonded to the airfoil at 5% and 50% chord from the LE. This configuration is chosen because it is a good compromise between the restrictions of the aircraft geometry and the determined pin locations (5% and 40% for high lift output) from the analysis in Section 5.2. Figure 5.7 shows one of the two bimorph airfoils (airfoil labeled T1) employing four (two on each face) MFC M8557-P1 type actuators.

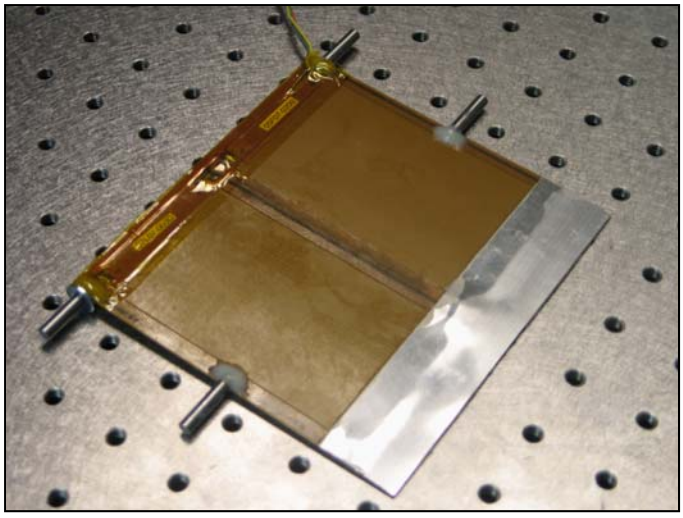

Figure 5.7: Prototype variable-camber bimorph airfoil (T1) with four MFC M8557-P1 actuators, 127 mm chord and 133 mm span.

The bimorph is fabricated by sandwiching a 0.027 mm thick stainless-steel sheet and bonding the laminate under vacuum. The MFCs are aligned at the LE in the chordwise direction. Two layers of 25.4 μm thick stainless-steel metal (passive material) are bonded to the TE to complete the total chord to 127 mm. Stainless-steel (instead of a fiber composite) is chosen due to several reasons. First, as shown in section D.2, the MFC bimorph device with no substrate material has the highest deformation when compared to a bimorph without substrate; therefore a bimorph without a substrate is the first choice. On the other hand, the experimental VTOL aircraft has a pre-determined control surface span which is in the order of 100 mm. However, the MFC actuators come in standard sizes, with the largest commercially available size having an 85 mm x 57 mm active area. In order to make a control surface with full spanwise coverage of the active material, it was decided to have two MFC M8557-P1 type actuators placed side-to-side in the spanwise direction. At this point it was necessary to "connect" the two MFC patches with a substrate. Since thin stainless-steel sheet metals 1) have a uniform thickness distribution and 2) are readily available, the thinnest available stainless-steel sheet metal (from McMaster-Carr, Aurora, OH, USA) was chosen as the substrate material. The experimental analysis presented in Section D.2 shows that a bimorph with 0.027 mm thick stainless-steel substrate indeed has very large deflections when compared to a fiber-composite substitute. The challenge with the fiber-composite substrates is that they have 1) relatively nonuniform thickness distribution (due to in-

house vacuum bagging techniques) and 2) are relatively thick when compared to the commercial sheet metals (also due to in-house fabrication limitations).

5.3.2. Ducted-Fan Aircraft Wind Tunnel Experiments

The preliminary motivation for the variable-camber airfoil concept presented in this chapter is to determine the potential effectiveness of the thin bimorph control surfaces for an experimental VTOL MAV designed by AVID LLC, VA, USA. One of the two variable-camber airfoil prototypes (presented in Section 5.3.1), mounted at the exit of the ducted-fan aircraft, is shown in Figure 5.8. The ducted-fan is mounted on its side for wind tunnel testing.

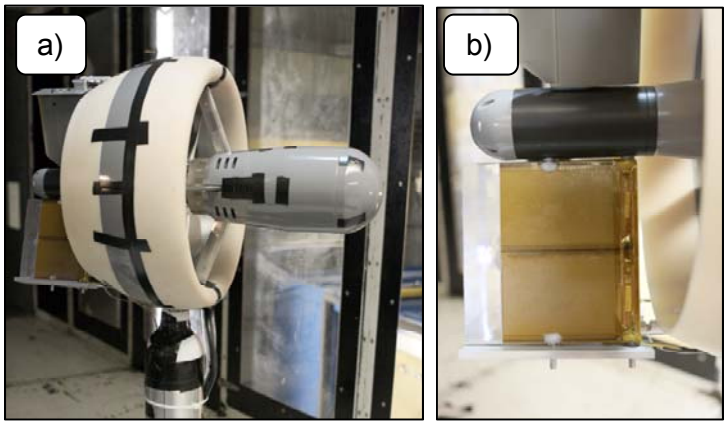

Figure 5.8: a) AVID LLC ducted-fan vehicle model installed in Virginia Tech 6 ft x 6 ft Stability Tunnel. b) Close-up of the thin morphing control surface installed in the ducted-fan vehicle. The airflow is from right to left.

The morphing control surface concept is initially evaluated through wind tunnel tests of the ducted-fan vehicle shown in Figure 5.8. These tests are conducted at a maximum fan flow speed of 45 m/s and maximum free-stream speed of 10 m/s. The morphing airfoil demonstrated high lift output and no adverse deformation due to high aerodynamic loads. Most importantly, a structural failure (or buckling) and an aerodynamic instability is not observed at the fan speeds of 45 m/s. Due to the publishing restriction on these wind tunnel tests, the quantitative results are not presented in this dissertation.

A custom, lightweight bipolar amplifier (weighing 151 grams and capable of ±2 kV four channel output with 0-10 Hz bandwidth) is fabricated and used during the wind tunnel tests. The design and evaluation of amplifier is presented in Section 6.3.1). The initial wind tunnel tests

proved the feasibility of the airfoil design. While the VTOL aircraft application drove a thin variable-camber airfoil design that can handle high dynamic pressure and symmetric deflection, the developments presented in this chapter can easily be applied to a wide range of aerodynamic implementations; therefore the followings sections present data on the conventional 2D aerodynamic coefficients.

5.3.3. 2D Wind Tunnel Setup

Wind tunnel tests are performed in a custom, low-speed, open circuit wind tunnel facility with a 2D test-section configuration. The wind tunnel is specifically designed and built for the research presented in this dissertation. A detailed description (of the wind tunnel *Version 1*) can be found in Appendix E. A manual beam-balance is used to measure lift and drag forces generated by the airfoil. Flow velocity measurements are conducted with a Flow-Kinetics Pitot-static tube. The maximum measured spatial variation of the flow profile (for *Version 1*) is $U_{Velocity} = \pm 0.54$ m/s at 15.3 m/s; therefore the flow is assumed spatially uniform for coefficient calculations. The turbulence of the flow in the empty test section is measured by standard hot wire anemometry technique. A turbulence intensity of 0.60 % is measured from 0.1 Hz - 50 kHz band-pass filtered signal for the current test speed of 15 m/s. The wind tunnels tests are conducted at an average speed of 15 m/s.

5.3.4. Baseline Flat Plate Airfoil Response

An aluminum, thin, flat-plate airfoil is selected as a baseline to variable-camber airfoil tests. This baseline information is necessary because of the lack of low Reynolds number experiments in high turbulence settings. The geometry of the airfoil is adapted from a flat plate airfoil extensively studied by Mueller [1999], and Pelletier and Mueller [2000]. The flat plate airfoil is tested for lift and drag coefficients at an average flow speed of 15 m/s and a chord Reynolds number of 127,000. The airfoil geometry is presented in Figure 5.9.

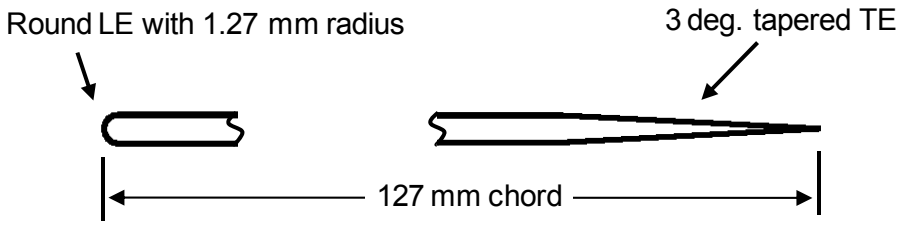

Figure 5.9: Important geometric features of the 2.00% thick flat plate aluminum airfoil.

Refer to Section F.1 for pictures of the airfoil and the mounting of the airfoil in the wind tunnel test section. The flat plate airfoil has a thickness of t = 2.54 mm (2.0% of chord), span of b = 133 mm and a chord of c = 127 mm. The airfoil has a round LE with 1.27 mm radius, and a 3° tapered TE. The airfoils tested in this chapter have an approximate 1.5 mm gap between the airfoil ends and the tunnel walls (see Appendix E for the illustrations of the 2D test section). Mueller and Burns [1982] show that gap sizes around 0.5% of the span are usually acceptable and do not affect the results. For the airfoils tested here, the gap is approximately 1.13%. Although the gap dimension is small, the percentage is still higher than recommended because of the small span of the airfoils. The possible effects of this gap size will be discussed in the following sections. Tunnel wall effects and buoyancy corrections were applied as necessary using the techniques found in Appendix E.

Figure 5.10 presents comparison of flat plate lift and drag coefficient data from the current research to the ones tested by Mueller [1999], Pelletier and Mueller [2000], and Selig and Donovan [1989]. XFOIL results are also presented. The data from the current evaluation represents the average of AOA sweep-up and sweep-down tests. The averaging is done because of the lack of aerodynamic hysteresis.

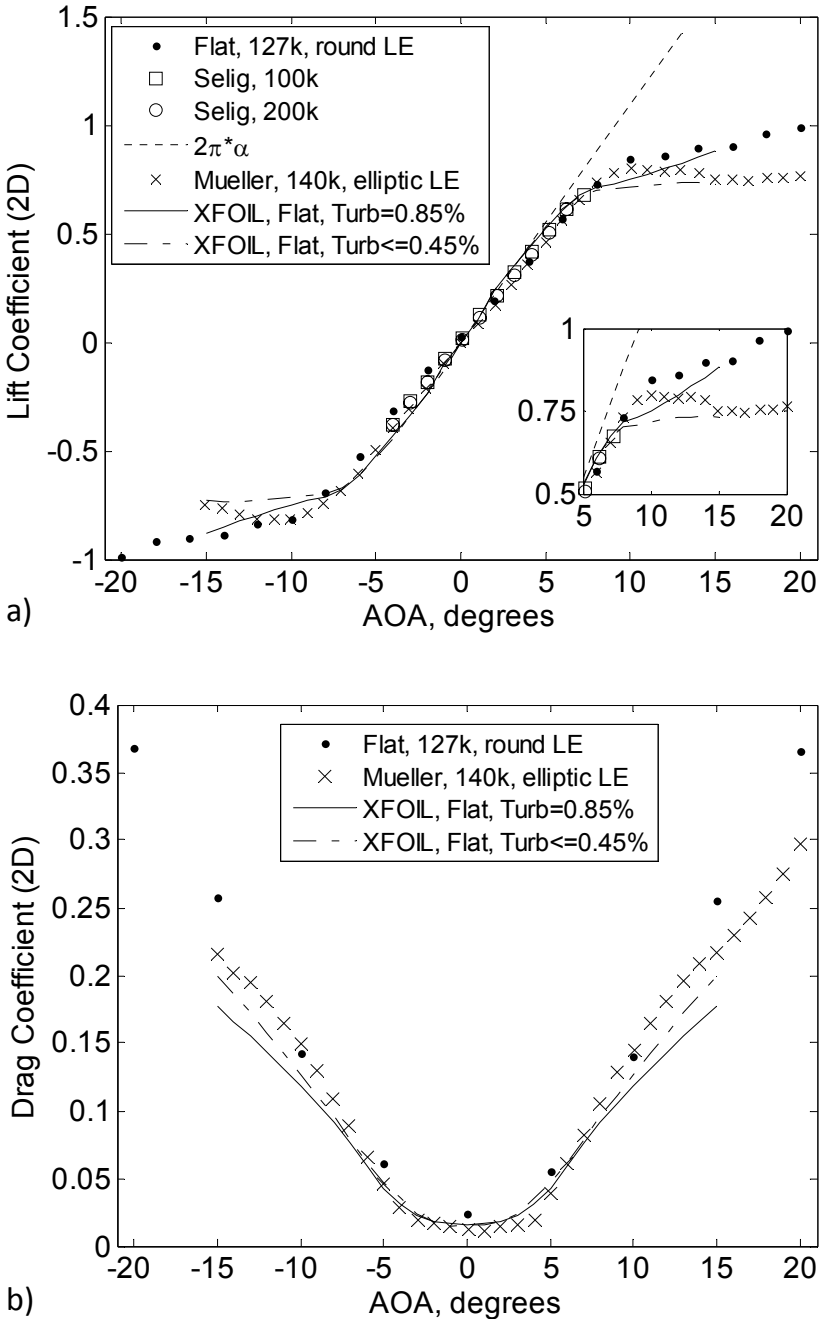

Figure 5.10: a) Lift and b) drag coefficients vs. angle of attack comparison for three thin flat-plate airfoils.

The lift-curve slope matches well for all tests shown which are slightly lower than the theoretical slope of 2π/rad and the XFOIL prediction. The Reynolds number has negligible effect on the lift coefficient. XFOIL does predict slightly lower lift for AOA above 8°; however the effect of turbulence is consistent with the experiments. Maximum lift coefficient uncertainty is

$U_{CL,max} = \pm 0.055$ which is mostly due to low frequency variation of velocity. The lift curve slope is consistent to data reported in Hoerner [1975] for a thin flat-plate. The drag coefficient from the flat plate airfoil shows a slightly higher trend at lower angles when compared to data reported by Mueller. Zero degree drag coefficient is 0.024 for the variable-camber airfoil. There are several reasons for this difference. First, note that Mueller reports an elliptical LE with ratio of $5t/2$ where the airfoil studied here has a circular LE. At zero degree AOA, a sharper LE is expected to create less drag. Second, the turbulence levels in different facilities must be noted. Mueller reports 0.05% turbulence intensity over the range of tests conducted. A 0.80 mm gap between the wing and the end-plates is also reported. Selig reports 0.358% rms turbulence for 0.01 Hz cutoff frequency, and 0.064% rms turbulence for 1 Hz cutoff frequency, at a Reynolds number of 100,000. Finally, the thin airfoil studied here is supported by four pins (two on each end) that are bonded at 5% and 50% chord. The cylindrical stainless-steel pins are 4.8 mm in diameter and extended 4.8 mm into the flow. The drag coefficient for a finite-length cylinder in a cross-flow is approximately 1.1 as reported by Hoerner [1993]. This translates into a corrected drag coefficient of 0.018 at zero AOA for the morphing airfoil. Mueller reports approximately 0.013 for zero degree drag coefficient. The difference in drag is acceptable considering the maximum drag coefficient uncertainty of $U_{CD,max} = \pm 0.014$.

5.3.5. Variable-Camber Airfoil Structural Response

The shape of the variable-camber bimorph airfoil at a given condition must be measured accurately due to the hysteretic nature of the piezo-composite bimorph. A nonlinear model is not addressed in this chapter. The shape measurement is also necessary to observe the additional deformation (if any) due to aerodynamic loading. In the current work, the shape is predicted by measuring the displacement of the airfoil mid-span section at two locations simultaneously. The measurement is taken using two Micro-Epsilon laser displacement sensors. With the known axis of rotation of the airfoil, an airfoil shape is fitted to the two measured displacements and the third know axis location. This approximation method is validated for accuracy using two methods: 1) The shape of the flat-plate airfoil is calculated and verified; 2) Shape recognition using a digital camera is employed on the variable-camber airfoil for one test case. Figure 5.11 illustrates displacement sensor locations (Laser 1 and Laser 2) and the fitted airfoil shapes to the measured points with laser sensors.

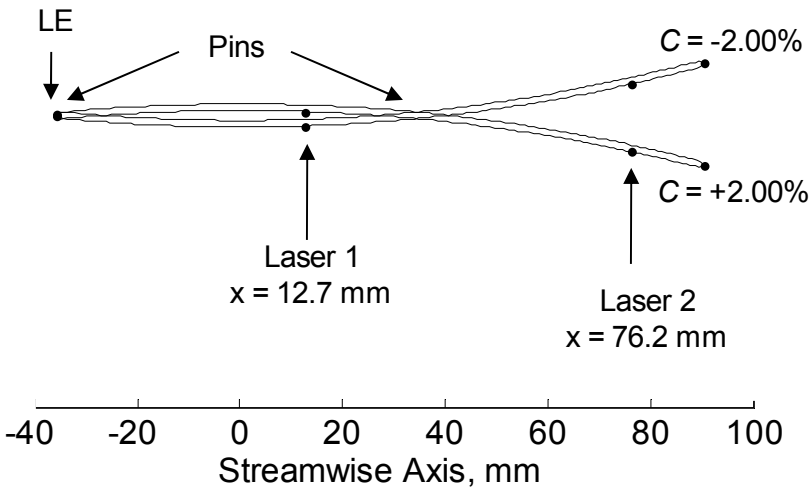

Figure 5.11: Illustration of the fitted airfoil shapes to two laser measurement points.

In Figure 5.11, the leading edge and trailing edge locations are computed using the fitted profile with arc-length of 127 mm. The AOA and the effective camber are calculated for the arc fit. The percent-camber is the percentage of the height over the chord of the circular arc.

Figure 5.12 shows the actual displacement of the airfoil end-section digitized from a series of photos for a peak-to-peak voltage sweep. Since the airfoil is in a bimorph configuration, MFCs on the opposite side are actuated with an opposite field and with 3-to-1 fixed ratio. The higher of the two supply voltages is used for labeling in the plots. A negative sign simply indicates actuation in the reverse direction as indicated in Figure 5.12.

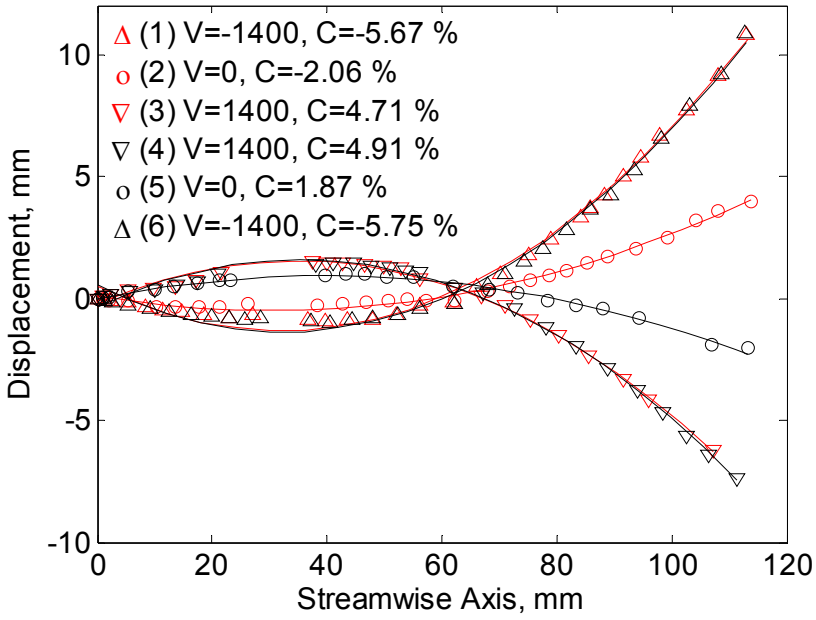

Figure 5.12: Airfoil end-section measurements with a digital camera. Legend shows test order, voltage (*V*) and camber (*C*) of the circular-arc fit (shown by solid lines).

In Figure 5.12, the actuation voltage is swept from -1400 V to 1400 V and swept back to -1400 V. The effect of piezoelectric hysteresis can be observed in the difference between deflection at zero voltage during the positive and negative voltage sweeps. However, the deflection is very repeatable, as seen at the maximum positive and negative voltage levels. Figure 5.12 also shows that a circular-arc is a good approximation; however the actual shape does deviate from a circular arc. Most of this deviation occurs between the two pin points and for the high camber cases because the support mounts on the balance resist the motion of the pins attached to the airfoil. There is a small and consistent offset between the two measurement methods which is presented in Figure 5.13.

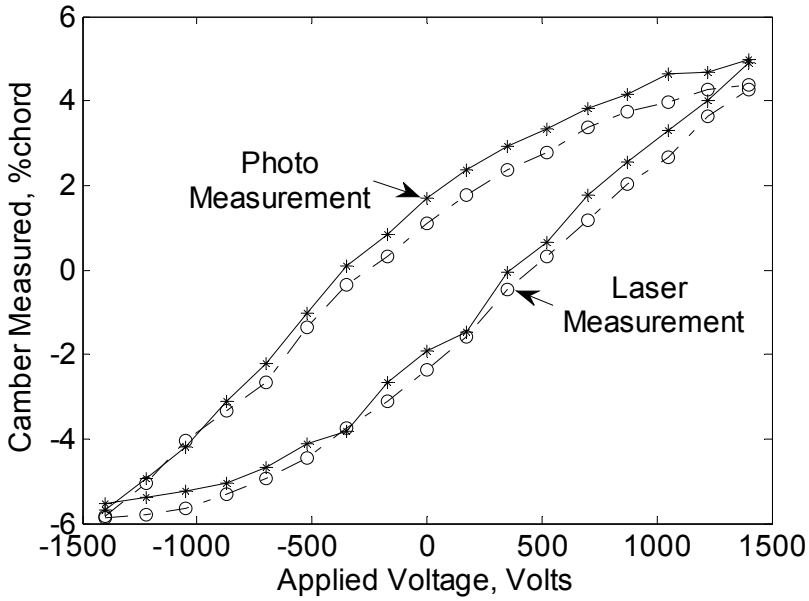

Figure 5.13: Comparison of two deflection measurement techniques.

The 95% confidence interval of this offset is taken as the uncertainty of camber measurements with lasers, which is $U_{\%camber} = \pm 0.37$. Note that the lasers measure the mid-span section where the photo method measures the end-section. No visible spanwise variation of shape is observed, however such variation is inherent in a composite airfoil due to fabrication limitations and the shape of the MFC actuator. Since the camber calculation from laser measurements is in good agreement with the photo method, aerodynamic experiments are conducted with the lasers.

5.3.6. Aerodynamic Response: AOA Sweep at Fixed Voltage

The variable-camber airfoil is tested for its lift and drag performance at a flow speed of 15 m/s. The airfoil, mounted in the wind tunnel test section is presented in Figure 5.14. The experimental measurement of lift, flow velocity and other parameters is the same as the procedure outlined in Section 5.3.4. Two different test schemes are followed. The first evaluation is performed by setting the voltage of the bimorph at a fixed value, then sweeping the support angle (β) up and down. The complete list of voltages (in order) is: 0V (+β), 0V (-β), 700V (+β), 1400V (+β), -700V (-β), and -1400V (-β). For positive voltages, angle β is swept from -4° to 20° then back to -4°. For negative voltages, angle β is swept from 4° to -20° then back to 4° degrees. Once the angle sweep is completed, the voltage is changed. The procedure outlined here is

necessary for correct identification and separation of two possible sources of nonlinear phenomena: 1) Aerodynamic hysteresis, and 2) Piezoceramic material hysteresis. These nonlinear effects will be discussed as the results are presented in the following pages.

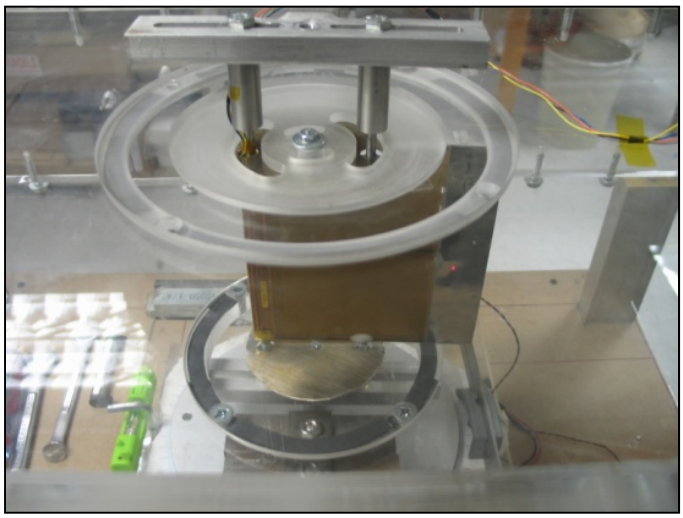

Figure 5.14: Thin variable-camber bimorph airfoil inside of the clear acrylic 2D test section and mounted on the manual beam-balance. The airflow is from left to right.

In order to identify deformation due to aerodynamic loading, baseline deflection measurements are taken with zero flow velocity. The comparison of wind-on and wind-off conditions confirmed that there is no measurable deformation (chordwise or spanwise) due to aerodynamic loading. All plots in the following sections represent the aerodynamically loaded data for consistency. Since the flow induced deformations are small, the theoretical analysis is valid (at least for 5% - 50% pin location configuration). The comparison of theoretical analysis and experiments are therefore omitted in the following figures, and the reader is referred to Figure 5.10 (which shows good agreement in the AOA = ±10° range).

The TE displacement (calculated from the laser displacement measurements) during the aerodynamic experiments is presented in Figure 5.15. Note that the angle of the support points (β) is given as the independent variable for most of the figures which is necessary for clear presentation of the data. The angle β is swept up and down for all voltage levels to change the aerodynamic loading on the cambered airfoil. Aerodynamic hysteresis is not expected due the blunt LE and the turbulence level of the flow. Since no hysteresis is observed in the experiments,

all plots related to the "first test scheme" present the average of sweep up and sweep down curves.

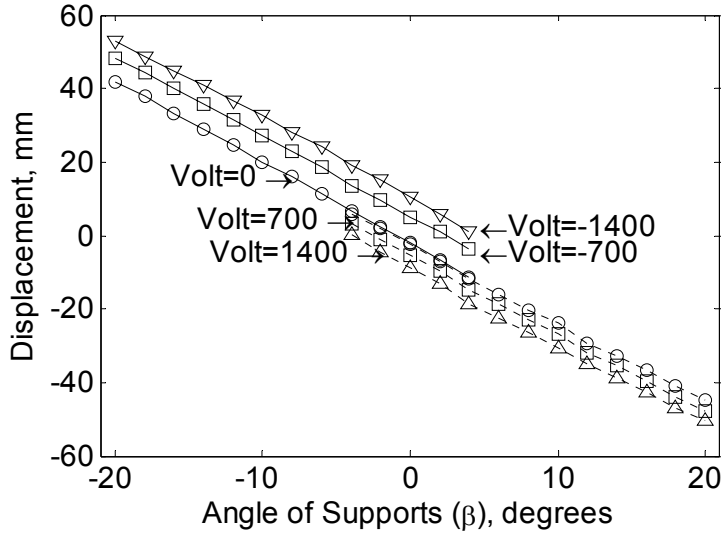

Figure 5.15: Displacement of the trailing edge due to voltage input and the change in β. $Re_{chord} = 1.27 \times 10^5$.

The AOA and effective camber values (also derived from the laser displacement measurements) are given in Figure 5.16.

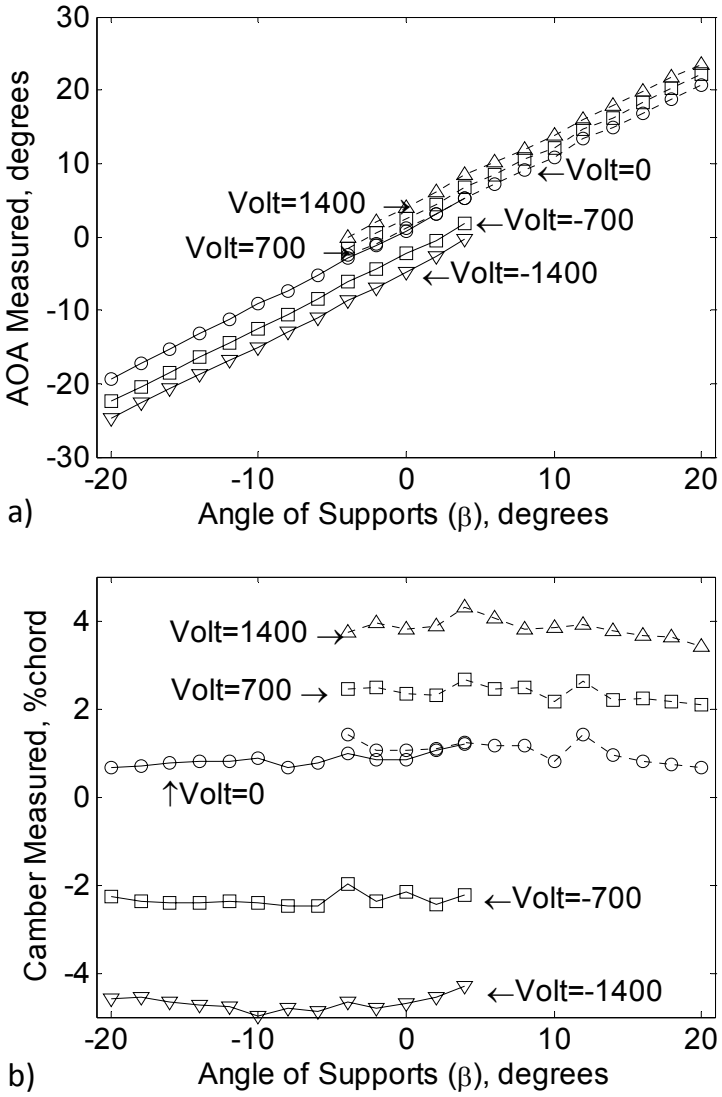

Figure 5.16: a) Angle of attack change due to voltage input and the change in β; b) Effective camber of the circular-arc fit due to voltage input and the change in β. Re_{chord} = 1.27×10^5.

The voltage-geometry relationship appears linear (and independent of β) since voltage is changed only when a β sweep is completed. It is observed that the AOA and camber are not zero for the zero degrees β and zero volt condition. This is caused by the residual shape that piezo-ceramic bimorph holds from previous tests (not reported here). This is a typical characteristic of a hysteretic piezoceramic actuator that goes through high deformations. The measured change in AOA and camber is consistent with assumptions made in Section 5.2. The camber of the airfoil at zero voltage is approximately 0.75% chord. As the support angle is swept up and down, no

conclusive deformation is observed due to the change of aerodynamic load distribution on the airfoil. As predicted by the model presented in Section 5.2, the airfoil sustains aerodynamic loading at 15 m/s. Figure 5.17 presents the experimental results for lift and drag coefficients vs. angle of supports.

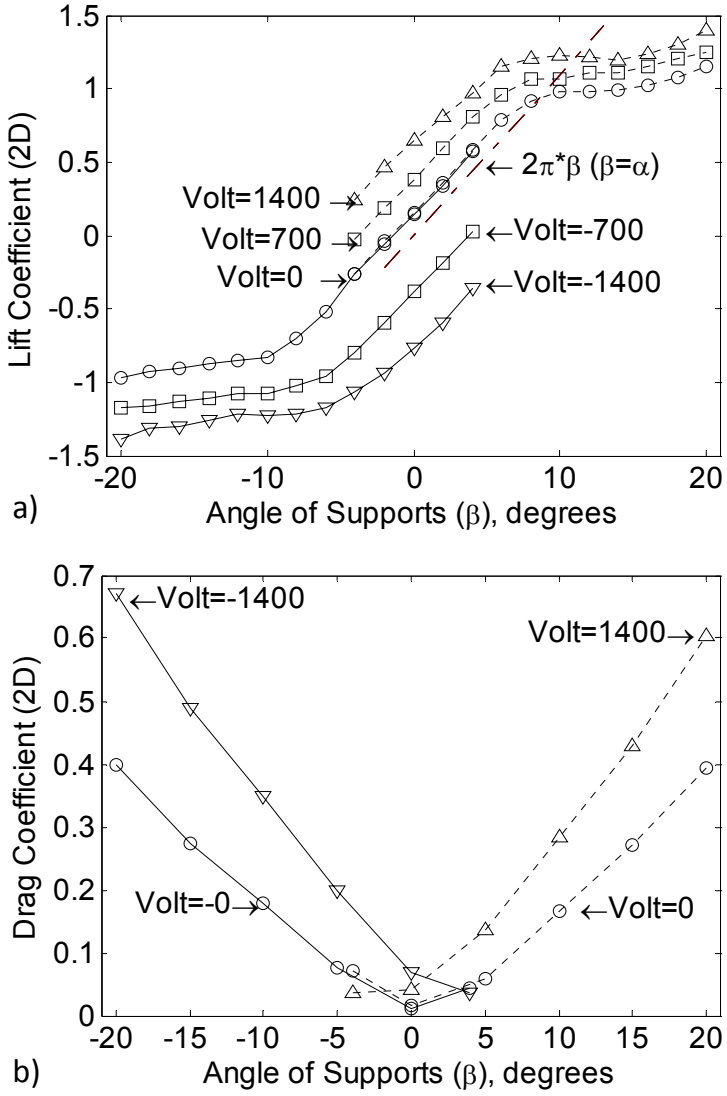

Figure 5.17: a) Lift and b) drag coefficient (2D) of the variable-camber airfoil at 15 m/s. $Re_{chord} = 1.27 \times 10^5$.

The lift coefficient curve for the zero voltage has a slight offset due to the residual camber (and the induced angle) as noted in the displacement measurements. The large voltage-induced peak-to-peak change in lift at zero degrees should be noted. Significant lift change is

observed at zero degree of support angle. A lift coefficient of -0.76 at -1400 V and 0.64 at 1400 V is observed which results in a total lift change of 1.40 through voltage excitation.

5.3.7. Aerodynamic Response: Voltage Sweep at Fixed Support Angle

The first test scheme concluded that the aerodynamic hysteresis was negligible for the thin variable-camber airfoil. A second test scheme is designed to identify the hysteresis of the morphing airfoil due to its piezoceramic bimorph nature. The experimental setup and measurements are the same as the previous tests, however, only a fixed support angle of zero degrees is considered while the applied voltage is changed. The test is started at -1400 V. After force and displacement measurements are taken, the voltage is incremented by 175 V up to 1400 V, which is labeled as "Sweep Up" curve. The voltage is then swept down from 1400 V to -1400 V in steps of 175 V. The calculated TE displacement (derived from the laser displacement measurements) is presented in Figure 5.18.

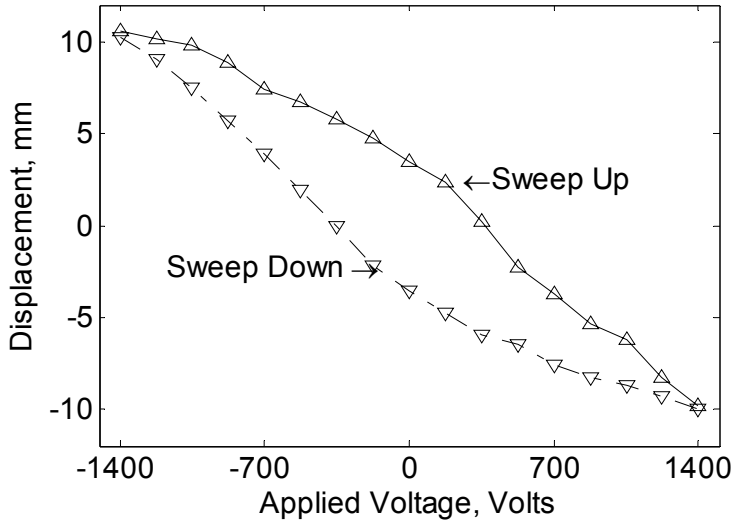

Figure 5.18: Displacement of the trailing edge due to voltage input. Re_{chord} = 1.27x10^5.

Figure 5.19 present the camber and the AOA of the airfoil. As with the previous tests, all plots represent the aerodynamically loaded airfoil. The nonlinear voltage-geometry relationship is due to piezoceramic hysteresis, which can be a made linear with a Preisach model [Preisach, 1935] (not addressed in this chapter) and feedback control if desired. The two measurement curves indicate that an increase in voltage magnitude above 1400 V will result in higher

deformations without reduction in its rate of change. This is desired since the MFCs can safely be actuated up to 1700 V which will increase operational envelope of the airfoil.

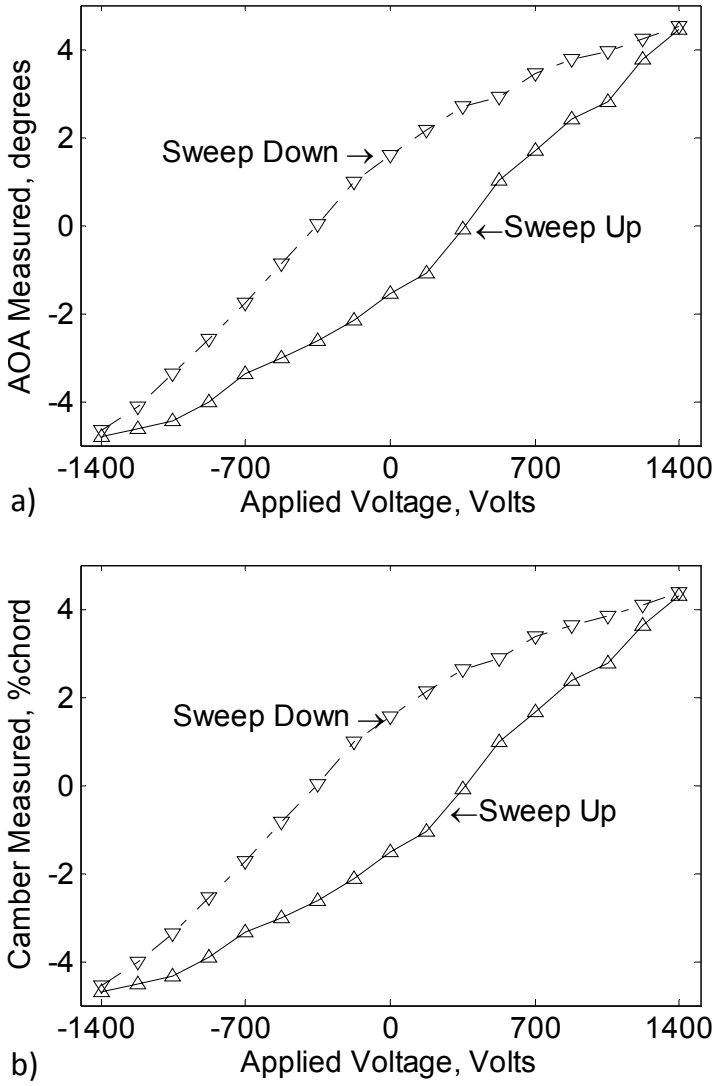

Figure 5.19: a) AOA of the circular-arc fit due to voltage input. b) Camber induced by voltage input. β = 0°, Re_{chord} = 1.27x10^5.

The magnitudes of the AOA and camber curves are almost identical which is due to the geometric property of a circular-arc for small deformations. Negative camber values simply indicate that actuation is in the negative direction. Figure 5.20 shows the lift and drag coefficients vs. voltage input for the variable-camber airfoil at 15 m/s flow speed.

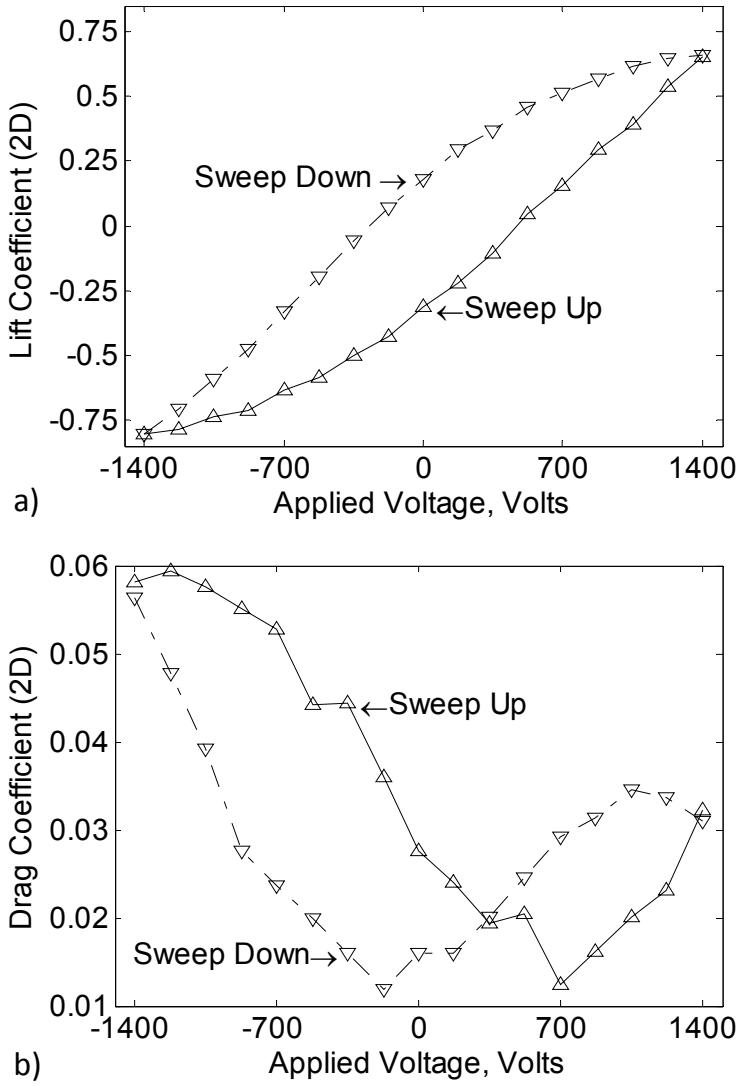

Figure 5.20: a) Lift and b) drag coefficient (2D) of the variable-camber airfoil from experiments at 15 m/s. β = 0°, Re_{chord} = 1.27x10^5.

The lift coefficient is measured as 0.657 at +1400 V and -0.807 at the -1400 V. As noted for the displacement plot, the end slopes of the two curves indicate that higher lift can be achieved if voltage is increased. A change of 1.46 in lift coefficient is measured for the peak-to-peak voltage input. Similar to the lift coefficient, the drag data is biased to the left, where higher drag is observed for negative voltage region. The drag curves are not as smooth as the lift curves because the magnitude of the drag forces generated are closer to the balance uncertainty of $U_{CD,max}$ = ±0.014 as reported earlier. When drag and lift are evaluated, a significant change in lift

can be achieved for a small drag penalty. Such results confirm an important motivation of using a variable-camber airfoil.

5.3.8. Comparison of Different Airfoils

A lift and drag coefficient comparison of different airfoils is given in Figure 5.21. Two airfoils are presented: 1) Variable-camber airfoil, 2) Flat plate with 2.00% thickness. The data for variable-camber airfoil (from Figure 5.20) are plotted against the measured, voltage-induced AOA (from Figure 5.19). In other words, there is no rotation of the airfoil supports for the morphing airfoil data presented. The plot also allows a clear representation of the lift generation by coupled camber and AOA change. The comparison is given to allow the reader to evaluate the variable-camber airfoil with respect to a standard airfoil subject to same Reynolds number and turbulence intensity. A desired comparison would be to an airfoil with a control surface; however this is not addressed due to the experimental complexity. Tests are conducted at 15 m/s and a chords $Re_{chord} = 1.27 \text{x} 10^5$.

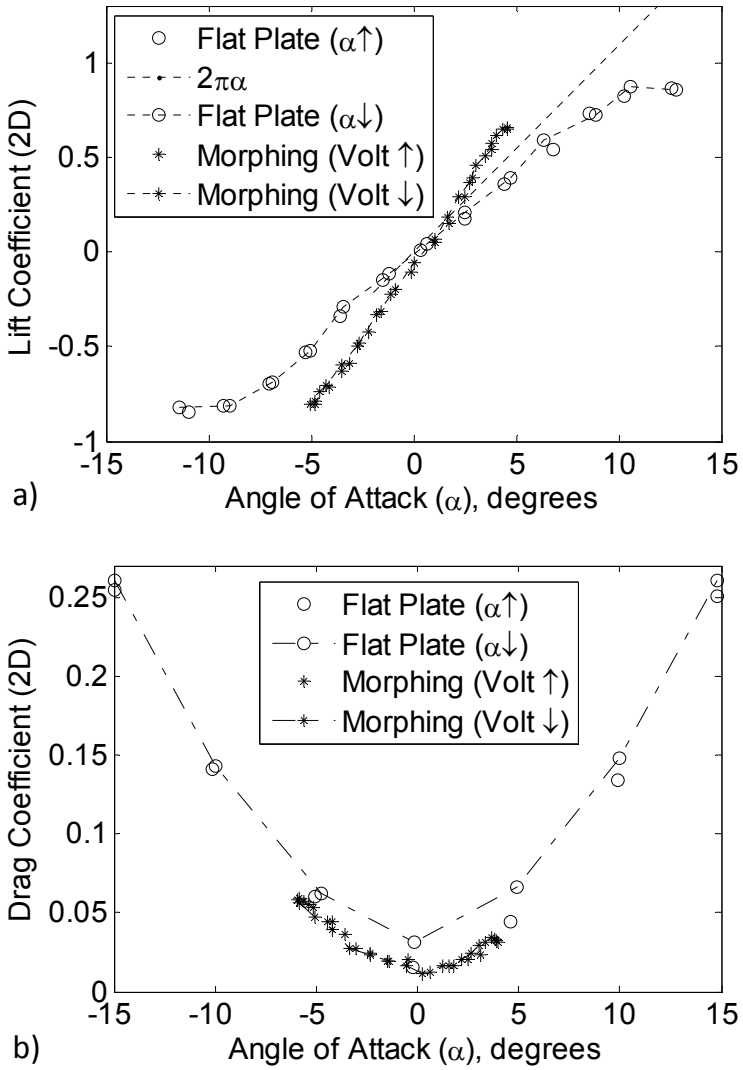

Figure 5.21: a) Lift and b) drag coefficient (2D) comparison for two thin airfoils. Re_{chord} = $1.27x10^5$.

There is a significant difference in lift curve slope (0.153 per-degree) when compared to flat-plate lift slope (0.081 per-degree). The increase of lift slope is due to coupled camber and AOA induced by voltage input. Drag is observed higher for the flat-plate airfoil (due to its relatively thicker LE) when compared to the thin bimorph airfoil. The uncertainty in the measurement (as reported earlier) must also be considered when comparing the two results. Since the variable-camber airfoil is aimed at generating forces for vehicle control, performance in lift is considered more important than the performance in drag.

The overall performance of the airfoils are compared by looking at the *L/D* ratio presented in Figure 5.22. Data for both airfoils represent the average of sweep-up and sweep-down curves.

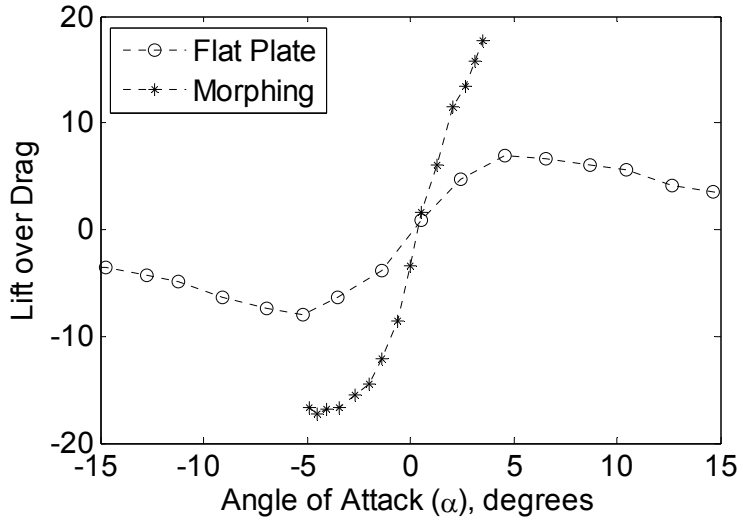

Figure 5.22: Lift over drag (2D) comparison for two thin airfoils. Re_{chord} = 1.27x10^5.

The variable-camber airfoil produces an *L/D* ratio of -17.3 at -1225 V (α = -4.52°) and an *L/D* ratio of 17.8 at +1400 V (α = +3.48°). The flat plate in the current research shows a maximum *L/D* of -8.02 at -5.17° AOA. In comparison to the flat plate airfoil, the variable-camber airfoil generates a significant change in lift-over-drag; however even higher *L/D* values are expected. As noted earlier, the drag from the flat plate airfoil is significantly higher than tests published by Mueller [1999], and Pelletier and Mueller [2000] due to the configuration of the wind tunnel. Refer to Section 5.3.3 and Appendix E for a detailed explanation.

5.4. Conclusions

The prototype presented in this chapter is a variable-camber airfoil with simply-supported boundary conditions. Aerodynamic and static deflection characterization under aerodynamic loads is presented. Wind tunnel results show comparable effectiveness to conventional actuation systems. The MFC bimorph demonstrated adequate control authority for aerodynamic open-loop shape control. The fabricated prototype demonstrated adequate stiffness at a tested flow speed of 15 m/s. An average lift coefficient increase of 1.46 is observed purely due to peak-to-peak

actuation voltage. The concept showed a small increase of drag with actuation voltage, making it an efficient variable lift generation device. A maximum 2D *L/D* ratio of 17.8 can be achieved through voltage excitation. The concept is also tested in the wind tunnel and verified to generate high control outputs in the VTOL ducted-fan vehicle.

CHAPTER 6

MACRO-FIBER COMPOSITE ACTUATED CASCADING BIMORPH THICK AIRFOIL

In Chapter 5, a variable-camber bimorph thin airfoil concept employing Macro-Fiber Composites is designed and tested to produce relatively large aerodynamic forces. A thin bimorph configuration is used to create the airfoil surface. Although a thin bimorph structure is easy to implement, it is well known that thin airfoils are more susceptible to flow separation. The maximum lift generation is relatively low for a thin airfoil when compared to its thick counterpart. To address this issue, a novel variable-camber airfoil employing two cascading bimorph surfaces (with MFC actuators) and a single four-bar (compliant box) mechanism as the internal structure is proposed. The unique choice of boundary conditions (induced by the compliant box) allows a variable and smooth deformation in both directions from a flat camber line. The compliant box allows for a desired thickness between the two cascading bimorph surfaces; hence the airfoil is significantly thicker that it's single bimorph counterpart (as shown in Chapter 5). This chapter focuses on actuation modeling and response characterization under aerodynamic loads.

The chapter is organized as follows. First, the airfoil concept is introduced and a parametric examination of the aerodynamic response is demonstrated (that optimizes kinematic parameters of the airfoil). Next, the fabricated concept, employing eight MFC M8557-P1 type actuators in a bimorph configuration, is presented. Wind tunnel experiments are discussed for the 12.6% maximum thickness, 127 mm chord variable-camber airfoil. Aerodynamic and structural performance results are presented for a flow rate of 15 m/s and Reynolds number of 127,000. Nonlinear effects due to aerodynamic and piezoceramic hysteresis are identified and discussed. Finally, the experimental results are compared to conventional, symmetric NACA and other airfoils.

6.1. Cascading Bimorph Variable-Camber Airfoil Concept

The high strain and high structural deflection requirement under aerodynamic loads creates the need for novel mechanisms to be employed along with piezoceramic actuation. Using the knowledge gained from Chapter 5, a novel airfoil is designed to provide bi-directional aerodynamic vectoring by employing two cascading bimorphs. The design employs two active surfaces in the top and bottom surfaces of the airfoil which are pinned at the trailing edge. These active surfaces are chosen to be MFC actuated bimorphs. A compliant parallelogram (box structure) is used to create the desired boundary conditions to the leading end of the bimorph surfaces. Figure 6.1 shows the kinematic model and the parameters of the airfoil.

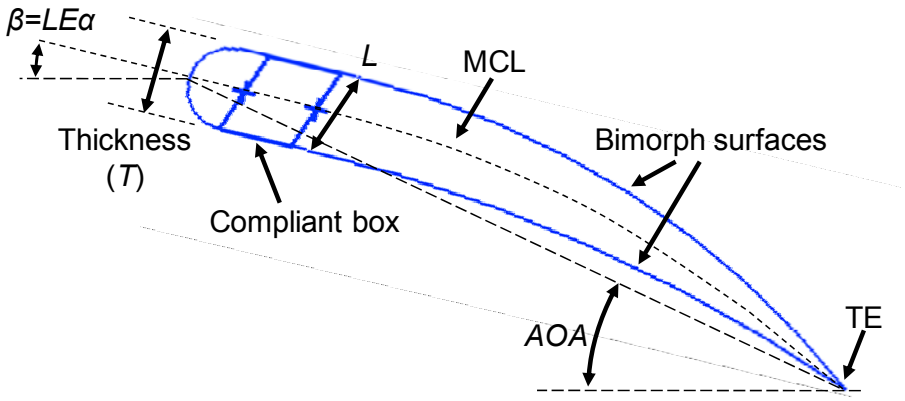

Figure 6.1: Novel airfoil design and geometric parameters. Morphed state is illustrated.

In the figure, β is the LE incidence angle and MCL is the mean-camber-line. The compliant box can simply be described as a four-bar mechanism. The two parallel bars that connect top and bottom surfaces have constant length (L). The airfoil can be mounted to an aircraft either at the center or at the ends of the vertical bars. The change in camber of the active surface of the airfoil causes the box to comply and generate a shear-like motion while keeping the end-slope of the bimorphs equal to each other. When the airfoil is in the non-actuated state, the link length (L) is equivalent to the LE thickness (T) of the airfoil. The initial percent thickness ($Th = L/chord*100$) is calculated at the zero volt state. It is important to note that the concept proposed here consists of 1) the two active unimorph or bimorph surfaces and 2) the three boundary conditions that are necessary to connect the surfaces and create a compliant mechanism. That is to say, the LE geometry is not proposed here, and it can be tailored to the specific application. In this chapter, the LE is designed to be elliptic due to geometric constraints

of the VTOL aircraft (presented in Section 5.3.2 and shown in Figure 5.8). Figure 6.2 shows a few possible geometric configurations, with different link lengths and voltage inputs.

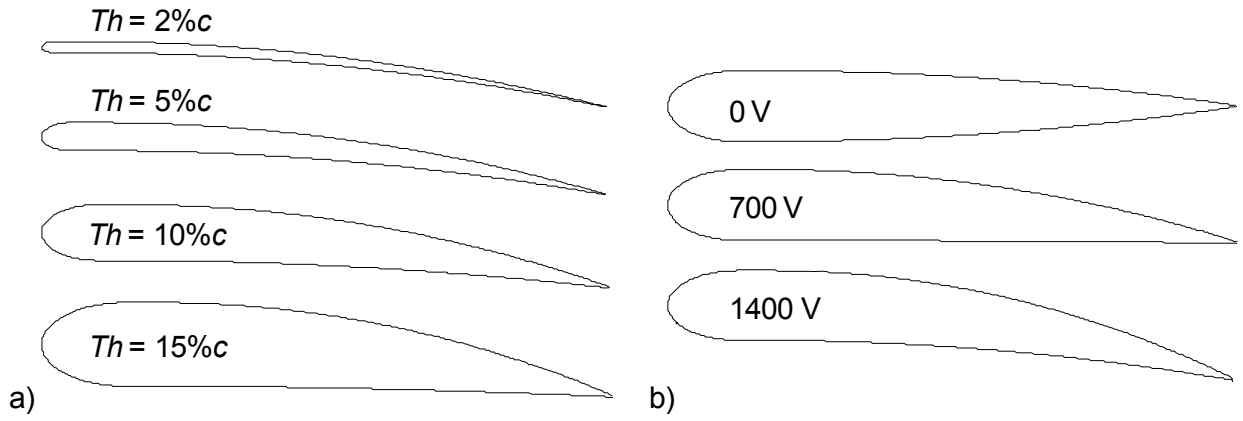

Figure 6.2: a) Airfoil design with different vertical link lengths. b) Effect of voltage input for an airfoil with 13.0% chord thickness.

The airfoil thickness is determined depending on the application, where an optimum configuration can be achieved for a desired function of various aerodynamic coefficients. The theoretical comparison of airfoils with different thicknesses is presented in the following section. Once the thickness is chosen, voltage could be applied to induce camber in both directions from a zero camber state.

6.2. Theoretical Aerodynamic Analysis

The theoretical analysis method presented here aims to determine optimal thickness ratio of the airfoil for high lift authority. For the analysis presented in this section, the airfoil is assumed to have a smooth and continuous surface and with a TE gap of 0.05% chord. A constant curvature is assumed for each surface of the active section due to the high chordwise coverage of the active material. An approximate slope of 2.86% camber-per-kV is assumed for each active surface for the theoretical analysis. The linear assumption simply corresponds to 4.86% camber at 1700 V, 4.00% at 1400 V, and 2.00% at 700 V. A MATLAB based program is developed to drive 2D panel method software XFOIL [XFOIL, Drela, 1989]. XFOIL software is employed to calculate lift and drag coefficients and the pressure distribution. For XFOIL simulations, a 0.05% chord trailing edge gap and an approximate 0.85% turbulence level is assumed. It must be noted

that XFOIL predictions for AOA above maximum lift angle are not accurate. Due to the limitation of the deflection of the piezo-composite bimorph, XFOIL analysis presented here never passes beyond this AOA limit. Figure 6.3 shows the effective geometric parameters of the airfoils (illustrated in Figure 6.2) as a function of thickness and actuation voltage. All results presented in this section are for a LE incidence angle of zero degrees ($\beta = 0°$).

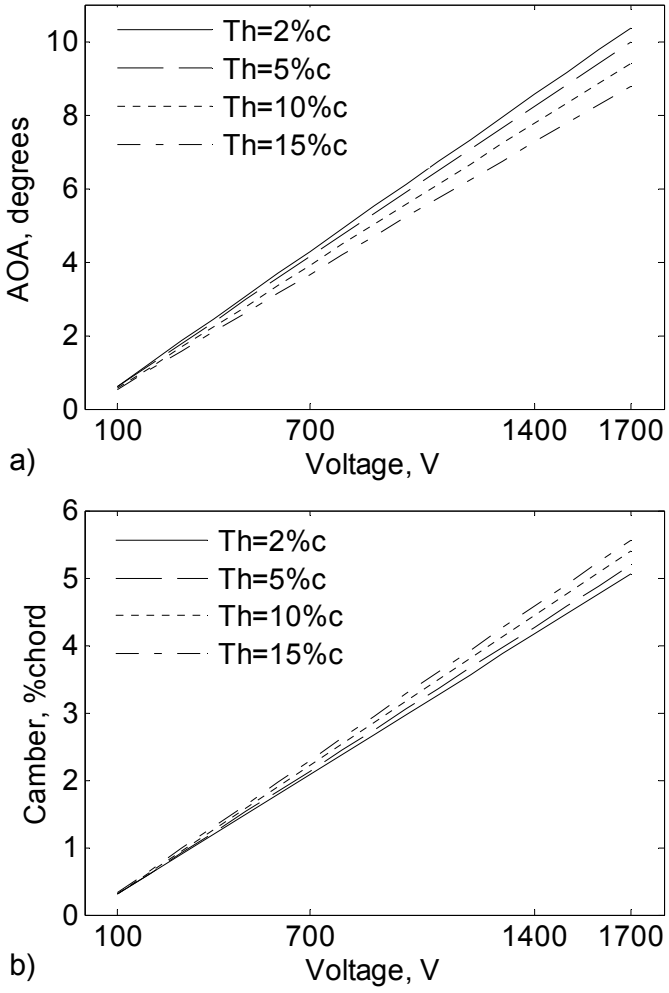

Figure 6.3: Theoretical (2D) change in geometry. a) Angle of attack and b) effective camber.

Note that both camber and AOA values are zero for zero volt actuation due to the linear assumption. The AOA of the airfoil is decreased as the thickness is increased which is caused by the change in location of the LE with respect to the TE. In contrast, the effective camber of the novel airfoil increases as the thickness is increased. This is because the mean-camber-line (the line that is equally distant from the top and bottom surface) forms a higher displacement with the

increased thickness. Figure 6.4 shows the theoretical change in lift coefficient for the airfoil with 127 mm chord. The airfoil is subjected to 15 m/s freestream velocity.

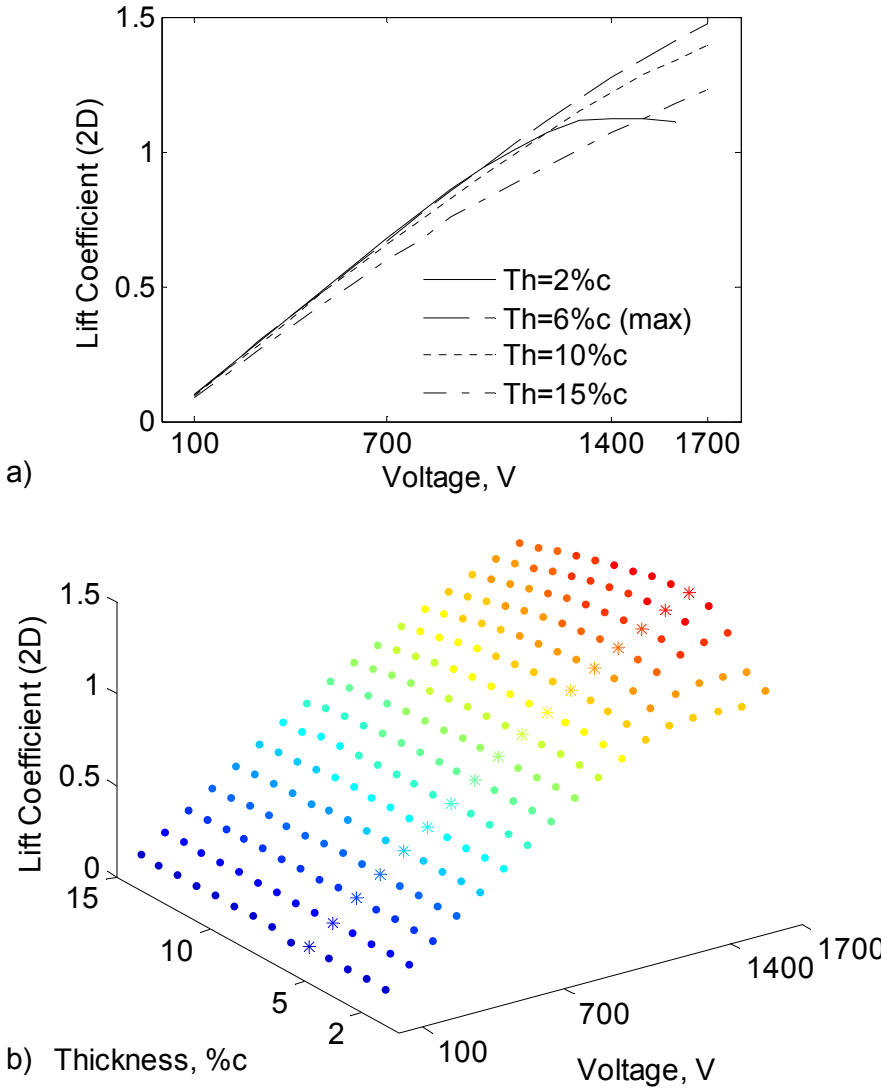

Figure 6.4: Theoretical (2D) lift coefficient for novel airfoil subjected to freestream velocity of 15 m/s. a) 2D and b) 3D plots. $Re_{chord} = 1.27 \times 10^5$.

The 2% thick airfoil reaches the CL_{max} of 1.12 at 1400 V due to early separation. In contrast, the 6% thick airfoil shows the highest lift trend. Figure 6.5 presents the theoretical drag coefficient results.

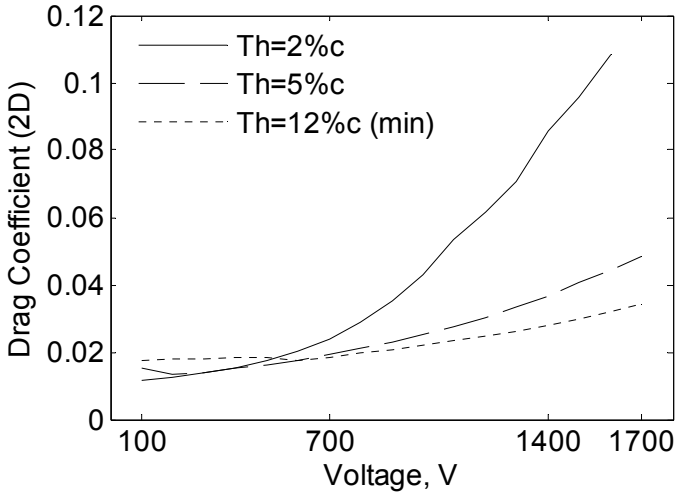

Figure 6.5: Theoretical (2D) drag coefficient for novel airfoil subjected to freestream velocity of 15 m/s. Re_{chord} = 1.27x10^5.

The 12% thick airfoil shows the lowest drag coefficient trend. Considering the stiffness of the airfoil, the flow induced deformation is assumed negligible at 15 m/s. A smooth surface is assumed for the analysis which is the main reason for deviation of lift curve from actual performance around CL_{max}. As reported in literature, XFOIL predicts slightly high lift coefficient and low drag coefficient when compared to experimental results therefore the predictions must be viewed as an upper boundary to actual performance. Figure 6.6 shows a comparison of lift-over-drag vs. actuation voltage.

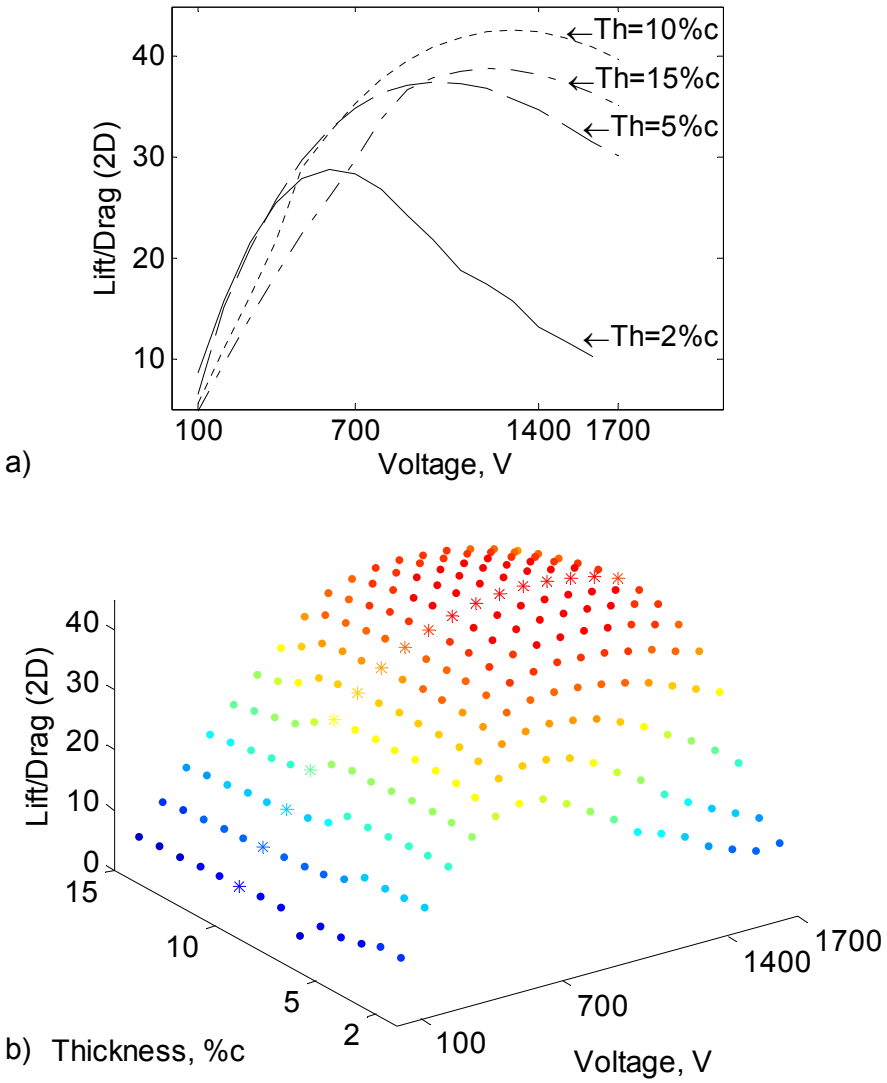

Figure 6.6: Theoretical (2D) L/D for novel airfoil at 15 m/s. a) 2D and b) 3D plots. Re_{chord} = $1.27x10^5$.

The maximum theoretical *L/D* is 42.6 for the 10% thick airfoil at 1300 V. This operation point corresponds to a camber of 4.12% and an AOA of 7.21°. The 2% thin airfoil shows the lowest *L/D* trend due to early stall and LE separation. Overall, the aerodynamic analysis clearly shows that a single bimorph airfoil (which is approximately 1%*c* thick) is not as effective as generating lift force when compared to a thick airfoil at the same surface curvature (and excitation voltage).

6.3. Structural and Aerodynamic Experiments

This section presents the structural and aerodynamic experiments conducted on a variable-camber airfoil prototype. First, the fabricated airfoil is introduced. The preliminary evaluation of the airfoil in a VTOL application is presented next. The 2D wind tunnel experimental setup is introduced. Finally, the experimental measurement of the structural and aerodynamic response is presented.

6.3.1. Variable-Camber Airfoil Specifications

Using the conclusions derived from the analysis presented in Section 6.2 and the geometric constraints of the VTOL aircraft (previously introduced in Section 5.3.2), two MFC actuated thick airfoils are fabricated. The compliant box mechanism is designed to keep the thickness to approximately 6% chord and allow free shear motion due to piezoceramic actuation. The elliptical leading edge is designed so that it could be mounted to the mounting bar directly or to the moving link (vertical link). In the latter case, the leading edge rotates with the vertical link in the opposite direction of the trailing edge. The gap between the leading edge and the rest of the airfoil is closed with a small flexible strip for smooth transition between the two surfaces. Figure 6.7 shows one of the two "identical" airfoils (sample labeled A2) employing eight (four on each bimorph) MFC M8557-P1 type actuators. The fabricated airfoil has 15 mm thickness, 127 mm chord and 133 mm span. The airfoil is 12% chord thick (instead of the desired 6% chord thickness for maximum lift authority) due to in-house fabrication limitations. The bimorphs are fabricated by sandwiching a 0.027 mm thick stainless-steel material with the MFC actuators and bonding the laminate under 0.8 Atm vacuum for approximately 24 hours. The substrate is chosen to be as thin as possible (to realize maximum displacement induced by voltage), and still have desired spanwise rigidity. The discussion of the substrate choice is previously presented in Section 5.3.1. The MFCs are aligned at the TE in the chordwise direction for both bimorph surfaces.

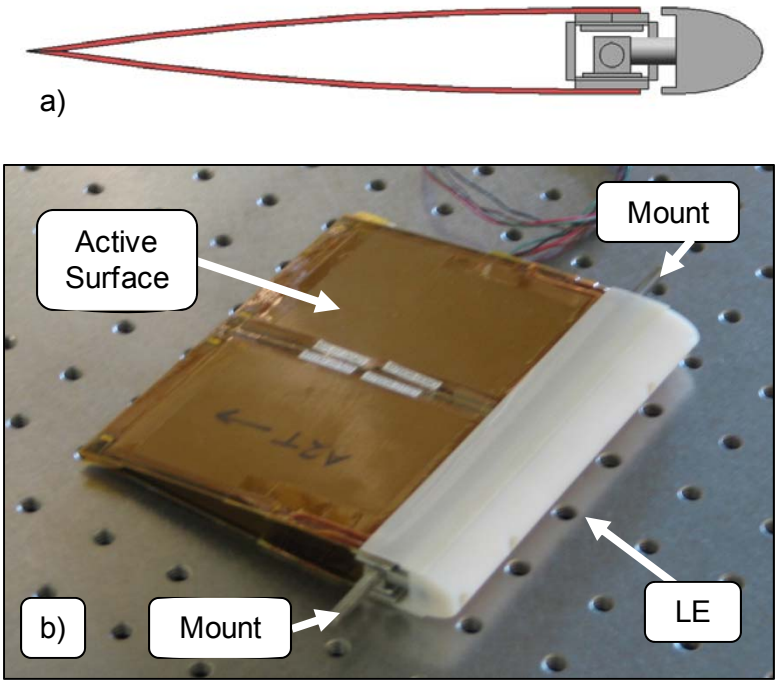

Figure 6.7: Novel variable-camber airfoil with eight MFC M8557-P1 actuators, 127 mm chord and 133 mm span. a) Final CAD model and b) fabricated airfoil (A2).

Bench-top static displacement tests are conducted to quantify the response of the airfoil. A custom, lightweight bipolar amplifier, weighing 151 grams and capable of ±2 kV four channel output, is fabricated and used during the tests. Note that the MFC actuators have a typical voltage range of -500 V to 1500 V. Since the airfoil has two surfaces, both in a bimorph configuration, MFCs on the opposite side are actuated with opposite voltage polarity and with 3-to-1 fixed ratio. Figure 6.8 shows the experimental setup.

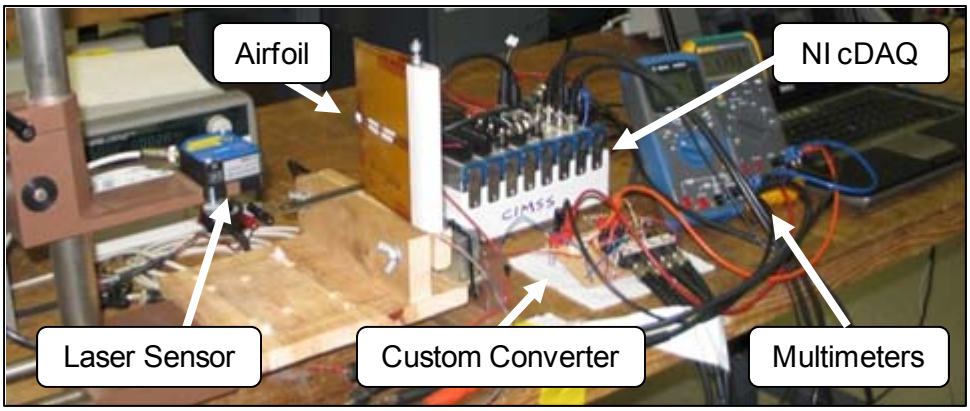

Figure 6.8: Experimental setup for airfoil displacement measurements with custom four channel bipolar converter.

The converter is controlled (with a reference signal) using a National Instruments (NI) cDAQ data acquisition system. The amplifier has a 5 V source input supplied by an Agilent DC power supply. This power supply is used in order to measure the current draw (hence the power consumption) by the amplifier. The high voltage output (of the converter) to the MFCs are measured by two digital multimeters. The displacement of the airfoil is measured with a Micro Epsilon optoNCDT 1401-200 laser displacement sensor. The displacement is measured at 86 mm from center of the compliant box (the mounting rod), which is equivalent to a distance of 118 mm from the leading edge. Figure 6.9 shows one of the airfoils at three different actuation levels.

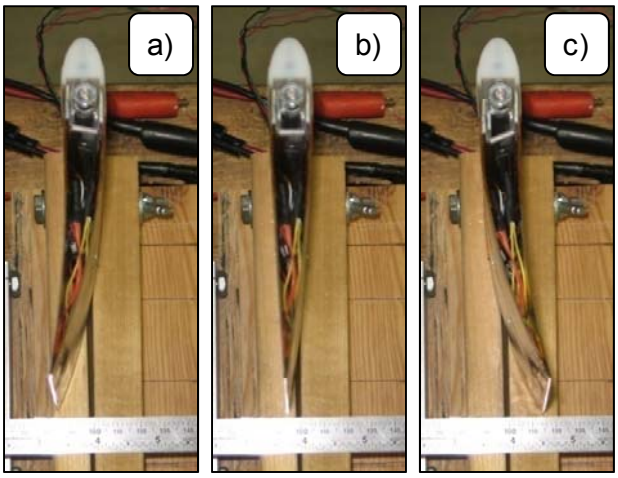

Figure 6.9: Displacement of the novel airfoil at three static voltage levels. a) -1500 V, b) 0 V, c) +1500 V.

Static voltage sweep tests are conducted to determine the nonlinearity of the amplifier voltage output and the airfoil displacement. First, a voltage level is set and steady state displacement is achieved. Next, the measurements are taken. Figure 6.10 presents the voltage output of the amplifier, and the displacement of the airfoil is plotted against the user input parameter labeled as the actuation percentage.

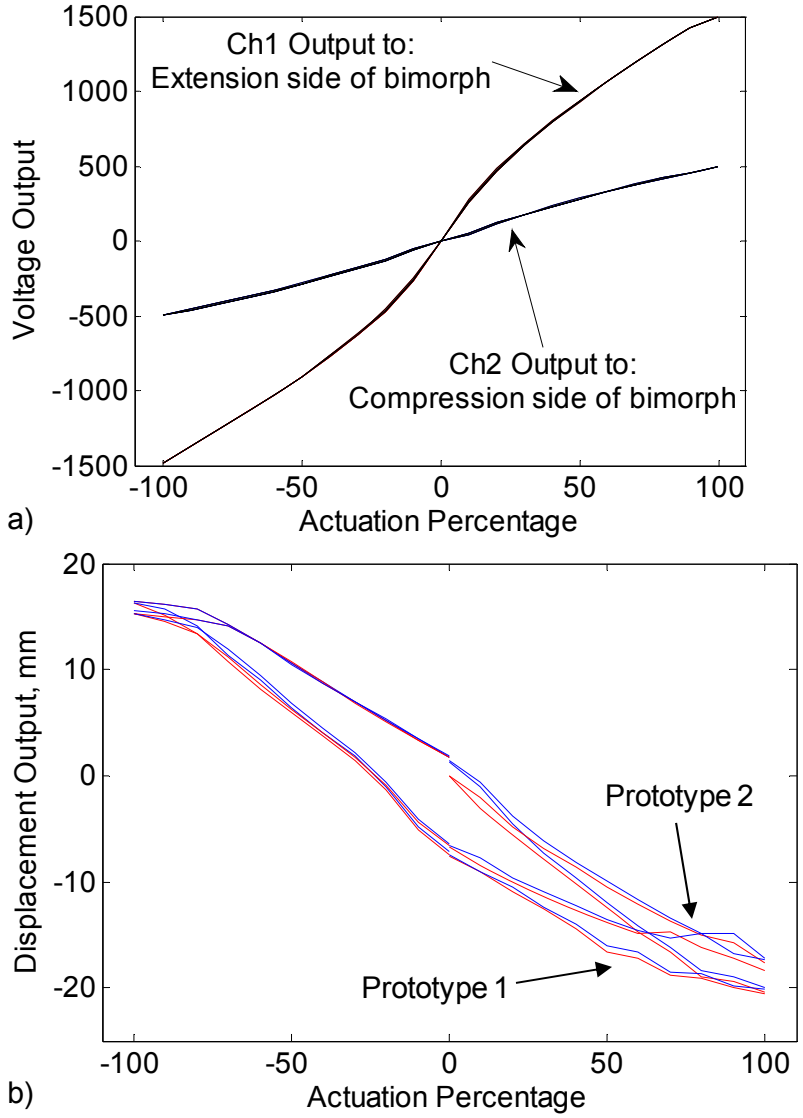

Figure 6.10: Amplifier voltage output and airfoil displacement response to user input. a) Voltage input-output relationship of the custom converter and b) displacement output of the two thick airfoils, A1 and A2 labeled Prototype 1 and Prototype 2 respectively.

The plots represent total of four loops (two loops for each airfoil) starting from -100% to +100% and back to -100%. The output of the amplifier is slightly nonlinear for both low and high side outputs. The amplifier output can be linearized by a simple analytic function if desired. The displacement of the airfoils shows hysteresis due to piezoceramic nature of the MFC actuators. Note that each airfoil is tested twice, and both of these runs produce consistent displacement outputs. There is a small difference in the displacement output between the two airfoils for the positive actuation. This is expected considering the limited in-house fabrication methods. Both airfoils show very high displacement outputs relative to other (monolithic) piezoceramic devices.

6.3.2. Ducted-Fan Aircraft Wind Tunnel Experiments

The two fabricated thick airfoils are initially evaluated through wind tunnel tests of the VTOL ducted-fan aircraft. The ducted-fan, mounted on its side for wind tunnel testing, and the two fabricated morphing airfoils, mounted at the exit of a ducted-fan, is shown in Figure 6.11. The peak-to-peak displacement of the variable-camber airfoil (induced by voltage) is shown.

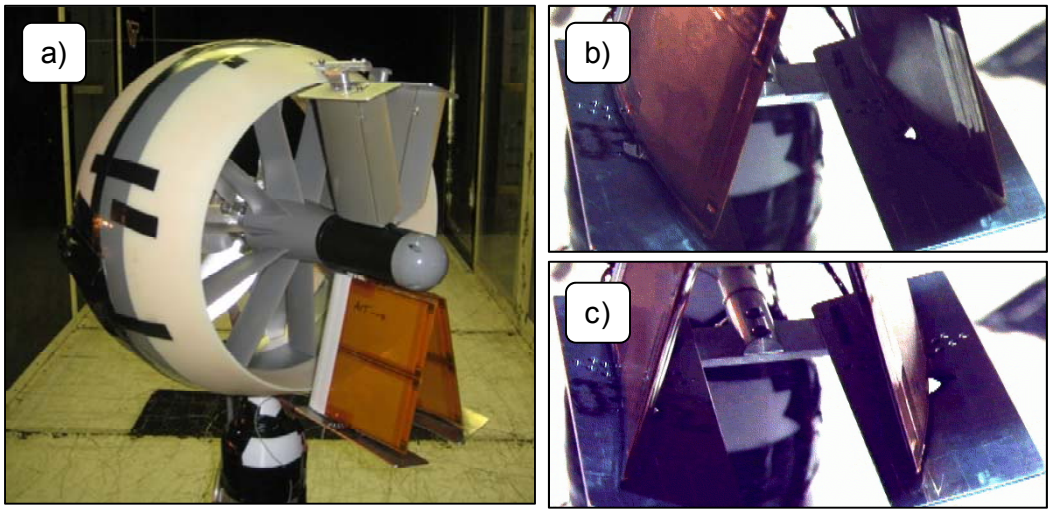

Figure 6.11: a) Ducted-fan vehicle model installed in Virginia Tech 6 ft x 6 ft Stability Tunnel, b,c) close-up of the two morphing control surfaces installed at the exit of the ducted-fan. Peak-to-peak actuation is shown.

The wind tunnel tests are conducted at a maximum fan flow speed of 45 m/s and maximum free-stream speed of 10 m/s. The morphing airfoil demonstrated high force outputs and no adverse deformation due to high aerodynamic loads. As noted earlier, the quantitative

results are not presented in this dissertation due to the publishing restriction on the wind tunnel tests of the VTOL aircraft. In order to prove the concept as a complete system, the custom bipolar amplifier is used during these wind tunnel tests.

The VTOL application required a variable-camber airfoil design that can handle high dynamic pressure and symmetric deflection; however, the developments presented in this chapter can easily be applied to a wide range of aerodynamic applications. Therefore, the following sections focus on fundamental (and isolated) airfoil characteristics, quantified in terms of conventional two-dimensional aerodynamic coefficients.

6.3.3. 2D Wind Tunnel Setup

Wind tunnel tests are performed in the custom, low-speed, open circuit wind tunnel (*Version 3.2*) as described in Appendix E. A custom balance that incorporates two load cells (from Transducer Techniques) is employed to measure lift and drag forces generated by the airfoil. A stepper-motor driven rotary table is used to set the angle of the airfoils tested. The airfoils tested in this section have an approximate 1.5 mm gap between the wing ends and the tunnel walls. Mueller and Burns [1982] show that gap sizes around 0.5% of the span are usually acceptable and do not affect the results. For the airfoils tested here, the gap is approximately 1.13%. Although the gap dimension is small, the percentage is still higher than recommended because of the low span of the airfoils. The possible effects of this gap size will be discussed in the following sections.

Preliminary tests are conducted to characterize the flow in the empty test section. Flow velocity during these tests is observed using a Flow-Kinetics Pitot-static tube and a Setra 267 pressure transducer. For the horizontal axis velocity measurements, a mean velocity of 15.4 m/s is measured and the 95% confidence interval uncertainty is $U_{Velocity,X} = \pm 0.40$ m/s. For the vertical axis measurements, the mean velocity is 15.2 m/s and the 95% confidence interval uncertainty is $U_{Velocity,Y} = \pm 0.54$ m/s. Approximately 4% maximum difference from mean is calculated independent of Pitot-static probe location; therefore the flow is assumed spatially uniform for aerodynamic coefficient calculations. The boundary layer will be discussed in the next section.

The streamwise turbulence of the flow in the empty test section is measured by standard hot wire anemometry technique. The lowest turbulence is observed at 15 m/s and the highest at 2 m/s. In summary, 0.60% turbulence intensity is calculated from 0.1 Hz - 50 kHz band-pass

filtered signal for the current test speed of 15 m/s. The turbulence of the wind tunnel used in this section is relatively larger than tunnels used in the research area due to the lack of flow straighteners/screens upstream of the inlet nozzle (see *Version 3.2* wind tunnel setup in Appendix E).

6.3.4. Baseline Aerodynamic Experiments on NACA Airfoils

A rapid-prototyped NACA 0009 airfoil is selected as a baseline to the variable-camber airfoil. The NACA 0009 airfoil is tested for lift and drag coefficients at an average flow speed of 15 m/s and a chord Reynolds number of 127,000. The fabricated airfoil has a maximum thickness of 11.3 mm, span of b = 133 mm and a chord of c = 127 mm. Refer to Section F.2 for details of the airfoil and the mounting of the airfoil in the 2D test section. The wind tunnel wall effects and buoyancy corrections are described in Appendix E.

Figure 6.12 presents comparison of NACA 0009 lift and drag coefficient data from the custom wind tunnel to different tests by Michael S. Selig of University of Illinois (UIUC) in two publications: Selig et al. [1995] (labeled as Selig-1), and Selig et al. [1989] (labeled as Selig-2). The references and respective Reynolds numbers are presented in the legend of the figures. The measurements are recorded at a rate of 100 Hz for a period of 60 seconds in order to get an accurate mean. The data for AOA sweep-up and sweep-down curves are presented for the current research, however there was no measurable aerodynamic hysteresis observed. The tests are conducted at 15 m/s and a chord Reynolds number of 127,000.

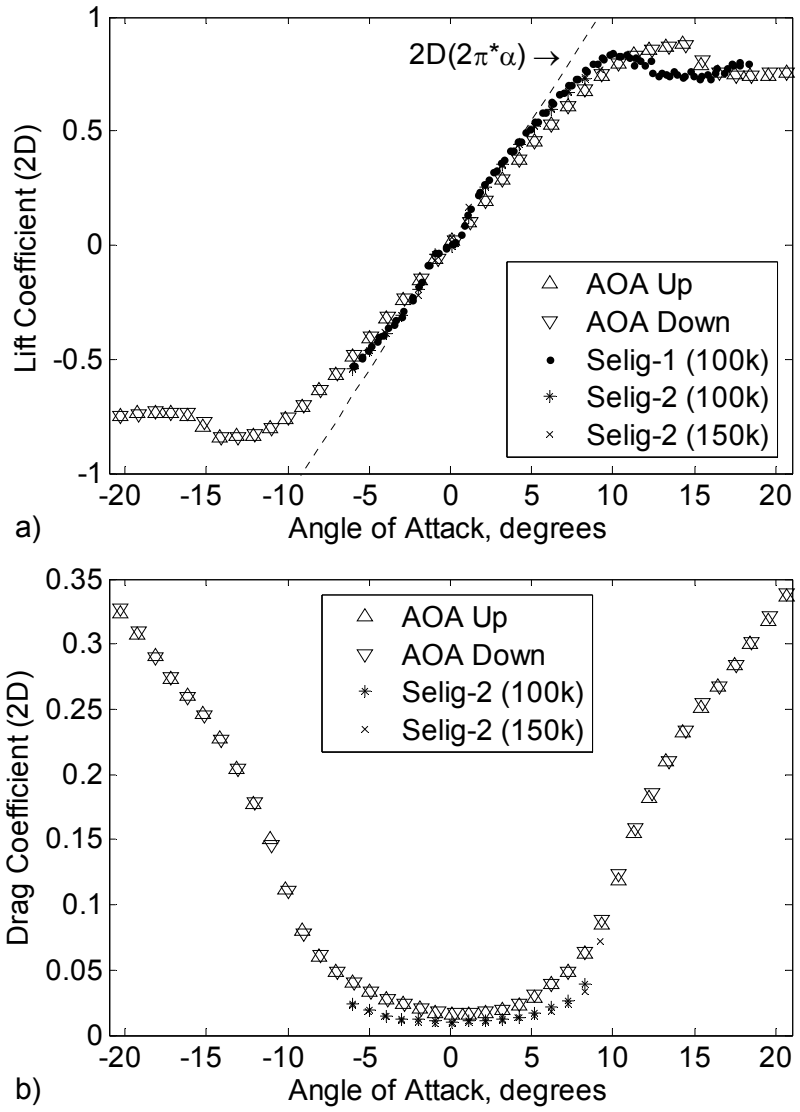

Figure 6.12: a) Lift and b) drag coefficients vs. angle of attack comparison for NACA 0009 airfoils.

The lift-curve-slope matches relatively well considering the effect of turbulence. The Reynolds number has negligible effect on the lift coefficient and there is no aerodynamic hysteresis. The drag coefficient from current evaluation shows a slightly higher trend at lower angles when compared to data reported by Selig. Zero degree drag coefficient is 0.0158 for the NACA 0009 airfoil tested here. Selig reports approximately 0.0087 at *Re* = 150,000 and 0.0096 at *Re* = 100,000 for zero degree drag coefficient of the NACA 0009 airfoil.

There are three main reasons for the difference in measured lift and drag between the two facilities compared in this section: 1) The span of the airfoils are designed so that the root and tip

is as close to the wind tunnel walls as possible. At high AOA, a small amount of 3D flow exists through the 1.5 mm gap between the airfoil and the test section walls. This flow is AOA dependent because the pressure gradient between the pressure and suction side increases as the AOA is increased. 2) The relatively large difference of turbulence levels in the two facilities must be noted. Selig et al. [1995, 1989] reports 0.358% rms turbulence for 0.01 Hz cutoff frequency, and 0.064% rms turbulence for 1 Hz cutoff frequency, at a Reynolds number of 100,000. 3) Finally, the airfoil tested in this section is a rapid-prototyped airfoil with some roughness along the spanwise direction. It is known that that NACA 0009 airfoils used by Selig et al. [1995, 1989] have smoother surfaces.

The experimental measurements are prone to the relative errors induced by uncertainty in setting the airfoil angle, flexibility in the balance system, and a small amount of friction in the balance pivots. The absolute values have uncertainties due to several parameters such as air density, flow velocity measurements and the theoretical wall and BL corrections. The uncertainty analysis of each measurement is conducted by following the AIAA Standard [AIAA]. The lift coefficient uncertainty is $U_{CL,max} = \pm 0.055$, and drag coefficient uncertainty is $U_{CD,max} = \pm 0.014$. The major source for the uncertainty is the low frequency variation of the flow velocity.

6.3.5. Displacement Field due to Voltage Excitation

Due to the nature of the piezo-composite bimorph, the airfoil is expected to have a residual but predictable curvature due to hysteresis, even for a short-circuit condition. A nonlinear model is not addressed in this chapter; instead the shape of the airfoil at each test condition is measured directly. This measurement is also necessary to observe the additional deformation (if any) due to aerodynamic loading.

To obtain geometric parameters during the experiments, a fast and accurate method had to be employed using two laser displacement sensors, and a digital camera. First, a calibration experiment is conducted for each airfoil. All geometric parameters are calculated from the image of the airfoil end-section from the camera and correlated to the two laser displacement sensor measurements at the mid-span section. The laser measurements are taken using two Micro-Epsilon laser displacement sensors with 100 μm dynamic resolution, mounted on the side-wall of the acrylic test-section. High spatial resolution can be obtained with the camera at the penalty of increase in test time. The measurement is taken without air flow in order to limit aerodynamic

effects. A direct correlation is obtained and the rest of the aerodynamic experiments are conducted with the laser sensors.

As noted earlier, the MFC actuators have a voltage range of approximately -500 V to 1500 V. Since the airfoil has two surfaces, both in a bimorph configuration, MFCs on the opposite side are actuated with an opposite field and with 3-to-1 fixed ratio. The higher of the two excitation voltages is used for labeling in the plots. A negative sign simply indicates actuation in the reverse direction. The standard definition of camber is used here, where percent-camber is the percentage of the height over the chord of the mean-camber-line. Figure 6.13 shows the displacement of the airfoil end section digitized from a series of six photos for a peak-to-peak voltage sweep.

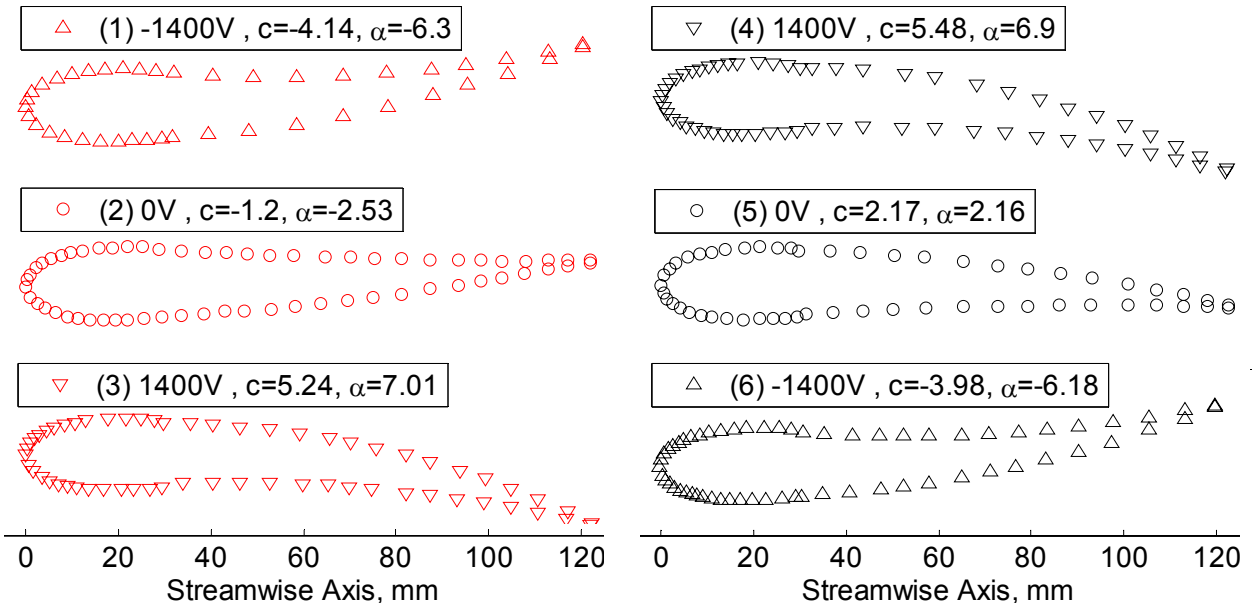

Figure 6.13: Composite plot of the airfoil end-section measurements with a digital camera. Legends show test order, voltage (*V*) and the calculated camber (*C*) and AOA (*α*).

The actuation voltage is swept from -1400 V to 1400 V and swept back to -1400 V. The effect of piezoelectric hysteresis can be observed from the difference between deflection at 0 V for the "up" and "down" sweeps. However, it should also be noted that the deflection is repeatable, as seen at the maximum positive and negative voltage levels. Figure 6.13 shows that the actual outline of the airfoil does deviate from the theoretical (and desired) airfoil. Most of this deviation occurs due to the interface between the active section and the rapid-prototyped leading section.

6.3.6. Aerodynamic Response: Angle Sweep at Fixed Voltage

This section presents the fixed voltage aerodynamic experiments on the variable-camber airfoil. The measurement and calculation of lift, drag and flow velocity is similar to the procedure outlined in the Section 6.3.4. The variable-camber airfoil is tested for its lift and drag performance at a flow speed of 15 m/s. Overall, two different test schemes are followed. The first evaluation is performed by setting the voltage of the bimorph at a fixed value, then sweeping the support angle (β) up and down. The complete list of voltages (in order) is: 1) -1500 V, 2) -700 V, 3) 0 V, 4) +1500 V, 5) +700 V, 6) 0 V. The support angle is swept from -20° to 20° and back to -20° in one degree increments. Once the angle sweep is completed, the voltage is changed. The procedure outlined here is necessary for correct identification and separation of two possible sources of nonlinear phenomena: 1) Aerodynamic hysteresis, and 2) Piezoceramic material hysteresis. These nonlinear effects will be discussed as the results are presented in the following pages.

In order to identify deformation due to aerodynamic loading, baseline deflection measurements are taken with zero flow velocity. The comparison of wind-on and wind-off conditions confirmed that there is no measurable deformation due to aerodynamic loading. All plots in the following sections represent the aerodynamically loaded data for consistency. Note that the angle of the support points (β) is given as the independent variable for the figures in this section which is necessary for clear presentation of the data. The angle β is swept up and down for several voltage levels, however, aerodynamic hysteresis was not observed. The lack of aerodynamic hysteresis is expected due the turbulence level of the flow. The AOA and effective camber values derived from the laser displacement measurements are presented in Figure 6.14.

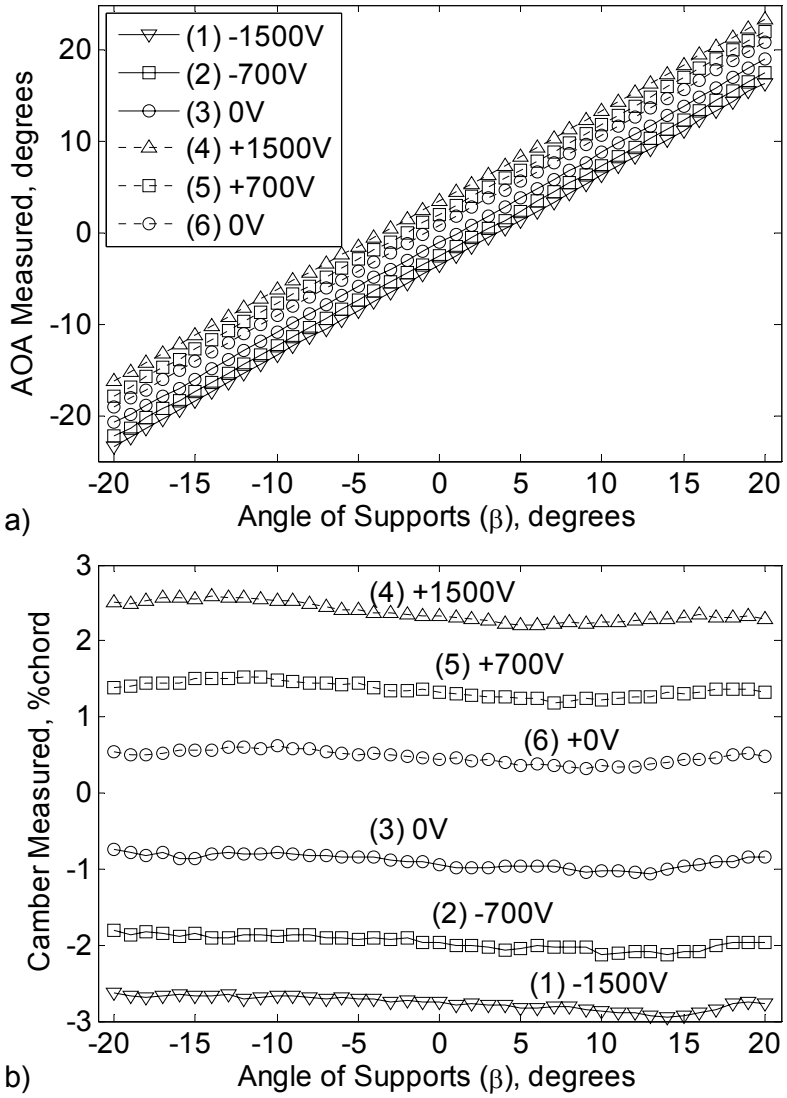

Figure 6.14: a) AOA and b) effective camber variation of the airfoil due to voltage input and the change in β. Re_{chord} = 1.27x10^5.

The measured change in AOA and camber is consistent with geometric predictions. The voltage-geometry relationship appears linear (and independent of β and magnitude of loading) since voltage is changed only when a β sweep is completed. It is observed that both AOA and camber is a non-zero value at zero volts. This is caused by the piezoceramic hysteresis (residual shape from a previous actuation test) which is a typical characteristic of an actuator that goes through high deformation. The hysteresis effect can be used to reduce power consumption of the overall system, where the airfoil can carry a range of external loads without consuming any power (except the transient effort to reach the desired position). As the support angle is swept up

and down, no conclusive deformation is observed due to the change of aerodynamic load distribution on the airfoil. The airfoil sustains aerodynamic loading at 15 m/s. Figure 6.15 presents the experimental results for lift and drag coefficients vs. angle of support.

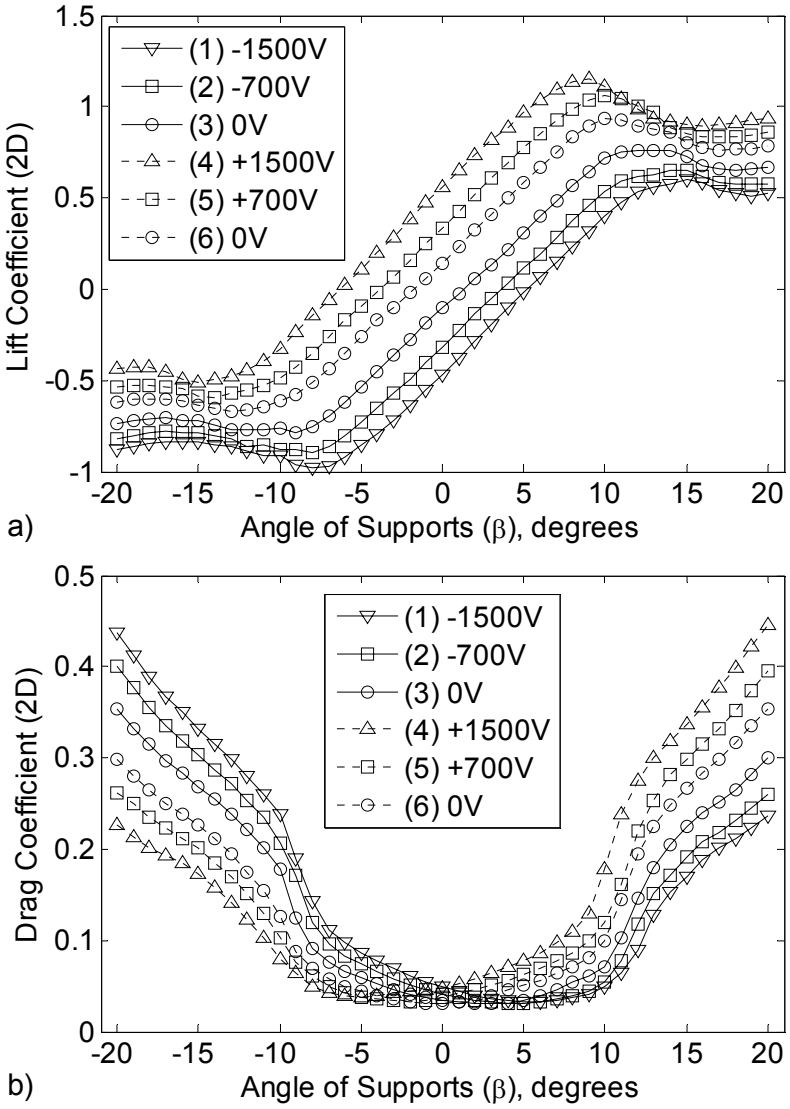

Figure 6.15: a) Lift and b) drag coefficient (2D) of the variable-camber airfoil at 15 m/s. Re_{chord} = 1.27x10^5.

The lift coefficient curves for the zero voltage levels have a slight offset due to the residual camber (and the induced angle) as noted earlier. The large voltage-induced peak-to-peak change in lift at zero degrees should be noted. Significant lift change is observed at zero degree of support angle. A lift coefficient of -0.47 at -1500 V and 0.56 at 1500 V is observed which

results in a total lift change of 1.03 through voltage excitation at $\beta = 0$. Minimum drag observed is 0.032.

6.3.7. Aerodynamic Response: Voltage Sweep at Fixed Support Angle

The first test scheme (presented in Section 6.3.6) concluded that the aerodynamic hysteresis was negligible for the morphing airfoil tested. A second test scheme is designed to identify the hysteresis of the morphing airfoil due to its piezoceramic bimorph nature. The experimental setup and measurements are the same as the previous tests, however, only a fixed support angle of zero degrees is considered while the applied voltage is changed. The test is started at -1500 V. After force and displacement measurements are taken, the voltage is incremented by 100 V up to 1500 V, which is labeled as "Sweep Up" curve. The voltage is then swept down from 1500 to -1500 V in 100 V steps. As with the previous section, all plots represent the aerodynamically loaded airfoil. Figure 6.16 present the measured AOA and the camber of the airfoil.

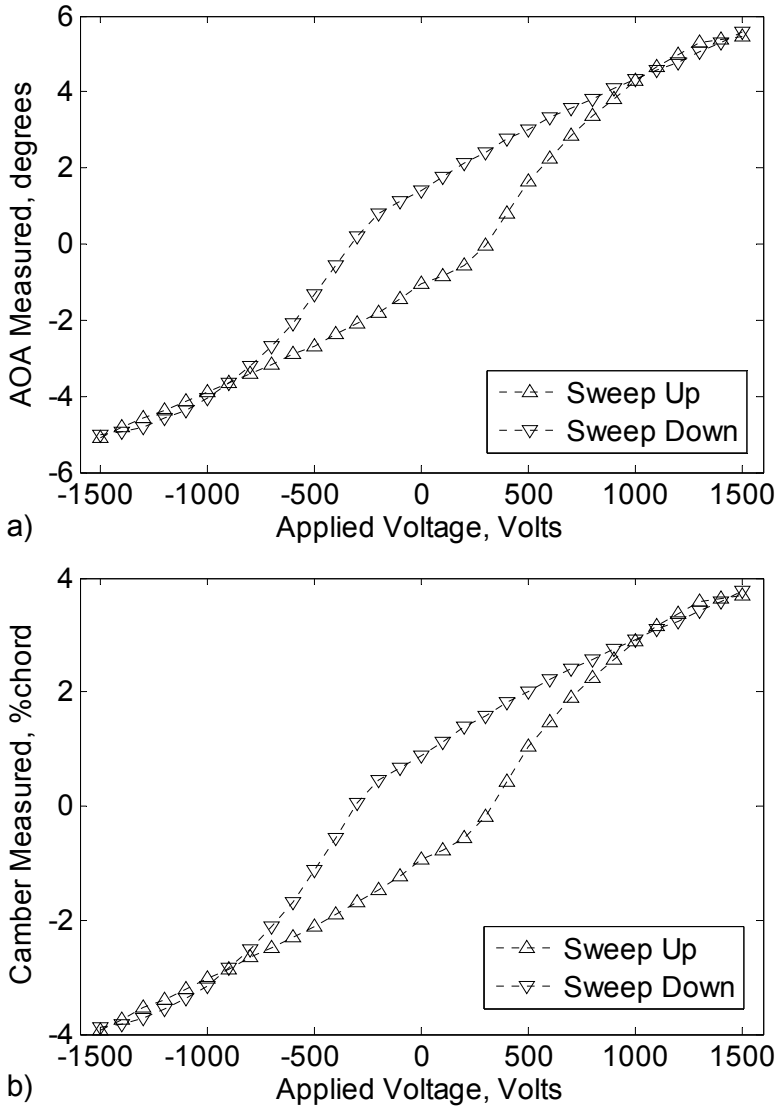

Figure 6.16: a) AOA and b) effective camber of the variable-camber airfoil induced by voltage input at β = 0°. Re_{chord} = 1.27x10^5.

A 10.7° AOA change and 7.59% camber change is observed for the peak-to-peak actuation range. The nonlinear voltage-geometry relationship is due to piezoceramic hysteresis, which requires a feedback control if linearization is desired. The two measurement curves indicate that an increase in voltage magnitude above 1500 V will result in a slightly higher deflection. This is desired since the MFCs can safely be actuated up to 1700 V. Negative camber values simply indicate that actuation is in the negative direction. Figure 6.17 shows the lift and drag coefficient vs. voltage input for the variable-camber airfoil at 15 m/s flow speed.

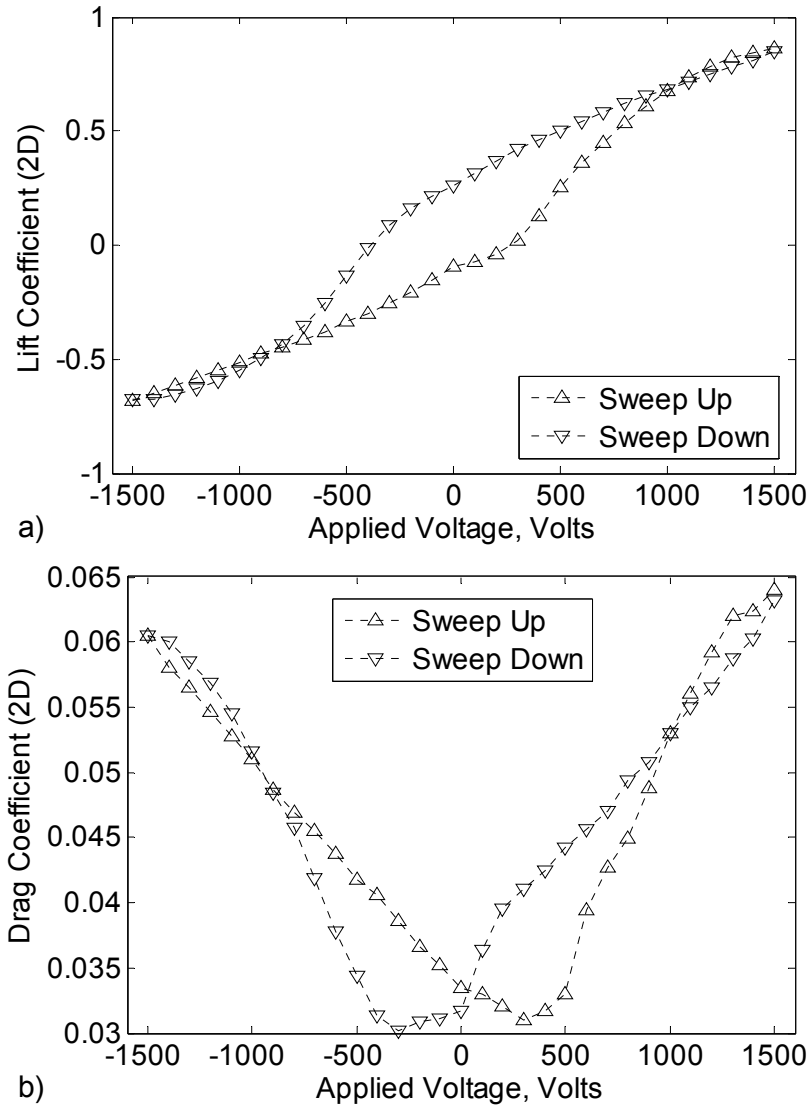

Figure 6.17: 2D aerodynamic response: a) Lift and b) drag coefficients of the variable-camber airfoil at 15 m/s. Re_{chord} = 1.27x10^5.

The lift coefficient is measured as -0.677 at -1500 V and 0.865 at +1500 V. The end slopes of the two curves indicate that higher lift can be achieved if the voltage is increased. A change of 1.54 in lift coefficient is calculated for the peak-to-peak voltage input. High drag is observed for the airfoil due to relatively blunt LE and the discontinuities on the surface caused by fabrication method. When drag and lift are evaluated together, a significant change in lift can be achieved for a small drag penalty. Such results confirm an important motivation of using a variable-camber airfoil without articulated surfaces.

6.3.8. Comparison of Variable-Camber Concept to Fixed Camber Airfoils

An aerodynamic comparison of the variable-camber airfoil to other similar (in shape) fixed-camber airfoils is presented in this section. The purpose is to show the advantages of continuously coupled camber-AOA actuation when compared to the mechanical AOA actuation. Four airfoils are presented: 1) Novel, variable-camber airfoil, 2) NACA 0009 airfoil, 3) NACA 0013 airfoil and 4) a rapid prototyped (RP) airfoil generated from the profile of the variable-camber prototype (at zero camber state). The fourth airfoil is tested to determine the effects of the surface roughness. The NACA 0009 has 11.3 mm, and the NACA 0013 airfoil has a maximum thickness of 16.5 mm. The variable-camber and the RP airfoils have an equivalent thickness of 15 mm. Figure 6.18 shows the profiles of the rapid-prototyped airfoils with 133 mm span, 127 mm chord and a finite TE thickness of 1.0 mm.

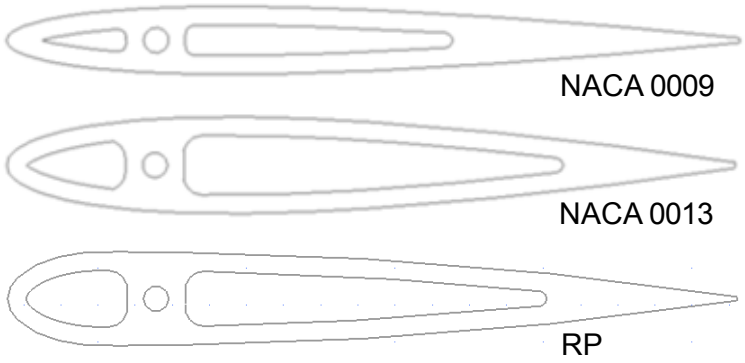

Figure 6.18: Profiles of rapid prototyped airfoils.

Lift and drag measurements are conducted at 15 m/s and at a chord Reynolds number of 127,000. The data is corrected for wall effects as outlined in the previous section. For the variable-camber airfoil, the true AOA (the voltage-induced AOA) is given as the independent variable. The mounting angle (β) is zero. In other words, there is no rotation of the airfoil supports for the morphing airfoil data presented. This allows a "fair" comparison between the fixed and variable-camber airfoils. Note that the AOA is calculated by photo calibration described earlier; hence it introduces a negligible uncertainty to the original data presented in Figure 6.17. The lift and drag comparison is given in Figure 6.19. Note that the arrows in the legend specify the direction of sweep of voltage (*Volt*) and AOA (α).

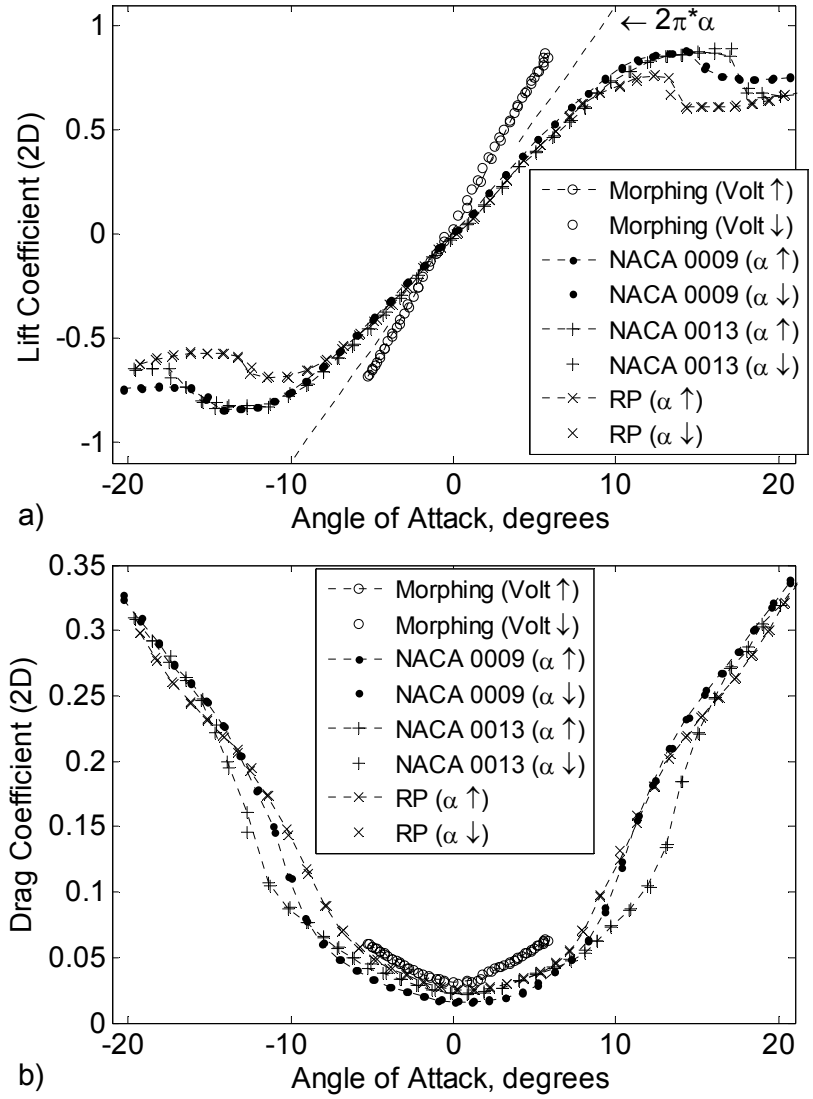

Figure 6.19: 2D aerodynamic response: a) Lift and b) drag coefficient comparison of four airfoils at 15 m/s. Re_{chord} = 1.27x10^5.

There is a significant increase in lift due to camber induced by voltage input. A lift curve slope of 0.144 per-degree is measured which exceeds the NACA 0009 lift slope (0.083 per-degree) by 72%. The plot shows the clear advantage of the lift generation by coupled camber-AOA change induced by voltage. The NACA 0013 and the RP airfoils develop similar lift-curve-slope however, NACA 0013 achieves a slightly higher Cl_{max}. As noted earlier, high experimental drag is observed for the morphing airfoil due to its relatively blunt (elliptical) LE when compared to the LE of NACA 0009 airfoil. The variable-camber prototype tested here does not have a continuous surface as desired due to in-house fabrication limitations. This is evident

when the morphing airfoil at zero AOA is compared to its rapid-prototyped replica airfoil (RP) with continuous and relatively smooth surface. Since the variable-camber airfoil is aimed at generating lift forces for vehicle control, performance in lift is considered more important than the performance in drag. The overall performance comparison of the airfoils is conducted by looking at the lift-over-drag (*L/D*) ratio presented in Figure 6.20.

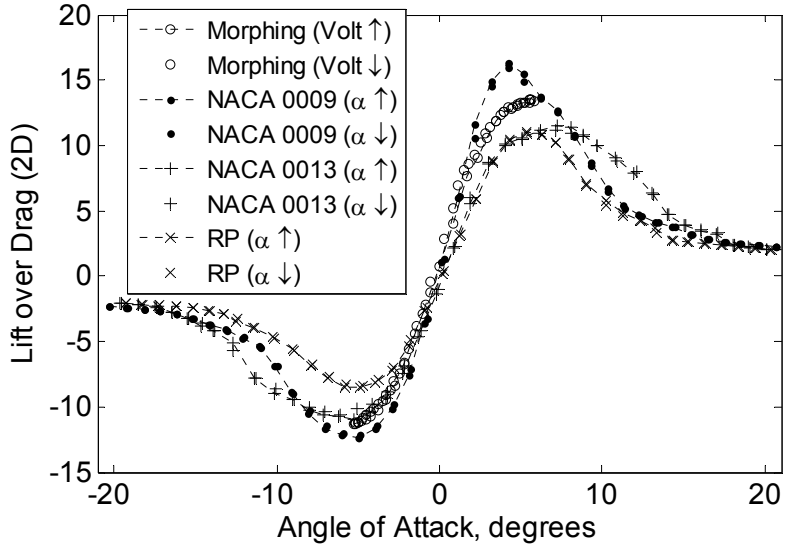

Figure 6.20: Lift over drag (2D) comparison of four airfoils at 15 m/s. Re_{chord} = 1.27x10^5.

The variable-camber airfoil produces a maximum *L/D* ratio of 13.4 at 1500 V (α = 5.78°) and an *L/D* ratio of -11.2 at -1500 V (α = -5.20°). The NACA 0009 airfoil produces a maximum *L/D* ratio of 16.3 at α = 4.21° and an *L/D* ratio of -12.3 at α = -4.97°. The variable-camber airfoil has higher *L/D* performance when compared to the fixed-camber airfoils with similar thickness (NACA 0013 and RP). In comparison to the conventional airfoils, the morphing airfoil generates a comparable change in lift-over-drag.

6.4. Conclusions

The variable-camber cascading bimorph airfoil concept presented in this chapter is designed to take advantage of aerodynamic loads to reduce control input moments and increase control effectiveness. The wind tunnel results show comparable effectiveness to conventional actuation systems. MFCs demonstrate adequate control authority for aerodynamic shape control. The concept shows adequate stiffness at a tested flow speed of 15 m/s. An average lift coefficient

change of 1.54 is observed purely due to peak-to-peak actuation voltage. The concept showed a small increase of drag with actuation voltage, making it an efficient variable lift generation device. A maximum *L/D* ratio of 13.4 can be achieved through voltage excitation. Finally, a 72% increase in lift curve slope is achieved when compared to a NACA 0009 airfoil. Compared to previously published results, the concept presented in this research demonstrates high force outputs and frequency bandwidth (although not demonstrated in this chapter). The concept is also tested and verified to generate high control outputs in the VTOL ducted-fan vehicle.

CHAPTER 7

LOW REYNOLDS NUMBER FLOW CONTROL WITH PIEZOCERAMIC COMPOSITE AIRFOILS

In Chapter 2, it was demonstrated that unimorph actuators with Macro-Fiber Composites are capable of high strain outputs and they can easily achieve curvatures commonly seen in airfoil surfaces. This chapter employs piezoceramic actuators (MFC unimorphs) for flow separation delay and for forced attachment of separated flow seen in airfoils at low Reynolds numbers. This flow regime corresponds to the operational envelope for small unmanned air vehicles, and micro air vehicles. To reduce separation, periodic excitation to the flow around the leading edge of the airfoil is induced by MFC actuated clamped-free unimorphs.

The chapter is organized as follows: First, two airfoil concepts (with flow control feature) are introduced. Next, a parametric examination is conducted to identify the substrate properties of an MFC unimorph actuator to output high deformations at the desired frequency for lift improvement at post-stall angles. Finally, different modes of flow control are evaluated in the wind tunnel and results are discussed. The optimum frequency and amplitude for increasing lift coefficient are identified experimentally. Along with aerodynamic force and structural displacement measurements, helium bubble flow visualization is used to verify existing separated flow, and the attached flow induced by flow control. The lift coefficient enhancement induced by several flow control techniques is compared.

7.1. Design of the Airfoil with Flow Control Feature

The design of an airfoil with flow control features is a complex procedure that requires coupled analysis of fluid and structure response. In this chapter, the aim is to introduce an MFC actuated flow control device to 1) a standard NACA airfoil and 2) the variable-camber airfoil presented in Chapter 6. For flow control purposes, the NACA four-digit airfoils are of interest,

particularly NACA 0009 and NACA 0015 airfoils have been studied by Greenblatt and Wygnanski [2000] and Seifert et al. [2000]. A review by Greenblatt and Wygnanski [2000] of wide variety of airfoil data indicates that, for the vast majority of cases, the optimum reduced frequencies (F^+) for separation control are in the range of $0.3 \leq F^+ \leq 4$. The reduced frequency is defined as:

$$F^+ = \frac{f_e X_{TE}}{U_\infty} \tag{7.1}$$

where f_e is the periodic excitation frequency, X_{TE} is the excitation location from the trailing edge and U_∞ is the frestream velocity. From the experimental data available from Greenblatt and Wygnanski [2000], F^+ values in the range of 0.3 - 4.0 shows improvement of lift for the angle-of-attack range of 16° - 22° for flow excitations around the leading edge.

The flow control airfoils are designed to have nine distributed (along the spanwise direction) clamped-free beam type MFC unimorph actuators in the airfoil leading-section. The clamped-free beams are selected because they provide large displacements with low input voltages at their resonance frequency. Two restrictions are considered when determining the chordwise placement of the actuator, hence the excitation location (X_{TE}). First, for separation delay, the flow excitation must be before the separation location. Second, the excitation device must not alter the baseline shape of the airfoil. Due to these reasons, the free-end of each cantilever is designed to face towards the leading edge. The free-ends of the clamped-free unimorphs are located 7.0% chord distance from the LE, and equivalently, 151 mm from the TE. Using Eq. (7.1), and considering the range of F^+ that are of interest, the target excitation frequency is selected as $f_e = 125\,Hz$. The unimorph beams will be designed to have resonance at 125 Hz (for optimized performance in terms of power consumption and displacement output), and different F^+ values will be evaluated simply by adjusting the air velocity (U_∞).

7.1.1. Symmetric Airfoil

The first airfoil concept (with the flow control feature) is a symmetric (non-variable-camber) airfoil. A NACA 0010 airfoil profile with 163 mm chord is selected as baseline. Figure 7.1 shows the evolution of the airfoil from a conventional NACA 0010 to a "NACA 0010 with cavity for flow the control unimorph actuators".

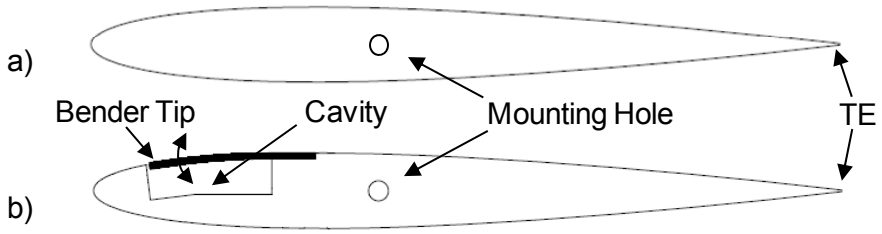

Figure 7.1: Illustration of a) a standard NACA 0010 airfoil and b) the airfoil design with flow control feature.

A set of wind tunnel tests are conducted on the symmetric airfoil. These results will be discussed later.

7.1.2. Variable-Camber Airfoil

The same flow control feature (shown in Figure 7.1) is employed as the leading-section of the variable-camber airfoil shown in Figure 6.7. Figure 7.2 shows the second proposed design that incorporates the NACA 0010 leading section with flow control cavity and the MFC actuated variable-camber trailing-section.

Figure 7.2: Illustration of the variable-camber airfoil with flow control feature.

In this design, the baseline airfoil is the MFC actuated variable-camber airfoil. The elliptic leading section (shown in Figure 6.1 and Figure 6.7) is switched with the leading section of a NACA 0010 airfoil as shown in Figure 7.2. The fabricated variable-camber airfoil with NACA 0010 leading section and with flow control cavity is shown in Figure 7.3. The airfoil has a 16 mm thickness, 133 mm span, 163 mm chord and a finite TE thickness of 1.0 mm. A latex skin covers the whole airfoil, including the benders.

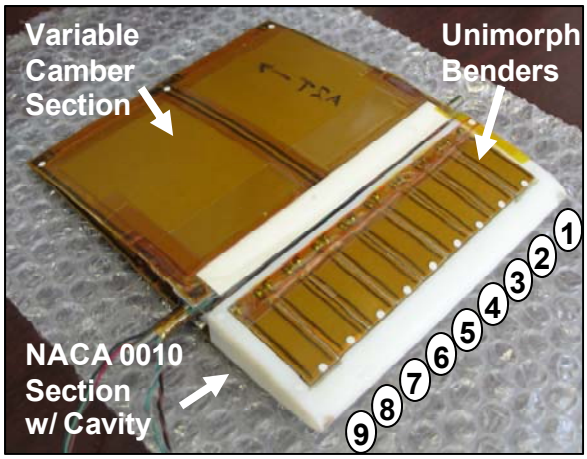

Figure 7.3: Variable-camber airfoil with NACA 0010 LE geometry with cavity and nine unimorph benders (labeled 1-9). The latex skin covering the airfoil is not shown.

The design shown in the figure has nine unimorph actuators. Each unimorph has a MFC M2807-P1 type actuator bonded on a stainless-steel substrate. There is also a tip-mass bonded to these actuators close to the free end. Figure 7.4 illustrates the actuated shape of the variable-camber airfoil with flow control leading-section.

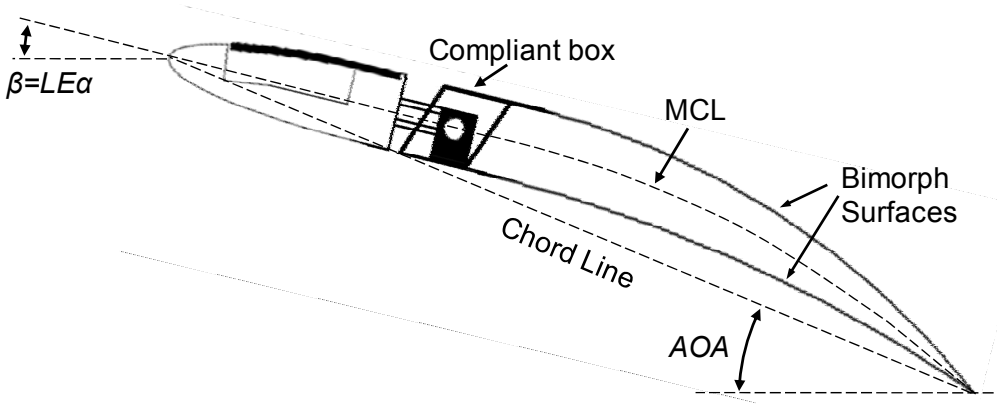

Figure 7.4: Illustration of the variable-camber airfoil and geometric parameters.

In the figure, β is the LE incidence angle and MCL is the mean-camber-line. The compliant box can simply be described as a four-bar mechanism. The two parallel bars that connect top and bottom surfaces have constant length. The change in camber of the active surface of the airfoil causes the box to comply and generate a shear-like motion while keeping the end-slope of the bimorphs equal to each other. The variable-camber trailing-section is previously discussed in Chapter 6.

7.2. Design of Flow Control Actuators

The actuators used for flow control are clamped-free benders that are composed of an MFC bonded on a metal substrate with epoxy. The linear electromechanical vibration model of such actuator is briefly described in Section 2.1. Here, a parametric evaluation is conducted using the solution given in Eq. (2.18). A damping ratio of 0.005 is assumed for all modes. The solution is found for different Young's modulus and thickness ratio of substrate with respect to the constant MFC active area thickness of 0.305 mm. Aluminum, brass and stainless-steel are chosen as possible substrate materials due to their availability, and well controlled geometric and material properties. The Young's moduli for aluminum, brass and steel substrates are taken as 70 GPa, 105 GPa, and 200 GPa respectively. The Young's modulus of the piezoceramic fibers is taken as 64 GPa. The typical epoxy choice for bonding the substrate and MFC layers is 3M DP460 and its shear strength is approximately 31 MPa. As previously noted, the epoxy thickness has a variation of ±0.02 mm between each sample and this variation is an important source of error between the model and experiments. Here, the mass densities of the aluminum, brass, and steel substrates are taken as 2700 kg/m^3, 9000 kg/m^3, and 7800 kg/m^3 respectively. The maximum tip displacement (around 1st bending resonance frequency) of the cantilevered MFC M2807-P1 unimorph in response to harmonic excitation is shown in Figure 7.5.

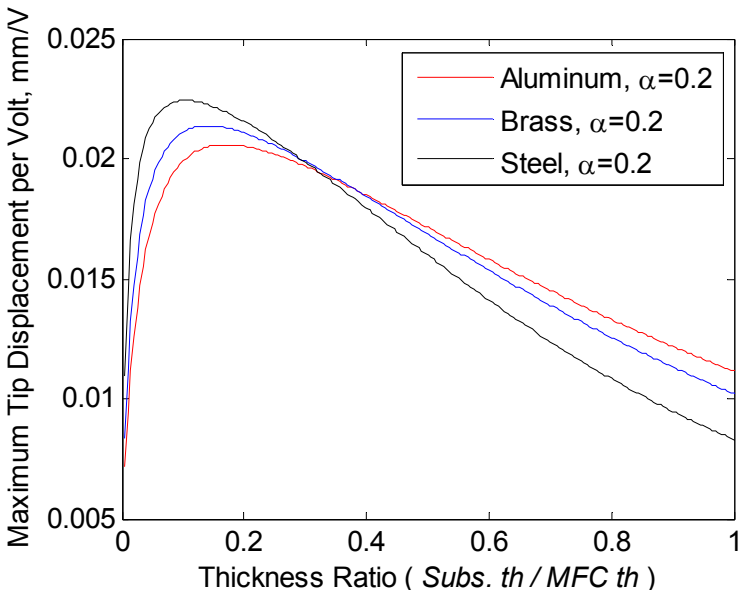

Figure 7.5: Analytical maximum tip displacement per volt for a range of thickness ratios in response to harmonic excitation.

The empirical electric field correction factor (α) presented in Section 2.1 is taken into account in the electromechanical model used here. The resonance frequency of the unimorph actuator is affected by its moment of inertia and the mass per length. Therefore the maximum tip displacement of the unimorph free-end occurs at different frequencies for different substrate materials and thicknesses. The effect of the material axial stiffness shows as change in the maximum displacement (at optimum thickness ratio). The steel substrate shows the highest displacement, however at a thinner substrate when compared to a unimorph with aluminum substrate. These results are previously verified in Chapter 2 and in the literature [Inman and Cudney, 2000]. It must be noted that changes in α shifts the magnitudes only, however the behavior (shown in Figure 2.4) stays the same. This section focuses on linear dynamic actuation, so the model prediction is not applicable to a high-voltage (and possibly hysteretic and geometrically nonlinear) actuation. The 1st bending resonance frequency variation for harmonic excitation is shown in Figure 7.6.

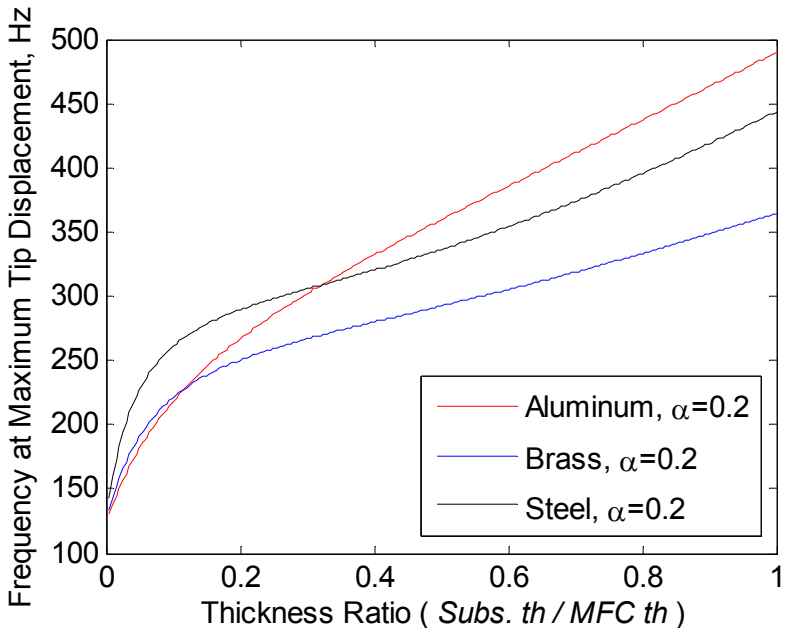

Figure 7.6: First bending resonance frequency variation for a range of thickness ratios in response to harmonic excitation.

The results presented in Figure 7.5 and Figure 7.6 are important to note. In order to achieve high displacement, required to effectively excite the flow, a certain thickness ratio of MFC and substrate material has to be chosen (assuming that the length of the actuator is not a

variable). This choice locks the 1st bending resonance frequency; however the resonance frequency has to be matched to the "optimum" flow control frequency (f_e) in order to obtain maximum energy induction to flow with minimum electrical energy consumption. For the airfoils shown in Figure 7.1 and Figure 7.2, a thickness ratio of 1.0% is required for a unimorph actuator with stainless-steel substrate, resulting in the "targeted" 1st bending resonance of 125 Hz.

7.2.1. Actuation Response of MFC M2807-P1 Unimorphs

Using the conclusions derived from the previous section and considering the aerodynamic loading, a unimorph design with thickness ratio of approximately 0.2 (20%) is chosen instead of 0.01 (1%). The 1% thickness ratio or the structural optimum thickness ratio (~ 10%) is not selected due to the limitations of in-house fabrication and the limitations of the material properties of the stainless-steel substrate. This increase in the substrate thickness requires the tuning of the 1st bending resonance frequency to 125 Hz by adding a tip mass, which will be addressed in the next section.

Nine "identical" unimorphs are fabricated by bonding an MFC M2807-P1 type actuator to a 36.3 mm long, 12.7 mm wide and 50.4 μm thick stainless-steel metal substrate with 3M DP460 epoxy. Samples are bonded in vacuum bag (at 0.8 Atm) to minimize variation in epoxy thickness, and air gaps, hence achieving a minimum variation in dynamic response. Each sample employs an M2807-P1 type MFC actuator manufactured by Smart Material Inc. which uses the *33* mode of piezoelectricity. The M2807-P1 type is chosen because it is the shortest commercially available MFC actuator. Total overhang length of the unimorphs are 26.75 mm.

The frequency response prediction of the model is compared to the experimental case for the MFC unimorphs. A Polytec PDV-100 laser vibrometer and a Siglab 20-42 frequency analyzer is used to measure and analyze the tip-velocity-to-excitation-voltage FRFs of the cantilevers. An HP model 6825A bipolar amplifier (with 1x gain) is used to buffer the excitation voltage to the MFC actuator. The excitation signal is a 1 Vpeak sine tone with 1 Hz – 5 kHz bandwidth. A virtual sine sweep is used for the FRF measurements, where the excitation is a pure sine tone at constant frequency. The frequency is incremented only when transients are decayed from the previous frequency. This method is utilized to avoid windowing and transients

caused by more common (and faster) techniques, such as a chirp excitation. Figure 7.7 shows the one (out of nine) clamped-free unimorph specimens.

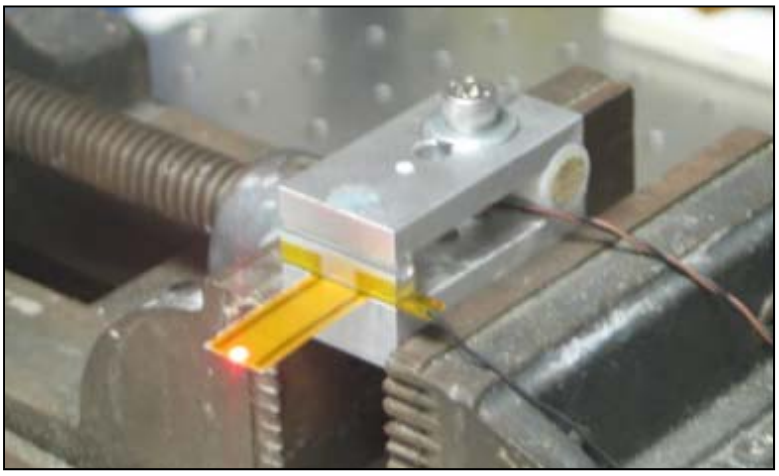

Figure 7.7: One of the MFC M2807-P1 unimorphs clamped for testing.

The FRFs (defined here as tip-velocity-to-excitation-voltage) obtained from model predictions are plotted in Figure 7.8 along with the experimental results for the nine "identical' unimorphs with stainless-steel substrates. The FRFs are in good agreement especially for the mode of interest.

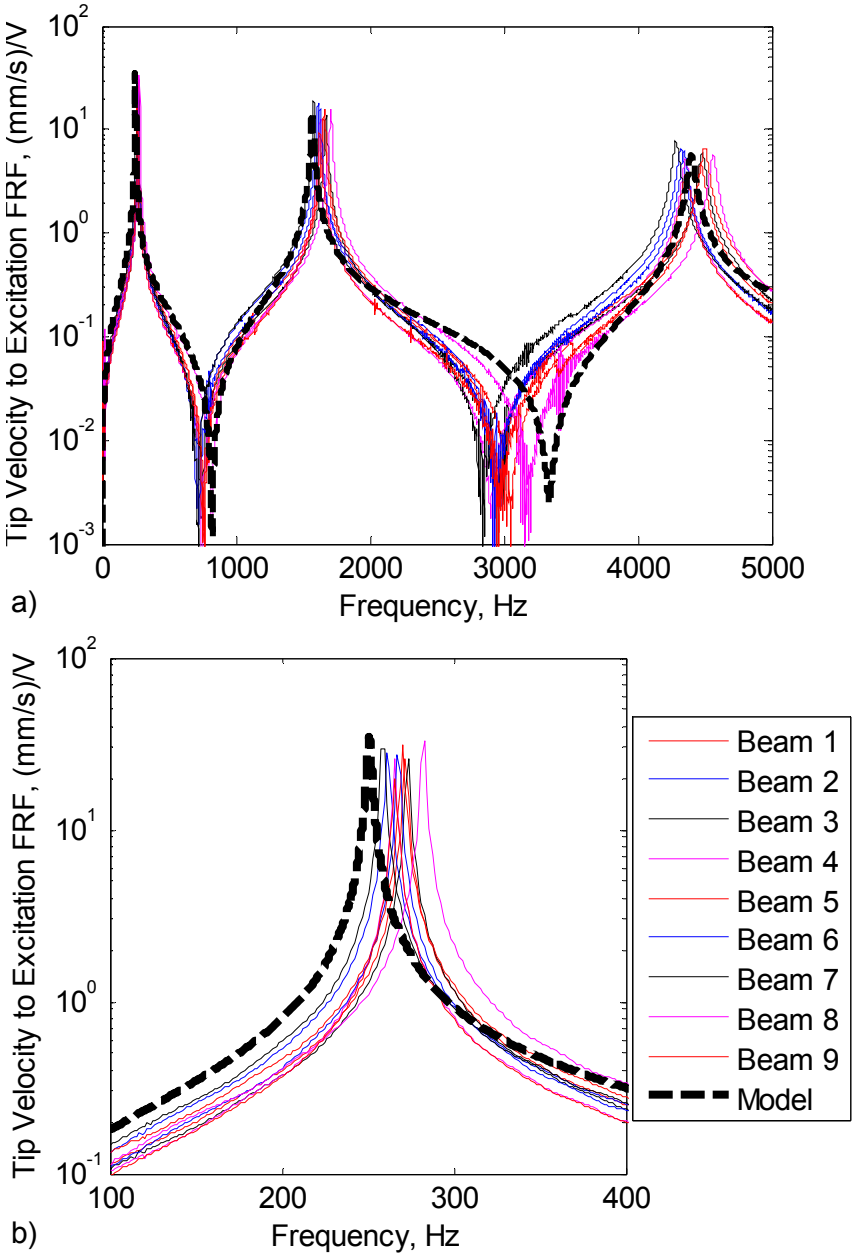

Figure 7.8: Tip velocity FRF comparison of experiments to model for nine "identical" MFC M2807-P1 clamped-free unimorphs with 50.4 μm thick stainless-steel substrate. No tip-mass. a) Complete test spectrum and b) zoom to 1st bending operating resonance.

The unimorphs, clamped on a rigid structure and without any tip-mass, have their 1st bending resonance frequency around 270 Hz. Theoretical bending stiffness is used in the model prediction; therefore a very small mismatch between the experimental and the model prediction is observed for the first natural frequency. The prediction for higher modes shows a shift in the

same direction relative to the shift observed in the first frequency. Considering the Euler-Bernoulli assumptions, this is expected since it over-predicts the natural frequencies (due to effectively stiffer assumptions of material behavior). The MFC actuated unimorph is a slender body however it includes nonlinearities due to MFCs composite nature (including piezoceramic hysteresis). The nonuniform shear layer (at the epoxy interface) is also neglected here which is another source of variation of the structure from the model assumptions. The reader is referred to Section 2.1 for additional discussion on the model,

7.3. Symmetric Airfoil: Structural and Aerodynamic Response

The NACA 0010 airfoil concept (shown in Figure 7.1b) with leading-section cavity is evaluated here for its structural and aerodynamic response. The airfoil has a 16 mm thickness, 133 mm span, 163 mm chord and a finite TE thickness of 1.0 mm. The airfoil mounted in the wind tunnel test section is shown in Figure 7.9.

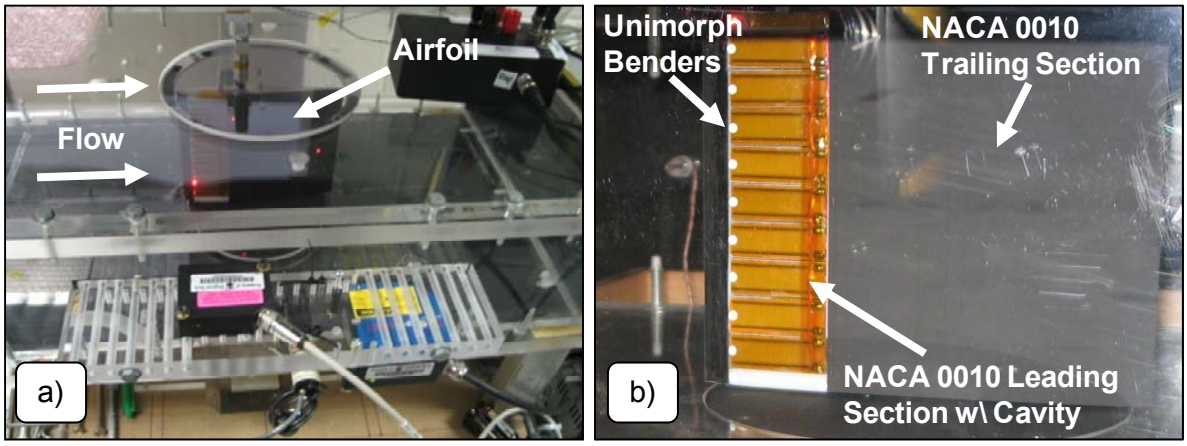

Figure 7.9: Flow control airfoil with NACA 0010 geometry with nine unimorphs. a) The 2D test section and b) the airfoil in the test section and mounted on the load balance.

The design shown in the figure has the nine unimorph actuators. As noted earlier, the necessary increase of the substrate thickness resulted in a 1st bending frequency around 270 Hz with ±13 Hz variation. In order to tune the natural frequency to the target value of 125 Hz, a small tip-mass (a small nut) is bonded to each unimorph actuator (on the inside surface), close to the free end of the actuators. The location of each tip-mass is adjusted so that the variation of the natural frequency is ±1 Hz between the nine actuators.

7.3.1. Structural Response

To measure the out-of-plane vibration response of the whole airfoil, two "modes" of excitation are considered: a) Symmetric and b) asymmetric. In symmetric actuation, all nine benders are theoretically "in phase" meaning that the same voltage polarity is applied. In contrast, for the asymmetric actuation, the polarity of each adjacent bender is reversed. Figure 7.10 presents the magnitude of the velocity-per-excitation response of a) averaged "active" free-end of the nine unimorphs and b) two "passive" locations on the airfoil such as the bottom and top end-sections around the leading edge. The bottom end-section of the airfoil is close to the unimorph #1 (as shown in Figure 7.9) and to the floor of the 2D test section. Similarly, the top end-section of the airfoil is close to unimorph #9 and to the ceiling of the test section. During these tests, the airfoil is mounted in the test section (and on the load balance) hence the measured response is due to the dynamics of the coupled balance and airfoil system. The boundary conditions considered for structural tests are the same as the ones that will be used for aerodynamic tests. The wind tunnel test section and the load balance will be discussed in the next section. The airflow is turned off during the structural tests in order to reduce the noise in the measurements. A simple comparison of the structural response (not presented here) between the flow-on and flow-off conditions showed that the measured shift in frequency response (due to fluid-structure interaction) is negligible at 5 m/s. The measurements are conducted using a single-point laser vibrometer (Polytec OFV-303) and a frequency analyzer system (Siglab 20-42). A chirp signal with 10 Hz to 1 kHz bandwidth is used for exciting the unimorphs. A TREK 50/750 high voltage amplifier (with 175x gain) is used to buffer the excitation signal. For the symmetric excitation, a 35 Vpeak signal with 35 V offset is used. For the asymmetric excitation, only a 35 Vpeak signal is used. All unimorphs are connected electrically in parallel for both symmetric and asymmetric excitations.

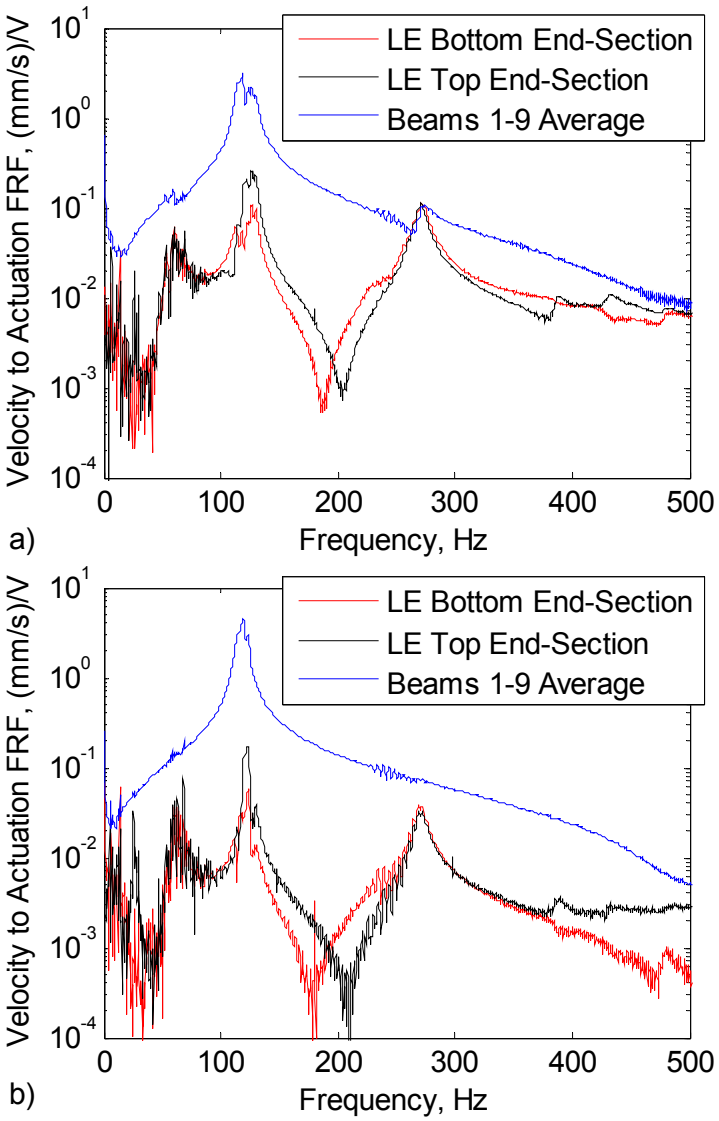

Figure 7.10: Velocity-to-actuation FRFs measured on various locations of the airfoil. a) Symmetric and b) asymmetric actuation.

In the figure, both symmetric and asymmetric cases are shown. The base loading generated on the clamped end of the benders, the airfoil in our case, is higher for symmetric actuation when compared to the asymmetric case. Due to the larger coupling between the airfoil and the benders in the symmetric case, the relative displacement (with respect to the test section and the airflow) of the benders are lower when compared to the asymmetric case around 125 Hz; however this is not the case for response at 50 Hz and 268 Hz. In fact, around 268 Hz, the displacement of the unimorph free-end is in the same order of magnitude as the leading edge of the airfoil. The relatively high coupling shown here is expected due to the simple fact that the

benders, whether actuated symmetrically or asymmetrically, have a total mass in the same order of magnitude of rest of the airfoil. In an actual aerodynamic application, the active elements will likely be very small compared to the rest of the structure, hence the base of the clamped-free benders act more like a rigid structure.

The single-point laser vibrometer measurements are useful to quantify the structural response; however the effect of the load balance on the airfoil dynamics must also be quantified. Therefore, the out-of-plane structural response is further investigated using a scanning laser Doppler vibrometer (SLDV) system. A Polytec VibraScan system with OFV 055 Scan Head, OFV 3001 S Controller, and a Vib-Z-010 data acquisition unit is used. Polytec's PSV software (version 7.44) is used for hardware control, acquisition and post processing. A TREK 50/750 high voltage amplifier (with 175x gain) is used to buffer the excitation signal. A chirp signal with 10 Hz – 1 kHz bandwidth and 158 Vpeak amplitude is used for excitation. Figure 7.11 presents the operating deflection shapes of the airfoil excited with 158 Vpeak asymmetric harmonic excitation, mounted in the test section (and on the load balance).

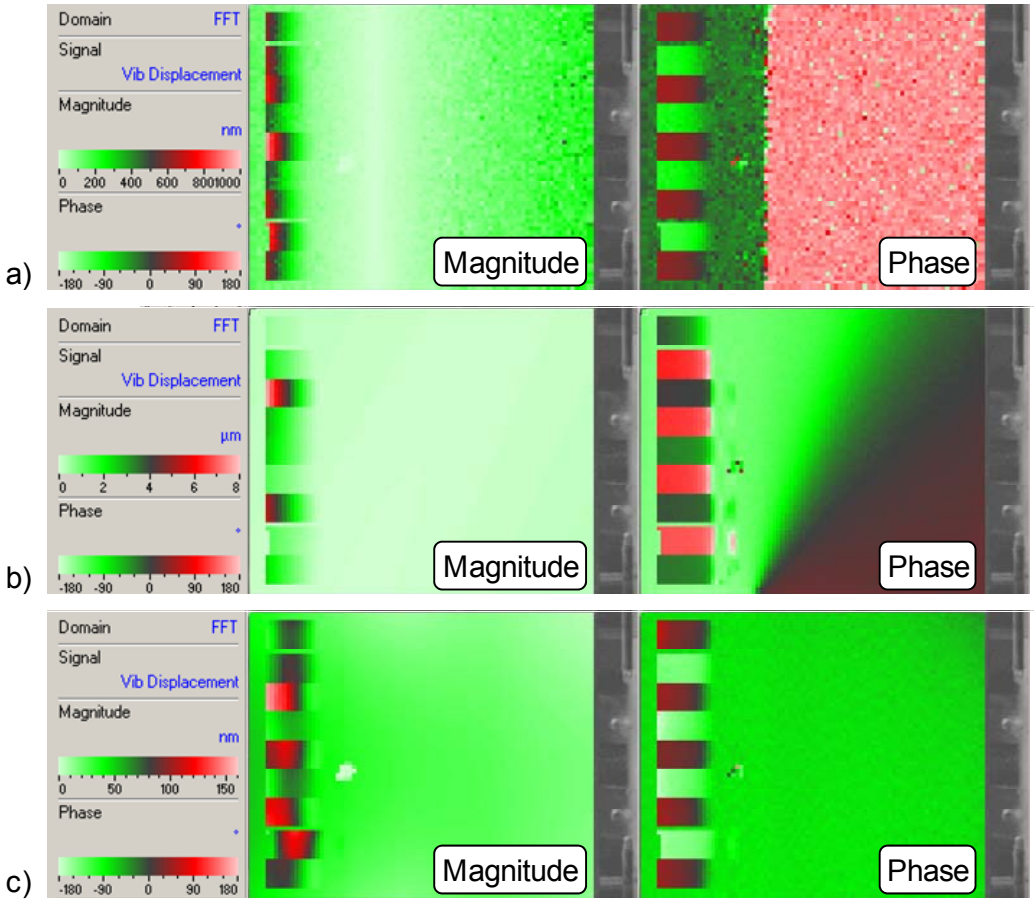

Figure 7.11: Displacement response of the airfoil to 158 Vpeak asymmetric harmonic excitation. a) 50 Hz, b) 125 Hz, c) 268 Hz. Airfoil is mounted on the load-balance.

The phase plots for all frequencies confirm the asymmetric (out-of-phase) excitation. At 50 Hz, the leading edge and trailing edge of the airfoil shows small deformation. From the phase plot in Figure 7.11b, the rigid-body torsional mode (about the spanwise mount axis) is clearly visible; hence the operating deflection shape is due to coupled airfoil and balance dynamics. At 125 Hz, the displacement is dominated by the unimorph benders, with negligible contribution from the airfoil and the load balance. Finally, at 268 Hz, the operating deflection shape is a combination of (out-of-plane) rigid-body displacement of the airfoil and the displacement of the benders. Both at 50 Hz and 268 Hz, the displacement (or the aerodynamic effects) of the LE (which is in front of the bender free-end) can't be neglected. However, at 125 Hz the displacement is dominated by the benders only. Figure 7.12 presents the operating deflection shapes of the airfoil excited with symmetric harmonic excitation, mounted in the test section (and on the load balance).

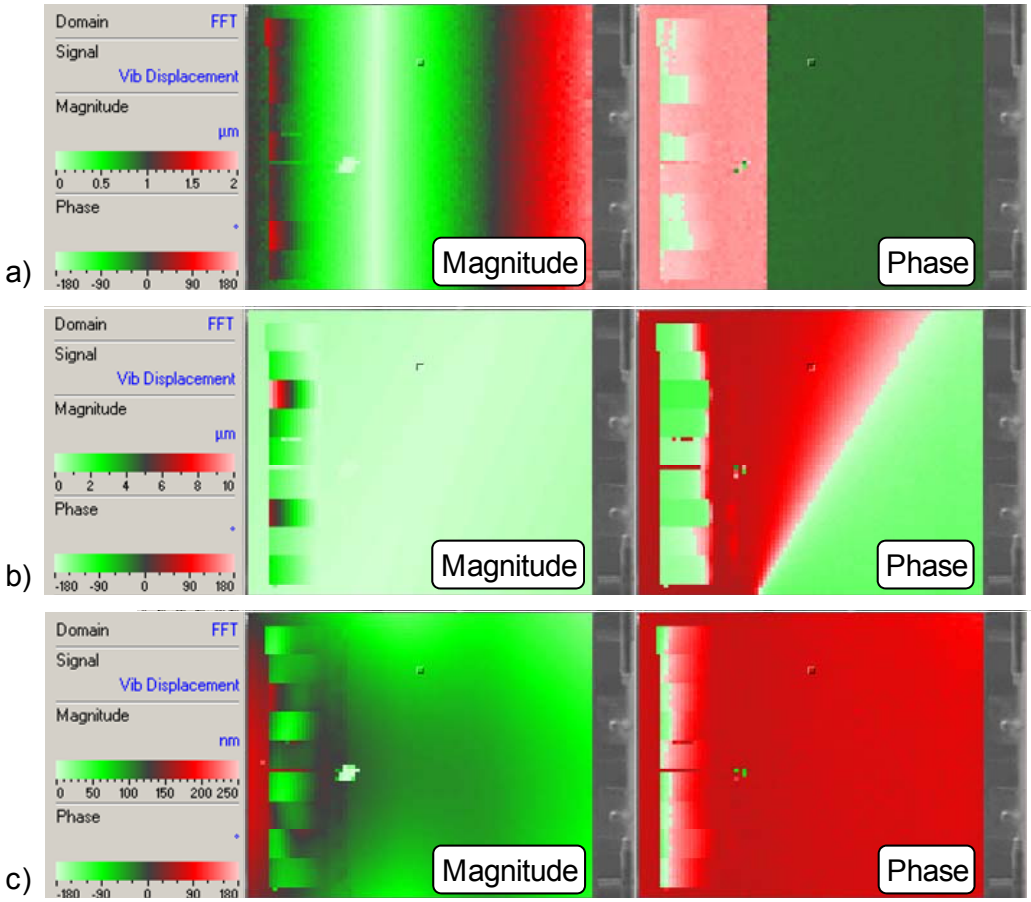

Figure 7.12: Displacement response of the airfoil to 158 Vpeak symmetric harmonic excitation. a) 50 Hz, b) 125 Hz, c) 268 Hz. Airfoil is mounted on the load-balance.

As observed with the asymmetric excitation, the symmetric excitation produces the same operating deflection shapes, however with higher magnitude coupling between the benders and the rest of the airfoil. At 50 Hz, the trailing edge displacement is approximately same as the bender free-end. At 125 Hz, there is negligible displacement of the airfoil. Finally, at 268 Hz, the LE displacement is actually higher than most of the benders. As with the asymmetric case, at 50 Hz and 268 Hz, the operating deflection shape is due to the coupled system of the benders, the airfoil, and the load balance.

7.3.2. Power Consumption

Total current and power consumption of the nine unimorph benders are presented in Figure 7.13. Since there is negligible difference in current draw between the symmetric and asymmetric excitations, only the symmetric mode is presented. The current-input-to-excitation-

voltage FRF is measured with the Siglab 20-42 system. The excitation signal is a 100 - 400 Vpeak sine tone in the 10 Hz – 2 kHz bandwidth. The results from the 10 Hz – 500 Hz bandwidth are reported here. A virtual sine sweep is used for the FRF measurements, where the excitation is a pure sine tone at constant frequency. Three averages are taken in each frequency increment. A TREK 623B high voltage amplifier (with 1000x gain) is used to supply the high voltage. The current and output voltage is measured using the monitoring outputs available on the amplifier.

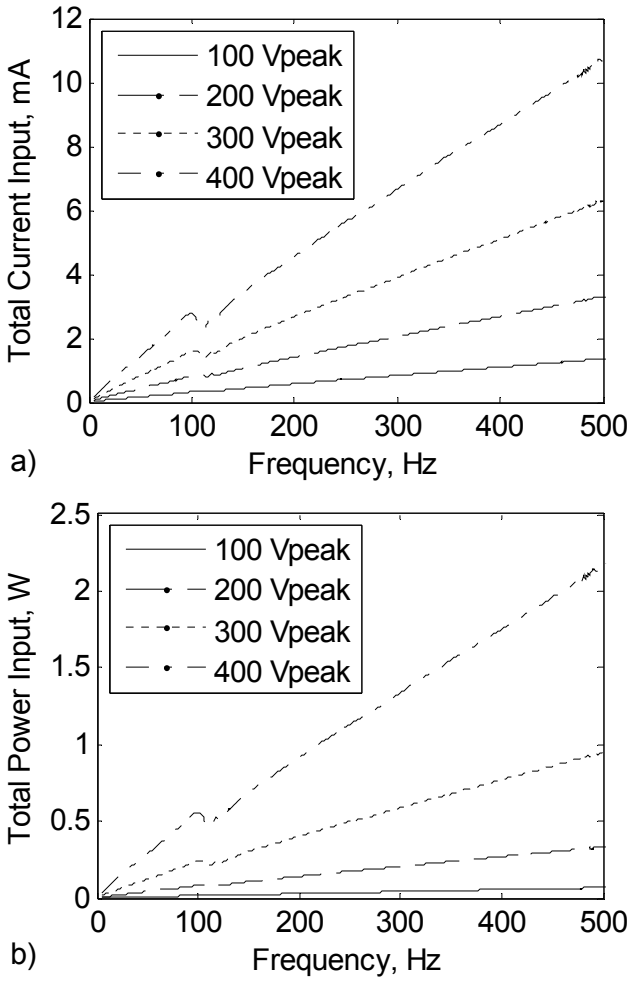

Figure 7.13: Total a) current and b) power consumption of nine unimorphs mounted on the airfoil. The airfoil is mounted on the balance in the test section.

Note that the power reported here includes the actual consumed power as well as the reactive power; therefore it is an upper bound to the actual consumed power consumption of the actuators. The reactive power can be stored in an external capacitor; however (in the experiments

reported here) it is dissipated through the output impedance of the amplifier. Current and power consumption is consistent with the response of a highly capacitive piezoelectric device. The current draw (theoretically) approaches zero as the frequency is reduced. The total power consumption is relatively low, allowing the use of on-board lightweight amplifiers for high-voltage source.

7.3.3. 2D Wind Tunnel Setup

Wind tunnel tests are performed in the low-speed, open circuit wind tunnel with a 2D test-section configuration. Refer to wind tunnel *Version 4* in Appendix E for more details. A custom load balance is used which incorporates two load cells (model MLP-10 from Transducer Techniques) to measure lift and drag forces generated by the airfoil. A stepper-motor driven rotary table is used to set the angle of the airfoils tested. The system is fully automated with an NI 6062E data acquisition card and a LabVIEW based code in order to eliminate human error, and minimize the uncertainties in load measurements.

The streamwise turbulence of the flow in the empty test section is measured by standard hot wire anemometry technique using a TSI IFA-100 anemometer. An average 0.19% turbulence intensity is measured from the 0.1 Hz high-pass filtered hot wire signal for the current average test speed of 5 m/s. Tunnel wall effects and buoyancy corrections were applied as necessary using the techniques outlined in Appendix E. The measured boundary layer displacement thickness is approximately 1.86 mm. Since there is a 1.50 mm gap between the tunnel wall and the airfoil, the applied reduction in span is 0.15% of the actual span [Fox et al., 2004].

7.3.4. Aerodynamic Response

Lift and drag measurements are conducted at 5 m/s (F^+=3.78) and at a chord Reynolds number of 58,000. Additional tests are conducted up to the flow velocity of 20 m/s; however, due to the increase in percent turbulence (as a function of velocity), the flow control method becomes ineffective at higher velocities. Therefore, only the results at 5 m/s are presented. Aerodynamic coefficients are measured for a range of parameters. Following parameters (or types) of excitation are considered: 1) Frequency of excitation (between 0 - 300 Hz), 2) amplitude of excitation (up to 490 Vpeak), 3) symmetric and asymmetric excitation, 4) spanwise (2D) or mid-span (3D) excitation. These excitation methods are introduced in the following paragraphs.

In order to find the frequencies of interest, several AOA sweeps are conducted in the 0 - 300 Hz frequency range. As noted earlier, the benders with tip-mass have their first bending resonance frequency around 125 Hz. Coupled with the rest of the airfoil and the load balance, the spatial distribution of the displacement amplitude of the whole system is frequency dependent. In fact, significant vibration response of the whole airfoil is observed at 50 Hz and 268 Hz in addition to bender resonance of 125 Hz. So, when sweeping the frequencies, the amplitude of excitation is "adjusted", simply meaning that the measured average-displacement-to-excitation FRF of the nine unimorph benders is inverted and applied to the benders to achieve constant displacement output. This results in high excitation levels in off-resonance frequencies, and low excitation levels around resonance, hence resulting in (approximately) constant displacement of the benders across the frequency sweep. Note that the inversion of the FRF is required for parametric analysis in this section. Once the effective frequencies are found, the benders can be designed to have matching resonance at the identified frequency, hence having large outputs with small voltage inputs. The inversion process is demonstrated in Figure 7.14. In the figure, 1) the excitation frequency (f_e), 2) the average-displacement-to-excitation and 3) the desired excitation voltage is presented as a function of the reduced frequency (F^+). It is important to note two observations. First, the excitation (to the flow) is assumed to be completely due to the displacement of the tip of the benders due to the very large difference in the displacement response of the airfoil leading edge and the bender free end at 125 Hz. Refer to Section 7.3.1 for more details. Second, the reported velocity and displacement measurements of the airfoil and the benders (on the airfoil) are absolute (i.e., the laser vibrometer is fixed to the floor which is independent of the wind tunnel test-section).

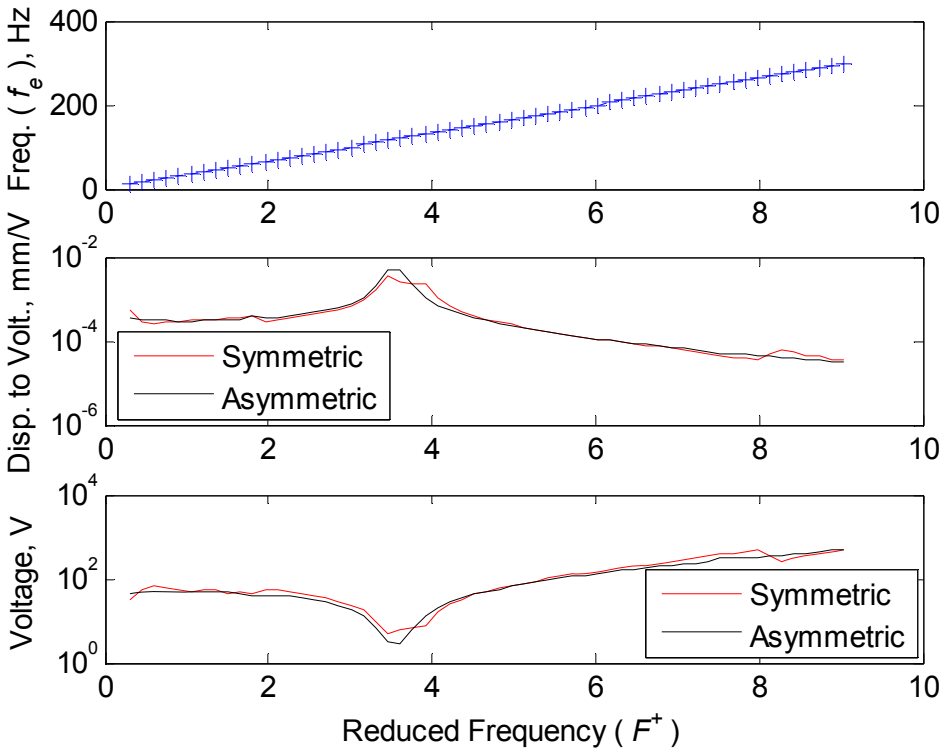

Figure 7.14: Calculation of symmetric and asymmetric excitation voltages from the experimentally measured average-displacement-to-excitation FRFs.

In addition to the excitation frequency and amplitude, two "modes" of excitation are considered: a) Symmetric and b) asymmetric. As noted earlier, in symmetric actuation, all nine benders are theoretically "in phase" meaning that the same voltage polarity is applied. In contrast, for the asymmetric actuation, the polarity of each adjacent bender is reversed.

Finally, the spanwise variation of the actuation is evaluated. In the simplest case, actuating all nine benders symmetrically, theoretically causes a 2D (chordwise only) induced flow. If asymmetrically actuated, a local 3D flow between adjacent benders are expected, however due to the repeated pattern of the "out-of-phase bender pairs" the overall flow over the wing section is still likely to be 2D. In contrast, if a few of the benders are actuated, and others assumed to be inactive, then a 3D flow (spanwise in addition to chordwise flow) is possible. Note that 3D flow can be achieved to the extent that the 2D test section allows.

Figure 7.15 shows the percent change in 2D aerodynamic response of the airfoil to a constant displacement, asymmetric, 2D excitation with constant bender displacement amplitude. The percent change of an aerodynamic coefficient is defined as:

$$\Delta C_{l,d,L/D}(f_e,\alpha) = \frac{C_{l,d,L/D}(f_e,\alpha) - C_{l,d,L/D}(0,\alpha)}{C_{l,d,L/D}(0,\alpha)} * 100 \qquad (7.2)$$

where C_l is lift coefficient, C_d is the drag coefficient, L/D is lift-over-drag, α is AOA, and $C_{l,d,L/D}(0,\alpha)$ is the aerodynamic response of the airfoil with no excitation. Note that the majority of the measured data is removed from these plots to improve clarity of the data that is of interest. Only the data around 50, 125, and 268 Hz are presented.

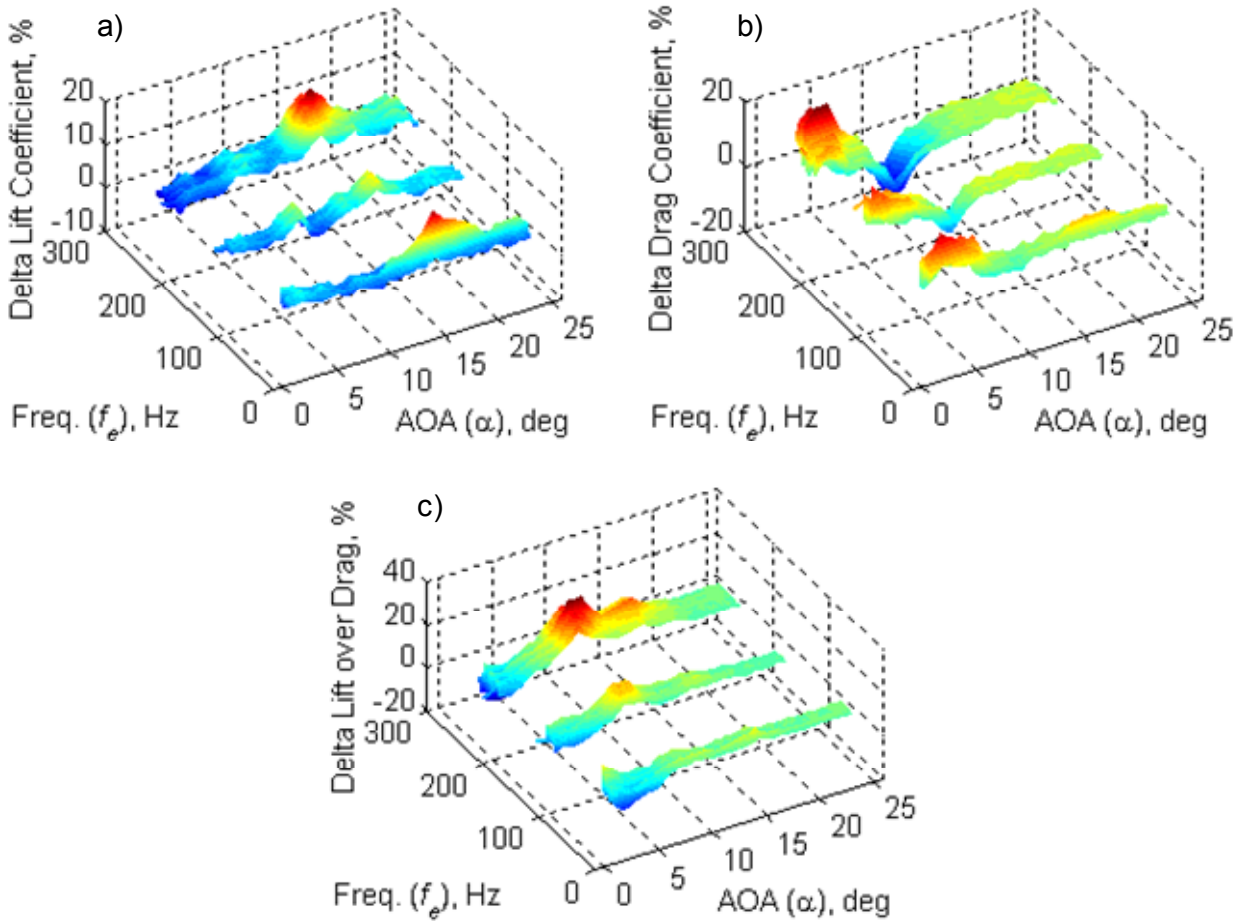

Figure 7.15: Change in a) lift, b) drag and c) lift-over-drag response (2D) due to frequency and AOA at 5 m/s. Asymmetric harmonic excitation with constant displacement amplitude. Re_{chord} = 5.85 x10^4.

Figure 7.16 shows the percent change in aerodynamic response of the airfoil to a constant displacement, symmetric, 2D excitation with constant bender displacement amplitude. Note that

the changes in aerodynamic coefficients are higher for the symmetric excitation when compared to the asymmetric excitation.

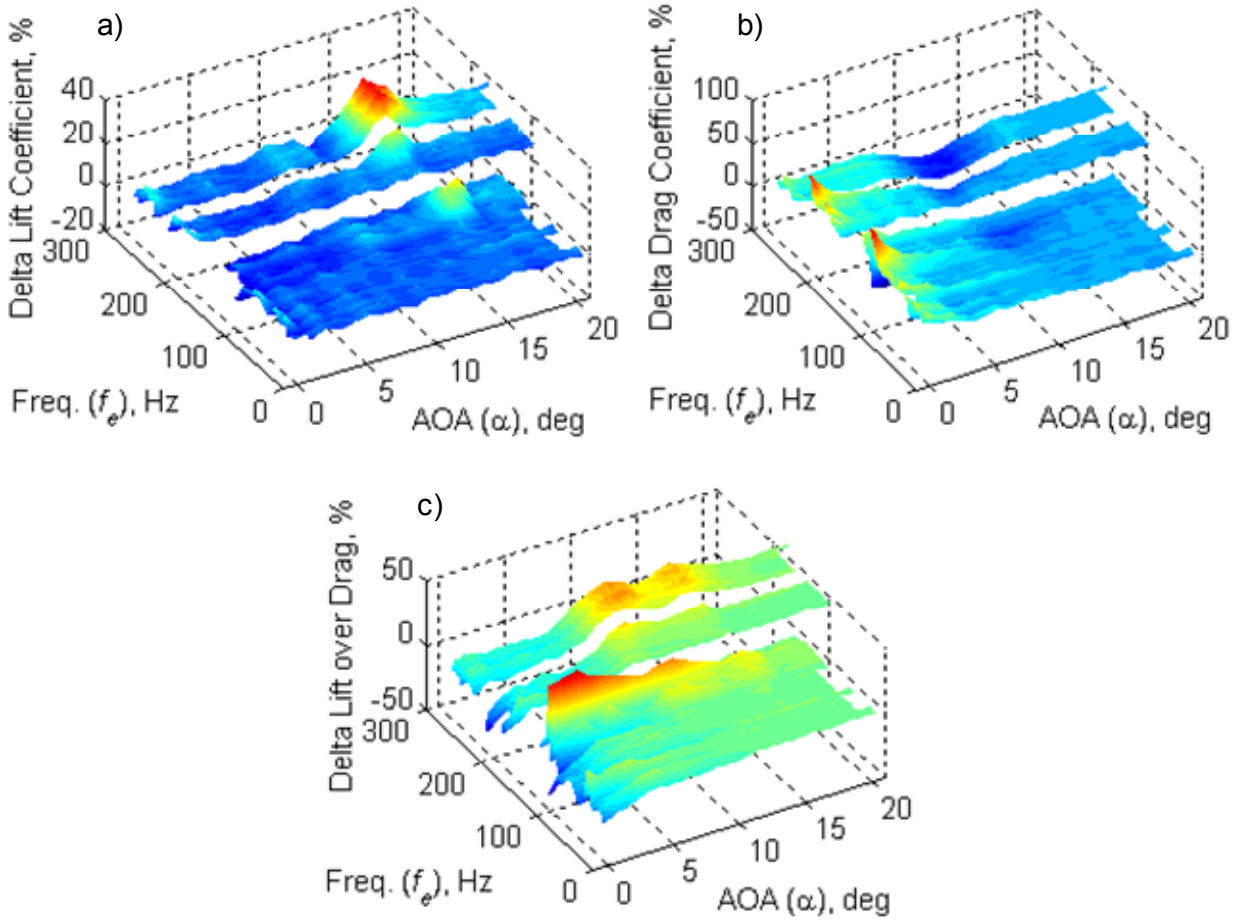

Figure 7.16: Change in a) lift, b) drag and c) lift-over-drag response (2D) due to frequency and AOA at 5 m/s. Symmetric harmonic excitation with constant displacement amplitude. Re_{chord} = 5.85 x10^4.

Consistent with the structural response, significant aerodynamic change is observed at 50 Hz, 125 Hz and 268 Hz. For both symmetric and asymmetric results, the highest improvement in lift is observed at 268 Hz. However, the operating deflection shape at 268 Hz is dominated by the rigid-body motion of the airfoil (which is induced by the corresponding resonance of the load-balance at 268 Hz). Similar effect is seen at 50 Hz, where the motion is dominated by the rigid-body torsional motion. These two excitation frequencies are important to note qualitatively; however they will be neglected in the following aerodynamic coefficient analysis due to the following reasons: 1) Since the structural response at these two frequencies are unique to the

load-balance and the test section configuration, the boundary conditions may not be reproducible by other researchers; 2) The response at these frequencies are amplified due to the resonance of the load-balance, therefore excessive excitation levels are necessary to get the same displacements for an airfoil that is not constrained by the same boundary conditions; 3) Operating deflection shapes at these frequencies show displacements at the LE as well as the benders' free end. Since the relative effectiveness of these excitation sources is unknown, no conclusion can be drawn on the sole effectiveness of the unimorph benders.

Figure 7.17 shows the lift coefficient comparison of two cases, where all benders are active (2D mode): 1) Airfoil with benders exposed but with no excitation (Off); 2) Airfoil excited at 125 Hz with 400 Vpeak. These two plots represent one of many multi-parameter tests that have been conducted to correctly identify the frequency and mode of excitation for effective flow control.

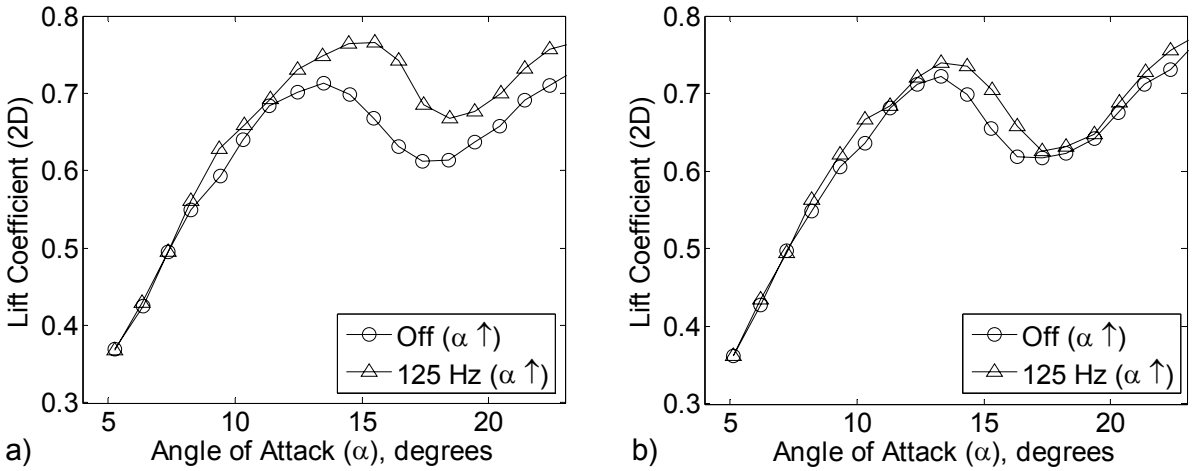

Figure 7.17: Lift coefficient response to 2D excitation mode where all benders are active. At constant voltage of 400 Vpeak and at 5 m/s. Re_{chord} = 5.85 x10^4. a) Symmetric and b) asymmetric actuation.

If we compare the active excitation at 125 Hz with the excitation "Off" case, we note the significant increase in the 12 to 20 degree AOA region (post-stall angles). The symmetric 2D excitation at 125 Hz results in a maximum lift coefficient increase of 17.7% at 16.5 degrees. It is known (from experimental data not shown here) that going from a smooth NACA 0010 airfoil to an airfoil with "rough" clamped-free structures around the LE impacts the aerodynamic response. The design tested here can be fabricated with higher precision resulting in a smoother

surface and an aerodynamic response closer to the original NACA 0010; however due to in-house fabrication limitations this is not addressed.

As noted earlier, one can theoretically induce 3D flow (with spanwise component) by simply actuating some benders while turning others off. In the test case presented here, all of the benders except for the three benders in the mid-span region are taped over. This way, symmetric and asymmetric excitations can be realized for a 3D configuration. As before, two cases are presented in Figure 7.18 for the 3D excitation mode.

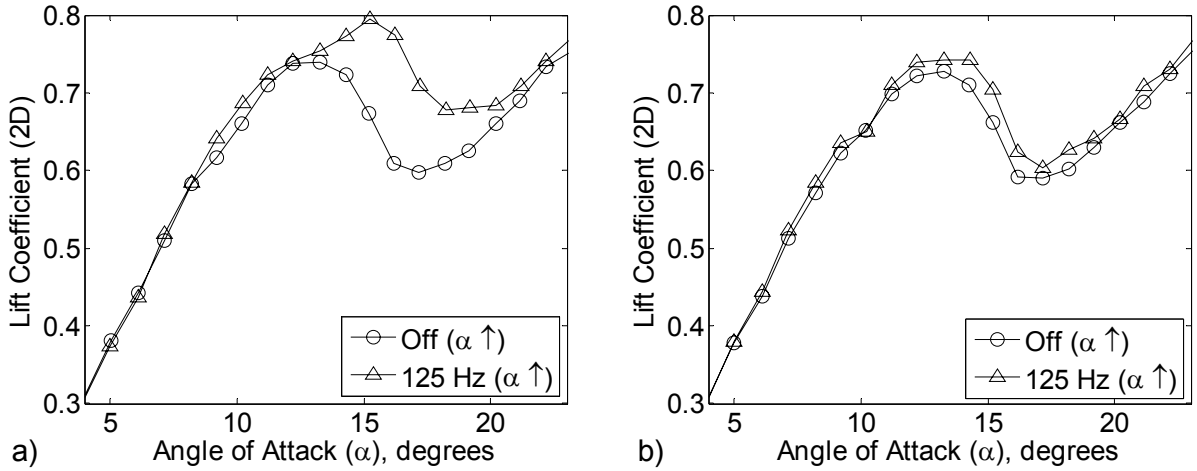

Figure 7.18: Lift coefficient response to 3D excitation mode where only three mid-span benders are active. At constant voltage of 400 Vpeak and at 5 m/s. Re_{chord} = 5.85 x10^4. a) Symmetric and b) asymmetric actuation.

Similar to the 2D case, the symmetric 3D excitation results in higher lift when compared to asymmetric 3D mode. The symmetric 3D actuation at 125 Hz results in a maximum lift coefficient increase of 27.5% at 16.2 degrees (post-stall lift enhancement). The asymmetric 3D actuation at 125 Hz results in a maximum increase of 6.66% increase at 15.2 degrees. The results are summarized in Table 7.1.

Table 7.1: Aerodynamic results for the airfoil at 5 m/s. Re_{chord} = 5.85x10^4, f_e=125 Hz, F^+=3.78. [Sym = Symmetric, Asym = Asymmetric]

Control	Mode	Cl_{max} (AOA)	ΔCl_{max} (%)	Cl (α=15.3°)	ΔCl (%)	Cd (α=15.3°)	ΔCd (%)	L/D (α=15.3°)	$\Delta L/D$ (%)
OFF	2D	0.713 (13.5°)	--	0.668	--	0.191	--	3.51	--
	3D	0.739 (13.3°)	--	0.674	--	0.207	--	3.26	--
ON	2D Sym	0.765 (15.5°)	+7.3	0.765	+15	0.202	+5.8	3.78	+7.7
	2D Asym	0.740 (13.3°)	+3.8	0.704	+5.4	0.212	+11	3.32	-5.4
	3D Sym	0.795 (15.3°)	+7.6	0.795	+18	0.212	+2.4	3.74	+15
	3D Asym	0.742 (14.3°)	+0.4	0.705	+4.6	0.212	+2.4	3.33	+2.1

In Table 7.1, the 4th column presents the Cl_{max} (and the respective AOA) for each test configuration. The maximum Cl_{max} of 0.795 is achieved by the airfoil with 3D symmetric excitation at 15.3° AOA. The following columns present the aerodynamic coefficients at the reference AOA of 15.3°; hence the percent change in the aerodynamic coefficients are "normalized" with the maximum possible lift across all excitation scenarios. Although only three benders are used (instead of nine), the 3D excitation mode results in the highest lift improvement at post-stall angles. Since only three benders are used for the 3D excitation mode, the power consumption is significantly lower than the 2D excitation mode (where all nine benders are active). Finally, the lift increase results are verified by HE bubble flow visualization technique shown in Figure 7.19.

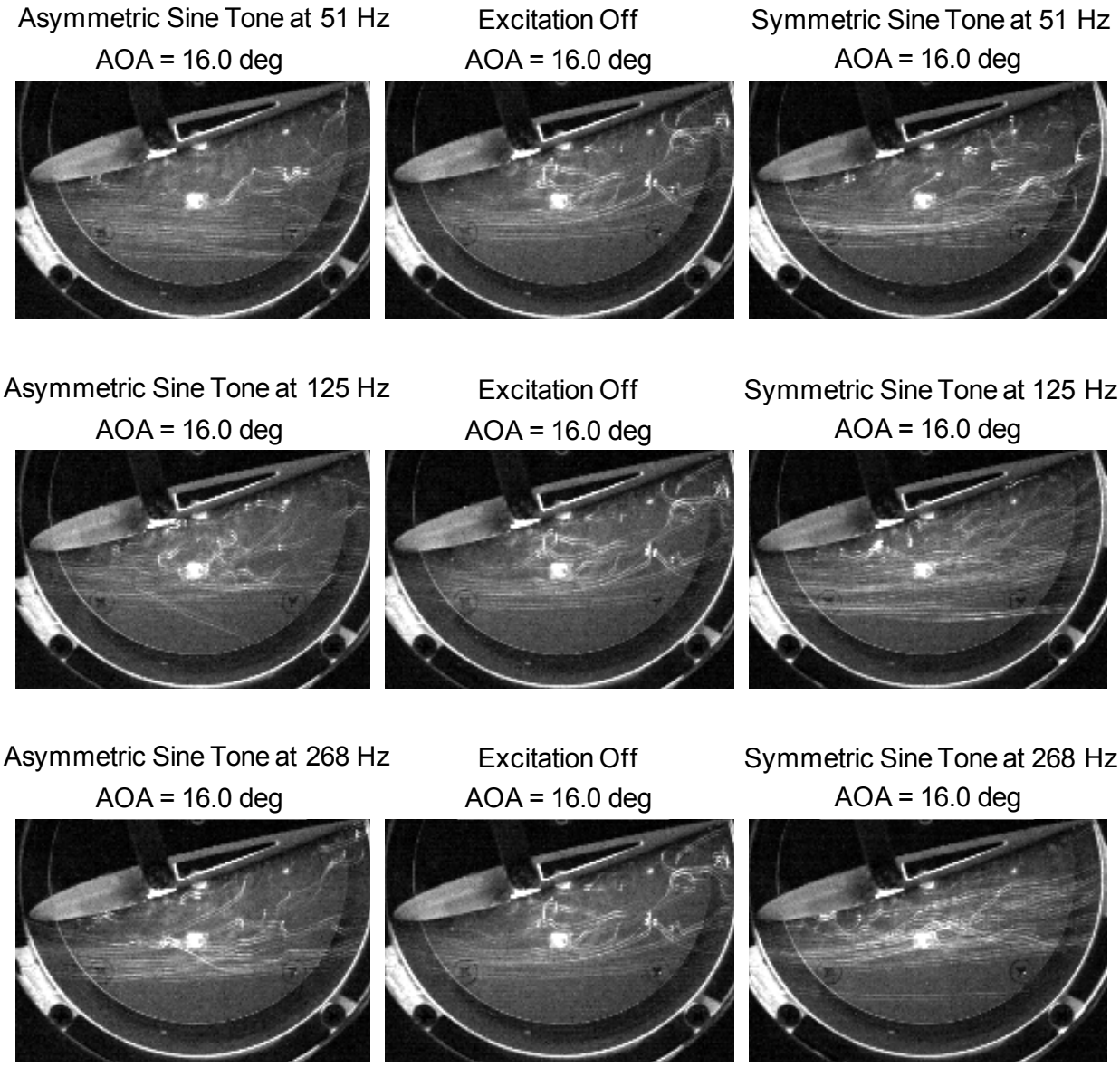

Figure 7.19: Flow visualization for 3D excitation at 16° AOA and 5 m/s. Re_{chord} = 5.85x10^4.

The flow visualization confirms the load measurements shown in Figure 7.18. The symmetric excitation at 125 Hz shows significantly more attached flow when compared the airfoil with no excitation. Significant flow attachment is also seen at 51 Hz and 268 Hz.

7.4. Variable-Camber Airfoil: Aerodynamic Response

The previous results (presented in Section 7.3) showed that one can induce 3D flow (with spanwise component) by simply actuating some benders while turning others off. This potentially can cause large increase in aerodynamic forces for small consumption in power. By

reducing the density of the active elements in the spanwise direction, the airfoil can be simpler and weigh less. The analysis presented in this section examines the effect of spanwise distribution of the active elements to the aerodynamic forces and coefficients. The tests employ the variable-camber airfoil shown in Section 7.1.2. By using the variable-camber airfoil, the flow control effectiveness is evaluated for asymmetric airfoils. Since the effect of excitation amplitude and frequency are determined from the analysis before, the analysis here is limited to the flow excitation frequency of $f_e = 125\ Hz$ (F^+=3.78) and the amplitude of *Vpeak* = 500 V.

The wind tunnel tests are performed in the low-speed, open circuit wind tunnel with a 2D test-section configuration. Refer to wind tunnel *Version 5* in Appendix E for more details. An average 0.14 % turbulence intensity is measured from 0.1 Hz - 10 kHz band-pass filtered signal for the current average test speed of 5 m/s. Lift and drag measurements are conducted at 5 m/s and at a chord Reynolds number of 58,000. Additional tests are conducted up to the flow velocity of 20 m/s; however, due to the increase in percent turbulence (as a function of velocity), the flow control method becomes ineffective at higher velocities (and not reported here). Figure 7.20 shows the variable-camber airfoil (mounted on the balance) in the 2D test section.

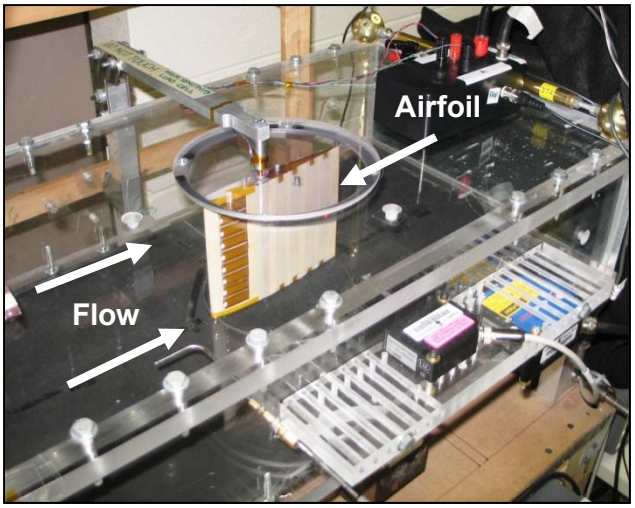

Figure 7.20: Variable-camber airfoil with flow control feature installed in the test section.

Aerodynamic coefficients are measured for a range of parameters. The two parameters tested are: 1) Camber of the airfoil, 2) Spanwise distribution of excitation. Figure 7.21 represents the aerodynamic response to the complete test parameter space that has been conducted to correctly identify the most effective spanwise distribution of flow control. Each flow control case

is tested at average 0.25%, 2.65% and 4.35% camber (of the whole airfoil), which are induced by 0 V, 700 V and 1400 V excitation voltages (to the variable-camber trailing section) respectively.

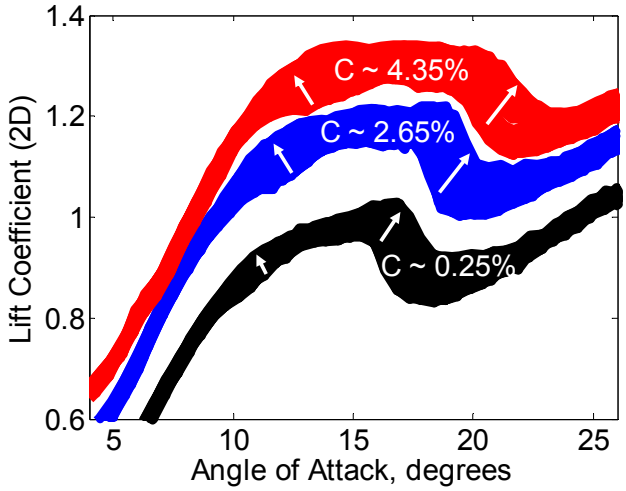

Figure 7.21: Lift coefficient (2D) comparison for all cases for three camber values at 5 m/s. Re_{chord} = 5.85x104, f_e = 125 Hz, F^+ = 3.78, Vpeak = 500 V.

The lower boundary of each area corresponds to the case without flow control (for the corresponding camber value). When the active excitation at 125 Hz is compared against the excitation off case, a significant lift coefficient increase is noted for the 12 to 20 degree AOA region (post-stall angles) for all three discrete camber conditions. The results of interest are summarized in Table 7.2 for 15 cases of spanwise distribution (of the nine flow control actuators). For example, the first row in Table 7.2 corresponds to flow control excitation by only one actuator which is located in mid-span. In Figure 7.3, this actuator is the $(5)^{th}$ bender. Case 2 corresponds to mid three benders (4), (5) and (6) excited, benders (1), (2), (3), (7), (8) and (9) not excited. The label *C* corresponds to percent camber of the airfoil. Cl_{max} and α are the maximum lift coefficient and the corresponding AOA. ΔCl_{max} is the percent increase of Cl_{max} from flow-control-off to flow-control-on condition. The *Max.* ΔCl is the highest percent increase in *Cl* at a fixed AOA (α), usually in the post-stall AOA region (16-22°). L/D_{max} is the maximum lift-over-drag. Similarly, *Max.* $\Delta L/D$ is the highest percent increase in lift-over-drag at a fixed AOA (α), also in the post-stall region. The main parameter of interest, the percent change of an aerodynamic coefficient, is previously defined in Eq. (7.2).

Table 7.2: Effect of spanwise distribution of flow control at 5 m/s. Re_{chord} = 5.85x10^4, f_e = 125 Hz, F^+ = 3.78, Vpeak = 500 V.

Case	Config.	C (%)	Cl_{max}	α (°)	ΔCl_{max} (%)	Max. ΔCl (%)	α (°)	L/D_{max}	Max. $\Delta L/D$ (%)	α (°)
1	oooo•oooo	0.20	n/a	n/a	n/a	n/a	n/a	n/a	n/a	n/a
		2.60	1.18	17.6	2.5	5.5	11.1	11.6	6.6	6.4
		4.38	1.29	16.6	0.8	4.8	13.1	10.8	7.8	13.6
2	ooo•••ooo	0.22	n/a	n/a	n/a	n/a	n/a	n/a	n/a	n/a
		2.63	1.17	17.7	1.6	10.4	18.7	11.6	7.7	13.1
		4.36	1.30	17.1	1.2	6.1	20.1	11.1	7.8	7.5
3	oo•••••oo	0.22	0.98	15.9	1.4	4.7	16.8	8.9	8.6	6.6
		2.64	1.18	17.8	2.1	6.7	18.3	10.2	9.5	11.2
		4.36	1.33	16.7	3.5	12.8	20.7	10.0	17.8	13.2
4	o•••••••o	0.25	1.00	16.3	2.8	12.7	16.8	9.7	14.8	11.2
		2.64	1.20	18.2	2.7	12.6	18.7	12.8	13.1	12.1
		4.36	1.34	17.1	3.1	11.0	20.6	11.6	16.1	13.6
5	•••••••••	0.24	1.01	16.4	4.1	16.4	16.9	9.2	15.5	10.8
		2.64	1.20	18.8	2.9	14.8	18.8	10.7	15.0	5.5
		4.36	n/a	n/a	n/a	n/a	n/a	n/a	n/a	n/a
6	•ooooooo•	0.25	n/a	n/a	n/a	n/a	n/a	n/a	n/a	n/a
		2.64	1.20	18.2	3.3	14.1	18.7	15.7	31.6	6.0
		4.33	1.31	16.1	1.4	7.1	20.6	11.4	7.4	5.9
7	••ooooo••	0.24	1.02	16.4	5.0	16.0	16.9	10.3	20.6	9.3
		2.65	1.19	17.8	3.2	14.1	18.8	10.5	13.6	11.3
		4.32	1.32	17.2	2.2	8.8	20.7	9.8	8.4	14.2
8	•••ooo•••	0.24	1.03	16.9	5.2	18.4	16.9	10.3	21.4	10.3
		2.65	1.20	18.3	2.9	15.0	18.8	9.6	7.8	11.8
		4.32	1.34	14.7	3.8	11.7	20.7	9.8	14.4	13.7
9	••••o••••	0.25	1.03	16.8	4.0	16.3	17.3	11.2	14.4	10.8
		2.65	1.19	18.7	2.1	13.7	19.2	11.4	8.0	12.7
		4.32	1.33	15.1	2.6	10.2	20.6	10.0	6.8	14.1
10	ooo•o•ooo	0.25	1.00	15.8	0.8	3.9	16.8	11.3	7.4	7.1
		2.66	1.18	14.7	1.0	5.4	18.2	12.9	7.1	12.2
		4.29	1.30	16.5	0.8	4.5	20.0	11.2	6.1	6.8
11	oo•ooo•oo	0.26	1.00	15.4	0.3	1.4	20.4	10.9	1.2	19.9
		2.68	1.21	17.8	2.5	10.5	18.8	10.5	7.9	12.3
		4.29	1.31	18.1	2.2	6.6	21.1	10.1	8.3	12.6
12	o•ooooo•o	0.26	1.01	15.8	0.4	6.5	16.8	10.4	9.7	16.3
		2.67	1.21	17.8	2.1	6.8	18.7	12.5	4.6	11.7
		4.28	1.30	17.0	0.6	5.2	20.5	11.4	8.0	5.3
13	oo••o••oo	0.26	1.00	15.9	0.2	6.3	16.9	10.2	29.0	13.9
		2.68	1.22	18.4	3.0	12.6	18.9	10.4	12.3	12.3
		4.27	1.31	16.6	1.1	6.0	20.1	10.1	8.5	11.5
14	o••ooo••o	0.26	1.01	15.9	1.3	7.3	16.9	9.6	4.9	7.7
		2.69	1.21	18.4	2.9	12.7	18.9	10.1	20.0	11.8
		4.26	1.32	18.1	2.5	8.9	20.6	10.1	12.5	12.6
15	o•••o•••o	0.26	1.01	16.4	2.7	8.5	16.9	9.5	13.0	10.9
		2.69	1.22	18.9	3.4	15.4	18.9	9.9	19.8	16.3
		4.26	1.32	18.1	3.2	10.2	20.6	9.4	13.1	13.1

In Table 7.2 the 4th column presents the Cl_{max} (and the corresponding AOA on the 5th column) for each case. The maximum increase in Cl_{max} is achieved by case 8, where the mid three benders are off and the side three benders are on. Although only six benders are used (instead of nine), case 8 results in the highest lift improvement at post-stall angles. Note that case 8 is analogous to the 3D excitation mode (with 3 mid-span benders employed) presented in Section7.3.4. Figure 7.22 shows the lift coefficient comparison of the flow control off and flow control on cases for three camber values. The figure shows the AOA sweep up and down curves (with negligible difference in between the two).

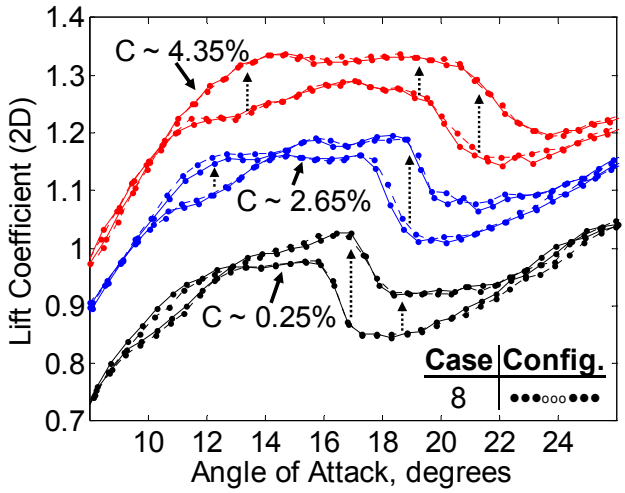

Figure 7.22: Lift coefficient (2D) comparison for case 8 for three camber values at 5 m/s. Re_{chord} = 5.85x10^4, f_e = 125 Hz, F^+ = 3.78, Vpeak = 500 V.

Total current and power consumption of the nine unimorph benders are measured during each test. The current and output voltage is measured using the monitoring outputs available on the Trek 623B amplifier. Current and power consumption is consistent with the response of a highly capacitive piezoelectric device. The current draw (theoretically) approaches zero as the frequency is reduced. A consistent average power-per-bender of 110 mW_{RMS} is measured at 500 Vpeak actuation. The total power consumption by case 8 is 639 mW_{RMS}. An efficiency measure, $\Delta Cl_{max} / Power$ is measured as 0.070 $1/W_{RMS}$ for case 8.

Note that the use of the flow control technique would be intermittent in most aircraft applications (and needed only at high AOA). The power consumption during the flow control effort is not a critical issue (compared to the increase of lift performance); however the "efficiency" measure is still considered here. The highest increase in lift coefficient per

consumed power, ΔCl_{max} / *Power,* is achieved by case 6. In this configuration, only two benders are active, located near the ends of the airfoil (and by the 2D test section walls). The total power consumption is 218 mW_{RMS} and the ΔCl_{max} / *Power* is 0.127 $1/W_{RMS}$ for case 6. The lift coefficient response is presented in Figure 7.23.

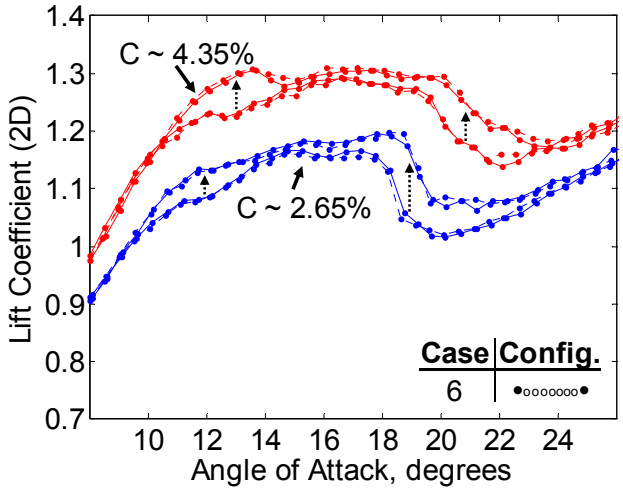

Figure 7.23: Lift coefficient (2D) comparison for case 6 for two camber values at 5 m/s. Re_{chord} = 5.85x10^4, f_e = 125 Hz, F^+ = 3.78, Vpeak = 500 V.

It is also important to look at the change in lift-over-drag, (and indirectly to effect of flow control to drag coefficient). Figure 7.24 shows the *L/D* response of case 8 at 4.35% camber value (induced by 1400 V_{DC} excitation to the MFCs on the variable-camber trailing section).

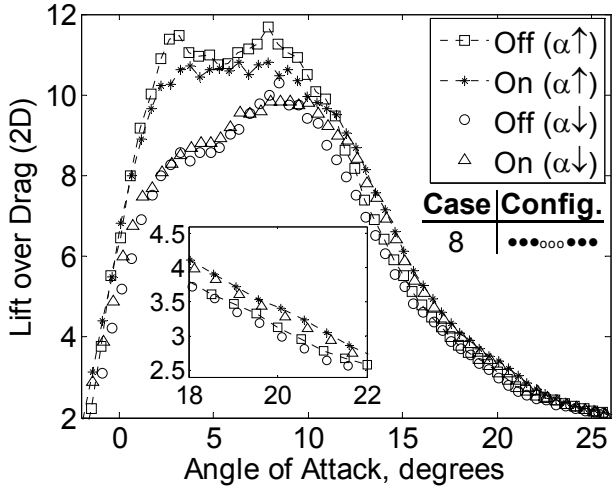

Figure 7.24: Lift-over-Drag (2D) comparison for case 8 for 4.35% camber at 5 m/s. Re_{chord} = 5.85x10^4, f_e = 125 Hz, F^+ = 3.78, Vpeak = 500 V.

With the flow excitation on, there is an increase in *L/D* in the post-stall region which is the region of interest. In almost all cases, the flow control does increase drag (therefore reduce *L/D*) at low AOA. For both on and off cases, the *L/D* values measured for this airfoil is relatively low due to high drag caused by the latex-covered, relatively "rough" surface of the airfoil. It is known (from experimental data not shown here) that going from a smooth NACA 0010 airfoil to an airfoil with relatively "rough" latex covered surface around the LE impacts the aerodynamic response. The design tested here can be fabricated with higher precision resulting in a smoother surface; however due to in-house fabrication limitations this is not addressed.

7.5. Conclusions

This chapter presented the design and wind tunnel evaluation of a flow control airfoil with 1) a symmetric NACA 0010 profile and 2) a cascading bimorph variable-camber airfoil. MFC actuated unimorphs are used to introduce energy to the flow.

The first set of wind tunnel experiments show that significant increase in lift can be achieved with 2D and 3D excitation modes. Symmetric and asymmetric excitations show different aerodynamic response due to the structural characteristics of the airfoil and its boundary conditions (i.e. the load balance). Overall, the symmetric 3D actuation results in the maximum lift enhancement at post-stall region at the lowest power consumption. A maximum lift coefficient increase of 27.5% is achieved at f_e=125 Hz, with the 3D symmetric excitation mode at 5 m/s and F^+=3.78.

The second set of wind tunnel test show further evidence that significant increase in lift can be achieved by the proper distribution of excitation sources in the spanwise direction. As before, the 3D excitation achieves higher lift enhancement at post-stall region with lower power consumption when compared to uniform excitation (2D). A maximum lift coefficient increase of 18.4% is achieved at f_e=125 Hz, with the identified 3D symmetric excitation mode at 5 m/s and F^+=3.78. Cl_{max} is increased 5.2% from the baseline.

CHAPTER 8

PIEZOCERAMIC HYSTERESIS MODELING USING PREISACH MODEL

Hysteresis is a type of nonlinearity that contains memory, thus there may be several outputs for a given input. In general, smart materials exhibit large hysteresis, so open-loop or feedback control laws may result in "amplitude dependent" phase-shifts and harmonic distortions. These phase shifts are indeed identified in Chapter 2 and Chapter 4 for MFC unimorphs and bimorphs respectively. The hysteresis effects are large when the input signals go through peak-to-peak actuation values. The structural and aerodynamic response of the two airfoils presented in Chapter 5 and Chapter 6 revealed significant hysteresis. In this chapter, the classical (scalar) Preisach model is used to predict large hysteresis observed in: 1) two of the MFC bimorphs examined in Section 4.4 and Section D.2, 2) the simply-supported thin airfoil examined in Chapter 5, and 3) the cascading bimorph thick airfoil evaluated in Chapter 6.

This chapter will first discuss the hysteresis that is typically observed in smart material systems. Next, the classical Preisach model is introduced and implemented for monotonically increasing and decreasing inputs. Next, the experimental setup is presented and the hysteresis response prediction of the cases listed above is shown. The chapter concludes with a brief discussion of the results.

8.1. Background of Hysteresis Nonlinearity

The background of hysteresis and the Preisach model is described in Mayergoyz [2003] in detail. Other well known works are by Smith [2005], Visintin [1994]. One of the early investigations of the Preisach model for ferroelectric compounds are by Sreeran et al. [1993] and by Hughes and Wen [1997]. These researchers discuss both the unified framework provided by Preisach model for PZT, magnetic compounds and shape memory alloys, and construct inverse

filters to compensate for hysteresis. Other investigations (e.g., Ge and Jouaneh [1995, 1996] and Robert et al. [2001]) focus on extensions of the theory for characterization and control design in systems employing piezoceramic transducers. Webb et al. [2000] discuss an adaptive hysteresis model for model reference control with actuator hysteresis. Song et al. [2005] discuss the tracking control of a piezoceramic unimorph beam using inverse Preisach model. Choi et al. [2004] present a fast Preisach modeling method for shape memory alloy actuators using major hysteresis loops. Viswamurthy and Ganguli [2007] present the modeling and compensation of piezoceramic actuator hysteresis for helicopter vibration control.

Hysteresis can be observed in static and dynamic events. Static events include systems with slow changing inputs, but they are not stationary as the name suggests. In dynamic events, the inputs and the response are fast changing, so time effects can't be ignored. Hysteresis falls into two categories, scalar and vector. The first category, scalar hysteresis is described as nonlinearities with memory which reveals itself through branching. Looping is described as a special kind of branching where input is bounded by fixed values. Scalar and static hysteresis can further be split into two categories: 1) Hysteresis nonlinearities with local memories and 2) hysteresis nonlinearities with non-local memories. The first case, hysteresis with local memories is the simplest form of hysteresis nonlinearity. The system can have only one of the two outputs for any input. The past events exert their influence on the future events through the current value of output for a transducer with this type of hysteresis. In the second case, there are an infinite number of outputs for any input. The future value of output depends on both the current value of output and the past extremum of the input. The second category is vector hysteresis. Scalar hysteresis (discussed previously) is a special case of vector hysteresis. In the vector case, both inputs and outputs are vectors, with two and three dimensional vectors being the most relevant to practical applications. In vector hysteresis nonlinearity, the past extremum values of input along all possible directions may affect future values of output.

8.2. The Classical Preisach Model

The Preisach model is introduced in a landmark publication by F. Z. Preisach [1935] in the German academic journal, "*Zeitschrift für Physik*". Since then, it has become a widely accepted model of hysteresis. The Preisach model is a completely intuitive (or phenomenological) approach for describing physical mechanisms of magnetization. The model is

originally developed for ferromagnetic materials however it is later realized that physics of piezoceramic and shape memory alloy (SMA) hysteresis is similar to that of ferromagnetics. Somewhat in parallel with the developments in the magnetic, the Preisach model was independently invented and then extensively studied and tested for adsorption hysteresis by Everett and Whitton [1952] and his collaborators. Krasnosel'skii and Pokrovskii [1983], a Russian mathematician, separated the physical definition, and represented the model in a purely mathematical form, which is a spectral decomposition of operators.

Mayergoyz's book [2003] is one of the most cited sources for the Preisach model; therefore this section follows similar description and representation of hysteresis nonlinearity by the Preisach model. The mathematical treatment of hysteresis is completely phenomenological with the Preisach model, meaning that it provides no insight to physical cause of hysteresis. There are fundamental models of hysteresis which attempt to explain experimental facts from first principles; however these models are not employed in this chapter.

The mathematical description is as follows. Consider an infinite set of simple hysteresis operators as shown in Figure 8.1. The input is u, output is $\hat{\gamma}_{\alpha\beta}u$ where α is the switching value for the increasing inputs and the β is the switching value for decreasing inputs. The constraint $\alpha \geq \beta$ is required.

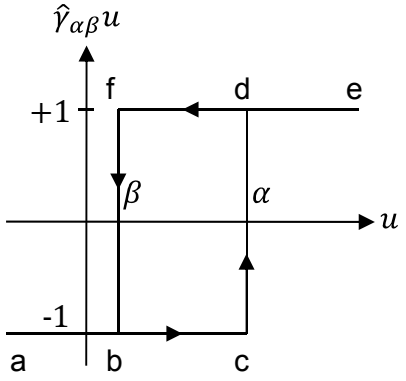

Figure 8.1: A simple relay operator.

The operator represents the hysteresis with local memory. When the input is monotonically increasing from $-\infty$, the output starts at a value of -1. The output switches at α and stays at +1 until $+\infty$. Similar response results due a monotonically decreasing input, where

the output switches from +1 to -1 at the input value of β. Mathematically, the following relationship can be written:

$$\begin{aligned} &if\ \frac{du}{dt} \geq 0\ then\ \hat{\gamma}_{\alpha\beta}u(t) = +1, \\ &if\ \frac{du}{dt} < 0\ then\ \hat{\gamma}_{\alpha\beta}u(t) = -1. \end{aligned} \tag{8.1}$$

Now consider the arbitrary weight function $\mu(\alpha, \beta)$ which is referred to as the Preisach function. The Preisach model is then defined as:

$$f(t) = \hat{\Gamma}u(t) = \iint_{\alpha \geq \beta} \mu(\alpha, \beta)\, \hat{\gamma}_{\alpha\beta}u(t)\, d\alpha\, d\beta \tag{8.2}$$

where $\hat{\Gamma}$ is the Preisach hysteresis operator. The model is analogous to a system of parallel connected two-position switches. The effect of each switch is first multiplied by a weight function, and then integrated over the domain. The Preisach hysteresis nonlinearity is constructed by superposition of simple $\hat{\gamma}_{\alpha\beta}$ operator with local memories to represent the complex operator $\hat{\Gamma}$. Functional analysis and spectral decomposition are a few, well known examples of the superposition method. The complex operator usually has a non-local memory.

The Preisach model depends on a special diagram technique that constitutes the mathematical foundation. The graphical method allows the model to detect local input extrema, accumulate them and choose the right branches of hysteresis nonlinearity. In order to represent the hysteresis behavior of a system, the Preisach function $\mu(\alpha, \beta)$ has to be identified from experimental measurements. The numerical implementation of the Preisach model is relatively simple because the two dimensional integrals can be avoided.

8.2.1. Geometric Definition

The properties of the model can be described from its geometric interpretation. There is a one-to-one correspondence between the operators $\hat{\gamma}_{\alpha\beta}$ and points (α, β) of the half plane described by $\alpha \geq \beta$. Figure 8.2 shows the $\alpha - \beta$ plane and the triangle T.

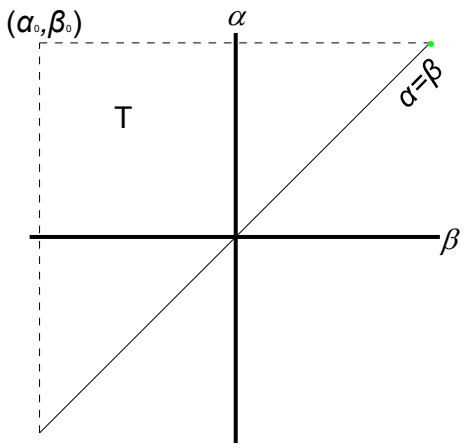

Figure 8.2: Illustration of the limiting triangle.

The vertex of this triangle (α_0, β_0) is given by $\beta_0 = -\alpha_0$. The triangle, *T*, is called the "limiting triangle." The Preisach function, $\mu(\alpha, \beta)$, is finite and assumed zero outside of *T*. This property of the Preisach function does cover the important class of hysteresis nonlinearities with closed major loops.

First, we assume an input value $u(t)$ that is less than β_0 at time t_0. In this case, all $\hat{\gamma}$ operators are equal to -1. This means that all of the "switches" are in the "down" or "off" position. This particular state is called the "negative saturation" for $f(t)$. Next, the input is monotonically increased until time t_1 to reach a value u_1. As the input is increased, all of the $\hat{\gamma}$ operators with "up switching value" α less than the current value of the input are switched up to +1. This causes the division of the limiting triangle two areas, where the $S^+(t)$ area consists of (α, β) points for the operators with +1 value and $S^-(t)$ area consists of (α, β) points for the operators with -1 value. The latter area represents the switches that are still in the "down" position because the input did not reach the corresponding up switching value for those operators. Figure 8.3 demonstrates the $\alpha - \beta$ plane for a monotonically increasing input from the negative saturation state.

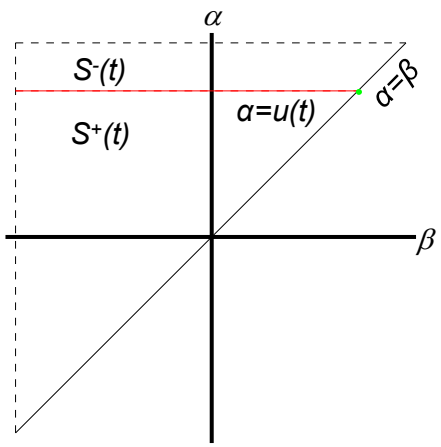

Figure 8.3. A monotonically increasing input from negative saturation.

The horizontal line, $\alpha = u(t)$ moves up as the input is increased. We assume that the input reaches a maximum value at u_1 at time t_1. At this point, the input is stationary with $\alpha = u_1 = u(t_1)$. This is illustrated in Figure 8.4

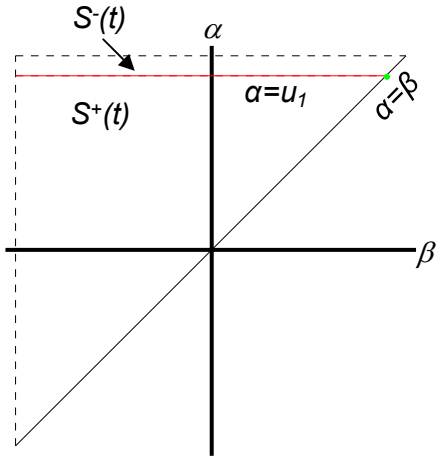

Figure 8.4: The termination of the monotonically increasing input.

During the monotonic increase, all $\hat{\gamma}$ operators are moving on the *abcde* path shown in Figure 8.1. Following the monotonic increase, the input is monotonically decreased until time t_2 to reach the value u_2. As the input is decreased, all $\hat{\gamma}$ operators with β value above the input value starts to switch down to a value of -1. Since the α and β axes are perpendicular, the boundary (or interface) between the positive switches ($S^+(t)$) and the negative switches ($S^-(t)$)

is now defined by two lines that are perpendicular to each other. This line is denoted by $L(t)$. Figure 8.5 shows the $\alpha - \beta$ plane for the monotonically decreasing input.

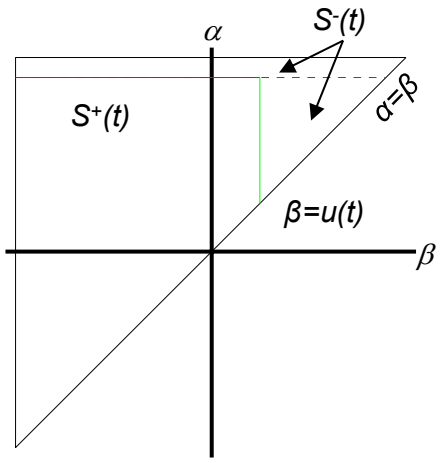

Figure 8.5: Monotonically decreasing input.

As the input is decreased, the vertical part of the interface $L(t)$ moves from right to left. This vertical line is defined by $\beta = u(t)$. The movement is terminated when the input reaches a minimum value of u_2 at time t_2. The intersection of the two lines that form $L(t)$ is defined by $\alpha = u_1 = u(t_1)$ and $\beta = u_2 = u(t_2)$. The corresponding $\alpha - \beta$ plane is given in

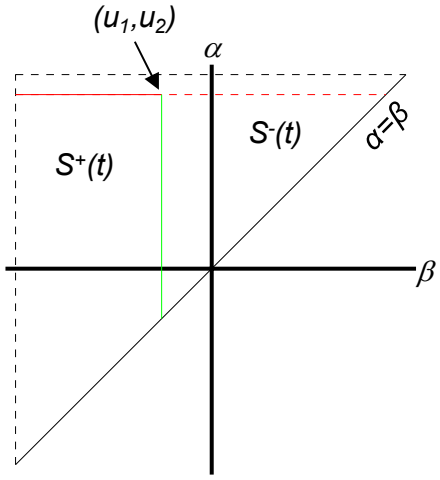

Figure 8.6: The $\alpha - \beta$ plane after a monotonically increasing input followed by a monotonically decreasing input.

Now, the input is increased again to a value of $u_3 < u_1$ as shown in

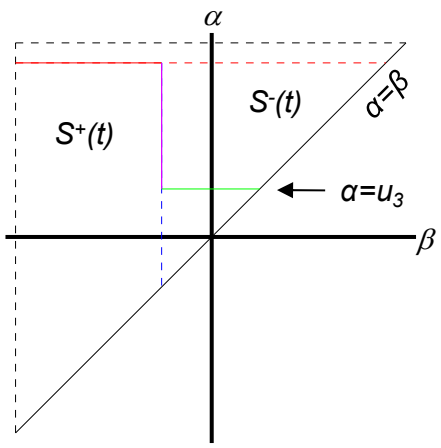

Figure 8.7: Illustration of a third input that is monotonically increasing.

Next, we assume a decreasing input to a minimum value of $u_4 > u_2$ at time t_4. This input results in a new vertical link to form on the $L(t)$ interface. A new vertex is formed at $\alpha = u_3$ and $\beta = u_4$. This step is illustrated in Figure 8.8.

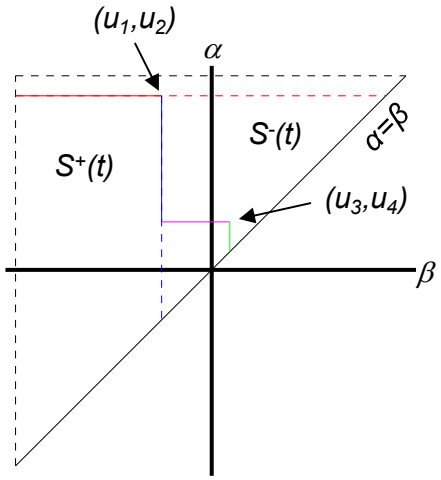

Figure 8.8: Illustration of the final decreasing input.

Using the illustrations given above, the following conclusion can be reached: At any instant of time, the limiting triangle T is divided into two sets where $S^+(t)$ consists of (α, β) points that correspond to $\hat{\gamma}$ operators with +1 value and $S^-(t)$ consists of (α, β) points that correspond to $\hat{\gamma}$ operators with -1 value. The interface $L(t)$ is a staircase line whose vertices have α and β coordinates that are equivalent to the local maxima and minima of the input respectively (for the previous instants of time). This intersection line always connects to the hypotenuse (of

the limiting triangle) which is defined by $\alpha = \beta$. The final link is horizontal (and moves up) if the input is increased and it is vertical (and moves down) if the input is decreased. Figure 8.9 shows the two possible positions of the final link.

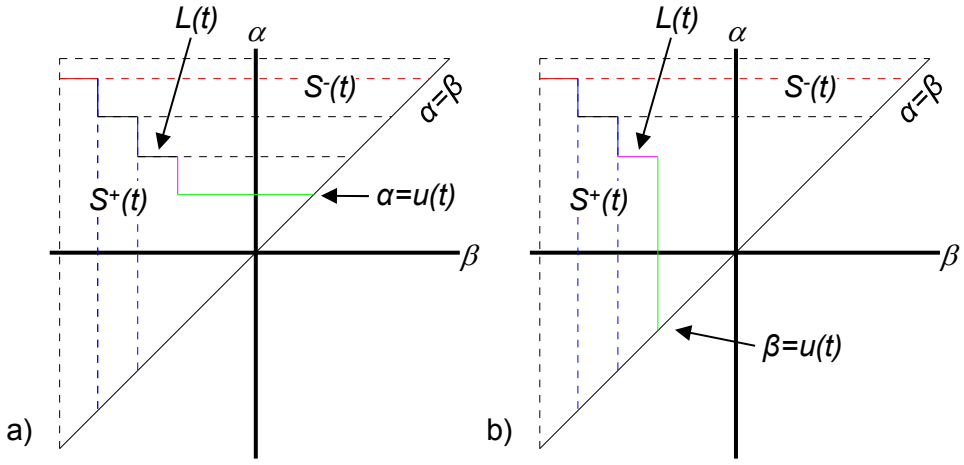

Figure 8.9: Illustration of the two positions of the final link. a) Increasing and b) decreasing final inputs.

Since there is always two areas that create the limiting triangle, the integral, given in Eq. (8.2), can be divided into two integrals over the $S^+(t)$ and $S^-(t)$ domains:

$$f(t) = \hat{\Gamma}u(t) = \iint_{S^+(t)} \mu(\alpha,\beta)\,\hat{\gamma}_{\alpha\beta}u(t)\,d\alpha\,d\beta + \iint_{S^-(t)} \mu(\alpha,\beta)\,\hat{\gamma}_{\alpha\beta}u(t)\,d\alpha\,d\beta. \tag{8.3}$$

Equation (8.3) can be simplified by using the following property of the $\hat{\gamma}$ operator:

$$\begin{aligned} &if\ (\alpha,\beta) \in S^+(t)\ then\ \hat{\gamma}_{\alpha\beta}u(t) = +1, \\ &if\ (\alpha,\beta) \in S^-(t)\ \ then\ \hat{\gamma}_{\alpha\beta}u(t) = -1. \end{aligned} \tag{8.4}$$

Substituting Eq. (8.4) in to (8.3), we get:

$$f(t) = \iint_{S^+(t)} \mu(\alpha, \beta)\, d\alpha\, d\beta - \iint_{S^-(t)} \mu(\alpha, \beta)\, d\alpha\, d\beta. \tag{8.5}$$

Equation (8.5) states that the output depends on the subdivision of the limiting triangle T into positive and negative sets.

In summary, the geometric definition presented here, which describes the staircase division between the two sets, is the mechanism of memory formation. The Preisach model, in general, describes hysteresis nonlinearities with nonlocal memories. The geometric definition is fully equivalent to the analytical definition of the model. However, the geometric definition is considered more convenient for further generalization of the model. Some modifications can be made in the following areas: 1) New and more general rules for the subdivision of the limiting triangle can be used. The staircase division can be substituted with smooth and analytical functions. 2) Different weight functions $\mu^+(\alpha, \beta)$ and $\mu^-(\alpha, \beta)$ can be defined for the positive and negative (α, β) sets.

8.2.2. Properties of the Model

There are three main properties of the Preisach model:

Property 1) The output value of f^+, in the state of positive saturation is equal to the negative of f^-, in the negative saturation. In positive saturation, where all switches are up, the input is more than α_0 and the output is:

$$f^+ = \iint_T \mu(\alpha, \beta)\, d\alpha\, d\beta. \tag{8.6}$$

In negative saturation, where all switches are down, the input is less than β_0, and the output is:

$$f^- = -\iint_T \mu(\alpha, \beta)\, d\alpha\, d\beta. \tag{8.7}$$

The saturation values remain constant for $u(t) \geq \alpha_0$ and $u(t) \leq \beta_0$. Partly due to this reason, the Preisach model does not describe the reversible components of hysteresis nonlinearities.

Property 2) The Wiping-Out Property shows that not all past extremum values are accumulated into the memory. Some past extremum values can be "wiped-out" by subsequent

input variations. For example, consider the finite decreasing input sequence $\{u_1, u_3, u_5, u_7\}$ of local input maxima and an increasing input sequence $\{u_2, u_4, u_6, u_8\}$ of local input minima. The $\alpha - \beta$ diagram can be seen in Figure 8.10.

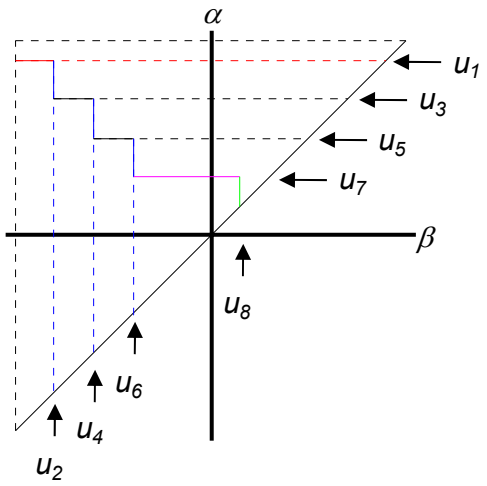

Figure 8.10: Illustration of the finite decreasing input sequence.

Now, we assume an increasing input to $u(t_9) = u_9$ which is above u_3. The horizontal link that is formed by $\alpha = u_9$ moves up in the vertical direction. This way, all past inputs with $\alpha < u_9$ are wiped-out. Figure 8.11 demonstrates the erasing of previous local maxima, minima and the vertices that are associated with them.

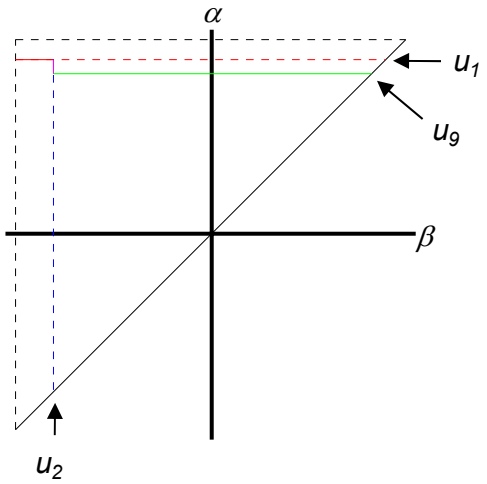

Figure 8.11: Illustration of wiping-out of past input.

The wiping-out property works in the same manner for a set of monotonically decreasing inputs. The definition of the wiping-out property, from Mayergoyz [2003], is as follows: "Each local input maximum wipes-out the vertices of $L(t)$ whose α coordinates are below this maximum, and each local minimum wipes-out the vertices whose β coordinates are above this minimum."

The analytical formulation of the wiping-out property is as follows. First, consider the input variation shown in Figure 8.12 for the interval $t_0 \leq t \leq t'$.

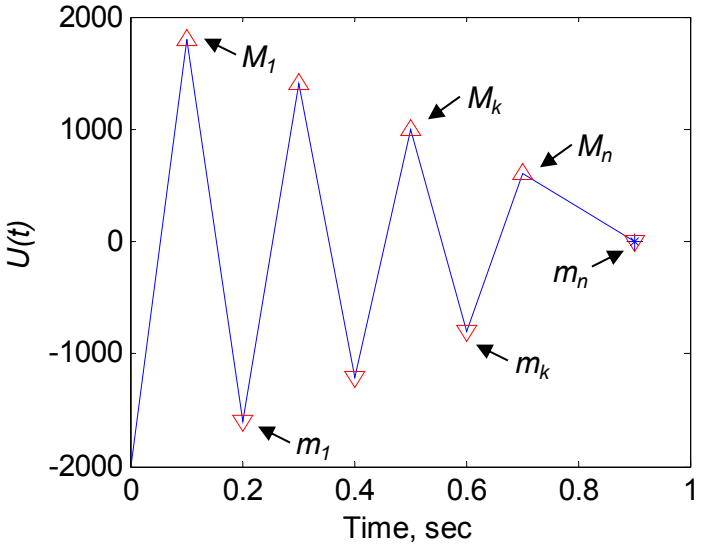

Figure 8.12: Example time history of input.

At time t_0, the input is below β_0 where all switches are in the down position, hence the system is in the state of negative saturation. In the time interval $[t_0, t']$, there is a global maximum at time t_1^+ with value M_1. Then, we have:

$$M_1 = \max u(t) \ \ in \ [t_0, t'], \qquad u(t_1^+) = M_1. \tag{8.8}$$

All previous input maxima are wiped-out by $u(t_1^+)$. Now, we consider the global input minimum in the $[t_1^+, t']$ time interval denoted by m_1 at time t_1^-. Then, we have:

$$m_1 = \min u(t) \ \ in \ [t_1^+, t'], \qquad u(t_1^-) = m_1. \tag{8.9}$$

All input extrema are wiped-out, in the $[t_1^+, t_1^-]$ interval, by the m_1 global minimum. The argument above can be continued for all pairs of maximum (M_k) and minimum (m_k) where

$$M_k = \max u(t) \ \ in \ [t_{k-1}^-, t'], \qquad u(t_k^+) = M_k \tag{8.10}$$

and

$$m_k = \min u(t) \ \ in \ [t_k^+, t'], \qquad u(t_k^-) = m_k \tag{8.11}$$

where t_{k-1}^- is the time for previous input minima and t_k^+ is the time for input maxima. The index, k is equal to $k = 1,2, \dots, n$. Only the alternating series of "dominant" input maxima (M_k) and minima (m_k) are accumulated by the Preisach model. All intermediate input extrema are erased. The α and β coordinates of the vertices of interface $L(t')$ are equal to M_k and m_k respectively. Note that the alternating series of dominant extrema is modified with time.

Property 3) The Congruency Property is another property of the Preisach model that is valid for periodic input variations. Let $u_1(t)$ and $u_2(t)$ be two inputs that may have different past histories. Starting from t_0, the two inputs are subjected to same two consecutive extremum values, u_+ and u_-. These inputs result in minor hysteresis loops. Figure 8.13 shows the $\alpha - \beta$ diagram for $u_1(t)$ and $u_2(t)$.

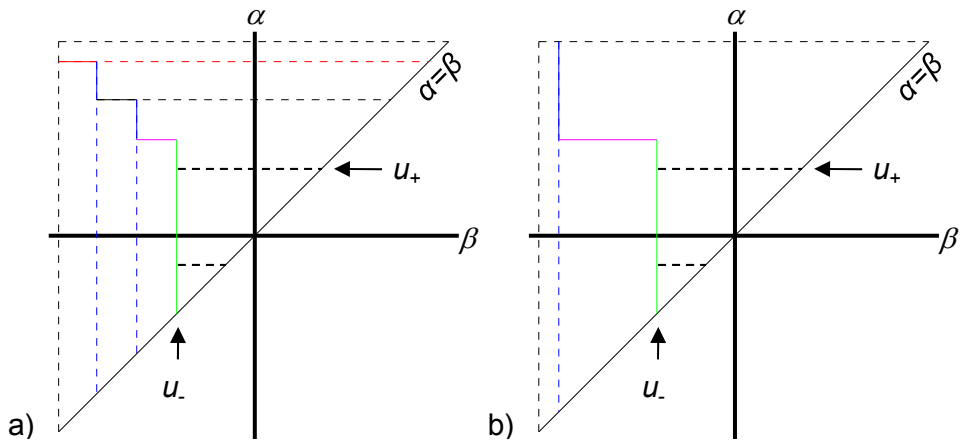

Figure 8.13: $\alpha - \beta$ diagram for a) $u_1(t)$ and b) $u_2(t)$.

This input sequence results in the periodic shape variations for the two interfaces, $L_1(t)$ and $L_2(t)$, which produces periodic variations of outputs $f_1(t)$ and $f_2(t)$. Figure 8.14 shows the input-output plot for the two inputs $u_1(t)$ and $u_2(t)$.

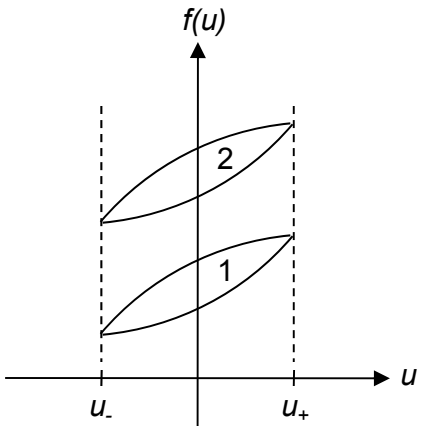

Figure 8.14: Input-output plot of two congruent inputs.

The position of these two loops are different in the vertical $f - axis$. The difference is due to the past histories of the two inputs. These two curves are congruent, therefore a translation of the two curves in the $f - axis$ will cause the two curves to coincide. The following definition is given for the congruency property: "All minor hysteresis loops corresponding to back-and-forth variations of inputs between the same two consecutive extremum values are congruent."

8.2.3. Identification of the Model

This section deals with the identification of the Preisach (weight) function $\mu(\alpha, \beta)$ for the Preisach model. The set of first-order transition curves (that are experimentally obtained) will be used for the identification. These curves are defined as follows: First, the input is decreased below β_0 which brings all $\hat{\gamma}$ operators to state of negative saturation. Next, the input is monotonically increased until it reaches some value α'. The corresponding $\alpha - \beta$ diagram and the $f - u$ plot is presented in Figure 8.15.

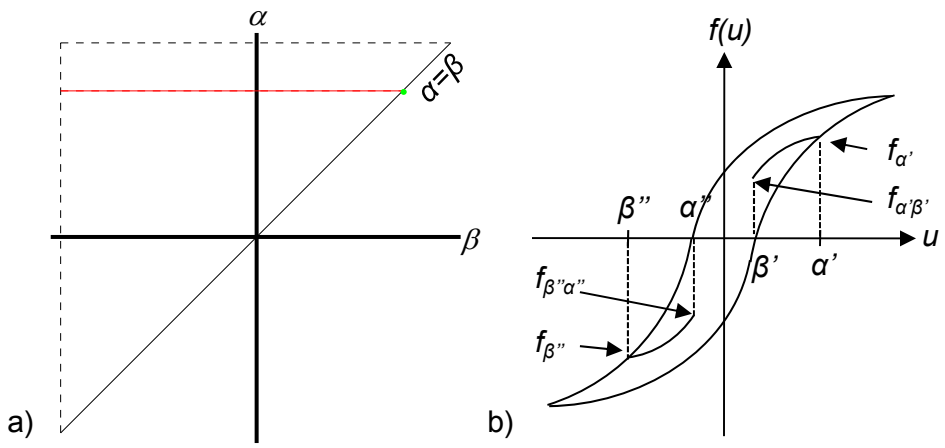

Figure 8.15: Illustration of the first-order transition curve. a) $\alpha - \beta$ diagram and b) $f - u$ plot.

Starting from the negative saturation state, the ascending curve of the major loop is followed. This is called the limiting ascending branch. The output is $f_{\alpha'}$ where the input is $u(t) = \alpha'$. The first-order transition curve is formed by the monotonic increase (from β_0) followed by a monotonic decrease. The curve is formed by the first reversal of input. The notation $f_{\alpha'\beta'}$ is used for the output of the transition curve that comes after the limiting ascending branch (that is terminated at $f_{\alpha'}$). The input is equal to β' at $f_{\alpha'\beta'}$. Figure 8.16 illustrates the new $\alpha - \beta$ diagram as a result of the first reversal of the input.

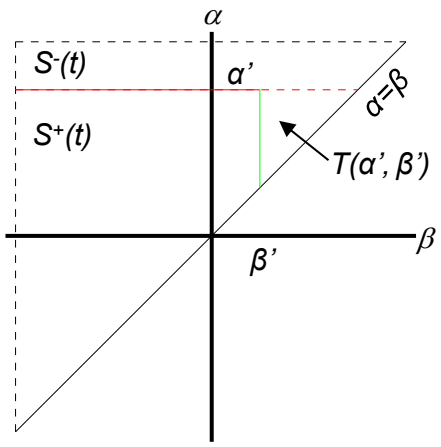

Figure 8.16: $\alpha - \beta$ diagram for the first-order transition curve.

We can define the following function:

$$F(\alpha', \beta') = \frac{1}{2}\left(f_{\alpha'} - f_{\alpha'\beta'}\right). \tag{8.12}$$

This function is equal to one-half of the output increments along the first-order transition curve. Now, we need to express this function in terms of the Preisach function $\mu(\alpha, \beta)$. From Figure 8.15a and Figure 8.16, we see that the triangle $T(\alpha', \beta')$ is added to the negative set S^- and removed from the positive set S^+ as a result of the monotonic decrease from $u = \alpha'$ to $u = \beta'$. Using this fact and Eq. (8.5), we find that the Preisach model will match the output increments if $\mu(\alpha, \beta)$ satisfies:

$$f_{\alpha'\beta'} - f_{\alpha'} = -2 \iint_{T(\alpha', \beta')} \mu(\alpha, \beta)\, d\alpha\, d\beta. \tag{8.13}$$

By comparing Eq. (8.12) and Eq. (8.13), we get:

$$F(\alpha', \beta') = \iint_{T(\alpha', \beta')} \mu(\alpha, \beta)\, d\alpha\, d\beta. \tag{8.14}$$

The integral over the triangle $T(\alpha', \beta')$ can be written as the following double integral:

$$F(\alpha', \beta') = \int_{\beta'}^{\alpha'} \left(\int_{\beta}^{\alpha'} \mu(\alpha, \beta)\, d\alpha \right) d\beta. \tag{8.15}$$

By differentiating Eq. (8.15) twice, we get:

$$\mu(\alpha', \beta') = \frac{-\partial^2 F(\alpha', \beta')}{\partial \alpha' \partial \beta'}. \tag{8.16}$$

Using Eq. (8.12), the weight function becomes:

$$\mu(\alpha', \beta') = \frac{1}{2} \frac{\partial^2 f_{\alpha'\beta'}}{\partial \alpha' \partial \beta'}. \tag{8.17}$$

The first derivative of $f_{\alpha'\beta'}$ with respect to β' is:

$$\frac{\partial f_{\alpha'\beta'}}{\partial \beta'} = \tan(\theta(\alpha', \beta') \tag{8.18}$$

where $\theta(\alpha', \beta')$ is the angle between the $u - axis$ and the tangent of the first-order transition curve $f_{\alpha'\beta'}$ at the input $u = \beta'$. From Eq. (8.17) and Eq. (8.18), we get:

$$\mu(\alpha', \beta') = \frac{1}{2}\frac{\partial \tan\theta(\alpha', \beta')}{\partial \alpha'}. \tag{8.19}$$

The Preisach function is positive if $\tan\theta(\alpha', \beta')$ is a monotonically increasing function of α' for any fixed β'. This condition is satisfied if 1) all first-order transition curves are monotonically increasing functions of β' and 2) they do not intersect inside the major loop but merge together at the point where the descending and ascending major loops meet. The $\tan\theta(\alpha', \beta')$ term should increase as a function of α' for any fixed β' in order for the first-order transition curves to merge. Figure 8.17 shows two types of first-order transition curves inside the corresponding major loop. These two types are described as 1) increasing-decreasing ($\beta_0 - \alpha' - \beta'$) and 2) decreasing-increasing ($\alpha_0 - \beta'' - \alpha''$) first-order transition curves.

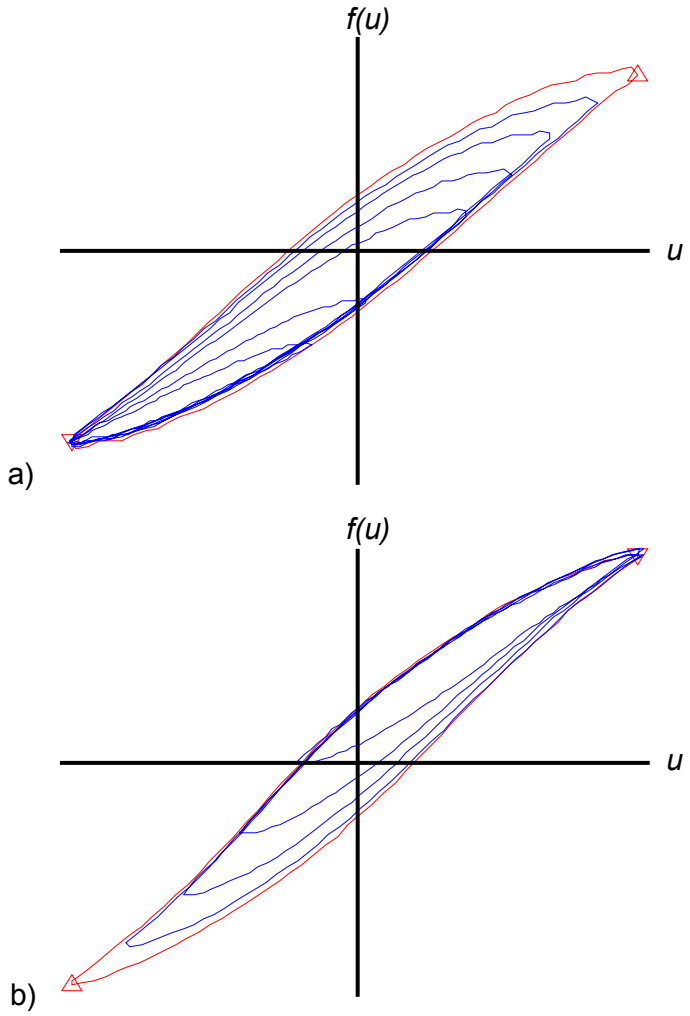

Figure 8.17: Two types of first-order transition curves. a) Increasing-decreasing and b) decreasing-increasing.

For positive $\mu(\alpha,\beta)$, $F(\alpha',\beta')$ is a 1) monotonically increasing function of α' for any fixed β' and 2) monotonically decreasing function of β' for any fixed α'.

In order to show that the first-order transition curves are matching, we consider the following case when $\beta' = \beta_0$. This means that the input started from the negative saturation and ended back at negative saturation after monotonically increasing and decreasing. We have:

$$f_{\alpha'\beta_0} = f^{-}. \tag{8.20}$$

From Eq. (8.13) and Eq. (8.20), we get:

$$f^- - f_{\alpha'} = -2 \iint_{T(\alpha',\beta_0)} \mu(\alpha,\beta)\, d\alpha\, d\beta. \tag{8.21}$$

The Preisach model matches the output increment, $f^- - f_{\alpha'}$, along the limiting ascending branch. On the other hand, for $\alpha' = \alpha_0$ we have:

$$f_{\alpha_0} = f^+. \tag{8.22}$$

Similarly, from Eq. (8.21) and Eq. (8.22), we get:

$$f^- - f^+ = -2 \iint_T \mu(\alpha,\beta)\, d\alpha\, d\beta \tag{8.23}$$

where $T = T(\alpha_0, \beta_0)$ is the limiting triangle. Since the major hysteresis loops are assumed symmetric here, the following can be written:

$$f^+ = -f^-. \tag{8.24}$$

From Eq. (8.23) and Eq. (8.24), we get:

$$f^- = -\iint_T \mu(\alpha,\beta)\, d\alpha\, d\beta. \tag{8.25}$$

From the analysis above, we conclude that the first-order transition curves are matched. These curves are attached to the limiting ascending branch, and each of them are formed when a monotonic increase along this branch is followed by an input decrease. These curves are called first-order decreasing transition curves.

By repeating the analysis above for first-order decreasing transition curves, a similar expression can be derived for $\mu(\alpha,\beta)$ by using the first-order increasing transition curves. Each of these curves are formed by a decrease along the limiting decreasing branch (starting at α_0), followed by an increase in input. The notation $f_{\beta''}$ will be used for the value for the descending curve along the limiting descending branch. This value is achieved when the input is decreased from some value above α_0 to $u = \beta''$. The notation $f_{\alpha''\beta''}$ indicates the output of the first-order increasing transition curve that starts from the limiting descending branch at point $f_{\beta''}$ for input

$u = \alpha''$. Figure 8.18 presents the $\alpha - \beta$ diagrams and the $f - u$ plot for the first-order increasing transition curve.

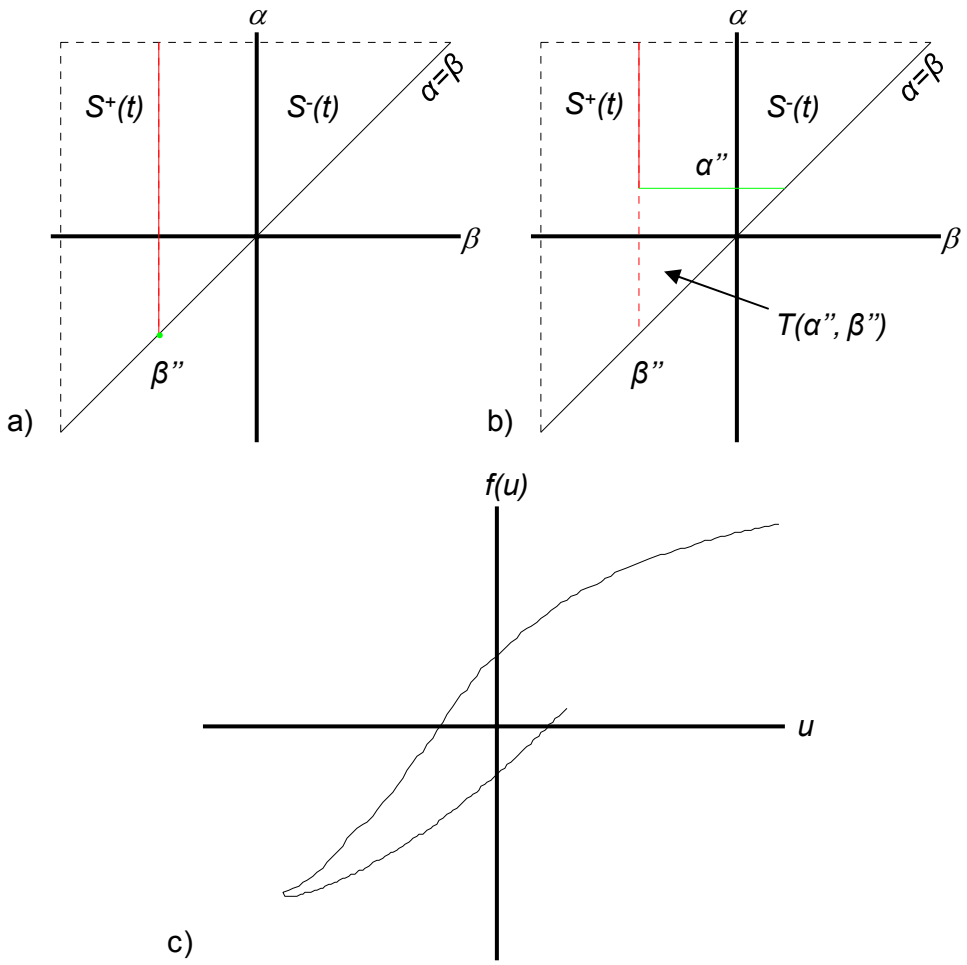

Figure 8.18: Illustration of the first-order increasing transition curve. a) First decrease followed by b) the first increase and c) the corresponding $f - u$ plot.

Using the following function:

$$F(\alpha'', \beta'') = \iint_{T(\alpha'', \beta'')} \mu(\alpha, \beta)\, d\alpha\, d\beta \tag{8.26}$$

and from Figure 8.18, and Eq. (8.5), we get:

$$F(\alpha'', \beta'') = \frac{1}{2}\left(f_{\beta''\alpha''} - f_{\beta''}\right). \tag{8.27}$$

As before we find the solution:

$$\mu(\alpha'', \beta'') = \frac{-\partial^2 F(\alpha'', \beta'')}{\partial \alpha'' \partial \beta''} \tag{8.28}$$

which is the exact same solution as Eq. (8.16). From the analysis above, the first-order decreasing and increasing transition curve are congruent. The following properties can be written:

$$\beta'' = -\alpha' \quad and \quad \alpha'' = -\beta' \tag{8.29}$$

then, we have:

$$f_{\beta''} = -f_{\alpha'} \quad and \quad f_{\beta''\alpha''} = -f_{\alpha'\beta'}. \tag{8.30}$$

From Eq. (8.12), Eq. (8.27), Eq. (8.29) and Eq. (8.30), we get:

$$F(\alpha'', \beta'') = F(\alpha', \beta'). \tag{8.31}$$

Substituting Eq. (8.29) into Eq. (8.31), we get:

$$F(-\beta', -\alpha') = F(\alpha', \beta') \tag{8.32}$$

and substituting Eq. (8.29) and Eq. (8.31) into Eq. (8.28), we get:

$$\mu(-\beta', -\alpha') = \frac{\partial^2 F(\alpha', \beta')}{\partial \alpha' \partial \beta'}. \tag{8.33}$$

Using Eq. (8.16) and Eq. (8.33), we have:

$$\mu(-\beta', \alpha') = \mu(\alpha', \beta'). \tag{8.34}$$

The Eq. (8.32) and Eq. (8.34) shows the mirror symmetry of functions $F(\alpha, \beta)$ and $\mu(\alpha, \beta)$ with respect to line $\alpha = \beta$. If this line is the interface between the positive and negative sets, $S^+(t)$ and $S^-(t)$, then the output is equal to $f(t) = 0$.

8.2.4. Representation Theorem

This theorem provides the necessary and sufficient conditions for the representation of actual hysteresis nonlinearities by the Preisach model. The theorem states that: "The wiping-out property and the congruency property constitute the necessary and sufficient conditions for a hysteresis nonlinearity to be represented by the Preisach model on the set of piece-wise monotonic inputs." See Mayergoyz [2003] for the detailed proof of this theorem.

For the purposes of the discussion here, it is important to note that the representation theorem reveals the limits of the Preisach model. These limits are in phenomenological terms, therefore the model is physically universal. The theorem allows for the explanation of the "statistical instability" of the Preisach model. The Eq. (8.16) for $\mu(\alpha, \beta)$ is derived from Eq. (8.14). This means that the weight function can always be determined if the integrals of $\mu(\alpha, \beta)$ over the triangles $T(\alpha', \beta')$ are experimentally found. These integrals can be found from the first-order transition curves and also from the higher-order transition curves. As the theory requires, if these transition curves are congruent and the wiping-out property holds, the integrals will have same value, regardless of the order of the transition curves used. The statistical instability arises when the actual hysteretic transducer does not exactly satisfy the wiping-out and congruency properties. In this case, the Preisach model becomes an approximation of the actual hysteresis nonlinearity.

Theoretically, all of the transition curves can be used to calculate the weight functions $\mu(\alpha, \beta)$ because all of them will lead to the same result. From a practical point of view, the first-order transition curves are preferred because 1) it is easier to obtain these curves experimentally and 2) the measurements of these curves start from the negative (or positive) saturation state (which is well defined).

8.2.5. Limitations and Assumptions

In summary, the classical Preisach model has some intrinsic limitations. The most important of them are: 1) The model describes hysteresis nonlinearities which exhibit congruency of minor loops formed for the same reversal values of input. 2) The model is rate-independent in nature and it does not account for dynamic properties of hysteresis nonlinearity. 3) The model describes hysteresis nonlinearities with wiping-out property. Only one dominant cycle is required to wipe-out the previous cycle. 4) A scalar output exhibits hysteretic variation

with respect to only one scalar input. 5) The classical Preisach model deals only with scalar hysteresis nonlinearities.

From the summary above, certain restrictions and assumptions have to be made in order to apply the classical Preisach model to the piezocomposite samples driven in the quasi-static frequency range. As stated above, the classical Preisach model deals with scalar outputs in response to one scalar input. However, it is known that the strain output of a piezoceramic material is a function of two variables: electric field and mechanical stress. In order to help the discussion, the linear electromechanical constitutive relationships is given here as an example, From Section 1.1.5, the linear constitutive relationship, given by $S_{ij} = s^E_{ijkl}T_{kl} + d_{kij}E_k$, demonstrates that the mechanical strain S is a function of the mechanical stress T and the applied electric field E. Refer to Eq. (1.1) for description of other terms. In actuality, the coefficients of stress and strain are nonlinear due to hysteresis and this nonlinearity can't be neglected for high amplitude inputs with varying extrema. However, the linear constitutive relationship is still useful to aid the discussion here. In this chapter, it is assumed that the mechanical stress, for the experimental cases considered here, is either negligible or it is proportional to the electric field. From the linear constitutive analogy, the piezoelectric constant (d) assumes a new effective value, therefore the strain is assumed to be a function of only one variable. In addition, the external aerodynamic loads (for the airfoil samples) are neglected here because they are known to be minimal from the experimental observations presented in Chapter 5 and Chapter 6. The aerodynamic loading is expected to be more dominant at high flow velocities (and high dynamic pressures) and may require the employment of the vector Preisach model.

8.3. Numerical Implementation of the Preisach Model

The Preisach model can be numerically implemented by using 1) Eq. (8.5) to compute the output $f(t)$ and 2) Eq. (8.17) to determine the weight function $\mu(\alpha, \beta)$. There are two difficulties that arise. First, it is difficult to evaluate the double integrals of Eq. (8.5). Second, the evaluation of the derivatives (for Eq. (8.17)) will amplify the noise that is in the experimental measurements. Another approach can be used to avoid these two issues. We first start with Eq. (8.5). Note that the staircase interface, $L(t)$, seperates the two sets, positive S^+ and negative S^-. The vertices of the interface are defined by $\alpha = M_k$ and $\beta = m_k$. First, a monotonically decreasing input will be discussed.

8.3.1. Monotonically Decreasing Input

Figure 8.19 demonstrates the $\alpha - \beta$ diagram for a monotonically decreasing input where the final link of the interface $L(t)$ is vertical.

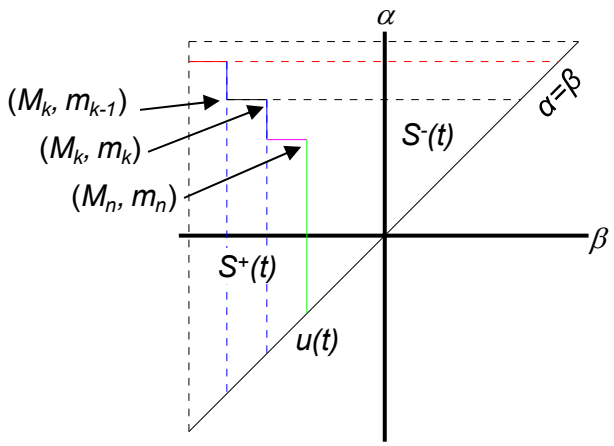

Figure 8.19: $\alpha - \beta$ diagram for a monotonically decreasing final input.

M_k and m_k form the series of dominant input extrema. By adding and subtracting the integral of $\mu(\alpha, \beta)$ over $S^+(t)$, the Eq. (8.5) can be written as:

$$f(t) = -\iint_T \mu(\alpha, \beta)\, d\alpha\, d\beta + 2 \iint_{S^+(t)} \mu(\alpha, \beta)\, d\alpha\, d\beta \tag{8.35}$$

where T is the limiting triangle. Using Eq. (8.14), we get:

$$\iint_T \mu(\alpha, \beta)\, d\alpha\, d\beta = F(\alpha_0, \beta_0). \tag{8.36}$$

Now, the positive set $S^+(t)$ can be subdivided into n trapezoids denoted θ_k. We now have:

$$\iint_{S^+(t)} \mu(\alpha, \beta)\, d\alpha\, d\beta = \sum_{k=1}^{n(t)} \iint_{\theta_k(t)} \mu(\alpha, \beta)\, d\alpha\, d\beta. \tag{8.37}$$

The number $n(t)$ and the shape $\theta_k(t)$ of the trapezoids is a function of time. Each trapezoid can be represented as a difference of two triangles, $T(M_k, m_{k-1})$ and $T(M_k, m_k)$. We now have:

$$\iint_{\theta_k(t)} \mu(\alpha,\beta)\, d\alpha\, d\beta = \iint_{T(M_k,m_{k-1})} \mu(\alpha,\beta)\, d\alpha\, d\beta - \iint_{T(M_k,m_k)} \mu(\alpha,\beta)\, d\alpha\, d\beta \tag{8.38}$$

where $m_0 = \beta_0$ for $k = 1$. Using Eq. (8.14), we get:

$$\iint_{T(M_k,m_{k-1})} \mu(\alpha,\beta)\, d\alpha\, d\beta = F(M_k, m_{k-1}) \tag{8.39}$$

and

$$\iint_{T(M_k,m_k)} \mu(\alpha,\beta)\, d\alpha\, d\beta = F(M_k, m_k). \tag{8.40}$$

Using Eq. (8.38), Eq. (8.39) and Eq. (8.40), we get:

$$\iint_{\theta_k(t)} \mu(\alpha,\beta)\, d\alpha\, d\beta = F(M_k, m_{k-1}) - F(M_k, m_k). \tag{8.41}$$

Using Eq. (8.35), Eq. (8.36), Eq. (8.37) and Eq. (8.41), we get:

$$f(t) = -F(\alpha_0, \beta_0) + 2\sum_{k=1}^{n(t)} [F(M_k, m_{k-1}) - F(M_k, m_k)]. \tag{8.42}$$

The current value of the input $u(t)$ is equal to m_n. The Eq. (8.42) can be written as:

$$\begin{aligned} f(t) = -F(\alpha_0, \beta_0) + 2\sum_{k=1}^{n(t)-1} [F(M_k, m_{k-1}) - F(M_k, m_k)] \\ + 2\big[F(M_n, m_{n-1}) - F\big(M_n, u(t)\big)\big]. \end{aligned} \tag{8.43}$$

This expression is for the monotonically decreasing input.

8.3.2. Monotonically Increasing Input

If the input $u(t)$ is monotonically increased, the final link of the interface $L(t)$ is horizontal as shown in Figure 8.20.

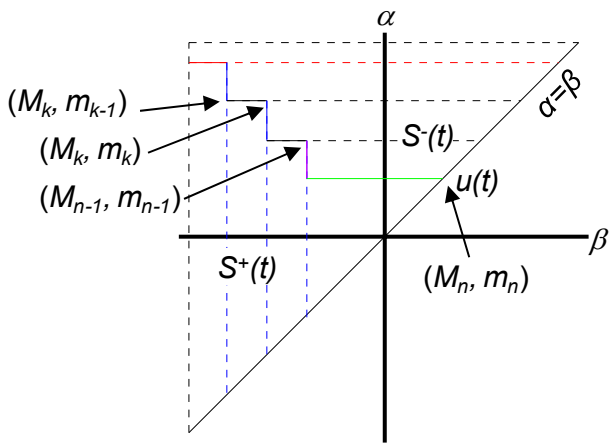

Figure 8.20: $\alpha - \beta$ diagram for a monotonically increasing final input.

This case is realized when $m_n(t) = M_n(t) = u(t)$. Using Eq. (8.14), we have:

$$F(M_n, m_n) = F\big(u(t), u(t)\big) = 0. \tag{8.44}$$

Using Eq. (8.42) and Eq. (8.44), the output $f(t)$ for a monotonically increasing input becomes:

$$f(t) = -F(\alpha_0, \beta_0) + 2\sum_{k=1}^{n(t)-1}[F(M_k, m_{k-1}) - F(M_k, m_k)] + 2F(u(t), m_{n-1}). \tag{8.45}$$

8.3.3. Explicit Final Form

Equation (8.12) can be used to compute the function $F(\alpha, \beta)$ with the experimentally measured increasing-decreasing first-order transition curves. Using Eq. (8.12), the Eq. (8.43) and Eq. (8.45) can be re-written as:

$$f(t) = f^{-} + \sum_{k=1}^{n(t)-1} (f_{M_k m_k} - f_{M_k m_{k-1}}) + f_{M_n u(t)} - f_{M_n m_{n-1}} \tag{8.46}$$

and

$$f(t) = f^{-} + \sum_{k=1}^{n(t)-1} (f_{M_k m_k} - f_{M_k m_{k-1}}) + f_{-m_{n-1}} - f_{-m_{n-1}\,-u(t)} \tag{8.47}$$

which is in terms of the experimental data of the first-order transition curves. In the expression, f^{-} is the positive saturation of the output. Eq. (8.46) and Eq. (8.47) are the explicit expressions of the output $f(t)$ in terms of the experimentally measured data. In Eq. (8.47), the last two terms are transformed by using Eq. (8.12) and Eq. (8.32). In this chapter, the following form of Eq. (8.47) is used:

$$f(t) = f^{-} + \sum_{k=1}^{n(t)-1} (f_{M_k m_k} - f_{M_k m_{k-1}}) + f_{u(t)} - f_{u(t) m_{n-1}}. \tag{8.48}$$

This expression if for a monotonically increasing input.

Eq. (8.46) and Eq. (8.48) can also be written in terms of the decreasing-increasing first-order transition curves. For a monotonically decreasing input, the response becomes:

$$f(t) = f^{+} + \sum_{k=1}^{n(t)-1} (f_{m_k M_k} - f_{m_k M_{k-1}}) + f_{u(t)} - f_{u(t) M_{n-1}} \tag{8.49}$$

where f^{+} is the maximum saturation output value. Similarly, the monotonically increasing input has the following form:

$$f(t) = f^{+} + \sum_{k=1}^{n(t)-1} (f_{m_k M_k} - f_{m_k M_{k-1}}) + f_{m_n u(t)} - f_{m_n M_{n-1}}. \tag{8.50}$$

These expressions are used in the following experimental predictions.

8.4. Application to Piezocomposite Bimorphs

The classical Preisach model is applied to: 1) Two cantilevered bimorph beams (Samples B6 and B2 employing two MFC M8507-P1 type actuators each. Refer to Table 4.1 and Section D.2 for more information on these samples). 2) The simply-supported thin airfoil. (Refer to Chapter 5 for detailed information). 3) The cascading bimorph thick airfoil. (Refer to Chapter 6 for more information).

8.4.1. Model Development

A MATLAB code is developed to predict the output of the clamped-free MFC bimorph actuator with hysteresis nonlinearity. First, the $f_{\alpha\beta}$ are computed using the experimentally measured first-order transition curves. Next, Eq. (8.46) and Eq. (8.48) are used (along with increasing-decreasing first-order transition curves) or Eq.(8.49) and Eq. (8.50) are used (along with decreasing-increasing first-order transition curves) to predict the output to a piecewise monotonically increasing and decreasing input $u(t)$. Following steps are followed:

Step 1) A square mesh covering the limiting triangle (T) is constructed.

Step 2) Discretized set of first-order transition curves are entered.

Step 3) Input history and the current value of input are entered.

Step 4) The alternating series of dominant input extrema $\{M_k, m_k\}$ is calculated by using Eq. (8.10) and Eq. (8.11). This series is updated for each step of time.

Step 5) The mesh values $f_{\alpha\beta}$ needs to be evaluated. This is done by first determining the particular square (or triangular) cells (in the $\alpha - \beta$ diagram) to which points (M_k, m_k), (M_k, m_{k-1}) and $(M_n, u(t))$ belong. Next, the values of $f_{\alpha\beta}$ is computed at these points by means of interpolation of the mesh values of $f_{\alpha\beta}$ at the vertices of the square (or triangular) cells. The interpolation is based on the following local approximation to $f_{\alpha\beta}$ in each square mesh cell:

$$f_{\alpha\beta,square} \cong C_0 + C_1\alpha + C_2\beta + C_3\alpha\beta. \tag{8.51}$$

The coefficients are found by matching the values of $f_{\alpha\beta}$ in the cell vertices. For triangular cells (adjacent to the line $\alpha = \beta$), the approximation is given by:

$$f_{\alpha\beta,triangle} \cong C_0 + C_1\alpha + C_2\beta. \tag{8.52}$$

Step 6) Using the computed values of $f_{\alpha\beta}$, the current output value is computed by using Eq. (8.46) and Eq. (8.48) (or Eq. (8.49) and Eq. (8.50)).

8.4.2. Experimental Setup

As noted earlier, there are a total of four samples that are considered in this chapter: 1) two of the MFC bimorphs examined in Section 4.4 and Section D.2, 2) the simply-supported thin airfoil examined in Chapter 5, and 3) the cascading bimorph thick airfoil evaluated in Chapter 6. All of these samples are in the bimorph electromechanical configuration.

The displacement of the samples (at a single point) is considered as the dependent variable. An MTI Instruments LTC-200-100-SA laser displacement sensor is employed to measure the displacement of the specimens. The independent variable is the excitation voltage. A TREK 623B high voltage amplifier is used to supply the input voltage to the MFCs. An NI cDAQ data acquisition system with an NI 9215 input module (with isolated 4 channels, 16 bit conversion) and an NI 9263 output module (with 16 bit conversion) is used to control the multi-parameter experiment. A triangle wave with variable amplitude and constant frequency is used to actuate the samples for both first-order transition curve measurements and the evaluation measurements. The deformation (due to excitation voltage) is recorded for 10 complete cycles and these cycles are averaged for the transition curve measurements.

Two electrical configurations are considered: 1) Asymmetric excitation and 2) symmetric excitation. In the asymmetric excitation, the voltage divider circuit (presented in Chapter 4) is employed. Using a pair of 1 MOhm and 3 MOhm resistors, the circuit (shown in Figure 4.8) is constructed for the tests presented in this chapter. The circuit results in a 3-to-1 division of the input voltage (from the TREK amplifier). For example, if 2 kV is applied to the circuit, the "front" MFC (which faces towards the laser displacement sensor) receives 1.5 kV which induces a bending motion away from the laser; hence resulting in a positive displacement. At the same time, the "rear" MFC (which faces away from the laser) receives -500 V and induces a bending motion away from the laser; hence resulting in an asymmetric bimorph actuation. The same 3-to-1 division is also applied for a -2 kV excitation. In the asymmetric configuration maximum voltages applied are -2 kV and +2 kV resulting in peak-to-peak actuation of both MFCs. On the

other hand, the symmetric electrical configuration (1-to-1) does not use the voltage divider. The opposing MFCs are connected to the amplifier in opposite polarities; therefore resulting in an electrically symmetric bimorph actuation. In the symmetric configuration, the maximum voltage is limited to -400 V and +400 V due to the - 500 V limit on the MFC actuator.

For the measurement of the increasing-decreasing first-order transition curves, the excitation voltage is started at -2 kV for the 3-to-1 configuration and -400 V for the 1-to-1 configuration. A triangle wave (at 0.5 Hz) is used to bring the voltage to the desired α' value (for the corresponding minor loop) and back to β_0. First, the major loop is obtained, which is limited by -2 kV and +2 kV for the 3-to-1 configuration, and -400 V and +400 V for the 1-to-1 configuration. The α' value is swept (with decreasing amplitude) from α_0 to β_0 in 40 increments, resulting in 100 V and 20 V α' resolution for the 3-to-1 and 1-to-1 configurations respectively. It is important to note that a saturation loop, between α_0 and β_0, is applied before the acquisition of each α' minor loop.

The measurement of the decreasing-increasing first-order transition curves is similar to the discussion above. The major loop acquisition is started at +2 kV (for 3-to-1) or +400 V (for 1-to-1) which are the maximum saturation input levels. The minor loops (and the corresponding β'' value) are swept from β_0 to α_0 with decreasing amplitude also in 40 increments.

There are several important observations on the samples employed in this chapter. For the bimorph sample B6, 1) there is no substrate material and 2) the two Kapton layers (which are part of the packaging of the MFC actuator, see Figure 1.1b) are assumed to have negligible bending stiffness. The bimorph sample B2, and the two piezocomposite airfoils have substrate materials. More specifically, both of the airfoils experience constraints due to the boundary conditions and the internal configuration. Possible errors arising from these observations will be discussed later.

It is also important to note the electrical field applied to each MFC on the bimorphs. In the experiments, two excitation conditions are used. In the symmetric, 1-to-1 electrical configuration, same-amplitude and opposite-polarity electric field is applied to the "opposing" active material on the bimorph. In this configuration, the neutral-axis is assumed to coincide with the geometric midline of the bimorph. In the asymmetric, 3-to-1 electrical configuration, one MFC receives a maximum of +1500 V where the "opposing" MFC receives -500 V. In this configuration, the neutral-axis of the bimorph is no longer aligned with the geometric midline.

8.4.3. Cantilevered Bimorph Beams

Two bimorphs beams are considered in this section. These samples are 1) B2 and 2) B6. Sample B2 is bimorph actuator with two MFC M8507-P1 type actuators and with a 0.027 mm thick stainless-steel substrate. Sample B6 also employs two MFC M8507-P1 actuators, however it has no substrate. Refer to Section 4.4 and Section D.2 for the details of these two samples. Figure 8.21 shows the important components of the experimental setup. The free length of the bimorph B2 is 86.65 mm and the laser measurement location is 80.88 mm from the clamped base. The free length of the bimorph B6 is set to 85.90 mm and the laser measurement location is 80.60 mm from the clamped base.

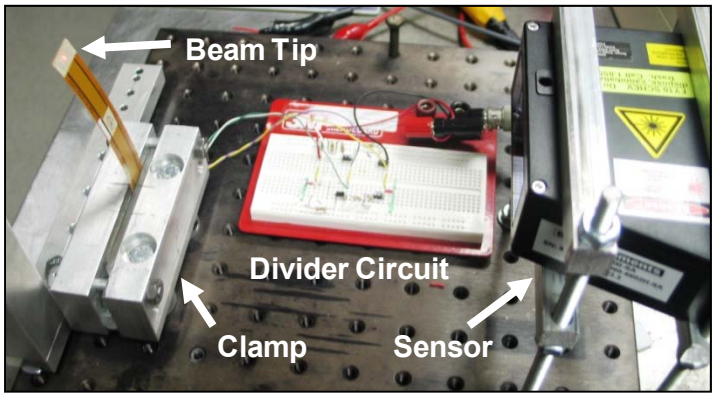

Figure 8.21: Experimental setup for hysteresis tests of bimorph beams.

First, the first-order transition curves are measured. Refer to 8.4.2 for the measurement procedure of these curves. Since bimorph sample B6 does not have any substrate, the discussion of the results are started with the sample B6. Figure 8.22 presents the increasing-decreasing ($\beta_0 - \alpha' - \beta_0$) and decreasing-increasing ($\alpha_0 - \beta'' - \alpha_0$) first-order transition curves measured for bimorph beam sample B6. Theoretically, these two types of first-order curves are symmetric, meaning that the 180° rotation of one curve should result in a matching pair between the two types. The curves correspond to the 3-to-1 electrical configuration.

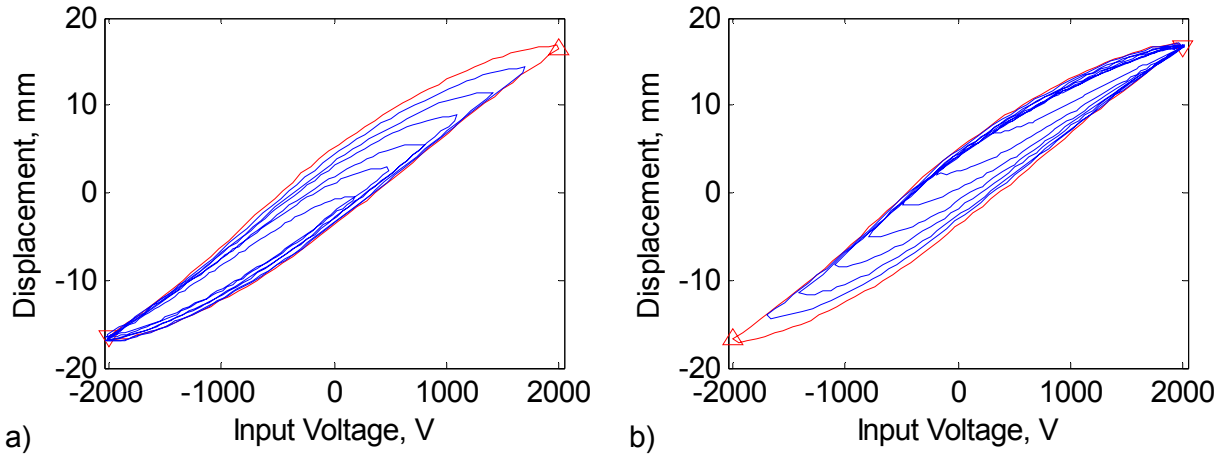

Figure 8.22: First-order transition curves for bimorph beam sample B6 in 3-to-1 configuration. a) Increasing-decreasing and b) decreasing-increasing.

As noted earlier, a total of 40 curves are measured; however most for these curves are removed for the plots in order to aid presentation. The first-order transition curves for the 1-to-1 configuration is presented in Figure 8.23.

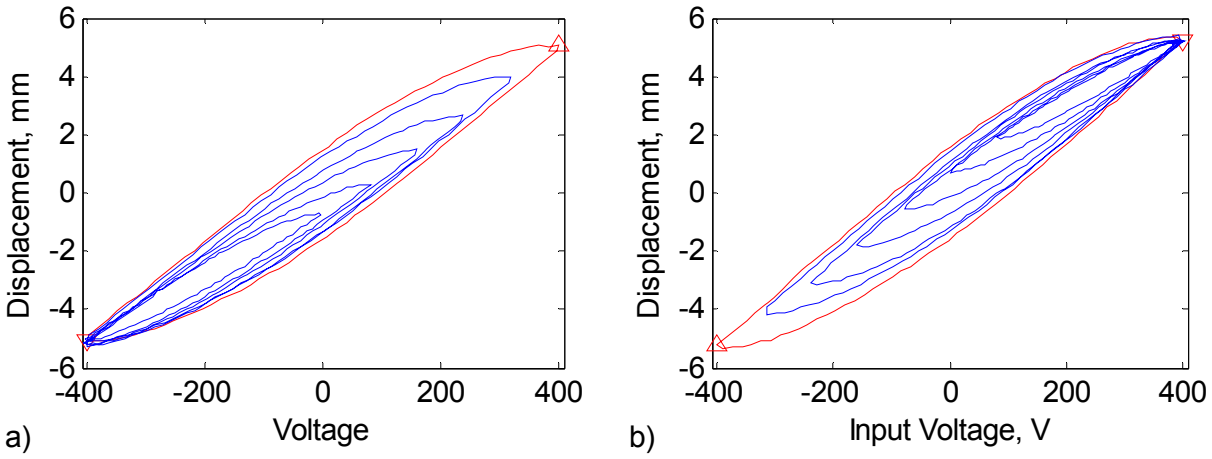

Figure 8.23: First-order transition curves for bimorph beam sample B6 in 1-to-1 configuration. a) Increasing-decreasing and b) decreasing-increasing.

The transition curves for both 3-to-1 and 1-to-1 configurations have similar shapes. After the measurement of these curves, the Preisach model can be constructed. First, the wiping-out property is examined. Two input signals (with different time history) are used to excite the samples. The deformation is measured and compared to the prediction of the Preisach model. These tests are simultaneously used to 1) check that the samples behave as the Preisach model

requires and 2) check the proper implementation of the model by the MATLAB code. Figure 8.24 presents the response to a wiping-out experiment on the bimorph beam sample B6 in the 3-to-1 electrical configuration.

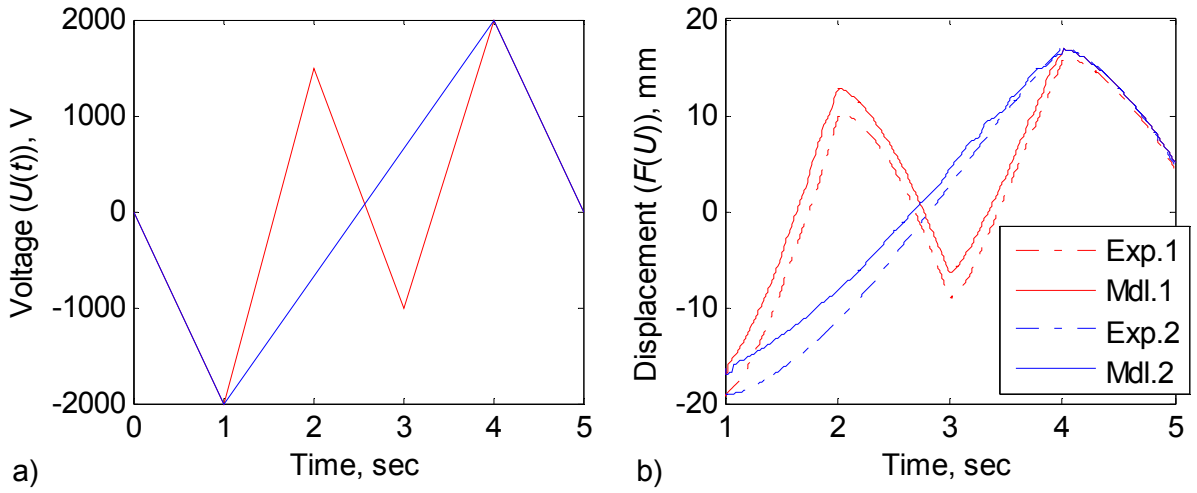

Figure 8.24: Wiping-out evaluation of bimorph beam sample B6 in 3-to-1 configuration. a) Voltage input and b) displacement output time histories.

Note that the two input signals, shown in Figure 8.24a, have identical outputs in the [0,1] second time frame and in the [4,5] second time frame. Figure 8.24b shows the matching experimental final descent in the [4,5] second time frame confirming that the previous input history is wiped out. The Preisach model also predicts the wiping-out very well. The set of increasing-decreasing first-order transition curves are used to make the prediction shown in Figure 8.24b. The same test is also conducted starting at the positive saturation point. In this case, the decreasing-increasing first-order transition curves are employed. Figure 8.25 shows the wiping-out evaluation of the bimorph sample B6 and the Preisach model prediction with the decreasing-increasing transition curves.

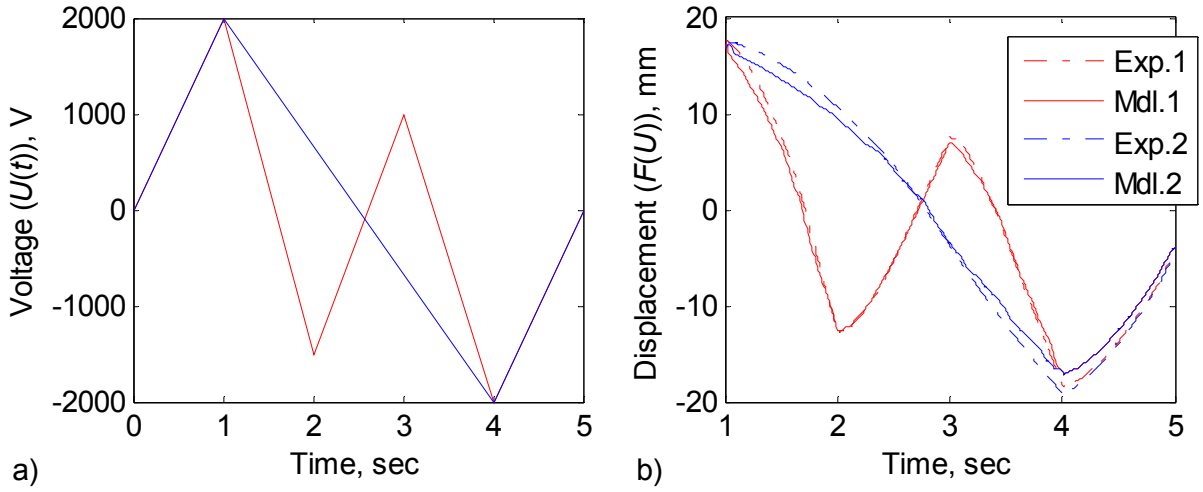

Figure 8.25: Wiping-out evaluation of bimorph beam sample B6 in 3-to-1 configuration. a) Voltage input and b) displacement output time histories.

Similar to the increasing-decreasing curves, the decreasing-increasing curves result in a very good prediction of the wiping-out property. The wiping-out property is also checked for the 1-to-1 electrical configuration. Figure 8.26 presents the test results for the bimorph sample B6 in the 1-to-1 configuration.

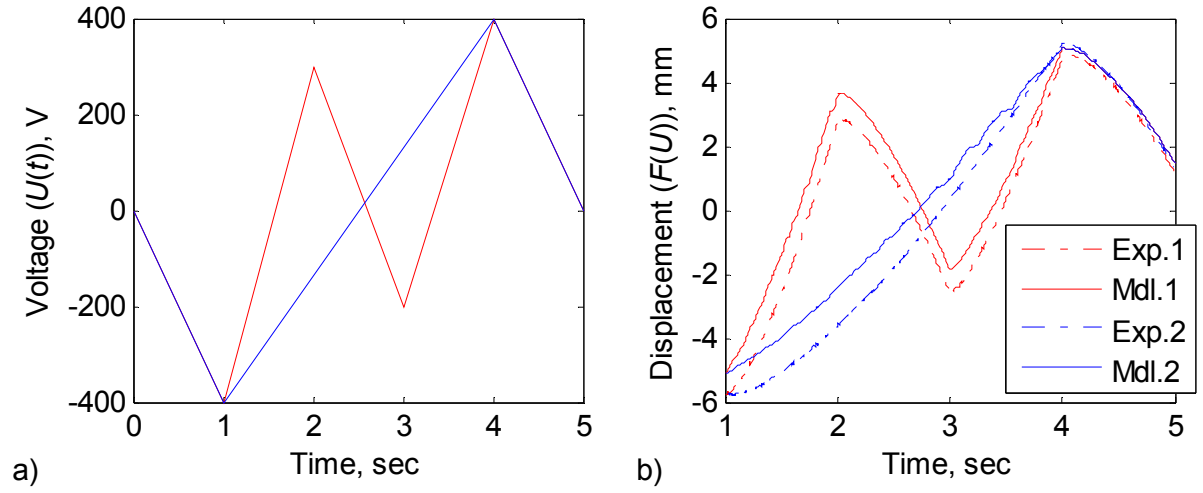

Figure 8.26: Wiping-out evaluation of bimorph beam sample B6 in 1-to-1 configuration. a) Voltage input and b) displacement output time histories.

The model uses the increasing-decreasing first-order transition curves for the prediction shown in Figure 8.26b. The wiping out property holds for the electrically symmetric actuation mode of bimorph sample B6. The test is repeated for the evaluation of the model using the

decreasing-increasing first-order transition curves. The corresponding results are presented in Figure 8.27

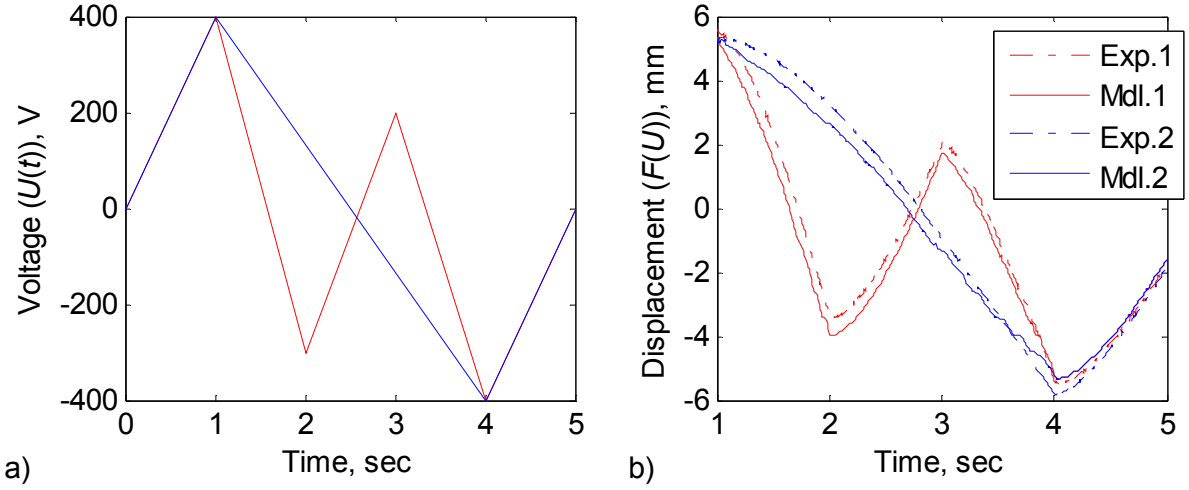

Figure 8.27: Wiping-out evaluation of bimorph beam sample B6 in 1-to-1 configuration. a) Voltage input and b) displacement output time histories.

The bimorph sample B6 successfully "passed" the wiping-out property evaluation for both 3-to-1 and 1-to-1 electrical configurations. The tests are repeated at 1 Hz and 5Hz in order to determine the inertial effects in addition to the tests presented for 0.5 Hz. These additional tests are presented in Section G.1.

The second property of the Preisach model is the congruency property. Another set of two input time histories are generated and applied to the samples to check for this property. First, the 3-to-1 electrical configuration is evaluated. The increasing-decreasing transition curves are used in the model prediction. Figure 8.28 shows the corresponding congruency test results for the bimorph sample B6. In the congruency tests, the two input time histories share same output in the [0,1] second time frame and in the [3,7] second time frame. As a result, the congruency of the two outputs are expected in the [4,7] second time frame.

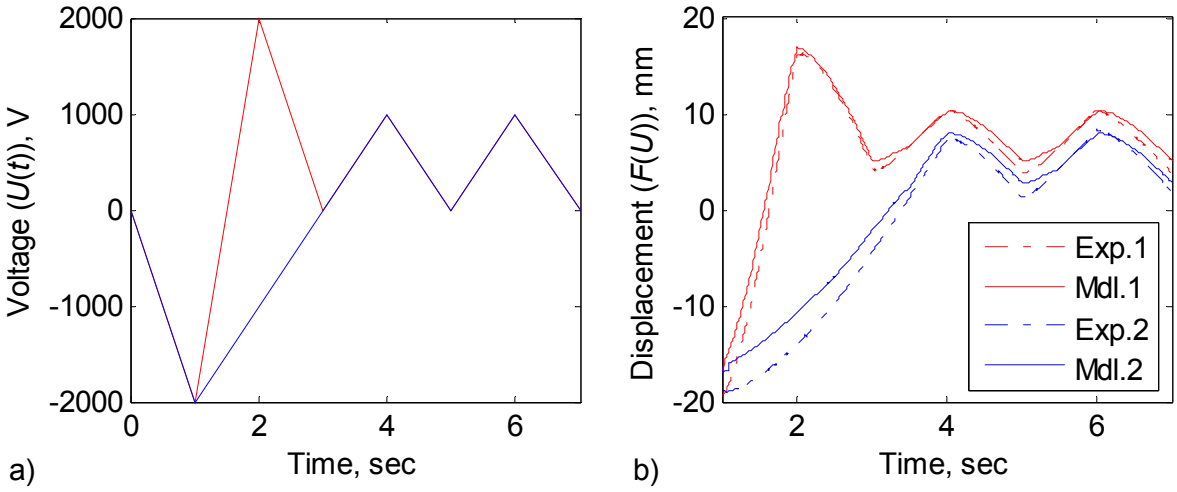

Figure 8.28: Congruency evaluation of the bimorph beam sample B6 in 3-to-1 configuration. a) Voltage input and b) displacement output time histories.

Both the sample and the model demonstrate the congruency of the two outputs in the [4,7] second time frame. The output has the same form; however at a different mean value due to the previous time history in the [1,4] second time frame. Figure 8.29 shows the response to a similar congruency test and the model prediction using the decreasing-increasing first-order transition curves.

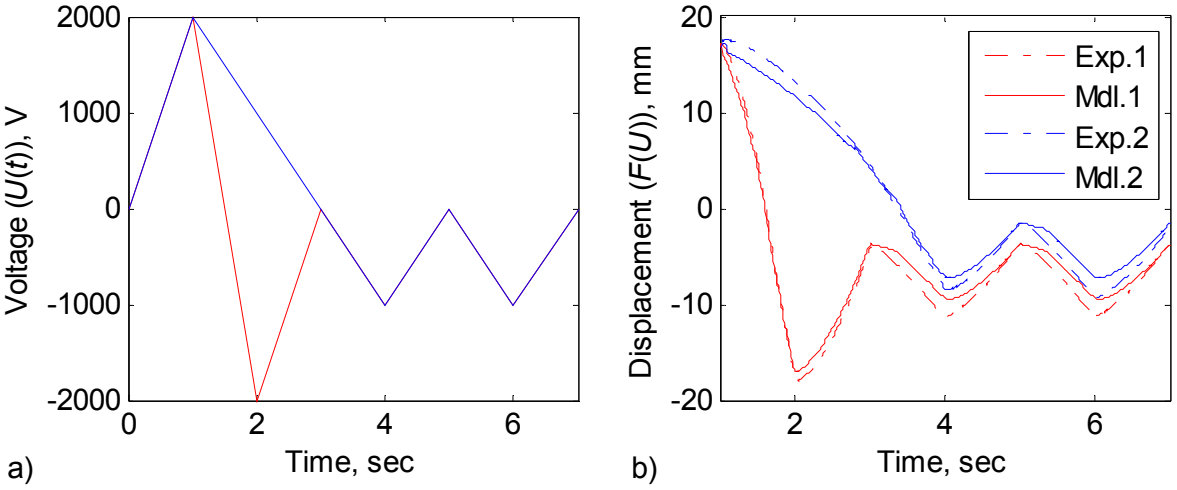

Figure 8.29: Congruency evaluation of the bimorph beam sample B6 in 3-to-1 configuration. a) Voltage input and b) displacement output time histories.

As observed before, the decreasing-increasing curves also predict the congruency property well. The congruency evaluation is continued for the 1-to-1 electrical configuration for the bimorph sample B6. The increasing-decreasing transition curves are used in Figure 8.30.

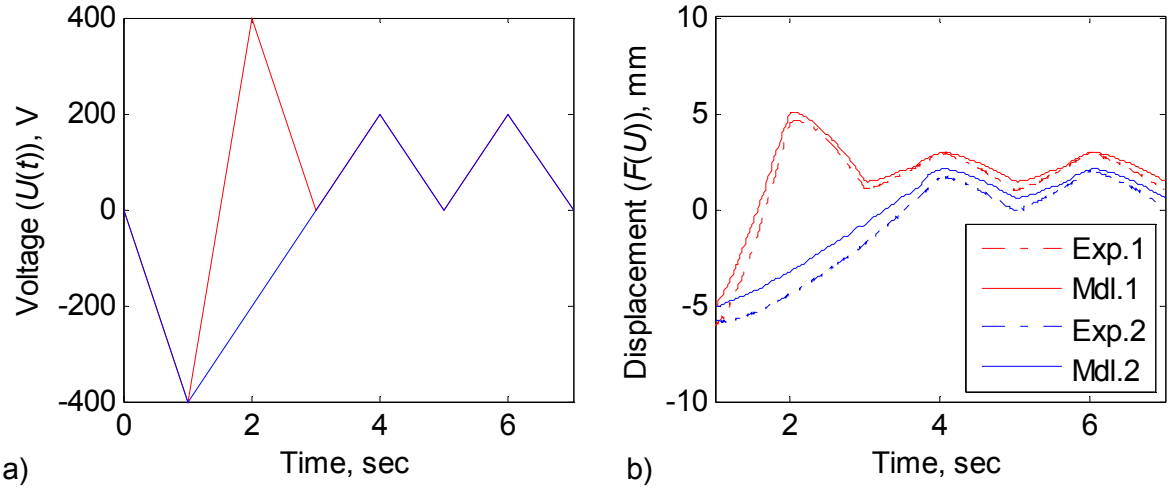

Figure 8.30: Congruency evaluation of the bimorph beam sample B6 in 1-to-1 configuration. a) Voltage input and b) displacement output time histories.

The congruency evaluation is concluded for bimorph sample B6 with the use of the decreasing-increasing first-order transition curves. The corresponding test results are presented in Figure 8.31.

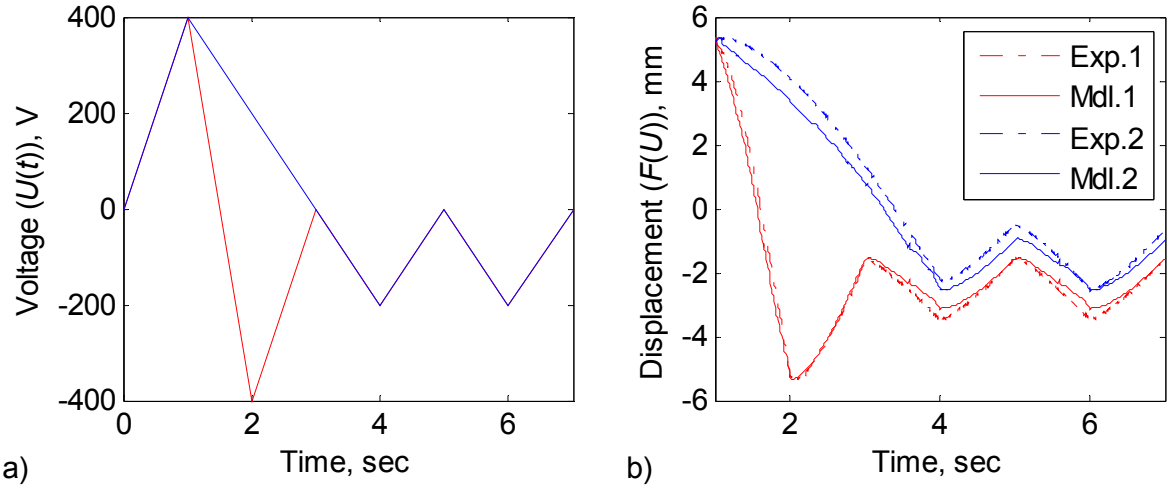

Figure 8.31: Congruency evaluation of the bimorph beam sample B6 in 1-to-1 configuration. a) Voltage input and b) displacement output time histories.

The analysis above demonstrates that the bimorph sample B6 complies to both wiping-out and congruency properties of the Preisach model. The 3-to-1 and 1-to-1 electrical configurations are also compliant with the two properties. Additional test results are presented in Section G.1.

The evaluation of the model (for bimorph sample B6) is conducted by a decaying input time history that "oscillates" between consecutive decaying extrema. This type of signal accumulates more and more memory as time passes; therefore the prediction error is expected to be higher when compared to the input time histories presented before. Figure 8.32 shows the response of the bimorph sample B6 and the model prediction for the 3-to-1 electrical configuration. Two types of input signals (and the corresponding response) are presented which employ both the increasing-decreasing and the decreasing-increasing first-order transition curves.

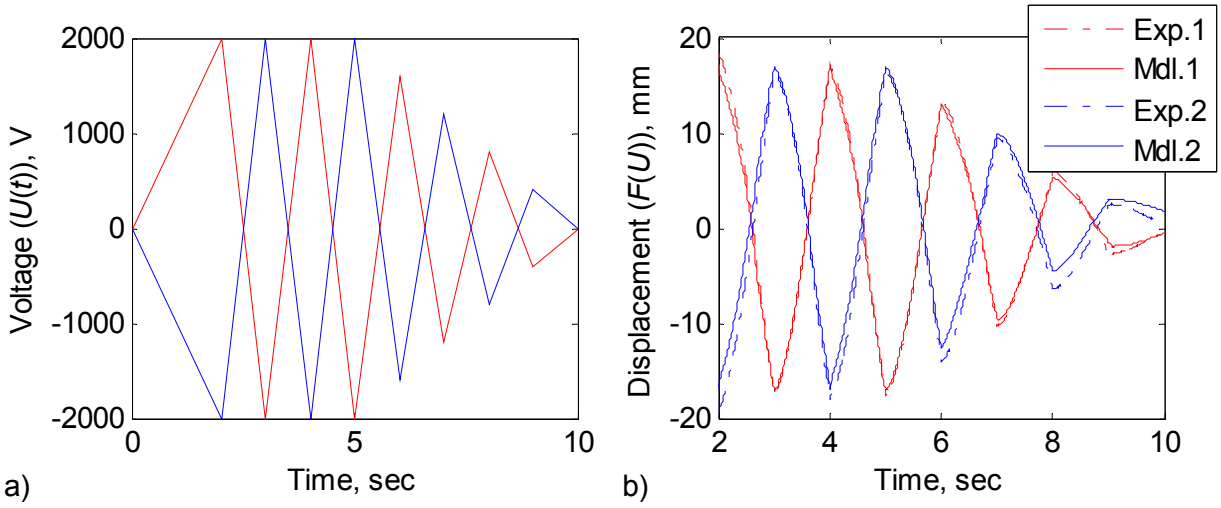

Figure 8.32: Decaying triangle input signal response of bimorph sample B6 in 3-to-1 configuration. a) Voltage input and b) displacement output time histories.

The maximum error (in the presented time frame) between the model and the experiment is 5.53% and 5.47% for the two cases. The error is given in terms of the full-scale displacement. The decaying input test is repeated for the 1-to-1 electrical configuration in Figure 8.33.

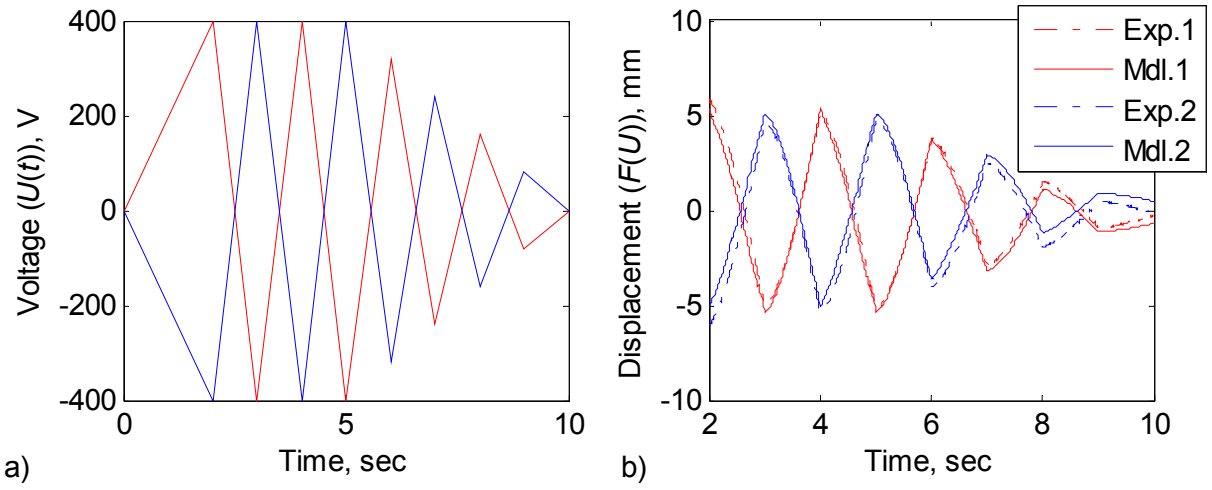

Figure 8.33: Decaying triangle input signal response of bimorph sample B6 in 1-to-1 configuration. a) Voltage input and b) displacement output time histories.

In both Figure 8.32 and Figure 8.33, the model has a small and constant offset from the experimental predictions. This offset is caused by initial displacement of the sample at the saturation input voltage (α_0 or β_0). The saturation deflection measured with the first-order transition curves is usually different than the saturation deflections observed in the arbitrary input tests. The main reason for this is that the first-order transition curves are averaged from approximately 10 loops for every minor loop and the major loop; therefore they represent a time-averaged where time-dependent effects are removed (i.e., creep). The second, less dominant reason is the very small inertial effects due to the use of a 0.5 Hz triangle input signal. The first-order transition curves can be obtained at much lower rates to reduce the dynamic effects; however the creep effects will be increased. The maximum error (in the presented time frame) between the model and the experiment is 7.21% for both cases.

The hysteresis modeling is extended to the second cantilevered bimorph specimen. As noted earlier, the bimorph sample B2 employs two MFC M8507-P1 actuators and a 0.027 mm thick stainless-steel substrate. The free length of the bimorph B2 is 86.65 mm and the laser measurement location is 80.88 mm from the clamped base. Refer to Figure 8.21 for the experimental setup. Similar to the analysis of sample B6 (above), several wiping-out, congruency and arbitrary input experiments are conducted for the sample B2. Only a few cases of the complete test matrix are presented in this section and the reader is referred to Appendix G for the complete set of experimental results. First, the increasing-decreasing and decreasing-

increasing first-order transition curves are presented for bimorph sample B2 for the 3-to-1 electrical configuration in Figure 8.34.

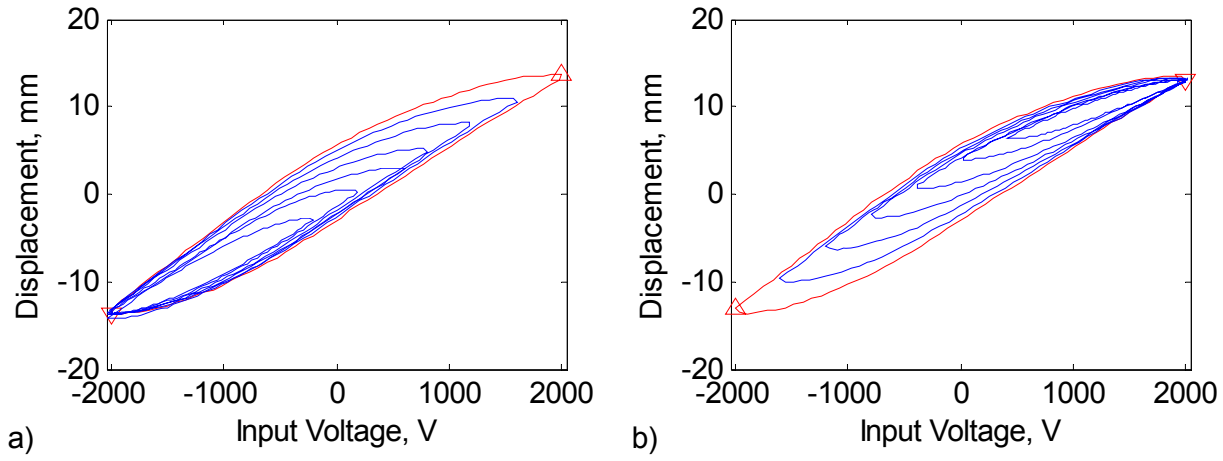

Figure 8.34: First-order transition curves for bimorph beam sample B2 in 3-to-1 configuration. a) Increasing-decreasing and b) decreasing-increasing.

Figure 8.35 presents the first-order transition curves for the bimorph sample B2 in the 1-to-1 electrical configuration.

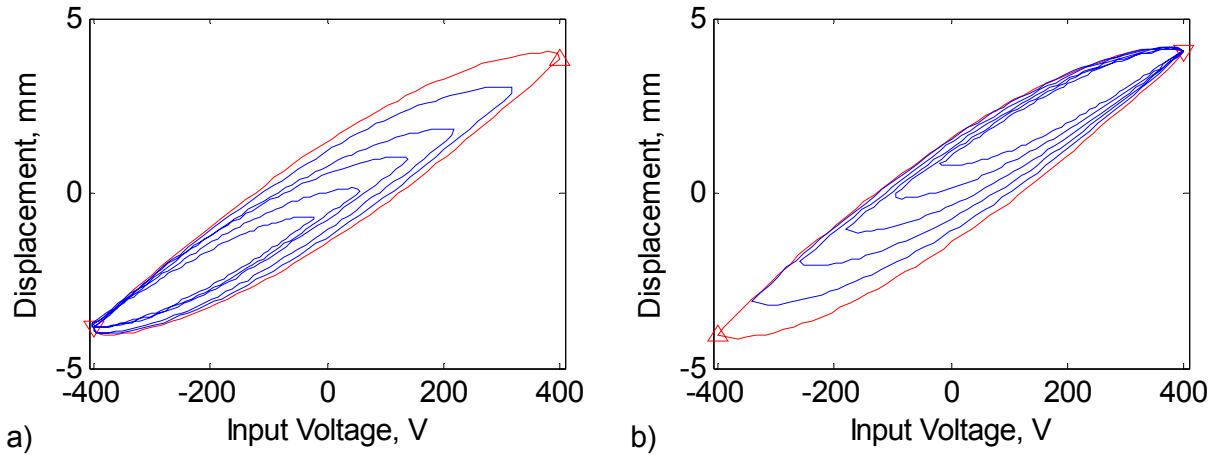

Figure 8.35: First-order transition curves for bimorph beam sample B2 in 1-to-1 configuration. a) Increasing-decreasing and b) decreasing-increasing.

First, the wiping-out property is examined for the 3-to-1 electrical configuration. Figure 8.36 shows the response of the bimorph to two input signals with different time history in the [1,4] second time frame.

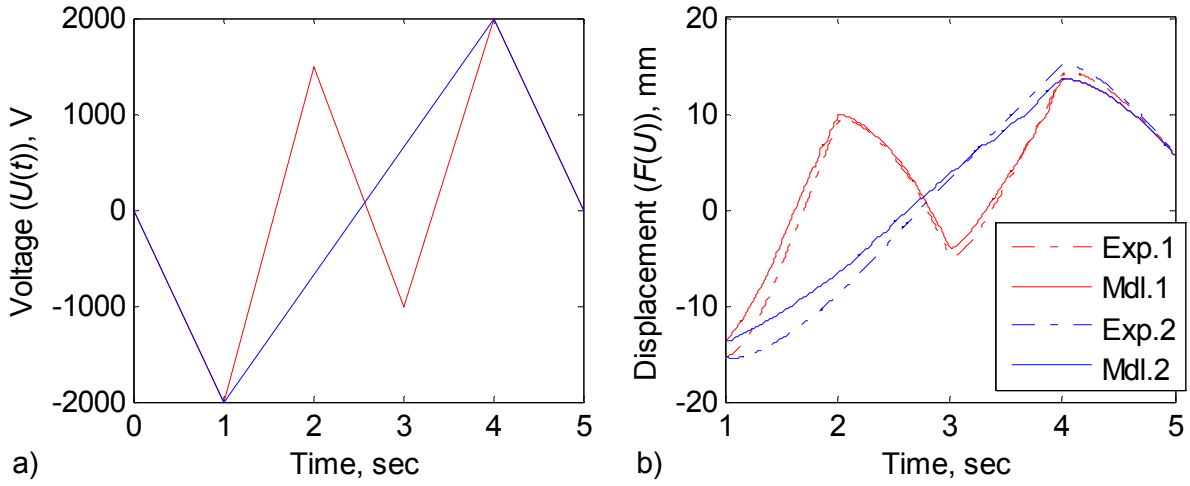

Figure 8.36: Wiping-out evaluation of bimorph beam sample B2 in 3-to-1 configuration. a) Voltage input and b) displacement output time histories.

The increasing-decreasing first order transition curves are used for the prediction presented in Figure 8.36b. The evaluation is also conducted for the 1-to-1 electrical configuration. Figure 8.37 presents the results from the wiping-out experiment applied to bimorph B2 in the 1-to-1 electrical configuration.

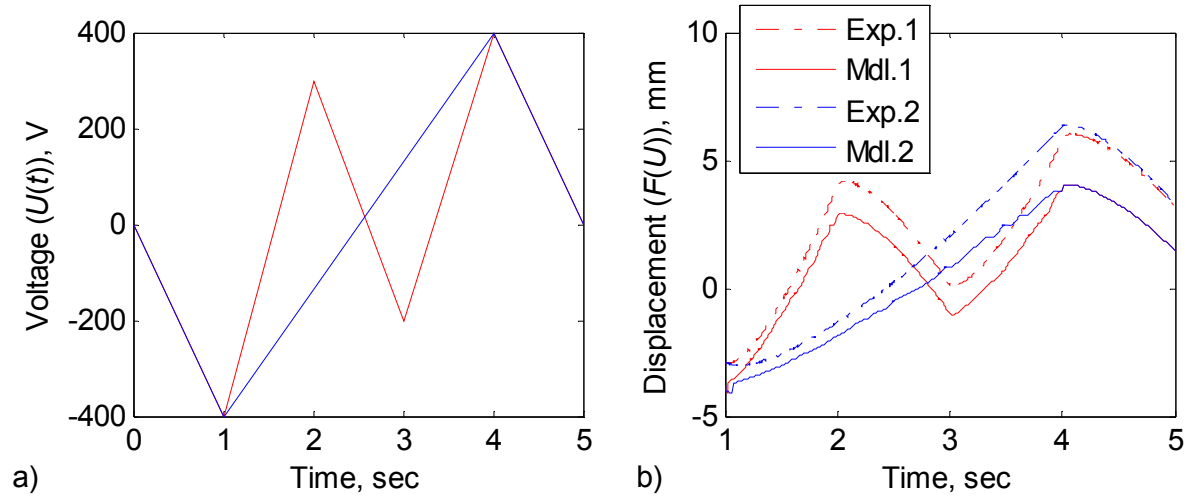

Figure 8.37: Wiping-out evaluation of bimorph beam sample B2 in 1-to-1 configuration. a) Voltage input and b) displacement output time histories.

The wiping-out property is observed for both in the experiment and in the model; however there is constant displacement offset between the actual displacement and the model prediction. This is an excellent demonstration of a low amplitude input variation (i.e., -400 V to

400 V peak-to-peak excitation in the 1-to-1 configuration) with unknown high-amplitude past input history (i.e., -2 kV to +2 kV peak-to-peak excitation in the 3-to-1 configuration). In Figure 8.37, the model is "unaware" of the previous high amplitude wiping-out tests that resulted in dominant extrema in the "memory" of the piezoceramic material. In summary, the bimorph sample B2 passed the wiping-out property examination.

The congruency property is also checked for the sample B2. As before, another set of two input time histories are generated and applied to the sample to check for this property. First, the 3-to-1 electrical configuration is evaluated. The increasing-decreasing transition curves are used in the model predictions. Figure 8.38 shows the first congruency test result for the bimorph sample B2 in the 3-to-1 electrical configuration. In the congruency tests, the two input time histories share same output in the [0,1] second time frame and in the [3,7] second time frame. As a result, the congruency of the two outputs are expected in the [4,7] second time frame.

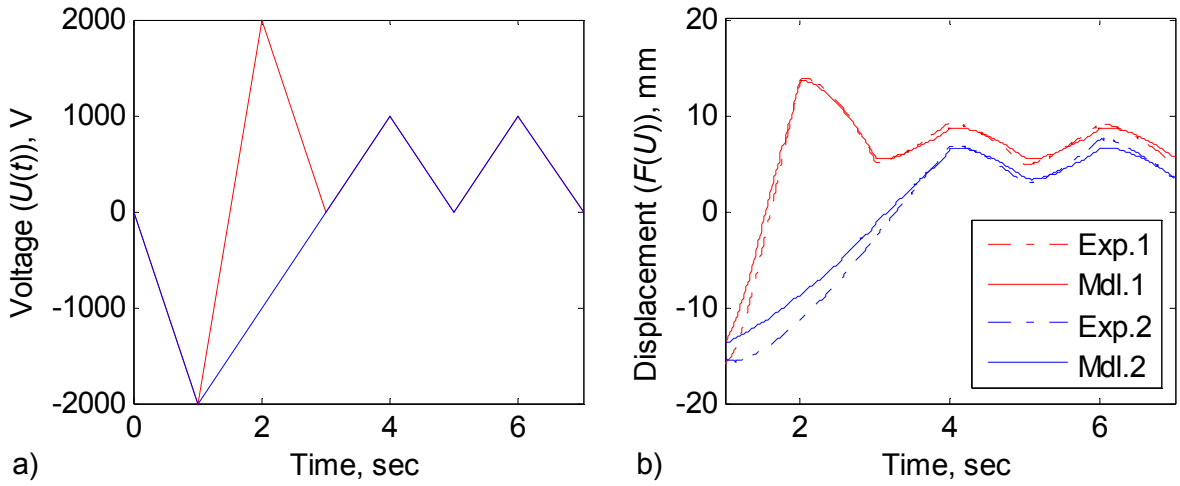

Figure 8.38: Congruency evaluation of the bimorph beam sample B2 in 3-to-1 configuration. a) Voltage input and b) displacement output time histories.

The bimorph sample B2 shows an excellent congruency in the 3-to-1 electrical configuration. The evaluation is extended to the 1-to-1 configuration and results are presented in Figure 8.39.

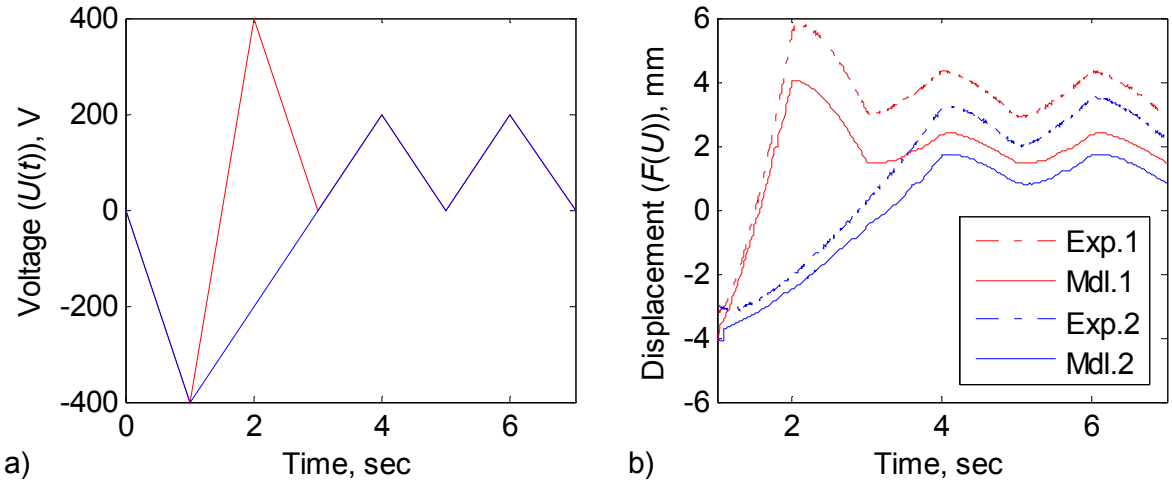

Figure 8.39: Congruency evaluation of the bimorph beam sample B2 in 1-to-1 configuration. a) Voltage input and b) displacement output time histories.

The congruency property is also demonstrated very well, both in the model and the experiment, for the 1-to-1 electrical configuration of the bimorph sample B2. As observed before in the low amplitude (1-to-1) wiping-out tests, the model is "unaware" of the previous extrema that is in the memory of the sample. In summary, the bimorph sample B2 also complies with the two properties of the Preisach model.

Finally, the evaluation of the model prediction for bimorph sample B2 is conducted by a decaying input time history that "oscillates" between consecutive decaying extrema. As noted earlier, this type of signal accumulates more and more memory as time passes; therefore the prediction error is expected to be higher when compared to the input time histories presented before. Figure 8.40 shows the response of the bimorph sample B2 and the model prediction for the 3-to-1 electrical configuration. Two types of input signals (and the corresponding response) are presented which employ both the increasing-decreasing and the decreasing-increasing first-order transition curves.

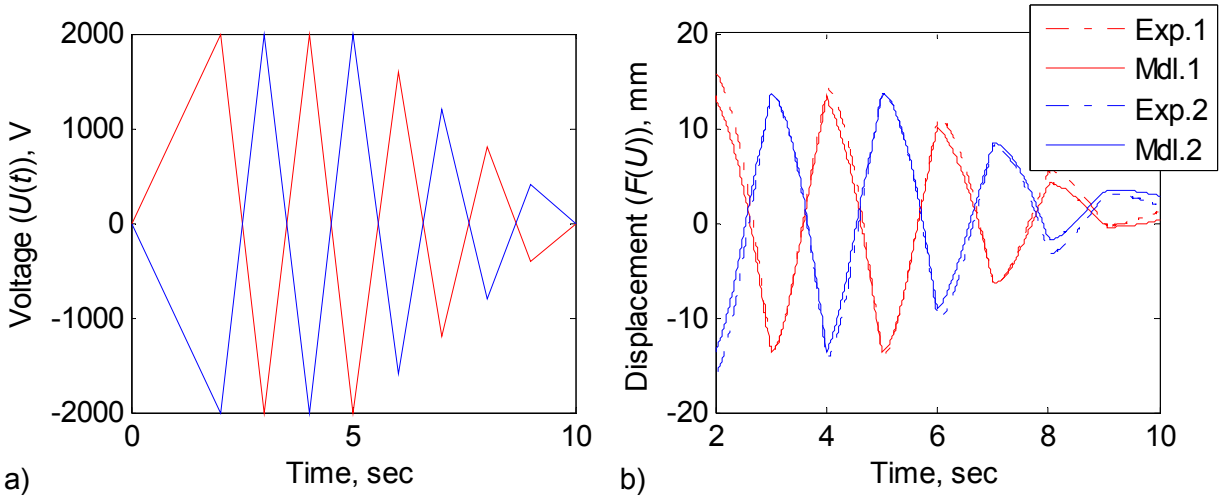

Figure 8.40: Decaying triangle input signal response of bimorph sample B2 in 3-to-1 configuration. a) Voltage input and b) displacement output time histories.

The maximum error (in the presented time frame) between the model and the experiment is 7.47% and 7.05% for the two cases. The decaying input test is repeated for the 1-to-1 electrical configuration for bimorph sample B2 in Figure 8.41.

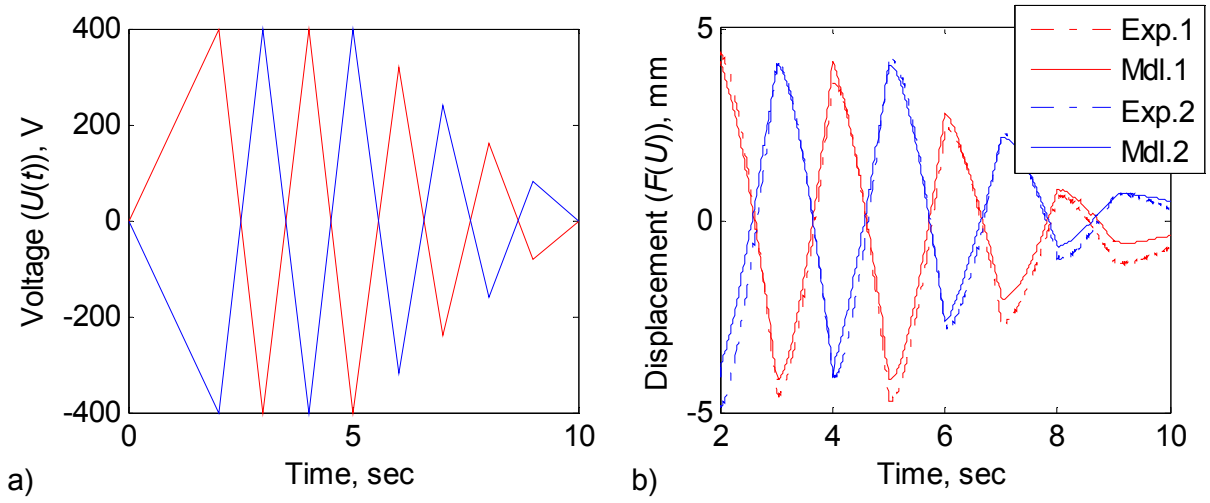

Figure 8.41: Decaying triangle input signal response of bimorph sample B2 in 1-to-1 configuration. a) Voltage input and b) displacement output time histories.

The maximum error (in the presented time frame) between the model and the experiment is 9.02% and 11.8% for the two cases. Note that the error is given in terms of the full-scale displacement. Similar to the observations made for sample B6, both Figure 8.40 and Figure 8.41

shows a small and constant offset between the model prediction and the experimental measurements. This offset is caused by initial displacement of the sample at the saturation input voltage (α_0 or β_0). The reasons for this offset are explained in detail at the end of the evaluation of sample B6. Additional test results (at 1 Hz and 5 Hz) are presented in Section G.2.

Overall, the Preisach model is capable of predicting the hysteresis observed in two bimorph samples, one with substrate and one without. Both electrical configurations, 3-to-1 and 1-to-1, are evaluated and predicted well by the model. Finally, the increasing-decreasing and decreasing-increasing first-order transition curves are found to be successful in developing the $f_{\alpha'\beta_0}$ and $f_{\beta''\alpha_0}$ databases for the Preisach model respectively.

8.4.4. Simply-Supported Thin Airfoil

The hysteresis modeling is extended to the simply-supported thin airfoil examined in Chapter 5. The specific thin airfoil sample employed here, labeled T1, is a variable-camber thin bimorph airfoil with four MFC M8557-P1 actuators, 127 mm chord and 133 mm span. Four total stainless-steel pins (two on each end) are bonded to the airfoil at 5% and 50% chord (6.35 mm and 63.5 mm respectively) from the leading edge. The bimorph is fabricated by sandwiching a 0.027 mm thick stainless-steel sheet and bonding the laminate under vacuum. The MFCs are aligned at the LE in the chordwise direction. Two layers of 0.027 mm thick stainless-steel metal (passive material) are bonded to the ends on the MFC actuators to complete the total chord to 127 mm. Stainless-steel (instead of a fiber composite) is chosen due to several reasons. Refer to Section 5.3.1 for more details on the airfoil design. The laser displacement measurement is taken at a single point that is 113 mm from the leading edge. Figure 8.42 shows the experimental setup.

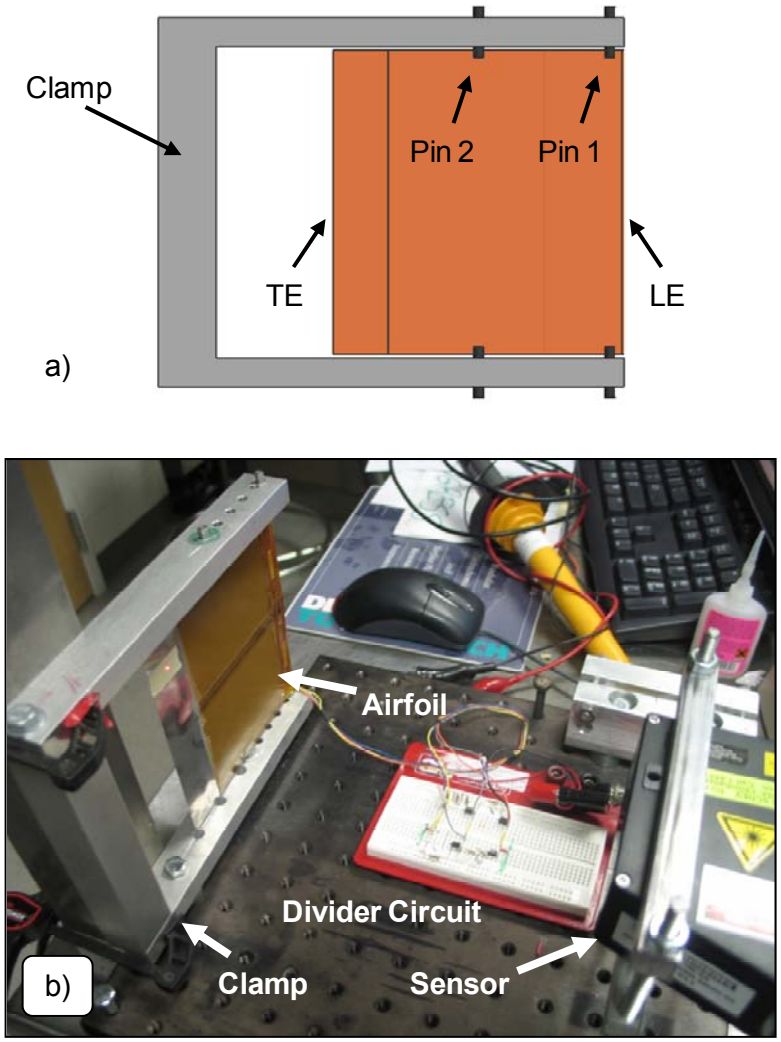

Figure 8.42: Experimental setup for hysteresis tests of thin simply-supported airfoil. a) Illustration of the clamping and boundary conditions and b) test setup.

Only a few cases of the complete test matrix are presented in this section and the reader is referred to Section G.3 for the complete set of experimental results. First, the increasing-decreasing and decreasing-increasing first-order transition curves are presented for airfoil sample T1 for the 3-to-1 electrical configuration in Figure 8.43.

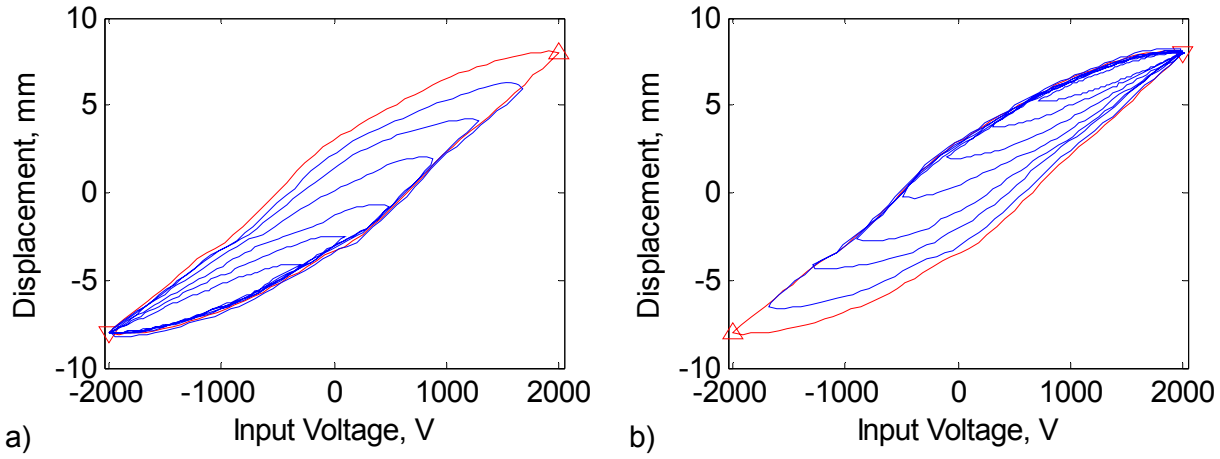

Figure 8.43: First-order transition curves for thin airfoil sample T1 in 3-to-1 configuration. a) Increasing-decreasing and b) decreasing-increasing.

The wiping-out property is presented in Figure 8.44 for the 3-to-1 electrical configuration.

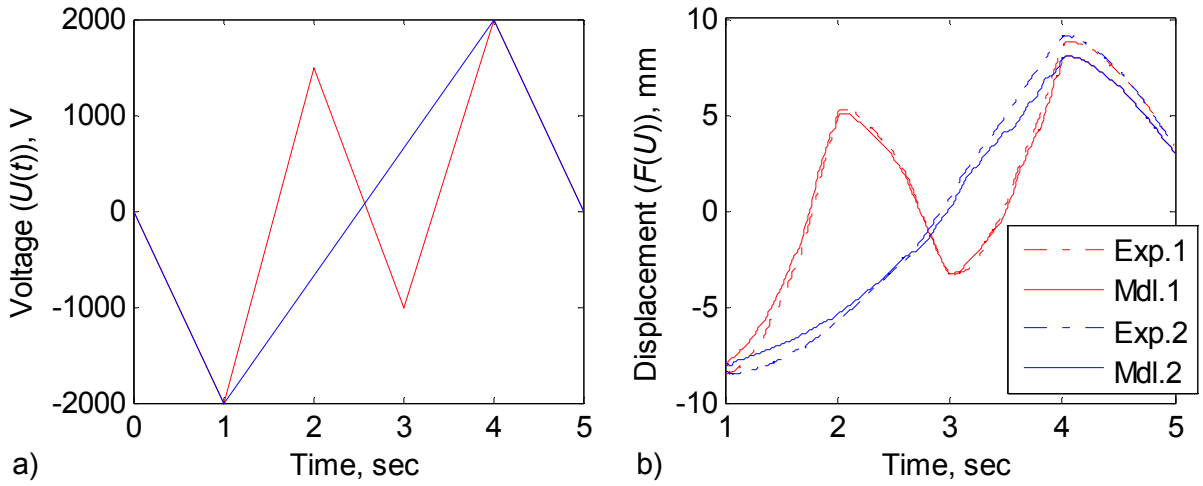

Figure 8.44: Wiping-out evaluation of thin airfoil sample T1 in 3-to-1 configuration. a) Voltage input and b) displacement output time histories.

The wiping-out property holds for 3-to-1 configuration (shown in Figure 8.44) and for 1-to-1 configuration (shown in Section G.3).

The congruency property is demonstrated in Figure 8.45 for the thin airfoil in the 3-to-1 configuration.

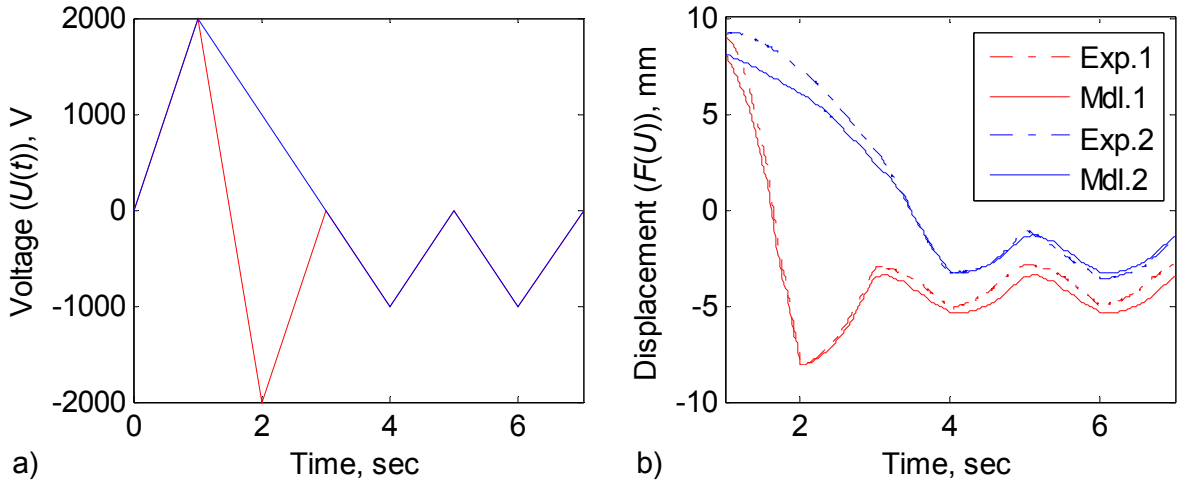

Figure 8.45: Congruency evaluation of thin airfoil sample T1 in 3-to-1 configuration. a) Voltage input and b) displacement output time histories.

The congruency property also holds for 3-to-1 configuration (shown in Figure 8.45) and for 1-to-1 configuration (shown in Section G.3).

Finally, the evaluation of the model prediction for thin airfoil sample T1 is conducted by a decaying input time history that "oscillates" between consecutive decaying extrema. Figure 8.46 shows the response of the thin airfoil and the model prediction for the 3-to-1 electrical configuration. Two types of input signals (and the corresponding response) are presented which employ both the increasing-decreasing and the decreasing-increasing first-order transition curves.

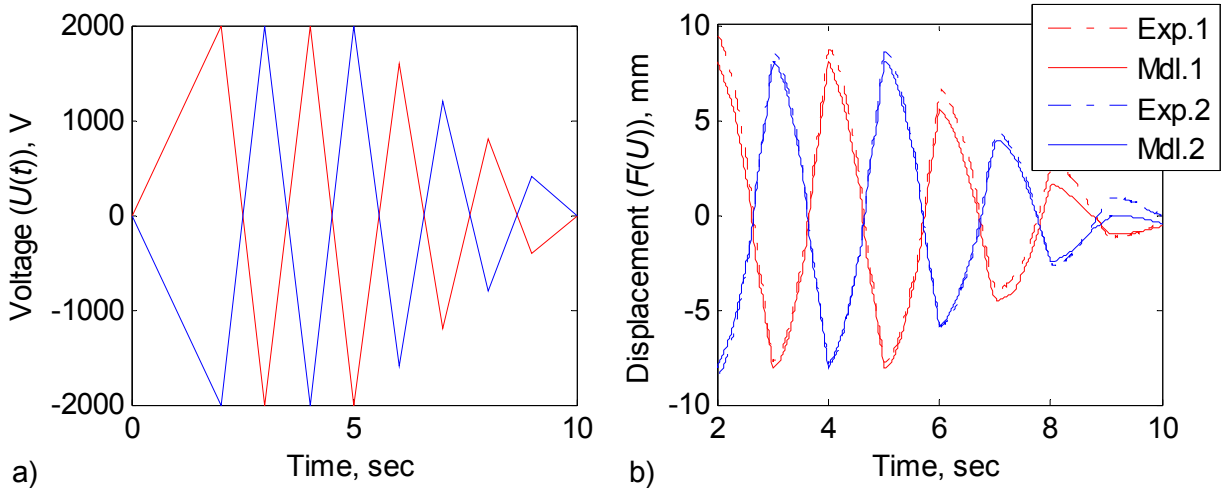

Figure 8.46: Decaying triangle input signal response of thin airfoil sample T1 in 3-to-1 configuration. a) Voltage input and b) displacement output time histories.

Similar to the observations made for bimorph beam samples B6 and B2, Figure 8.46 shows a small and constant offset between the model prediction and the experimental measurements for the thin airfoil. The maximum error (in the presented time frame) between the model and the experiment is 5.58% and 5.50% for the two cases. Note that the error is given in terms of the full-scale displacement.

In summary, the Preisach model is capable of predicting the hysteresis observed in the simply-supported thin airfoil sample T1. This results is expected because the thin airfoil is essentially in the same electromechanical configuration as the bimorph beam sample B2 (which has a 0.027 mm thick stainless-steel substrate. Both electrical configurations, 3-to-1 and 1-to-1, are evaluated and predicted well by the model. Finally, the increasing-decreasing and decreasing-increasing first-order transition curves are found to be successful in developing the $f_{\alpha'\beta_0}$ and $f_{\beta''\alpha_0}$ databases for the Preisach model respectively.

8.4.5. Cascading Bimorph Thick Airfoil

The hysteresis modeling is also extended to the cascading bimorph thick airfoil examined in Chapter 6. The specific thick airfoil sample employed here, labeled A1, is a variable-camber airfoil with eight MFC M8557-P1 actuators (two cascading bimorphs), 127 mm chord and 133 mm span. The airfoil has 15 mm thickness. The two bimorphs used in the airfoil are fabricated by sandwiching a 0.027 mm thick stainless-steel material with the MFC actuators. Refer to section 6.3.1 for detailed information on the thick airfoil design. The laser displacement measurement is taken at a single point that is 113 mm from the leading edge. The mounting rod of the airfoil is 25.4 mm from the leading edge. Figure 8.47 shows the experimental setup.

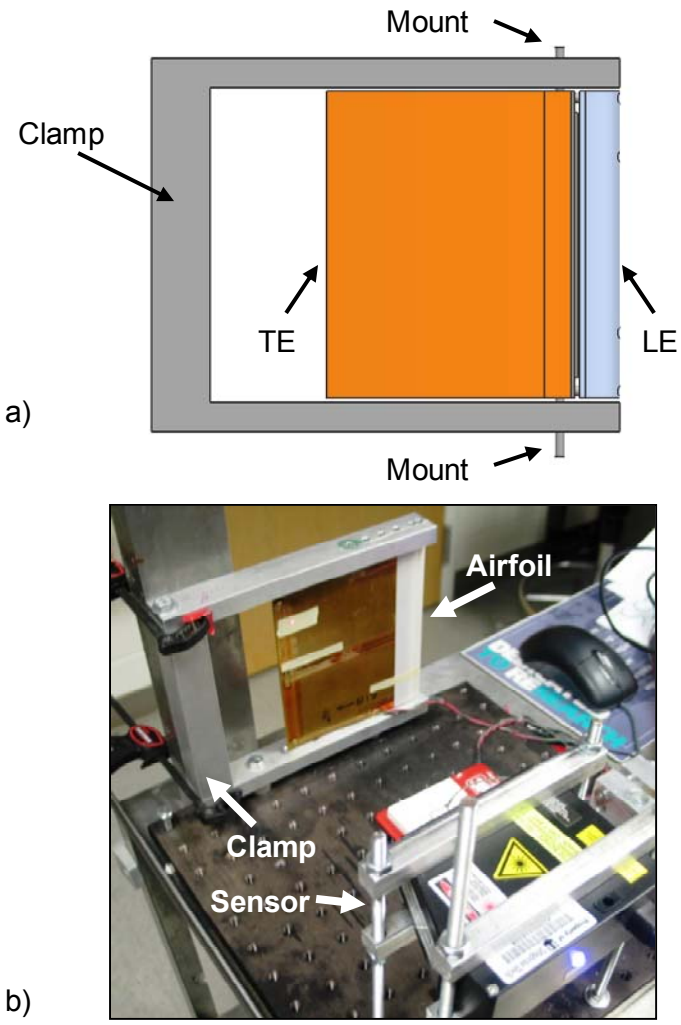

Figure 8.47: Experimental setup for hysteresis tests of cascading bimorph thick airfoil. a) Illustration of the clamping and boundary conditions and b) test setup.

Only a few cases of the complete test matrix are presented in this section and the reader is referred to Section G.4 for the complete set of experimental results. First, the increasing-decreasing and decreasing-increasing first-order transition curves are presented for airfoil sample A1 for the 3-to-1 electrical configuration in Figure 8.48.

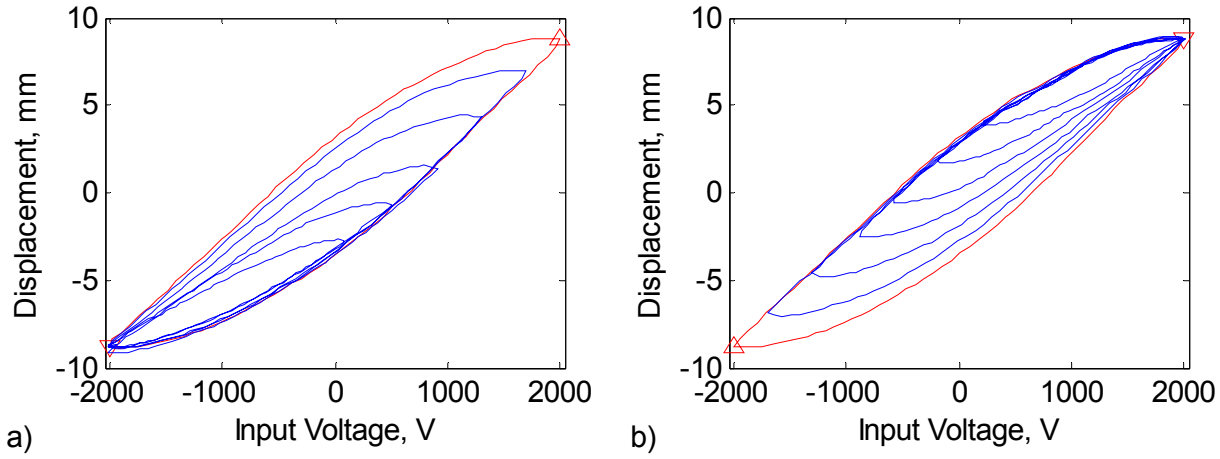

Figure 8.48: First-order transition curves for thick airfoil sample A1 in 3-to-1 configuration. a) Increasing-decreasing and b) decreasing-increasing.

The wiping-out property is presented in Figure 8.49 for the 3-to-1 electrical configuration.

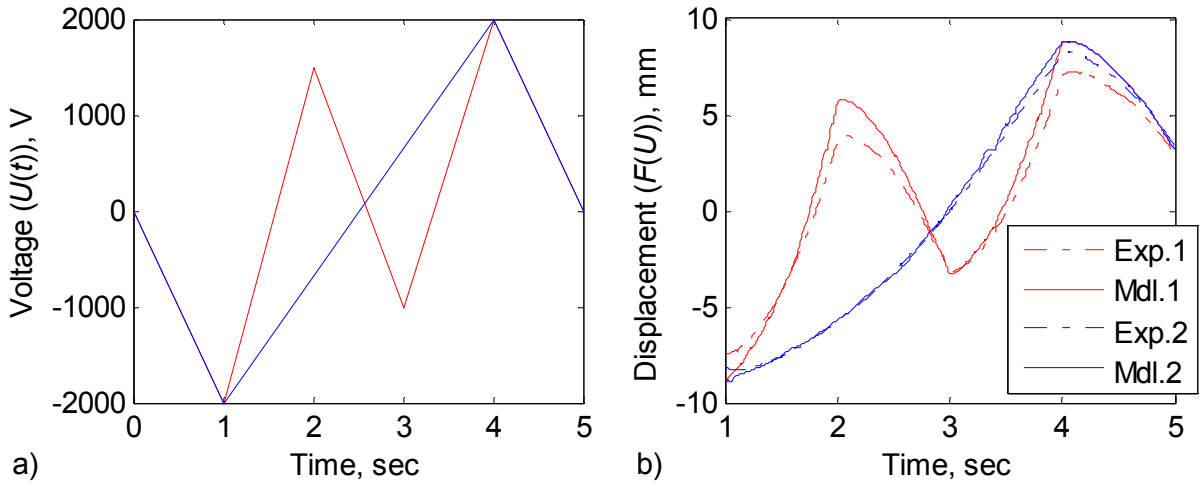

Figure 8.49: Wiping-out evaluation of thick airfoil sample A1 in 3-to-1 configuration. a) Voltage input and b) displacement output time histories.

The wiping-out property holds for 3-to-1 configuration (shown in Figure 8.49) and for 1-to-1 configuration (shown in Section G.4).

The congruency property is demonstrated in Figure 8.50 for the thick airfoil in the 3-to-1 configuration.

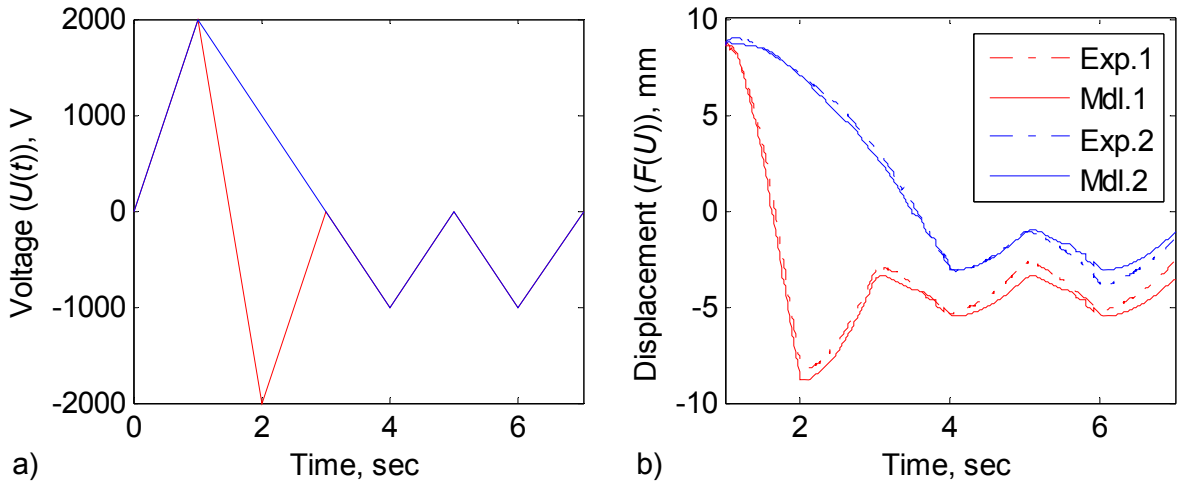

Figure 8.50: Congruency evaluation of thick airfoil sample A1 in 3-to-1 configuration. a) Voltage input and b) displacement output time histories.

The congruency property also holds for 3-to-1 configuration (shown in Figure 8.50) and for 1-to-1 configuration (shown in Section G.4).

Finally, the evaluation of the model prediction for thick airfoil sample A1 is conducted by a decaying input time history that "oscillates" between consecutive decaying extrema. Figure 8.51 shows the response of the thick airfoil and the model prediction for the 3-to-1 electrical configuration. Two types of input signals (and the corresponding response) are presented which employ both the increasing-decreasing and the decreasing-increasing first-order transition curves.

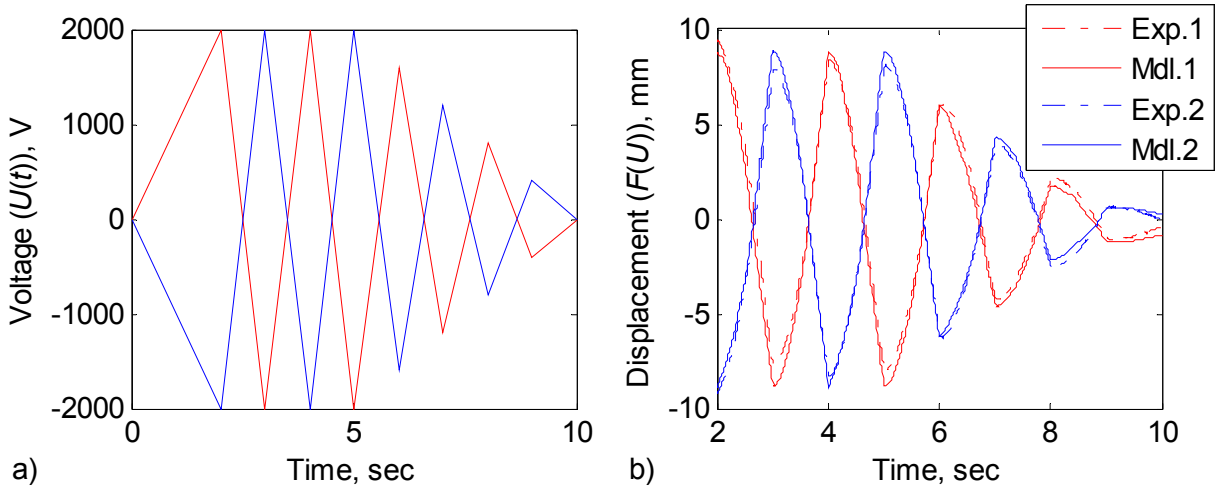

Figure 8.51: Decaying triangle input signal response of thick airfoil sample A1 in 3-to-1 configuration. a) Voltage input and b) displacement output time histories.

Similar to the observations made for bimorph beam samples B6 and B2 and the thin airfoil sample T1, Figure 8.51 shows a small and constant offset between the model prediction and the experimental measurements for the thin airfoil. The maximum error (in the presented time frame) between the model and the experiment is 6.17% and 5.50% for the two cases. Note that the error is given in terms of the full-scale displacement.

In summary, the Preisach model is capable of predicting the hysteresis observed in the cascading bimorph thick airfoil sample A1. This result is very important because the model is predicting three coupled hysteresis phenomena (arising from 1) each cascading bimorphs and 2) the compliant-box mechanism) at the same time. Both electrical configurations, 3-to-1 and 1-to-1, are evaluated and predicted well by the model. As noted for the previous three samples, the increasing-decreasing and decreasing-increasing first-order transition curves are found to be successful in developing the $f_{\alpha'\beta_0}$ and $f_{\beta''\alpha_0}$ databases for the Preisach model respectively for the thick airfoil.

8.5. Conclusions

This chapter presented the application of the classical Preisach model to predict hysteresis observed in: 1) two MFC bimorph beams, 2) the simply-supported thin airfoil, and 3) the cascading bimorph thick airfoil. The Preisach model is capable of predicting the hysteresis observed in all of the samples tested. Both electrical configurations, 3-to-1 and 1-to-1, are evaluated and predicted well by the model. The increasing-decreasing and decreasing-increasing first-order transition curves are found to be successful in developing the $f_{\alpha'\beta_0}$ and $f_{\beta''\alpha_0}$ databases for the Preisach model respectively for all samples.

CHAPTER 9

CONCLUSIONS AND FUTURE WORK

This research presented a detailed theoretical and experimental analysis of the aerodynamic and electromechanical systems that are necessary for a practical implementation a piezocomposite airfoil. This chapter first summarizes the conclusions derived in the previous chapters. Next, the academic publications that stemmed from the current research are listed. Finally, recommendations are made for the future direction of the research.

9.1. Summary of Results

Chapter 2 discussed the electromechanical response of Macro-Fiber Composite based unimorph structures in comparison to other piezoelectric materials. An electromechanical model is introduced to predict the necessary structural features that result in large electrically induced deformations. Overall, the MFC actuator demonstrated the highest actuation capability due to 1) its use of the *33* mode (due to interdigitated electrodes), 2) its flexibility (due to fibrous ceramics). From a practical perspective, the MFC actuators are far superior to other evaluated piezoelectrics in this research due to their flexibility and ease of application. It is also demonstrated that the single crystal piezoelectrics can improve the actuation performance when compared to polycrystalline ceramics; however only under certain electromechanical conditions.

Chapter 3 presented experimental results on energy harvesting from base excited unimorph clamped-free beams. The main goal of this chapter is to determine the capabilities of Macro-Fiber Composites coupled to a structure as a multifunctional transducer. In summary, the clamped-free unimorph energy harvester with MFCs demonstrated the lowest harvesting capability (per ceramic mass) due to its low capacitance. On the other hand, the MFCs are considered superior (for aircraft applications) to other piezoelectrics evaluated in the research due to their flexibility and ease of application. Monolithic polycrystalline and single crystal piezoelectrics do offer better energy harvesting capabilities when compared to fibrous,

interdigitated polycrystalline piezoceramics (such as MFCs); however the application of monolithic piezoelectric materials is not practical for large strain aerodynamic applications.

Chapter 4 demonstrated a novel, lightweight voltage divider circuit that enables the peak-to-peak actuation of Macro-Fiber Composite based bimorph devices (with asymmetric voltage input range). The experimental results show that the proposed circuit allows the division of the input voltage so that: 1) The MFC that is in extension receives +1500 V (which is the maximum positive voltage), and 2) the MFC that is in compression receives -500 V (which is the maximum negative voltage). The circuit also allows the actuation in the opposite direction without any physical changes (i.e., not using any electromechanical switches). The experimentally determined input-output relationship shows an excellent linear trend. An MFC bimorph is used to further demonstrate the wide bandwidth operation capability of the circuit.

Chapter 5 presented a simply-supported thin bimorph airfoil that can take advantage of aerodynamic loads to reduce control input moments and increase control effectiveness. The structural boundary conditions of the design are optimized by solving the coupled fluid-structure interaction problem using a structural finite element method and a panel method based on the potential flow theory for fluids. The airfoil is tested in a wind tunnel for its 2D lift and drag coefficients at low Reynolds number flow. The wind tunnel results show comparable effectiveness to conventional actuation systems. The MFC bimorph demonstrated adequate control authority for aerodynamic open-loop shape control and adequate stiffness at a tested flow speed of 15 m/s. An average lift coefficient change of 1.46 is observed purely due to peak-to-peak actuation voltage. The concept showed a small increase of drag with actuation voltage, making it an efficient variable lift generation device. A maximum 2D *L/D* ratio of 17.8 can be achieved through voltage excitation. The concept is also tested in the wind tunnel and verified to generate high control outputs in the VTOL ducted-fan vehicle. The effects of piezoceramic hysteresis are identified for both structural and aerodynamic response.

Chapter 6 presented a novel variable-camber airfoil employing two cascading bimorph surfaces (with MFC actuators) and a single four-bar (compliant box) mechanism as the internal structure. The unique choice of boundary conditions (induced by the compliant box) allows a variable and smooth deformation in both directions from a flat camber line. The compliant box allows for a desired thickness between the two cascading bimorph surfaces; hence the airfoil is significantly thicker that it's single bimorph counterpart (as shown in Chapter 5). The fabricated

concept has a 12.6% maximum thickness, 127 mm chord and a 133 mm span. Aerodynamic and structural performance results are presented for a flow rate of 15 m/s and Reynolds number of 127,000. Nonlinear effects due to aerodynamic and piezoceramic hysteresis are identified and discussed. Finally, the wind tunnel results are compared to conventional, symmetric NACA and other airfoils. The wind tunnel results show comparable effectiveness to conventional actuation systems. MFCs demonstrate adequate control authority for aerodynamic shape control. The concept shows adequate stiffness at a tested flow speed of 15 m/s. An average lift coefficient change of 1.54 is observed purely due to peak-to-peak actuation voltage. The concept showed a small increase of drag with actuation voltage, making it an efficient variable lift generation device. A maximum *L/D* ratio of 13.4 can be achieved through voltage excitation. Finally, a 72% increase in lift curve slope is achieved when compared to a NACA 0009 airfoil. Compared to previously published results, the concept presented in this research demonstrates high force outputs and frequency bandwidth (although not demonstrated in this Chapter 6). The concept is also tested and verified to generate high control outputs in the VTOL ducted-fan vehicle.

Chapter 7 discussed the design and wind tunnel evaluation of a flow control airfoil with 1) a symmetric NACA 0010 profile and 2) a variable-camber profile. MFC actuated unimorphs are used to introduce energy to the flow. The electromechanical excitation modes are identified for lift improvement by delay of laminar separation bubble using piezoceramic induced periodic excitation to the flow near the leading edge of the airfoil. The effects of amplitude, frequency and spanwise distribution of excitation are determined experimentally using the wind tunnel. The first set of wind tunnel experiments show that significant increase in lift can be achieved with 2D and 3D excitation modes. Symmetric and asymmetric excitations show different aerodynamic response due to the structural characteristics of the airfoil and its boundary conditions (i.e. the load balance). Overall, the symmetric 3D actuation results in the maximum lift enhancement at post-stall region at the lowest power consumption. A maximum lift coefficient increase of 27.5% is achieved at f_e=125 Hz, with the 3D symmetric excitation mode at 5 m/s and F^+=3.78. The second set of wind tunnel test show further evidence that significant increase in lift can be achieved by the proper distribution of excitation sources in the spanwise direction. As before, the 3D excitation achieves higher lift enhancement at post-stall region with lower power consumption when compared to uniform excitation (2D). A maximum lift coefficient increase of

18.4% is achieved at f_e=125 Hz, with the identified 3D symmetric excitation mode at 5 m/s and F^+=3.78. Cl_{max} is increased 5.2% from the baseline.

Chapter 8 presented the effects of piezoceramic hysteresis for Macro-Fiber Composite actuated bimorph type devices. The hysteretic open-loop response is predicted using a phenomenological classical Preisach model. The Preisach model is capable of predicting the hysteresis observed in 1) two MFC bimorph beams, 2) the simply-supported thin airfoil, and 3) the cascading bimorph thick airfoil. Both electrical configurations, 3-to-1 and 1-to-1, are evaluated and predicted well by the model. The increasing-decreasing and decreasing-increasing first-order transition curves are found to be successful in developing the $f_{\alpha'\beta_0}$ and $f_{\beta''\alpha_0}$ databases for the Preisach model respectively for all samples.

9.2. Related Publications

Portions of this dissertation have been presented at various peer-reviewed journals and professional conferences. These works are the foundation for this dissertation. Below is a list of related published journal articles, and conference papers and presentations.

9.2.1. Journal Papers

Bilgen, O., Kochersberger, K. B., and Inman, D. J., "Novel, Bi-Directional, Variable Camber Airfoil via Macro-Fiber Composite Actuators," *AIAA Journal of Aircraft*, **47**(1), pp 303-314, 2010.

Bilgen, O., Kochersberger, K. B., and Inman, D. J., "Macro-Fiber Composite Actuated Simply-Supported Thin Morphing Airfoils," *Journal of Smart Material and Structures*, **19**, 055010, 2010.

Bilgen, O., Erturk, A., and Inman, D. J., "Analytical and Experimental Characterization of Macro-Fiber Composite Actuated Thin Clamped-Free Unimorph Benders," *ASME Journal of Vibration and Acoustics*, **132**(5), 051005, 2010.

Bilgen, O., De Marqui Junior, C., Kochersberger, K. B., and Inman, D. J., "Piezoceramic Composite Actuators for Flow Control in Low Reynolds Number Airflow," *Journal of Intelligent Material Systems and Structures*, fully accepted for publication July 15, 2010.

Bilgen, O., Kochersberger, K. B., Inman, D. J., and Ohanian, O. J., "Lightweight High Voltage Electronic Circuits for Piezoelectric Composite Actuators," *Journal of Intelligent Material Systems and Structures*, fully accepted for publication July 16, 2010.

Bilgen, O., De Marqui Junior, C., Kochersberger, K. B., and Inman, D. J., "Flow Control Techniques for Variable Camber Airfoils in Low Reynolds Number Airflow," *Journal of Intelligent Material Systems and Structures*, submitted May 21, 2010.

Bilgen, O., Wang, Y., and Inman, D. J., "Electromechanical Comparison of Cantilevered Beams with Multifunctional Piezoceramic Devices," *Mechanical Systems and Signal Processing*, submitted June 19, 2010.

9.2.2. Conference Papers and Presentations

Bilgen, O., Kochersberger, K. B., and Inman, D. J., "Lightweight High Voltage Electronic Circuits for Piezoelectric Composite Actuators," Presentation, Second Annual Center for Intelligent Material Systems and Structures Conference, Roanoke, VA, March 4, 2010.

Bilgen, O., De Marqui, C., Kochersberger, K. B., and Inman, D. J., "Flow Control via Piezoceramic Actuators with an Application to a Variable-Camber Airfoil via MFCs," Paper and Poster Presentation, 20th International Conference on Adaptive Structures and Technologies, Hong-Kong, China, October 20-22, 2009.

Bilgen, O., Kochersberger, K. B., and Inman, D. J., "Piezoceramic Actuated Variable-Camber Airfoils: Design, Modeling and Testing," Presentation, 1st Annual Center for Intelligent Material Systems and Structures Conference, Blacksburg, VA, August 20, 2009.

Bilgen, O., Ohanian, J. O., Kochersberger, K. B., and Inman, D. J., "Novel, Bi-Directional, Variable Camber Airfoil via Macro-Fiber Composite Actuators," AIAA 2009-2133, 50th AIAA/ASME/ASCE/AHS/ASC Structures, Structural Dynamics, and Materials Conference, Palm Springs, California, May 6, 2009.

Bilgen, O., Erturk, A., Inman, D. J., and Kochersberger, K. B., 'Macro-Fiber Composite Actuated Thin Clamped-Free Benders and Thin Simply-Supported Morphing Airfoils,' 19th International Conference on Adaptive Structures and Technologies, Ascona, Switzerland, October 6-9, 2008.

Bilgen, O., Kochersberger, K. B., and Inman, D. J., "A Novel Aerodynamic Vectoring Control Airfoil via Macro-Fiber Composite Actuators," AIAA-2008-1700, 49th

AIAA/ASME/ASCE/AHS/ASC Structures, Structural Dynamics, and Materials Conference, Schaumburg, Illinois, 7-10 April, 2008.

Bilgen, O., Kochersberger, K. B., and Inman, D. J., "An Experimental and Analytical Study of a Flow Vectoring Airfoil via Macro-Fiber-Composite Actuators," Proc. of SPIE Vol. 6930, SPIE Smart Structures & NDE 2008, San Diego, California, 9-13 March 2008.

9.3. Future Work

This research provides strong evidence that piezocomposite airfoils can be used in small unmanned aircraft. The structural and electromechanical response of the piezocomposite airfoils (and similar devices) is characterized in detail. On the other hand, fine position control of these systems is not addressed. In order to achieve fine position control (which is required from a flight control perspective,) further nonlinear modeling must be conducted to include 1) structural dynamic, 2) piezoceramic creep, and 3) aerodynamic loading effects in to the Preisach hysteresis model. This requires the employment of more generalized versions of the Preisach model (i.e., vector Preisach model). Once all of the nonlinear effects are compensated, linear feedback controllers can be used to achieve a desired response. In addition, adaptive control laws can achieve further improvement is the response of the piezocomposite airfoils and similar bimorph or unimorph devices.

REFERENCES

"AIAA Standard on Assessment of Experimental Uncertainty with Application to Wind Tunnel Testing," S-071A-1995, AIAA, New York, 1995.

Acharya, M., Emo, S., Bugajski, D., and Williams, D., "Smart Vanes for UCAV Engine Applications," 2nd AIAA Flow Control Conference, Portland, Oregon, AIAA 2004-2516, 28 June - 1 July 2004.

Albertani, R., Hubner, J. P., Ifju, P. G., Lind, R., and Jackowski, J., "Experimental Aerodynamics of Micro Air Vehicles," SAE World Aviation Congress and Exhibition, Paper 04AER-8, Nov 2004.

AM1505. Online data sheet for AM Power Systems dc-dc converter, [http://www.ampowersystems.net/thunder.htm]

ANSYS. Computer Software, version 12.0. [http://www.ansys.com/products/ansys12-new-features.asp]

Anton, S. R. and Sodano, H. A., "A review of power harvesting using piezoelectric materials (2003-2006)," *Journal of Smart Materials and Structures*, **16**, pp. 1, 2007.

Barlow, J. B., Rae, W. H., and Pope, A., *Low-Speed Wind Tunnel Testing*, 3 Sub edition, Wiley-Interscience, New York, NY, February 22, 1999.

Barrett, R. M., Vos, R., Tiso, P., and De Breuker, R., "Post-Buckled Precompressed (PBP) Actuators: Enhancing VTOL Autonomous High Speed MAVs," 46th AIAA/ASME/ASCE/AHS/ASC Structure, Structural Dynamics & Materials Conference, AIAA 2005-2113, Austin, Texas, Apr. 18-21, 2005.

Bartley-Cho, J. D., Wang, D. P., and West, M. N., "Development, Control, and Test Results of High-Rate, Hingeless Trailing Edge Control Surface for the Smart Wing Phase 2 Wind Tunnel Model," Smart Structures and Materials 2002: Industrial and Commercial Applications of Smart Structures Technologies, Proceedings of SPIE, Vol. 4698, 2002.

Bent, A. A., Active Fiber Composites for Structural Actuation, Ph.D. Dissertation, Massachusetts Institute of Technology, Cambridge, MA, 1997.

Bent, A. A. and Hagood, N. W., "Piezoelectric Fiber Composites with Interdigitated Electrodes," *Journal of Intelligent Material Systems and Structures*, **8**(11), 1997.

Bilgen, O., Kochersberger, K. B., and Inman, D. J., "Macro-Fiber Composite Actuators for a Swept Wing Unmanned Aircraft," *Aeronautical Journal*, Special issue on Flight Structures Fundamental Research in the USA, publication of Royal Aeronautical Society, **113**, No. 1144, 2009.

Bilgen, O., Kochersberger, K. B., Diggs, E. C., Kurdila, A. J., and Inman, D. J., "Morphing Wing Aerodynamic Control via Macro-Fiber-Composite Actuators in an Unmanned Aircraft," AIAA-2007-2741, AIAA Infotech @ Aerospace Conference, Rohnert Park, California, May 7-10, 2007.

Bilgen, O., Kochersberger, K. B., Diggs, E. C., Kurdila, A. J., and Inman, D. J., "Morphing Wing Micro-Air-Vehicles via Macro-Fiber-Composite Actuators," AIAA-2007-1785, 48th AIAA/ASME/ASCE/AHS/ASC Structures, Structural Dynamics, and Materials Conference, Honolulu, Hawaii, Apr. 23-26, 2007.

Cadogan, D., Smith, T., Lee, R., Scarborough, S., and Graziosi, D., "Inflatable and Rigidizable Wing Components for Unmanned Aerial Vehicles," AIAA 2003-6630, 44th AIAA/ASME/ASCE/AHS/ASC Structures, Structural Dynamics and Materials Conference, Norfolk, VA, April, 2003.

Cadogan, D., Smith, T., Uhelsky, F., and Mackusick, M., "Morphing Inflatable Wing Development for Compact Package Unmanned Aerial Vehicles," AIAA-2004-1807, 45th AIAA/ASME/ASCE/AHS/ASC Structures, Structural Dynamics and Materials Conference, Palm Springs, CA, April, 2004.

Ceracomp PMN-PZT. Online data sheet. [http://www.ceracomp.com/sub/sub03_01_05.php]

Choi, B.J., Lee, Y.J., and Choi, B.Y., "Fast Preisach modeling method for shape memory alloy actuators using major hysteresis loops," *Journal of Smart Materials and Structures*, **13**, pp. 1069-1080, 2004.

Cook-Chennault, K. A., Thambi, N., and Sastry, A. M., "Powering MEMS portable devices—a review of non-regenerative and regenerative power supply systems with special emphasis on piezoelectric energy harvesting systems," *Journal of Smart Materials and Structures*, **17**, 043001, 2008.

Crawley, E. F. and Anderson, E. H., "Detailed Models of Piezoceramic Actuation of Beams," *Journal of Intelligent Material Systems and Structures*, **1**(1), pp. 4-25, 1990.

Dosch, J. J., Calamita, J.P., and Inman, D. J., "Performance of a programmable structure," Smart Structures and Materials 1993: Mathematics in Smart Structures, Albuquerque, NM, USA, 1993.

Drela, M., 'XFOIL: An Analysis and Design System for Low Reynolds Number Airfoils,' Conference on Low Reynolds Number Airfoil Aerodynamics, University of Notre Dame, June 1989.

Erturk, A. and Inman, D. J., "A Distributed Parameter Electromechanical Model for Cantilevered Piezoelectric Energy Harvesters," *ASME Journal of Vibration and Acoustics*, **130**, 041002, 2008.

Erturk, A., Bilgen, O., Fontenille, M., and Inman, D. J., 2008, 'Piezoelectric energy harvesting from macro-fiber composites with an application to morphing-wing aircrafts,' 19th International Conference on Adaptive Structures and Technologies, Ascona, Switzerland, October 6-9, 2008.

Erturk, A. and Inman, D. J., "An Experimentally Validated Bimorph Cantilever Model for Piezoelectric Energy Harvesting from Base Excitations," *Journal of Smart Materials and Structures*, **18**, 025009, 2009.

Erturk, A., Anton, S. R., Bilgen, O., and Inman, D. J., "Effect of Material Constants and Mechanical Damping on Piezoelectric Power Generation," Proceedings, 22nd Biennial Conference on Mechanical Vibration and Noise (VIB) at the ASME Design Engineering Technical Conference, San Diego, CA, August 30 - September 2, 2009.

Everett, D. H. and Whitton, W. I., "A general approach to hysteresis," *Transactions of Faraday Society*, **48**, pp. 749-757 , 1952.

Fanson, J. L. and Caughey, T. K., "Positive position feedback control for large space structures," *AIAA Journal*, **28**, pp. 717-24, 1990.

Fox, R. W., McDonald, A. T., and Pritchard, P. J., *Introduction to Fluid Mechanics*, 6th ed., John Wiley & Sons, New York, NY, 2004.

Friswell, M. I., Inman, D. J., and Rietz, R. W., "Active damping of thermally induced vibrations," *Journal of Intelligent Material Systems and Structures*, **8**, pp. 678-85, 1997.

Gad-el-Hak, M., “Control of Low-Speed Airfoil Aerodynamics,” *AIAA Journal*, **28**(9), pp. 1537–1552, 1990.

Garcia, H. M., Abdulrahim, M., and Lind, R., “Roll Control for a Micro Air Vehicle Using Active Wing Morphing,” AIAA 2003~5347.

Ge, P. and Jouaneh, M., “Modeling hysteresis in piezoceramic actuators,” *Precision Engineering*, **17**, pp. 211-221, 1995.

Ge, P. and Jouaneh, M., “Tracking control of a piezoceramic actuator,” *IEEE Transactions on Control Systems Technology*, **4**(3), pp. 513-518, 2000.

Giurgiutiu, V., “Review of Smart-Materials Actuation Solutions for Aeroelastic and Vibration Control,” *Journal of Intelligent Material Systems and Structures*, **11**, July 2000.

Giurgiutiu, V., Chaudhry, Z., and Rogers, C. A., "Engineering Feasibility of Induced-Strain Actuators for Rotor Blade Active Vibration Control", Smart Structures and Materials '94 Conference, Orlando, Florida, Paper # 2190-11, SPIE Volume 2190, pp. 107-122, 13-18 February 1994.

Glezer, A., Amitay, M., and Honohan, A., “Aspects of Low- and High-Frequency Actuation for Aerodynamic Flow Control,” *Journal of AIAA*, **43**(7), pp. 1501 – 1511, 2005.

Goh, C. J. and Caughey, T. K., “On the stability problem caused by finite actuator dynamics in the collocated control of large space structures,” *International Journal of Control*, **41**, pp. 787-802, 1985.

Goh, C. J., “Analysis and Control of Quasi Distributed Parameter Systems,” in Department of Mechanical Engineering, California Institute of Technology, Pasadena, CA, pp. 54 , 1983.

Gomes, L. D., Crowther, W. J., and Wood, N. J., ”Towards A Practical Piezoceramic Diaphragm Based Synthetic Jet Actuator For High Subsonic Applications – Effect Of Chamber And Orifice Depth On Actuator Peak Velocity,” 3rd AIAA Flow Control Conference, San Francisco, California, AIAA 2006-2859, 5 - 8 June 2006.

Greenblatt, D. and Wygnanski, I. J., “The Control of Flow Separation by Periodic Excitation,” *Progress in Aerospace Sciences*, **36**, pp. 487-545, 2000.

Hagood, N. W. and Bent, A. A., “Development of Piezoelectric Fiber Composites for Structural Actuation,” 34th AIAA/ASME/ASCE/AHS/ASC Structures, Structural Dynamics and Materials Conference, La Jolla, CA, AIAA Paper No. 93-1717-CP, pp. 3625-3638, 1993.

Hagood, N. W., Kindel, R., Ghandi, K., and Gaudenzi, P., "Improving Transverse Actuation using Interdigitated Surface Electrodes," SPIE Paper No. 1917-25, 1993 North American Conference on Smart Structures and Materials, Albuquerque, NM, pp. 341-352, 1993.

High, J. W. and Wilkie, W. K., "Method of Fabricating NASA-Standard Macro-Fiber Composite Piezoelectric Actuators," NASA/TM-2003-212427, ARL-TR-2833, 2003.

Hoerner, S. F., *Fluid Dynamic Drag*, Hoerner Fluid Dynamics, June 1993.

Hoerner, S. F., *Fluid Dynamic Lift*, published by Mrs. Liselotte A. Hoerner, Hoerner Fluid Dynamics, P.O. Box 342, Brick Town, N.J. 08723, Chapter 2, 1975.

Hughes, D. and Wen, J.T., "Preisach modeling of piezoceramic and shape memory alloy hysteresis," *Journal of Smart Materials and Structures*, **6**, pp. 287-300, 1997.

Ifju, P. G., Ettinger, S., Jenkins, D. A., and Martinez, L., "Composite Materials for Micro Air Vehicles," SAMPE Annual Conference, Long Beach CA, May 6-10, 2001.

Ifju, P. G., Jenkins, D. A., Ettinger, S., Lian, Y., Shyy, W., and Waszak, M. R., "Flexible-Wing-Based Micro Air Vehicles," AIAA Annual Conference, AIAA-2002-0705. January 2002.

Inman, D. J. and Cudney, H. H., "Structural and Machine Design Using Piezoceramic Materials: A Guide for Structural Design Engineers," Final Report to NASA Langley Research Center, NASA Langley Grant NAG-1-1998, April 30, 2000.

Jha, A. K. and Kudva, J. N., "Morphing Aircraft Concepts, Classifications, and Challenges", Proceedings of SPIE Vol. 5388, 2004.

Joslin, R. D., "Aircraft Laminar Flow Control," *Annual Review of Fluid Mechanics*, **30**, pp. 1–29, 1998.

Kim, D. K. and Han, J. H., "Smart Flapping Wing using Macro-Fiber Composite Actuators," Proceedings of SPIE Vol.6173 61730F, pp. 1-9, 2006.

Kim, D. K., Kim, H. I., Han, J. H., Kwon, K. J., "Experimental Investigation on the Aerodynamic Characteristics of a Bio-mimetic Flapping Wing with Macro-Fiber Composites," *Journal of Intelligent Materials, Systems, and Structures,* **19**(3), pp. 423-431, March 2008.

Kim, D. K., Han, J. H., Kwon, K. J., "Wind Tunnel Tests for a Flapping Wing Model with a Changeable Camber using Macro-Fiber Composite Actuators," *Journal of Smart Materials and Structures*, **18**(2), 2009.

Krasnosel'skii, M. and Pokrovskii, A., *Systems with Hysteresis*, Nauka, Moscow, 1983.

Lazarus, K. B., Crawley, E. F., and Bohlmann, J.D., "Static Aeroelastic Control Using Strain Actuated Adaptive Structures," *Journal of Intelligent Materials, Systems, and Structures*, **2**, pp. 386-410, July 1991.

Leo, D. J. and Inman, D. J., "Pointing control and vibration suppression of a slewing flexible frame," *Journal of Guidance, Control, and Dynamics*, **17**, pp. 529-36, 1994.

Lesieutre, G. and Davis, C., "Can a Coupling Coefficient of a Piezoelectric Device be Higher Than Those of Its Active Material?" *Journal of Intelligent Materials Systems and Structures*, **8**(10), pp. 859-867, 1997.

Lloyd, J. M., "Electrical Properties of Macro-Fiber Composite Actuators and Sensors," M.S. Thesis, Mechanical Engineering Dept., Virginia Tech, Blacksburg, VA, June 22nd, 2004.

MATLAB. Computer Software, version R2009b. [http://www.mathworks.com/products/matlab/]

Mayergoyz, I., *Mathematical Models of Hysteresis and their Applications*, Series in Electromagnetism, Elsevier, New York, NY, 2003.

MFC M8507-P1. Online data sheet. [http://www.smartmaterial.us/media/Datasheet/MFC_ENG_WEB.pdf]

MFC M8528-P1. Online data sheet. [http://www.smart-material.com/MFC/P1_types.php]

MFC M8557-P1. Online data sheet. [http://www.smart-material.com/MFC/P1_types.php]

MIDE QP10N. Online data sheet. [http://www.mide.com/products/qp/qp10n.php]

Moses, R. W., Weisman, C. D., Bent, A. A., and Pizzochero, A. E., "Evaluation of New Actuators in a Buffet Loads Environment," SPIE 8th Annual International Symposium on Smart Structures and Materials, Newport Beach, CA, 2001.

Mueller, T. J., "Aerodynamic Measurements at Low Reynolds Numbers for Fixed Wing Micro-Air Vehicles," presented at the "Development and Operation of UAVs for Military and Civil Applications" course held at the von Karman Institute for Fluid Dynamics, Belgium, September 13-17, 1999.

Mueller, T. J. and Burns, T. F., "Experimental Studies of the Eppler 61 Airfoil at Low Reynolds Numbers," AIAA Paper 82-0345, January 1982.

Murray, J., Pahle, J., Thornton, S., Frackowiak, T., Mello, J., and Norton, B. "Ground and Flight Evaluation of a Small-Scale Inflatable-Winged Aircraft," AIAA 2002-0820, 40th AIAA Aerospace Sciences Meeting & Exhibit, Reno, NV, Jan. 14–17,2005.

Park, J. S. and Kim, J. H., "Analytical development of single crystal Macro Fiber Composite actuators for active twist rotor blades," *Journal of Smart Materials and Structures*, **14**, pp. 745-753, 2005.

Patel, M.P., Ng, T.T., Vasudevan, S., Corke, T.C., and He, C., "Plasma Actuators for Hingeless Aerodynamic Control of an Unmanned Air Vehicle," *AIAA Journal of Aircraft*, **44**(4), July–August 2007.

Pelletier, A. and Mueller, T. J., "Low Reynolds Number Aerodynamics of Low Aspect-Ratio, Thin/Flat/Cambered-Plate Wings," *AIAA Journal of Aircraft*, **37**(5), September-October 2000.

Pern, N. J., Jacob, J., and LeBeau, R., "Characterization of Zero Mass Flux Flow Control for Separation Control of an Adaptive Airfoil," AIAA Paper 2006-3032, 36th Fluid Dynamics Conference, June, 2006.

Prandtl, L., "Mutual Influence of Wings and Propeller," NACA Technical Notes No. 74, Extract from the First of the Gottingen Aerodynamic Laboratory, Chapter IV, Sec. 6, December 1921.

Preisach, F. Z., "Uber die Magnetische Nachwirkung," *Zeitschrift fur Physik*, **94**, pp. 277-302, 1935.

Priya, S. and Inman, D. J., *Energy Harvesting Technologies*, Springer, New York, NY, 2008.

PSI PZT-5A4E. Online data sheet for industry type 5A (Navy Type II) piezoceramic. [http://www.piezo.com/prodsheet3disk5A.html]

PSI PZT-5H4E. Online data sheet for industry type 5H (Navy Type VI) piezoceramic. [http://www.piezo.com/prodsheet2sq5H.html]

Ramakumar, K. and Jacob, J., "Flow Control and Lift Enhancement Using Plasma Actuators," AIAA Paper 2005-4635, 35th Fluid Dynamics Conference, June 2005.

Robert, G., Damjanovic, D. and Setter, N., "Preisach modeling of piezoelectric nonlinearity in ferroelectric ceramics," *Journal of Applied Physics*, **89**(9), pp. 5067-5074, 2001.

Rogers, E., Schwartz, A., and Abramson, J., "Applied Aerodynamics of Circulation Control Airfoils and Rotors," Annual forum proceedings of the American Helicopter Society, Vol. 2, Issue 41, pp. 479 – 490, 1985.

Roglin, R. L., Hanagud, S. V., and Kondor, S., “Adaptive Airfoils for Helicopters,” 35th AIAA Structures, Structural Dynamics, and Materials Conference, 1994.

Ruggiero, E., Park, G., Inman, D. J. and Wright, J., “Multi-Input, Multi-Output Modal Testing Techniques for a Gossamer Structure,” Proceedings, IMECE 02, 2002 ASME IMECE Adaptive Structures Symposium, November 17-22, New Orleans, LA, 2002.

Santhanakrishnan, A., Pern, N. J., Ramakumar, K., Simpson, A., and Jacob, J. D., “Enabling Flow Control Technology for Low Speed UAVs,” Infotech@Aerospace, Arlington, Virginia, AIAA 2005-6960, 26 - 29 September 2005.

Seifert, A., Greenblatt, D., and Wygnanski, I. J., “Active Separation Control: An Overview of Reynolds and Mach Numbers Effects,” *Aerospace Science and Technology*, **8**, pp. 569-582, 2000.

Seigler, T. M., Neal, D. A., Bae, J. S., and Inman, D. J., “Modeling and Flight Control of Large-Scale Morphing Aircraft,” *AIAA Journal of Aircraft*, **44**(4), July–August 2007

Selig, M. S., Donovan, J. F., and Fraser, D. B., *Airfoils at Low Speeds, Soartech 8*, published by H.A. Stokely, Virginia Beach, VA, 1989.

Selig, M. S., Guglielmo, J.J., Broeren, A.P., and Giguere, P., *Summary of Low-Speed Airfoil Data*, Vol. 1, Soartech Publications, Virginia Beach, VA, 1995.

Simpson, A. and Jacob, J., “Aerodynamic Control of an Inflatable Wing Using Wing Warping,” 35th AIAA Fluid Dynamics Conference and Exhibit, Toronto, Ontario Canada, AIAA 2005-5133, 6 - 9 June 2005.

Smith, R.C., *Smart Material Systems: Model Development*, SIAM Frontiers in Applied Mathematics, Philadelphia, PA, 2005.

Sodano, H. A., Lloyd, J., and Inman, D. J., "An Experimental Comparison between Several Active Composite Actuators for Power Generation," *Journal of Smart Materials and Structures*, **15**, pp. 1211-1216, 2006.

Sodano, H. A., Park, G., and Inman, D. J., “An investigation into the performance of macro-fiber composites for sensing and structural vibration applications,” *Mechanical Systems and Signal Processing*, **18**(3), pp. 683-697, May 2004.

Sodano, H. A., Peairs, D. M., Magliula, E. A., Park, G., and Inman, D. J., "The Use of Macro-Fiber Composites in Structural Vibration Applications," Proceeding of the 21st International Modal Analysis Conference (IMAC), February 3-6th, Kissimmee, FL, 2003.

Song, G., Zhao, J., Zhou, X., and De Abreu-Garcia, J.A., "Tracking control of a piezoceramic actuator with hysteresis compensation using inverse Preisach model," *IEEE/ASME Transactions on Mechatronics*, **10**(2), pp. 198-208, 2005.

SP5L. Online data sheet for high voltage diode. [http://www.deantechnology.com/pdf/download/Diodes.pdf]

Sreenan, P. N., Salvady, G. and Naganathan, N. G., "Hysteresis prediction for a piezoceramic material system," Proceedings of the 1993 ASME Winter Annual Meeting, New Orleans, LA, Volume AD-VOL 35, pp. 35-42, 1993.

Steadman, D. L., Griffin S. L., and Hanagud, S. V., "Structure-Control Interaction and the Design of Piezoceramic Actuated Adaptive Airfoils," AIAA-1994-1747, 1994.

Tarazaga, P. A., Inman, D. J., and Wilkie, W. K., "Control of a space rigidizable inflatable boom using macro-fiber composite actuators," *Journal of Vibration and Control*, **13**(7), pp. 935-950, 2007.

Torres, G. E., "Aerodynamics of Low Aspect Ratio Wings at Low Reynolds Numbers with Applications to Micro Air Vehicle Design," Ph.D. Dissertation, Aerospace and Mechanical Engineering Dept., University of Notre Dame, Indiana, April 2002.

Visintin, A., *Differential Models of Hysteresis*, Springer, Berlin, 1994.

Viswamurthy, S.R. and Ganguli, R., "Modeling and compensation of piezoceramic actuator hysteresis for helicopter vibration control," *Sensors and Actuators A*, **135**, pp. 801-810, 2007.

Vos, R., DeBreuker, R., Barrett, R., and Tiso, P., "Morphing Wing Fight Control Via Post-Buckled Precompressed Piezoelectric Actuators," *AIAA Journal of Aircraft*, **44**(4), pp. 1060-1069, July-August 2007.

Waszak, M. R., Jenkins, L. N., and Ifju, P. G., "Stability and Control Properties of an Aeroelastic Fixed Wing Micro Aerial Vehicle," AIAA-2001-4005, 2001.

Webb, G., Kurdila, A., and Lagoudas, D., " Adaptive hysteresis model for model reference control with actuator hysteresis," *Journal of Guidance, Control and Dynamics*, **23**(3), pp. 459-465, 2000.

Wickramasinghe, V. K., Chen, Y., Martinez, M., Kernaghan, R., and Wong, F., "Design and Verification of a Smart Wing for an Extremely-Agile Micro-Air-Vehicle," AIAA 2009-

2132, 50th AIAA/ASME/ASCE/AHS/ASC Structures, Structural Dynamics, and Materials Conference, Palm Springs, California, 4 - 7 May 2009.

Wilkie, W. K., Bryant, G. R., and High, J. W., "Low-Cost Piezocomposite Actuator for Structural Control Applications," SPIE 7th Annual International Symposium on Smart Structures and Materials, Newport Beach, CA, 2000.

Wilkie, W. K., Inman, D. J., Lloyd, J. M., and High, J. W., "Anisotropic Laminar Piezocomposite Actuator Incorporating Machined PMN-PT Single-Crystal Fibers," *Journal of Intelligent Material Systems and Structures*, **17**(1), pp. 15-28, January 2006.

Williams, R. B., "Nonlinear Mechanical and Actuation Characterization of Piezoceramic Fiber Composites," Ph.D. Dissertation, Mechanical Engineering Dept., Virginia Tech, Blacksburg, VA, March 22nd, 2004.

Wright. Information on Wright Brothers from Wikipedia.org. [http://en.wikipedia.org/wiki/Wright_brothers].

XFOIL. User Primer for XFOIL version 6.9. XFOIL: Subsonic Airfoil Development System," Massachusetts Institute of Technology. [http://web.mit.edu/drela/Public/web/xfoil/xfoil_doc.txt]

APPENDIX A

ADDITIONAL UNIMORPH ACTUATION RESULTS

This appendix presents additional information on the experiments and the unimorph specimens presented in Chapter 2.

A.1 Clamp Design for Cantilevered Beams

In order to evaluate cantilevered beams with piezoceramic materials, a clamp is designed and fabricated. The clamp is designed to apply a uniformly distributed pressure across the clamped base of the cantilevered specimen. Other (simpler) designs fail to apply uniform pressure to the clamped specimen causing 1) deviation from the (typically) assumed zero-slope boundary condition and 2) stress concentrations on the brittle piezoceramic material. Figure A.1 shows the clamp machined from aluminum stock material. The clamp consists of three main parts: 1) *base*, 2) *top plate* and 3) a *free bar*. A *clamping bolt* pulls the top plate to the base. The specimen and a free-to-rotate bar are squeezed between the top plate and base. There are two pins that allow a free motion of the three main parts (described above).

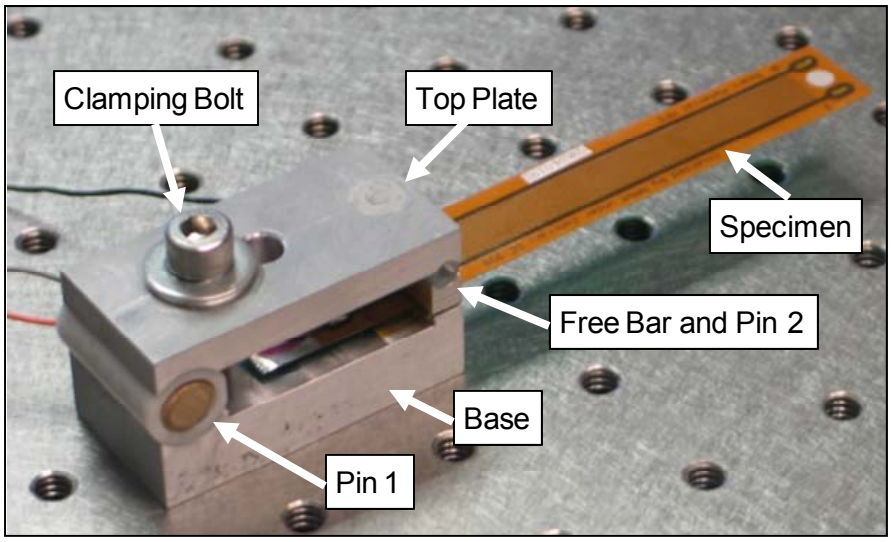

Figure A.1: The aluminum clamp used for cantilevered beam samples.

Since the *free bar* can rotate, it self-adjusts its angle to match the slope of the specimen. This allows for a range of specimens with different thicknesses to be clamped. Both the main structure and the pins are fabricated from lightweight materials to reduce the mass loading effect if the clamp is connected to a vibration exciter (or an electromagnetic shaker).

A.2 Geometric Properties of MFC M8507-P1 Actuator

Selected geometric properties of the MFC M8507-P1 type device is presented here. Figure A.2 shows the MFC actuator with attention to critical areas. Figure A.2a present the top view of the whole actuator. Figure A.2b is a microscope image of the area where the piezoceramic fibers (running horizontal to the page) end. Figure A.2c shows the area with uniform fiber and electrode (running vertical to the page) distribution. Finally, Figure A.2d presents the side transition area where electrode bus connects to (every other) interdigitated electrodes.

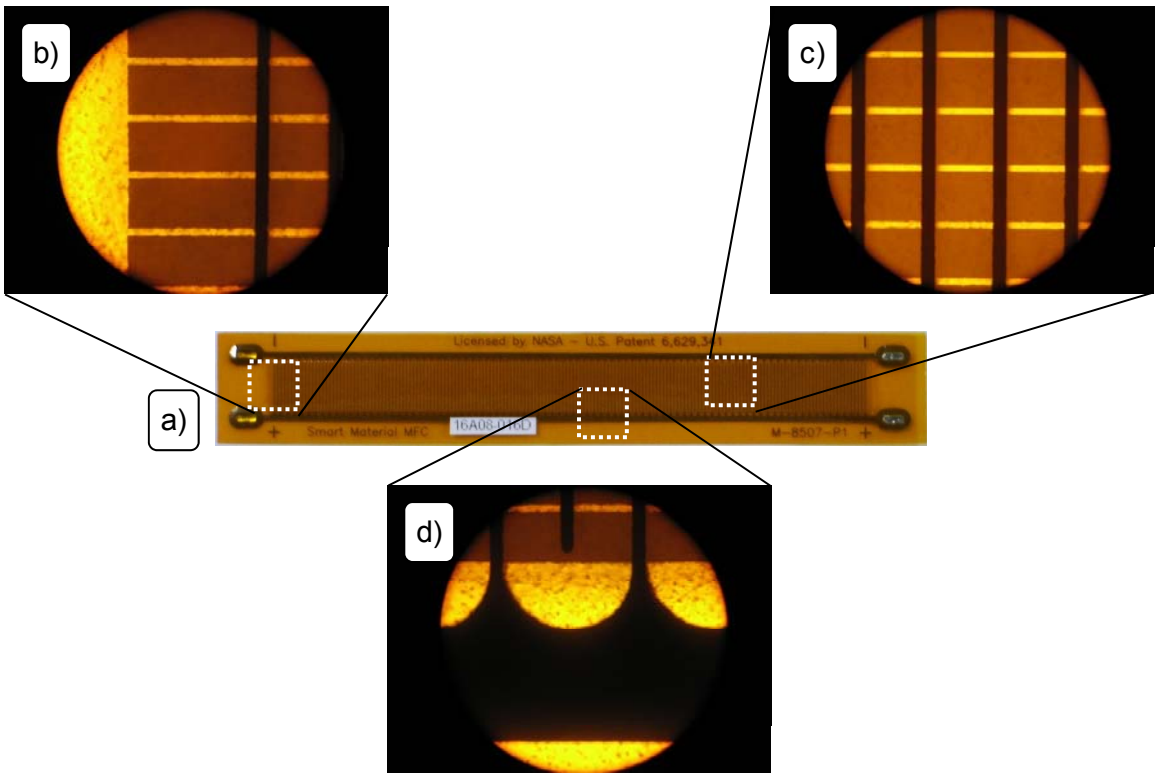

Figure A.2: Digital photograph of the MFC M8507-P1 type device. a) Top view, b) piezoceramic fiber ends, c) uniform active area and d) electrode bus connection to the interdigitated electrodes.

A Zeiss microscope with 10X lens and 10X eye piece is used to take these photos. The specific MFC model, used throughout this dissertation, has a total length of 102.38 mm and a total width of 16.28 mm. The active area is 0.305 mm thick. The inactive area (sides) is 0.142 mm thick. The piezoceramic fiber and electrode dimensions are originally presented in Section 2.1.1. Table A.1 presents the geometric properties of the MFC device. Some values could not be measured hence reported values from the manufacturer are used. In addition to the measurements conducted using the microscope, other measurements are taken with a digital caliper (for length measurements) and a digital micrometer (for thickness measurements).

Table A.1: Geometric properties of MFC M8507-P1 type piezoceramic device. Values reported by the manufacturer are indicated by '*'.

Property	Value	Unit	Axis
Overall			
Length	102.38	mm	x
Width	16.28	mm	y
Thickness, active	305	μm	z
Thickness, inactive	142	μm	z
Active Area			
Length*	85	mm	x
Width	7.3	mm	y
Piezoceramic Fiber			
Length*	85	mm	x
Width*	355	μm	y
Thickness*	180	μm	z
Spacing	51.25	μm	y
Epoxy Fiber			
length*	85	mm	x
Width	51.25	μm	y
Thickness*	180	μm	z
Spacing*	355	μm	y
Electrodes			
Length	7.3	mm	y
Width	97	μm	x
Thickness	n/a	n/a	z
Spacing	410	μm	x
Other			
Kapton Thickness	60	μm	z
Number of Electrodes	144	n/a	n/a
Number of Piezo Fibers	18	n/a	n/a

A.3 Analytical Response of Thin MFC M8507-P1 Unimorphs

This section presents additional results from the theoretical examination of the effects of 1) the substrate-to-MFC-actuator thickness ratio and 2) substrate modulus for MFC model

M8507-P1 actuated unimorph cantilevered beams. These results are provided to aid the discussion presented in Section 2.1.1.

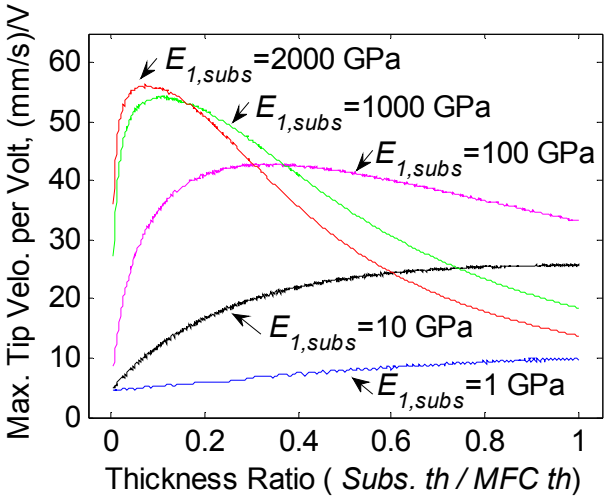

Figure A.3: Theoretical maximum tip velocity response to harmonic excitation for a range of substrate Young's moduli and thickness ratios. (α=0.2, ρ_{subs}=2700 kg/m^3)

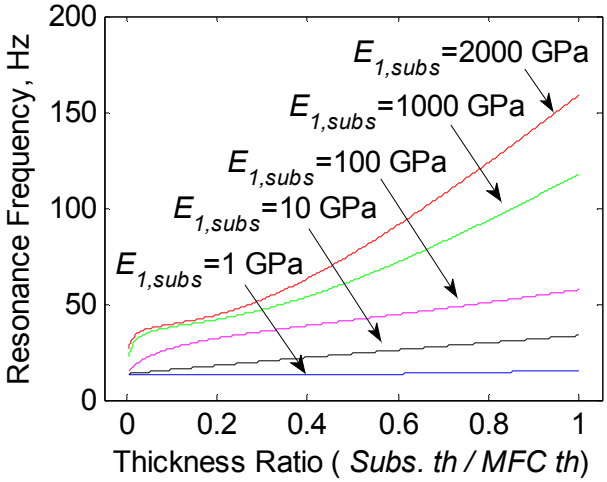

Figure A.4: Theoretical variation of 1st bending resonance frequency for a range of substrate Young's moduli and thickness ratios. (α=0.2, ρ_{subs}=2700 kg/m^3)

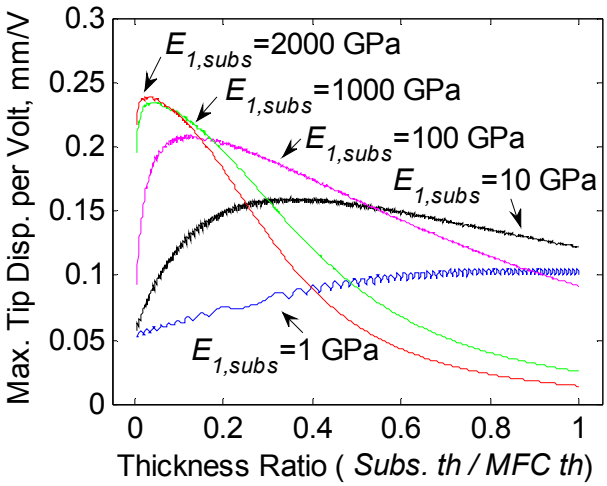

Figure A.5: Theoretical maximum tip displacement response to harmonic excitation for a range of substrate Young's moduli and thickness ratios. (α=0.2)

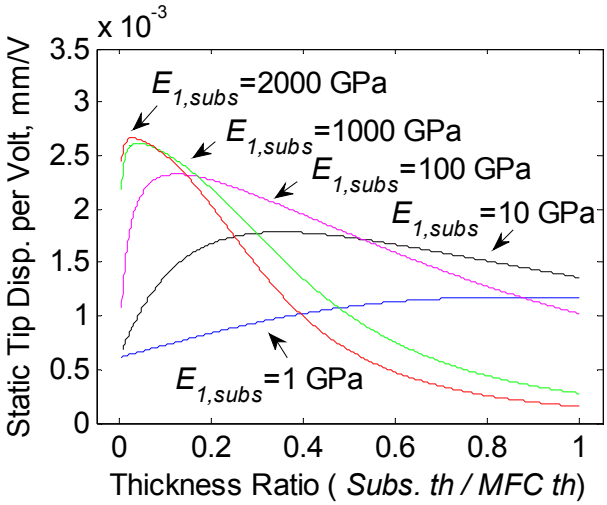

Figure A.6: Theoretical static tip displacement per volt for a range of substrate Young's moduli and thickness ratios. (α=0.2)

A.4 Experimental Response of Thin MFC M8507-P1 Unimorphs

This section presents the complete set of experimental and analytical frequency response function measurements on the unimorphs with MFC M8507-P1 type actuators. The experimental details are presented in Section 2.1.2. Figure A.7a through Figure A.12a presents the measured velocity-output-to-actuation-voltage FRFs of all 12 samples. Similarly, Figure A.7b through Figure A.12b presents the derived displacement-output-to-actuation-voltage FRFs Both magnitude and phase are shown for the experimental results and the linear model prediction. It is important to note that the wrapped experimental phase shows a constant offset due to the piezoceramic hysteresis. Only two samples are presented in one plot to aid the clear presentation of the data.

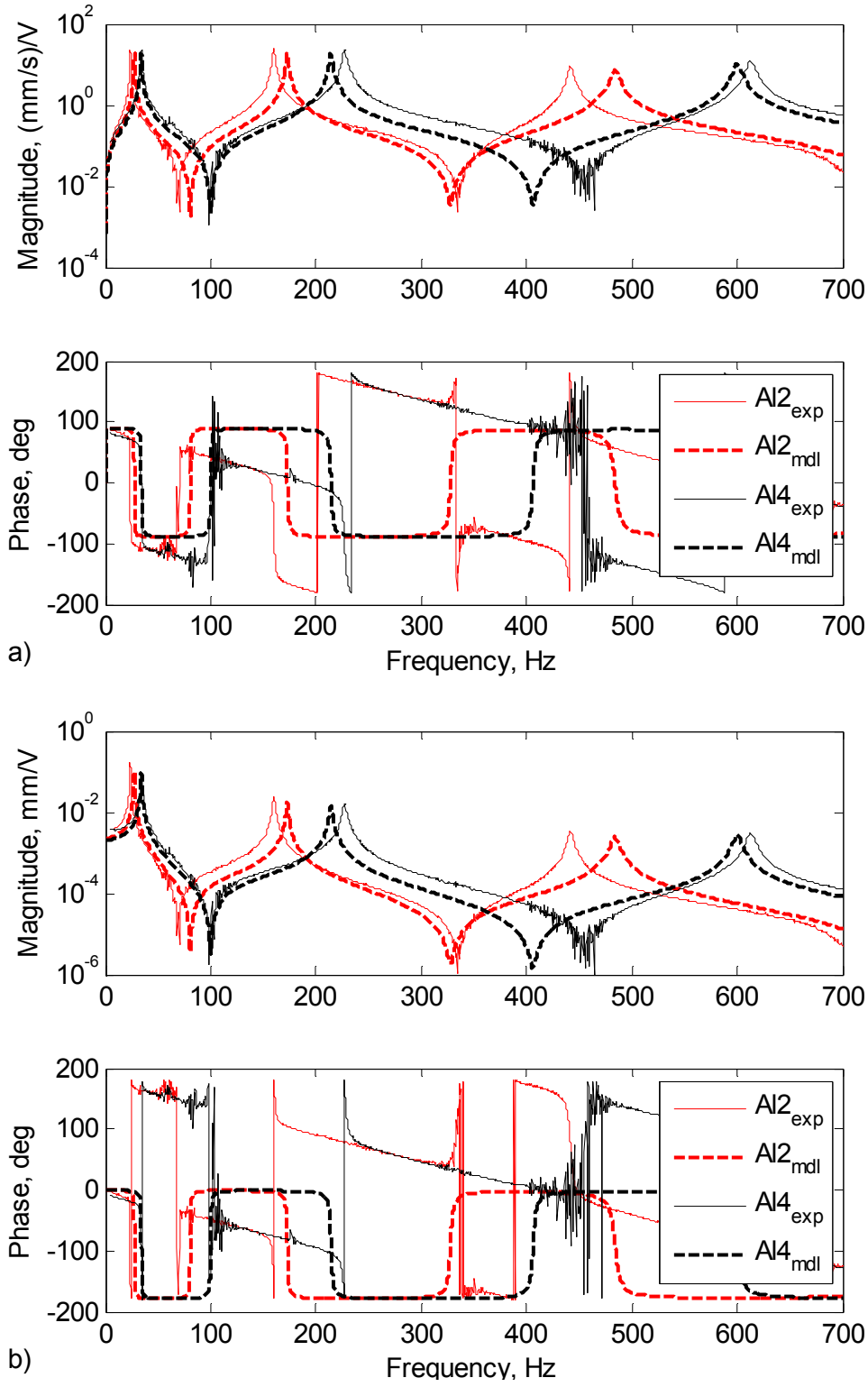

Figure A.7: Comparison of analytical and experimental a) Velocity and b) displacement - to-voltage-excitation FRFs of unimorph samples A2 and A4.

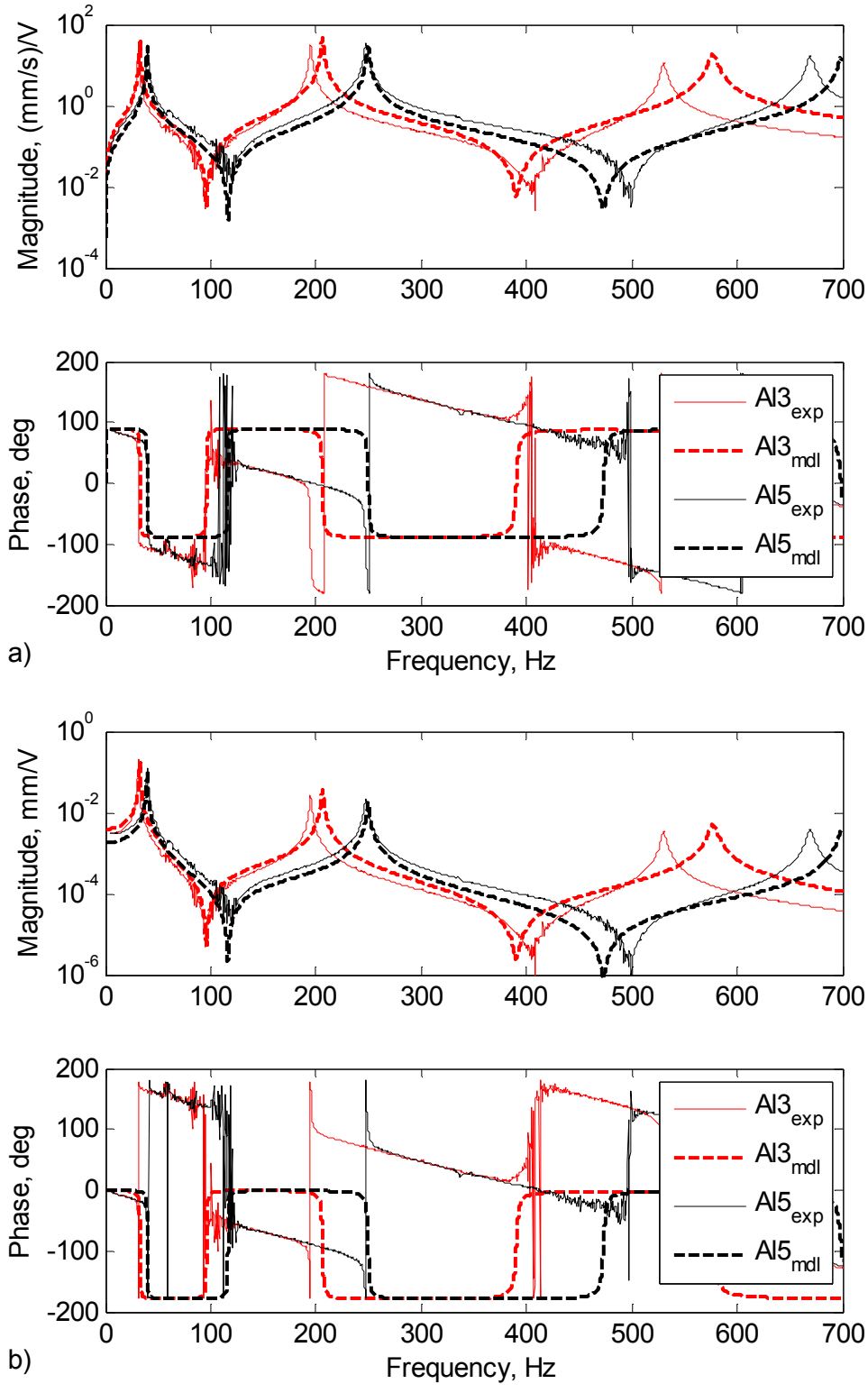

Figure A.8: Comparison of analytical and experimental a) Velocity and b) displacement - to-voltage-excitation FRFs of unimorph samples Al3 and Al5.

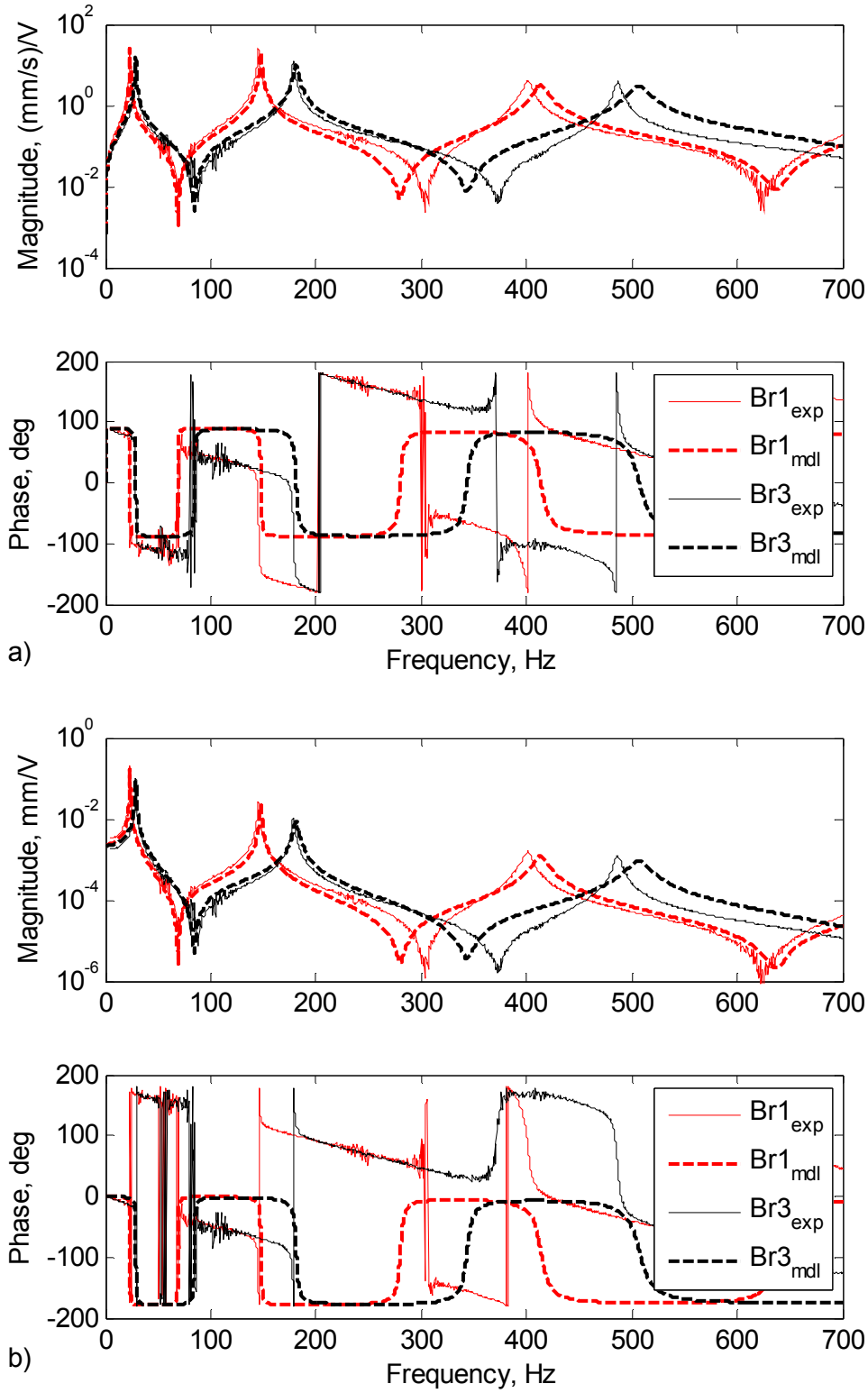

Figure A.9: Comparison of analytical and experimental a) Velocity and b) displacement - to-voltage-excitation FRFs of unimorph samples Br1 and Br3.

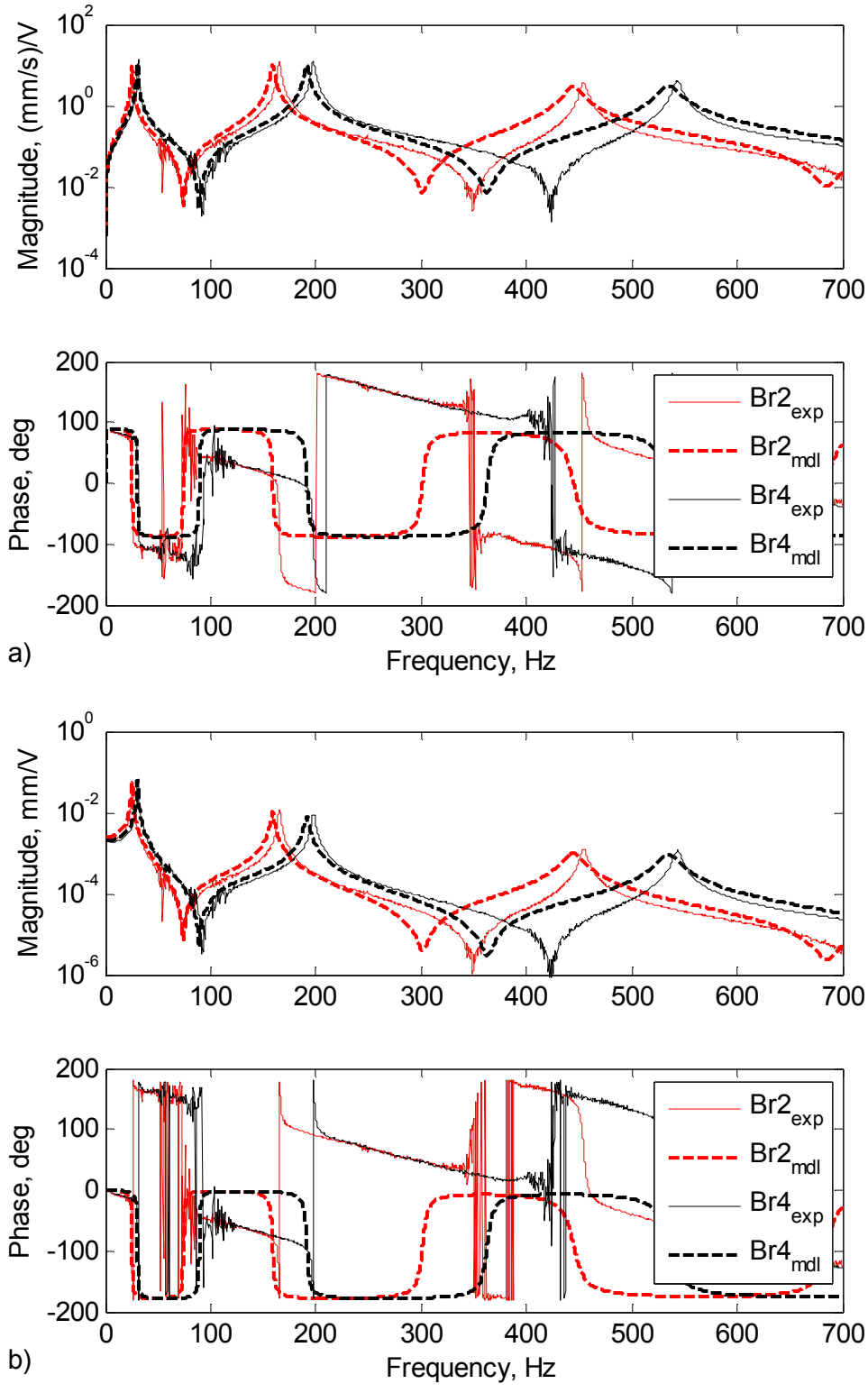

Figure A.10: Comparison of analytical and experimental a) Velocity and b) displacement - to-voltage-excitation FRFs of unimorph samples Br2 and Br4.

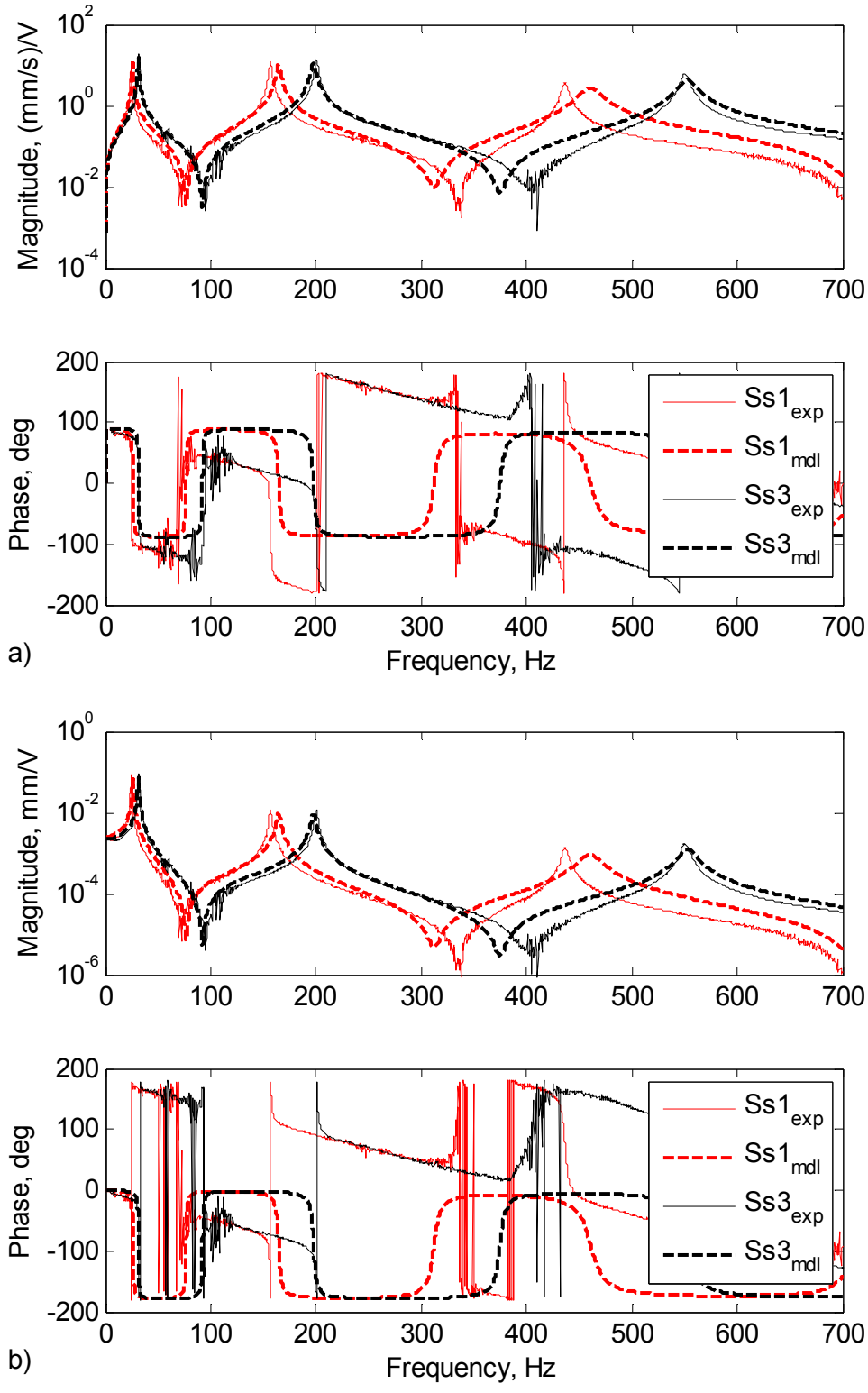

Figure A.11: Comparison of analytical and experimental a) Velocity and b) displacement - to-voltage-excitation FRFs of unimorph samples Ss1 and Ss3.

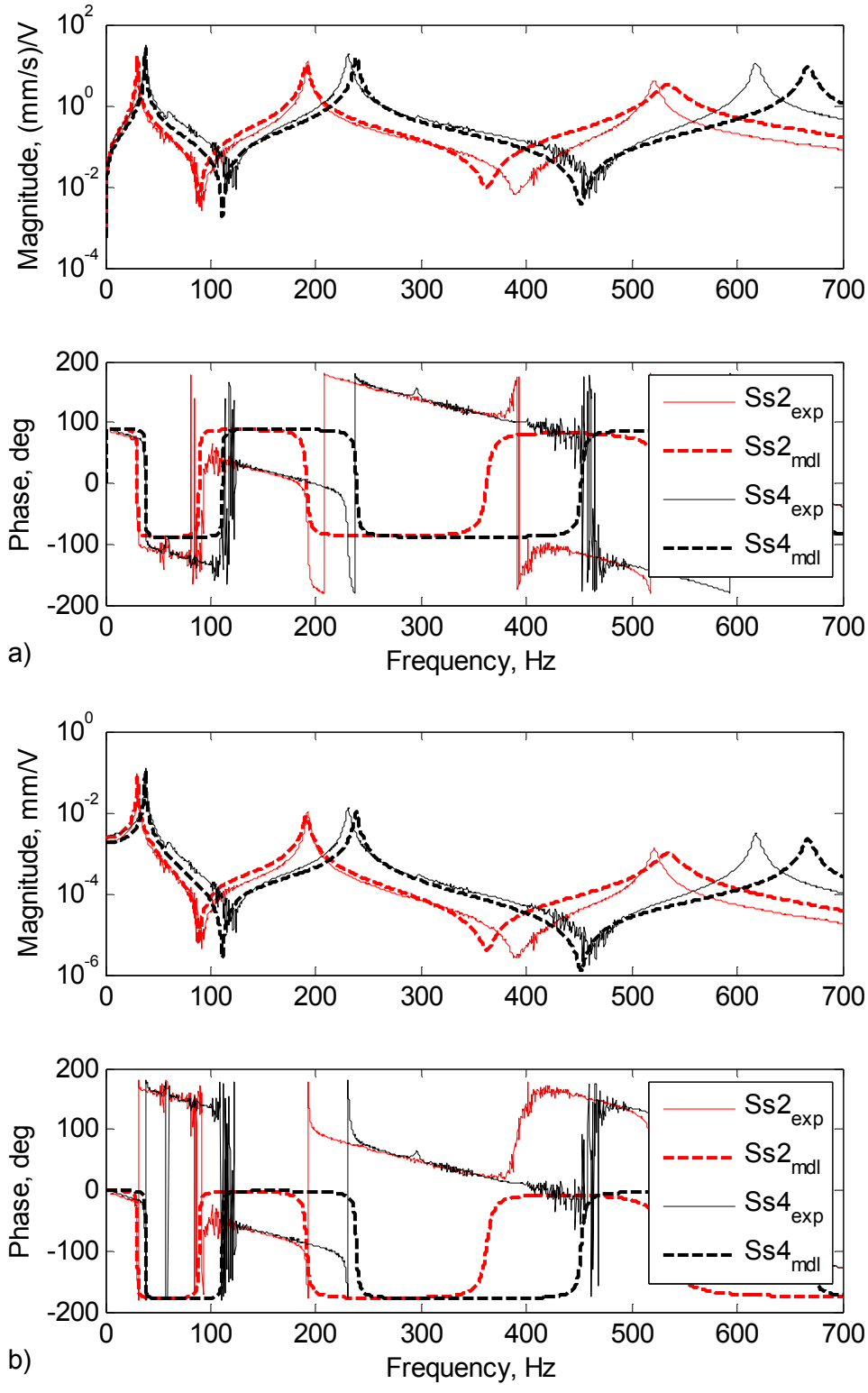

Figure A.12: Comparison of analytical and experimental a) Velocity and b) displacement - to-voltage-excitation FRFs of unimorph samples Ss2 and Ss4.

A.5 Properties of Single Crystal PMN-PZT Piezoelectrics

This section presents the properties of the single crystal PMN-PZT type piezoelectric specimens that are examined in Section 2.3 and Section 3.3.

Table A.2: Typical properties of Ceracomp *31* mode CPSC 160-95 PMN-PZT single crystal piezoelectric material. Values are reported by the manufacturer.

Property	Unit	Value
Density, ρ	gr/cm^3	8.0
Relative Dielectric Constant, K_3^T	n/a	7000
Dielectric Loss, $tan\delta$	n/a	0.005
Curie Temperature, T_C	°C	160
R-T Transition Temp., T_{RT}	°C	95
Electromechanical Coupling, k_{33}	n/a	0.93
Strain / applied field, d_{33}	pC/N	2000
Electromechanical Coupling, k_{31}	n/a	0.91
Strain / applied field, d_{31}	pC/N	-1850
Coercive Electric Field, E_C	kV/cm	4
Mechanical Quality Factor, Q_M	n/a	100

Table A.3: Description of symbols related to piezoelectric properties.

Property	Symbol	Unit
Capacitance	C	nF
Dielectric Loss	$tan\delta$	n/a
Resonance Frequency	f_r	kHz
Anti-Resonance Frequency	f_a	kHz
Impedance	Z_r	kOhm
Relative Dielectric Constant	K_3^T	n/a
Electromechanical Coupling	k_{31}	n/a
Strain / applied field	d_{31}	pC/N
Compliance	s_{11}^E	m^2/N
Mechanical Quality Factor	Q_M	n/a

Table A.4: Measured properties (by the manufacturer) of Ceracomp *31* mode CPSC 160-95 PMN-PZT single crystal piezoelectric materials without any substrate.

Crystal Sample	C (nF)	$\tan\delta$	f_r (kHz)	f_a (kHz)	Z_r (kOhm)	K_3^T	k_{31}	$-d_{31}$ (pC/N)	s_{11}^E (x10^{-12}) (m^2/N)	Q_M
5	22.43	0.01	21.0	34.2	0.02	4732	0.89	1619	78.7	34
6	22.52	0.01	21.0	34.2	0.01	4751	0.89	1622	78.7	45
7	21.91	0.01	21.2	34.0	0.01	4621	0.88	1568	77.3	42
8	21.70	0.01	21.4	34.2	0.01	4578	0.88	1542	75.8	44
9	22.14	0.01	21.2	33.6	0.01	4671	0.87	1563	77.3	40
10	22.60	0.01	21.0	33.8	0.01	4767	0.88	1612	78.7	39
11	22.33	0.01	21.0	34.0	0.01	4711	0.89	1609	78.7	45
12	20.32	0.01	21.6	34.0	0.01	4285	0.87	1462	74.4	44
13	22.43	0.01	21.0	34.2	0.02	4732	0.89	1619	78.7	34
14	22.52	0.01	21.0	34.2	0.01	4751	0.89	1622	78.7	45
15	21.91	0.01	21.2	34.0	0.01	4621	0.88	1568	77.3	42
16	21.70	0.01	21.4	34.2	0.01	4578	0.88	1542	75.8	44
17	22.14	0.01	21.2	33.6	0.01	4671	0.87	1563	77.3	40
18	22.60	0.01	21.0	33.8	0.01	4767	0.88	1612	78.7	39
19	22.33	0.01	21.0	34.0	0.01	4711	0.89	1609	78.7	45
Ave.	22.11	0.01	21.1	34.0	0.01	4663	0.88	1582	77.7	41
Std.Dev.	0.5829	0	0.192	0.214	0.004	123.1	0.0077	44.65	1.38	3.8

Table A.5: Measured mass characteristics of single crystal unimorph samples. The red texts indicate the estimated values.

Sample	Code	Type	*PZT Mass* (gr)	Subs.	*Subs. Mass* (gr)	*Tot. Mass* (gr)	*Glue Mass* (gr)
1	5H01	PZT-5H	0.3348	Al	0.1542	0.49008	0.00108
2	5H02	PZT-5H	0.3348	Ss	0.4496	0.78548	0.00108
5	SC05	PMN-PZT	0.3286	Ss	0.1223	0.45198	0.00108
6	SC06	PMN-PZT	0.3295	Ss	0.2994	0.62998	0.00108
7	SC07	PMN-PZT	0.3286	Ss	0.4496	0.77928	0.00108
8	SC08	PMN-PZT	0.3304	Ss	0.5892	0.92068	0.00108
9	SC09	PMN-PZT	0.3300	Ss	0.7319	1.06298	0.00108
10	SC10	PMN-PZT	0.3296	Al	0.0524	0.38308	0.00108
11	SC11	PMN-PZT	0.3300	Al	0.0977	0.42878	0.00108
12	SC12	PMN-PZT	0.3280	Al	0.1542	0.48328	0.00108
13	SC13	PMN-PZT	0.3287	Al	0.1980	0.52778	0.00108
14	SC14	PMN-PZT	0.3301	Al	0.3309	0.66208	0.00108
16	SC16	PMN-PZT	0.3268	Al	0.0490	0.37688	0.00108
17	SC17	PMN-PZT	0.3291	Ss	0.4450	0.77518	0.00108
20	5H20	PZT-5H	0.3068	Ss	0.1208	0.42868	0.00108
21	5H21	PZT-5H	0.3302	Ss	0.2973	0.62858	0.00108
22	5H22	PZT-5H	0.3411	Ss	0.4476	0.78978	0.00108
23	5H23	PZT-5H	0.3469	Ss	0.5865	0.93448	0.00108
24	5H24	PZT-5H	0.3489	Ss	0.7279	1.07788	0.00108
25	5A25	PZT-5A	0.3429	Ss	0.1216	0.4652	0.00070
26	5A26	PZT-5A	0.3561	Ss	0.2984	0.6565	0.00200
27	5A27	PZT-5A	0.3436	Ss	0.4466	0.7907	0.00050
28	5A28	PZT-5A	0.3587	Ss	0.5918	0.9509	0.00040
29	5A29	PZT-5A	0.3420	Ss	0.7300	1.0738	0.00180

APPENDIX B

ADDITIONAL UNIMORPH ENERGY HARVESTING RESULTS

This appendix presents additional experimental results from the energy harvesting characterization of cantilevered unimorph beam specimens presented in Chapter 3.

B.1 Additional Thin MFC Unimorph Results

This section presents the energy harvesting characteristics of thin unimorph beams with MFC M8507-P1 type piezoceramic devices. These results are presented to aid the discussion presented in Section 3.1.

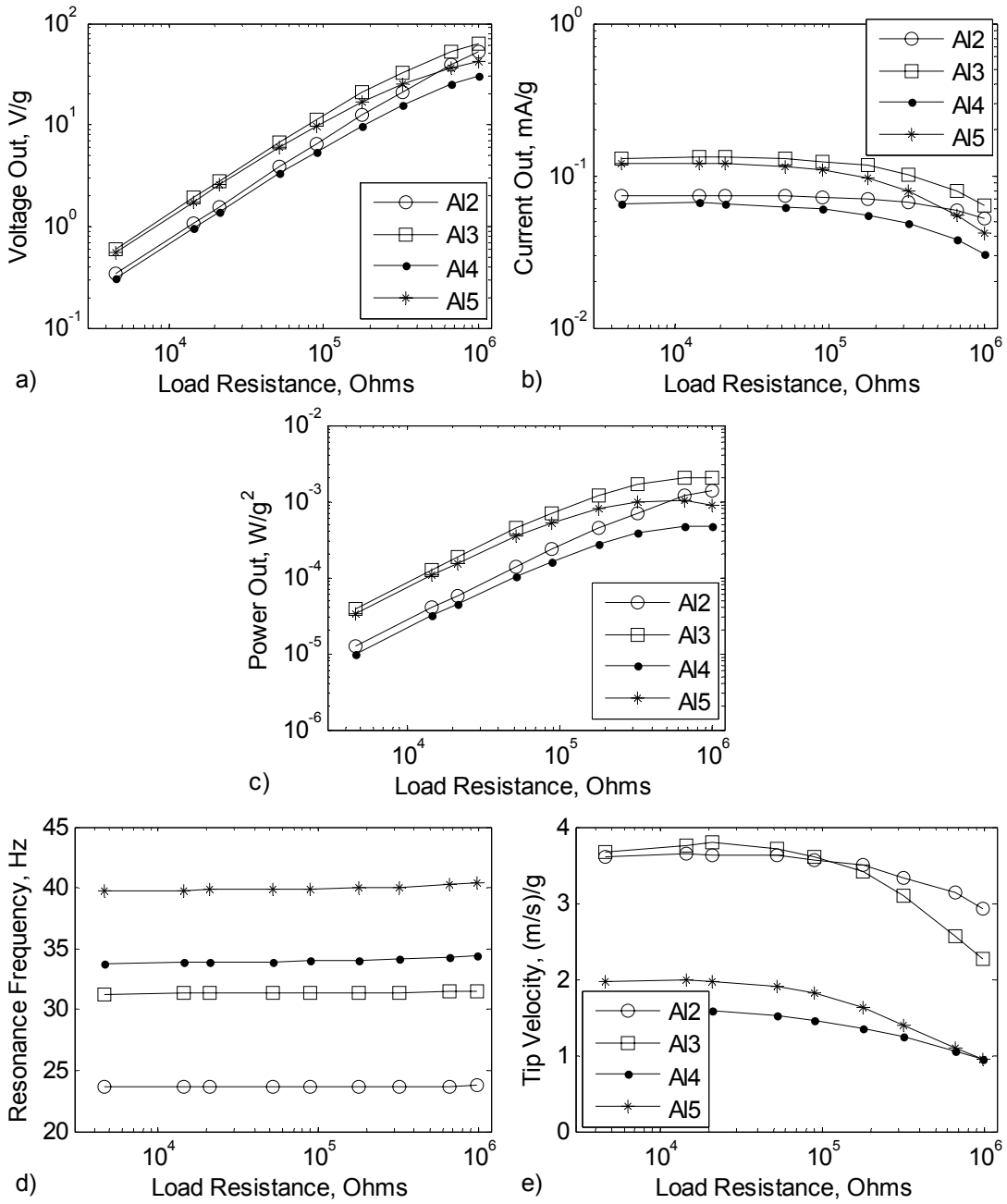

Figure B.1: a) Voltage-output, b) current-output, c) power-output, e) tip-velocity per-base-acceleration and d) corresponding resonance frequency of four unimorphs with aluminum substrates as a function of load resistance. Response is at the short circuit natural frequency (ω_{sc}).

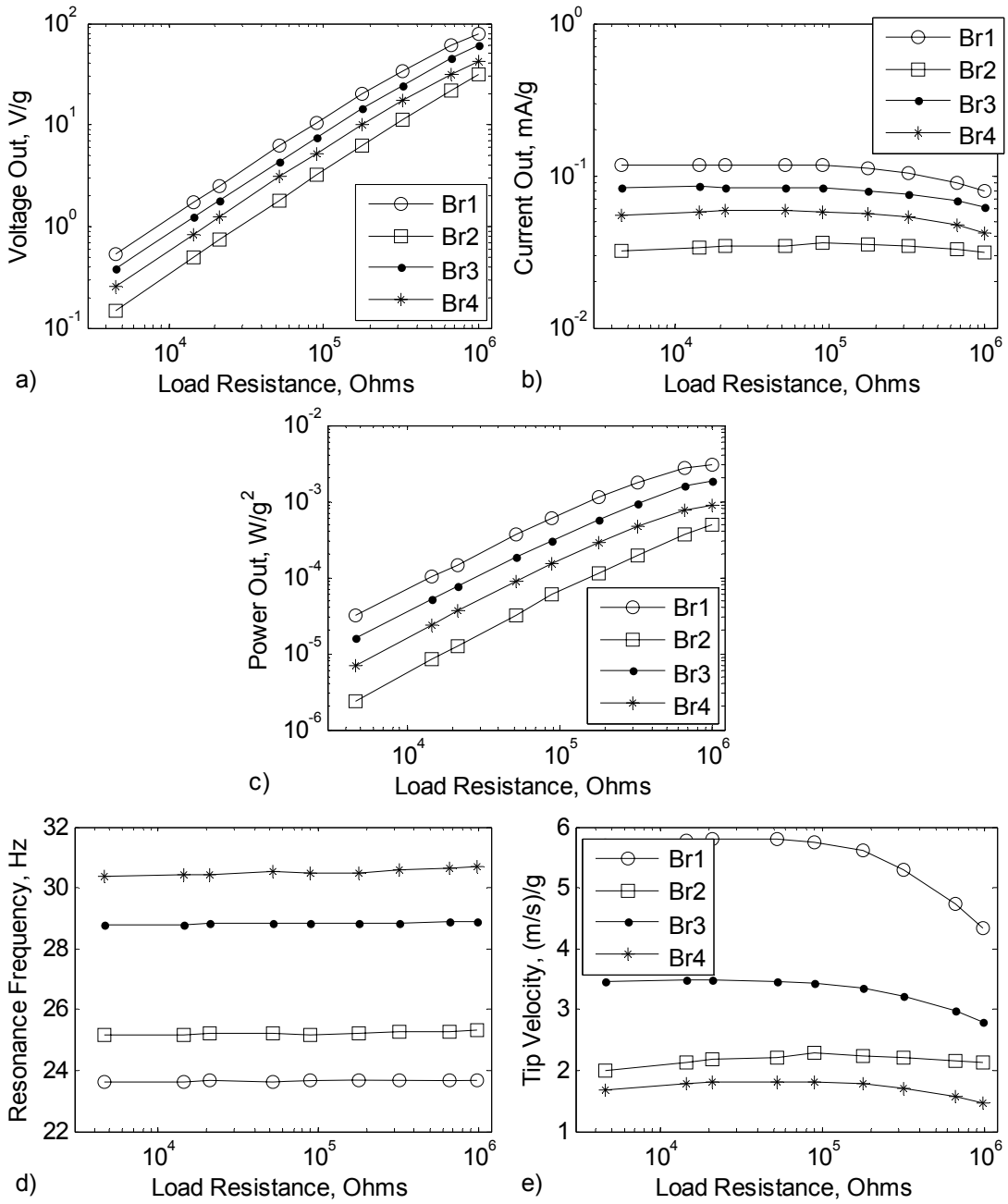

Figure B.2: a) Voltage-output, b) current-output, c) power-output, e) tip-velocity per-base-acceleration and d) corresponding resonance frequency of four unimorphs with brass substrates as a function of load resistance. Response is at the short circuit natural frequency (ω_{sc}).

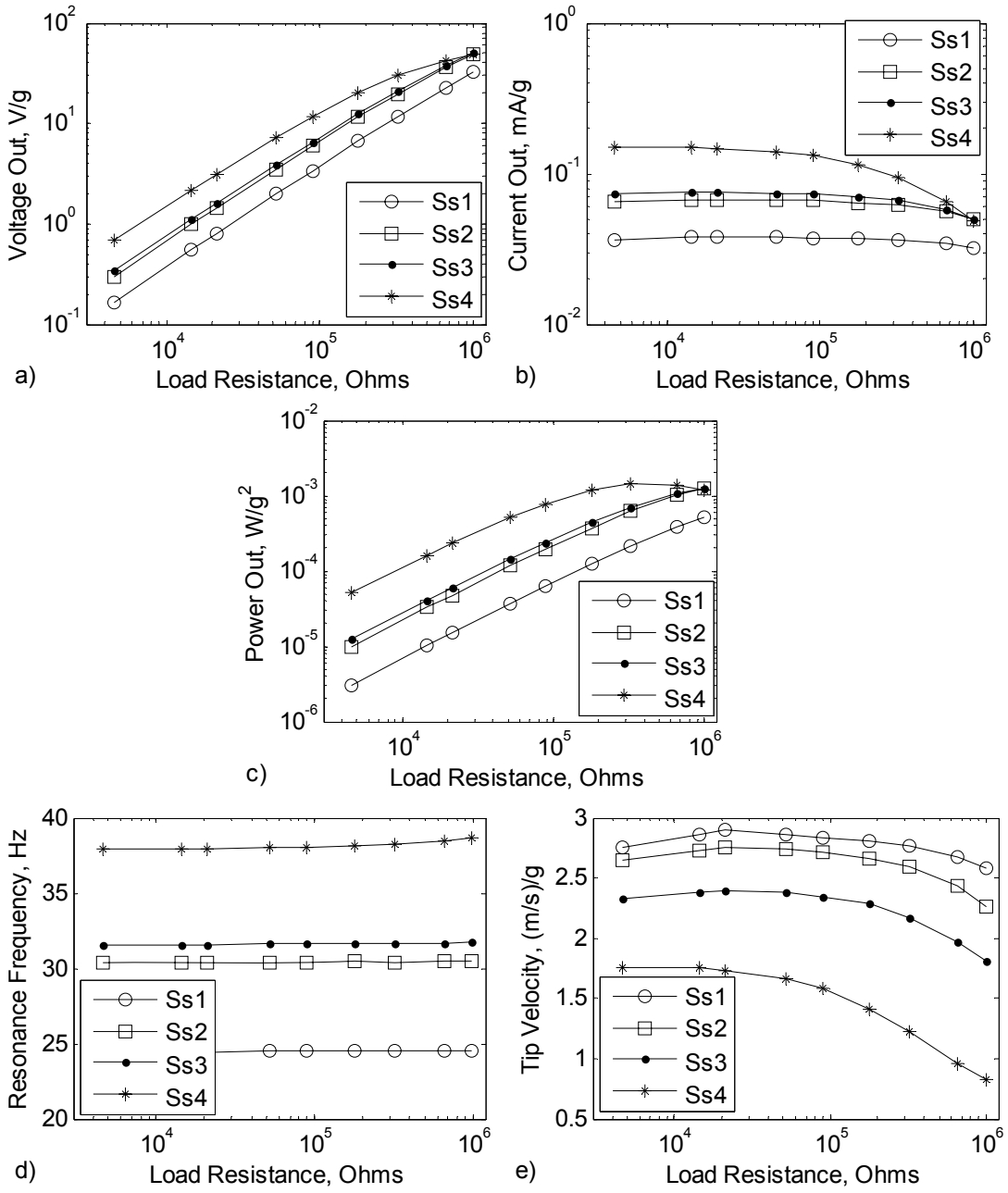

Figure B.3: a) Voltage-output, b) current-output, c) power-output, e) tip-velocity per-base-acceleration and d) corresponding resonance frequency of four unimorphs with stainless-steel substrates as a function of load resistance. Response is at the short circuit natural frequency (ω_{sc}).

B.2 Additional Thick Unimorph Results

This section presents the energy harvesting characteristics of thick unimorph beams with different types of piezoceramic devices. These results are presented to aid the discussion presented in Section 3.2.

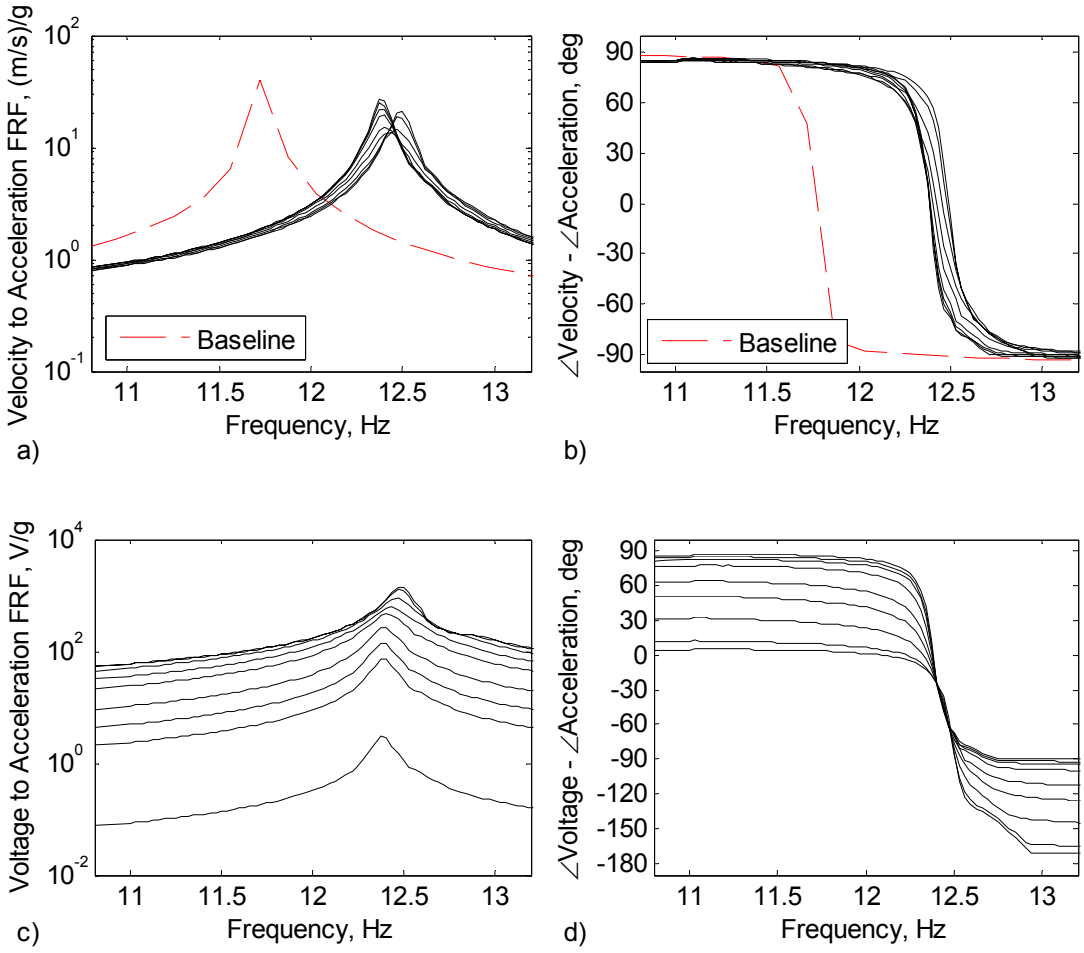

Figure B.4: Tip-velocity-to-harmonic-base-acceleration FRF a) magnitude and b) phase, and voltage-output-to-harmonic-base-acceleration FRF c) magnitude and d) phase for Beam 1 with PSI PZT-5A type piezoceramic.

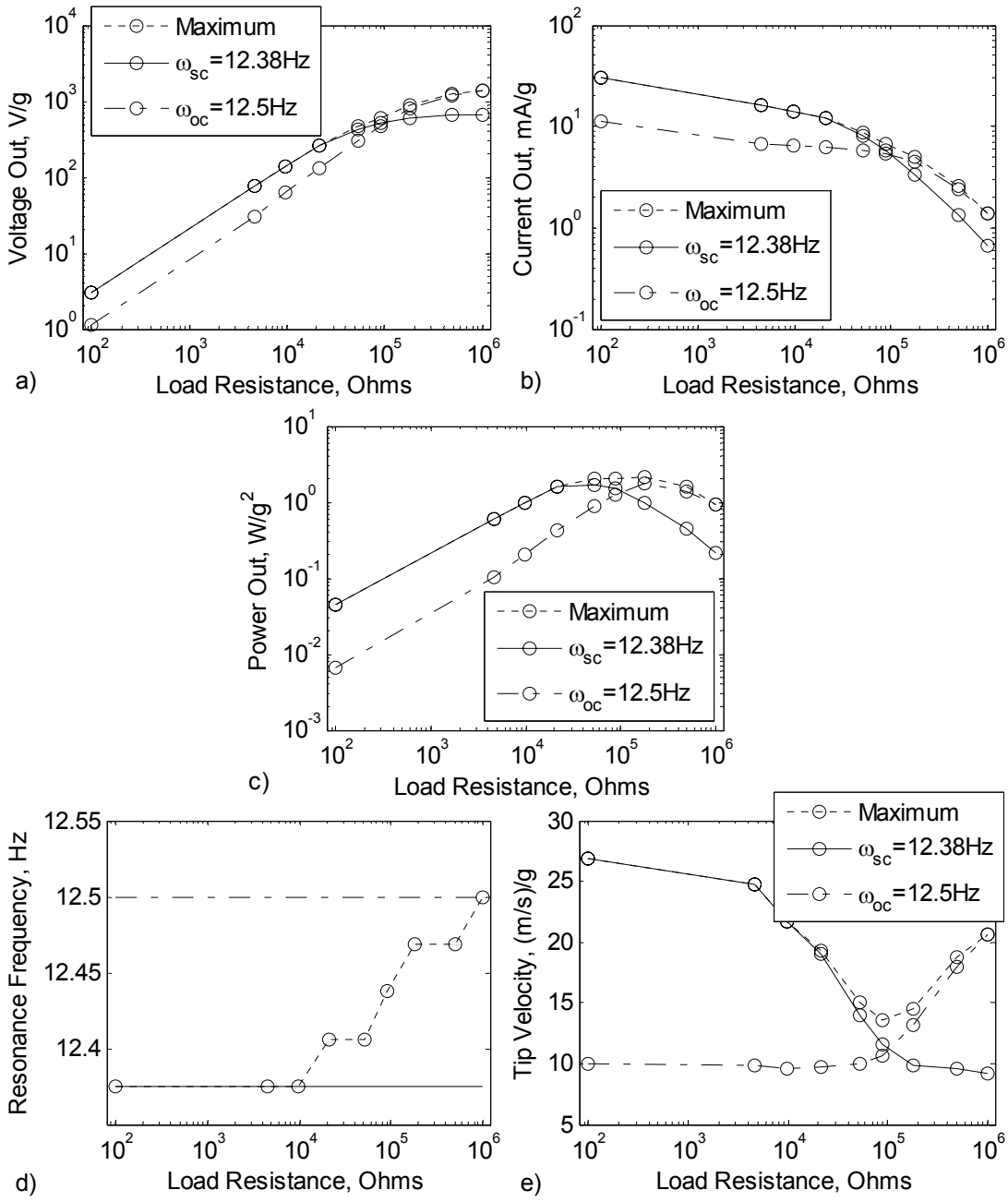

Figure B.5: a) Voltage-output, b) current-output, c) power-output, e) tip-velocity per-base-acceleration and d) corresponding resonance frequency of Beam 1 with PSI PZT-5A piezoceramic as a function of load resistance.

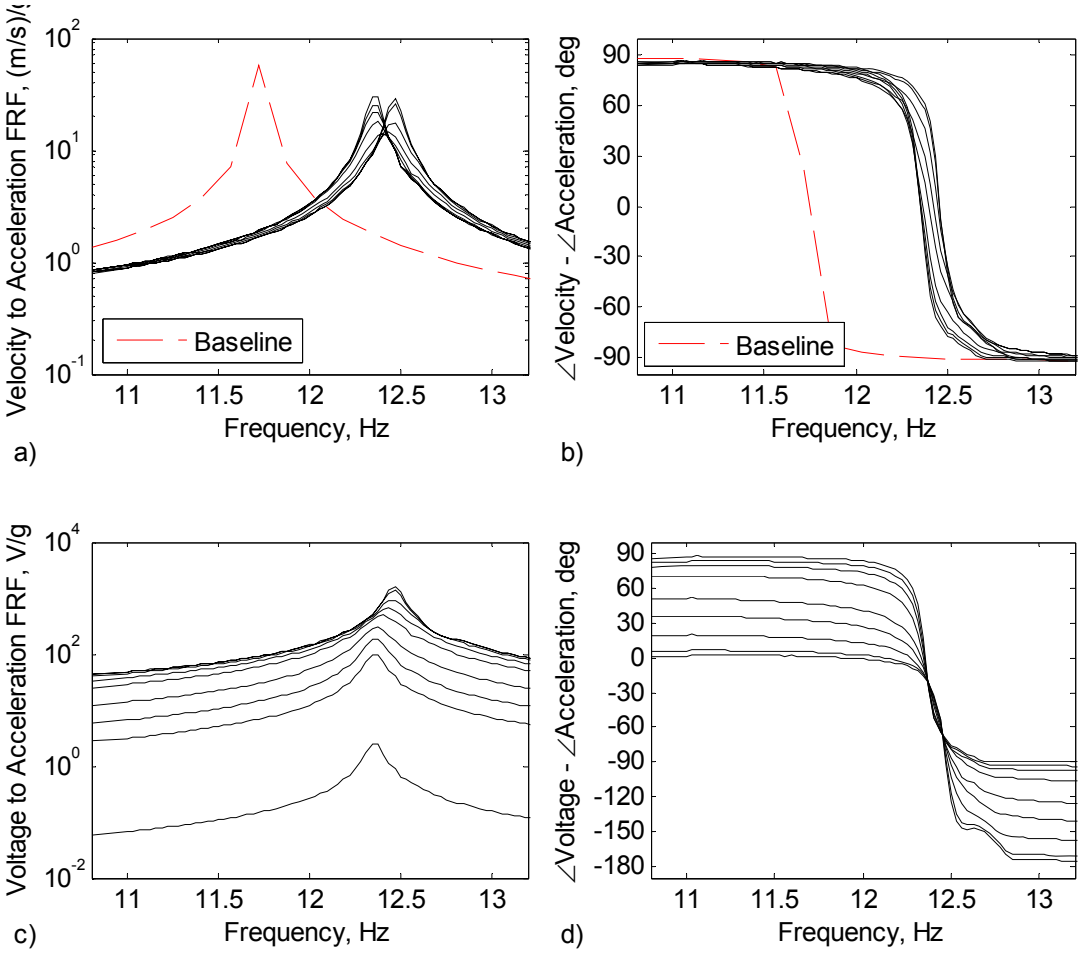

Figure B.6: Tip-velocity-to-harmonic-base-acceleration FRF a) magnitude and b) phase, and voltage-output-to-harmonic-base-acceleration FRF c) magnitude and d) phase for Beam 2 with PSI PZT-5H type piezoceramic.

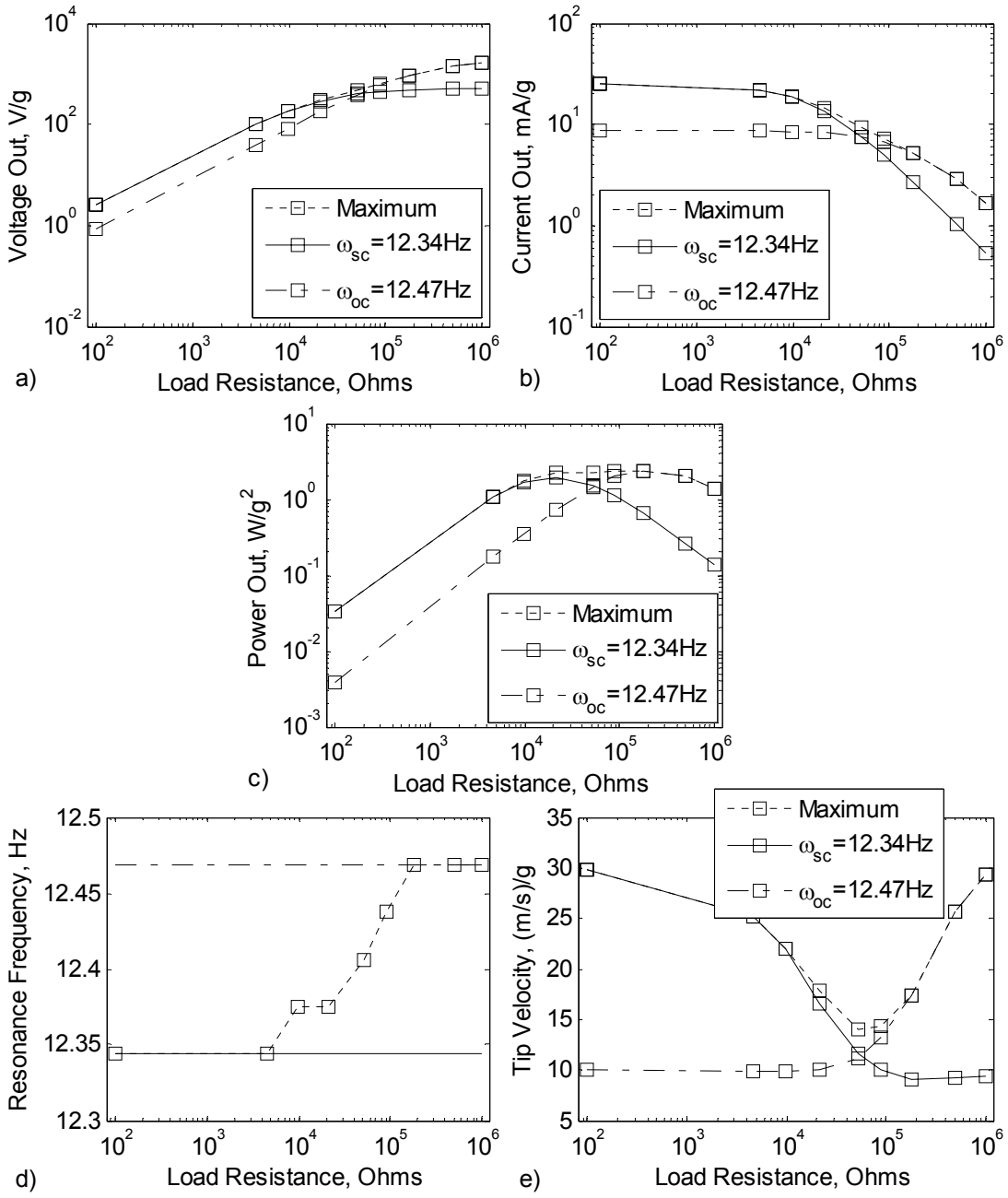

Figure B.7: a) Voltage-output, b) current-output, c) power-output, e) tip-velocity per-base-acceleration and d) corresponding resonance frequency of Beam 2 with PSI PZT-5H piezoceramic as a function of load resistance.

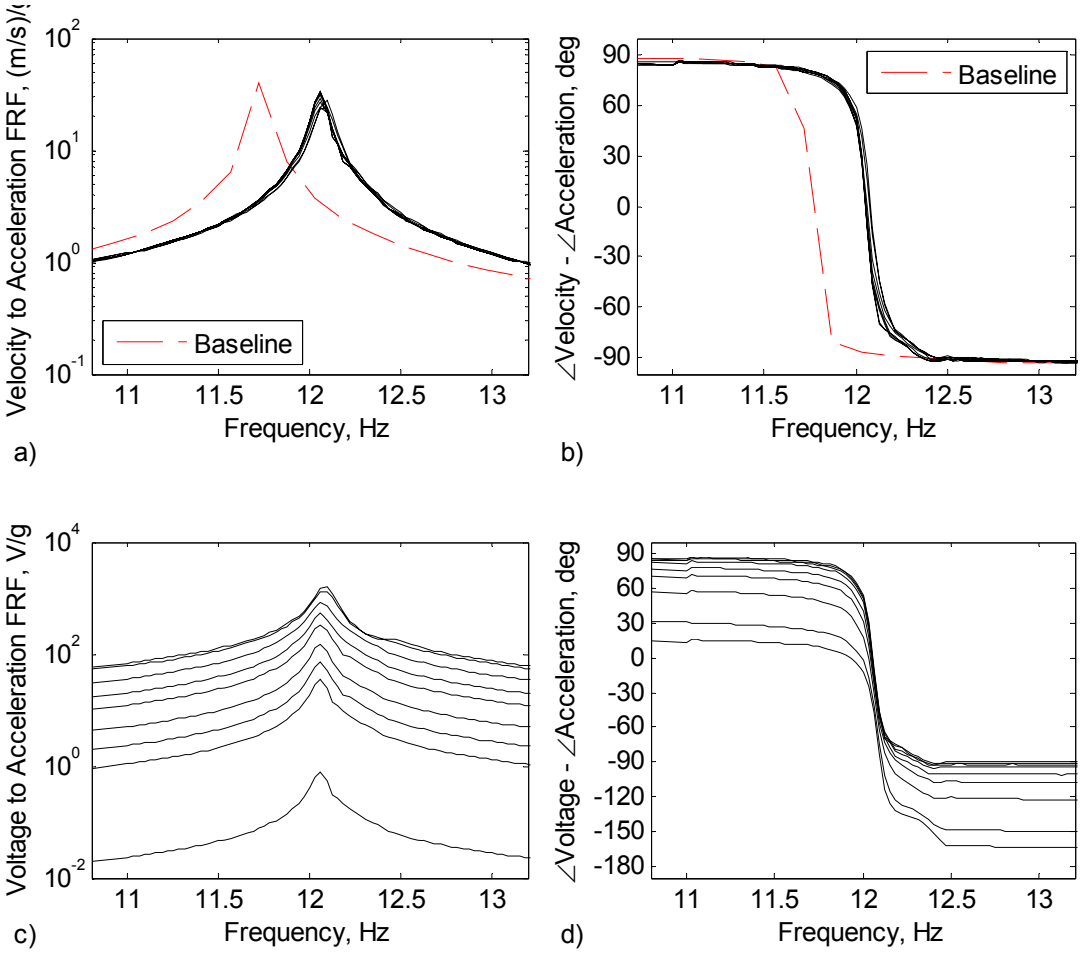

Figure B.8: Tip-velocity-to-harmonic-base-acceleration FRF a) magnitude and b) phase, and voltage-output-to-harmonic-base-acceleration FRF c) magnitude and d) phase for Beam 3 with MIDE QP10N type piezoceramic.

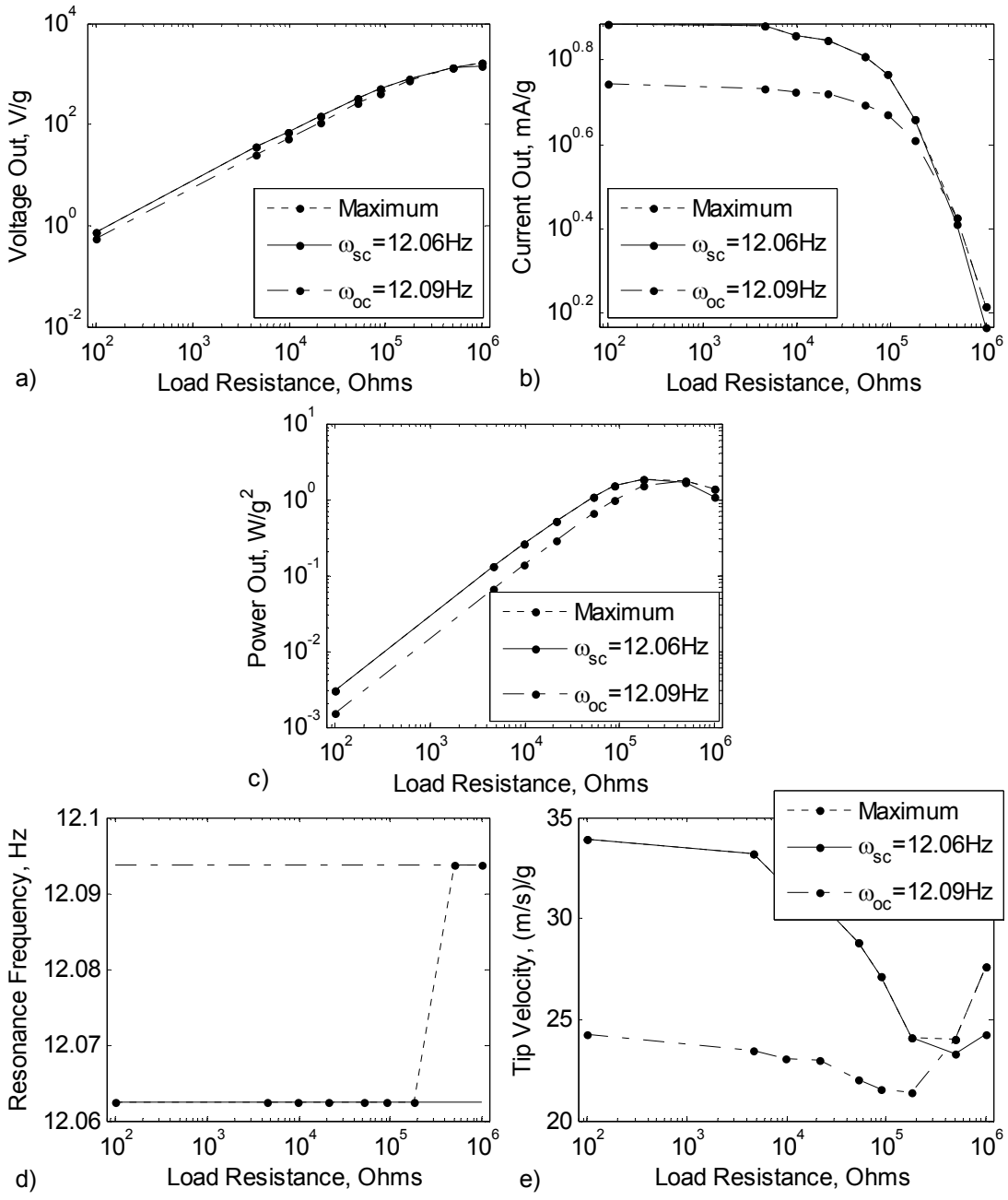

Figure B.9: a) Voltage-output, b) current-output, c) power-output, e) tip-velocity per-base-acceleration and d) corresponding resonance frequency of Beam 3 with MIDE QP10N piezoceramic as a function of load resistance.

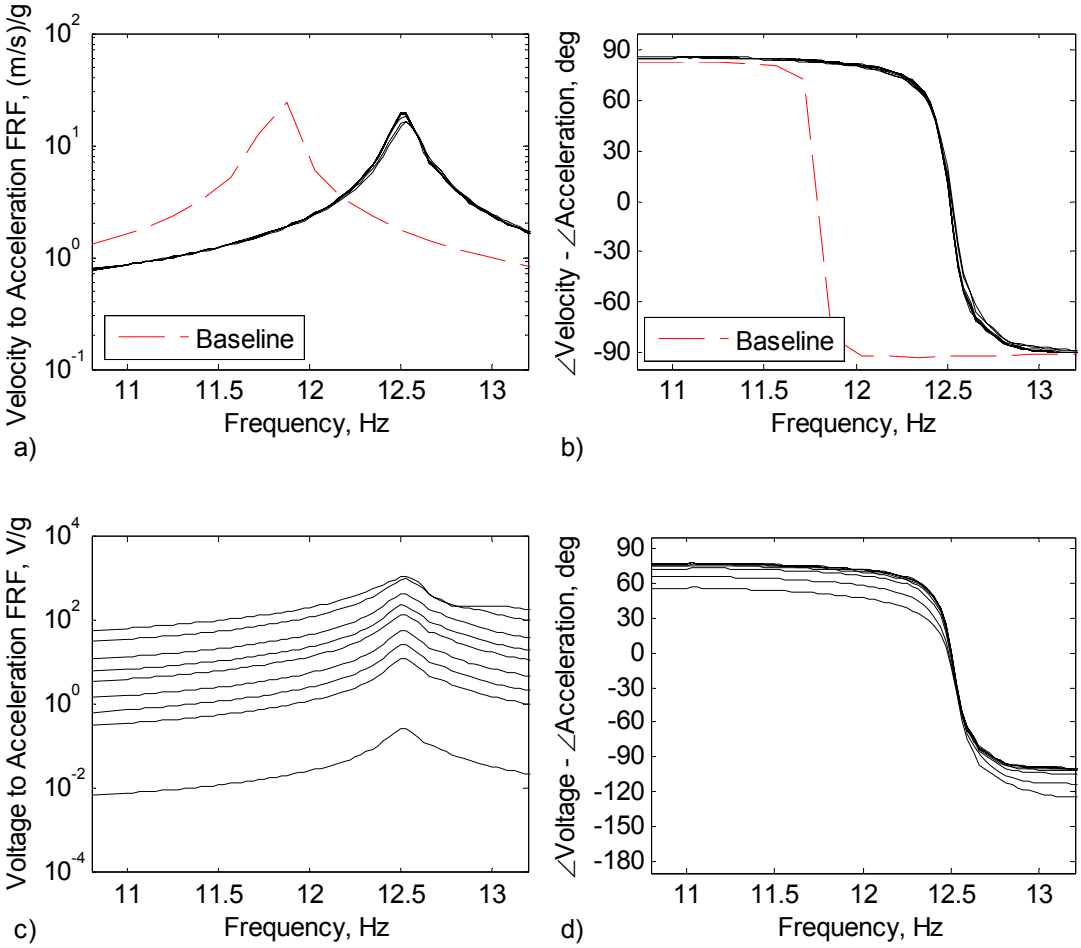

Figure B.10: Tip-velocity-to-harmonic-base-acceleration FRF a) magnitude and b) phase, and voltage-output-to-harmonic-base-acceleration FRF c) magnitude and d) phase for Beam 4 with MFC M8528-P1 type piezoceramic.

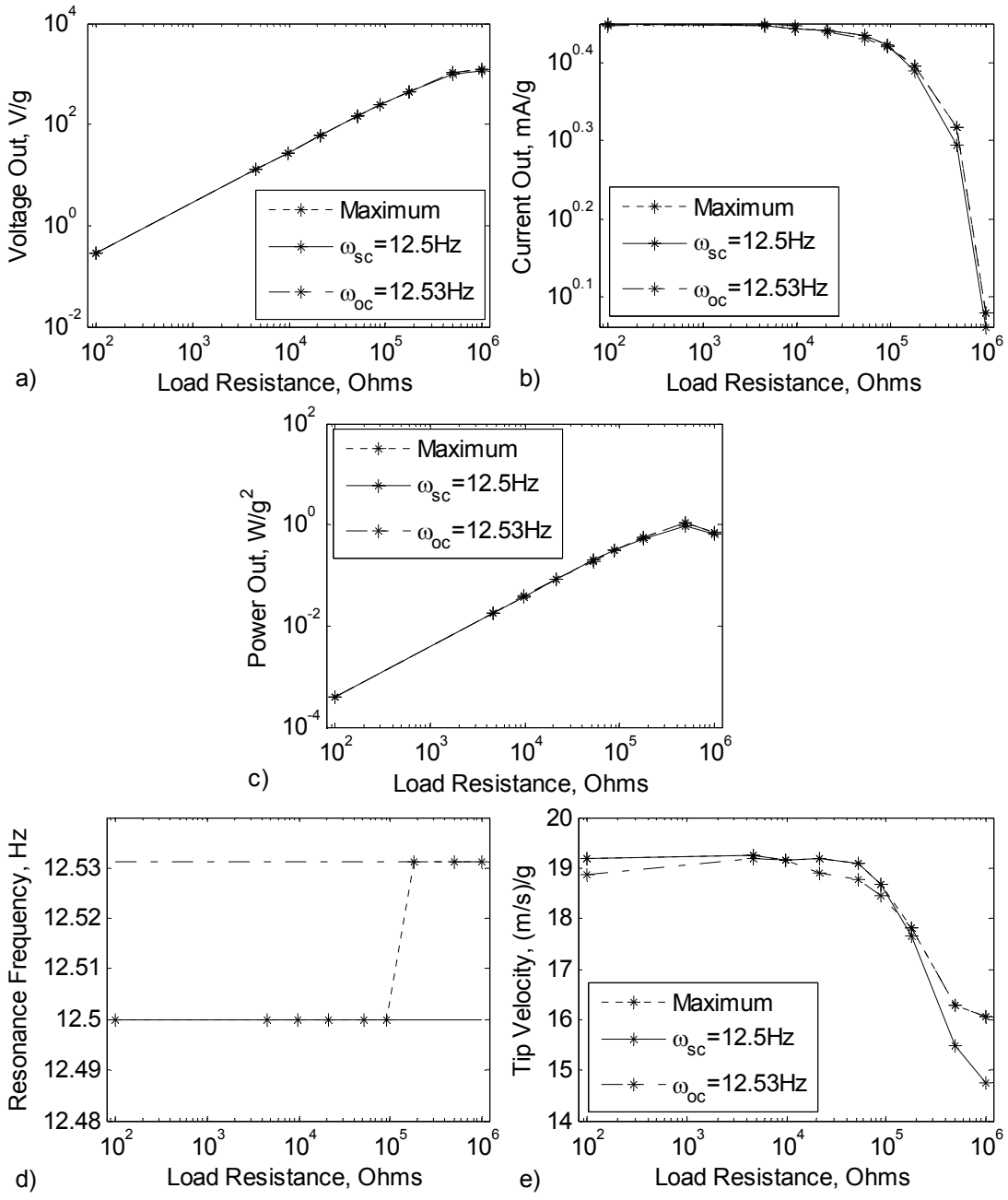

Figure B.11: a) Voltage-output, b) current-output, c) power-output, e) tip-velocity per-base-acceleration and d) corresponding resonance frequency of Beam 4 with MFC M8528-P1 piezoceramic as a function of load resistance.

B.3 Additional Single Crystal Unimorph Results

This section presents the energy harvesting characteristics of unimorph beams with polycrystalline and single crystal piezoelectric devices, and with different substrates. These results are presented to aid the discussion presented in Section 3.3.

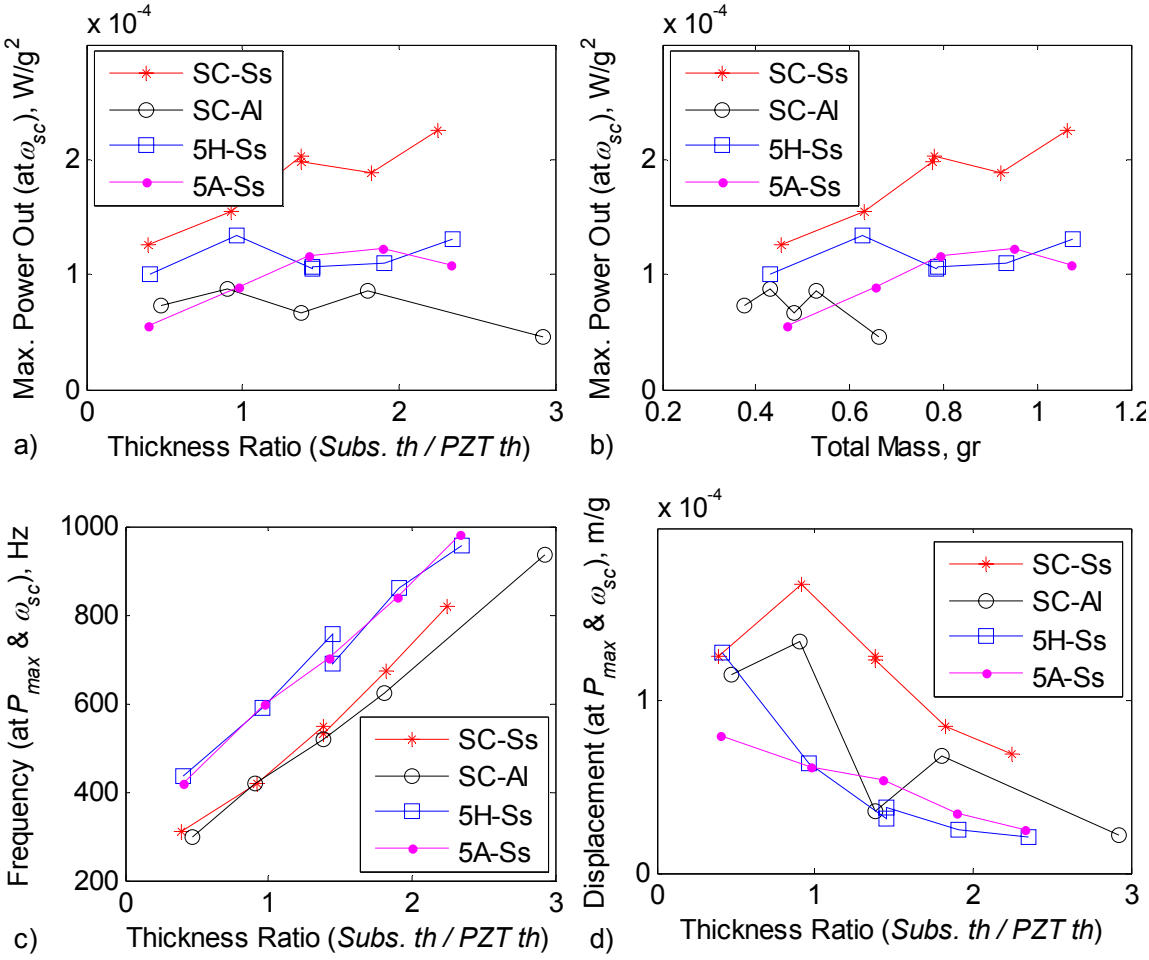

Figure B.12: Maximum-power-output-per-harmonic-base-acceleration as a function of a) thickness ratio and b) total unimorph mass. c) Frequency and b) displacement-per-base-acceleration at the maximum power operating condition as a function of thickness ratio. Response is at the short circuit natural frequency.

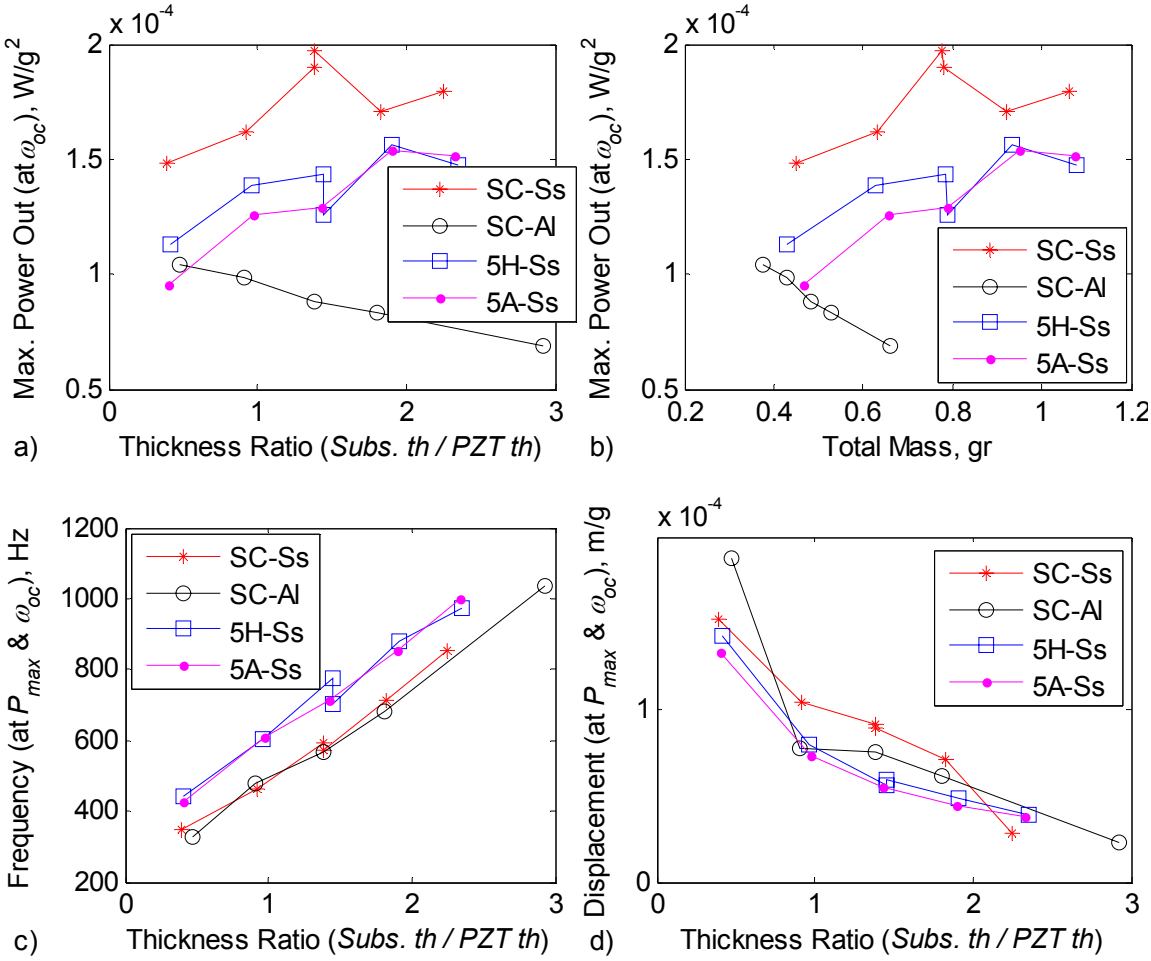

Figure B.13: Maximum-power-output-per-harmonic-base-acceleration as a function of a) thickness ratio and b) total unimorph mass. c) Frequency and b) displacement-per-base-acceleration at the maximum power operating condition as a function of thickness ratio. Response is at the open circuit natural frequency.

APPENDIX C

ELASTIC MODULUS MEASUREMENTS OF COMPOSITES

This section presents the experimental stress-strain measurements on several commercially available composite materials. The test data presented in this appendix are used to aid the design of the bimorph beam samples (presented in Section 4.4) and the bimorph airfoils presented in Chapter 5 and Chapter 6. The purpose of these tests is to determine the cured properties of fiber-epoxy composites. The two properties that are of interest are thickness (after the curing of the epoxy) and elastic modulus.

The tests are conducted at the Engineering Science and Mechanics Department of Virginia Tech. An Instron Model 4468 Electromechanical Test System (with capacity of 50 kN) is used along with two self-calibrating load cells (with 1 kN and 5 kN maximum load capacity). The crosshead extension speed is set to 0.50 mm/s for all stress-strain tests. Figure C.1 shows the experimental setup. A National Instruments (NI) LabVIEW based program is used to acquire the head extension and the force from the load cell. It is important to note the following: 1) The samples are rectangular trough the whole length (instead of the traditional "dog bone" shape) so there are significant stress concentrations around the clamped edges. This causes the fracture point to be lower than a dog-bone specimen. Since the research in this section aims to quantify the material axial modulus at the linear elastic region, these artificial stress concentrations can be neglected. 2) The crosshead (or the clamp) extension is used to measure the strain in the specimens instead of a typical extensometer setup. It is predicted that (if the samples slip from the clamp and the slip is not detected during post-processing) the strain measurements will be larger than actual strains while the loads are measured correctly. In all of the experiments, the slip conditions are detected. Also, several "identical" specimens are fabricated for each sample, and stress-strain measurements are checked for consistency.

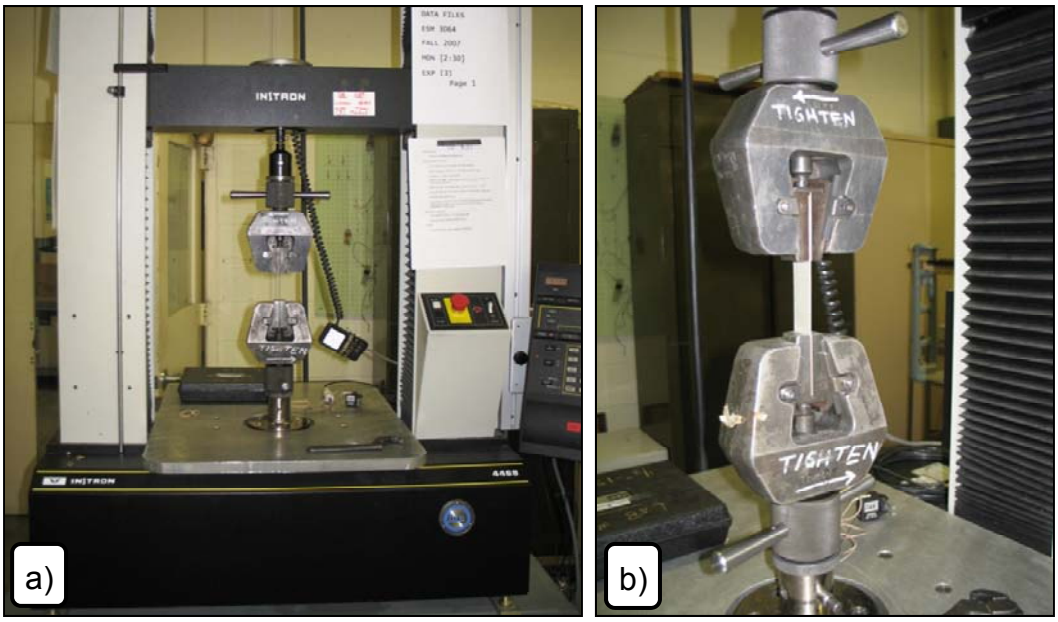

Figure C.1: Instron stress-strain test setup. a) The Instron 4468 equipment. b) Close-up of a specimen clamped for testing.

The composite samples are prepared by a standard vacuum bagging technique. The fiber-epoxy composite samples are cured under approximately 0.8 Atm vacuum at room temperature for 24 hours. A *West System* brand *205 -105 Fast Epoxy System* is used as the epoxy material. The fabrics are from three sources: 1) *Fibre Glast*, 2) *Wicks Aircraft Supply*, 3) *Hobbico.* An additional carbon fabric is also tested which was available in the laboratory. The carbon fabric is likely to be from the first two sources. Once the curing process is complete, the composite samples are trimmed to a rectangle with 140 mm total length and 25.4 mm width. Rectangular tabs are glued (to reduce stress concentrations due to clamping) to both ends of each specimen, leaving approximately 60 mm long (free-to-strain) test section. The clamp tips are also separated by 60 mm, therefore the free length of each specimen is taken as $l = 60\ mm$. Figure C.2 shows 15 (out of 16) specimens that are cured and trimmed. The figure shows some samples before and some after the Instron tests. The tested specimens are shown on the bottom left part of the figure. Each sample, labeled with a code name, has several "identical" specimens.

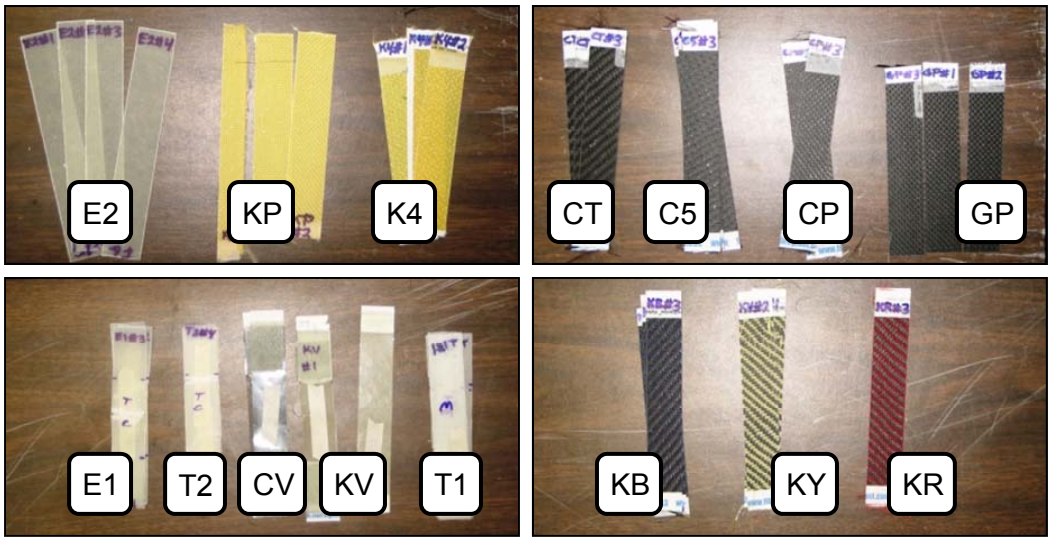

Figure C.2: Tested specimens representing 15 out of 16 sample composites.

The material and layup characteristics of all samples are presented in Table C.1. The *Code* column refers to the two character label that is shown in Figure C.2. The fabric density is presented with the standard units of oz/yd^2. The *Source* column presents the distributor of the fabrics and the respective part number.

Table C.1: Material properties of all samples.

Sample	Code	Material	Weave	Layers	oz/yd^2	Source
1	E1	Glass Fiber Thick	E Glass Cloth	1	8.90	Wicks (7781)
2	E2	Glass Fiber Thick	E Glass Cloth	2	8.90	Wicks (7781)
3	T1	Glass Fiber Thin	Cloth	1	2.00	Hobbico (5010)
4	T2	Glass Fiber Thin	Cloth	2	2.00	Hobbico (5010)
5	CI	Carbon Fiber	3k Plain	1	5.70	Lab
6	CP	Carbon Fiber	3k Plain	1	5.70	Fibre Glast (530)
7	C5	Carbon Fiber	5HS	1	10.10	Fibre Glast (660)
8	CT	Carbon Fiber	2x2 Twill	1	5.70	Fibre Glast (1069)
9	CV	Carbon Fiber	Veil	1	0.20	Fibre Glast (1064)
10	KY	Carbon/Kevlar	2x2 Twill	1	5.70	Fibre Glast (1065)
11	KB	Carbon/Kevlar	2x2 Twill	1	5.70	Fibre Glast (1066)
12	KR	Carbon/Kevlar	2x2 Twill	1	5.70	Fibre Glast (1067)
13	GP	Graphite Tape	3k Plain	1	5.70	Fibre Glast (598)
14	K4	Kevlar Fabric	4HS	1	5.00	Fibre Glast (549)
15	KP	Kevlar Tape	Plain	1	5.00	Fibre Glast (532)
16	KV	Kevlar Veil	Veil	1	0.25	Fibre Glast (1063)

Table C.2 shows the averaged results from the Instron tests. The material thickness is labeled as *th*, and the calculated elastic modulus is $E_1 = \sigma_1/\varepsilon_1$ where σ_1 is the measured axial stress and the ε_1 is the measured strain. The fracture stress and strain are σ_F and ε_F respectively. The tests where slip is detected are not used for averaging. Also note that not all tests achieved fracture; therefore the fracture values are not available.

Table C.2: Average measured properties of composite samples.

Sample	Code	*th*, mm	E_1, GPa	σ_F, GPa	ε_F, %
1	E1	0.305	99.9	2.89	3.58
2	E2	0.610	95.0	n/a	n/a
3	T1	0.140	96.1	2.02	2.44
4	T2	0.216	120.5	2.92	2.94
5	CI	0.305	183.3	n/a	n/a
6	CP	0.305	176.1	5.88	3.47
7	C5	0.546	165.3	n/a	n/a
8	CT	0.330	190.1	4.31	2.30
9	CV	0.114	24.3	0.21	0.59
10	KY	0.305	186.3	5.57	2.97
11	KB	0.305	89.7	3.30	4.74
12	KR	0.305	198.7	5.37	2.62
13	GP	0.318	180.5	4.49	2.38
14	K4	0.305	128.2	n/a	n/a
15	KP	0.330	92.3	n/a	n/a
16	KV	0.114	12.3	0.19	1.43

Table C.3 and Table C.4 show all tests that are conducted (which are then used to construct Table C.2). These tables are presented to show the variation of properties among the so called "identical" specimens from each composite sample. The *Note* column presents the test condition. A completely successful test (where specimen did not slip and fracture is achieved) is labeled "*1*". A failed test (where the specimen slipped from the clamps) is labeled with "*2*". A test that is valid in the linear elastic region, but is considered faulty beyond this range is labeled "*3*".

Table C.3: Complete test data. Part 1 of 2.

Test	Sample	*w*, mm	*th*, mm	E_1, GPa	σ_F, GPa	ε_F, %	Note
1	9	25.4	0.1143	23.3	0.226	0.733	1
2	9	25.4	0.1143	25.3	0.195	0.450	1
3	3	25.4	0.1397	97.5	2.060	2.433	1
4	3	25.4	0.1397	95.9	2.056	2.533	1
5	3	25.4	0.1397	96.0	2.001	2.367	1
6	3	25.4	0.1397	95.1	1.977	2.433	1
7	16	25.4	0.1143	12.3	0.187	1.433	1
8	4	25.4	0.2159	n/a	n/a	n/a	2
9	4	25.4	0.2159	n/a	n/a	n/a	2
10	4	25.4	0.2159	117.9	2.474	2.400	1
11	4	25.4	0.2159	122.0	3.178	3.300	1
12	4	25.4	0.2159	121.1	2.955	2.950	1
13	4	25.4	0.2159	121.1	3.074	3.100	1
14	1	25.4	0.3048	106.4	3.137	4.067	1
15	1	25.4	0.3048	99.3	2.695	3.183	1
16	1	25.4	0.3048	98.7	2.800	3.450	1
17	1	25.4	0.3048	95.1	2.944	3.633	1
18	2	25.4	0.6096	93.6	n/a	n/a	3
19	2	25.4	0.6096	95.0	3.037	4.933	1
20	2	25.4	0.6096	95.4	2.996	4.567	1
21	2	25.4	0.6096	96.0	2.940	5.700	1
22	8	25.4	0.3302	n/a	n/a	n/a	2
23	8	25.4	0.3302	n/a	n/a	n/a	2
24	8	25.4	0.3302	n/a	n/a	n/a	2
25	8	25.4	0.3302	n/a	n/a	n/a	2

Table C.4: Complete test data. Part 2 of 2.

Test	Sample	*w*, mm	*th*, mm	E_1, GPa	σ_F, GPa	ε_F, %	Note
26	8	25.4	0.3302	184.6	4.128	2.367	1
27	8	25.4	0.3302	191.7	4.263	2.217	1
28	8	25.4	0.3302	194.1	4.553	2.317	1
29	6	25.4	0.3048	n/a	n/a	n/a	2
30	6	25.4	0.3048	n/a	n/a	n/a	2
31	6	25.4	0.3048	174.8	5.528	2.850	1
32	6	25.4	0.3048	n/a	n/a	n/a	2
33	6	25.4	0.3048	177.7	6.110	3.533	1
34	6	25.4	0.3048	175.7	5.994	4.017	1
35	13	25.4	0.3175	179.1	4.503	2.400	1
36	13	25.4	0.3175	179.2	4.931	2.633	1
37	13	25.4	0.3175	183.3	4.047	2.117	1
38	11	25.4	0.3048	92.7	3.384	5.050	1
39	11	25.4	0.3048	86.6	3.074	4.400	1
40	11	25.4	0.3048	89.8	3.435	4.783	1
41	10	25.4	0.3048	186.6	5.877	3.067	1
42	10	25.4	0.3048	186.0	5.268	2.867	1
43	12	25.4	0.3048	203.7	5.471	2.567	1
44	12	25.4	0.3048	197.6	5.285	2.717	1
45	12	25.4	0.3048	194.8	5.366	2.567	1
46	14	25.4	0.3048	128.7	4.328	3.267	1
47	14	25.4	0.3048	129.8	n/a	n/a	3
48	14	25.4	0.3048	126.1	3.896	3.100	1
49	15	25.4	0.3302	91.2	n/a	n/a	3
50	15	25.4	0.3302	93.5	4.392	3.967	1
51	5	18.6	0.3048	184.0	n/a	n/a	3
52	5	25.4	0.3048	182.5	3.683	1.933	1
53	7	25.4	0.5461	161.7	n/a	n/a	3
54	7	25.4	0.5461	169.1	n/a	n/a	3
55	7	25.4	0.5461	164.9	n/a	n/a	3

Figure C.3 through Figure C.8 presents the calculated stress-strain plots for all test specimens. The (red) circles indicate the two points (on the assumed linear elastic region) where the elastic modulus, E_1, is calculated.

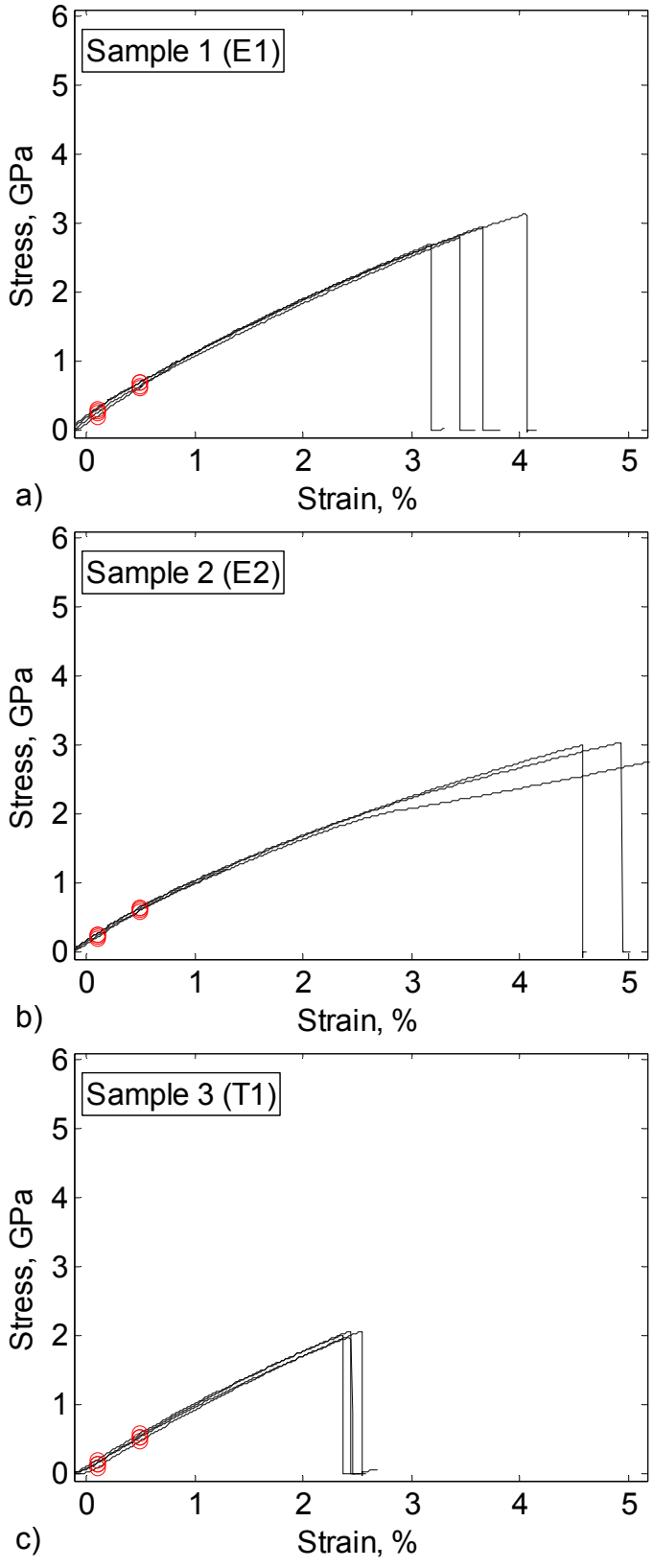

Figure C.3: Stress-strain plots for a) Sample 1, b) Sample 2 and c) Sample 3.

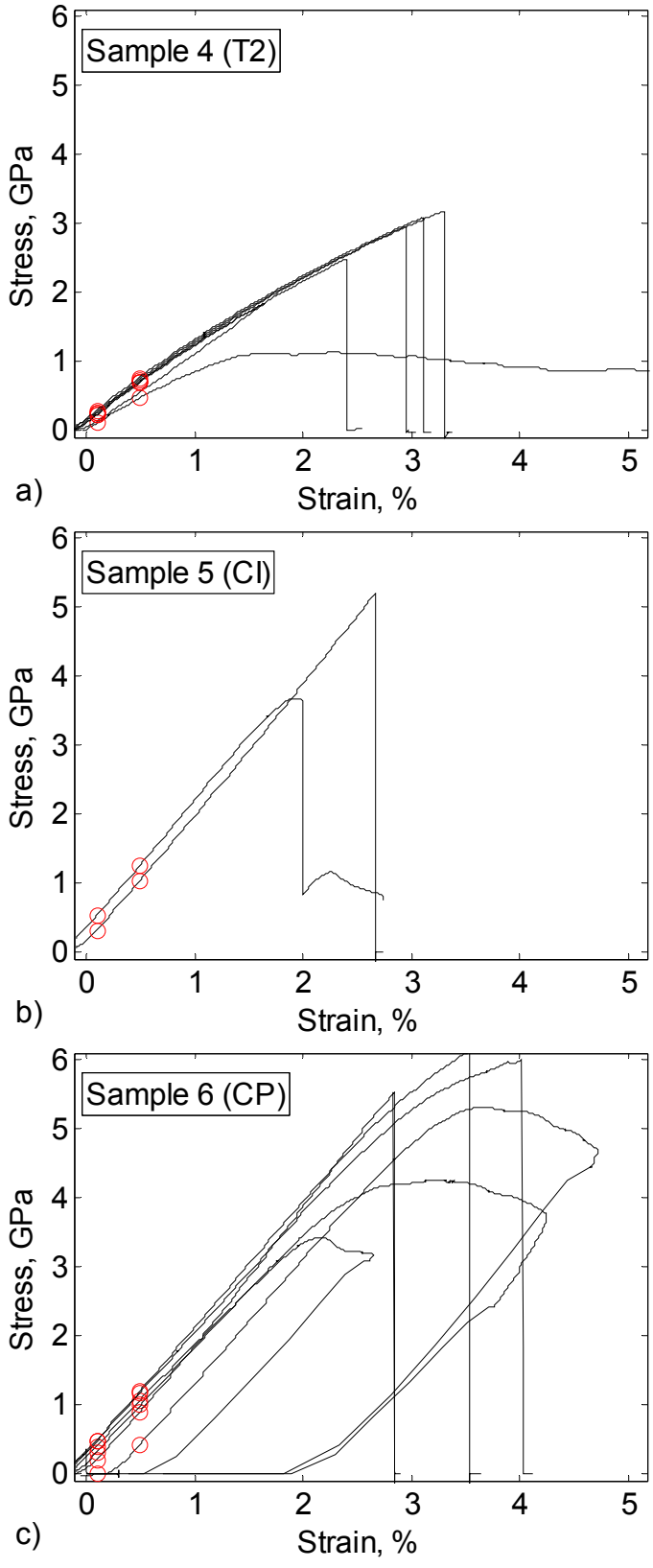

Figure C.4: Stress-strain plots for a) Sample 4, b) Sample 5 and c) Sample 6.

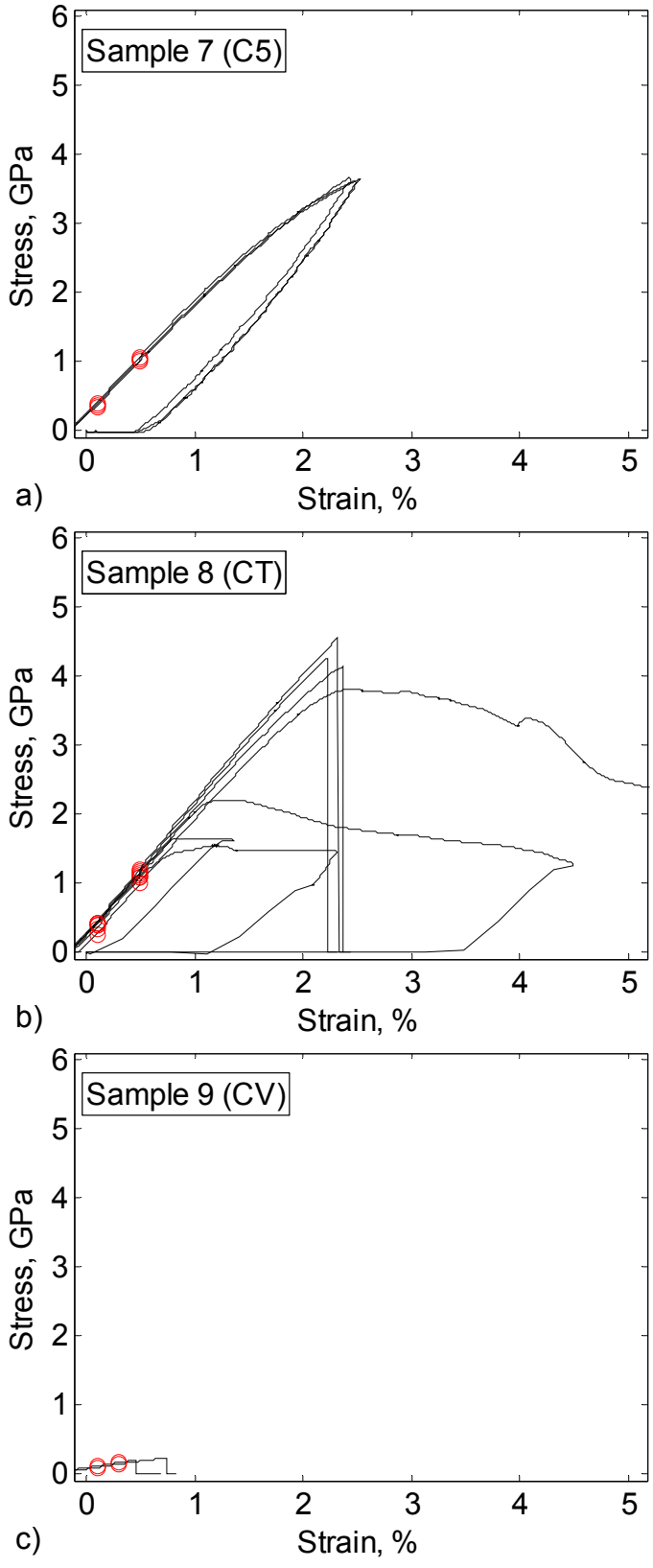

Figure C.5: Stress-strain plots for a) Sample 7, b) Sample 8 and c) Sample 9.

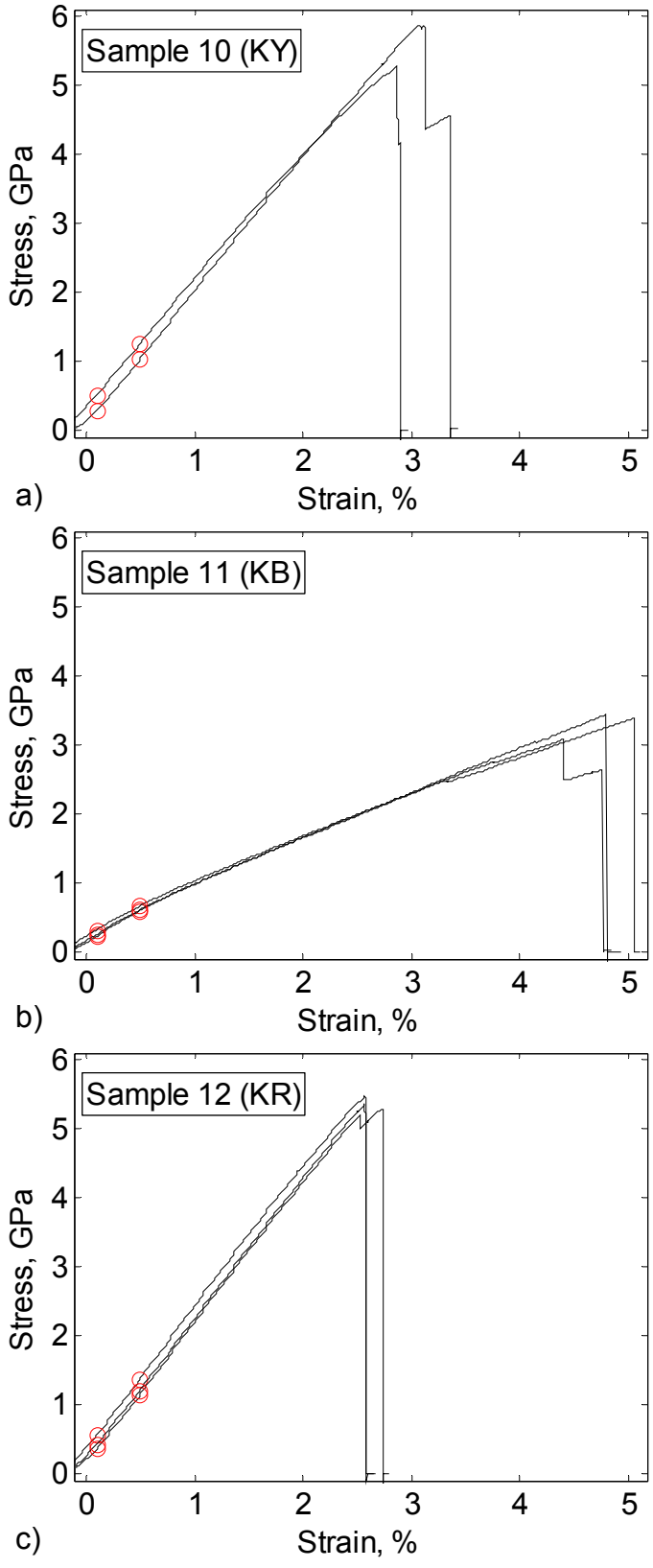

Figure C.6: Stress-strain plots for a) Sample 10, b) Sample 11 and c) Sample 12.

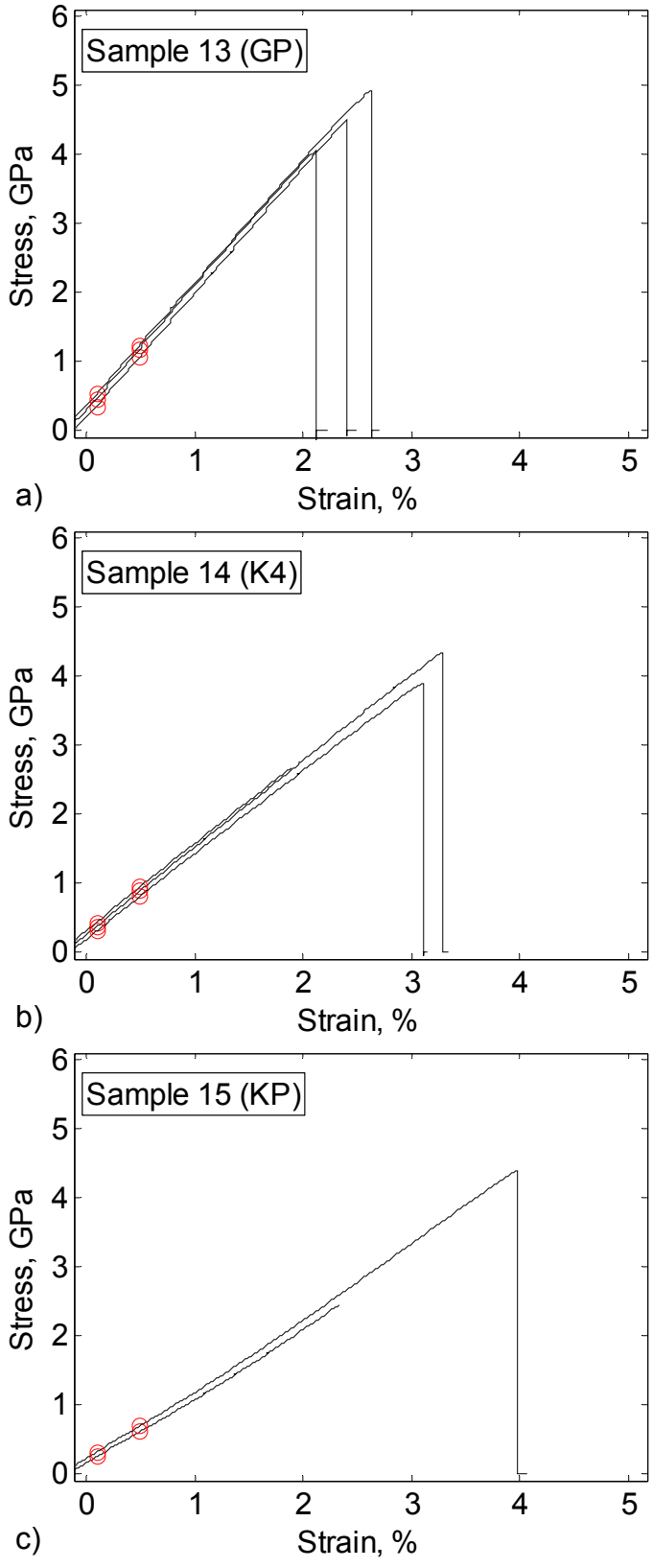

Figure C.7: Stress-strain plots for a) Sample 13, b) Sample 14 and c) Sample 15.

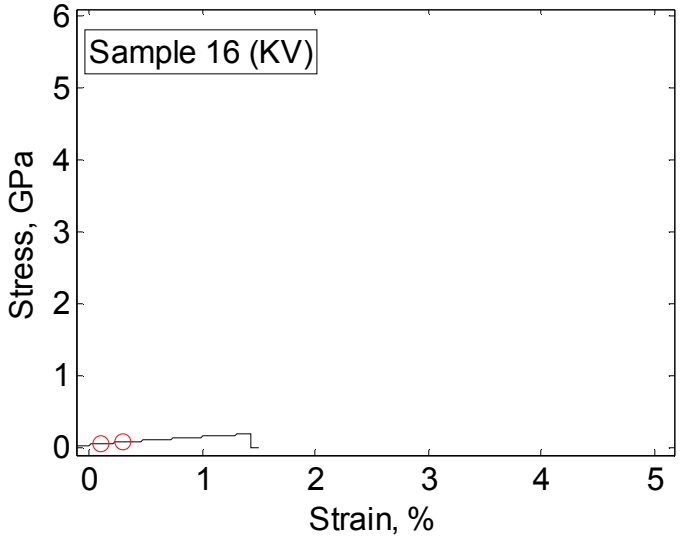

Figure C.8: Stress-strain plot for Sample 16.

APPENDIX D

ADDITIONAL MFC BIMORPH ACTUATION RESULTS

This appendix presents 1) electrical input-output relationships of several DC-DC converters (see Section 4.2.1) and 2) physical parameters and additional experimental data of the bimorph devices that are presented in Section 4.4.

D.1 DC-DC Converter Electrical Performance Results

This section presents additional electrical input-output characterization of several DC-DC converters to aid the discussion presented in Section 4.2.1.

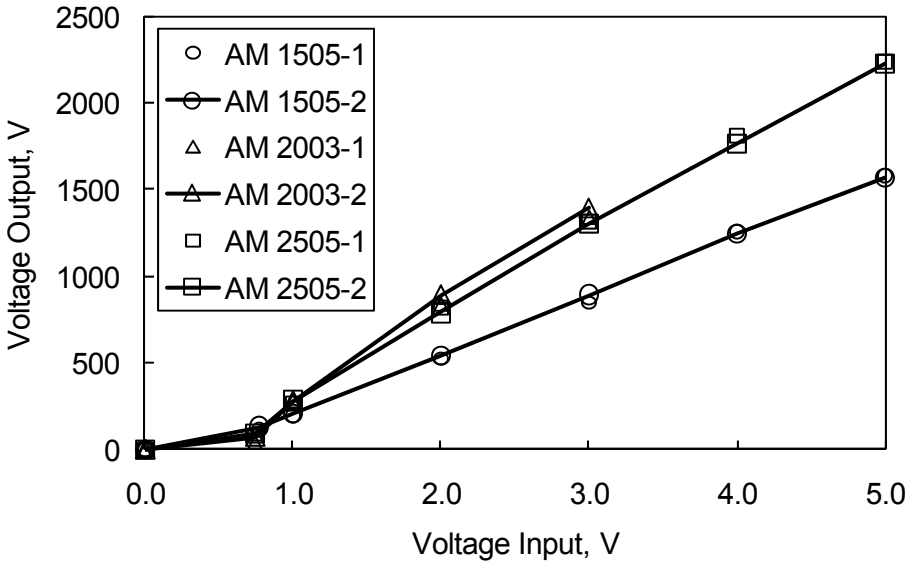

Figure D.1: Voltage input-output relationship of six AM Powers Systems DC-DC converters with a 5.01 MOhm load.

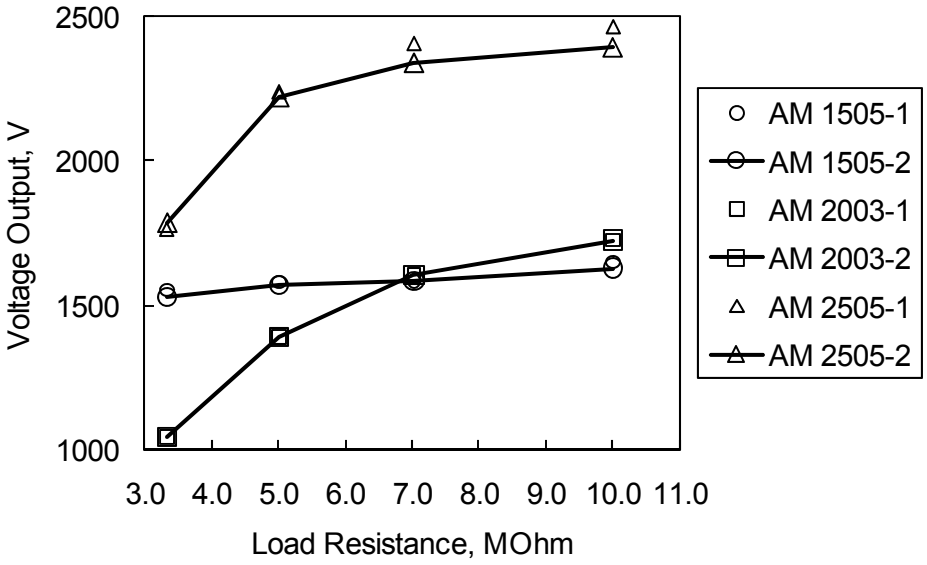

Figure D.2: Voltage output of six AM Powers Systems DC-DC converters at their maximum input voltage.

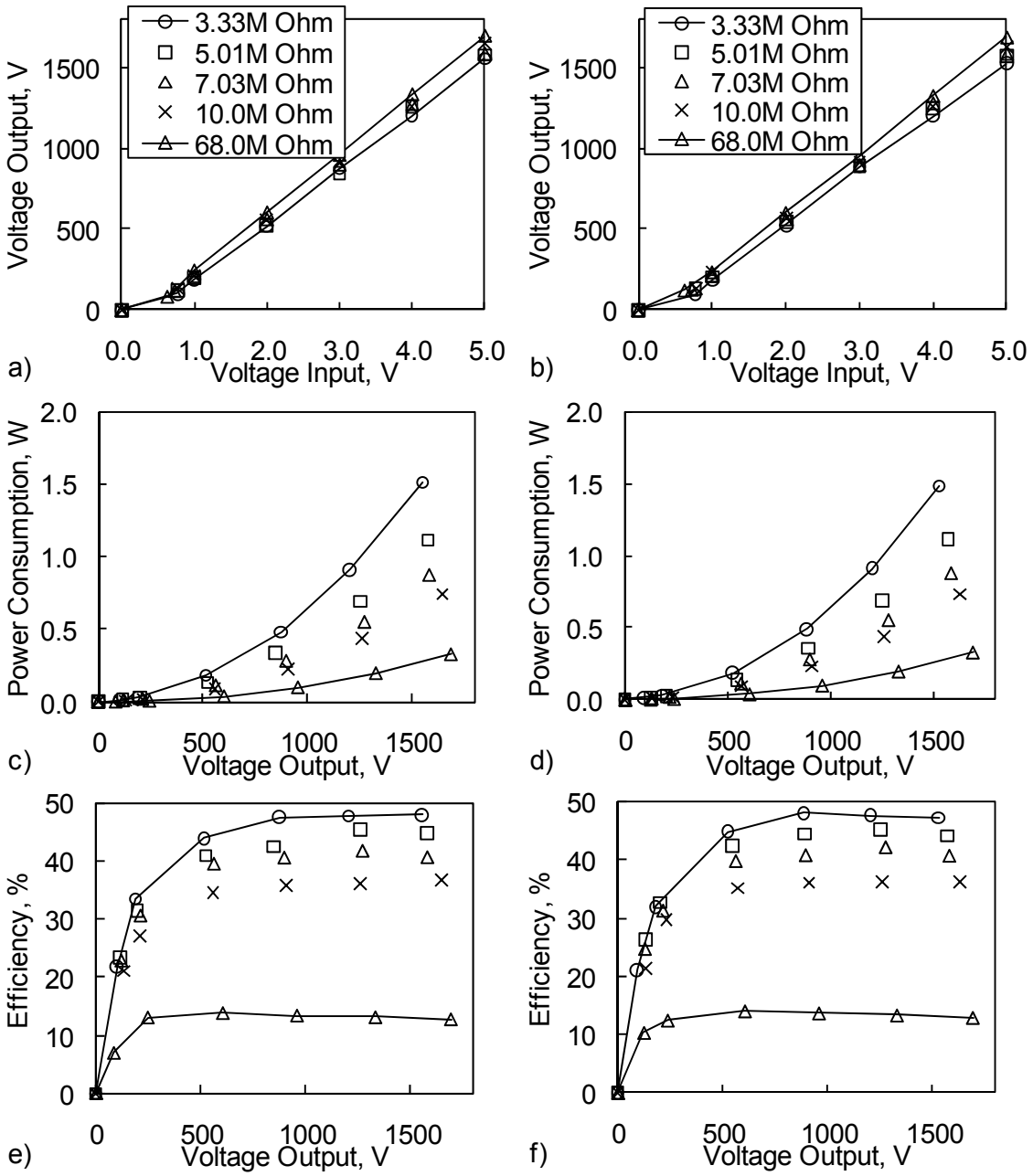

Figure D.3: The electrical response of two AM Power Systems model AM1505 DC-DC converters. a,c,e) AM1505-1, b,d,f) AM1505-2.

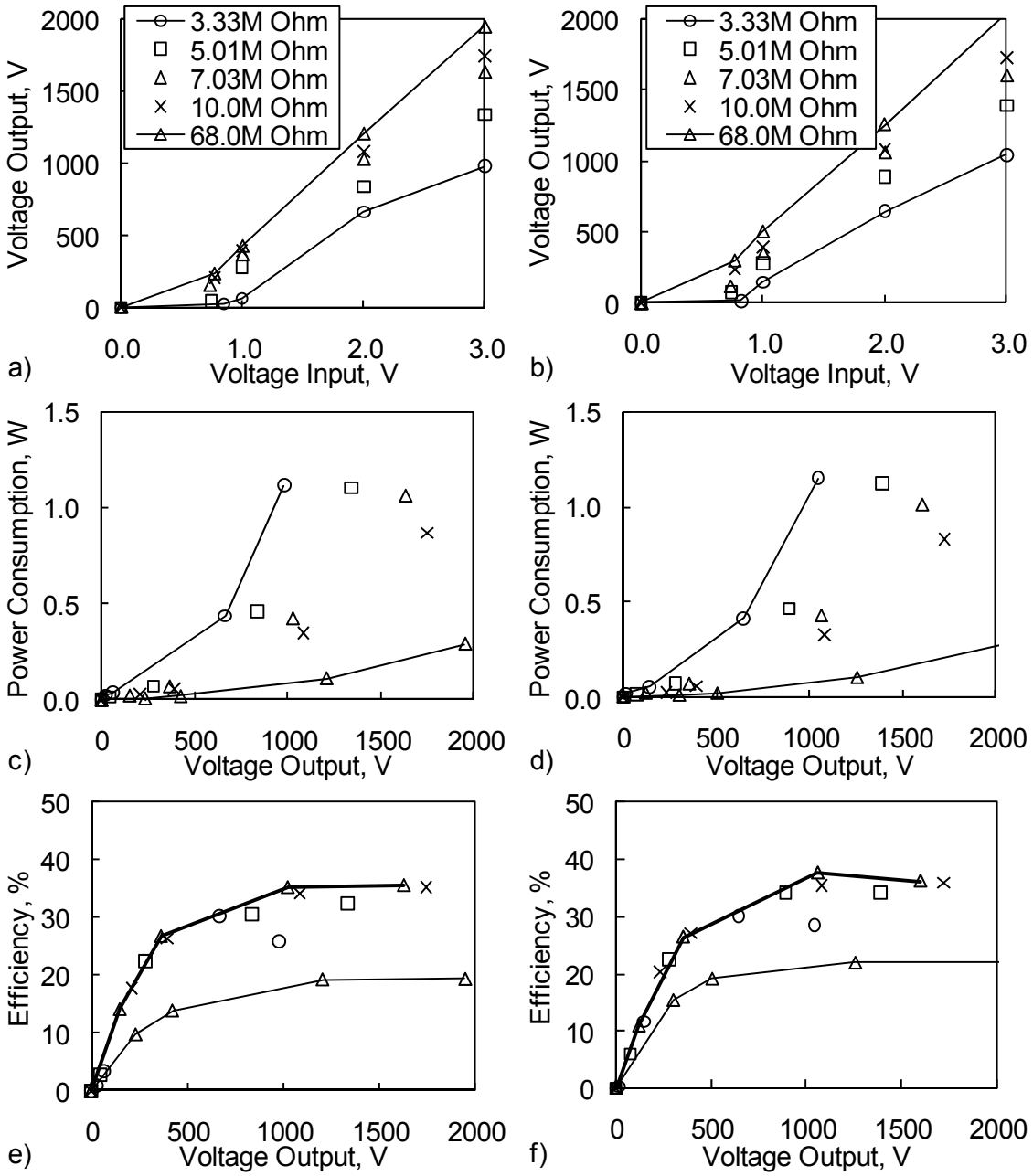

Figure D.4: The electrical response of two AM Power Systems model AM2003 DC-DC converters. a,c,e) AM2003-1, b,d,f) AM2003-2.

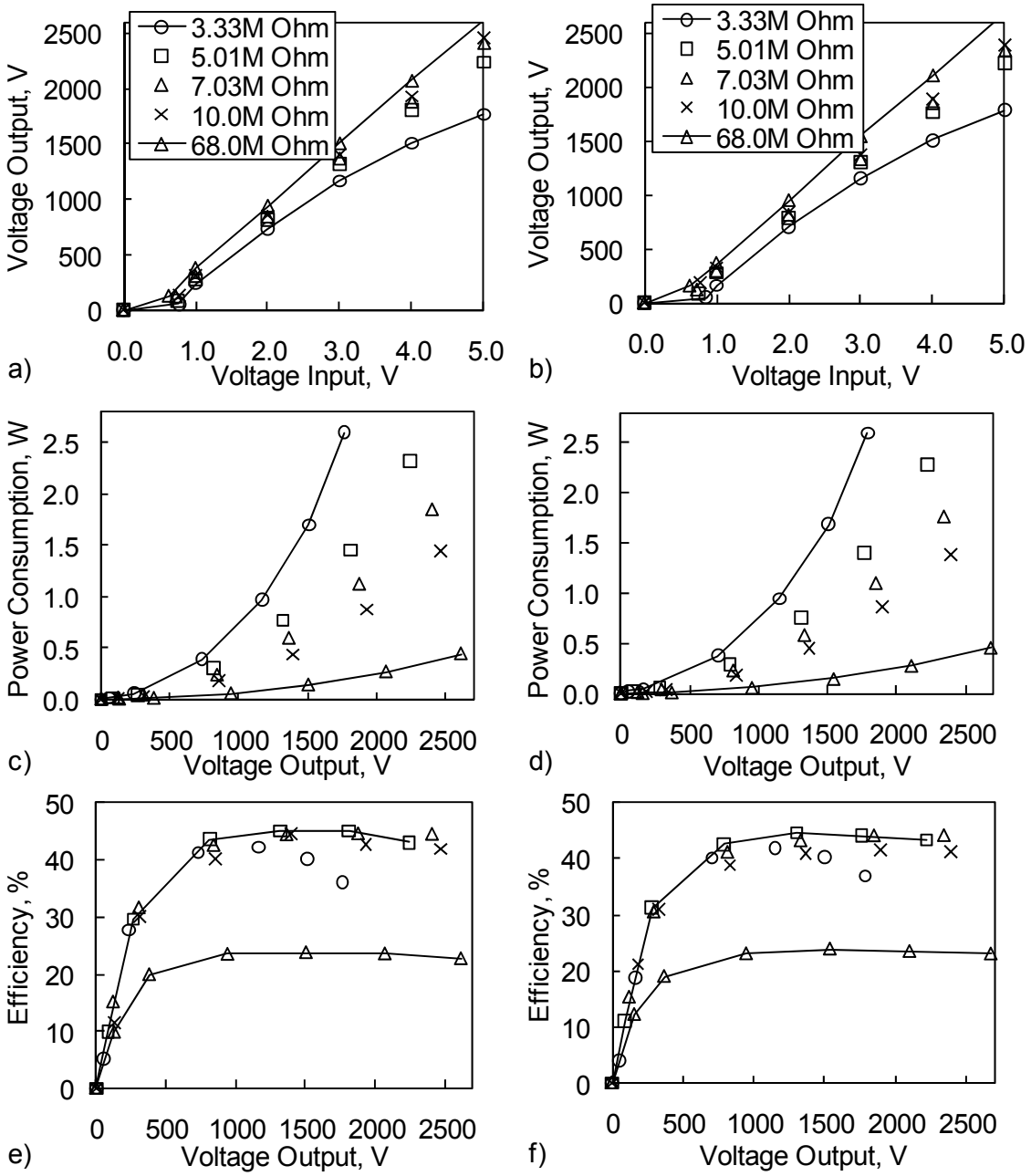

Figure D.5: The electrical response of two AM Power Systems model AM2505 DC-DC converters. a,c,e) AM2505-1, b,d,f) AM2505-2.

D.2 Bimorph Actuation Experiments

A total of seven bimorphs are fabricated by bonding two MFC M8507-P1 type actuators to both sides of a substrate material. Each unimorph is 16.28 mm wide and 102.38 mm long (which also correspond to the original size of the MFC M8507-P1 type actuator). The active area (with piezoceramic material) of MFC M8507-P1 type actuator is approximately 85.0 mm long and 7.00 mm wide. The epoxy (used for bonding the MFCs to the substrate) is set for cure in a vacuum bag at approximately 0.8 Atm vacuum. Figure D.6 shows six of the seven bimorphs labeled B1 – B6 respectively.

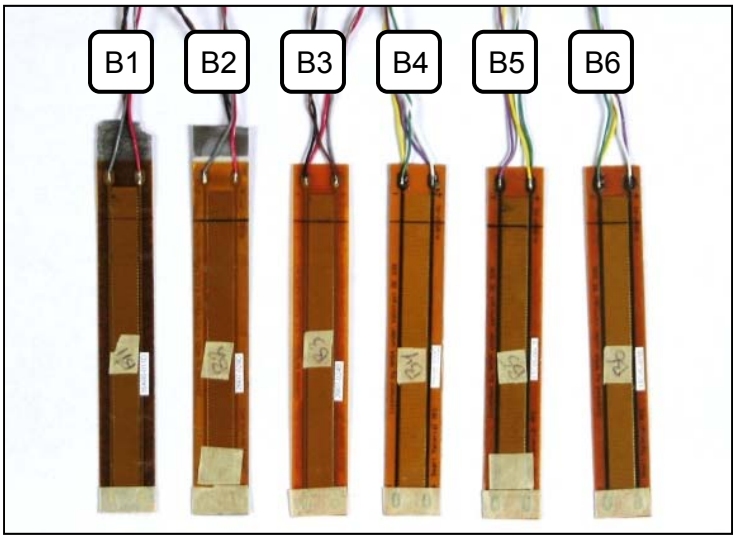

Figure D.6: Bimorph samples with MFC M8507-P1 type actuator.

Table D.1 presents the material properties of the substrate materials that are used for each bimorph. Additional substrate information can be found in Appendix C.

Table D.1: Material properties of substrates used in bimorphs.

Sample	Substrate	Notes	Source	Glue / Epoxy
B1	Carbon Veil / Epoxy	1 layer	Fibre Glast (1064)	West System 205+105
B2	Stainless-Steel	n/a	McMaster	3M DP460
B3	n/a	4% cambered	n/a	3M DP460
B4	Aluminum	n/a	McMaster	3M DP460
B5	Glass Fabric / Epoxy	Thin, 1 layer	Hobbico (5010)	West System 205+105
B6	n/a	n/a	n/a	3M DP460
B7	Glass Fabric / Epoxy	Thick, 1 layer	Wicks (7781)	West System 205+105

Note that sample B3 and B6 do not have substrates and bimorph B3 is a curved bimorph with approximately 4.0% camber. This curvature is achieved by curing the bimorph on a CNC machined mold in a vacuum bag. Structural parameters of the substrates are given in Table D.2.

Table D.2: Structural properties of substrates used in bimorphs.

Sample	E_1, GPa	Density*	*Tot. th*, mm	*Subs. th*, mm	*Glue th*, mm
B1	24.3	0.20 [oz/yd^2]	0.736	0.114	n/a
B2	200*	7800 [kg/m^3]	0.699	0.027	0.072
B3	n/a	n/a	0.632	0.000	0.032
B4	70*	2700 [kg/m^3]	0.718	0.055	0.063
B5	96.1	2.00 [oz/yd^2]	0.703	0.140	n/a
B6	n/a	n/a	0.605	0.000	0.005
B7	99.9	8.90 [oz/yd^2]	0.832	0.305	n/a

The data labeled with "*" indicates estimated (or assumed) values. Note that composite substrate density is presented in original units reported by the manufacturer. In addition, the composite densities are presented for the fabric material only; hence it does not include the cured substrate (with the epoxy). The glue thickness for composite substrates is not presented because this value is accounted in the cured composite thickness.

The complete set of results is presented here for the experiments introduced in Section 4.4. Figure D.7 shows the low frequency response of sample B1 to harmonic excitation at a constant voltage and frequency. Figure D.7a and b shows the peak (or peak-to-peak/2) displacement of the free end of the bimorph in 3D and 2D plots respectively. The phase angle between the displacement and input (reference) voltage is presented in Figure D.7c and d. It is important to note that the phase calculation assumes that the signal is a single harmonic with a fixed frequency. This is true for the reference voltage signal; however the displacement is nonlinear (due to piezoceramic hysteresis) which introduces a non-zero phase in the so-called quasi-static region.

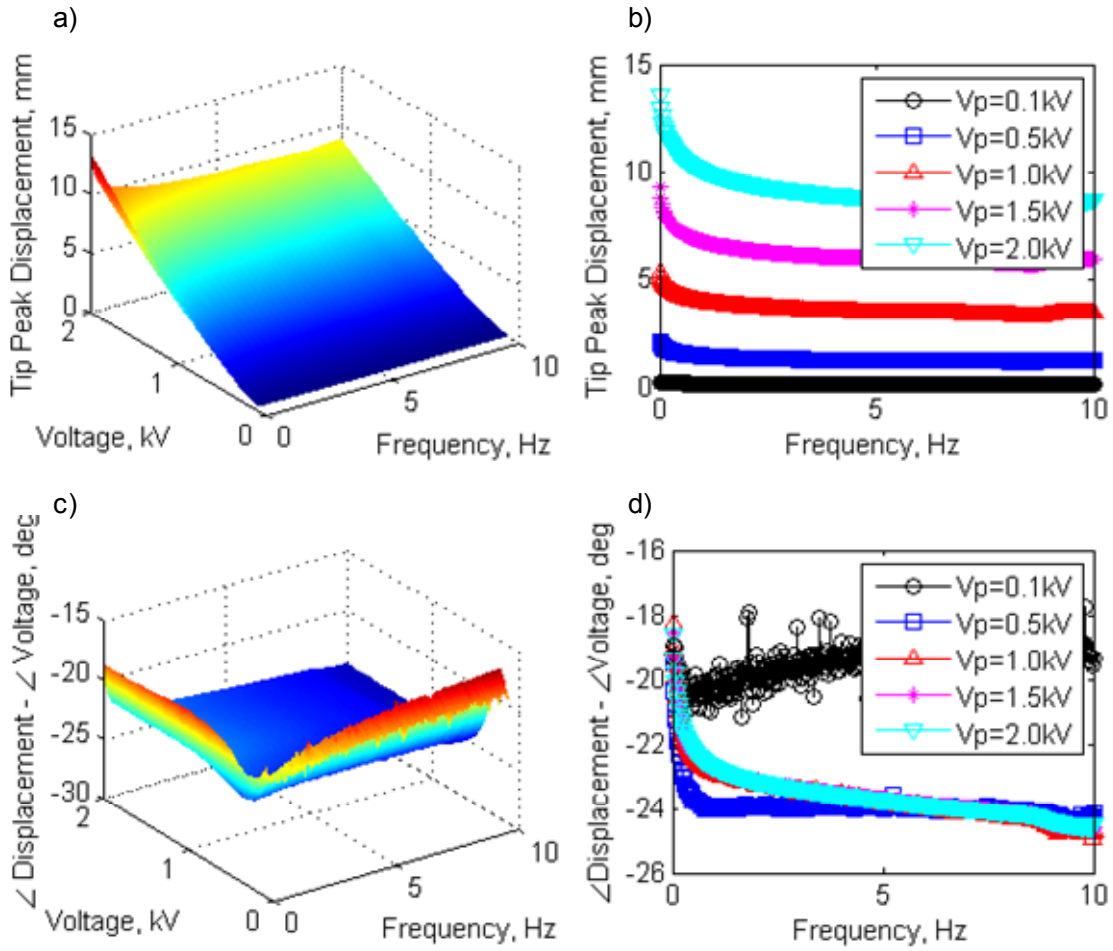

Figure D.7: Low frequency response of sample B1: a,b) Peak displacement of free-end, c,d) phase angle between displacement output and voltage input.

Figure D.8a and b presents the curvature of the beam. For the low frequency response, the operating deflection shape is assumed to be a circular arc (with constant curvature) because 1) the frequency of operation is well below the 1st natural frequency and 2) the active material covers (almost) the full length of the beam hence a uniform moment is induced (by the actuator) through the length of the beam. The power consumption of the beam is presented in Figure D.8c and d.

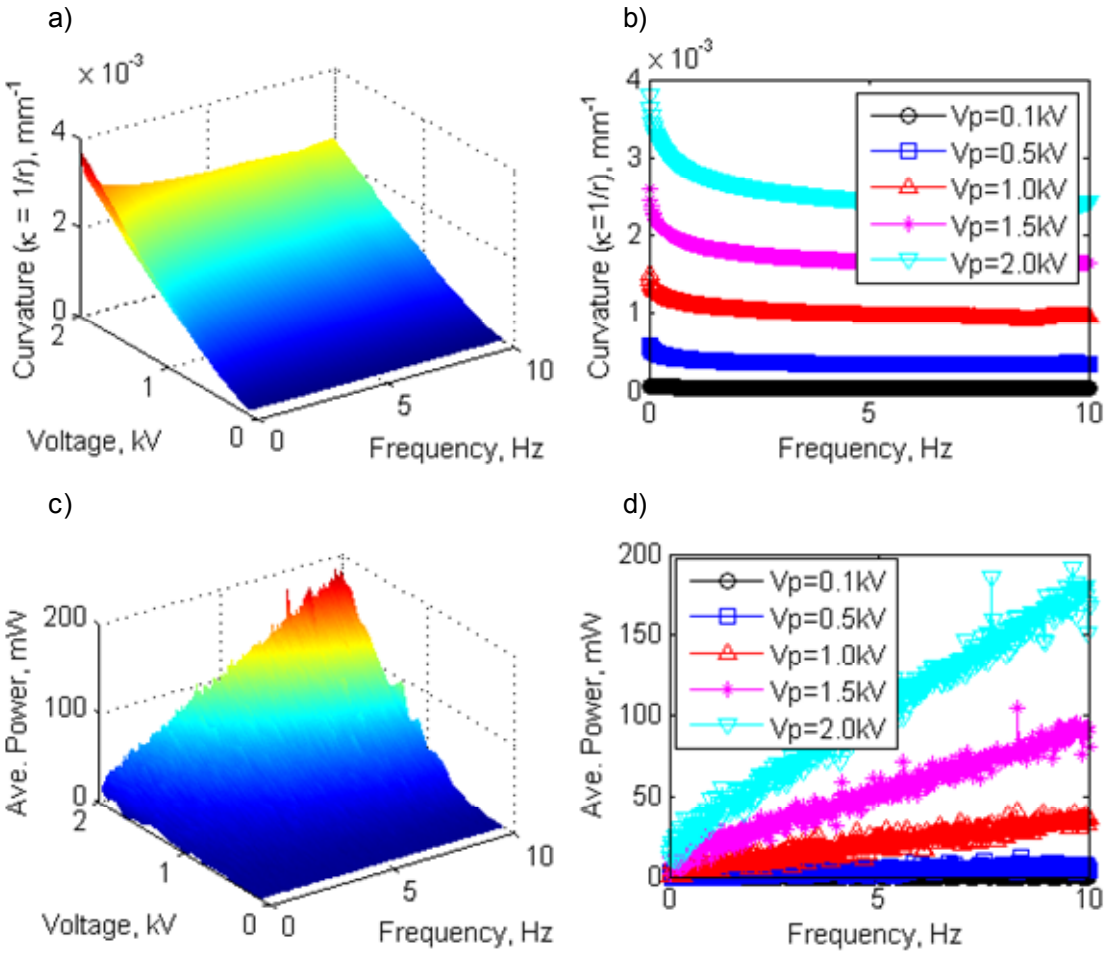

Figure D.8: Low frequency response of sample B1: a,b) Curvature and c,d) power consumption.

Figure D.9 shows the high frequency response of sample B1 to harmonic excitation at a constant voltage and frequency. Figure D.9a and b shows the peak (or peak-to-peak/2) displacement of the free end of the bimorph. The phase angle between the displacement and input (reference) voltage is presented in Figure D.9c and d.

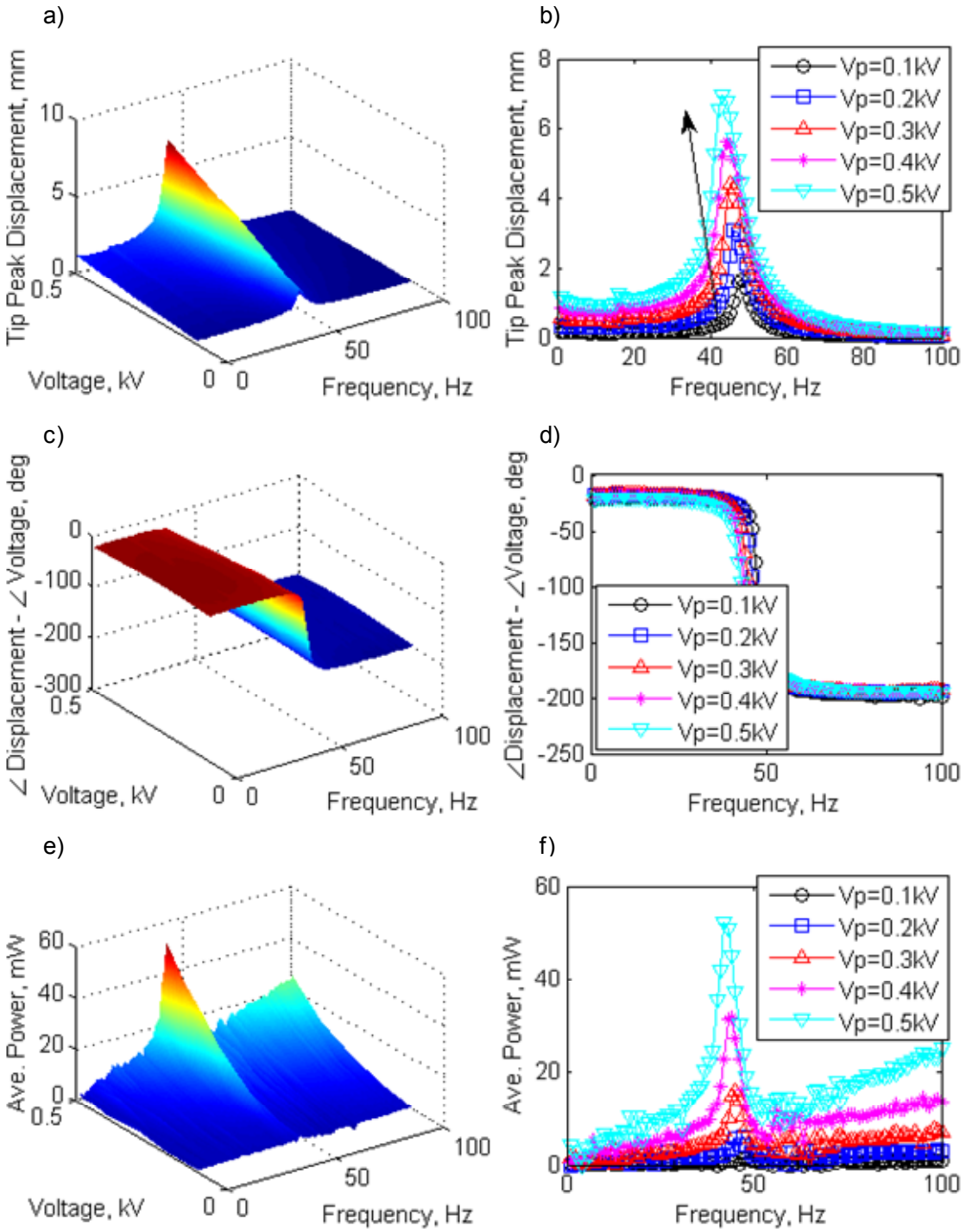

Figure D.9: High frequency response of sample B1: a,b) Peak displacement of free-end, c,d) phase angle between displacement output and voltage input, e,f) power consumption.

In Figure D.9b, an arrow indicates the resonance shift to lower frequencies, indicating that the beam is effectively getting "softer" as the peak voltage is increased. As noted earlier, the phase calculation assumes that the signal is a single harmonic with a fixed frequency. It is observed that the piezoceramic hysteresis appears like a phase shift throughout the spectrum. This is an expected result from a hysteretic actuator which is actuated by an input signal with constant amplitude.

Figure D.10 through Figure D.27 presents the same discussion (given above for sample B1) for samples B2 through B7. Same observations are made; hence the discussion is not repeated. The reader is referred to the figure captions for information.

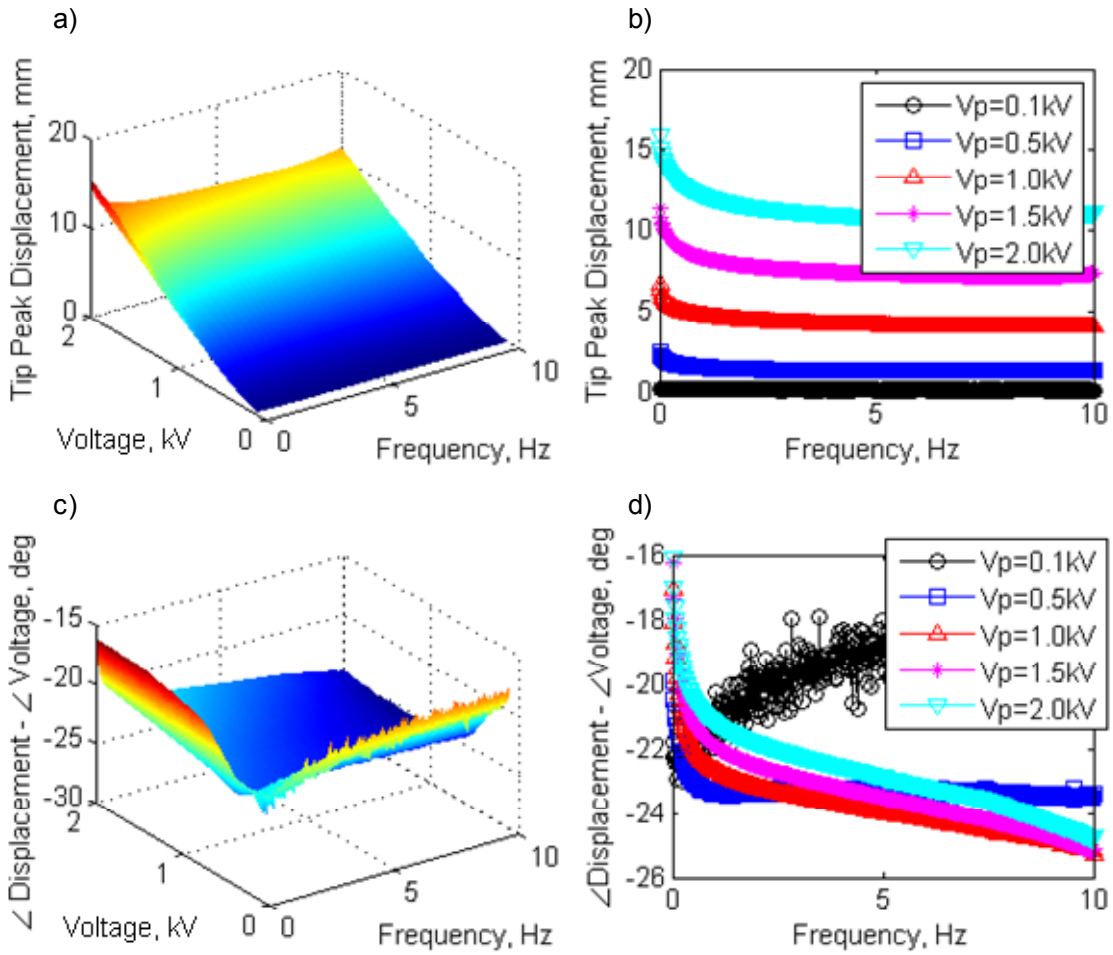

Figure D.10: Low frequency response of sample B2: a,b) Peak displacement of free-end, c,d) phase angle between displacement output and voltage input.

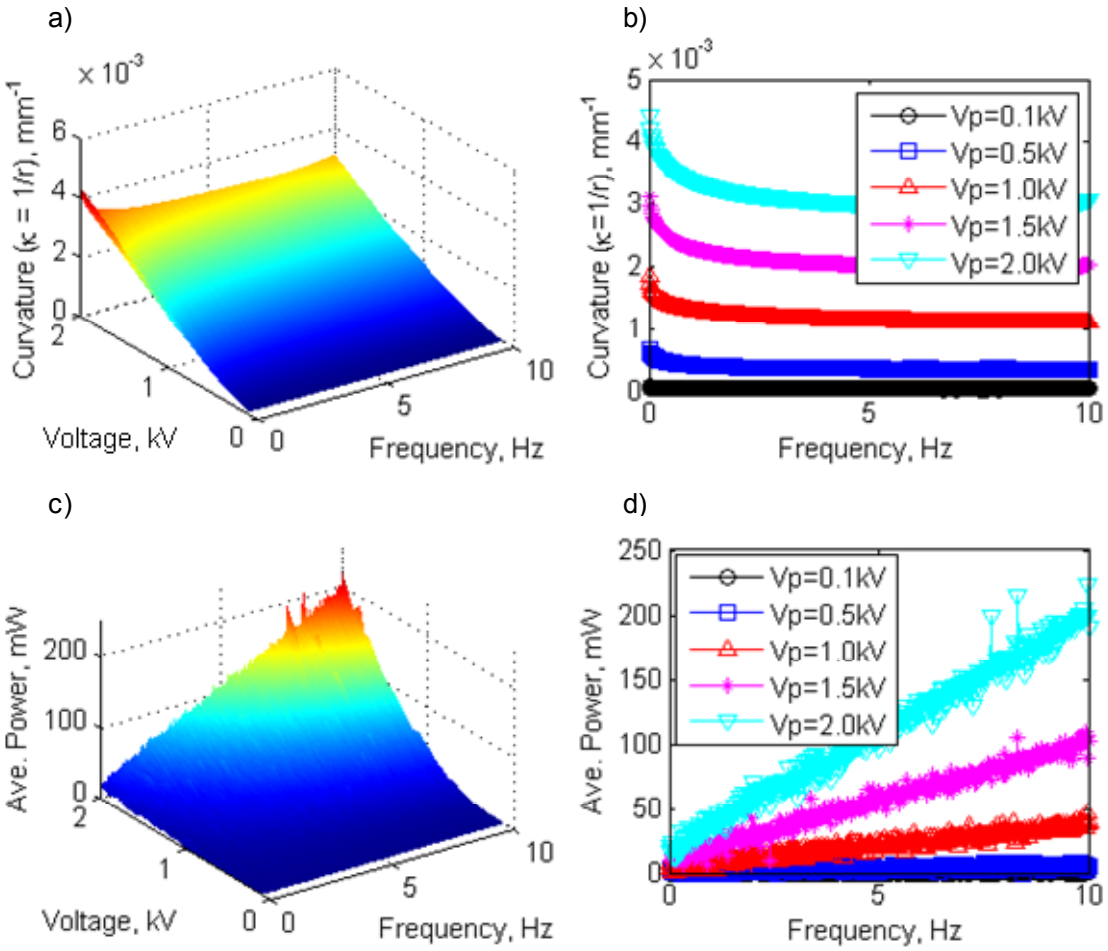

Figure D.11: Low frequency response of sample B2: a,b) Curvature and c,d) power consumption.

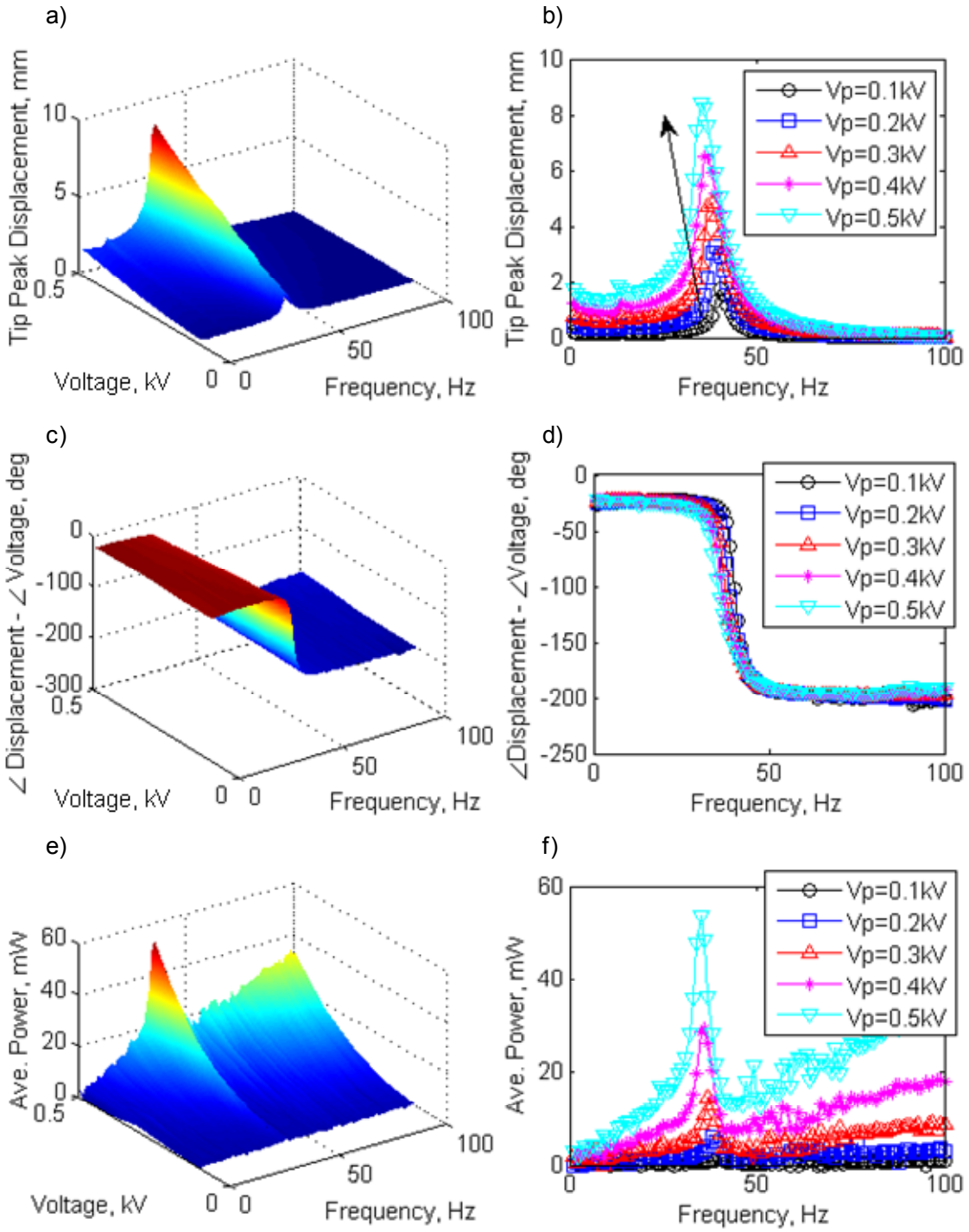

Figure D.12: High frequency response of sample B2: a,b) Peak displacement of free-end, c,d) phase angle between displacement output and voltage input, e,f) power consumption.

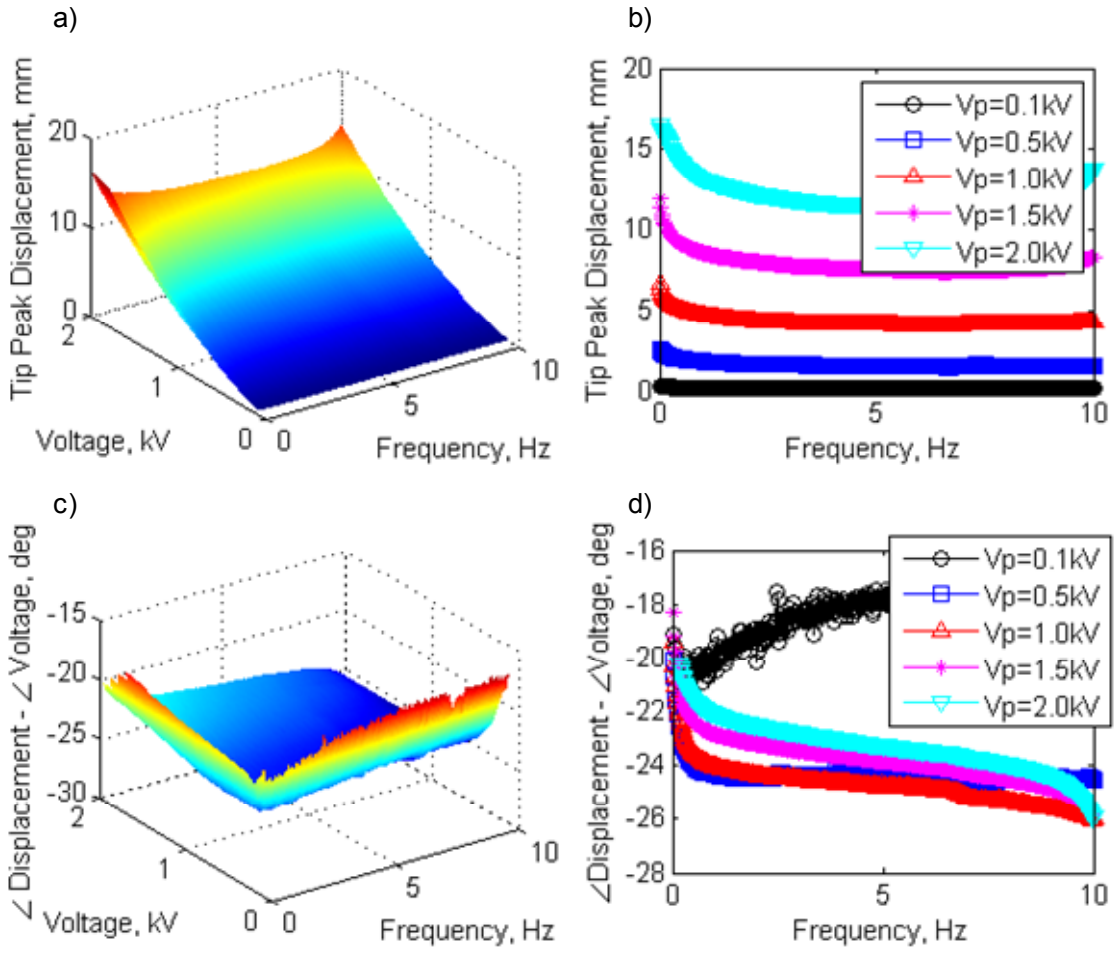

Figure D.13: Low frequency response of sample B3: a,b) Peak displacement of free-end, c,d) phase angle between displacement output and voltage input.

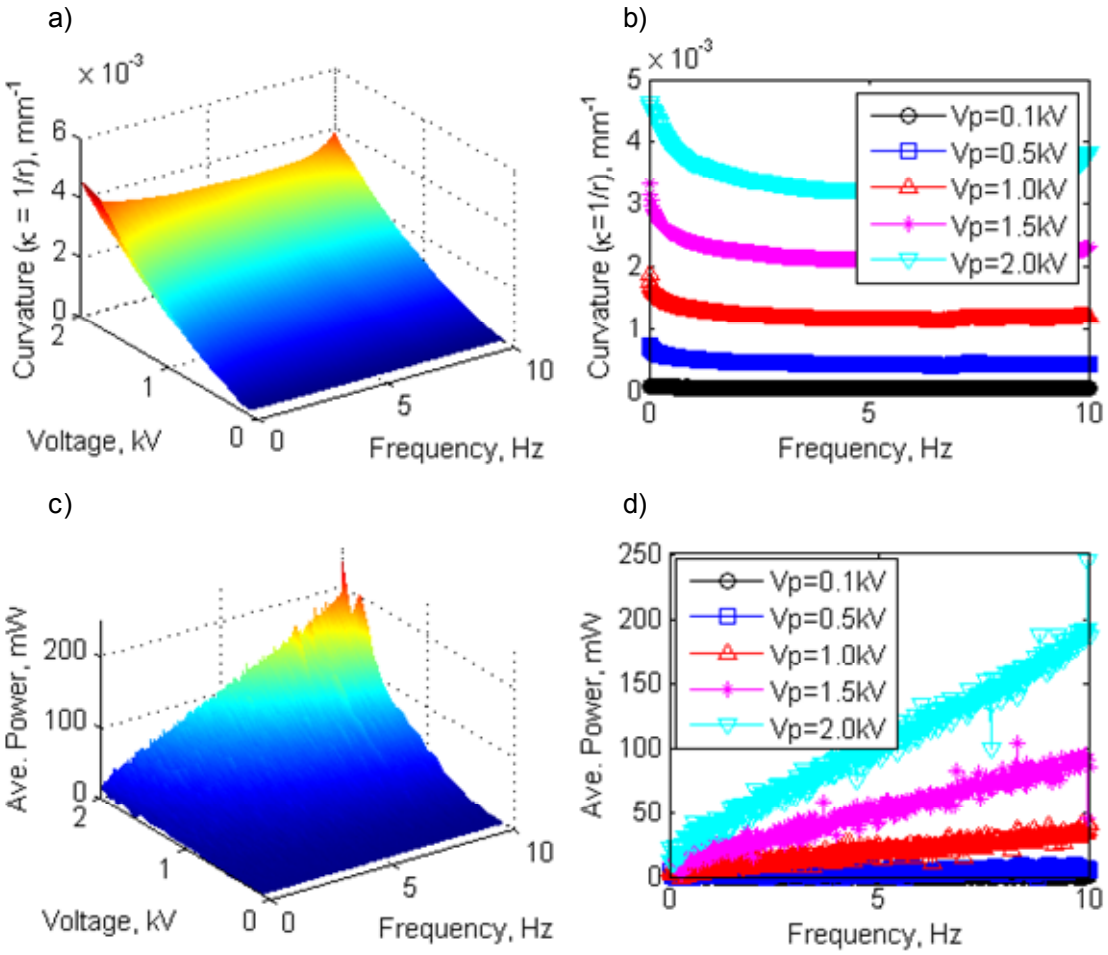

Figure D.14: Low frequency response of sample B3: a,b) Curvature and c,d) power consumption.

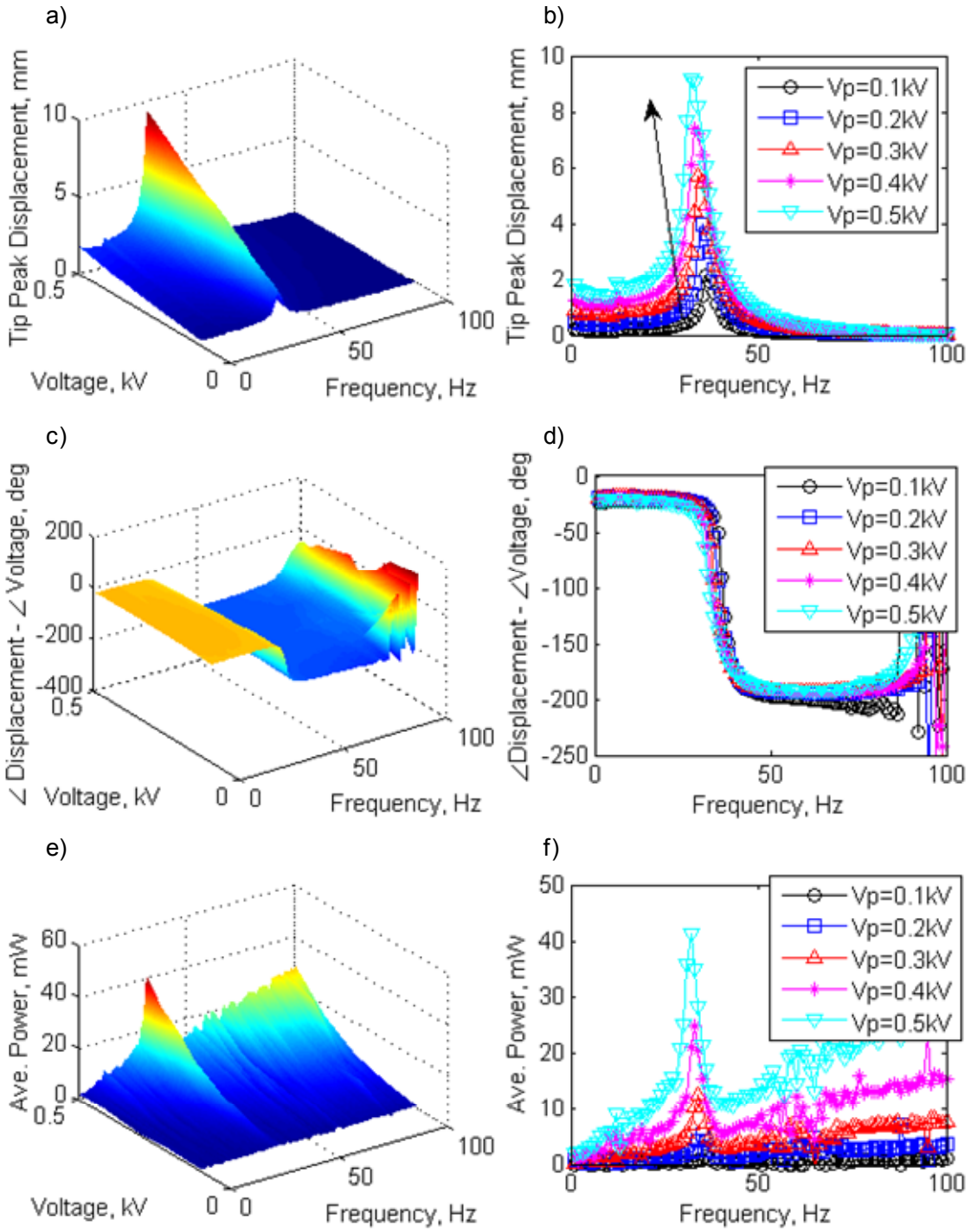

Figure D.15: High frequency response of sample B3: a,b) Peak displacement of free-end, c,d) phase angle between displacement output and voltage input, e,f) power consumption.

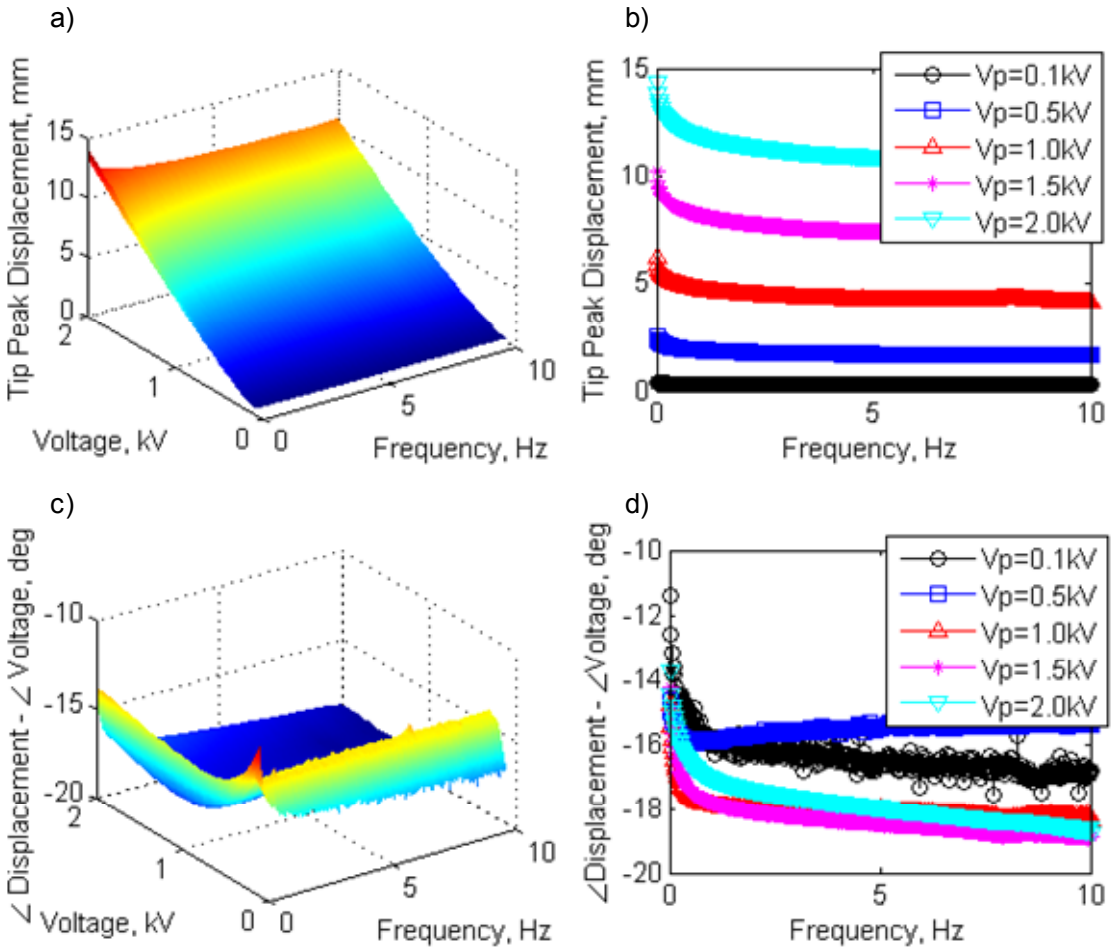

Figure D.16: Low frequency response of sample B4: a,b) Peak displacement of free-end, c,d) phase angle between displacement output and voltage input.

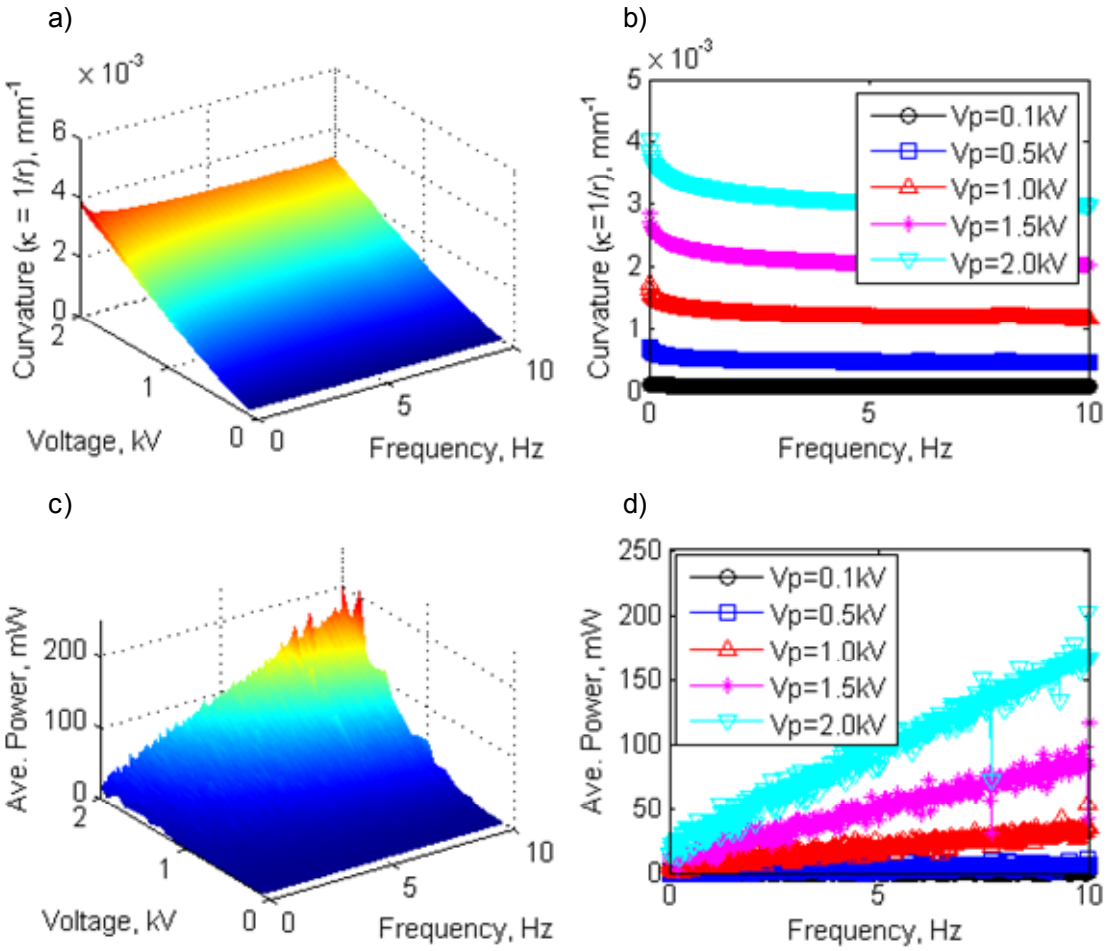

Figure D.17: Low frequency response of sample B4: a,b) Curvature and c,d) power consumption.

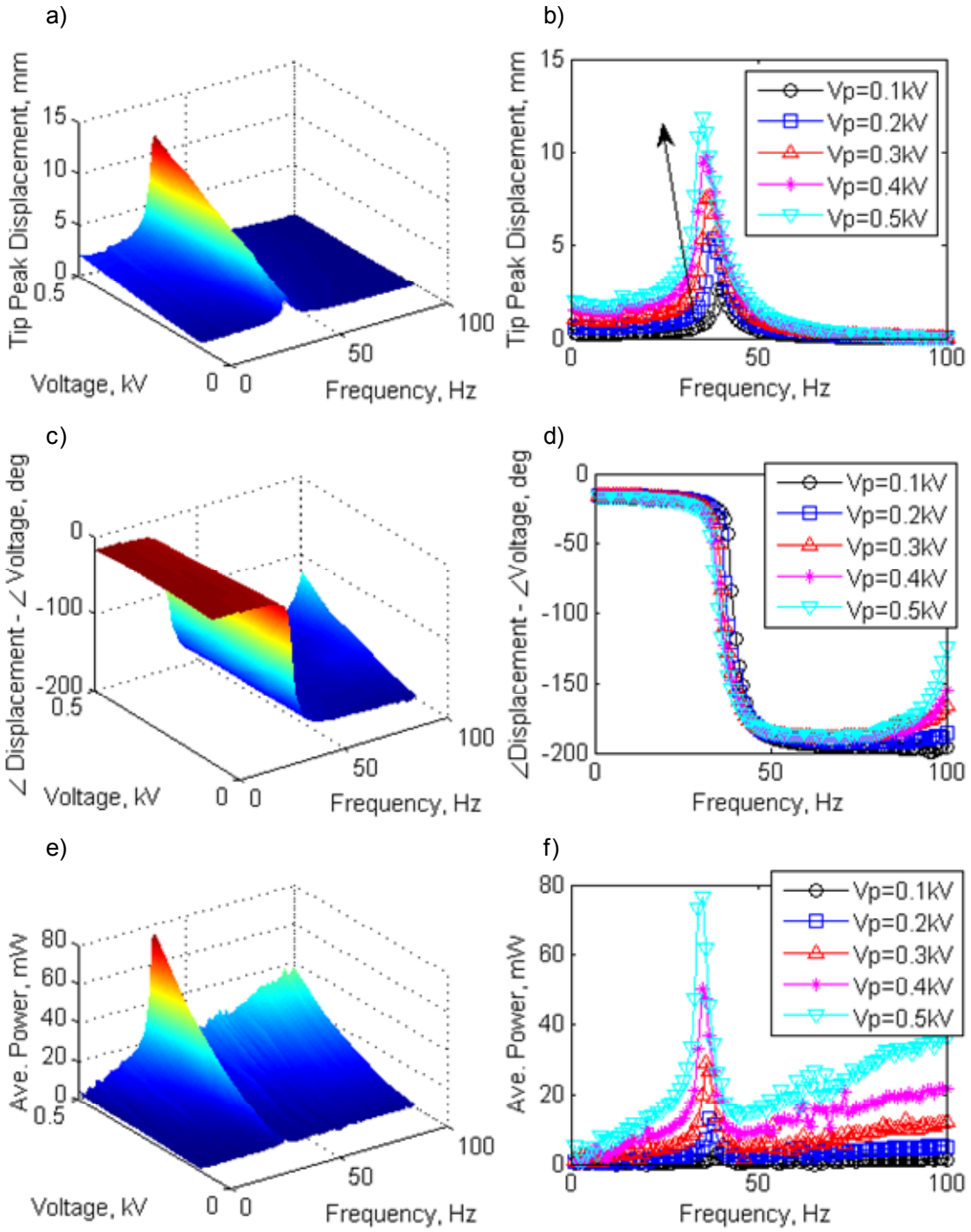

Figure D.18: High frequency response of sample B4: a,b) Peak displacement of free-end, c,d) phase angle between displacement output and voltage input, e,f) power consumption.

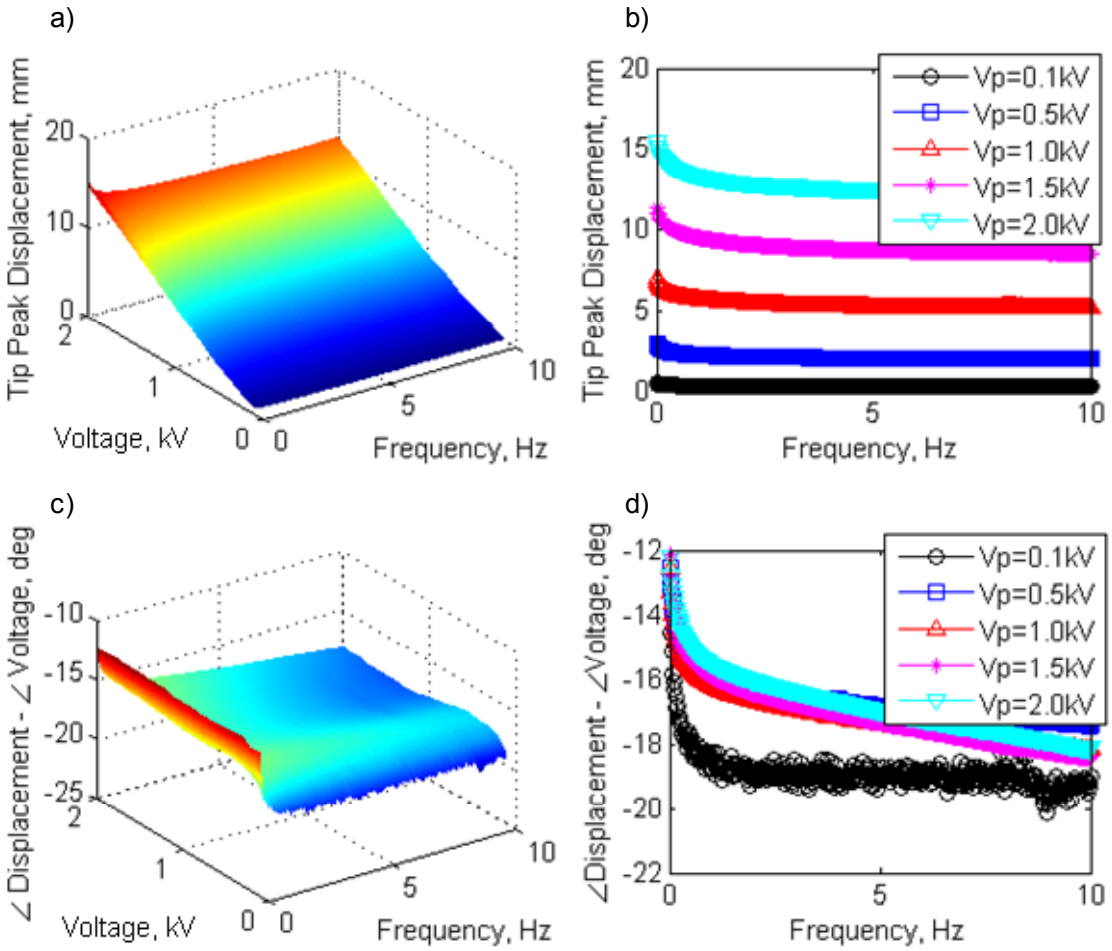

Figure D.19: Low frequency response of sample B5: a,b) Peak displacement of free-end, c,d) phase angle between displacement output and voltage input.

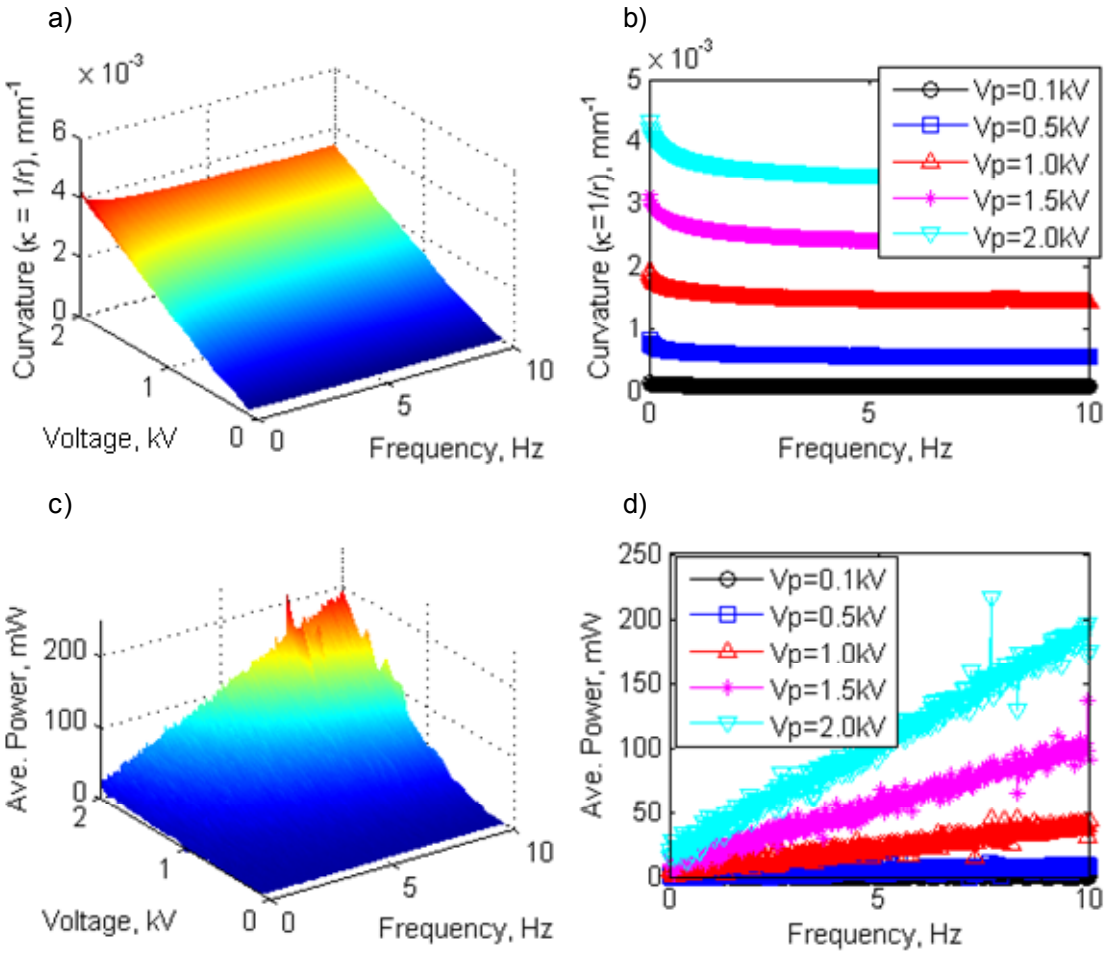

Figure D.20: Low frequency response of sample B5: a,b) Curvature and c,d) power consumption.

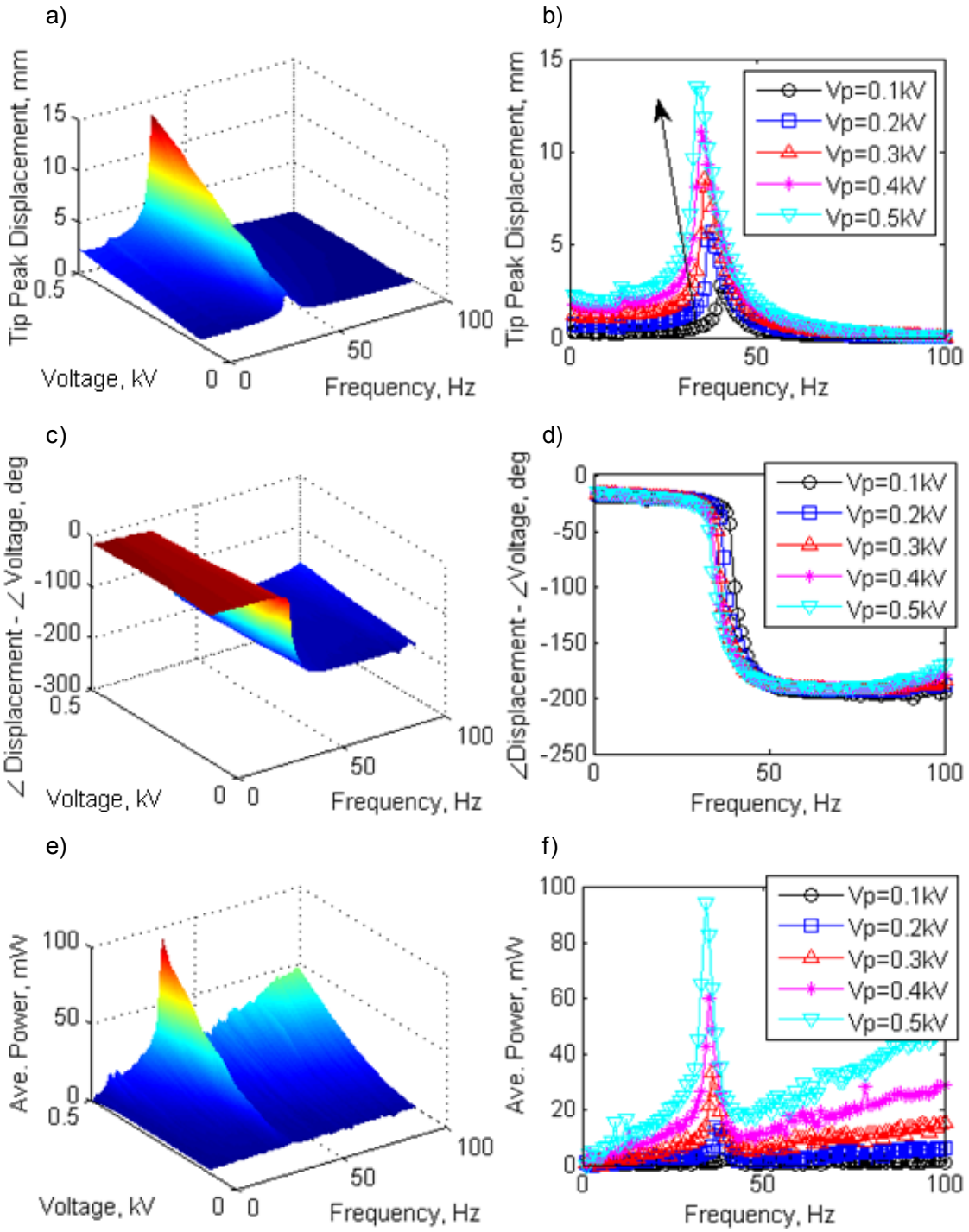

Figure D.21: High frequency response of sample B5: a,b) Peak displacement of free-end, c,d) phase angle between displacement output and voltage input, e,f) power consumption.

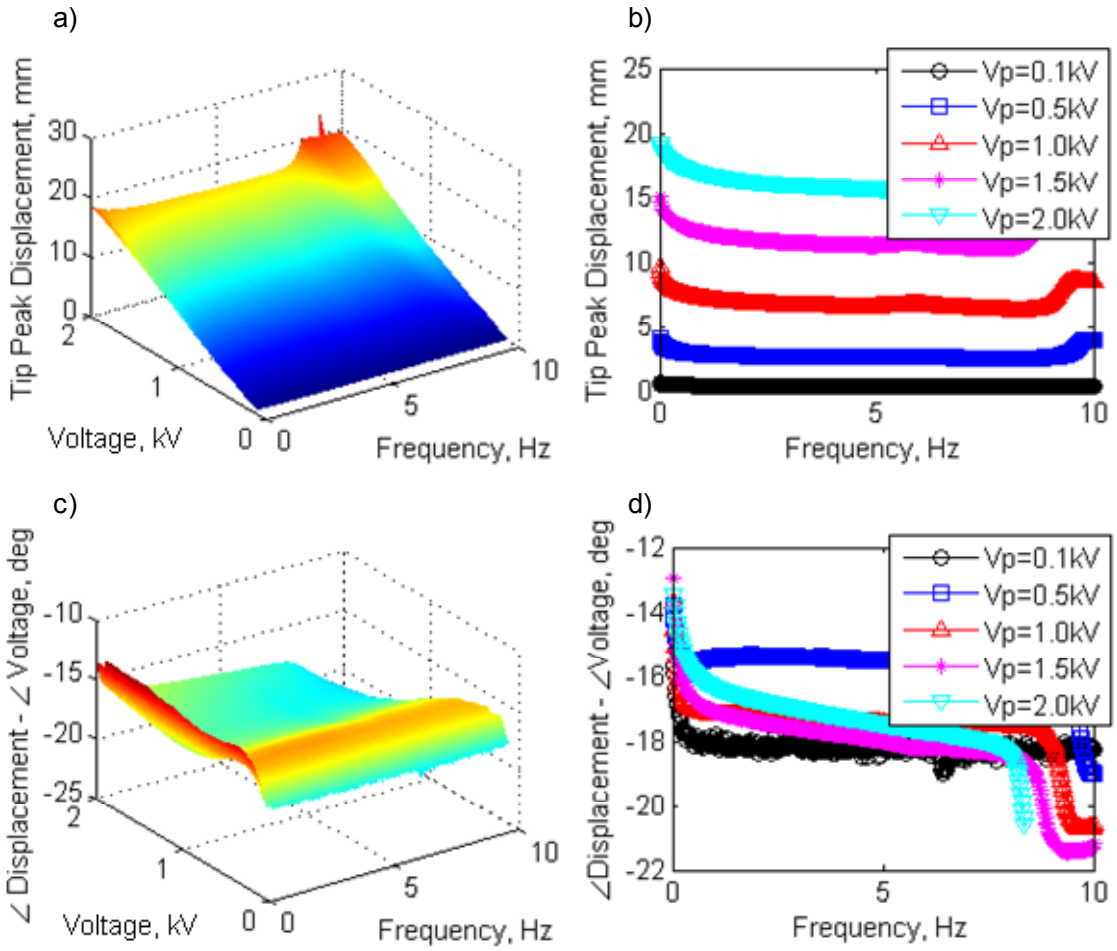

Figure D.22: Low frequency response of sample B6: a,b) Peak displacement of free-end, c,d) phase angle between displacement output and voltage input.

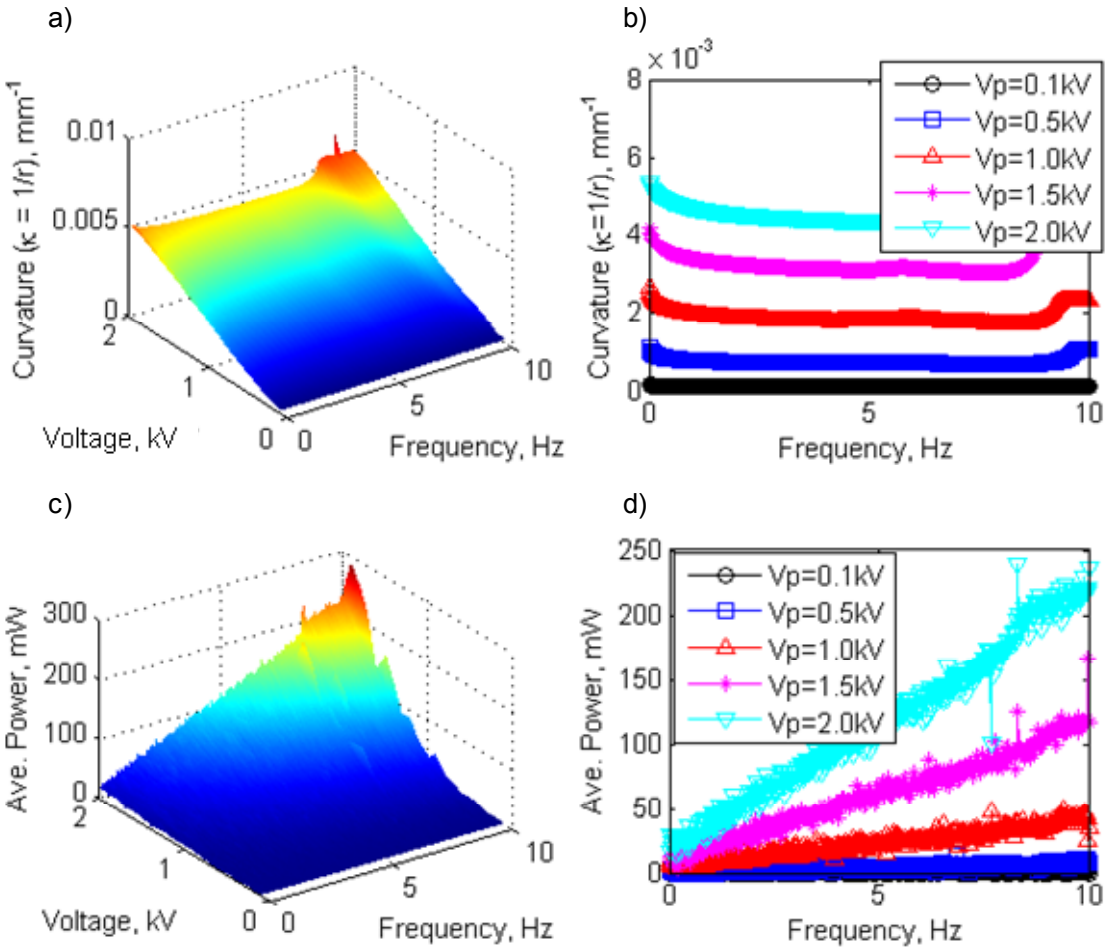

Figure D.23: Low frequency response of sample B6: a,b) Curvature and c,d) power consumption.

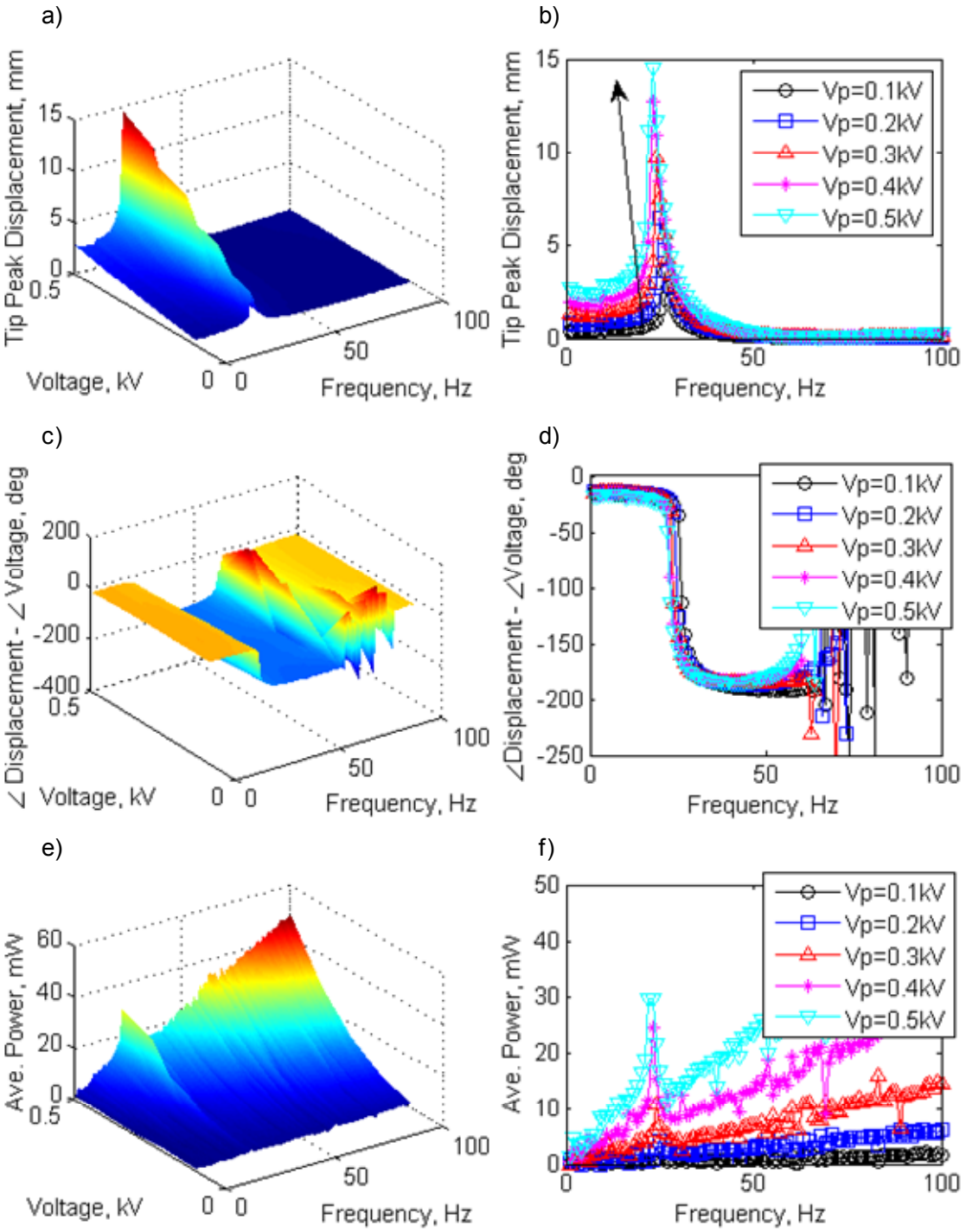

Figure D.24: High frequency response of sample B6: a,b) Peak displacement of free-end, c,d) phase angle between displacement output and voltage input, e,f) power consumption.

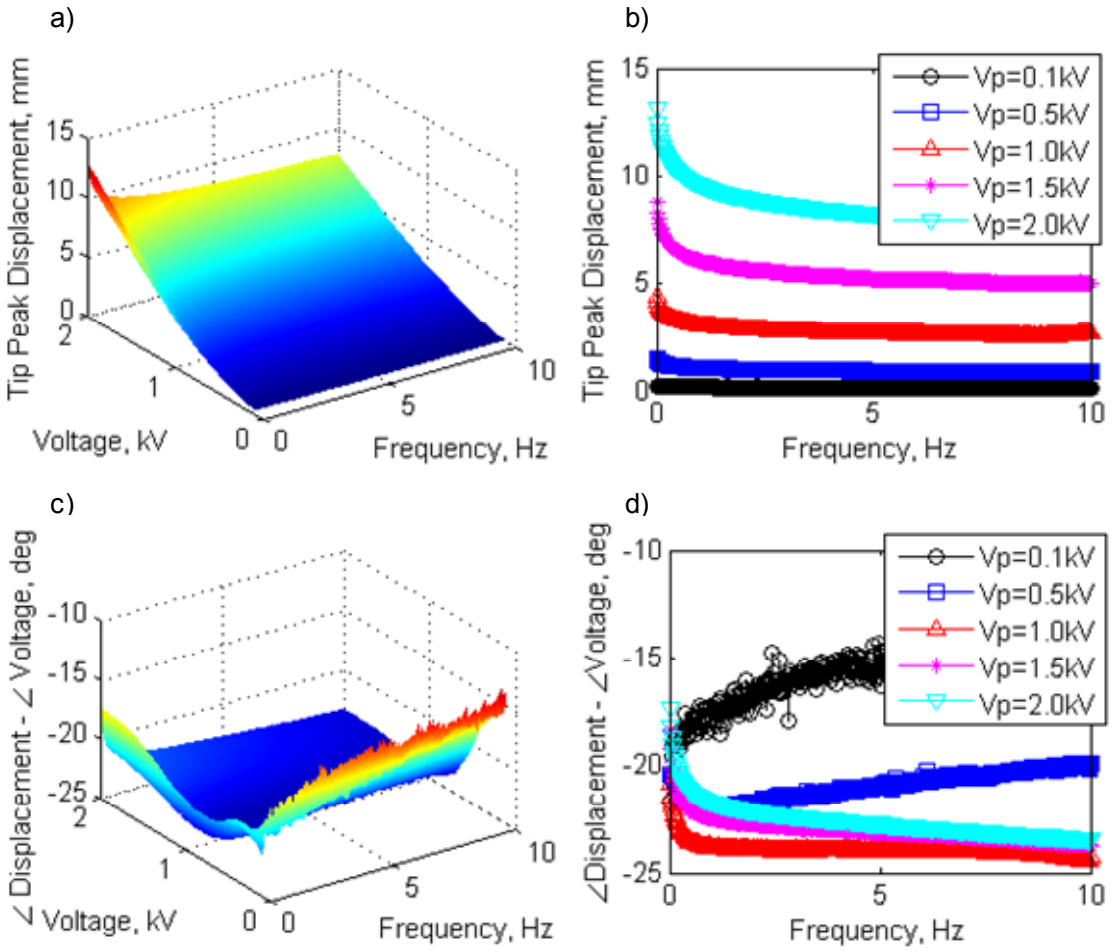

Figure D.25: Low frequency response of sample B7: a,b) Peak displacement of free-end, c,d) phase angle between displacement output and voltage input.

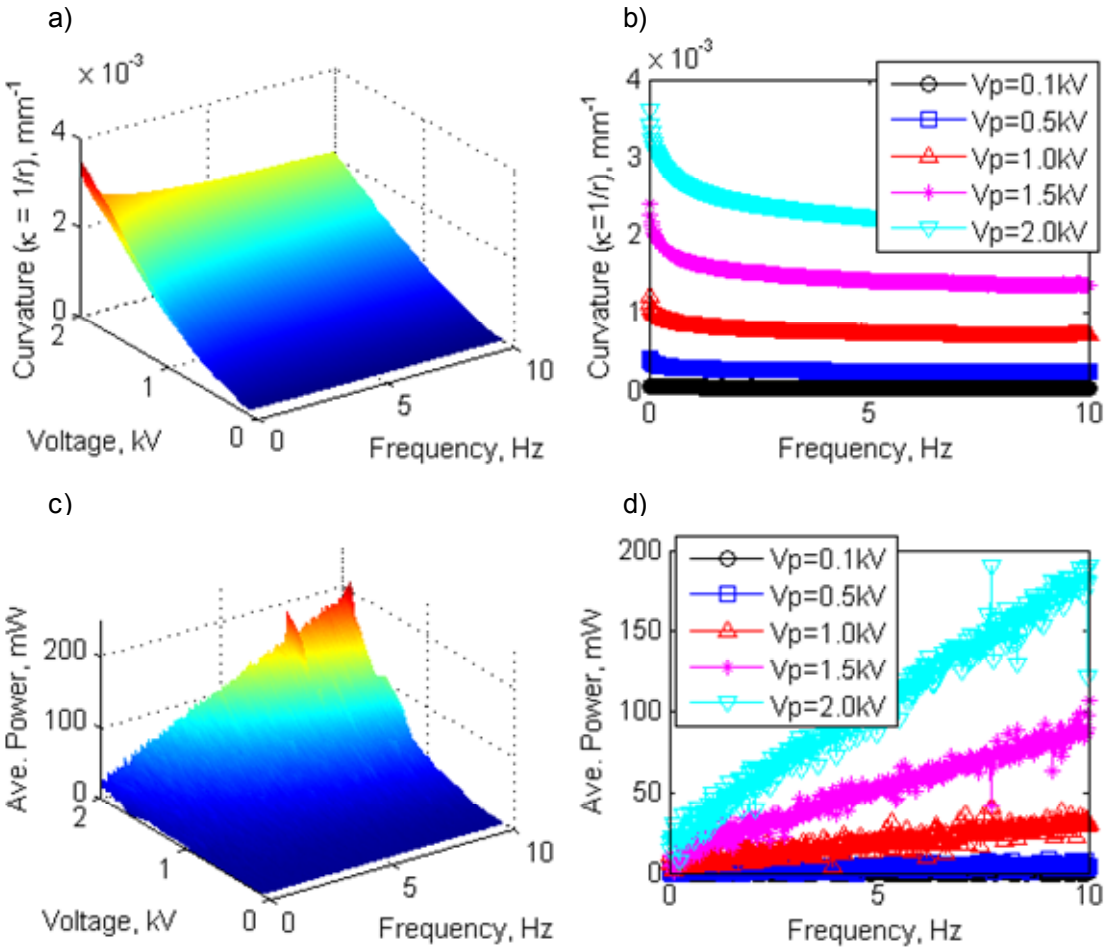

Figure D.26: Low frequency response of sample B7: a,b) Curvature and c,d) power consumption.

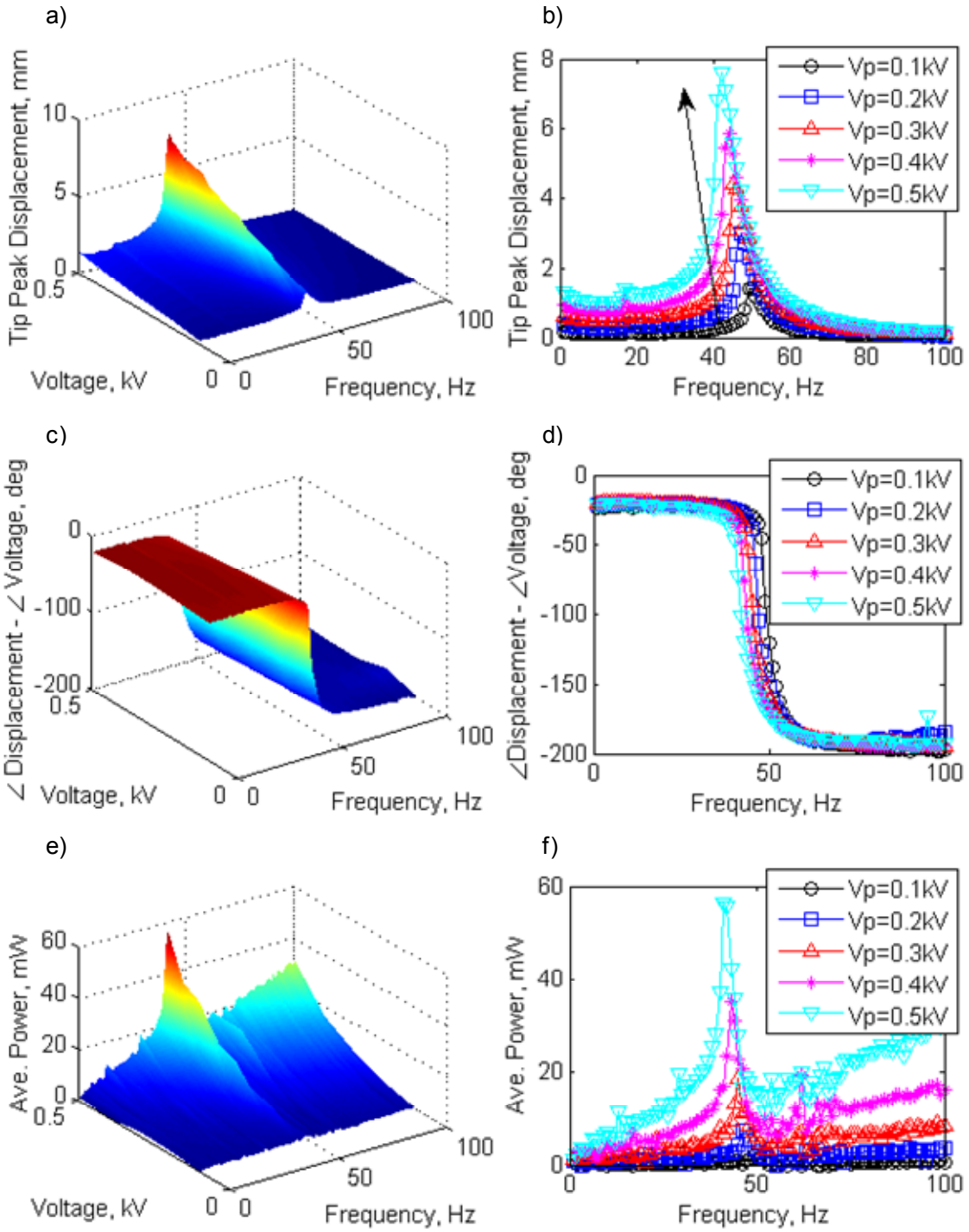

Figure D.27: High frequency response of sample B7: a,b) Peak displacement of free-end, c,d) phase angle between displacement output and voltage input, e,f) power consumption.

APPENDIX E

WIND TUNNEL FACILITY

The wind tunnel tests are performed in a low-speed, open circuit wind tunnel located at the Center for Intelligent Material Systems and Structures (CIMSS) in 381 Durham Hall, Blacksburg, VA. The wind tunnel setup and instrumentation is designed and fabricated specifically for the analysis of the airfoils discussed in this dissertation. The current version of the wind tunnel facility (version 5) is fully automated with a software controlled data acquisition unit with the following features: 1) The flow can be enabled\disabled, 2) the angle of the test specimen can be adjusted to 0.01° resolution, 3) uncoupled lift and drag forces can be measured simultaneously using two load cells, 4) the flow velocity and temperature of the flow can be monitored, 5) two separate excitation voltages can be applied to the test specimens, 6) the polarity of one of the excitation sources can be controlled with an electromagnetic relay, 7) the high voltage excitation sources can be enabled\disabled (for safety reasons), and 8) the displacement of the test specimen can be measured at two points simultaneously using two laser displacement sensors. Each of these instruments (and features) is discussed in the following sections.

The wind tunnel has six distinct versions from an aerodynamic and instrumentation point of view. Four of these iterations are relevant to the experimental results that are presented in the main text. Table E.1 presents the specifications of the wind tunnel versions. Note that U.S. customary units are used along with SI units in this appendix for practical reasons.

Table E.1: Versions of the CIMSS low-speed open-circuit wind tunnel facility.

	Version 1	**Version 2**	**Version 3.1**
Used in	Chapter 5 (Thin Airfoil)	n/a	n/a
Dates Used	Sep. 24 to Mar. 26, 2009	Mar. 09 to Mar. 11, 2009	Jun. 3 to July 26, 2009
Balance Type	Manual Beam Balance	Beam Balance w\ one load cell	Two load cells
Rotation Method	Manual	Manual	Rotary Table
Pitot Probe	w\ Setra Transducer	w\ Setra Transducer	w\ Setra Transducer
Static Ports	n\a	n\a	n\a
Inlet Type	Steel (open)	Steel (open)	Steel (open)
Screens	n\a	n\a	n\a
Flow Straightener	n\a	n\a	n\a

	Version 3.2	**Version 4**	**Version 5**
Used in	Chapter 6 (Thick Airfoil)	Chapter 7 (Section 7.3)	Chapter 7 (Section 7.4)
Dates Used	Jul. 31 to Aug. 7, 2009	Sep. 7, 2009 to Feb. 3, 2010	Feb. 20 to May 7, 2010
Balance Type	Two load cells	Two load cells	Two load cells
Rotation Method	Rotary Table	Rotary Table	Rotary Table
Pitot Probe	w\ Setra Transducer	w\ Setra Transducer	w\ Dwyer Transducer
Static Ports	w\ Dwyer Transducer	w\ Dwyer Transducer	w\ Setra Transducer
Inlet Type	Steel (open)	Wood - Acrylic	Wood - Acrylic
Screens	n\a	Two screens	Two screens
Flow Straightener	n\a	Straw Honeycomb	Alum. Honeycomb

The following sections present the design, instrumentation and the aerodynamic characteristics of the relevant versions of the wind tunnel.

E.1 General Characteristics

The wind tunnel is in an open circuit configuration as shown in Figure E.1. Two fans in serial (from Northern Tool + Equipment, FlowPro Classic Cooler Drum Fan, 23in., 1/3 HP, 7700 CFM, Model# 10289,) are used downstream of the test-section to generate the airflow. One of the fans is connected to a variable voltage output transformer (Part number 6994K17 from

McMaster-Carr). The second fan can be set to three settings (off, low and high). Both fans are automatically switched on and off with an electromechanical relay. The relay is powered by a simple buffer amplifier circuit. The control signal (to the buffer amplifier) is generated by the data acquisition system (described later in this section). The test section is connected to the fans with one rectangular duct (labeled DS-1) and a two-piece diverging nozzle (labeled DS-2 and DS-3 which has a lofted cross-section from the rectangular inlet (from DS-1) to the circular fans). This diverging nozzle is fabricated from a galvanized steel material by B&M Sheet Metal Shop, Inc., Roanoke, VA.

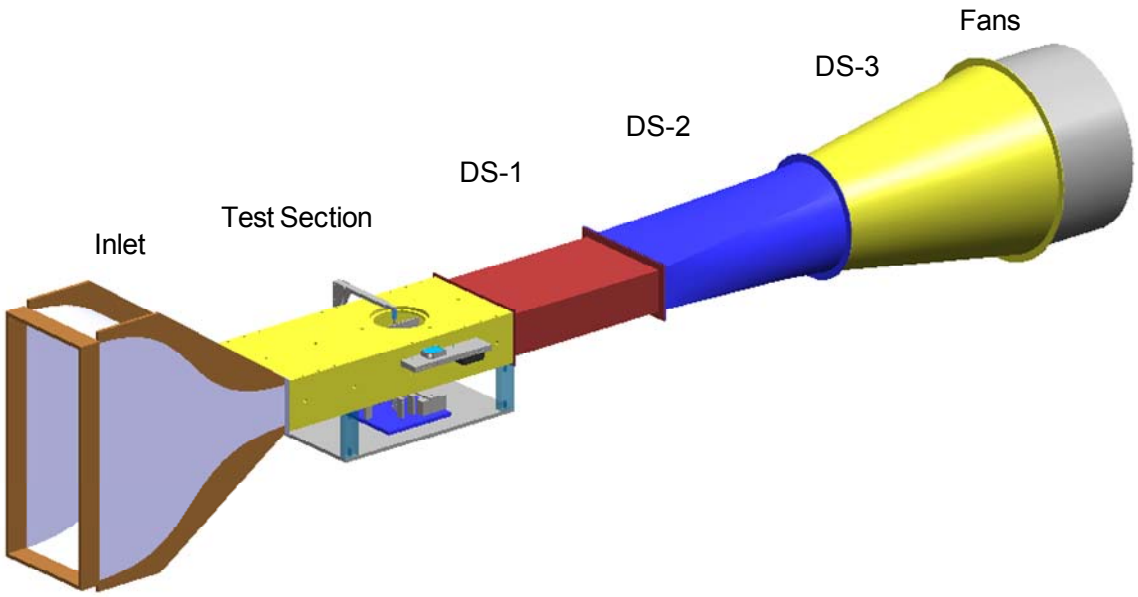

Figure E.1: CAD model of the version 5 wind tunnel facility.

The converging nozzle (labeled Inlet) is fabricated from several pieces of clear acrylic sheets and wood, and it has a 31.75" inlet height and 14.0" width. The nozzle converges to a 5.37" (136 mm) height (that matches the fixed height of the test section). The nozzle is 30.0" long (between the inlet and the outlet). There are two fiberglass screens (window screens) in series which are 3.50" apart from each other. These screens are upstream of the converging nozzle. An aluminum honeycomb flow straightener upstream of the screens (not shown in Figure E.1) is the first flow conditioning part of the wind tunnel. The pictures of the inlet nozzle (and the flow straightener) can be seen in Section E.1.3 and Section E.1.4. The downstream section 1 (DS-1) is rectangular cross-section duct with 24.0" length. The next section (DS-2) is 30.0" long. The final downstream section (DS-3) connects to the fans (in serial) and it is also 30.0" long.

The test section is constructed from four rectangular sheets of 0.75” thick acrylic purchased from McMaster-Carr, Aurora, OH. The test section is CNC machined and features holes for the static ports and the Pitot-static probe. There are also precision machined mounting holes (on the side walls of the test section) for the mount for two laser displacement sensors. The precise placement of the lasers allow for the accurate measurement of the deformation of the airfoils tested in this research. There are also two access openings, one 6.50” in diameter on the top wall (or the ceiling) and other 5.00” in diameter on the bottom wall (or the floor) of the test section. Figure E.2 presents the CAD model of the test section for the version 5 wind tunnel.

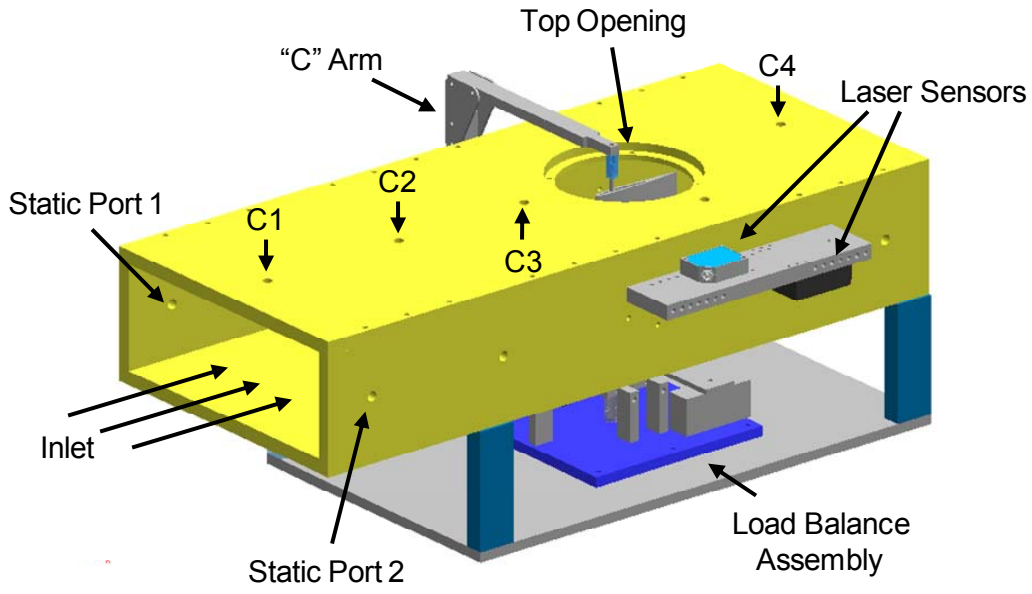

Figure E.2: CAD model of the test section of version 5 wind tunnel.

In Figure E.2, there are several “ports” (or holes) shown through the test section side walls and the top wall. The two ports on the side walls are connected together and used for static pressure measurements. The holes labeled C1 - C4 are used for buoyancy measurements with the Pitot-static tube. The calibration curves for the static ports, Pitot-static tube and the buoyancy calculations are presented later in this appendix.

Figure E.3 shows a simplified illustration of the side view of the 2D test section and the airfoil mount (“C” arm that connects the airfoil to the balance). This illustration of the inside of the test section is applicable to all of the wind tunnel tests presented in this dissertation. The differences in the each wind tunnel version arise due to the improvements that were applied to 1)

inlet converging nozzle and 2) the aerodynamic force measurement device (also referred to as load balance).

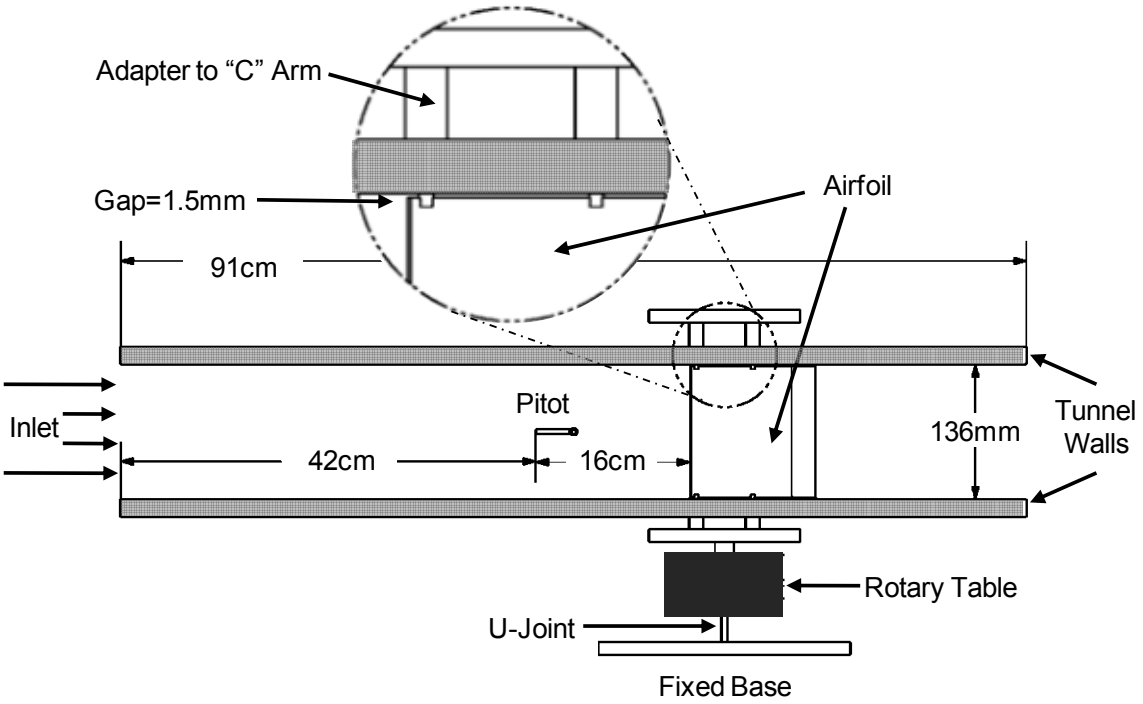

Figure E.3: Side view of the wind tunnel 2D test section.

The leading edge of the test article is located at 58 cm from the beginning of the test-section along the streamwise direction. The span axis is oriented normal to floor of the test section (and ground). The "C" shaped arm (labeled as "C" Arm later) surrounds the test section and supports the test airfoil without contacting the tunnel walls.

The airfoils tested in this dissertation have an approximate 1.5 mm gap between the airfoil ends and the tunnel walls. Mueller and Burns [1982] show that gap sizes around 0.5% of the span are usually acceptable and do not affect the results. Depending on the boundary layer (which is different for each wind tunnel version), the end-gap percentage is still higher than the recommended value because of the low span of the airfoils. The measured boundary layer for each relevant wind tunnel version and the possible effects of this gap size will be discussed in the following sections.

Figure E.4 presents the front view of the wind tunnel test section. As noted before (for Figure E.3), the illustration of the inside of the test section is applicable to all of the wind tunnel tests presented in this dissertation.

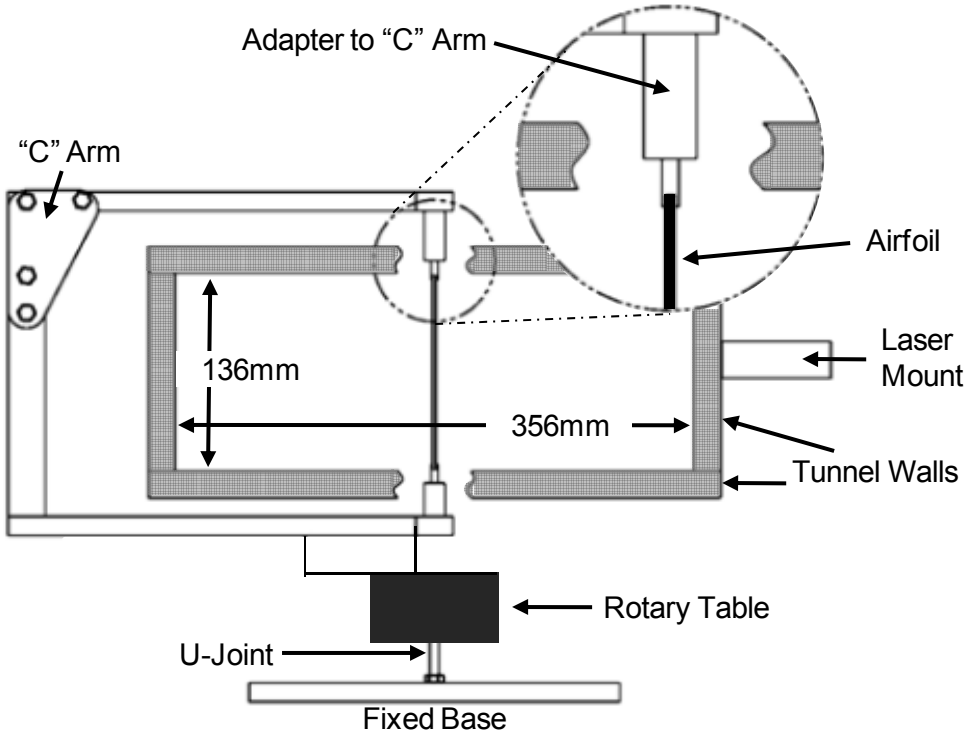

Figure E.4: Front view of the wind tunnel 2D test section.

Figure E.4 shows the “C” arm wrapping around the test section and supporting the airfoil from both ends. The laser mount, fixed to the side wall, holds two laser displacement sensors 1) model ILD 1401-200 and 2) model ILD 1800-200 from Micro-Epsilon, Raleigh, NC. Both lasers are powered by a regulated 20V DC voltage source from an Agilent E3648A DC power supply.

The aerodynamic lift and drag forces are measured with a custom designed load balance that incorporates two strain-gage based load cells (model MLP-10 from Transducer Techniques, Temecula, CA). Each load cell has a maximum load capacity of 10 lbs. The drag load cell is connected to a model TMO-1 signal conditioner, and the lift load cell is connected to a TMO-2 signal conditioner (both from Transducer Techniques). In order to reduce human interference, a stepper-motor driven rotary table (model B5990TS from Velmex, NY) is used to set the angle of the airfoils. The rotary table has a 90:1 gear ration and is driven by a Vexta model PK245-01AA 2-Phase DC stepper motor. The effective conversion ratio of the rotary table is 0.010 degree/step. The stepper motor is controlled by a Velmex Stepping Motor Controller (model VXM-1). The control of the rotary table is established by the data acquisition unit through an RS232 type serial communication port. Figure E.5 shows the CAD model of the load balance assembly with a NACA 0009 airfoil mounted on the “C” arm.

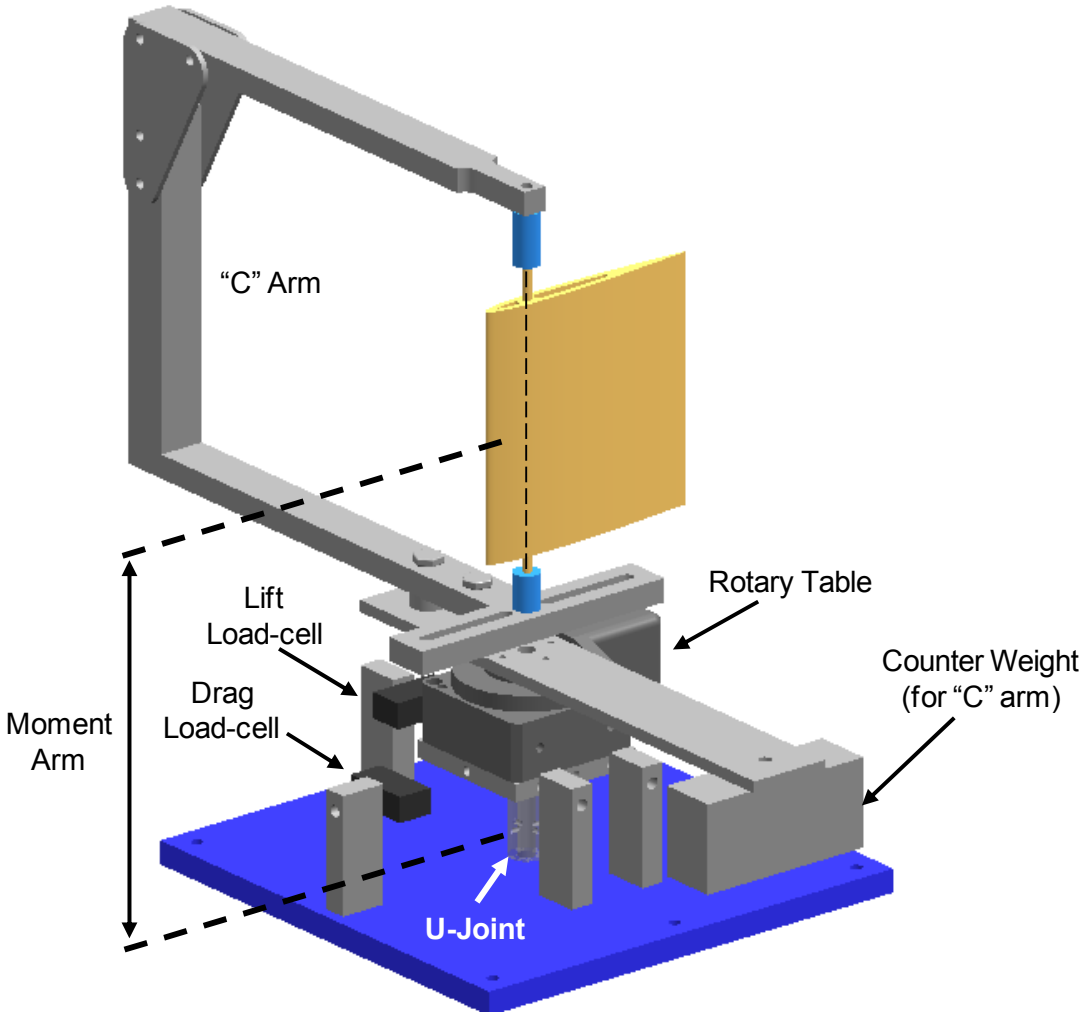

Figure E.5: CAD model of the load balance for version 5 wind tunnel.

The mechanism of the load balance is quite simple. First, the aerodynamic forces and moments (generated by the airfoil) are transferred to the "C" arm. The "C" arm is mounted on the "rotating" part of the rotary table. The loads are passed through the rotary table to its base. The base of the rotary table is connected to a U-Joint. The other side of the U-Joint is fixed to a stationary base plate that is connected to the wind tunnel test section. The connections described above allow the airfoil, the "C" arm and the rotary table to "rock" back-and-forth and side-to-side as one piece. The rotation (induced by pitch moment) is constrained by the U-Joint. Two orthogonal load cells are connected to the base of the rotary table to restrict the motion and sense the aerodynamic forces. The connection between each load cell and the rotary table is made by a thin rod (also known as a "sting"). This thin rod translates the axial forces while applying

negligible moment constrains to the load cell and the rotary table. The lift load cell is perpendicular to the flow, and the drag load cell is in-line with the flow.

Due to the precise alignment of load cells with respect to the wind tunnel test section, the cross-measurement between the lift and drag forces are measured to be very small and therefore neglected in the calculations. The conversion relationship of the voltages measured from the load cells to the aerodynamic forces experienced by the airfoil is calculated by a simple calibration experiment. A set of known forces are applied to the load balance using an additional beam (mounted externally on the load balance) and a set of weights attached to its end.

In Figure E.5, the Moment Arm is the distance between the rotation point of the U-Joint and the airfoil mid-span. The Moment Arm is measured to be 8.309”. Using this precise measurement, the calibration relationships presented Figure E.6 are obtained. The figure also presents the linear calibration formulas that are used to calculate the aerodynamic measurements that are related to the version 5 wind tunnel.

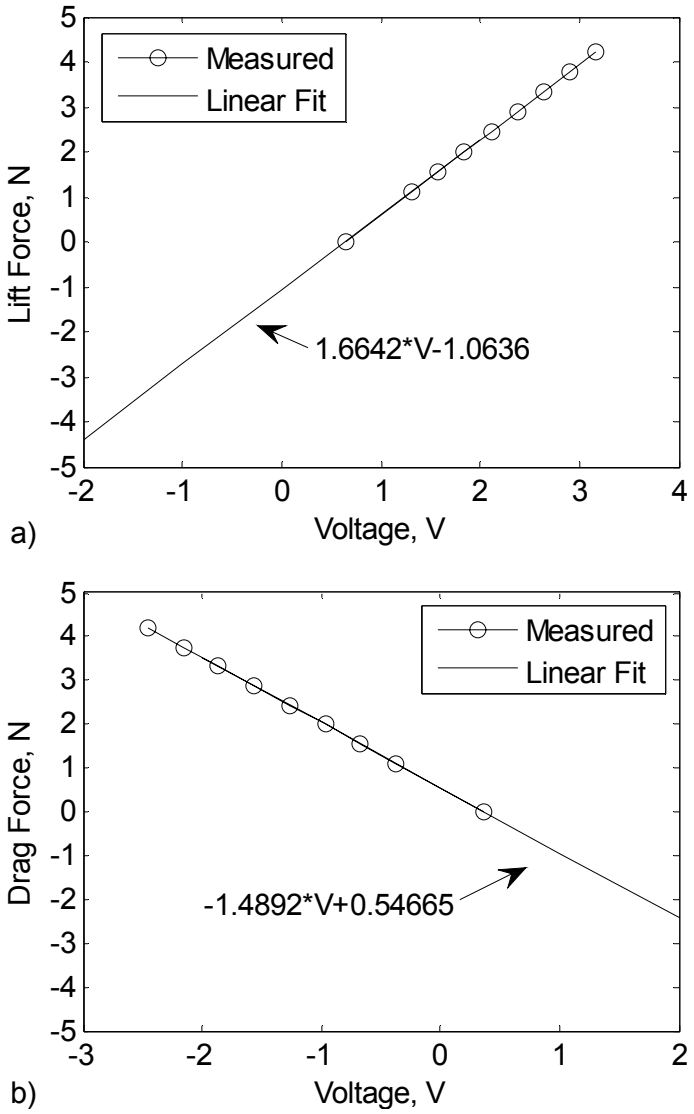

Figure E.6: Lift and drag forces as a function of the lift load cell and drag load cell voltage outputs respectively. Forces are assumed to be at the center of the test section (and at the mid-span of the airfoil).

The pressure from the static ports (Static Port 1 and 2 connected together) is measured with a model 668-5 transducer from Dwyer Instruments, Inc., Michigan City, IN. The Dwyer transducer has a 0-5" water-column (WC) range and a ±1% full-scale (FS) accuracy. Note that the static ports are connected to the "low" side of the transducer, where the "high" side is open to the atmosphere. The differential pressure from the Pitot-static probe is measured by a model 267 (part number: 2671-2R5-W-D-2D-G1-F-D) transducer from Setra Systems, Inc., Boxborough, MA. The Setra transducer has a 0-2.5" WC range with 0.25% FS accuracy. Figure E.7 presents

the calibration curves for the Setra and Dwyer differential pressure transducers. The measurement of the velocity in the test section is described later.

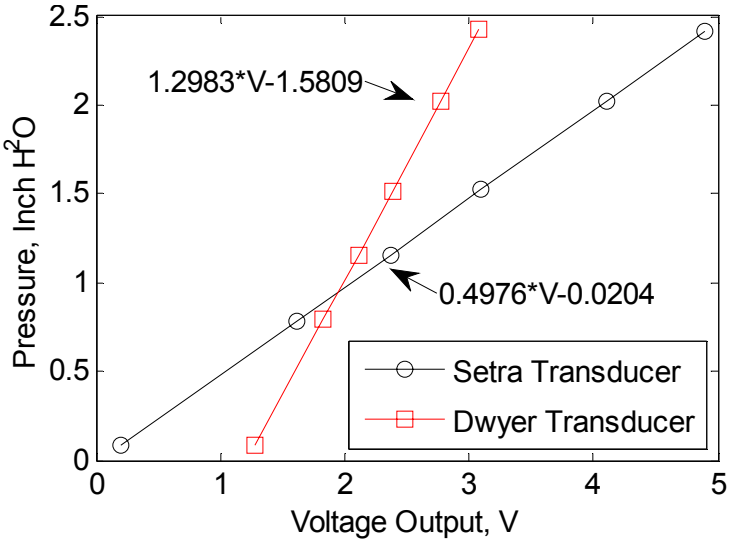

Figure E.7: Calibration curves for the Setra 267 and Dwyer 668-5 differential pressure transducers.

Note that the Dwyer transducer has a 4-20 mA output range, which is placed across an external precision resistor and converted to a voltage signal.

The temperature of the flow (inside of the test section) is measured downstream of the airfoil. A "J" type thermocouple wire is placed through the test section wall and into the flow. A model CCT-22 thermocouple signal conditioner from Omega Engineering Inc., Stamford, CT is used.

All of the measurement instruments above have a voltage output proportional to the physical parameters that they are measuring. These voltages are measured with a National Instruments (NI) model DAQCard-6062E (for PCMCIA) type data acquisition unit [NI DAQCard]. The card is coupled with a model SCC-68 break-out box. The data acquisition system has a 500 kS/s sampling speed and 12 bit 16 single-ended analog input channels, 2 analog outputs and 8 digital input/output (I/O) lines. The analog input has 17.945 mV accuracy at the maximum input range of ±10 V. The analog output has 10.568 mV accuracy at the maximum output range of ±10 V. The 16 single-ended channels are paired (using two 100 kOhm precision resistors to ground) so that 8 differential channels can be attained. Reader is referred to the E Series user manual for differential voltage input connections [NI E Series].

Table E.2: Connections for the DAQ system for version 5 wind tunnel setup.

Ch.	Connected to	Purpose
Analog Inputs		
AI0	Setra 267 pressure transducer	Static port pressure measurement
AI1	Omega CCT-22 thermocouple amplifier	Temperature of flow in test section
AI2	ILD 1401-200 CCD laser disp. sensor 1	Displacement of the airfoil around QC
AI3	ILD 1800-200 CCD laser disp. sensor 2	Displacement of the airfoil around TE
AI4	Dwyer 668-5 pressure transducer	Pitot-static pressure measurement
AI5	MLP-10 load cell with TMO-2 signal cond.	Lift force measurement
AI6	TREK 623B amplifier current monitor	Current consumption of actuators
AI7	MLP-10 load cell with TMO-1 signal cond.	Drag force measurement
Analog Outputs		
AO0	TREK 50/750 high voltage amp. (2 ch.)	Actuation of MFCs for camber actuation
AO1	TREK 623B high voltage amp.	Actuation of MFCs for flow control
Digital Outputs		
DIO0	Electromagnetic relay and buffer amp.	Control of two fans (on/off)
DIO1	Electromagnetic relay and buffer amp.	Control of polarity of TREK 50/750 output
DIO2	Electromagnetic relay and buffer amp.	Enable/disable both TREK amplifiers
DIO3	Electromagnetic relay and buffer amp.	Control of bender 5 (Group 1)
DIO4	Electromagnetic relay and buffer amp.	Control of benders 4 and 6 (Group 2)
DIO5	Electromagnetic relay and buffer amp.	Control of benders 3 and 7 (Group 3)
DIO6	Electromagnetic relay and buffer amp.	Control of benders 2 and 8 (Group 4)
DIO7	Electromagnetic relay and buffer amp.	Control of benders 1 and 9 (Group 5)

There are two analog outputs of the DAQ system. The first one (from AO0) controls the level of the high voltage output of two channels on the TREK 50/750 high voltage amplifier. This amplifier is configured to output voltages in the range of 0 - 1500 V. The first channel has a gain of 175 V/V. The second channel has a gain of 58 V/V. When an 8 V signal is applied to both channels, the first channel has an output of +1400 V and the second channel has an output of +464 V. These two unipolar signals are switched (for the correct terminals of the variable-camber bimorph airfoils presented in Chapter 5 and Chapter 6) using a quad single-pole-single-throw (SPST) type electromagnetic relay (also referred to as single-pole-four-throw). The quad relay is powered by a simple buffer amplifier which is controlled with the DIO1 digital output port of the DAQ system.

The second output of the DAQ system is connected to the TREK 623B high voltage amplifier through a Frequency Devices model 9002 low pass filter (LP) at 10 kHz cut-off frequency. The digital output (from the DAQ system) is LP filtered to remove the high frequency noise from the digital-to-analog (D\A) conversion with 12 bit resolution. This high voltage amplifier is used to generate excitation voltages in the 5 - 500 Hz bandwidth for the unimorph benders used in Chapter 7 for flow control purposes. The single output of the TREK 623B amplifier is distributed to the nine benders by five SPST type electromagnetic relays connected in parallel. These relays are powered with a dedicated buffer amplifier and controlled by the digital outputs (DIO3 - DIO7) of the DAQ system as presented in Table E.2.

For safety purposes during the long-period experiments, the high voltage amplifiers are enabled and disabled (depending on the test procedure) using an electromagnetic relay that is connected to the TTL enable function (of the amplifiers). During power outages, the NI DAQ system is not disturbed because it is connected to a battery powered laptop computer. The power source of the buffer amplifiers for the electromagnetic relays is connected a model Back-UPS CS 350 uninterruptible power supply (UPS) from APC, West Kingston, RI. In the event of a power outage, the relays and the data acquisition continues operation without sudden voltage changes and\or polarity changes.

The data acquisition (signal measurement and signal generation) is controlled with a computer program written in NI LabVIEW 8.5. Unless otherwise stated, the acquisition is conducted at 100 Hz sampling rate. Due to the multiplexed structure of the NI DAQCard-6062E, the slow acquisition speeds result in higher voltage measurement accuracy. Note that spill-over is an issue and it results in measurement of high amplitude signals from the previous channel (selected by the multiplexer) during the current measurement channel (with low amplitude signals). The reader is referred to NI website for important considerations of multi-channel measurements [NI E Series].

The following sections present the details of the wind tunnel facility that are specific to the version specified by the section title.

E.1.1 Wind Tunnel Version 1

Figure E.8 shows the first version of the wind tunnel setup with a galvanized steel inlet nozzle and two downstream fans. A custom manual beam balance is used in this wind tunnel

setup to measure aerodynamic forces. This wind tunnel version is employed in the aerodynamic measurements presented in Chapter 5 for the simply-supported thin variable-camber airfoil.

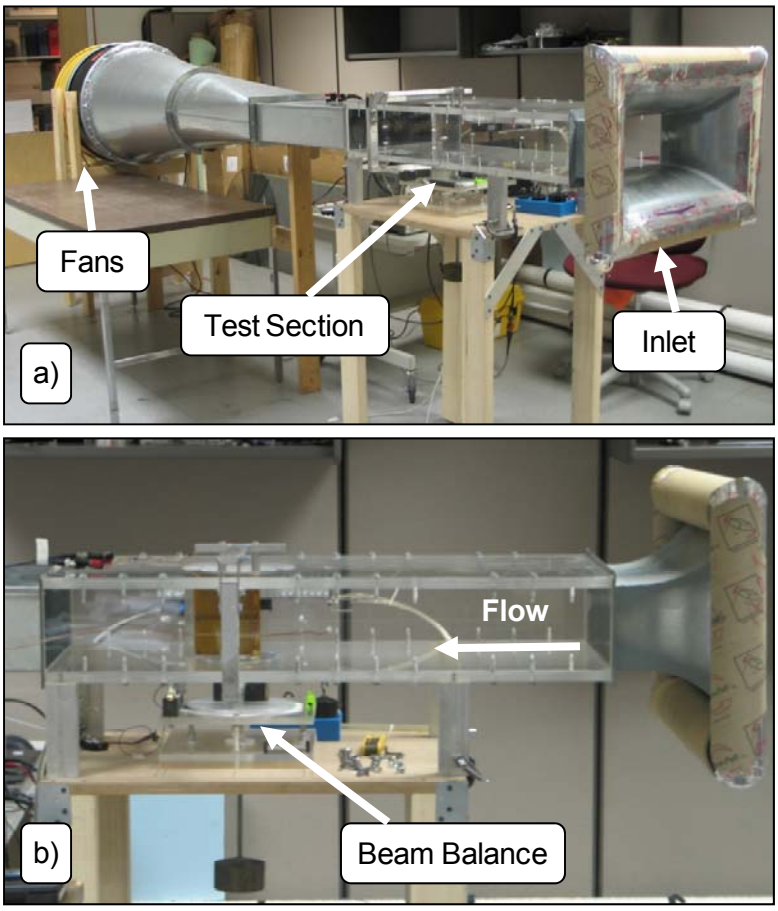

Figure E.8: a) Picture of the version 1 wind tunnel setup. b) Close-up of the acrylic test-section and inlet-nozzle.

The converging nozzle inlet is fabricated by B&M Sheet Metal Shop, Inc., Roanoke, VA. The nozzle has a 24.0" wide and 15.0" tall inlet section that converges to the 14.0" wide and 5.37" (136 mm) tall test section. Four paper tubes (packaging tubes) with 3.50" diameters are taped along the edges of the inlet of the converging nozzle to reduce turbulence and the separation of the ambient air that is accelerated into the test section. The custom manual beam balance is presented in Figure E.9

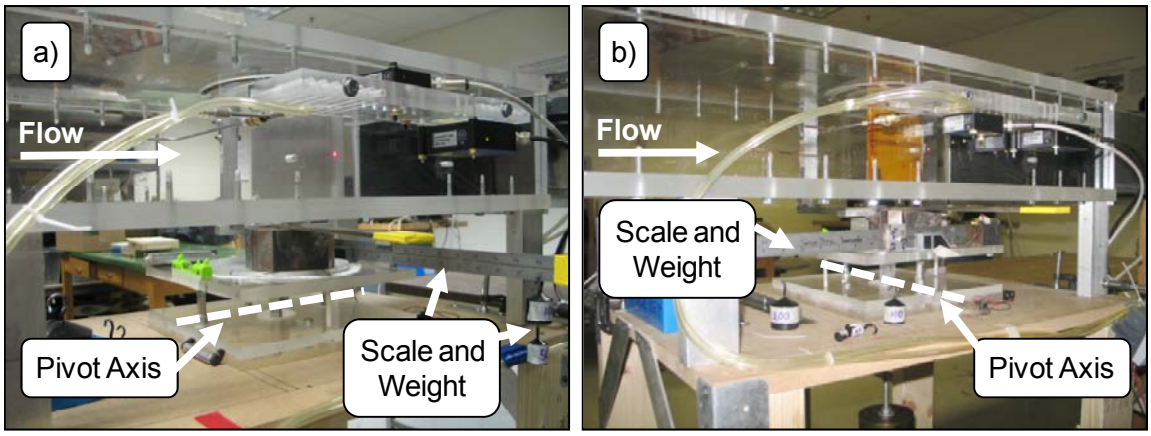

Figure E.9: The pictures of the custom beam balance for version 1 wind tunnel. The balance is in a) lift force and b) drag force measurement configurations.

The manual beam balance is easy to operate and allows the high accuracy measurement of lift and drag forces. Since there a no electrical devices on the manual beam balance, the measurement errors due to A/D conversion and other electrical issues (such as conversions) are eliminated. On the other hand, most of the measurements are conducted manually; therefore automation of the experiment for multiple parameters is not possible. The major disadvantages with the manual beam balance are: 1) the angle of the airfoil is set manually, 2) the tare (or counter) weight has to be adjusted on the scale manually to compensate for the moment generated by the aerodynamic forces, and 3) the lift and drag measurements cannot be conducted simultaneously.

E.1.2 Wind Tunnel Version 3.2

The version 3.2 wind tunnel setup is used for the aerodynamic measurements presented in Chapter 6 for the cascading bimorph thick airfoil. There are two major differences of this version from the previous ones. First, the manual beam balance (of version 1) is upgraded to a custom load balance system that incorporates two strain-gage based load cells (model MLP-10 from Transducer Techniques). This load balance is also used in the current version (version 5) of the wind tunnel setup. Figure E.10 presents the load balance setup on the version 3.2 wind tunnel.

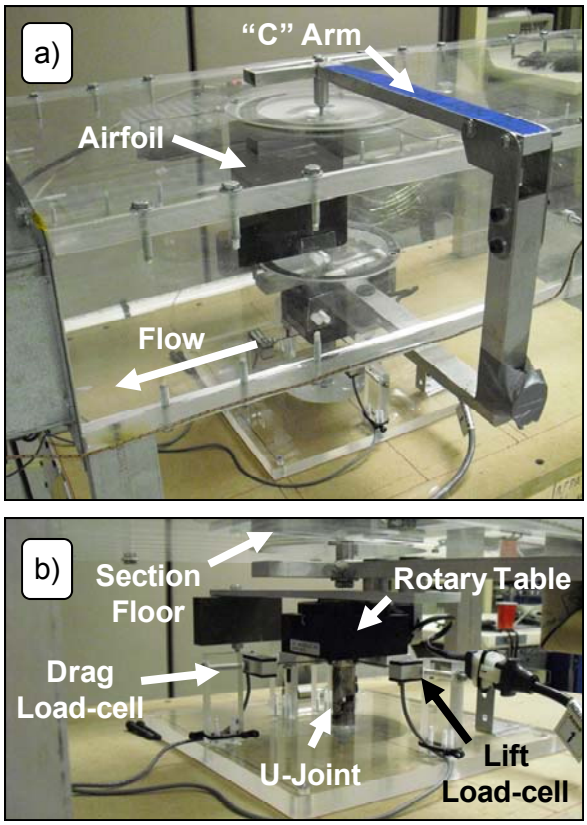

Figure E.10: Picture of load balance with two load cells.

In addition to the load cells, a rotary table allows the automated and precise adjustment of the angle of the airfoil with respect to the flow. These improvements in the load balance enable a fully automated wind tunnel setup. Refer to Figure E.5 for an accurate CAD model of the load balance.

The second major improvement is applied in order to measure the flow velocity in the test section with higher accuracy. Two static ports (or holes) are drilled on the test section. These holes are located 1.13" from the inlet of the test section. Refer to Figure E.2 for the placement of Static Port 1 and Static Port 2 on each of the side walls. These two static ports are connected together with a "T" connection which is also connected to the low input of the Dwyer 668-5 differential pressure transducer (for versions 3.2 and 4 of the wind tunnel). The Setra 267 pressure transducer is used with the Pitot-static tube for versions 3.2 and 4 of the wind tunnel. In addition to the static ports, four holes are drilled on the top wall (ceiling) of the test section. These holes are labeled C1 - C4 in Figure E.2. These holes are used for the placement of the Pitot-static tube during buoyancy measurements only. The holes C1 through C4 are located 1.13", 9.00", 16.5", and 31.88" from the inlet of the test section respectively. The buoyancy

calculations (and corrections) and the calibration of the flow velocity (with the use of the static ports and the Pitot-static tube) are presented later in this appendix.

E.1.3 Wind Tunnel Version 4

The version 4 wind tunnel setup is used for the aerodynamic measurements presented in Chapter 7 (section 7.3) for the airfoil with the flow control feature and the NACA 0010 trailing section. Figure E.11 shows the version 4 wind tunnel setup.

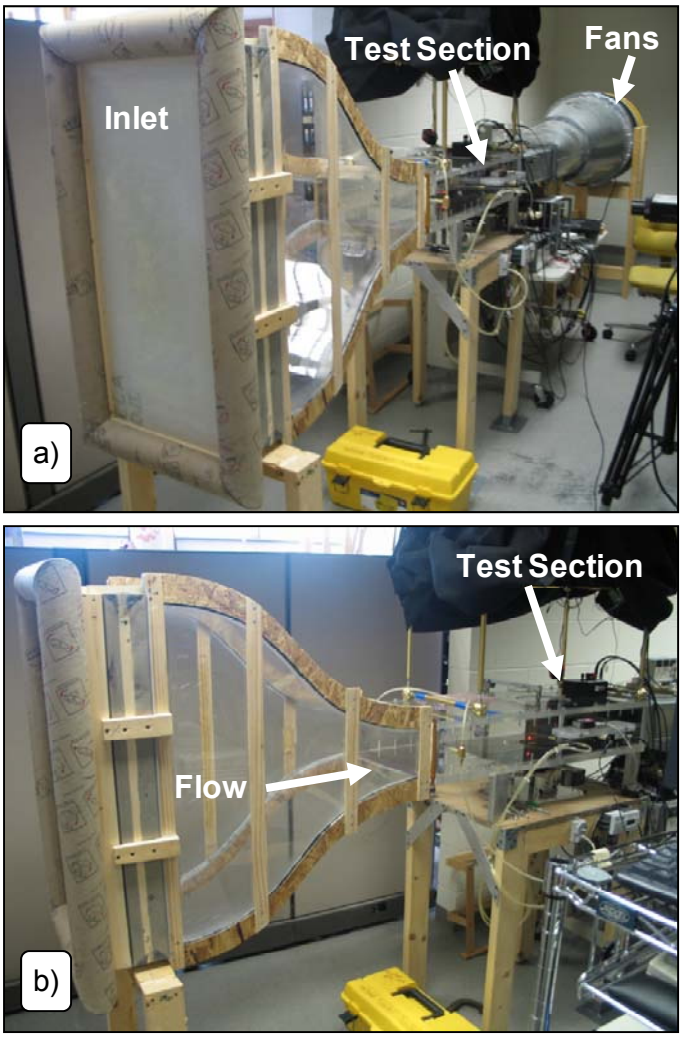

Figure E.11: Version 4 wind tunnel setup with a new converging nozzle inlet, two screens and a flow straightener made with drinking straws.

The version 4 wind tunnel is relocated (in 381 Durham Hall) to its current position. The electronic instrumentation and the test section are same as version 3.2; however the "open" galvanized steel inlet is upgraded to an aerodynamically improved converging nozzle inlet. The

new inlet is modeled via CAD and fabricated using several sheets of (flexible) 1/16” acrylic material (for the interior surface) and wood for the frame. As noted earlier, the inlet nozzle is 31.75” tall and 14.0” wide at the flow entrance. The nozzle converges to a 5.37” (136 mm) height at the flow exit (or test section entrance). The nozzle is 30.0” long (between the inlet and the outlet).

In addition to the new converging nozzle, two layers of fiberglass screens (window screens) are added ahead of the converging nozzle. As noted earlier, these screens are in series and they are 3.50” apart from each other. These screens are upstream of the converging nozzle and help reduce the turbulence of the incoming air. The first flow conditioning device (for version 4 wind tunnel) is a honeycomb structure fabricated from 0.25” diameter drinking straws that are cut into 3.0” length. The straws are stacked in a wooden box with 31.75” height and 14.00” width. The straws are glued together with a 3M spray adhesive. The edges of the honeycomb box are surrounded with four paper tubes (packaging tubes) with 3.50” diameter. These tubes are cut and glued along the edges of the honeycomb box to reduce turbulence and the separation of the ambient air that is accelerated into the test section.

E.1.4 Wind Tunnel Version 5

This section presents the final version of the wind tunnel setup. In addition to the improvements described for version 3.2 and version 4, two additional changes are applied. First, the Setra 267 pressure transducer is connected to the static ports because 1) it has higher accuracy and 2) the static ports are the primary source of the flow velocity measurements. The Dwyer 668-5 pressure transducer is then switched to the Pitot-static tube. Note that the Pitot-static tube is only employed during the buoyancy and calibration experiments (which are presented later in Section E.4). Second, the straw honeycomb is replaced with an aluminum honeycomb. Figure E.12 presents the final version of the wind tunnel facility with the aluminum honeycomb flow straightener.

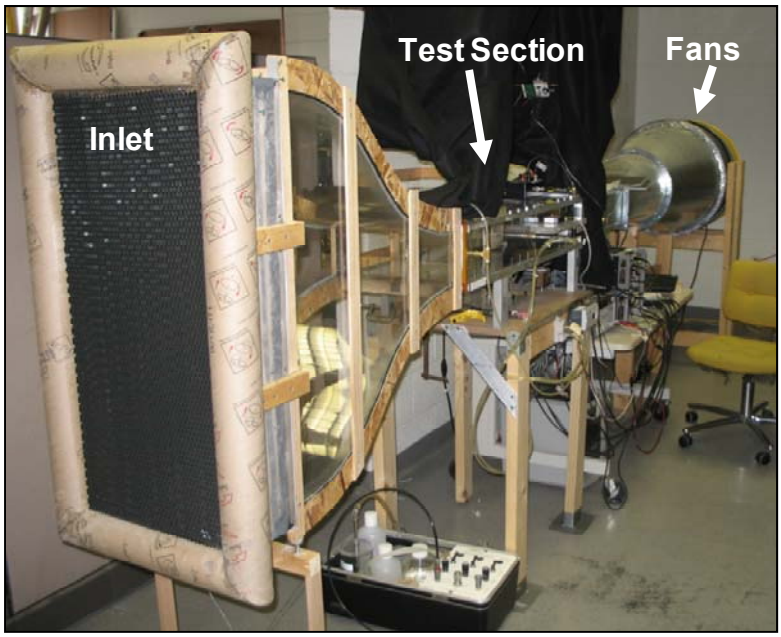

Figure E.12: Version 5 wind tunnel facility.

The aluminum honeycomb material is purchased from Texas Almet LP, Arlington TX. The honeycomb has 3/8" hexagonal cell size, 0.0026" cell wall thickness and a 3.00" depth. In comparison to the straw honeycomb structure, the aluminum honeycomb has "cleaner" edges and less pressure drop across it. It also has significantly more uniform thickness and cell geometry.

E.2 Velocity Profile

Preliminary tests are conducted to characterize the empty test section flow profile for each iteration (of the inlet converging nozzle). Flow velocity during these tests is observed using a Pitot-static tube from Flow-Kinetic LLC, Bryan, TX (model P06A-CF stainless-steel tube with 1/8" diameter and 6.5" insertion depth). The differential pressure from the Pitot-static probe is measured with a Setra 267 pressure transducer during the velocity profile characterization. The velocity profile is measured along the horizontal axis (68 mm from the top and bottom walls) and vertical axis (178 mm from each side wall). The Pitot-static probe is located 16.0 cm upstream of the airfoil. Figure E.3 demonstrates the placement of the Pitot-static tube for velocity profile measurements along the horizontal axis. The flow velocity at discrete locations are recorded for 20 seconds (sampled at 1 kHz) and averaged to get the mean velocity.

The following sections present the velocity profile of the wind tunnel versions (with significant differences in the inlet geometry).

E.2.1 Wind Tunnel Versions 1 through 3.2

This section presents the velocity profile of the wind tunnel versions 2 and 3.2. As noted earlier, a galvanized steel converging nozzle is employed in these versions of the wind tunnel. These two versions do not employ any turbulence reduction screens or flow straighteners upstream of the inlet nozzle. Figure E.13 presents the velocity profile of the wind tunnel versions 1 through 3.2.

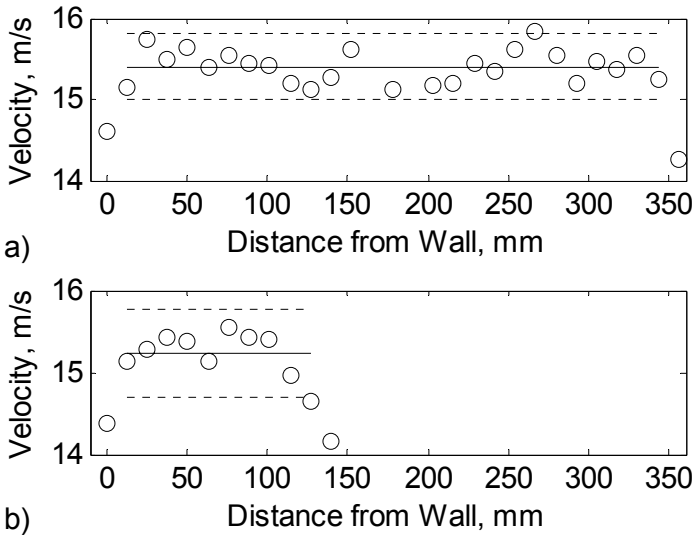

Figure E.13: Velocity profile of the empty test section of wind tunnel versions 1 through 3.2. Pitot-static sweep along the a) horizontal and b) vertical axes.

Although a 20 second sample is taken at each location, a variation of the mean value between each sample is still observed. There are two known sources of this variation: 1) Low-frequency disturbances in the laboratory and 2) converging nozzle geometry. Note that the wind tunnel used here is an open circuit facility and a longer sample time might remove the mean velocity variation due to the low-frequency disturbances in the laboratory. For the horizontal axis velocity measurements, a mean velocity (solid line) of 15.4 m/s is measured and the 95% confidence interval uncertainty (dotted lines) is $U_{Velocity,X}$ = ±0.40 m/s. For the vertical axis measurements, the mean velocity is 15.2 m/s and the 95% confidence interval uncertainty is $U_{Velocity,Y}$ = ±0.54 m/s. Approximately 4% maximum difference from the mean velocity is

calculated independent of Pitot-static probe location. The flow is assumed spatially uniform for coefficient calculations for the experimental results from version 1 and version 3.2 wind tunnel facilities.

E.2.2 Wind Tunnel Version 4

This section presents the velocity profile of the wind tunnel version 4. A custom acrylic\wood converging nozzle is employed in this version of the wind tunnel. Two fiberglass screens and a honeycomb flow straightener (fabricated using 0.25" diameter drinking straws) are employed upstream of the inlet nozzle. Figure E.14 presents the velocity profile of version 4 of the wind tunnel.

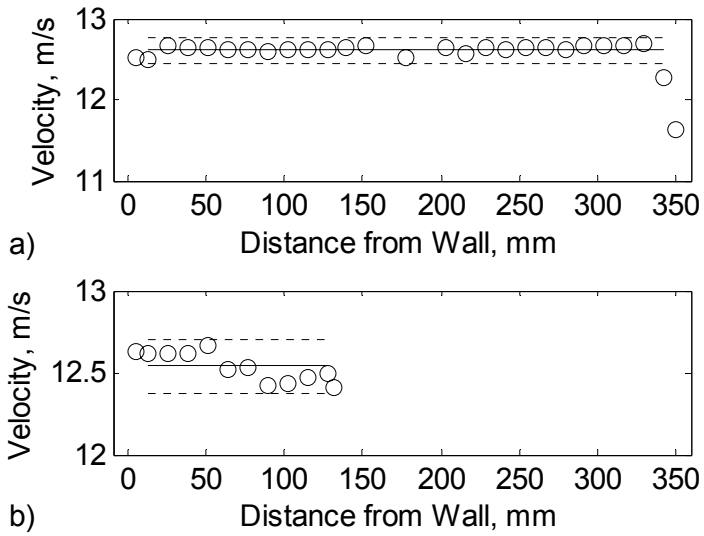

Figure E.14: Velocity profile of the empty test section of wind tunnel version 4. Pitot-static sweep along the a) horizontal and b) vertical axes.

Similar observations (as in versions 1 and 3.2) can be made on the behavior of the flow profile. For the horizontal axis velocity measurements, a mean velocity (solid line) of 12.6 m/s is measured and the 95% confidence interval uncertainty (dotted lines) is $U_{Velocity,X} = \pm 0.16$ m/s. For the vertical axis measurements, the mean velocity is 12.5 m/s and the 95% confidence interval uncertainty is $U_{Velocity,Y} = \pm 0.17$ m/s. Approximately 1.5% maximum difference from the mean velocity is calculated independent of Pitot-static probe location. The flow is assumed spatially uniform for coefficient calculations for the experimental results from version 4 wind tunnel

facility. The changes made to the converging nozzle inlet indeed show improved flow velocity profile (when compared to the previous versions).

E.2.3 Wind Tunnel Version 5

This section presents the velocity profile of the wind tunnel version 5 which is also the current version of the wind tunnel. A custom acrylic\wood converging nozzle is employed in this version of the wind tunnel. Two fiberglass screens and an aluminum honeycomb flow straightener (with 3/8" hexagonal cells) are employed upstream of the inlet nozzle. Figure E.15 presents the velocity profile of version 5 of the wind tunnel.

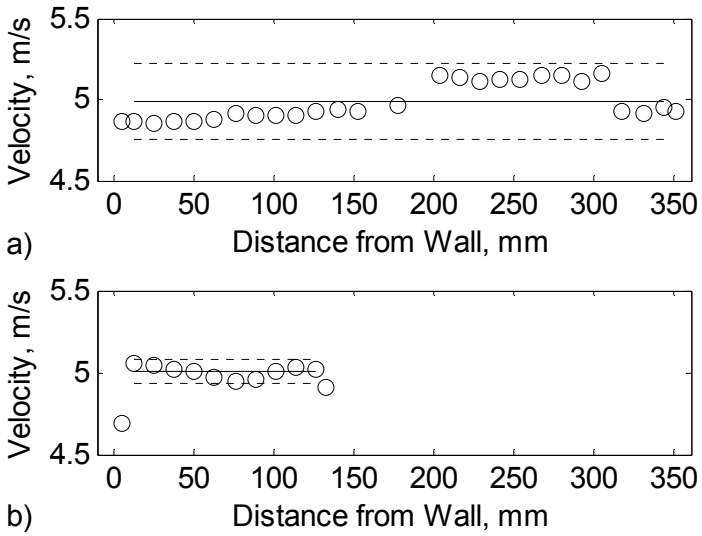

Figure E.15: Velocity profile of the empty test section of wind tunnel version 5. Pitot-static sweep along the a) horizontal and b) vertical axes.

Similar observations (as in version 4) can be made on the behavior of the flow profile. For the horizontal axis velocity measurements, a mean velocity (solid line) of 4.99 m/s is measured and the 95% confidence interval uncertainty (dotted lines) is $U_{Velocity,X} = \pm 0.22$ m/s. For the vertical axis measurements, the mean velocity is 5.01 m/s and the 95% confidence interval uncertainty is $U_{Velocity,Y} = \pm 0.07$ m/s. Approximately 4.5% difference (from horizontal axis measurements) and 1.5% difference (from vertical axis measurements) from the mean velocity is calculated independent of Pitot-static probe location. The flow is assumed spatially uniform for coefficient calculations for the experimental results from version 5 wind tunnel facility. It is important to note that the replacement of the straw honeycomb with the aluminum honeycomb

indeed improved the flow velocity profile (when compared to version 4). On the other hand, the variation of the flow velocity (due to low-frequency variations) is more dominant in the experiments presented in Section 7.4 (in comparison to Section 7.3), which employs a slower flow speed of 5.0 m/s. The low-frequency variation of the flow velocity is mainly due to the variation of the rotation of the blades (of the fans) at low fan speeds.

E.3 Turbulence Intensity

The turbulence of the flow in the empty test section is measured by standard constant temperature anemometry (CTA, and also known as hot wire anemometry) technique. A model 1210-T1.5 hot wire probe (from TSI Inc., Shoreview, MN) is used along with a model 55M01 CTA standard bridge (from Dantec Dynamics Inc., Ramsey, NJ). The hot wire probe is located at the center of the test-section for all turbulence tests (unless otherwise stated). The signal from the Dantec standard bridge is conditioned with a model 9002, 8 pole, 6 zero low pass (LP) filter (from Frequency Devices, Inc., Ottawa, IL) and a model 4302, dual 24 dB/octave high pass (HP) filter (from Ithaco, Ithaca, NY). After proper conversion of the measured voltages to velocity (V), the turbulence intensity (TI) is calculated by:

$$TI = \frac{V_{rms}}{V_{mean}} * 100. \tag{A.1}$$

The RMS of the velocity, V_{rms}, is calculated by:

$$V_{rms} = \sqrt{\frac{1}{n}\sum_{i=1}^{n}(V_i - V_{mean})^2} \tag{A.2}$$

where the index i represents each sample and n is the total number of samples. The turbulence intensity is measured at several velocities for different filter settings. The presentation of turbulence for different bandwidths is commonly used in the literature [Selig and McGranahan, 2004] to show the frequency components of the turbulence. Note that the each measurement is repeated four times. Turbulence is calculated from each set and averaged in order to get a better representation of the mean turbulence intensity.

The following sections present the turbulence intensity measurements that are specific to the version specified by the section title.

E.3.1 Wind Tunnel Version 1 through 3.2

Figure E.16 presents the turbulence intensity (as a function of mean flow velocity) at different low-pass (LP) filter settings for versions 1 through 3.2 of the wind tunnel. As noted earlier, the turbulence is measured at the center of the test section.

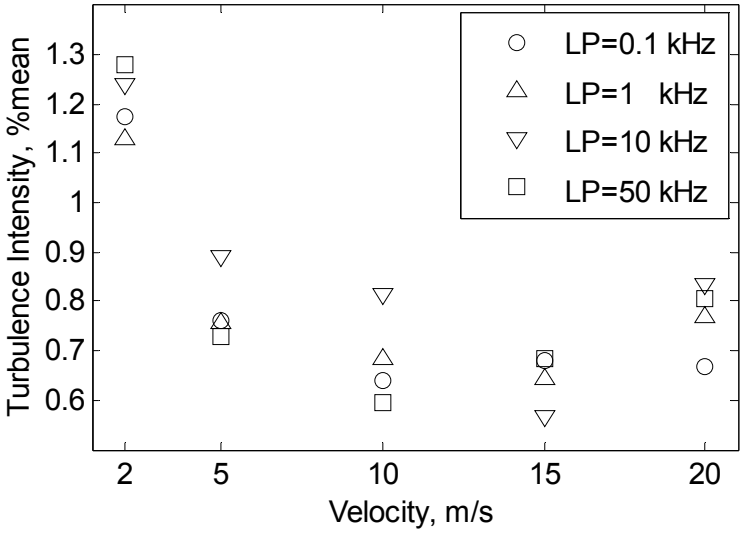

Figure E.16: Turbulence intensity vs. velocity at the center of the empty test section of versions 1 and 3.2 wind tunnel. The HP filter cut-off is to 0.1 Hz.

The effect of low pass filter is small and therefore not consistent at each velocity. This is caused by the reduction of "power" in the voltage signal (from the Dantec CTA standard bridge) at higher frequencies. At low signal amplitudes, the roll-off of the filter is simply not effective. The variation of the turbulence observed in the figure is dominated by the small changes in turbulence with time (due to low-frequency variations of the mean velocity). The turbulence is at the lowest intensity around 15 m/s and highest at 2 m/s average velocity. Figure E.17 presents the turbulence intensity (as a function of mean flow velocity) at different high-pass filter settings for versions 1 through 3.2 of the wind tunnel.

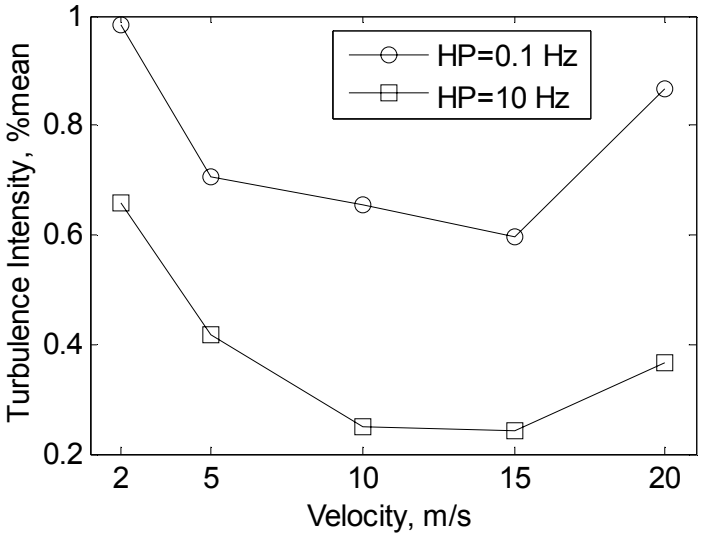

Figure E.17: Turbulence intensity vs. velocity at the center of the empty test section of versions 1 and 3.2 wind tunnel. The LP filter cut-off is set to 50 kHz.

In contrast, the effect of the high-pass filter is significant, and as expected, the turbulence appears to decrease as more of the low frequency content of the signal is filtered. The lowest turbulence is observed at 15 m/s and the highest at 2 m/s. In summary, 0.60 % turbulence intensity is calculated from 0.1 Hz - 50 kHz band-pass filtered signal for the test speed of 15 m/s. The turbulence of versions 1 and 3.2 wind tunnel setup at 15 m/s (used in Chapter 5 and Chapter 6 respectively) is relatively larger than tunnels used in the research area due to the lack of flow straighteners and screens upstream of the inlet nozzle.

Figure E.18 shows the turbulence intensity measured at different locations along the horizontal axis (of the test section) which is similar to the flow profile measurements presented in Section E.2. This turbulence intensity profile measurement is only available for the version1 and 3.2 wind tunnel setup.

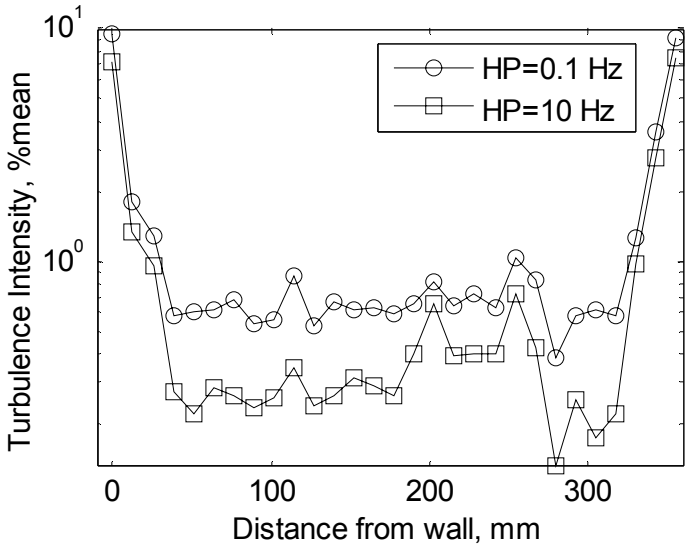

Figure E.18: Turbulence intensity profile along the horizontal axis. The data represents the empty test section of versions 1 and 3.2 wind tunnel setup at 15 m/s mean velocity. The LP filter cut-off is set to 50 kHz.

As expected, the turbulence intensity is quite high near the side walls. Although not measured, similar trend is expected at other mean velocities, and in between the top and bottom walls of the wind tunnel test section.

E.3.2 Wind Tunnel Version 4

Figure E.19 presents the turbulence intensity (as a function of mean flow velocity) at different band-pass filter settings for version 4 of the wind tunnel. As noted earlier, the turbulence is measured at the center of the test section. Since the power density of turbulence signal is low for frequencies above 10 kHz, the low-pass filter settings are set to be 0.1 kHz, 1 kHz and 10 kHz. The high-pass filter cut-off is set to 0.1 Hz and 10 Hz. As observed earlier, the effect of the LP filter is small indicating that the turbulence is dominated by the low frequency variations of the flow. In contrast, the effect of HP filter is significant. The trend of the turbulence intensity is significantly different than the observations made for the versions 1 and 3.2 wind tunnel setup with the converging nozzle without turbulence reduction screens and a flow straightener. The turbulence intensity (appears to) monotonically increase as the flow velocity is increased.

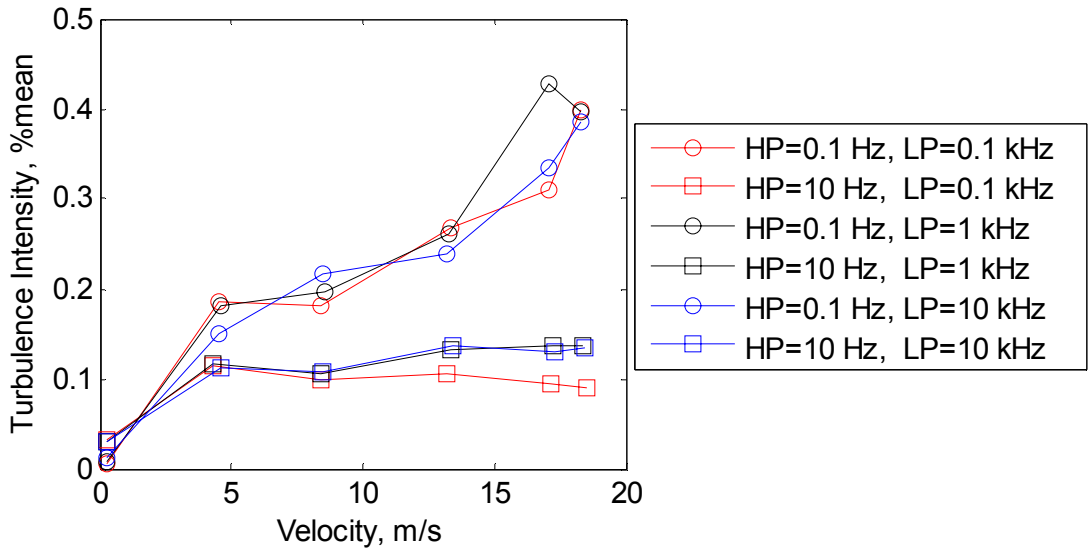

Figure E.19: Turbulence intensity vs. velocity at the center of the empty test section of version 4 wind tunnel at 4.5 m/s mean velocity.

Approximately 0.15% turbulence intensity is deduced from 0.1 Hz - 10 kHz band-pass filtered signal for the test speed of 4.5 m/s. Approximately 0.19% turbulence intensity is deduced from 0.1 Hz - 0.1 kHz band-pass filtered signal for the test speed of 4.6 m/s. Higher turbulence intensity is expected from the 10 kHz low-pass filtered signal when compared to the 0.1 kHz. The results presented in Figure E.19 further demonstrate that the turbulence intensity is dominated by low-frequency variations of the flow. In summary, approximately 0.19% turbulence intensity is assumed for the 0.1 Hz high-pass filtered signal at the test speed of 4.6 m/s. The turbulence of the version 4 wind tunnel setup (used in Section 7.3 for flow control experiments) is significantly lower than the version 3.2 due to the addition of the flow straightener and two turbulence reduction screens upstream of the inlet nozzle.

E.3.3 Wind Tunnel Version 5

Figure E.20 presents the turbulence intensity (as a function of mean flow velocity) from the 0.1 Hz - 10 kHz band-pass filtered CTA signal for version 5 of the wind tunnel. The flow straightener of the version 4 wind tunnel (fabricated with drinking straws) is replaced with the aluminum honeycomb with hexagonal cells. In addition to the effect of the new honeycomb flow straightener, the effect of the number of turbulence reduction screens are evaluated. Three

experiments are conducted, 1) without any screens, 2) with 1 screen and 3) with 2 screens in series. As noted earlier, the turbulence is measured at the center of the test section.

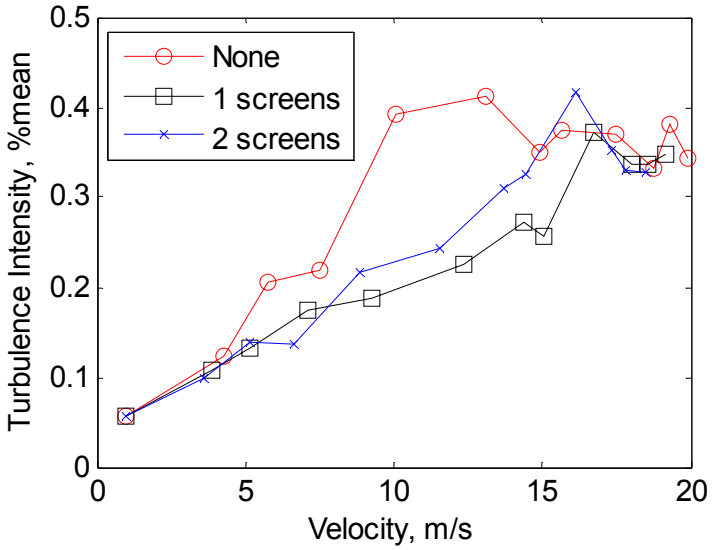

Figure E.20: Turbulence intensity vs. velocity at the center of the empty test section of version 5 wind tunnel from 0.1 Hz - 10 kHz band-pass filtered signal at 5.2 m/s mean velocity. The effect of turbulence reduction screens is presented.

As expected, the dependence of the turbulence intensity to the mean flow velocity is similar to the observations made for the version 4 wind tunnel setup. The turbulence intensity (appears to) monotonically increase as the flow velocity is increased.

In summary, approximately 0.14% turbulence intensity is deduced from the 0.1 Hz - 10 kHz band-pass filtered CTA signal at the test speed of 5.2 m/s. The turbulence of the version 5 wind tunnel setup (used in Section 7.4 for flow control experiments) is significantly lower than the version 3.2 and version 4 wind tunnel setups due to the addition and improvement of the flow straightener and due to the use of two turbulence reduction screens upstream of the inlet nozzle. Although a single turbulence reduction screen results in lower turbulence intensity in the operation range, the version 5 wind tunnel is kept with two turbulence reduction screens.

E.4 Buoyancy and Wall Corrections

Tunnel wall effects and buoyancy corrections were applied as necessary using the techniques found in Barlow et al. [1999]. The reported lift and drag coefficients (in this dissertation) are calculated and corrected by the following equations:

$$C_l = C_{lu}(1 - \sigma - 2\epsilon_{sb} - 2\epsilon_{wb}), \tag{A.3}$$

$$C_d = C_{du}(1 - 3\epsilon_{sb} - 2\epsilon_{wb}). \tag{A.4}$$

Barlow suggests several corrections due to the existence of the walls around the airfoil. The solid blockage term, ϵ_{sb}, and the wake blockage terms are explained in Allen and Vincenti [1944] and Maskell [1965] respectively. The C_{lu} and C_{du}, uncorrected lift and drag coefficients, are calculated by:

$$C_{lu} = \frac{F_{lift}}{\left(\frac{1}{2}\rho c b_r v_{qc}^2\right)}, \tag{A.5}$$

$$C_{du} = \frac{(F_{drag} - F_{bd})}{\left(0.5\rho c b_r v_{qc}^2\right)} \tag{A.6}$$

where F_{lift} and F_{drag} are the measured lift and drag forces (by the load balance), and F_{bd} is the drag on the airfoil caused by the longitudinal pressure gradient, ρ is the density of air, b_r is the reduced span (due to boundary layer displacement thickness) and v_{qc} is the flow speed calculated at the quarter-chord (QC) location. Note that density is calculated using the fixed absolute pressure in the laboratory and the temperature of the flow which is recorded during each test (using the "J" type thermocouple and the Omega CCT-22 signal conditioner). In addition to the corrections above, streamline curvature correction is applied where the angle-of-attack (α) is calculated by:

$$\alpha = \alpha_u + \frac{57.3}{2\pi}\left(\frac{\pi^2 c^2}{48h^2}\right)(C_{lu} + 4C_{m_{\frac{1}{4}u}}) \tag{A.7}$$

where α_u is the measured AOA, $h = 356\,mm$ is the section width, and the $C_{m_{\frac{1}{4}u}}$ is the (negligible) uncorrected pitch-moment coefficient.

Actual velocity and reduction in span is calculated as follows: First, a calibration test is conducted in the empty test section between static ports (sufficiently upstream of the airfoil location) and the Pitot-static tube located at different locations along the flow-axis. The velocity is measured with the Pitot-static tube at each location, and the development of boundary layer (BL) is calculated by applying Bernoulli's equation and conservation of mass. As noted earlier, the static ports are located 1.13" from the inlet of the test section. The Pitot-static tube is placed through the holes C1 through C4 as illustrated in Figure E.2. These measurements are repeated for several fan power settings (adjusted by the variable voltage output transformer that controls the fans).

The effect of the thickness of the boundary layer (δ) is calculated by assuming an equivalent displacement thickness (δ^*). The assumed velocity profile of the test section is shown in Figure E.21.

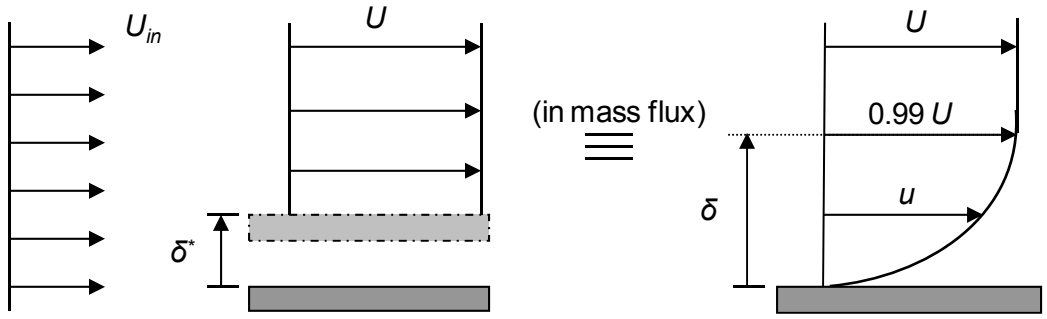

Figure E.21: Illustration of the velocity profile in the test section and the boundary layer thickness.

In Figure E.21, the U_{in} is the (assumed) uniform velocity at the inlet of the test section and U is the maximum velocity of the flow at the quarter-chord location of the airfoil. The displacement thickness, δ^*, is the effective (single-sided) change in the airfoil span. The displacement thickness reduces either the mass or the momentum flux by the same amount as the actual boundary layer [Fox et al., 2004]. For incompressible flow, the displacement thickness is equal to:

$$\delta^* = \int_0^\infty (1 - \frac{u}{U})\, dy \approx \int_0^\delta (1 - \frac{u}{U}) dy \tag{A.8}$$

where y is the distance from the wall (which is perpendicular to the flow). The integral is essentially zero for $y \geq \delta$ since $u \approx U$ at $y = \delta$. Assuming that the flow is turbulent and the 1/7 power velocity profile is applicable, the boundary layer thickness (at distance L from the inlet) is calculated by:

$$\delta_L = \frac{0.382}{Re_L^{1/5}} L \tag{A.9}$$

where Re_L is the Reynolds number at distance L from the inlet. Substituting

$$\frac{u}{U} = \left(\frac{y}{\delta}\right)^{1/7} = \eta^{1/7} \tag{A.10}$$

where η is the distance from the wall (y) normalized by the boundary layer thickness (δ), the boundary layer displacement thickness (at distance L from the inlet) becomes:

$$\delta_L^* = \delta_L \int_0^1 \left(1 - \eta^{1/7}\right) d\eta = \frac{\delta_L}{8}. \tag{A.11}$$

The reduced span is calculated by subtracting twice the displacement thickness from the part of the actual span of the airfoil (that is in the boundary layer) since the layer is developed both ends of the span.

The following sections present the buoyancy measurements that are specific to the version specified by the section title.

E.4.1 Wind Tunnel Version 3.2

Figure E.22 presents the static port pressure and the Pitot-static tube pressure for version 3.2 wind tunnel. Both pressure measurements are a function of the fan power in reality. The quarter-chord (QC) is located 24.25" downstream of the inlet of the test section. A linear fit is calculated for the QC using the spatial information in Figure E.22.

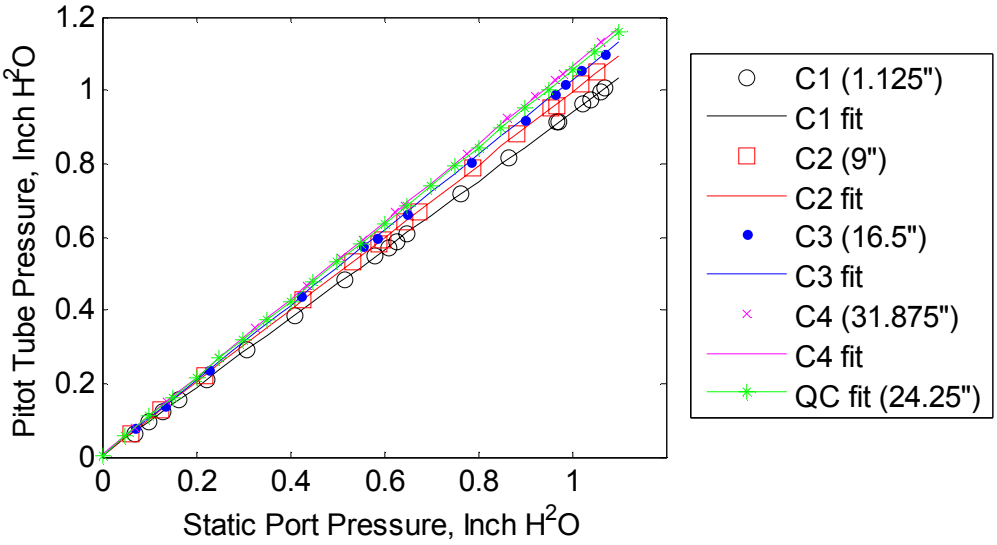

Figure E.22: Measurement of the static and Pitot-static pressures in the full wind tunnel velocity range (or fan power range).

Figure E.23 presents the longitudinal (also known as the streamwise) pressure gradient in the wind tunnel test section in the streamwise direction. The pressure gradient is measured using Pitot-static tube at different locations along the longitudinal direction with respect to the test section. This trend is deduced from the measurements presented Figure E.22.

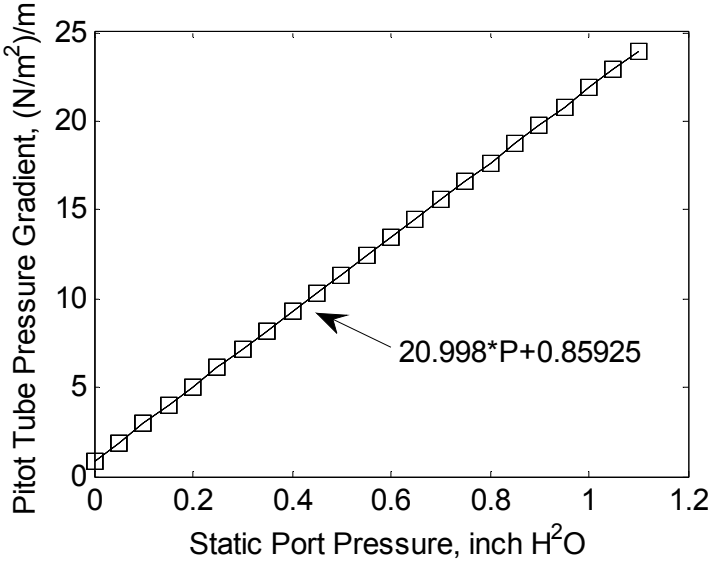

Figure E.23: Test section longitudinal pressure gradient for version 3.2 wind tunnel.

The relationship presented in Figure E.23 is used to calculate the drag on the airfoil caused by the longitudinal pressure gradient, F_{bd} depending on the measured static port pressure

(which is a function of the flow velocity). Note that the drag caused by the longitudinal pressure gradient is very small; therefore it has almost no influence on the coefficient calculations.

Figure E.24 presents the final calibration of Pitot-static-pressure-to-static-port-pressure ratio that applies to the QC location. This ratio is also deduced from the measurements presented in Figure E.22. At the quarter-chord location, the ratio is equal to 1.05. This means that the pressure measured during the aerodynamic experiments with the static ports must be multiplied by the pressure ratio of 1.05 in order to get the correct pressure drop at the quarter-chord location. This calibrated pressure could then be used to calculate the velocity of the flow at the quarter-chord.

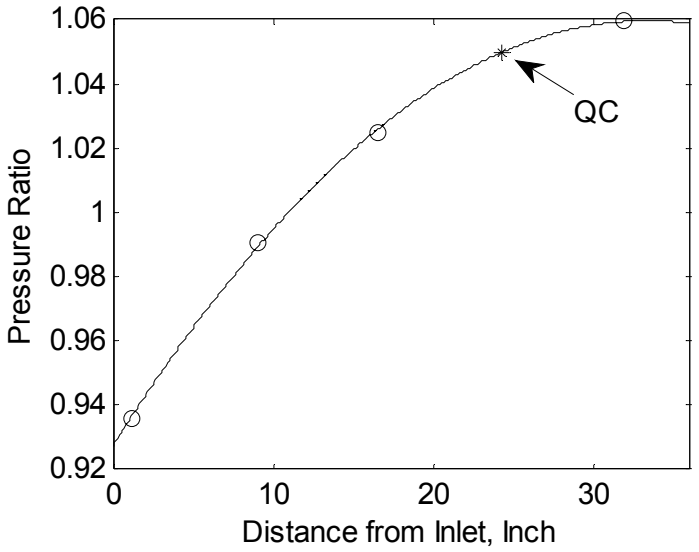

Figure E.24: Pitot-static-tube-pressure-to-static-port-pressure ratio for version 3.2 wind tunnel setup.

Figure E.25 presents the calculated boundary layer displacement thickness (from the calibration experiments presented above) assuming that 1) the flow is turbulent, 2) the boundary layer thickness is zero at station C1 and 3) 1/7 power velocity profile applies.

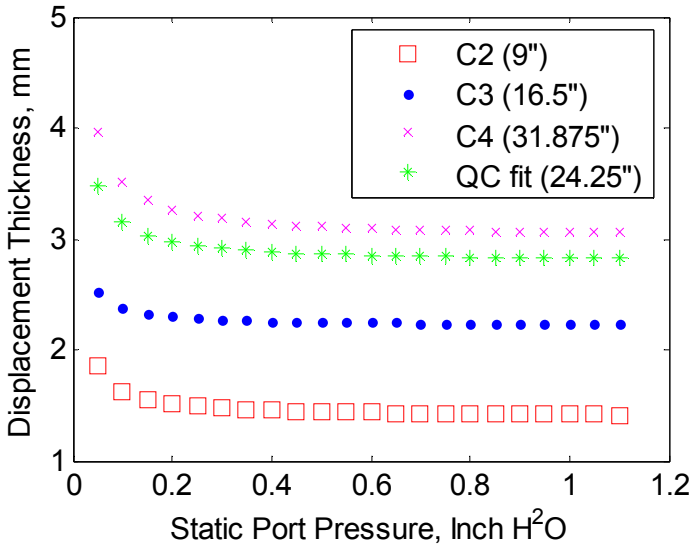

Figure E.25: Boundary layer displacement thickness for version 3.2 wind tunnel.

The calculation of the boundary layer displacement thickness assumes that the boundary layer thickness at station C1 (which is 1.13" from the inlet of the test section) is equal to zero. It is well known (from the literature) that the boundary layer is non-zero for similar duct geometries; therefore the boundary layer displacement thicknesses presented in this dissertation is a lower bound approximation of the actual boundary layer displacement thickness.

The actual BL displacement thickness (from the calibration experiment) is approximately 2.86 mm for the flow speed of 15.0 m/s (which corresponds to 0.50" H^20 static port pressure). Since there is a 1.50 mm gap between the tunnel wall and the airfoil, the applied reduction in span is approximately 1.66% of the actual span (b). On the other hand, assuming a 1/7 power velocity profile (also assuming that flow is turbulent) the theoretical BL height is calculated to be 16.27 mm. The theoretical displacement thickness is 2.03 mm at Reynolds number of 5.79×10^5 at quarter-chord location at 15 m/s [Fox et al., 2004].

E.4.2 Wind Tunnel Version 4

Figure E.26 presents the static port pressure and the Pitot-static tube pressure for version 4 wind tunnel. Both pressure measurements are a function of the fan power in reality. The quarter-chord (QC) is located 24.25" downstream of the inlet of the test section. A linear fit is calculated for the QC using the spatial information in Figure E.26.

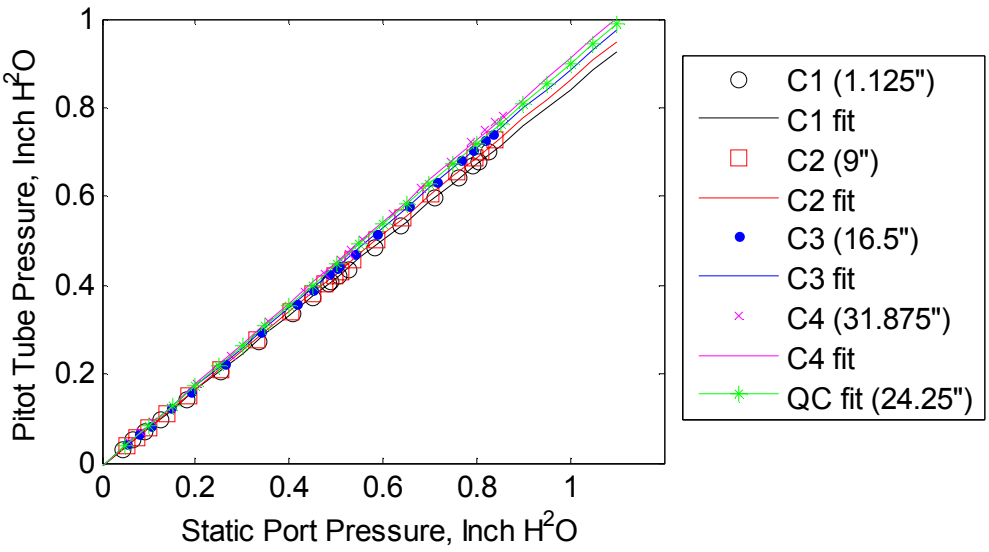

Figure E.26: Measurement of the static and Pitot-static pressures in the full wind tunnel velocity range (or fan power range).

Figure E.27 presents the longitudinal (also known as the streamwise) pressure gradient in the wind tunnel test section in the streamwise direction. The pressure gradient is measured using Pitot-static tube at different locations along the longitudinal direction with respect to the test section. This trend is deduced from the measurements presented Figure E.26.

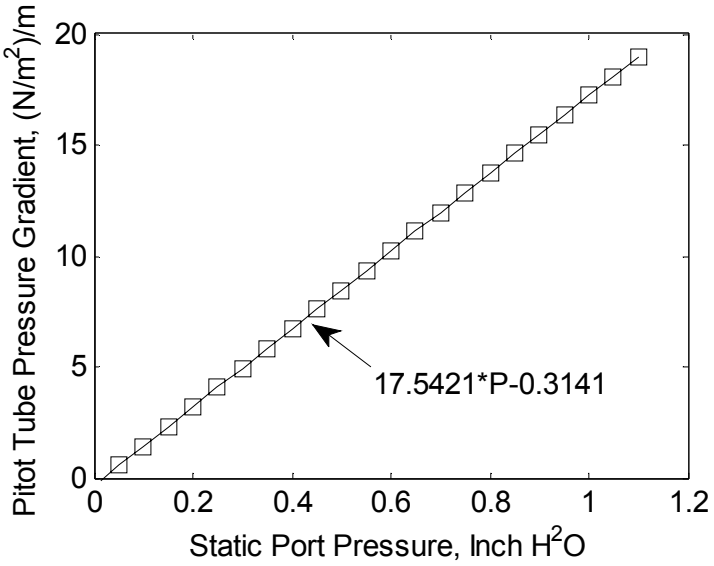

Figure E.27: Test section longitudinal pressure gradient for version 4 wind tunnel.

The relationship presented in Figure E.27 is used to calculate the drag on the airfoil caused by the longitudinal pressure gradient, F_{bd} depending on the measured static port pressure (which is a function of the flow velocity). Note that the drag caused by the longitudinal pressure gradient is very small; therefore it has almost no influence on the coefficient calculations.

Figure E.28 presents the final calibration of Pitot-static-pressure-to-static-port-pressure ratio that applies to the QC location. This ratio is also deduced from the measurements presented in Figure E.26. At the quarter-chord location, the ratio is equal to 0.908. This means that the pressure measured during the aerodynamic experiments with the static ports must be multiplied by the pressure ratio of 0.908 in order to get the correct pressure drop at the quarter-chord location. This calibrated pressure could then be used to calculate the velocity of the flow at the quarter-chord.

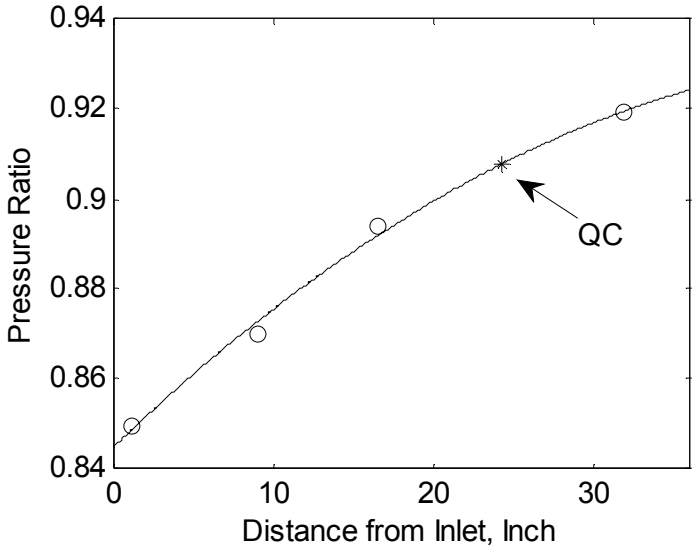

Figure E.28: Pitot-static-tube-pressure-to-static-port-pressure ratio for version 4 wind tunnel setup.

Figure E.29 presents the calculated boundary layer displacement thickness (from the calibration experiments presented above) assuming that 1) the flow is turbulent, 2) the boundary layer thickness is zero at station C1 and 3) 1/7 power velocity profile applies.

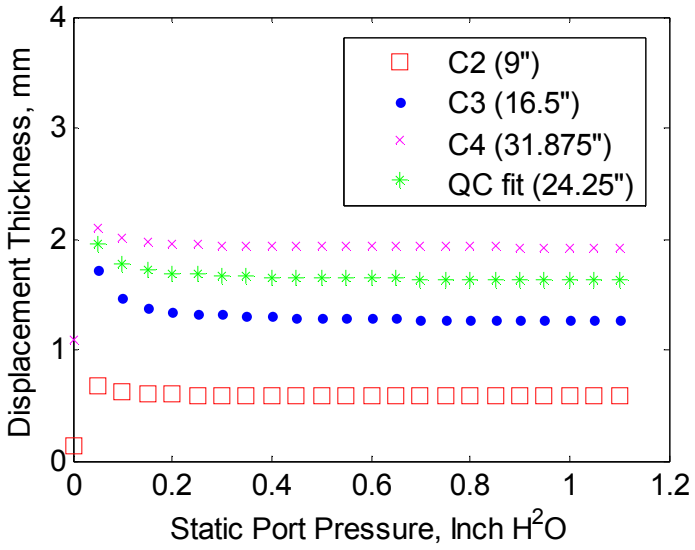

Figure E.29: Boundary layer displacement thickness for version 4 wind tunnel.

The calculation of the boundary layer displacement thickness assumes that the boundary layer thickness at station C1 (which is 1.13" from the inlet of the test section) is equal to zero. It is well known (from the literature) that the boundary layer is non-zero for similar duct geometries; therefore the boundary layer displacement thicknesses presented in this dissertation is a lower bound approximation of the actual boundary layer displacement thickness.

The actual BL displacement thickness (from the calibration experiment) is approximately 1.86 mm for the flow speed of 5.0 m/s (which corresponds to 0.073" H^20 static port pressure). Since there is a 1.50 mm gap between the tunnel wall and the airfoil, the applied reduction in span is approximately 0.15% of the actual span (b). On the other hand, assuming a 1/7 power velocity profile (also assuming that flow is turbulent) the theoretical BL height is calculated to be 20.26 mm. The theoretical displacement thickness is 2.53 mm at Reynolds number of 1.93×10^5 at quarter-chord location at 5.0 m/s [Fox et al., 2004].

E.4.3 Wind Tunnel Version 5

Figure E.30 presents the static port pressure and the Pitot-static tube pressure for version 5 wind tunnel. Both pressure measurements are a function of the fan power in reality. The quarter-chord (QC) is located 24.25" downstream of the inlet of the test section. A linear fit is calculated for the QC using the spatial information in Figure E.30.

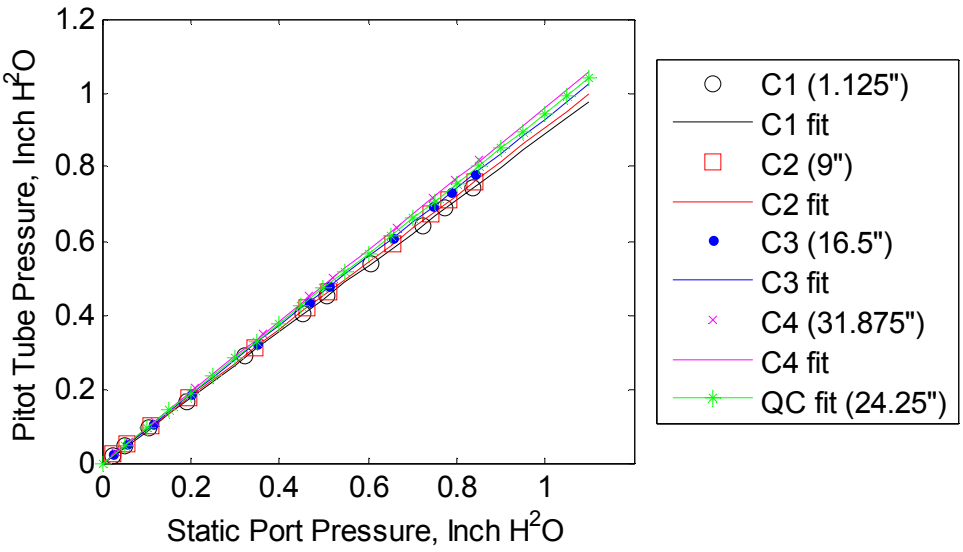

Figure E.30: Measurement of the static and Pitot-static pressures in the full wind tunnel velocity range (or fan power range).

Figure E.31 presents the longitudinal (also known as the streamwise) pressure gradient in the wind tunnel test section in the streamwise direction. The pressure gradient is measured using Pitot-static tube at different locations along the longitudinal direction with respect to the test section. This trend is deduced from the measurements presented Figure E.30.

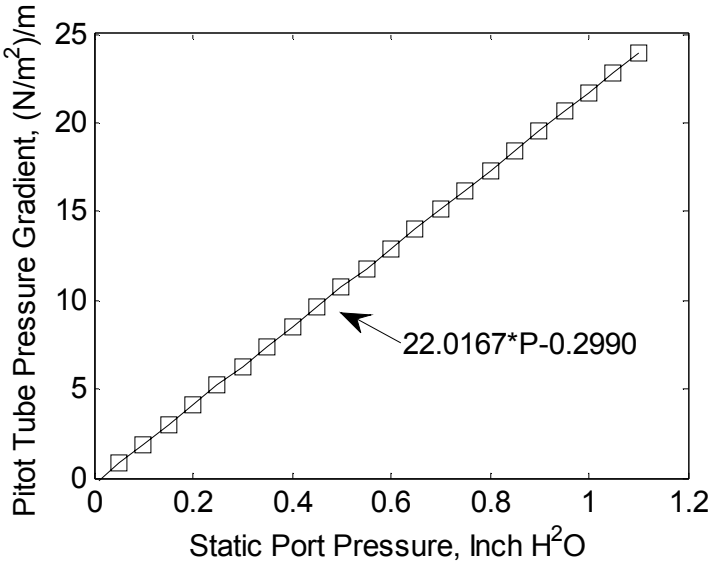

Figure E.31: Test section longitudinal pressure gradient for version 5 wind tunnel.

The relationship presented in Figure E.31 is used to calculate the drag on the airfoil caused by the longitudinal pressure gradient, F_{bd} depending on the measured static port pressure

(which is a function of the flow velocity). Note that the drag caused by the longitudinal pressure gradient is very small; therefore it has almost no influence on the coefficient calculations.

Figure E.32 presents the final calibration of Pitot-static-pressure-to-static-port-pressure ratio that applies to the QC location. This ratio is also deduced from the measurements presented in Figure E.30. At the quarter-chord location, the ratio is equal to 0.946. This means that the pressure measured during the aerodynamic experiments with the static ports must be multiplied by the pressure ratio of 0.946 in order to get the correct pressure drop at the quarter-chord location. This calibrated pressure could then be used to calculate the velocity of the flow at the quarter-chord.

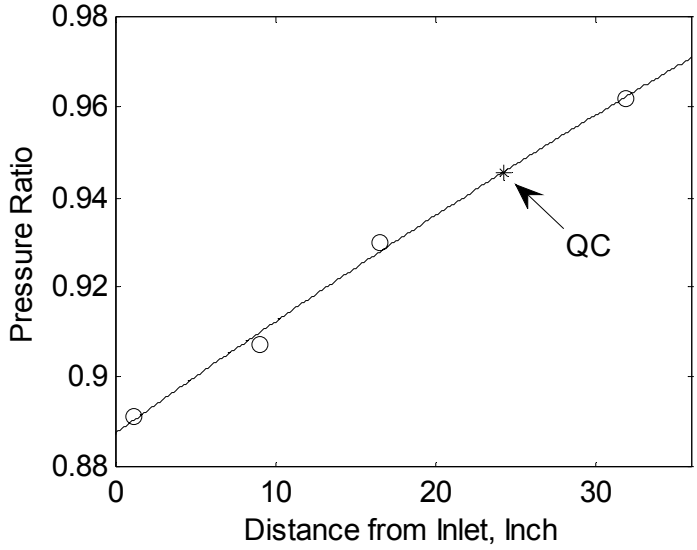

Figure E.32: Pitot-static-tube-pressure-to-static-port-pressure ratio for version 5 wind tunnel.

Figure E.33 presents the calculated boundary layer displacement thickness (from the calibration experiments presented above) assuming that 1) the flow is turbulent, 2) the boundary layer thickness is zero at station C1 and 3) 1/7 power velocity profile applies.

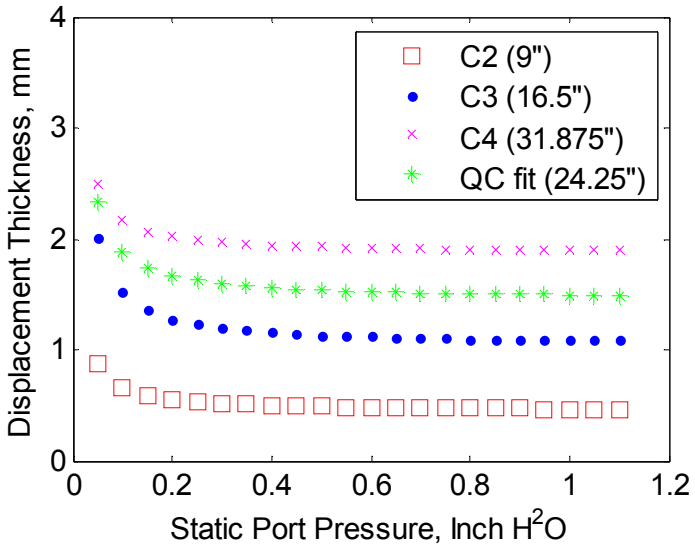

Figure E.33: Boundary layer displacement thickness for version 5 wind tunnel.

The calculation of the boundary layer displacement thickness assumes that the boundary layer thickness at station C1 (which is 1.13" from the inlet of the test section) is equal to zero. It is well known (from the literature) that the boundary layer is non-zero for similar duct geometries; therefore the boundary layer displacement thicknesses presented in this dissertation is a lower bound approximation of the actual boundary layer displacement thickness.

The actual BL displacement thickness (from the calibration experiment) is approximately 2.34 mm for the flow speed of 5.0 m/s (which corresponds to 0.063" H^20 static port pressure). Since there is a 1.50 mm gap between the tunnel wall and the airfoil, the applied reduction in span is approximately 0.86% of the actual span (b). On the other hand, assuming a 1/7 power velocity profile (also assuming that flow is turbulent) the theoretical BL height is calculated to be 20.26 mm. The theoretical displacement thickness is 2.53 mm at Reynolds number of 1.93×10^5 at quarter-chord location at 5.0 m/s [Fox et al., 2004].

E.5 References

Allen, H. J., and Vincenti, W.G., "Wall Interference in a Two-Dimensional-Flow Wind Tunnel with Consideration of the Effect of the Compressibility,' NACA TR 782, 1944.

Barlow, J. B., Rae, W. H. Jr., and Pope, A., *Low-Speed Wind Tunnel Testing*, 3rd ed., John Wiley & Sons, New York, 1999.

Fox, R. W., McDonald, A. T., and Pritchard, P. J., *Introduction to Fluid Mechanics*, 6th ed., John Wiley & Sons, New York, 2004.

Maskell, E. C., "A Theory of the Blockage Effects on Bluff Bodies and Stalled Wings in a Closed Wind Tunnel." ARC R&M 3400, 1965.

Mueller, T. J., and Burns, T. F., "Experimental Studies of the Eppler 61 Airfoil at Low Reynolds Numbers," AIAA Paper 82-0345, Jan. 1982.

NI DAQCard. National Instruments DAQCard-6062E data acquisition system website. [http://sine.ni.com/nips/cds/view/p/lang/en/nid/11918]

NI E Series. National Instruments E Series data acquisition systems' user manual. [http://www.ni.com/pdf/manuals/370503k.pdf]

Selig, M. S., and McGranahan, B. D., 'Wind Tunnel Aerodynamic Tests of Six Airfoils for Use on Small Wind Turbines,' Transactions of ASME, Vol. 126, Pg. 986-1000, November 2004.

APPENDIX F

ADDITIONAL AIRFOIL INFORMATION

This appendix presents additional information for the airfoils examined in this dissertation. The following sections present 1) the simply-supported symmetric and variable-camber thin airfoils (examined in Chapter 5), 2) the rapid-prototyped and variable-camber thick airfoils (examined in Chapter 6), and 3) symmetric and variable-camber airfoils with flow control feature (examined in Chapter 7).

F.1 Simply-Supported Thin Airfoils

The simply-supported airfoils are evaluated in Chapter 5. The first airfoil simply-supported airfoil is an aluminum flat plate airfoil. The flat plate airfoil has a thickness of t = 2.54 mm (2.0% of chord), span of b = 133 mm and a chord of c = 127 mm. The airfoil has a round LE with 1.27 mm radius, and a 3° tapered TE. Figure F.1 shows the aluminum airfoil.

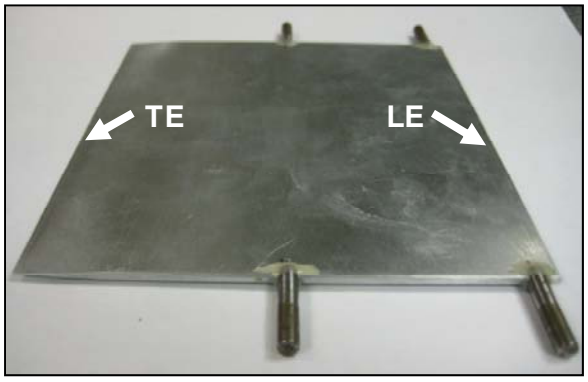

Figure F.1: Simply-supported thin aluminum airfoil with 133 mm span and 127 mm chord.

Figure F.2 shows the aluminum airfoil mounted in the 2D test section of version 1 wind tunnel.

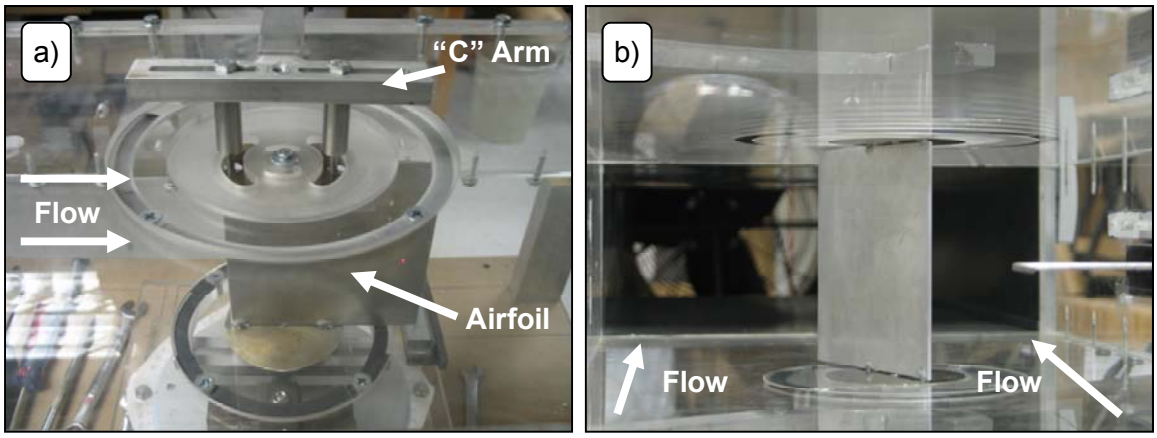

Figure F.2: Thin aluminum airfoil mounted in the 2D test section of version 1 wind tunnel. a) Top view and b) front view of the test section.

There are two variable-camber thin bimorph airfoils, referred to as airfoils T1 and T2 in Chapter 5 and Chapter 8. Each bimorph airfoil is fabricated by sandwiching a 0.027 mm thick stainless-steel sheet with four (two on each face) MFC M8557-P1 type actuators, and bonding the laminate under vacuum. The Macro-Fiber Composite (MFC) actuators are aligned at the LE in the chordwise direction. Two layers of 25.4 μm thick stainless-steel metal (passive material) are bonded to the TE to complete the total chord to 127 mm. Figure F.3 shows both of the thin bimorph variable-camber airfoils.

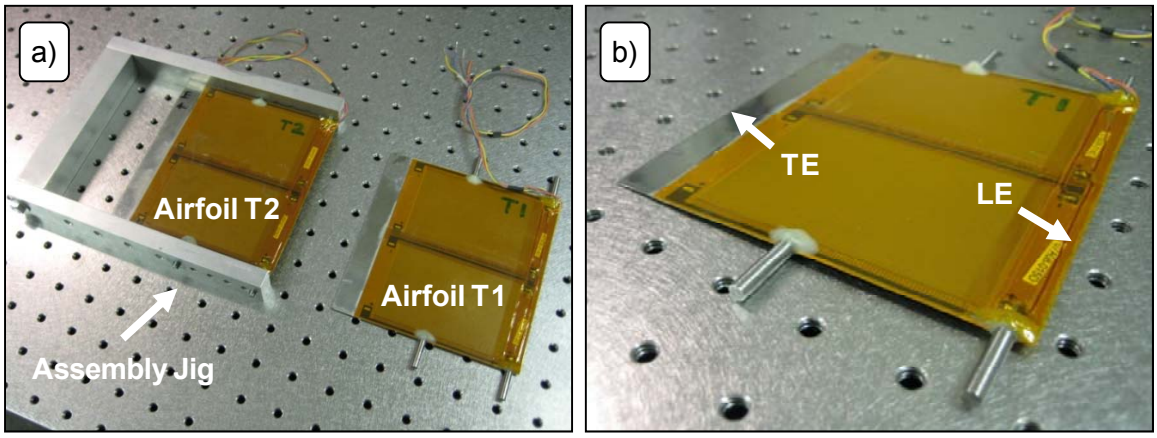

Figure F.3: a) Two variable-camber bimorph airfoils with four MFC M8557-P1 actuators each. b) Close-up of airfoil T1. (127 mm chord and 133 mm span)

Four total stainless-steel pins (two on each end) are bonded to each the airfoils at 5% and 50% chord from the LE. Figure F.4 presents the airfoil T1 mounted in the 2D test section for aerodynamic experiments.

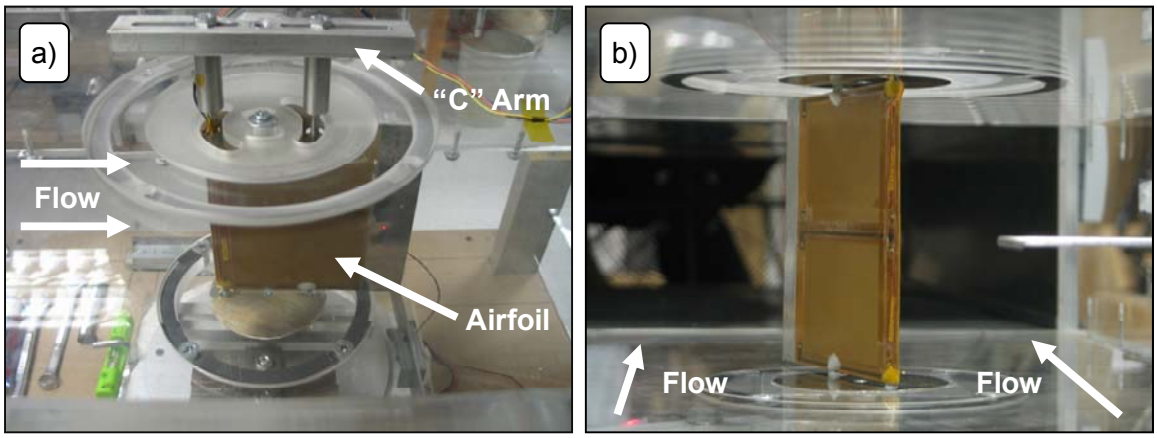

Figure F.4: Thin variable-camber airfoil (T1) mounted in the 2D test section of version 1 wind tunnel. a) Top view and b) front view of the test section.

The wind tunnel evaluations of these airfoils are presented in Chapter 5.

F.2 Symmetric and Variable-Camber Thick Airfoils

The thick airfoils are evaluated in Chapter 6. The first thick airfoil is a NACA 0009 profile airfoil fabricated using a rapid-prototype manufacturing method.

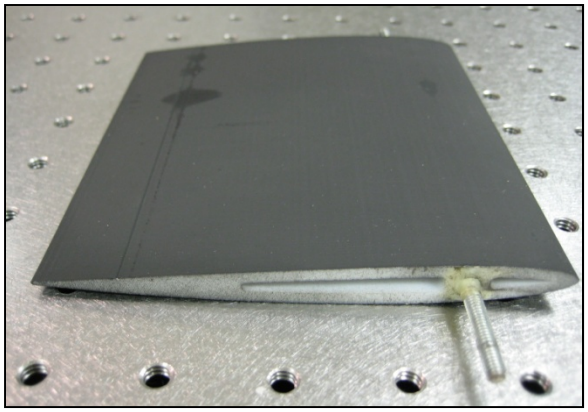

Figure F.5: NACA 0009 airfoil with 127 mm chord and 133 mm span.

The airfoil is fabricated using a Stratasys Dimension SST rapid-prototyping machine available at the Mechanical Engineering Department of Virginia Tech. A P400 ABS type material is used. The fabricated NACA 0009 airfoil has a maximum thickness of 11.3 mm, span of b = 133 mm and a chord of c = 127 mm. Figure F.6 shows the NACA 0009 airfoil mounted on the load balance of the version 3.2 wind tunnel setup.

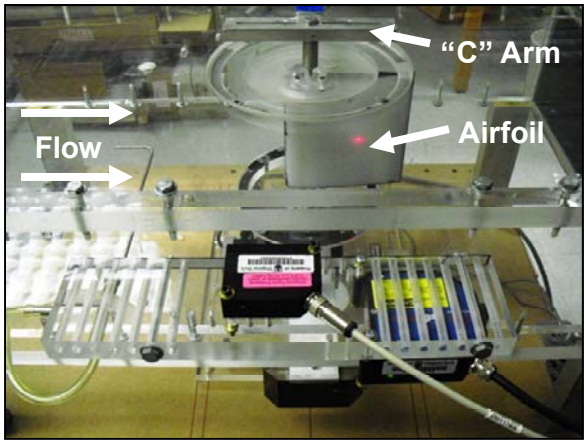

Figure F.6: Top view of NACA 0009 airfoil mounted in the 2D test section of version 3.2 wind tunnel.

Two cascading bimorph variable-camber thick airfoils are also fabricated. These airfoils (labeled A1 and A2) are first used in the wind tunnel evaluation of the ducted-fan aircraft (as shown in Section 6.3.2). The fabricated airfoils have 15 mm thickness, 127 mm chord and 133 mm span. The airfoils are approximately 12% chord thick. Each airfoil employs two cascading bimorphs that are fabricated by sandwiching a 0.027 mm thick stainless-steel material with the MFC actuators and bonding the laminate under 0.8 Atm vacuum for approximately 24 hours. The MFCs are aligned at the TE in the chordwise direction for both bimorph surfaces. Figure F.7 shows the final bonding process where the two cascading bimorphs are bonded to the compliant box mechanism using a 3M DP460 two-part epoxy. Several C-clamps are used to apply uniform pressure across the ends of the bimorphs. The compliant box mechanism is fabricated using several pieces of CNC machined beams glued on a Great Planes CA (cyanoacrylate) hinge (for model airplanes with stock number LXKIII). The hinges are purchased from Tower Hobbies, Champaign, IL. A Tower Hobbies Build-It CA (stock number LXPT38) thin glue is used to harden the CA hinge.

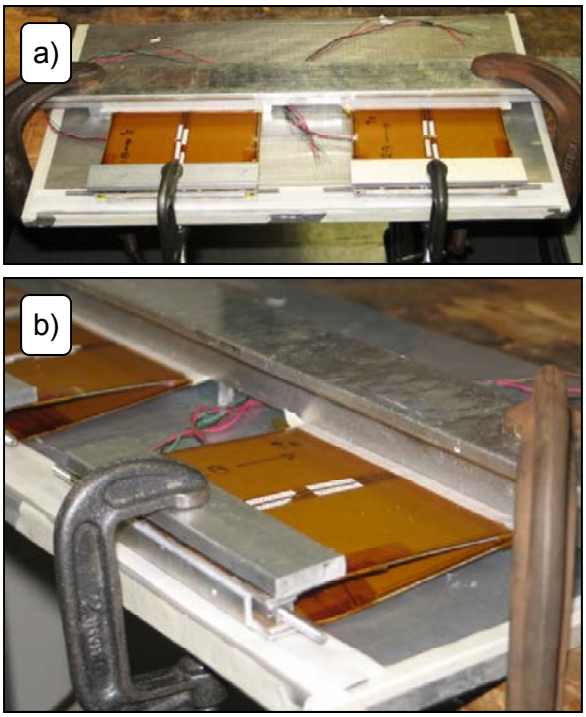

Figure F.7: a) Top and b) side views of the airfoils during the bonding process.

Both airfoils initially employed a rapid-prototyped leading edge for the ducted-fan wind tunnel experiments. The elliptical leading edge is fabricated using a rapid-prototype method by Solid Concepts, Valencia, CA. The rapid-prototype method is PolyJet and the material is VeroWhite83D. The surface finish is machine-finish and the surface treatment is wet\dry blast. Figure F.8 shows the current condition of the airfoils.

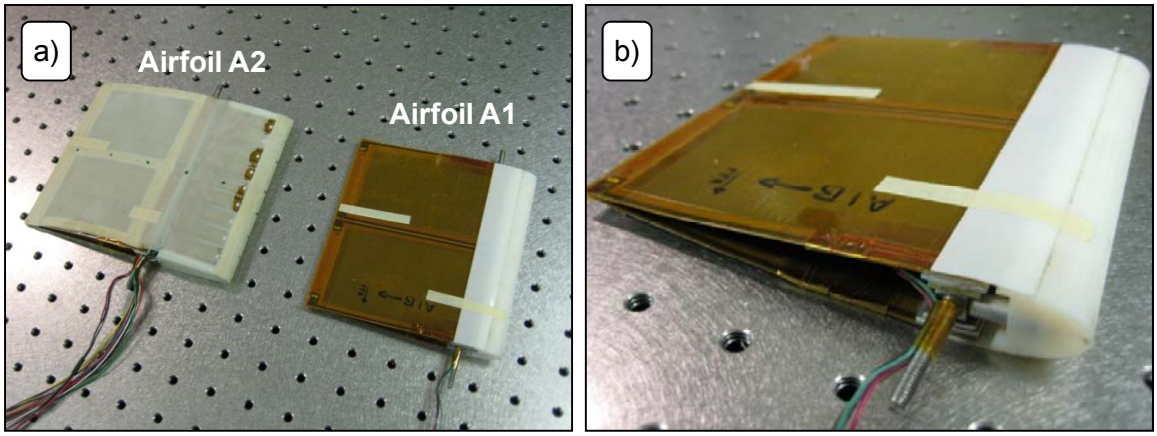

Figure F.8: The current condition of a) airfoils A1 and A2 and b) A1 alone.

The airfoil A1 is mostly employed in the wind tunnel experiments presented in Chapter 6. The airfoil A2 is discussed in the next section. Figure F.9 shows the airfoil A1 mounted on the load balance (and in the 2D test section) of version 3.2 wind tunnel.

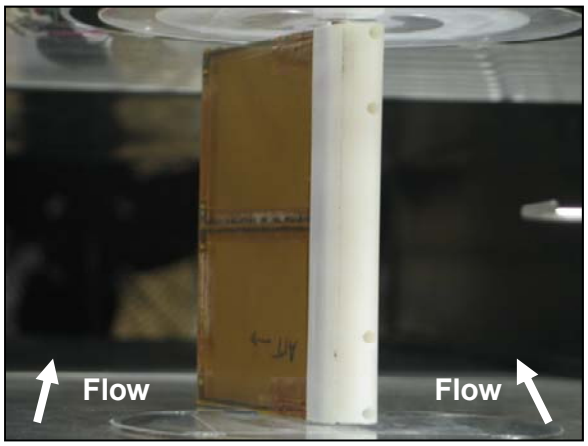

Figure F.9: Front view of the variable-camber thick airfoil (A1) mounted in the 2D test section of version 3.2 wind tunnel.

In addition to the rapid-prototyped NACA 0009 airfoil, two other airfoils are examined. Figure F.10 presents the NACA 0013 airfoil that is evaluated in Chapter 6.

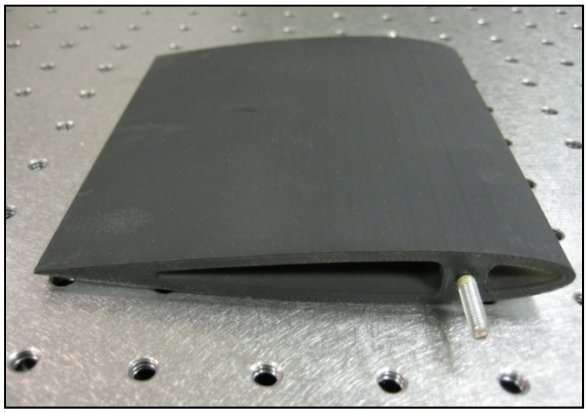

Figure F.10: NACA 0013 airfoil with 127 mm chord and 133 mm span.

The NACA 0013 airfoil has a maximum thickness of 16.5 mm. Figure F.11 shows the rapid prototyped airfoil (labeled RP) generated from the profile of the cascading bimorph variable-camber thick airfoil design (at zero camber state). This airfoil is examined to determine the influence of the surface roughness of the thick variable-camber airfoils (A1 and A2).

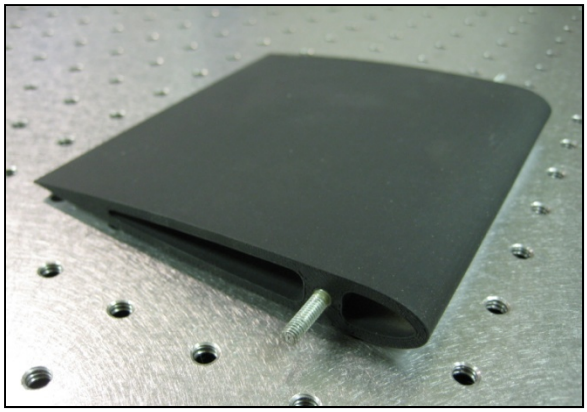

Figure F.11: Airfoil RP with 127 mm chord and 133 mm span.

The airfoil RP has a maximum thickness of 15 mm. Note that all of the rapid prototyped airfoils examined in Chapter 6 have 133 mm span, 127 mm chord and a finite TE thickness of 1.0 mm.

F.3 Airfoils with Flow Control Feature

This section presents the airfoils evaluated in Chapter 7. Two airfoils are examined in Chapter 7: 1) NACA 0010 airfoil with flow control feature and 2) variable-camber airfoil with flow control feature. Figure F.12 shows a two-piece rapid-prototyped NACA 0010 airfoil. The trailing section of this airfoil is used along with the flow control leading section (as shown in Section 7.3).

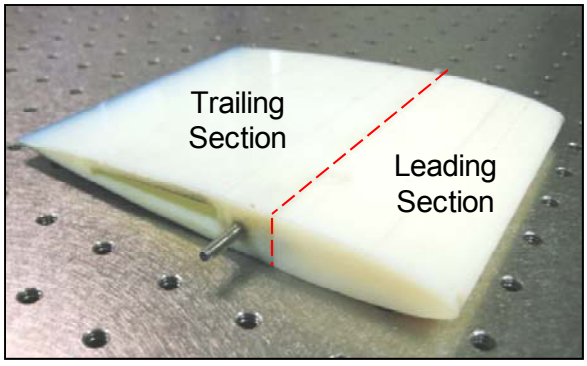

Figure F.12: Two-piece NACA 0010 airfoil with 163 mm chord and 133 mm span.

Both pieces of the airfoil (including the leading section with flow control feature presented in Section 7.3) are fabricated using a rapid-prototype method by Solid Concepts,

Valencia, CA. The rapid-prototype method is PolyJet and the material is VeroWhite83D. The surface finish is machine-finish and the surface treatment is wet\dry blast. The two sections are held together with two machine screws.

Figure F.13 shows the variable-camber airfoil with flow control leading section. This airfoil is composed of a rapid-prototyped leading section (with nine unimorph actuators) and the variable-camber trailing section (from airfoil A2). Additional details are presented in Section 7.4.

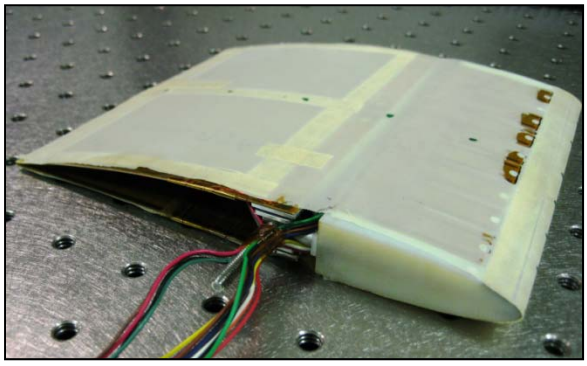

Figure F.13: Variable-camber airfoil (A2) with flow control leading section. The airfoil has a 163 mm chord and a 133 mm span.

The surface of the airfoil covered with a 0.006” thick abrasion-resistant natural latex rubber membrane (item number 8611K11 from McMaster-Carr). The latex is adhered to the original airfoil surface using a double-sided masking tape for smooth surfaces (item number 75985A666 from McMaster-Carr).

APPENDIX G

ADDITIONAL HYSTERESIS RESULTS

This appendix presents additional hysteresis modeling and experimental results for bimorphs examined in Chapter 8. The sections of the appendix present the following four samples. 1) The cantilevered bimorph beam labeled Sample B6. 2) The cantilevered bimorph beam labeled Sample B2. (Refer to Table 4.1 and Section D.2 for more information on these bimorph beam samples). 3) The simply-supported thin airfoil. (Refer to Chapter 5 for detailed information). 4) The cascading bimorph thick airfoil. (Refer to Chapter 6 for more information).

G.1 Bimorph Beam Sample B6

This section presents additional hysteresis modeling and experimental results for the cantilevered bimorph beam labeled Sample B6. Refer to Section 8.4.3 for the details of the experimental setup and the model description.

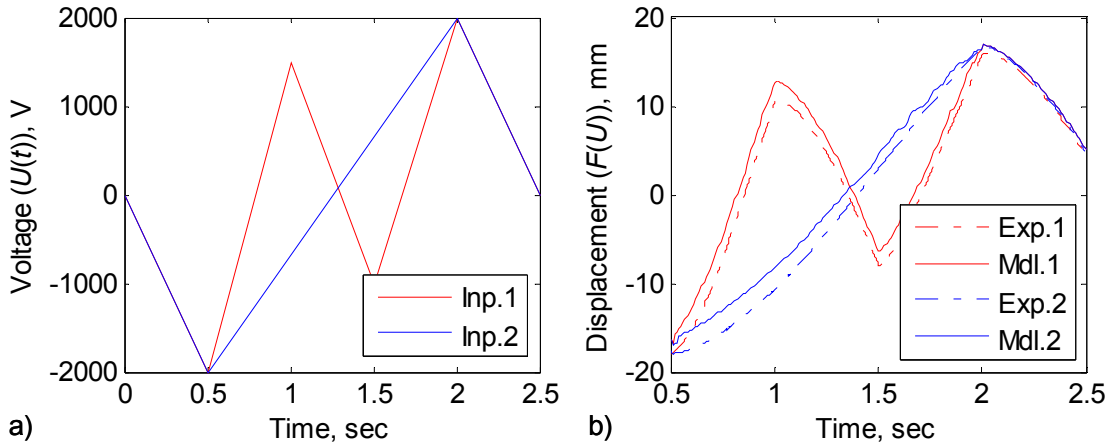

Figure G.1: Wiping-out evaluation of bimorph beam sample B6 in 3-to-1 configuration at 1 Hz. a) Voltage input and b) displacement output time histories.

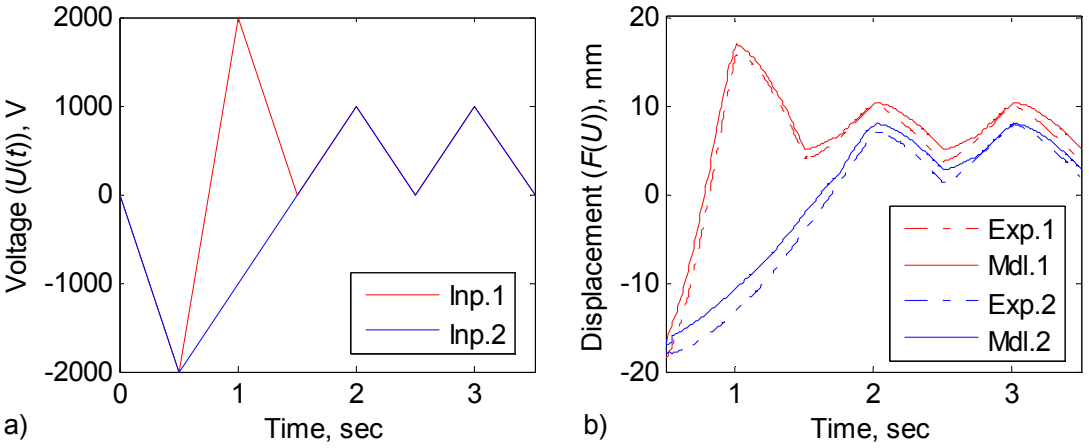

Figure G.2: Congruency evaluation of the bimorph beam sample B6 in 3-to-1 configuration at 1 Hz. a) Voltage input and b) displacement output time histories.

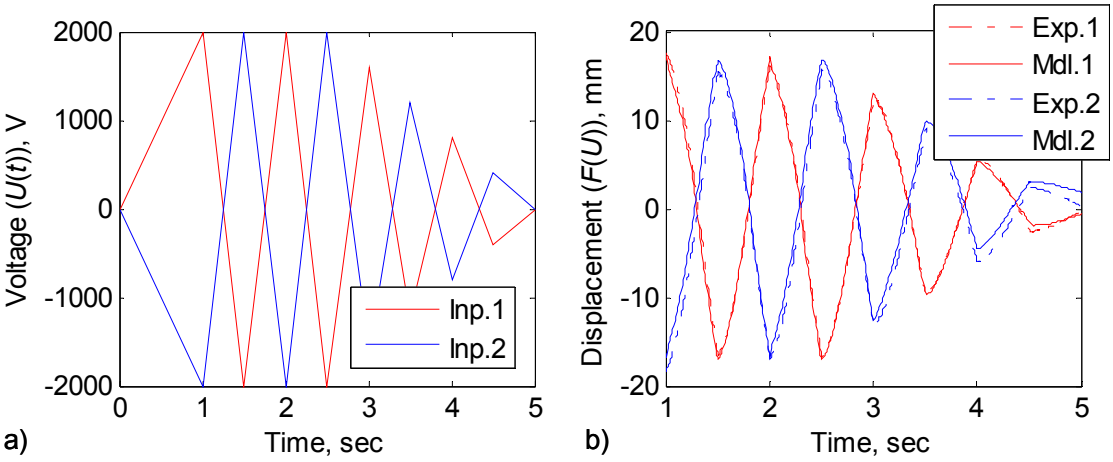

Figure G.3: Decaying triangle input signal response of bimorph sample B6 in 3-to-1 configuration at 1 Hz. a) Voltage input and b) displacement output time histories.

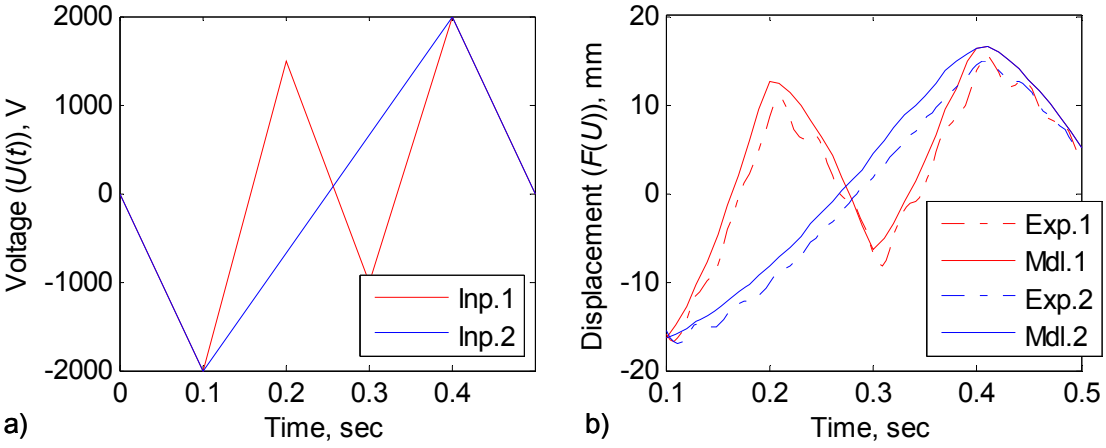

Figure G.4: Wiping-out evaluation of bimorph beam sample B6 in 3-to-1 configuration at 5 Hz. a) Voltage input and b) displacement output time histories.

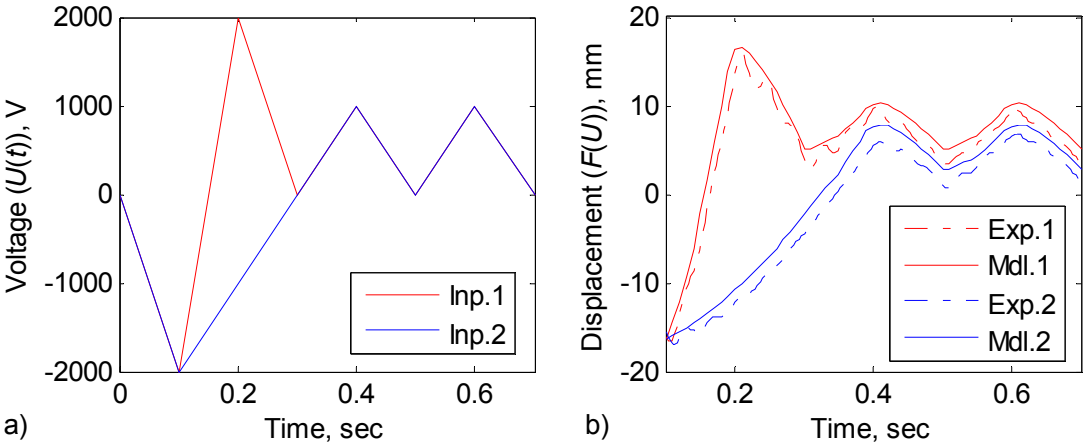

Figure G.5: Congruency evaluation of the bimorph beam sample B6 in 3-to-1 configuration at 5 Hz. a) Voltage input and b) displacement output time histories.

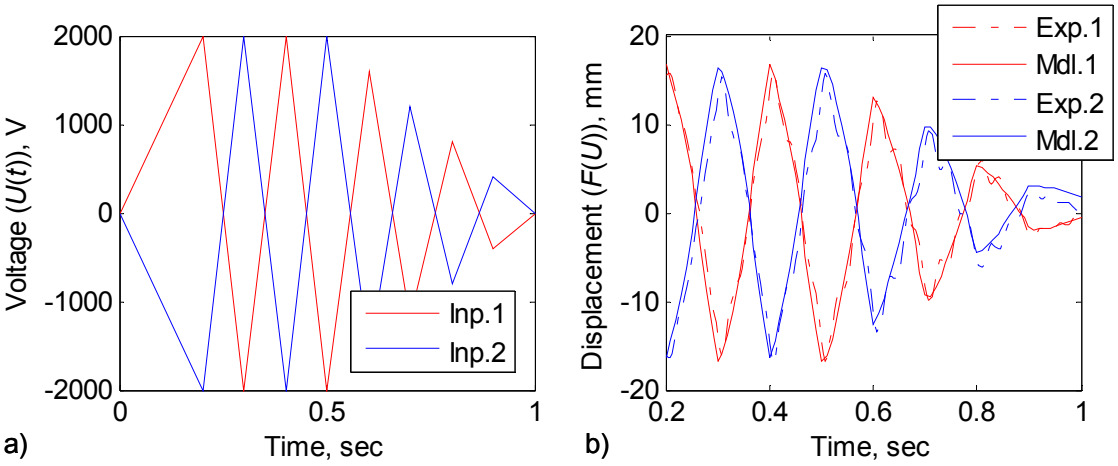

Figure G.6: Decaying triangle input signal response of bimorph sample B6 in 3-to-1 configuration at 5 Hz. a) Voltage input and b) displacement output time histories.

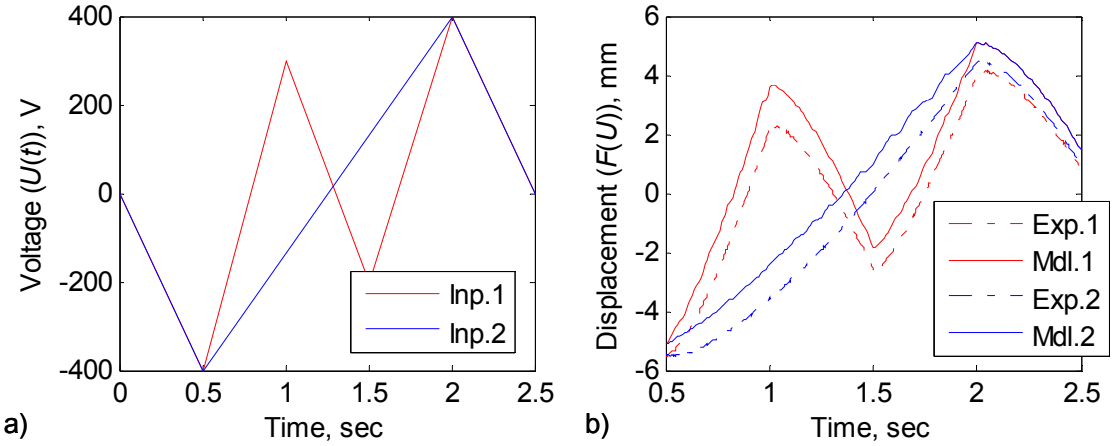

Figure G.7: Wiping-out evaluation of bimorph beam sample B6 in 1-to-1 configuration at 1 Hz. a) Voltage input and b) displacement output time histories.

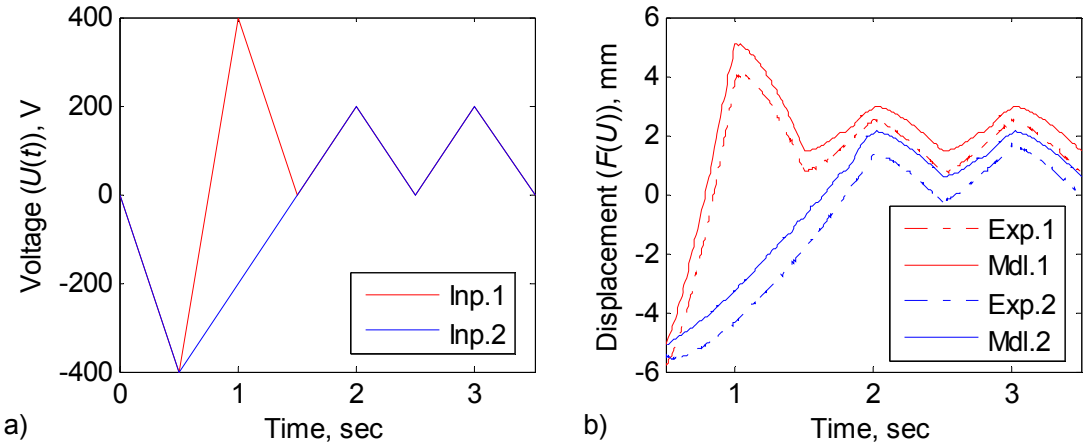

Figure G.8: Congruency evaluation of the bimorph beam sample B6 in 1-to-1 configuration at 1 Hz. a) Voltage input and b) displacement output time histories.

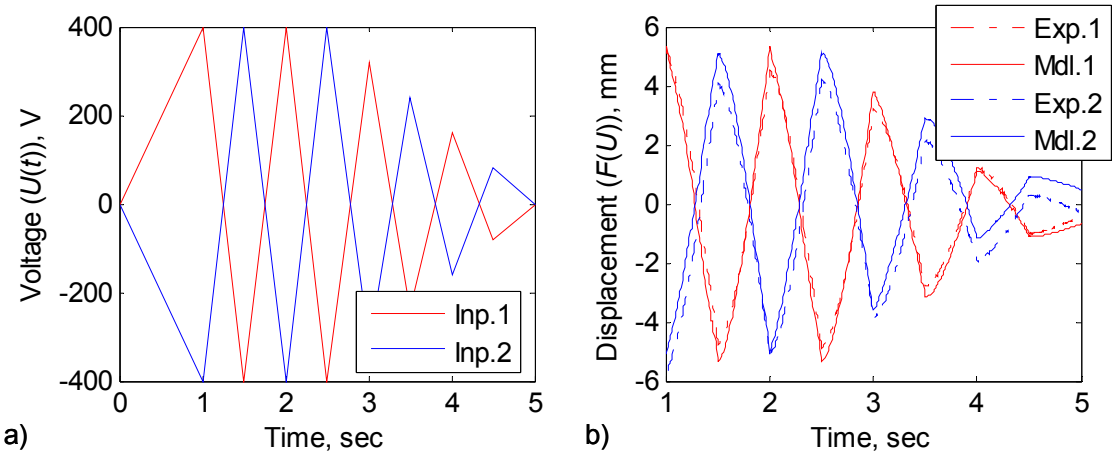

Figure G.9: Decaying triangle input signal response of bimorph sample B6 in 1-to-1 configuration at 1 Hz. a) Voltage input and b) displacement output time histories.

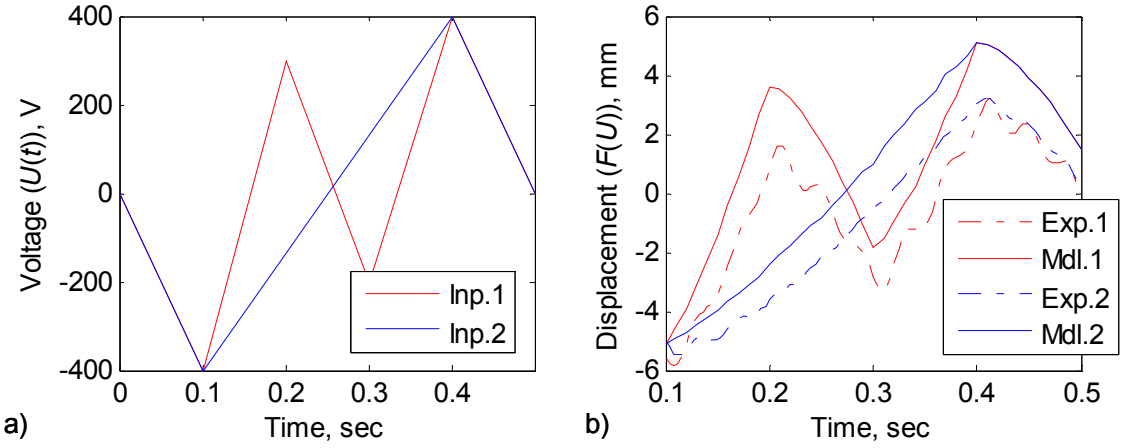

Figure G.10: Wiping-out evaluation of bimorph beam sample B6 in 1-to-1 configuration at 5 Hz. a) Voltage input and b) displacement output time histories.

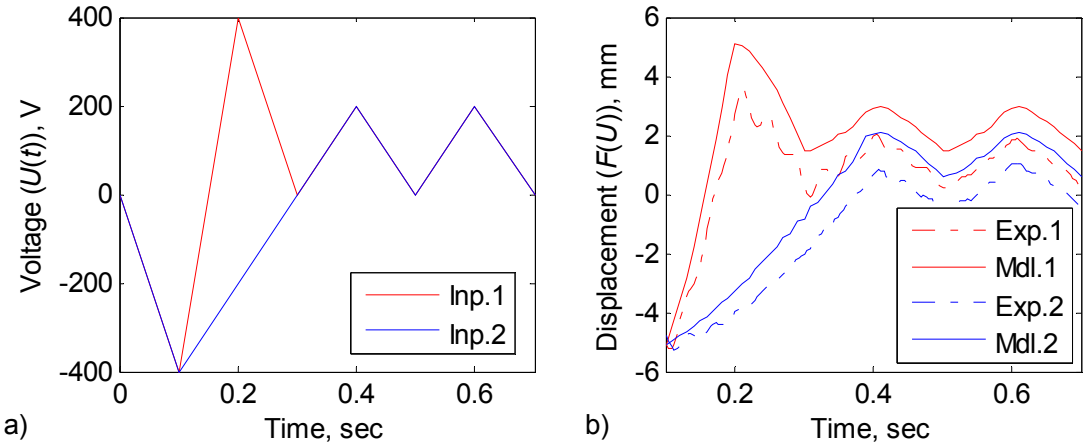

Figure G.11: Congruency evaluation of the bimorph beam sample B6 in 1-to-1 configuration at 5 Hz. a) Voltage input and b) displacement output time histories.

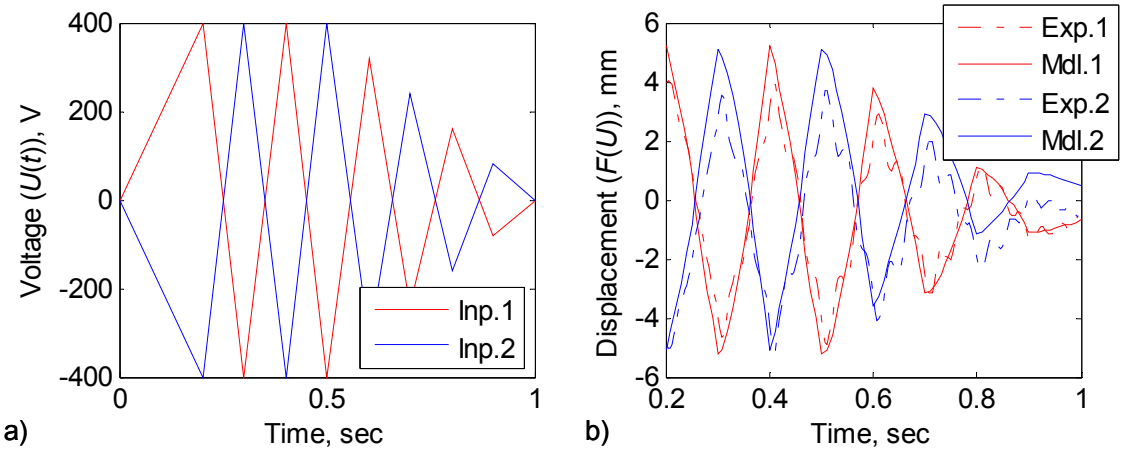

Figure G.12: Decaying triangle input signal response of bimorph B6 in 1-to-1 configuration at 5 Hz. a) Voltage input and b) displacement output time histories.

G.2 Bimorph Beam Sample B2

This section presents additional hysteresis modeling and experimental results for the cantilevered bimorph beam labeled Sample B2. Refer to Section 8.4.3 for the details of the experimental setup and the model description.

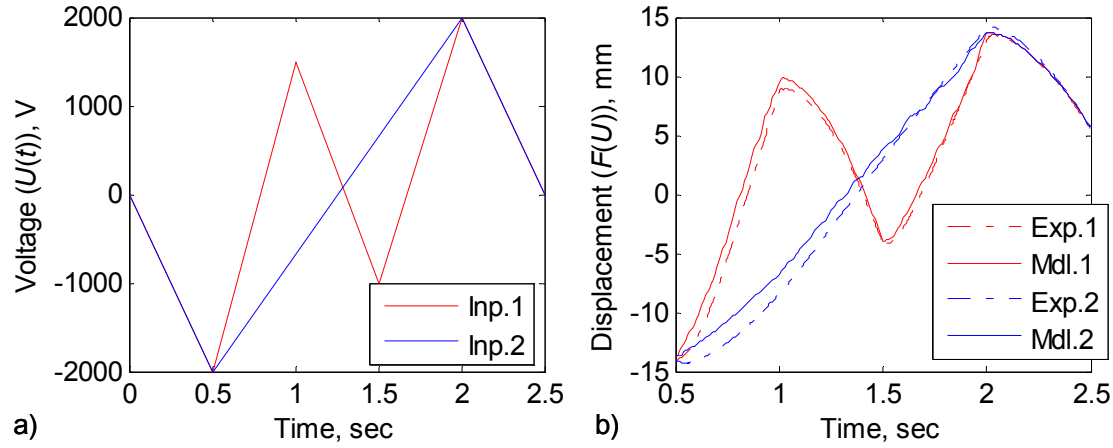

Figure G.13: Wiping-out evaluation of bimorph beam sample B6 in 3-to-1 configuration at 1 Hz. a) Voltage input and b) displacement output time histories.

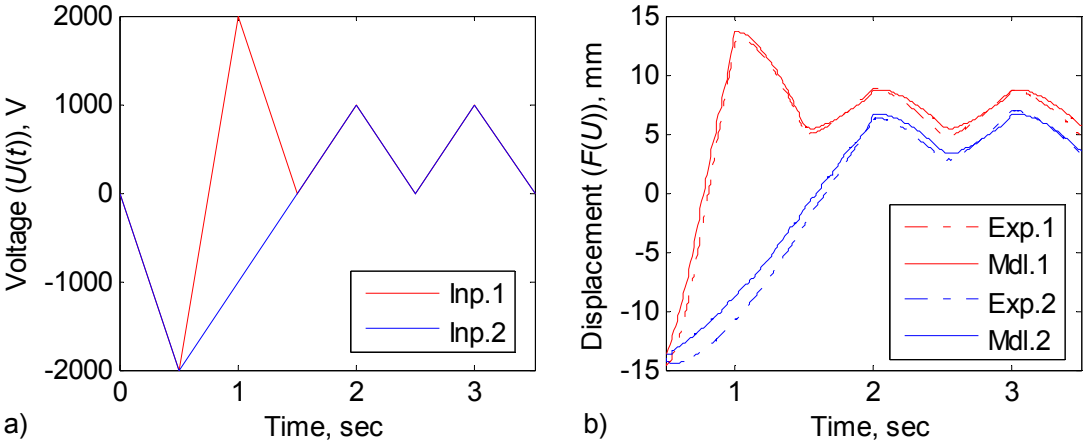

Figure G.14: Congruency evaluation of the bimorph beam sample B2 in 3-to-1 configuration at 1 Hz. a) Voltage input and b) displacement output time histories.

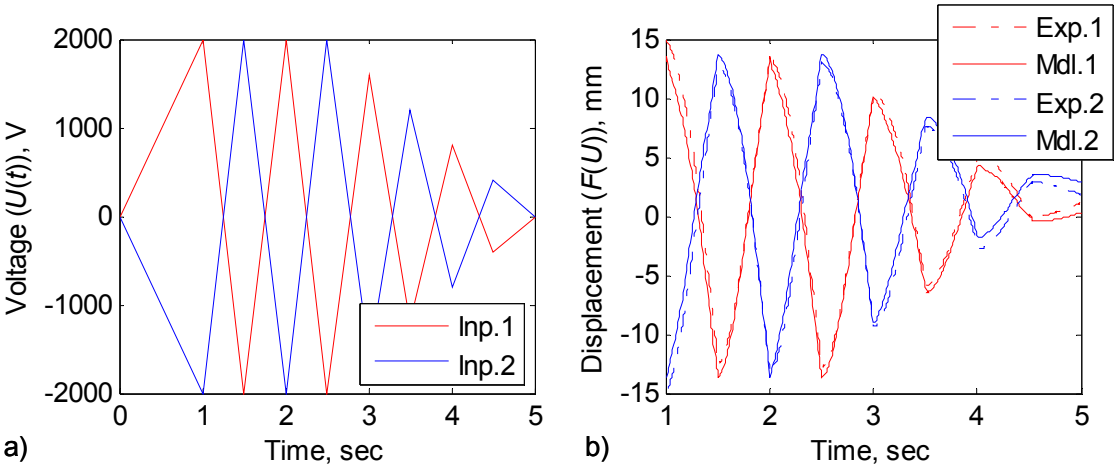

Figure G.15: Decaying triangle input signal response of bimorph B2 in 3-to-1 configuration at 1 Hz. a) Voltage input and b) displacement output time histories.

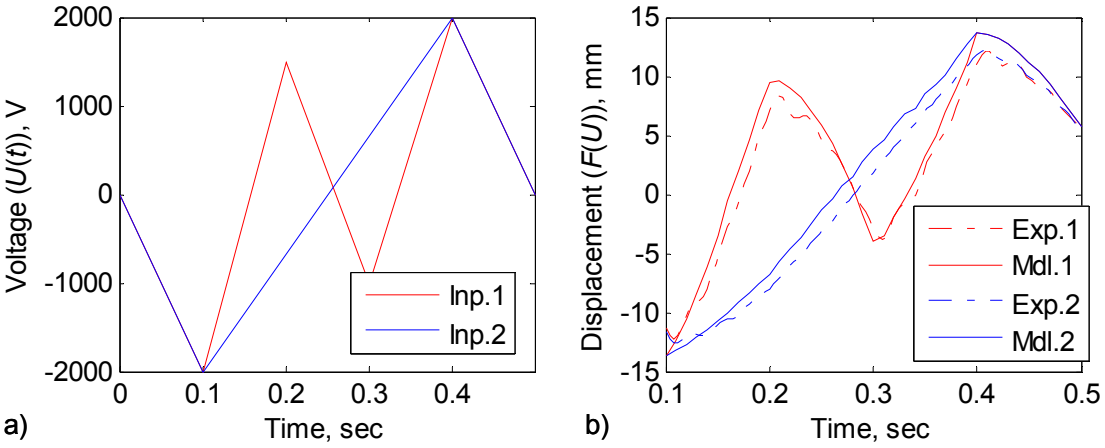

Figure G.16: Wiping-out evaluation of bimorph beam sample B6 in 3-to-1 configuration at 5 Hz. a) Voltage input and b) displacement output time histories.

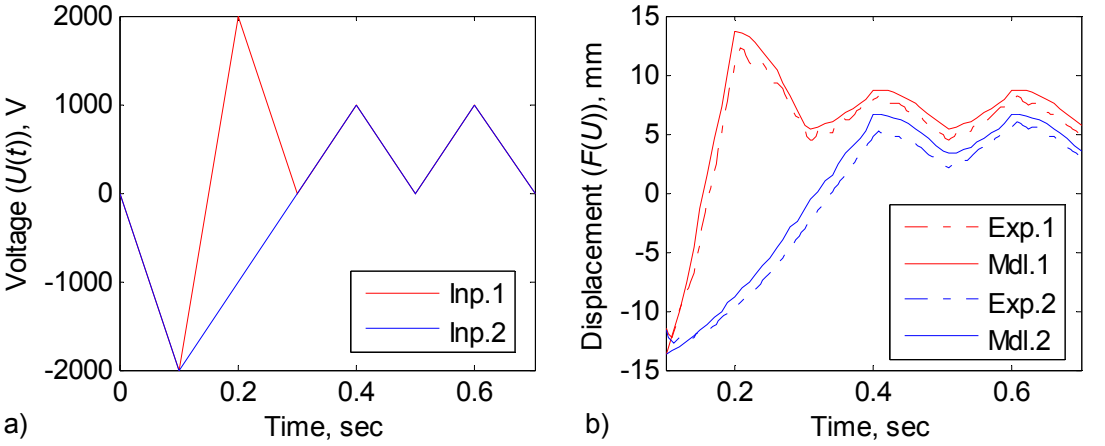

Figure G.17: Congruency evaluation of the bimorph beam sample B2 in 3-to-1 configuration at 5 Hz. a) Voltage input and b) displacement output time histories.

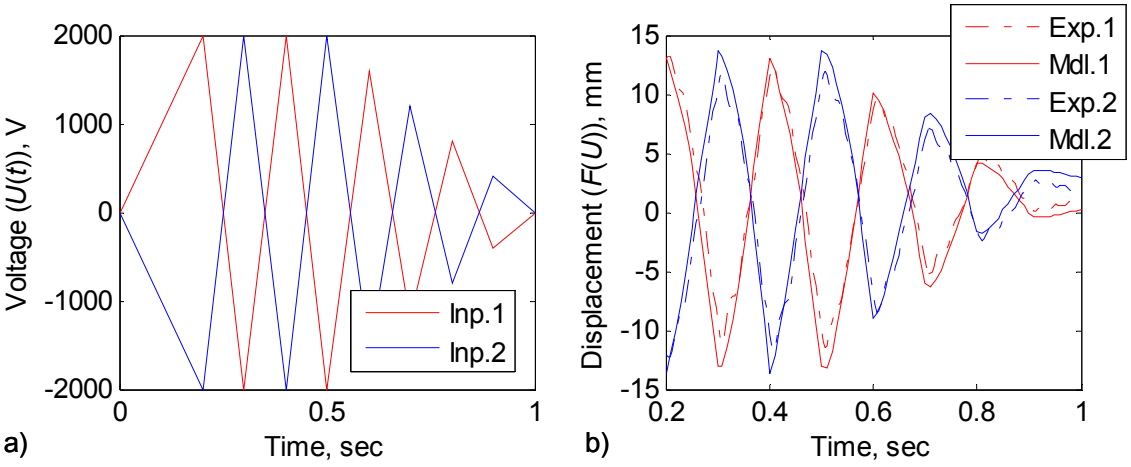

Figure G.18: Decaying triangle input signal response of bimorph B2 in 3-to-1 configuration at 5 Hz. a) Voltage input and b) displacement output time histories.

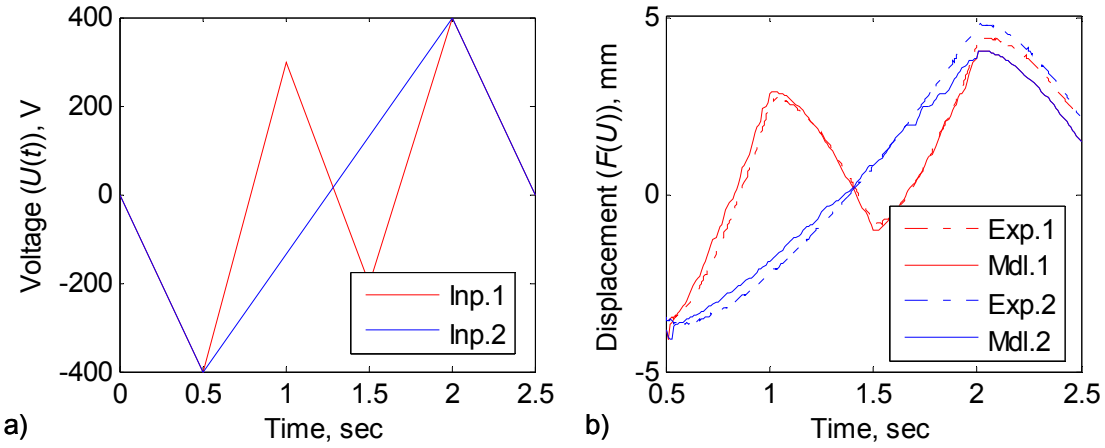

Figure G.19: Wiping-out evaluation of bimorph beam sample B6 in 1-to-1 configuration at 1 Hz. a) Voltage input and b) displacement output time histories.

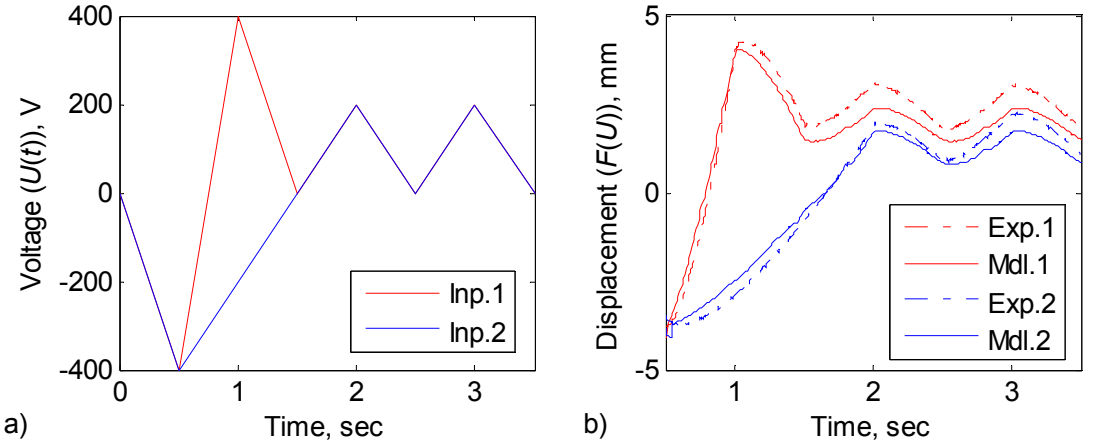

Figure G.20: Congruency evaluation of the bimorph beam sample B2 in 1-to-1 configuration at 1 Hz. a) Voltage input and b) displacement output time histories.

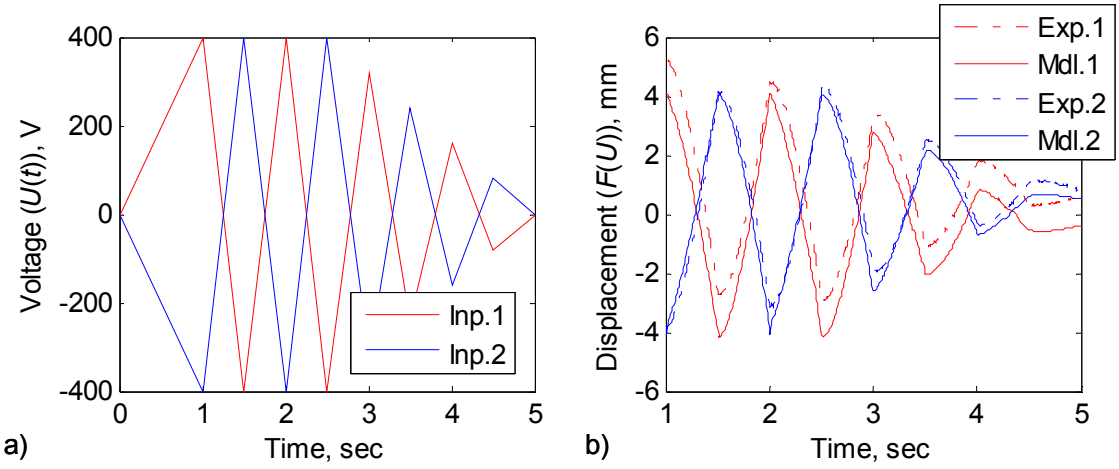

Figure G.21: Decaying triangle input signal response of bimorph B2 in 1-to-1 configuration at 1 Hz. a) Voltage input and b) displacement output time histories.

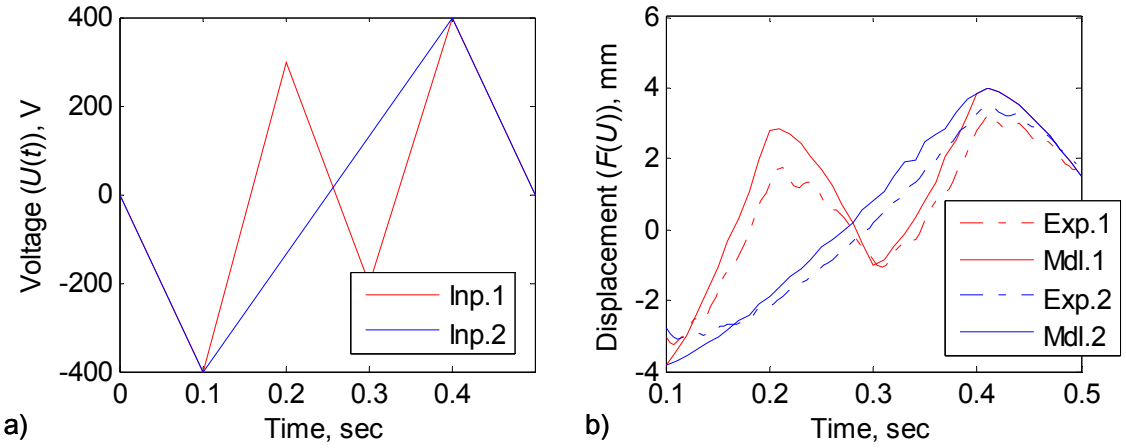

Figure G.22: Wiping-out evaluation of bimorph beam sample B6 in 1-to-1 configuration at 5 Hz. a) Voltage input and b) displacement output time histories.

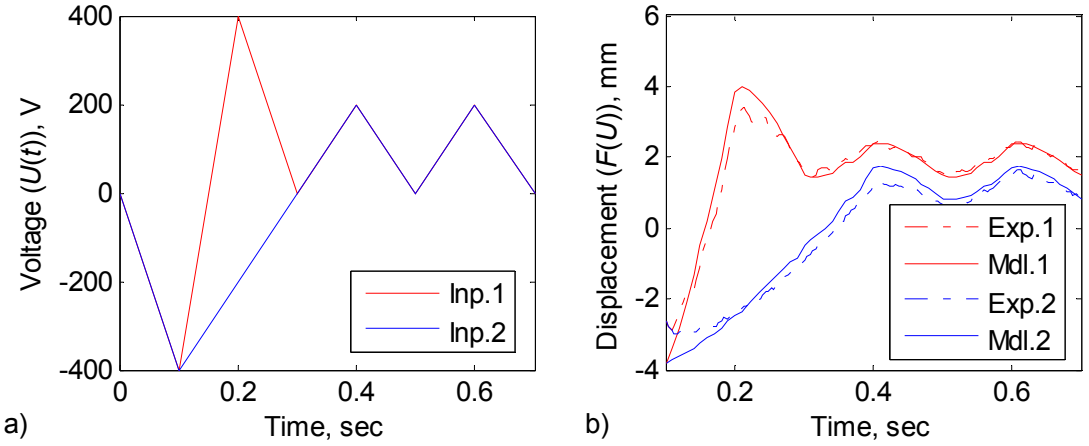

Figure G.23: Congruency evaluation of the bimorph beam sample B2 in 1-to-1 configuration at 5 Hz. a) Voltage input and b) displacement output time histories.

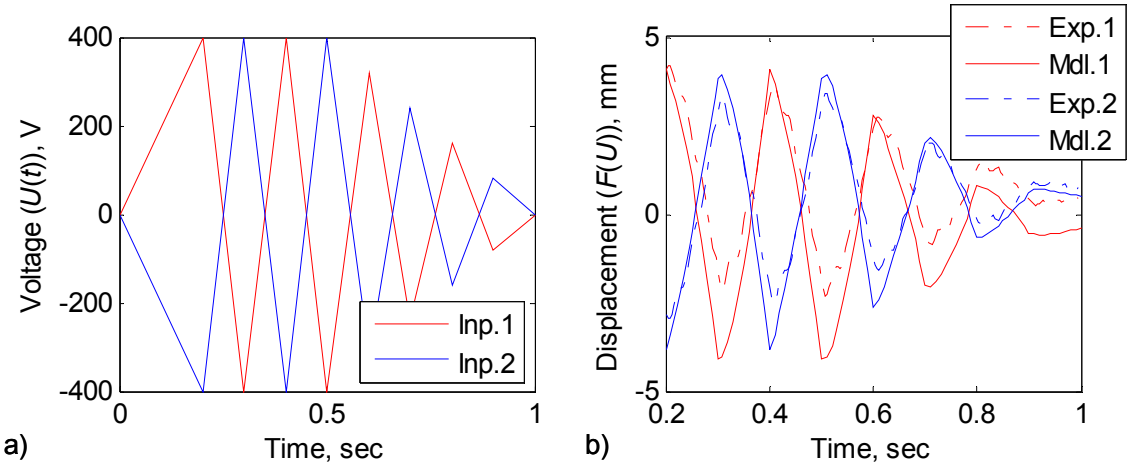

Figure G.24: Decaying triangle input signal response of bimorph B2 in 1-to-1 configuration at 5 Hz. a) Voltage input and b) displacement output time histories.

G.3 Simply-Supported Thin Airfoil

This section presents additional hysteresis modeling and experimental results for the simply-supported variable-camber thin airfoil labeled T1. Refer to Section 8.4.4 for the details of the experimental setup and the model description.

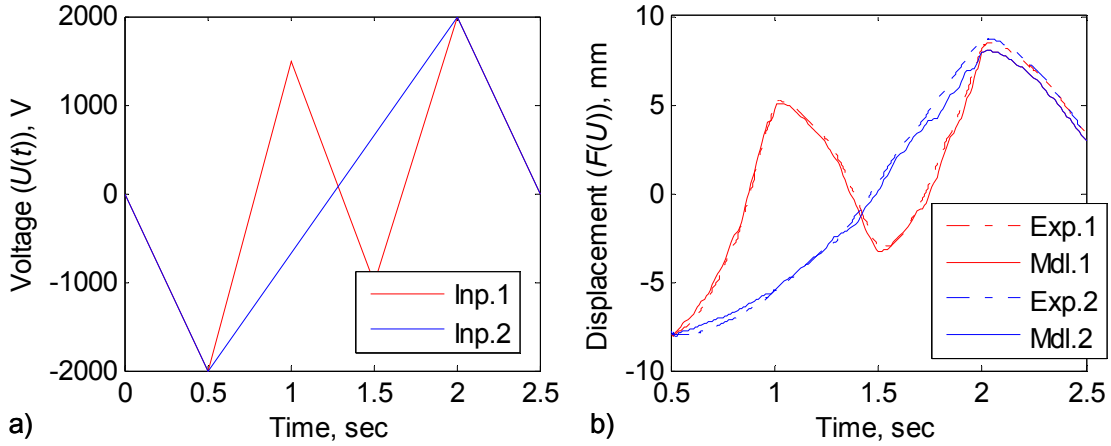

Figure G.25: Wiping-out evaluation of the thin airfoil sample T1 in 3-to-1 configuration at 1 Hz. a) Voltage input and b) displacement output time histories.

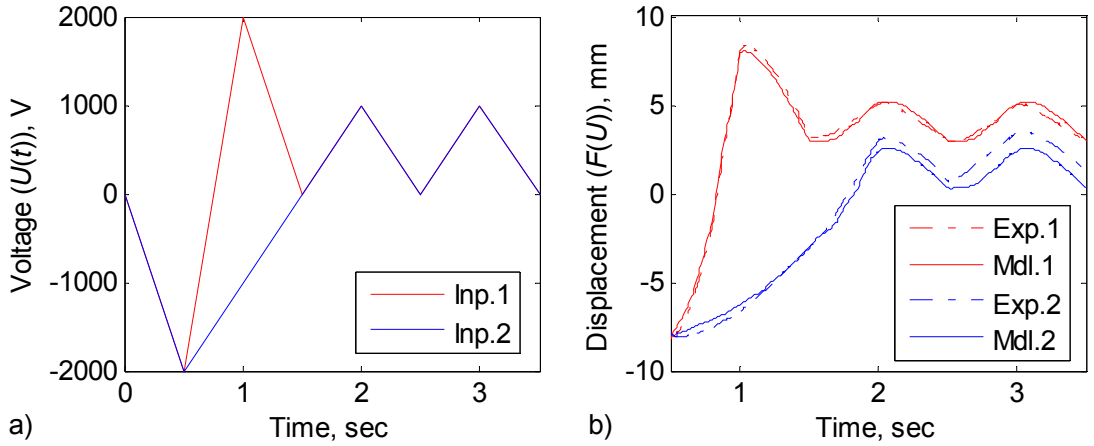

Figure G.26: Congruency evaluation of the thin airfoil sample T1 in 3-to-1 configuration at 1 Hz. a) Voltage input and b) displacement output time histories.

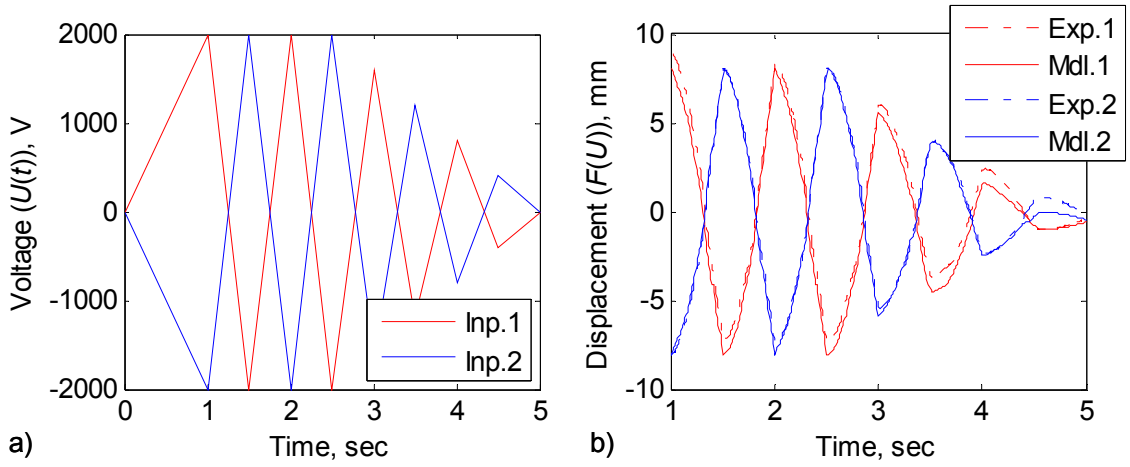

Figure G.27: Decaying triangle input signal response of airfoil sample T1 in 3-to-1 configuration at 1 Hz. a) Voltage input and b) displacement output time histories.

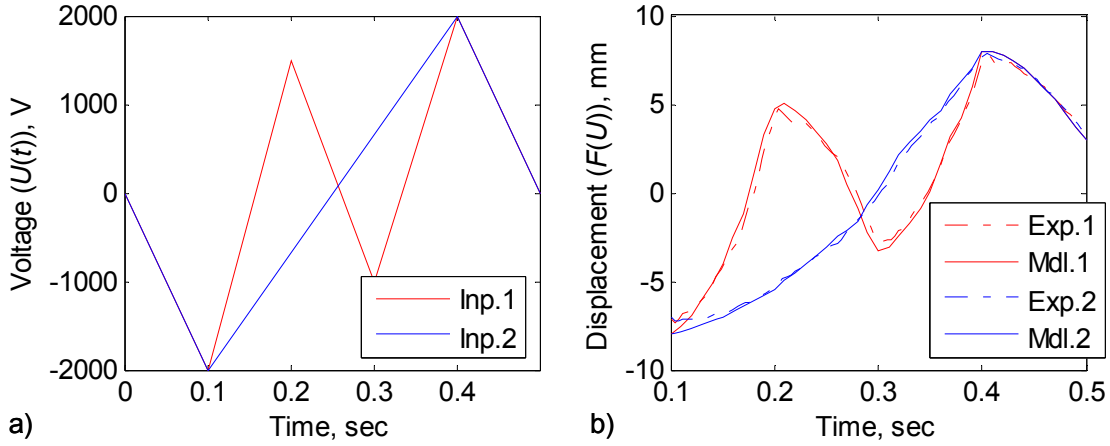

Figure G.28: Wiping-out evaluation of the thin airfoil sample T1 in 3-to-1 configuration at 5 Hz. a) Voltage input and b) displacement output time histories.

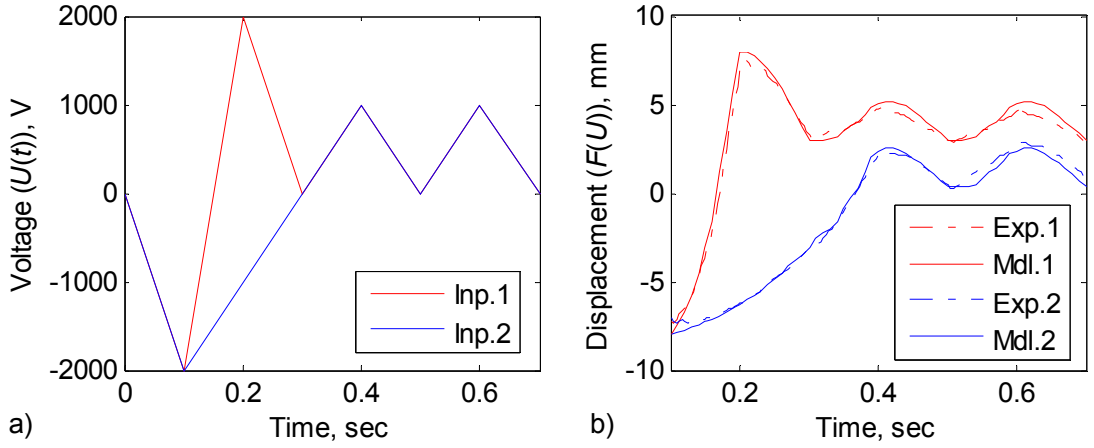

Figure G.29: Congruency evaluation of the thin airfoil sample T1 in 3-to-1 configuration at 5 Hz. a) Voltage input and b) displacement output time histories.

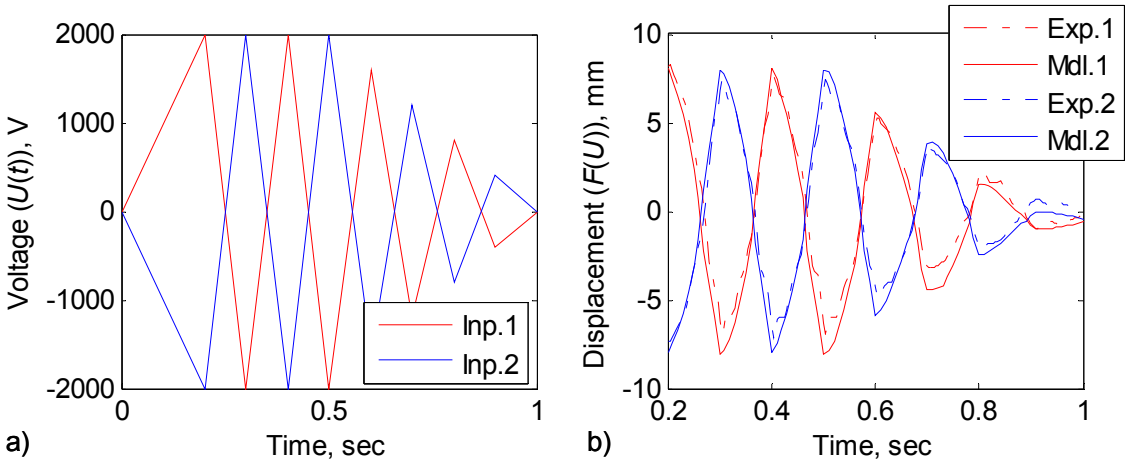

Figure G.30: Decaying triangle input signal response of airfoil sample T1 in 3-to-1 configuration at 5 Hz. a) Voltage input and b) displacement output time histories.

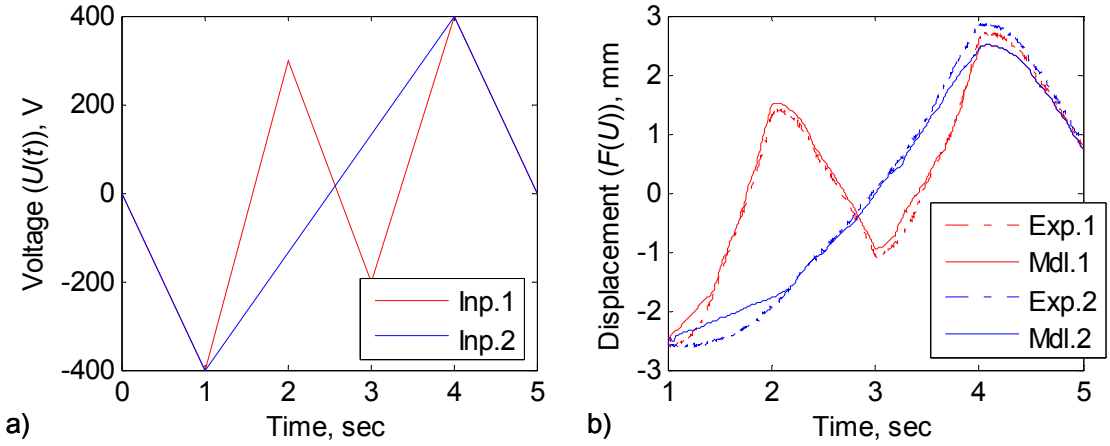

Figure G.31: Wiping-out evaluation of the thin airfoil sample T1 in 1-to-1 configuration at 0.5 Hz. a) Voltage input and b) displacement output time histories.

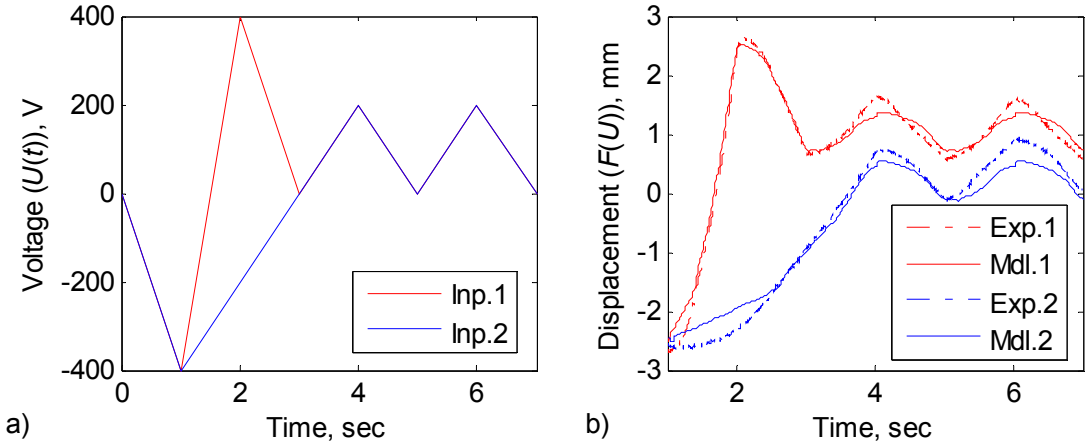

Figure G.32: Congruency evaluation of the thin airfoil sample T1 in 1-to-1 configuration at 0.5 Hz. a) Voltage input and b) displacement output time histories.

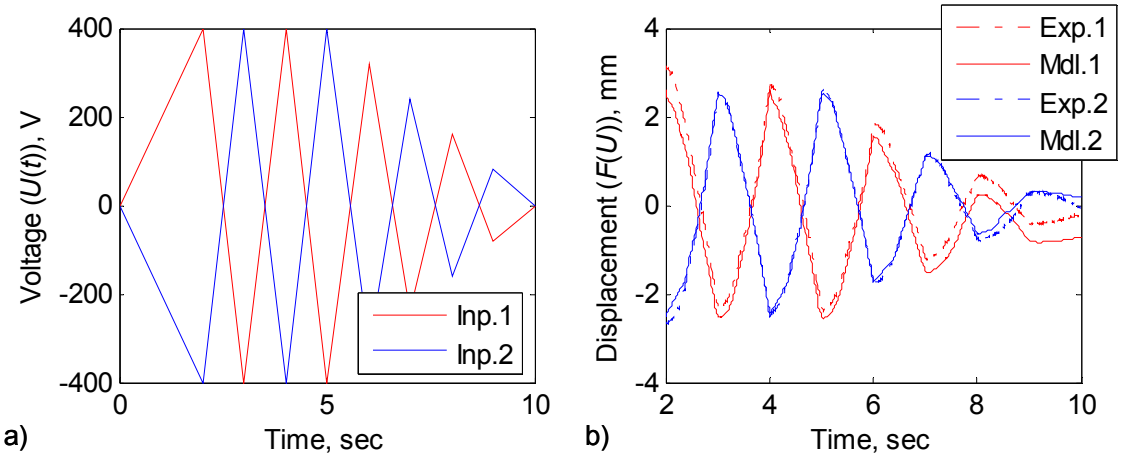

Figure G.33: Decaying triangle input signal response of airfoil sample T1 in 1-to-1 configuration at 0.5 Hz. a) Voltage input and b) displacement output time histories.

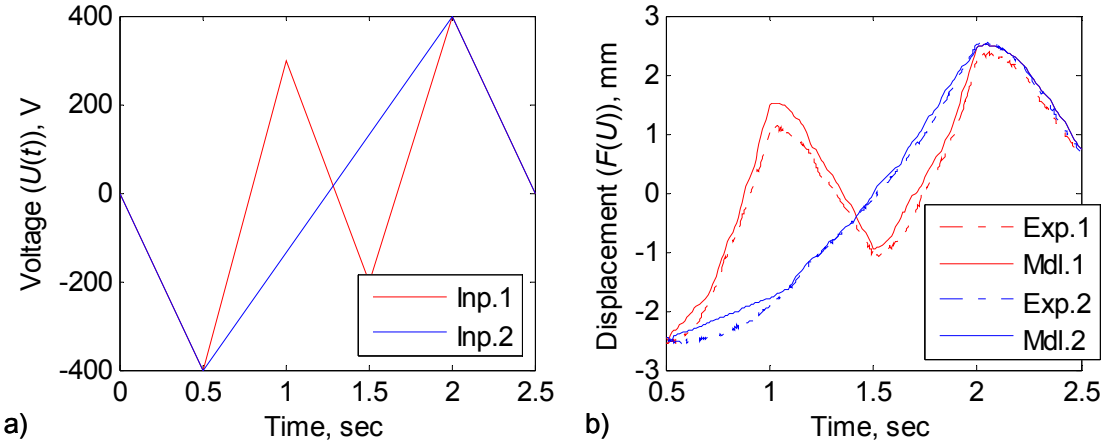

Figure G.34: Wiping-out evaluation of the thin airfoil sample T1 in 1-to-1 configuration at 1 Hz. a) Voltage input and b) displacement output time histories.

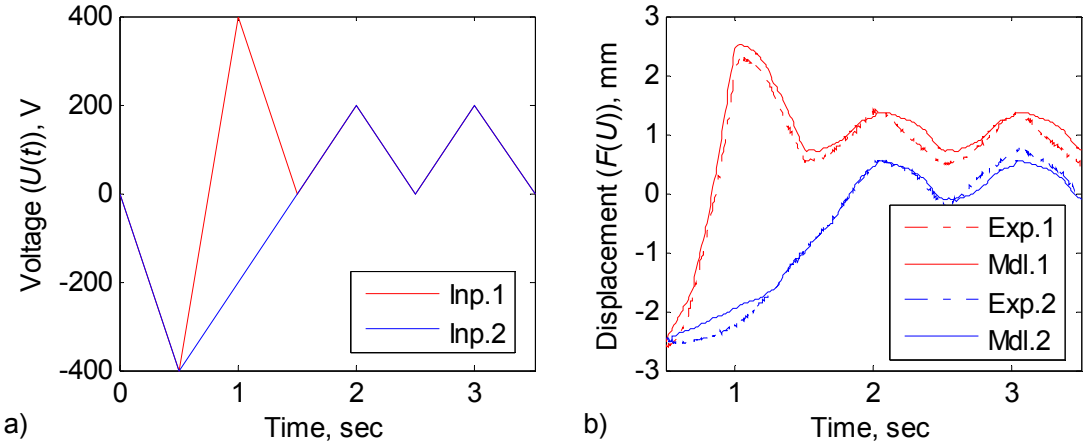

Figure G.35: Congruency evaluation of the thin airfoil sample T1 in 1-to-1 configuration at 1 Hz. a) Voltage input and b) displacement output time histories.

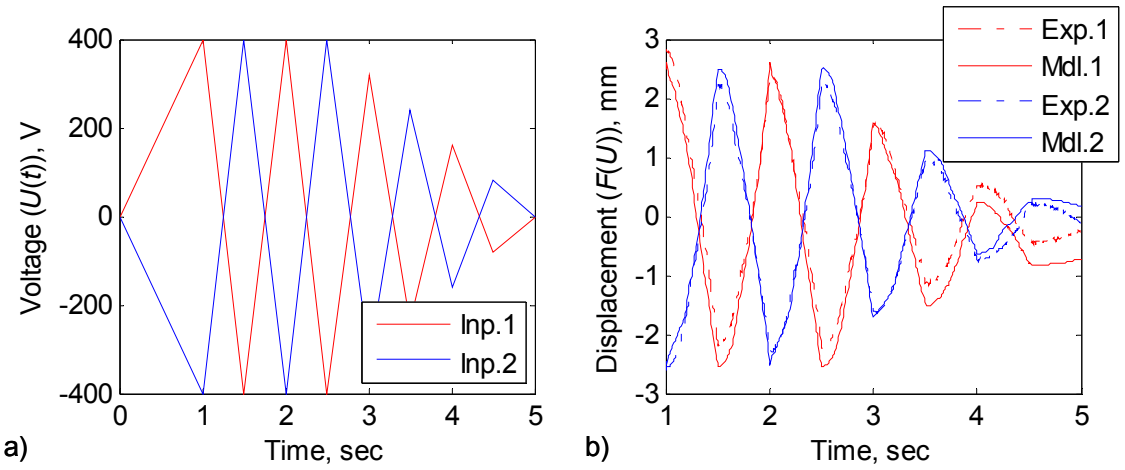

Figure G.36: Decaying triangle input signal response of airfoil sample T1 in 1-to-1 configuration at 1 Hz. a) Voltage input and b) displacement output time histories.

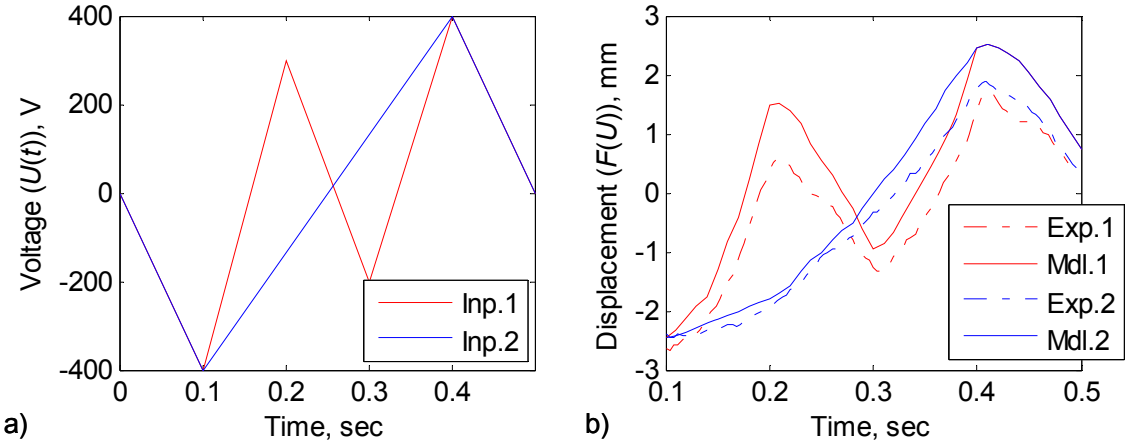

Figure G.37: Wiping-out evaluation of the thin airfoil sample T1 in 1-to-1 configuration at 5 Hz. a) Voltage input and b) displacement output time histories.

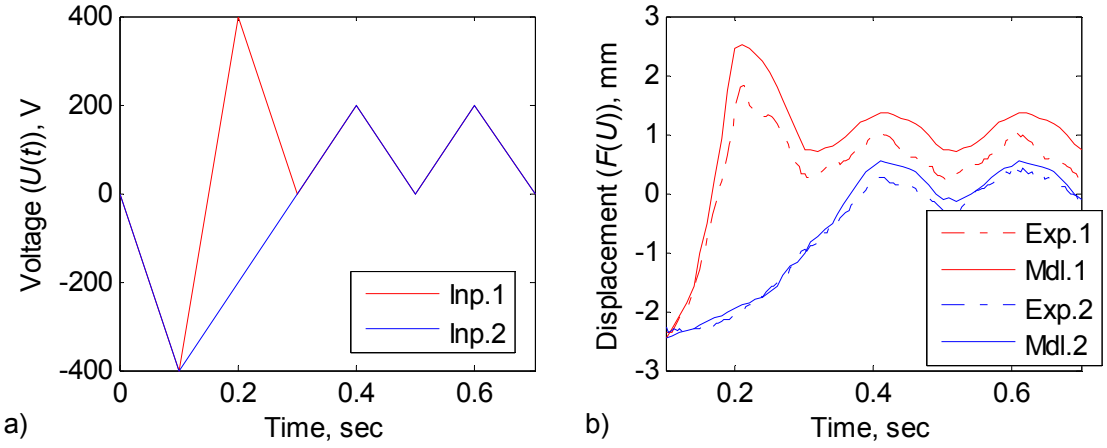

Figure G.38: Congruency evaluation of the thin airfoil sample T1 in 1-to-1 configuration at 5 Hz. a) Voltage input and b) displacement output time histories.

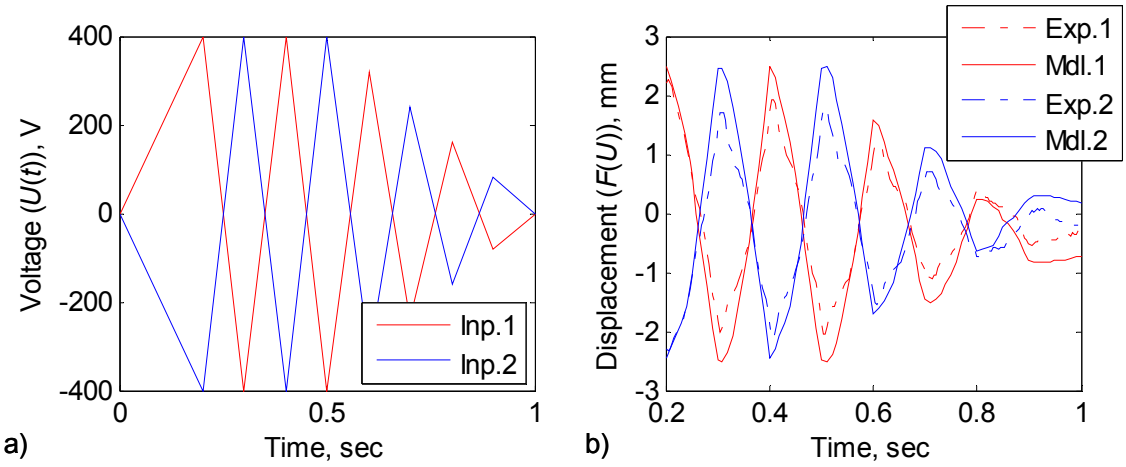

Figure G.39: Decaying triangle input signal response of airfoil sample T1 in 1-to-1 configuration at 5 Hz. a) Voltage input and b) displacement output time histories.

G.4 Cascading Bimorph Thick Airfoil

This section presents additional hysteresis modeling and experimental results for the cascading bimorph thick airfoil labeled A1. Refer to Section 8.4.5 for the details of the experimental setup and the model description.

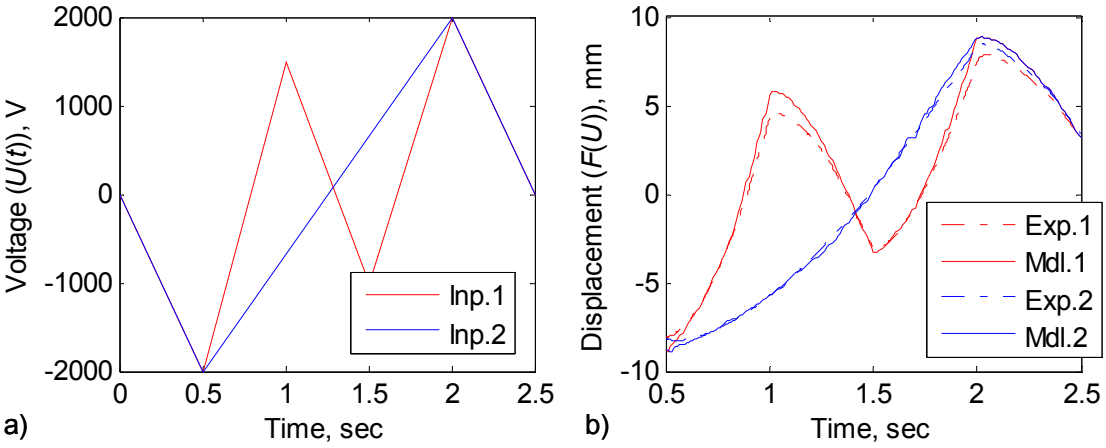

Figure G.40: Wiping-out evaluation of the thick airfoil sample A1 in 3-to-1 configuration at 1 Hz. a) Voltage input and b) displacement output time histories.

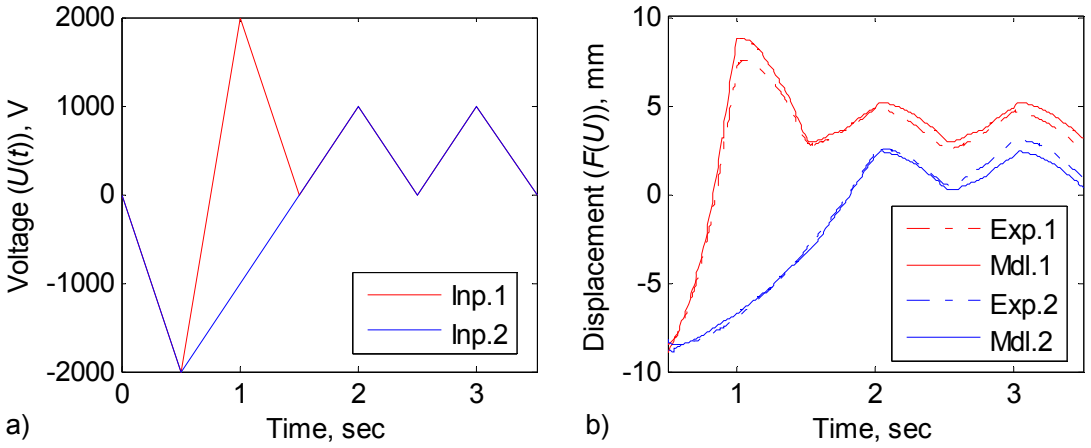

Figure G.41: Congruency evaluation of the thick airfoil sample A1 in 3-to-1 configuration at 1 Hz. a) Voltage input and b) displacement output time histories.

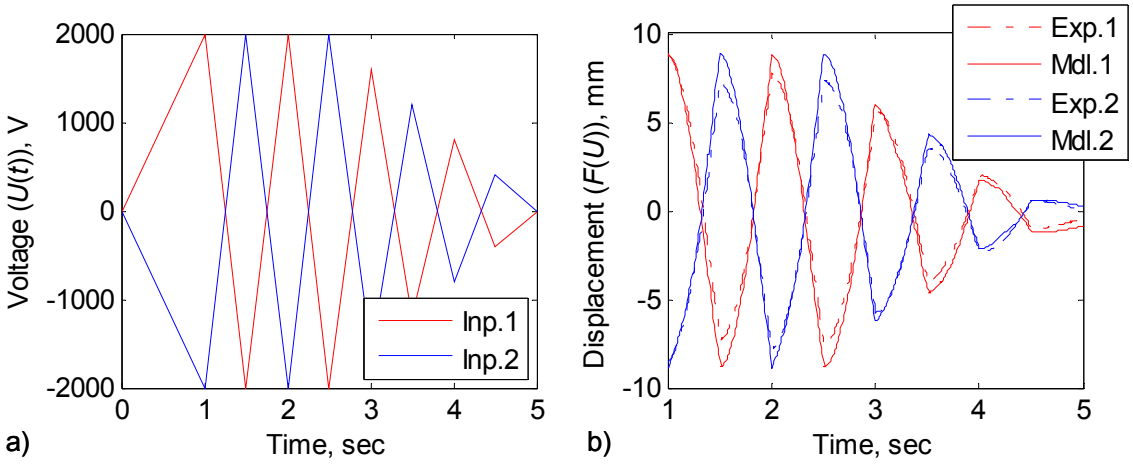

Figure G.42: Decaying triangle input signal response of airfoil sample A1 in 3-to-1 configuration at 1 Hz. a) Voltage input and b) displacement output time histories.

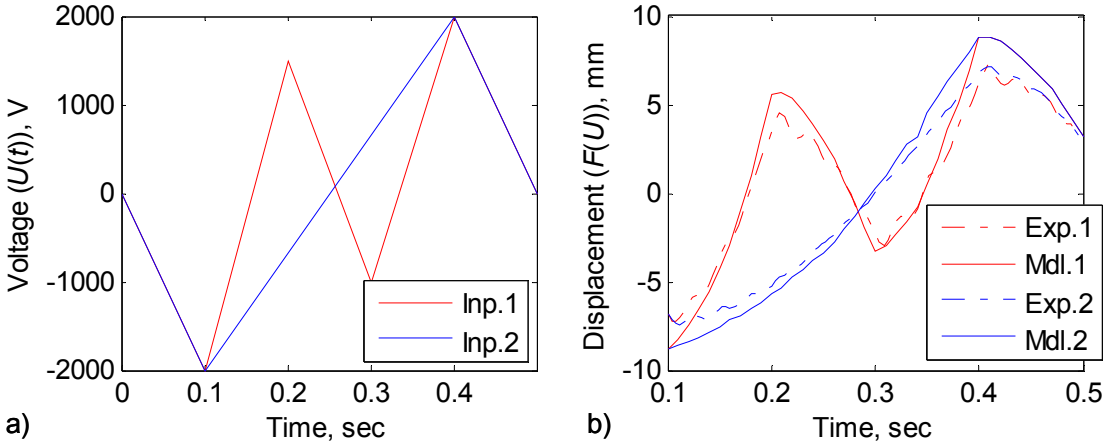

Figure G.43: Wiping-out evaluation of the thick airfoil sample A1 in 3-to-1 configuration at 5 Hz. a) Voltage input and b) displacement output time histories.

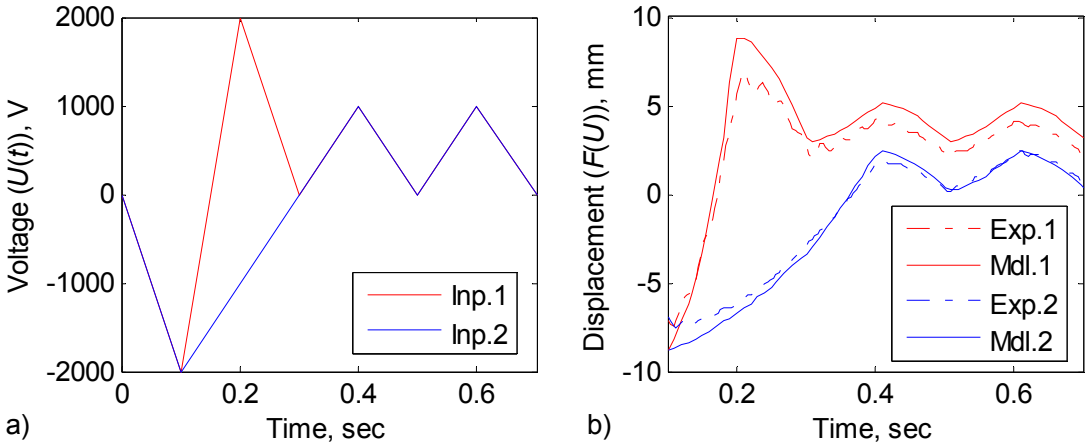

Figure G.44: Congruency evaluation of the thick airfoil sample A1 in 3-to-1 configuration at 5 Hz. a) Voltage input and b) displacement output time histories.

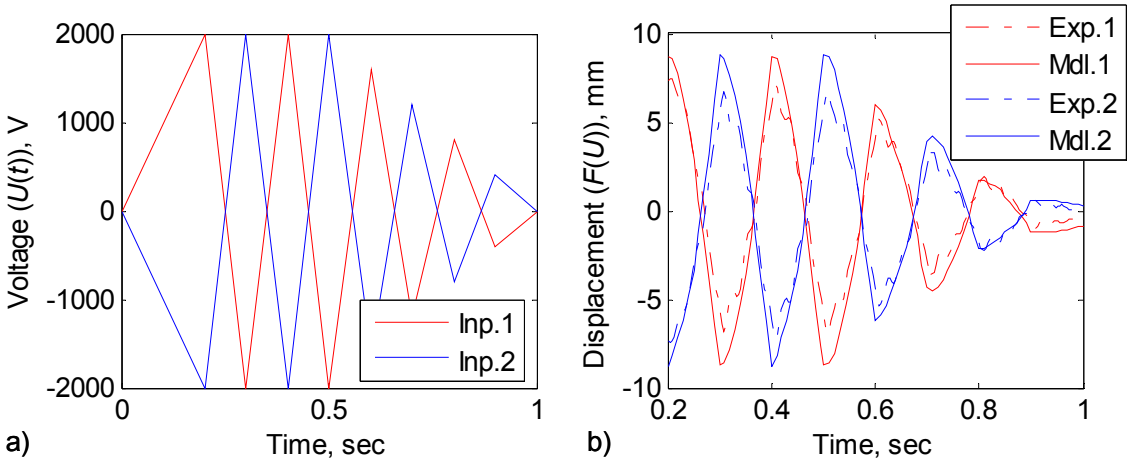

Figure G.45: Decaying triangle input signal response of airfoil sample A1 in 3-to-1 configuration at 5 Hz. a) Voltage input and b) displacement output time histories.

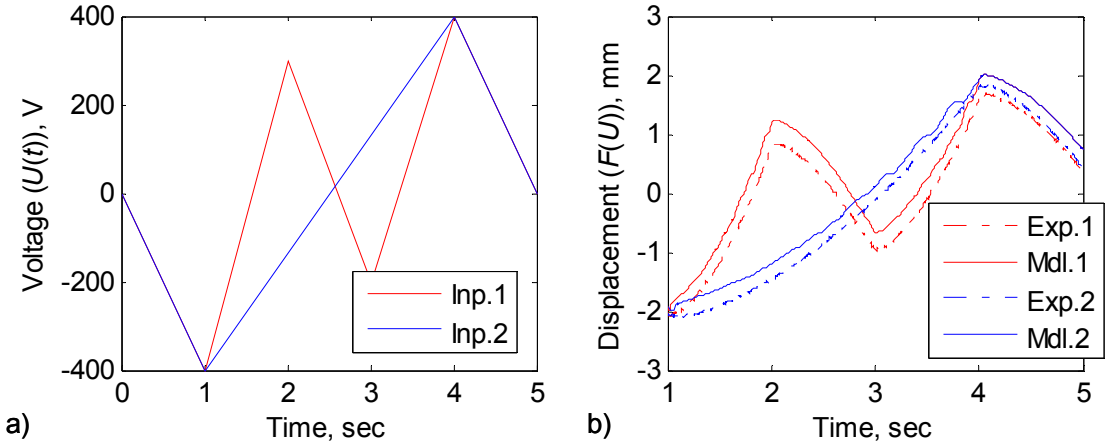

Figure G.46: Wiping-out evaluation of the thick airfoil sample A1 in 1-to-1 configuration at 0.5 Hz. a) Voltage input and b) displacement output time histories.

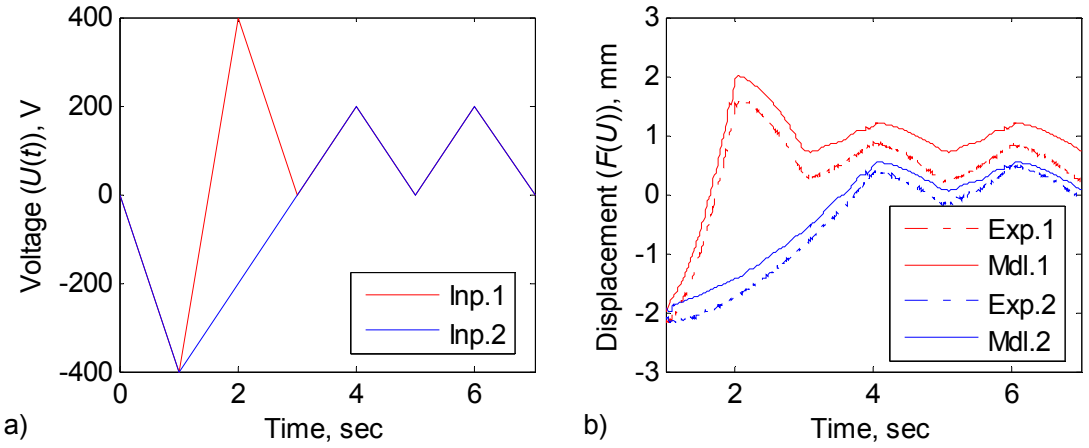

Figure G.47: Congruency evaluation of the thick airfoil sample A1 in 1-to-1 configuration at 0.5 Hz. a) Voltage input and b) displacement output time histories.

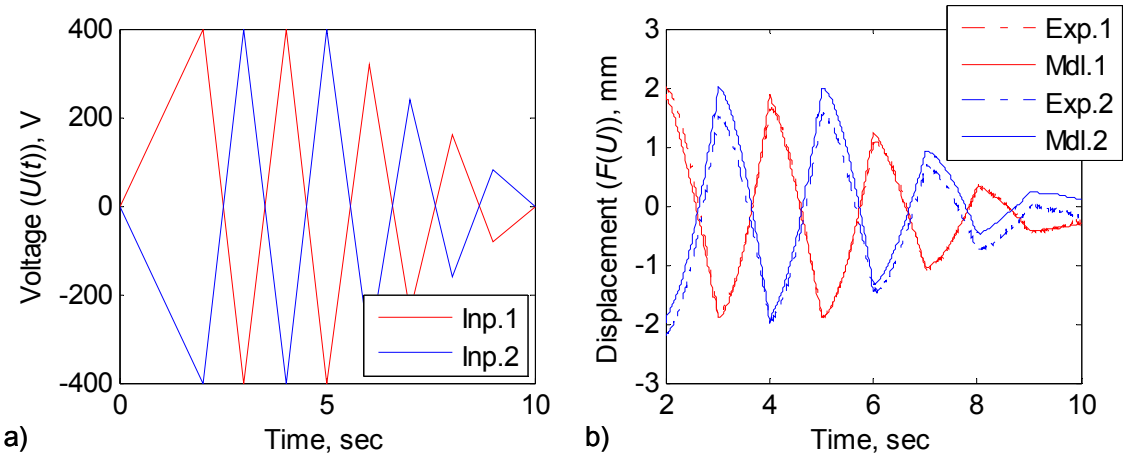

Figure G.48: Decaying triangle input signal response of airfoil sample A1 in 1-to-1 configuration at 0.5 Hz. a) Voltage input and b) displacement output time histories.

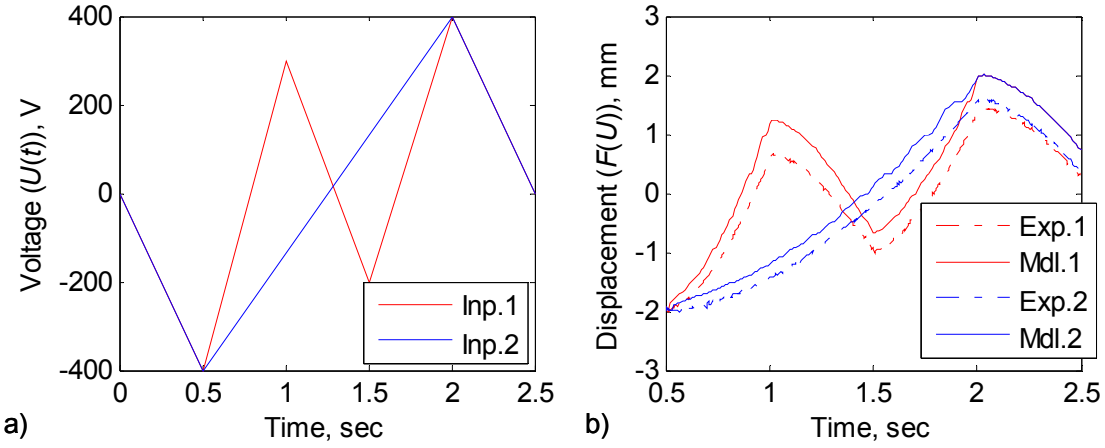

Figure G.49: Wiping-out evaluation of the thick airfoil sample A1 in 1-to-1 configuration at 1 Hz. a) Voltage input and b) displacement output time histories.

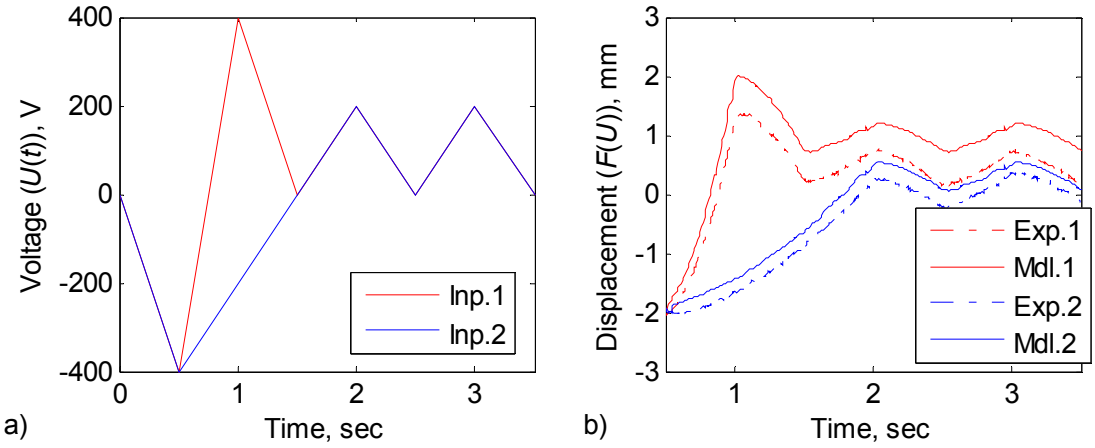

Figure G.50: Congruency evaluation of the thick airfoil sample A1 in 1-to-1 configuration at 1 Hz. a) Voltage input and b) displacement output time histories.

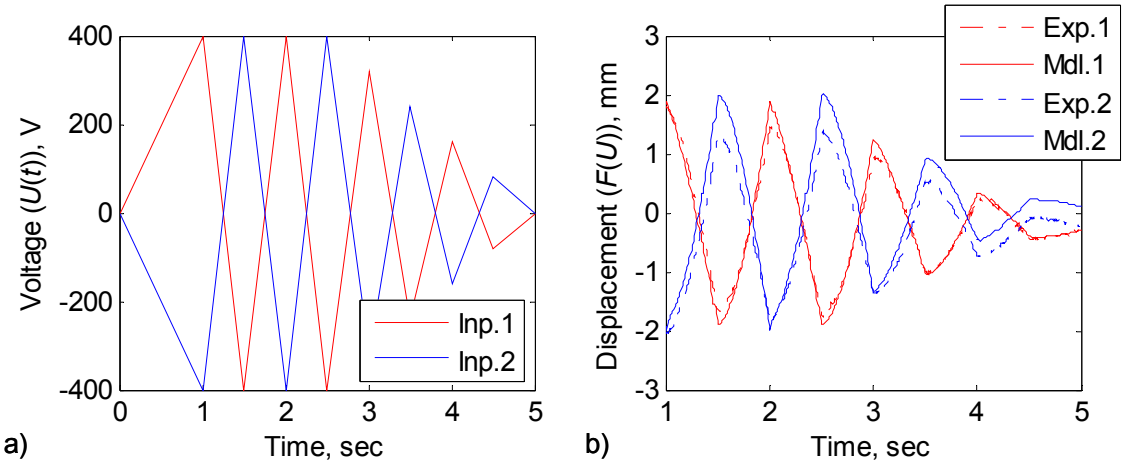

Figure G.51: Decaying triangle input signal response of airfoil sample A1 in 1-to-1 configuration at 1 Hz. a) Voltage input and b) displacement output time histories.

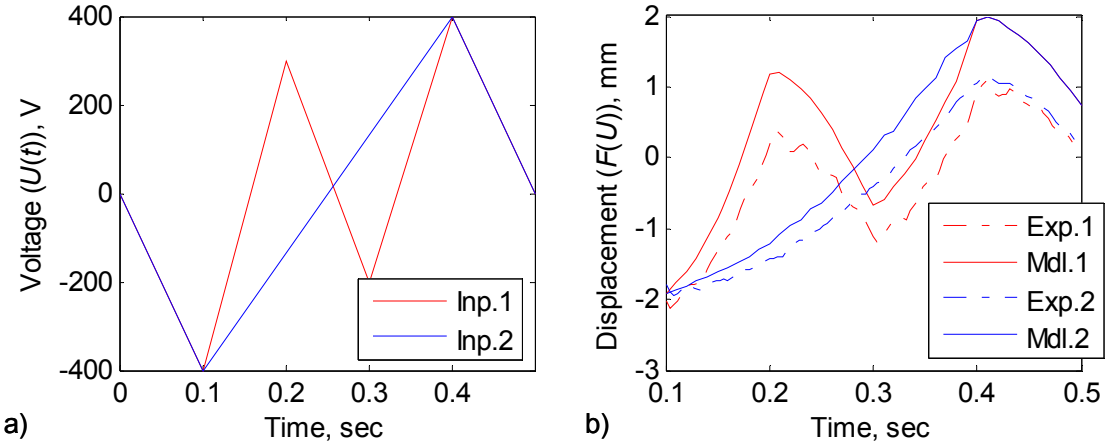

Figure G.52: Wiping-out evaluation of the thick airfoil sample A1 in 1-to-1 configuration at 5 Hz. a) Voltage input and b) displacement output time histories.

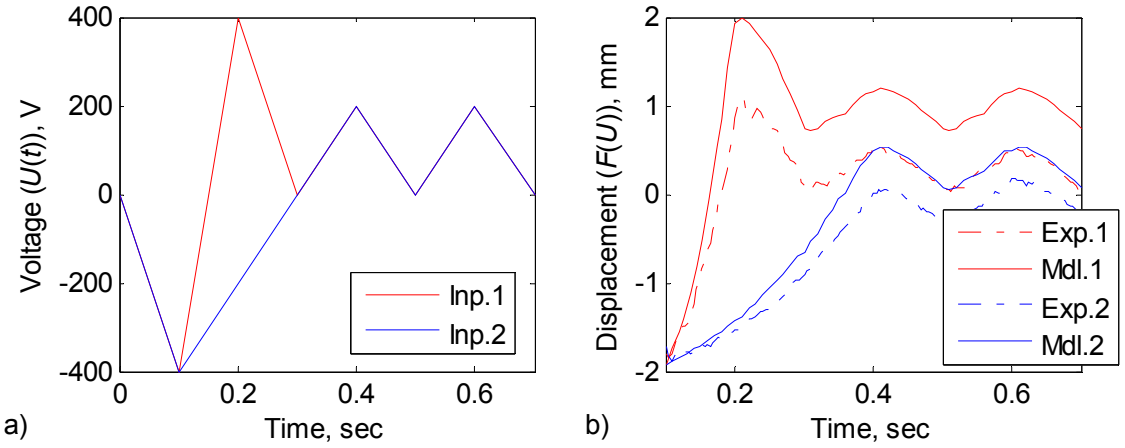

Figure G.53: Congruency evaluation of the thick airfoil sample A1 in 1-to-1 configuration at 5 Hz. a) Voltage input and b) displacement output time histories.

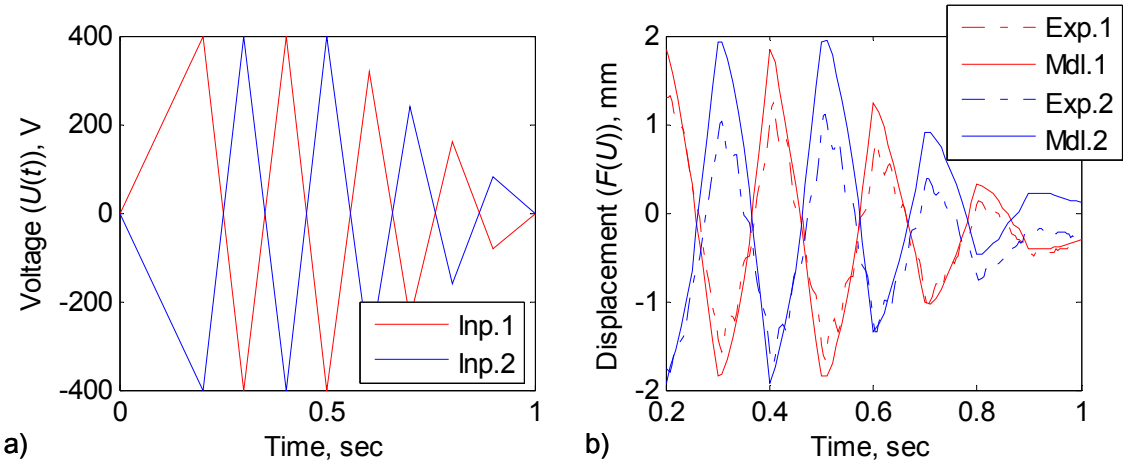

Figure G.54: Decaying triangle input signal response of airfoil sample A1 in 1-to-1 configuration at 5 Hz. a) Voltage input and b) displacement output time histories.